NGGM/MAGIC – Science Support Study During Phase A – CCN1

“MAGIC”

ESA Contract No. 4000134613/21/NL/FF/ab

Final Report

Issue 1.0

30/10/2023

Max-Planck-Institut für Gravitationsphysik
Albert-Einstein-Institut

ESA STUDY CONTRACT REPORT		
ESA Contract No: 4000134613/21/NL/FF/ab Contract Chance Notice 1 (CCN1)	Subject: Final Report NGGM/MAGIC – Science Support Study During Phase A – CCN1	Contractor: Technische Universität München
*ESA CR( ) No. ESA CR. No. 1 issue 1.0	No. of Volumes: 1 This is Volume No.: 1	Contractors Reference: Roland Pail
Abstract: Final Report of ESA study *NGGM/MAGIC – Science Support Study During Phase A – CCN1*		
The work described in this report was done under ESA Contract. Responsibility for the contents resides in the author or organisation that prepared it.		
Names of Authors: Roland Pail, Thomas Gruber, Petro Abrykosov, Philipp Zingerle, Pieter Visser, João Teixeira da Encarnação, Christian Siemes, Frank Flechtner, Christoph Dahle, Markus Hauk, Josefine Wilms, Sean Bruinsma, Jean-Charles Marty, Vitali Müller, Laura Müller		
** NAME OF ESA STUDY MANAGER: Ilias Daras DIV: Mission Science Division DIRECTORATE: Earth Observation Programmes	** ESA BUDGET HEADING	

Authors

Roland Pail (editor)
Thomas Gruber, Petro Abrykosov, Philipp Zingerle TUM
Pieter Visser, João Teixeira da Encarnação, Christian Siemes TUD
Frank Flechtner, Christoph Dahle, Markus Hauk, Josefine Wilms GFZ
Sean Bruinsma, Jean-Charles Marty CNES
Vitali Müller, Laura Müller AEI

Document Change Record

ISSUE /REV.	DATE	REASON FOR CHANGE	CHANGED PAGES / PARAGRAPHS
1.0	30 Oct 2023	Initial Issue	

Table of Contents

PREFACE

This Final Report reports on the results of the extended phase (Contract Change Notice 1) of the project "NGGM/MAGIC – Science Support Study During Phase A – CCN1". It addresses all tasks defined in the SoW and the corresponding work packages defined in the WBS, and is a compilation of the document deliverables (Technical Notes) D1-CCN1 to D7-CCN1 plus a TN resulting from an Ad-hoc question by ESA. The following Table summarizes the conents of this Final Report.

Part no.	Title	TN	version
1	ATBD of NGGM/MAGIC L2 and L3 products	D1-CCN1	2.0
2	Science Readiness Assessment (SRA) report	D2-CCN1	2.1
3	MRTD critical assessment and compliance report	D3-CCN1	2.0
4	E2E simulations: Description, results and analysis	D4-CCN1	3.1
5	NGGM/MAGIC science impact analysis	D5-CCN1	2.0
6	NRT concept: Description, results, analysis and applications	D6-CCN1	1.0
7	In-flight calibration of accelerometers	D7-CCN1	2.0
8	Ad-hoc: Impact of frozen vs. circular orbit for P2	AH1-CCN1	1.0

In addition, a summary of the main findings of this CCN1 project phase and the main conclusions are given in the Executive Summary.

EXECUTIVE SUMMARY

In November 2020 it was decided at ESA's Ministerial Conference to investigate a European next-generation gravity mission (NGGM) in Phase A as first Mission of Opportunity in the FutureEO Programme. The Mass-change And Geoscience International Constellation (acronym: MAGIC) is a joint investigation with NASA's MCDO study resulting in a jointly accorded Mission Requirements Document (MRD 2020) responding to global user community needs. The MAGIC mission will be composed of two pairs flying in different orbit planes. As baseline assumptions at the current stage of NGGM Phase A, the NASA/DLR–developed first pair (P1) of MAGIC will be in a near-polar orbit at altitude around 500 km, while the ESA–developed second pair (P2) NGGM will be in an inclined controlled orbit of 65–70 deg at approximately 400 km altitude.

According to the NGGM Mission Requirement Document (NGGM MRD 2023), NGGM has the aim to "extend and improve time series of satellite gravity missions by providing enhanced spatial and temporal resolution time-varying gravity field measurements with reduced uncertainty and latency to address the international user needs as expressed by IUGG and GCOS and demonstrate operational capabilities relevant for Copernicus."

On ESA side, the NGGM/MAGIC concept was investigated in two parallel industry Phase A studies, and was complemented by this "NGGM/MAGIC – Science Support Study during Phase A". The main results of the first phase of the Science Support Study were already reported, see: https://www.asg.ed.tum.de/iapg/magic/documents/. Additional invesitgations were performed in a Phase A extension of 8 months. The main results and conclusions of this extension phase are summarized in this document.

The majority of the numerical simulations and impact studies were based on the baseline constellation 5d_397_70, which has the following key parameters:

Satellite	Semi-major axis [m]	Eccentr.	Incl. [°]	Asc. node [°]	Arg.of perigee [°]	Mean anomaly [°]
P1-A	6871210.979	0.0016	89	359.98	27.78	331.51
P1-B	6871208.124	0.0016	89	359.98	29.17	331.95
P2-A	6780418.955	0.0008	70	2.34	5.46	353.82
P2-B	6780416.219	0.0008	70	2.34	8.46	352.68

Generally, two noise scenarios have been investigated in either scenario – product-noise-only (PO) and full-noise (FN). In case of PO, all time-variable gravity signal components are disregarded, and only the LOS-projected noise of individual instruments is considered as an error contributor to the low-low observations. Here, we consider only the two most dominant instruments – the ACC (SuperSTAR-type for P1, MicroSTAR-type for P2) and the LRI (for P1), or LTI (for P2), respectively (see **Figure E-1**). Further, tone errors, i.e. sinusoidal errors occurring at multiples of the orbital frequency, are considered. In case of FN, also the temporal variations of the gravity field in the form non-tidal atmosphere/ocean (AO) background model errors and ocean tide (OT) model errors are considered in addition.

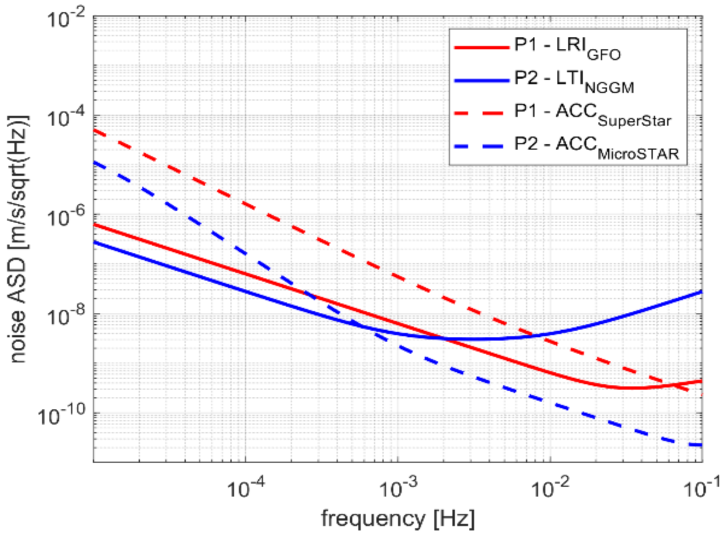

Figure E-1: Product noise specification (in terms of LOS projection) for 5d_397_70.

1) L2 algorithmic development

In the frame of this project, improved processing strategies for the optimum exploitation of NGGM/MAGIC data have been developed, implemented, numerically analyzed and compared to the performance of the baseline strategy.

a) Stochastic modelling of background model errors

After a successful study on the inclusion of stochastic models of ocean tide (OT) background model errors in the first phase (Abrykosov 2022b), in the extended phase we concentrated on the stochastic modelling of non-tidal atmosphere and ocean (AO) background models. It could be demonstrated that already a static error variance-covariance matrices (VCM) is beneficial for the reduction of aliasing stemming from AO errors, see **Figure E-2** (left), where different variants have been investigated. The investigation of time-variable VCMs was started, but is not yet successful (**Figure E-2**, right) and is still work in progress.

a) b)

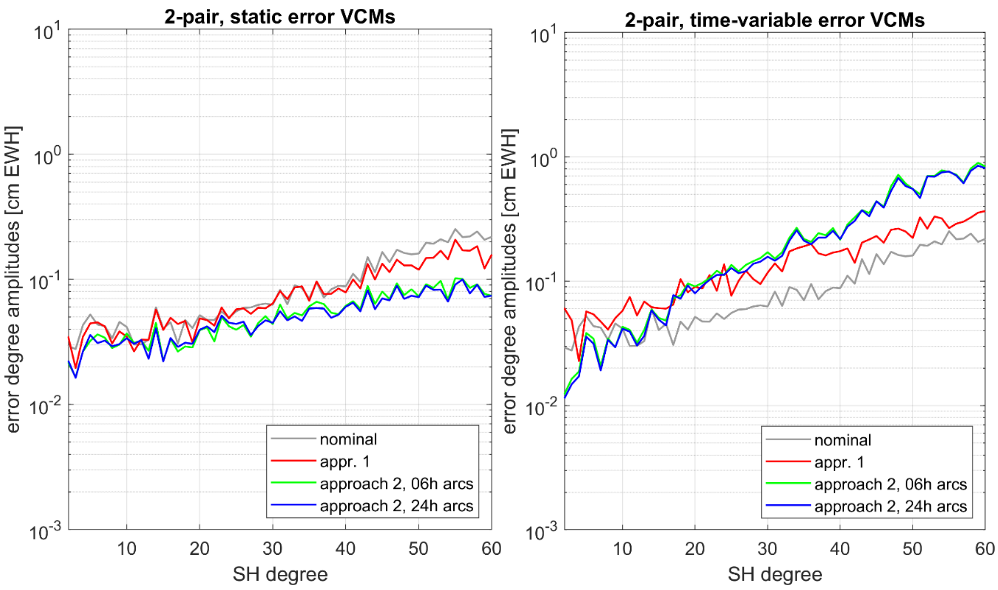

Figure E-2 Retrieval errors when using a) static AO error VCM, and b) time-variable error VCMs for different approaches.

b) Extended parameterization schemes

The performance of the DMD approach (Abrykosov et al. 2022a) in the frame of a double-pair-based gravity retrieval, was carried out on the basis of observation geometry of the baseline scenario 5d_397_70. It could be shown that the DMD approach has some advantages over the alternative "Wiese approach (Wiese et al. 2011).

a) b)

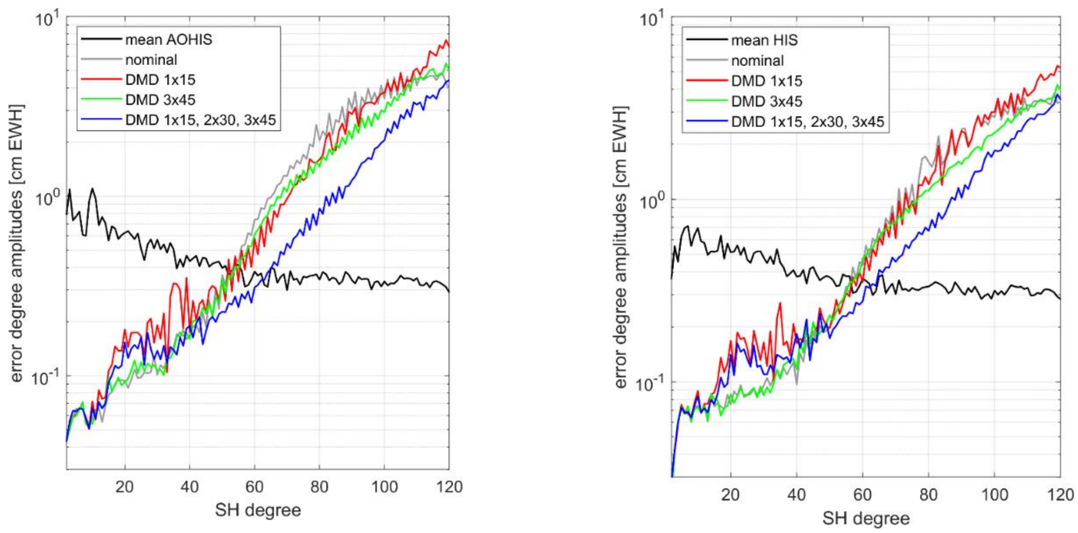

Figure E-3: Retrieval errors of the 30-day estimate obtained with various DMD parametrization schemes. a) Retrieval of the full AOHIS; b) retrieval of HIS (i.e. a priori BM-based AO de-aliasing is applied).

Especially in the case of very different relative weights of P1 and P2 due to the altitude difference and different instrumentation, the underlying normal equation system of the DMD is more stable. The DMD was also investigated for its potential to apply multiple sequential short-term estimates before solving for final, e.g. monthly, gravity products, and showed very promising results (Figure E-3).

The approach has to be seen in context with stochastic modelling of OT BM errors described in a). It indeed offers an added value, as it allows to utilize the benefit of both methodologies, but several effects still have to be studied in further detail.

c) Treatment of P1 – P2 transition zone artefacts

This WP was triggered by an open issue of the first phase: It was identified that in the double-pair solutions (based on a different scenario 3d_H), the polar regions which are only covered by the polar pair (P1) are sometimes degraded compared to the polar single-pair solutions. The tailored spherical cap regularization strategy (Metzler and Pail 2005), which constrains the double-pair solutions towards to P1-solution in the polar cap areas, without changing the solution in the regions covered by both pairs (|φ| < 70°) significantly, was modified and adapted to the current baseline scenario 5d_397_70, and a second comparable approach in space domain was implemented. Both approaches succeed to constrain the double-pair solution towards the polar pair in the polar areas (**Figure E-4**). However, the single-pair solution is not always superior to double-pair in polar cap areas, so that it is difficult to define a generalized strategy. It is recommended to apply a weak regularization towards polar-pair solution.

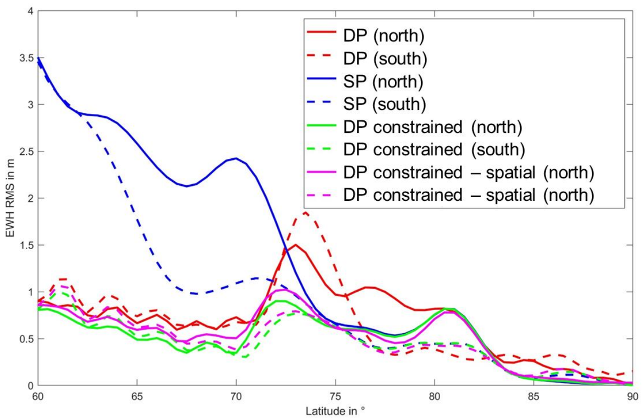

Figure E-4: EWH RMS per latitude for baseline scenario 5d_397_70: constraints toward single-pair solution applied in spectral and spatial domain.

d) HIS vs. AOHIS estimation

The nominal and the DMD method were applied to the 5d_397_70 scenario either with on-the-fly AOD1B de-aliasing, or without de-aliasing, followed by a posteriori subtraction of AO+AOerr. They show very similar results (**Figure E-5**). It is recommended to provide users with both a HIS and an AOHIS product. The nominal method will deliver the HIS signal, while the DMD method will result in the full AOHIS signal.

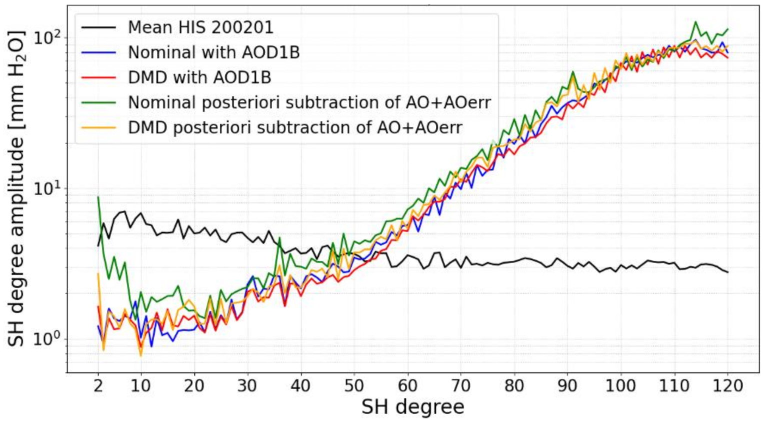

Figure E-5: Degree (error) amplitudes of various scenarios to evaluate HIS vs. AOHIS estimation.

e) Bump at around degree 80 in TUM full-noise 31-day solution

The monthly P1+P2 and P2-only 5d_397_70-based full-noise solutions of TUM have been shown to feature a “bump” in the spectral range between d/o ca. 75 and 90 (c.f. **Figure E-6**). Upon further investigation, it was also determined that the “bump” occurs in the same manner regardless of the chosen resolution of the estimated field as well as regardless of the underlying time interval over which the field is estimated (provided the respective solution’s intrinsic noise level is sufficiently low). It could ultimately be shown that the bump originates from the observation geometry coupled with the sampled time-variable signal, and can to a large extent be regulated by means of the applied co-variance matrix of observation errors. The stochastic modelling is very likely also the reason why the GFZ solutions do not feature a similar bump, as it is applied differently at TUM and GFZ.

The stochastic modelling in the nominal processing scheme was for now based exclusively on the specifications of the instrument noise. Due to the presence of time-variable gravity signal components in the observations, however, this method is, in a strict sense, flawed. Therefore, tweaking the observation VCM in a way that yields an optimal result cannot be regarded as incorrect either. However, an improved stochastic modelling is recommended for use in the future which takes into account the stochastics of all observation components. This concerns specifically the AOD and OTD background model errors in addition to the instrument noise as the most dominant error contributors. This “complete” stochastic modelling is expected to produce optimally tailored weighting to the respective set of observations, and to directly solve the issue of relative weighting between observations of different satellite pairs.

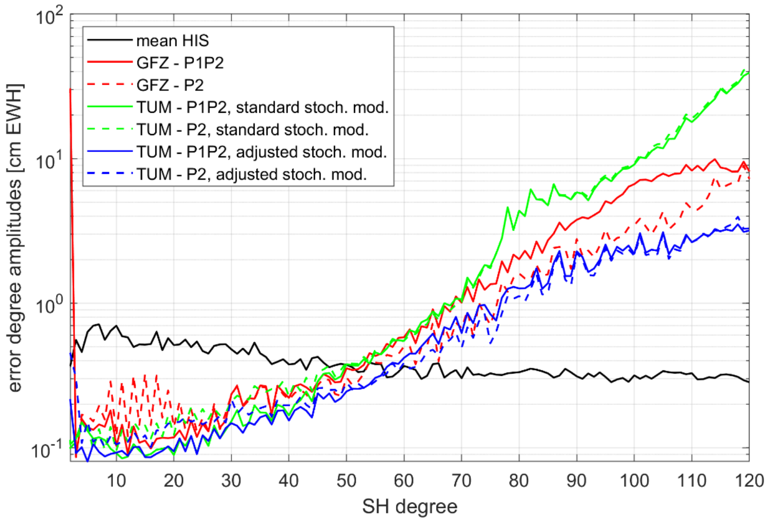

Figure E-6: Comparison of monthly full-noise solutions produced by TUM and GFZ on the basis of the 5d_397_70 observation geometry.

f) Fast-track processing strategy

A functional fast-track (NRT) retrieval scheme on the basis of a sliding window approach was already developed by Purkhauser and Pail (2019). This method was adapted by applying the DMD parametrization scheme instead of the Wiese approach, which facilitates the retrieval of gravity products over shorter time scales. In turn, this allows for a reduction of the latency time at which variations in temporal gravity can be computed, as comparisons can already be carried out on the basis of interval (de-aliasing) products. Evidently, the clear drawback is that a shorter latency also results in a reduced spatial resolution. However, there is freedom to compute interval fields over – in principle – arbitrary time intervals, which allows a better tailoring of the retrieval scheme to the user groups' requirements regarding latency times.

2) P2-only solutions

The performance of solutions which are only based on the inclined pair (P2) of the baseline scenario 5d_397_70 was evaluated. In order to account for the lack of observations in the polar regions, a spherical cap regularization (Metzler and Pail 2005) was applied for the regions $|\varphi|>70°$.

Due to the polar gaps, global metrics like degree error amplitudes do not work anymore, at least not without modifications. Therefore, it is recommended to assess the performance in the spatial domain, e.g. in terms of grids of equivalent water height difference, limited to the regions that are covered by the inclined pair.

Figure E-7 shows a comparison of the performance of the P2-only and the P1+P2 solution. It clearly demonstrates that the performance in those areas covered by P2 is dominated by P2. The relative contribution of P2 to the total P1+P2 solution is about 97%.

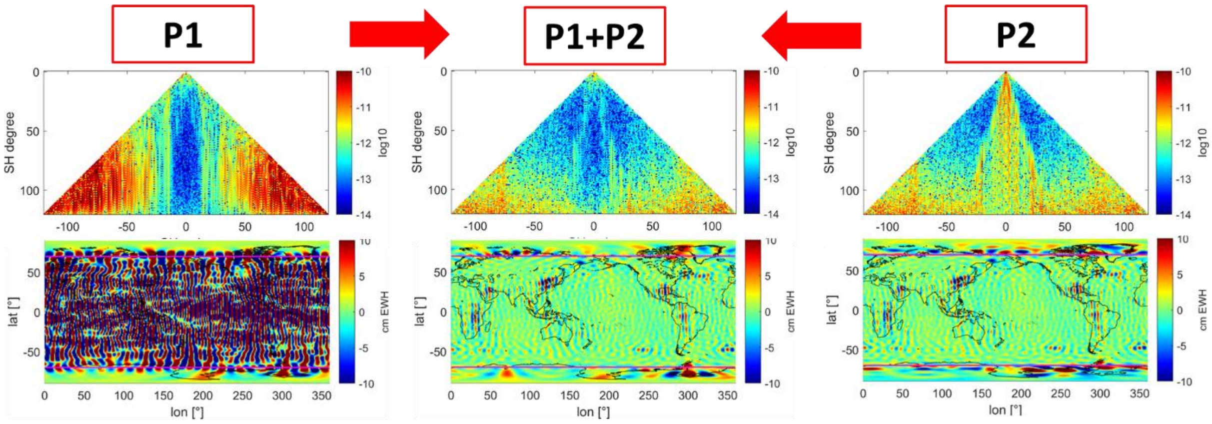

RMS [EWH] for $|\varphi| < 70°$

cm [EWH]	P1	P1+P2	P2
d/o 60	18.47	1.79	1.83
d/o 90	389.68	19.74	20.15

Figure E-7: Coefficients (top row), EHW differences up to SH degree 60 (middle row) and key statistics of P1, P2 and P1-P2 constellations based on baseline scenario 5d_397_70.

Regarding co-estimation of daily parameters applying the Wiese approach, the reduced spatial resolution of a single-pair P2 solution does not allow for similar retrieval quality as in P1+P2 scenario when evaluated to a max. spherical harmonic (SH) degree of 15, but still the P2-only solution performs much better than the polar pair P1-only solution. However, when reducing the max. SH degree to 10, the P2-only solution is competitive with the double-pair P1+P2 solution (**Figure E-8**).

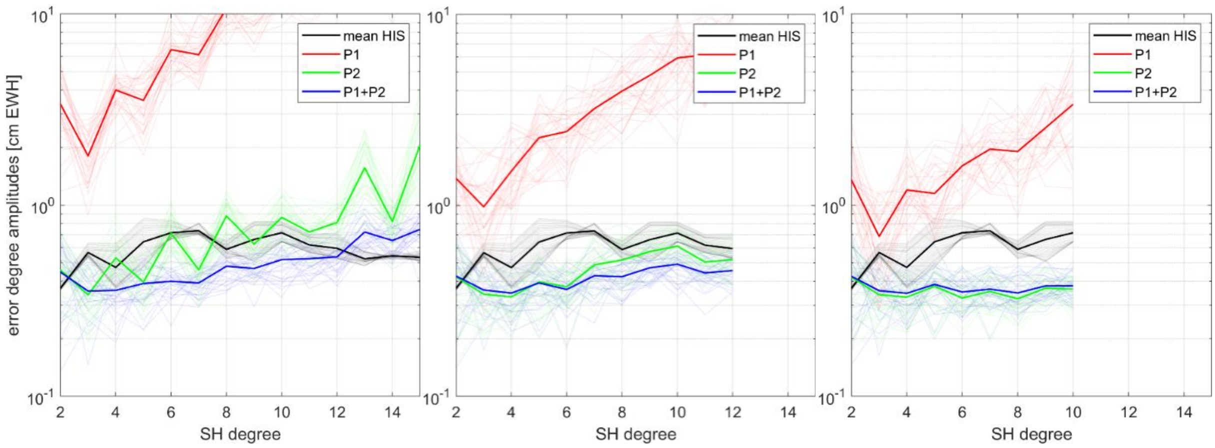

Figure E-8: Daily “Wiese” co-estimates with maximum SH degree a) 15, b) 12 and c) 10, for P1-only, P2-only and P1+P2 constellations.

3) Match against NGGM MRD requirements

All simulation scenarios performed in this study were evaluated in terms of cumulative EHW errors, and the results were compared against the NGGM MRD requirements (NGGM MRD 2023). The results are depicted in **Figure E-9** for P2 and in **Figure E-10** for P1+P2, respectively. Note that these were obtained with the optimal stochastic modelling (c.f. section 1.e).

In case of P2, all threshold requirements can be met fully for the 31-day retrieval. In case of the 5-day retrieval, only the threshold requirement for d/o 2 is missed.

In case of P1+P2, the threshold requirement for d/o 10 is just barely missed for the 31-day retrieval, while all others are met. For the 5-day retrieval, just like in case of P2-only, the threshold requirement at d/o 2 is not met. Additionally, the requirement at d/o 10 is just barely missed.

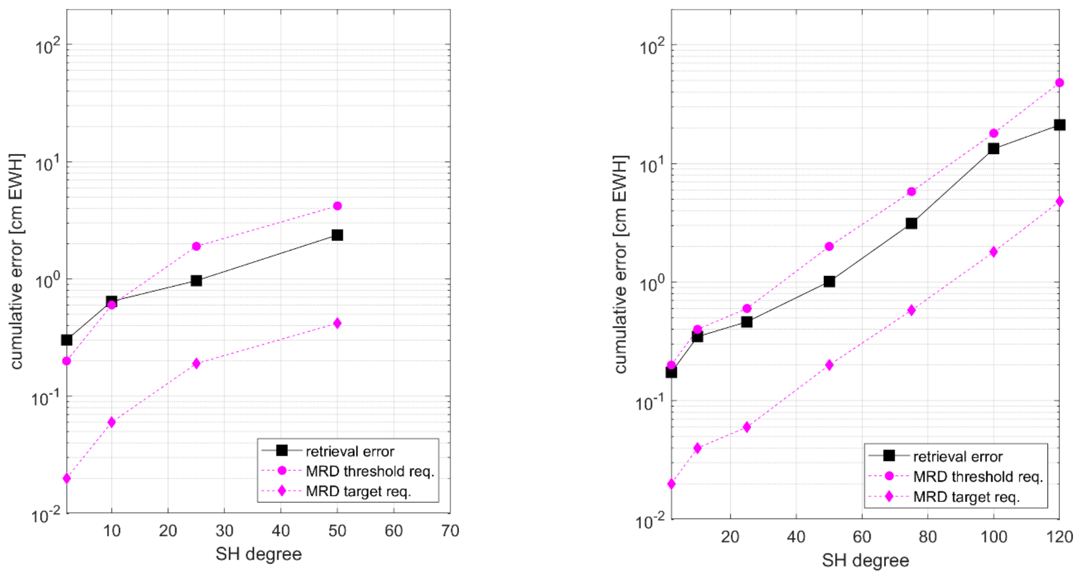

Figure E-9: Mean cumulative spatial error of 5-day (left) and 31-day (right) P2-based solutions evaluated in the latitude range [-70°,70°] and compared against the NGGM Level-2a requirements.

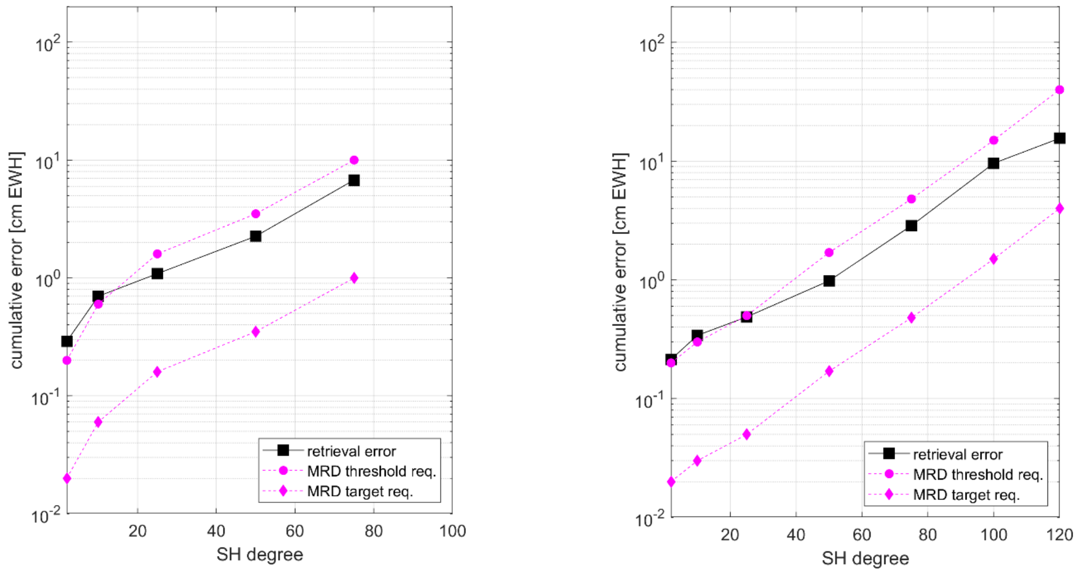

Figure E-10: Mean cumulative spatial error of 5-day (left) and 31-day (right) P1+P2-based solutions evaluated in the latitude range [-90°,90°] and compared against the MAGIC Level-2a requirements.

4) 3rd numerical simulator implementation at CNES

A third numerical simulator based on the GINS software was implemented at CNES. Closed-loop simulation results based on the baseline scenario 5d_397_i70 were compared against GFZ solutions and show similar results. Numerical problem with the stochastic modelling of product errors were solved toward the very end of the project. In summary, the development CNES simulator has made very good progress during this extended project phase, but it has not yet reached the same degree of maturity as the GFZ and TUM simulators.

5) Scientific impact analysis

The science impact analysis carried out in CCN1 in different fields of Earth Sciences revealed a strong benefit of the NGGM and MAGIC constellations over a polar-pair only GRACE-like mission. NGGM and MAGIC perform similarly well in most evaluation cases. This is shown exemplarily in terms of the root-mean-square difference (RMSD) for 405 river basins for a spatial resolution of 400 km in **Figure E-11**.

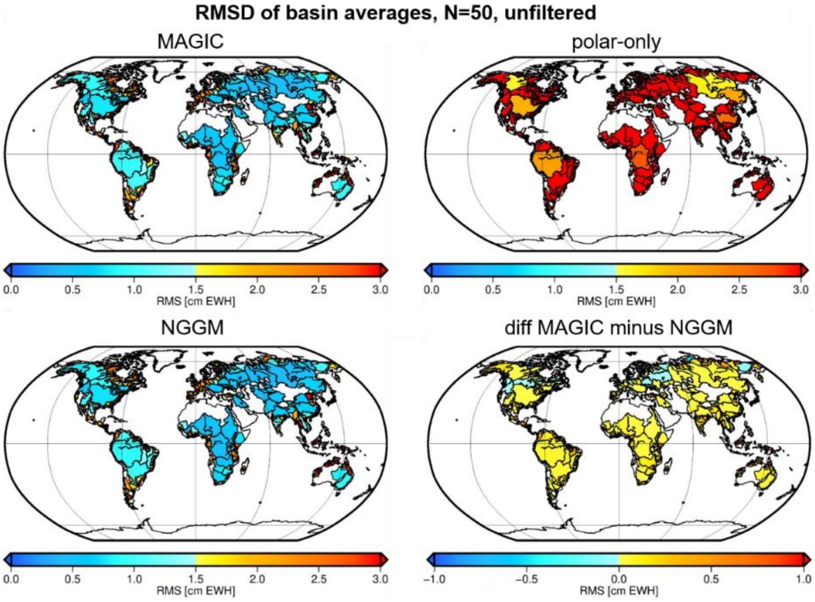

Figure E-11: Temporal RMSD of 5-days simulation output and reference solution truncated at N=50 for basin averaged time series of 405 river basins defined by the Global Runoff Data Center (GRDC): double-pair MAGIC mission (top left), polar-pair-only (top right) and NGGM (bottom left). The figure on the bottom right shows the difference between the MAGIC and the NGGM result.

For water storage variations in river basins, the scenarios with 5-day resolution largely fulfil the envisaged mission performance for short-term mass variations in hydrology. This similarly applies to the detection of wet and dry extremes of water storage anomalies at the level of individual 5-day intervals. While a polar-pair scenario is dominated by false positive alerts for extreme events, i.e., the exceedance of wet or dry thresholds while there is no such event, the lower noise of NGGM and MAGIC largely improves the ratio of correctly versus incorrectly detected hydrological extremes.

The accuracy of glacier mass change observations increases by orders of magnitude at mid latitudes, both a short and long time scales. As an example, **Figure E-12** shows a performance evaluation for a 12-year simulation. The noise level at the mid-latitude regions (Arctic Canada South, Iceland, and Southern Andes) is reduced by one order of magnitude when adding an inclined satellite pair. At higher latitudes, the double pair constellation still outperforms the single pair in all regions, although the noise reduction is less substantial. To which extent NGGM threshold or target requirements for can be met for these glacier mass change applications depends on the considered spatial resolution and on the region.

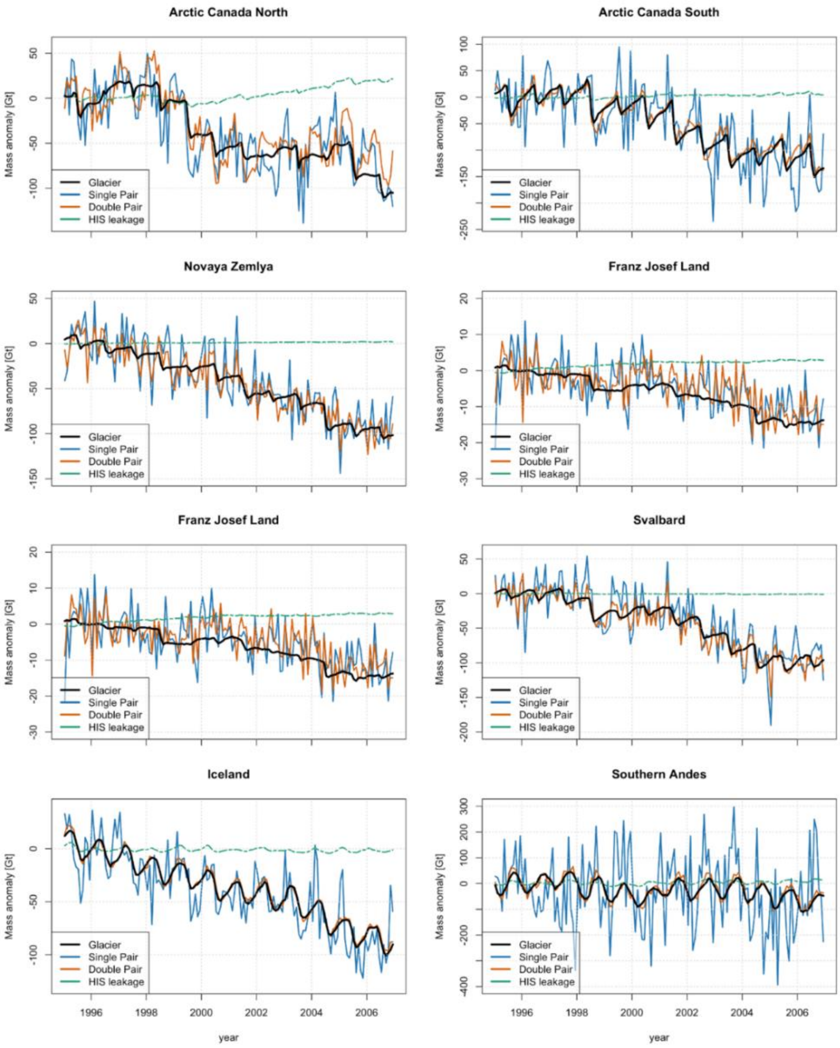

Figure E-12: Time series of mass variations in glacier regions retrieved from the 12-yr closed loop simulations for a single (blue) and dual (orange) pair mission concept. The green lines show the leakage signal from non-glacier components in the HIS model.

Furthermore, a dual-pair satellite configuration is shown to be able to detect 5-year running mean AMOC changes with an accuracy level that is comparable with (and independent of) the best in-situ measurements and thus is of great value for ocean climate monitoring. **Figure E-13** shows the actual model AMOC in the North Atlantic between 25°N and 45°N (black) and its reconstruction (blue) using the ideal simple weighting function. Very good agreement can be achieved for 5-year means or longer). Figure E-14 shows the related noise calculations, with the upper panels representing the actual time series of erroneous AMOC from fields truncated at degree 90, and the lower panels giving summary statistics for the same cases at different truncations. In panels a-e, black is for monthly values, blue for running annual mean, and pink for running 5-year mean. Thin lines (except the black lines in b) and c)) are single-pair noise, thick lines for double-pair noise, and dots for signal leakage. It is clear that the dual-pair noise is substantially below that for a single pair. The degree 90 truncation is the worst case for the single pair in this comparison, but comparing thick and thin lines with matching colours in

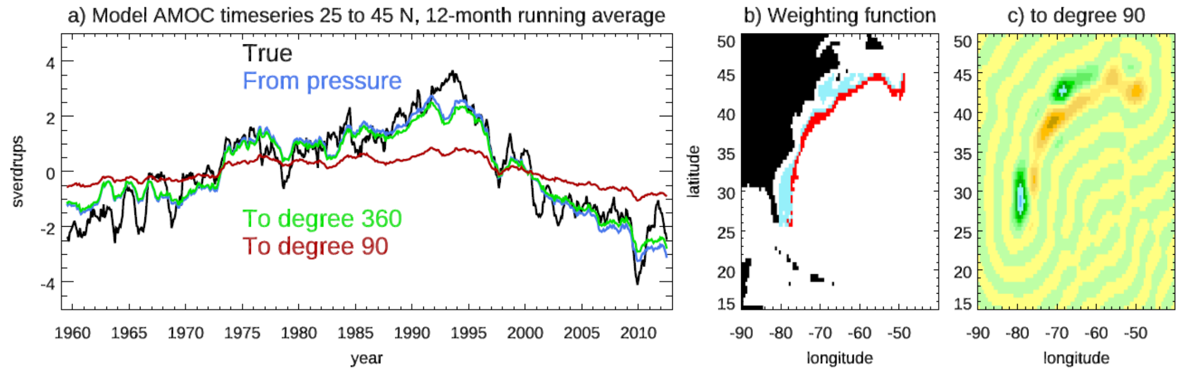

Figure E-13: AMOC and its reconstruction from boundary pressures in the 1/12 degree resolution NEMO ocean model: a) The true model AMOC (black), its reconstruction using pressures with the best, simple weighting function (blue), and when the pressure data are truncated at degree 360 (green) and 90 (red). b) simple weighting function used. c) simple weighting function truncated at degree 90.

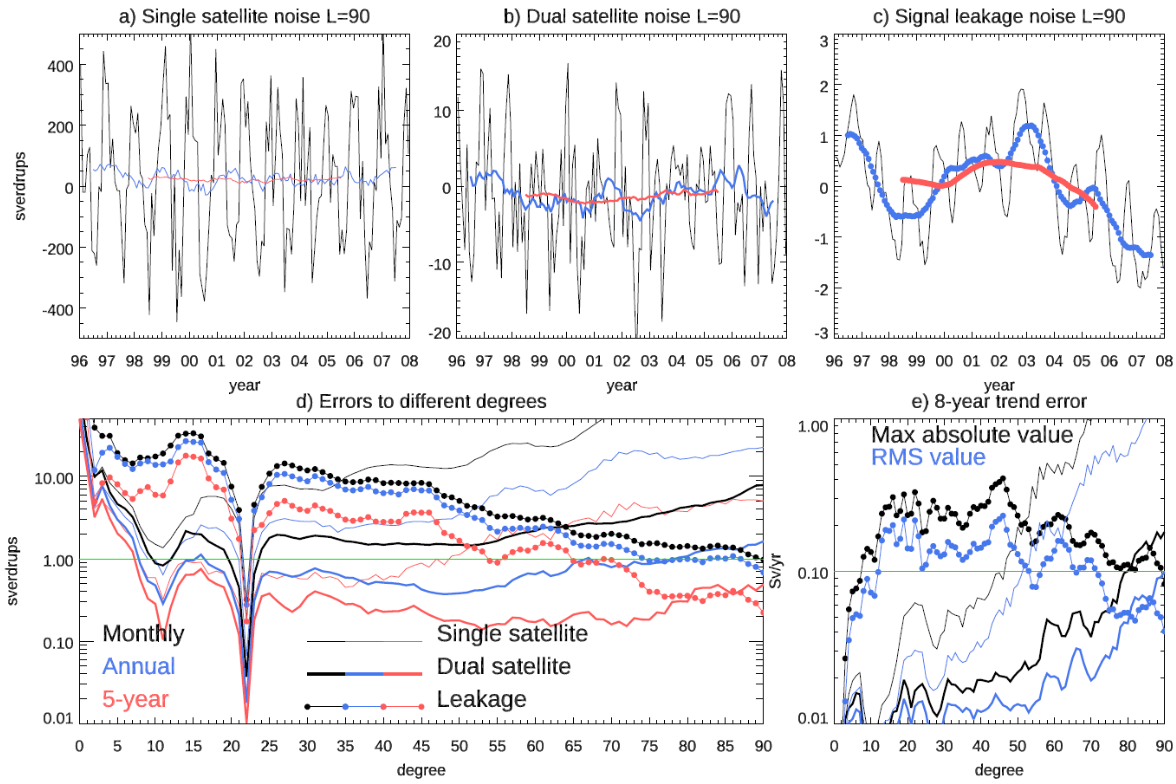

Figure E-14: Noise in the pressure-predicted AMOC retrieval under different observation scenarios. a) measurement noise in a single pair scenario, showing monthly values, running annual means, and running 5-year means for a retrieval truncated at degree 90. b) as for a), but using a two-pair scenario. c) leakage effects due to truncation for the "truth" model. d) Standard deviations of the above time series, but for different truncations. e) maximum absolute value and rms value of linear trends fitted to all 8-year subsets of the three noise time series, with no smoothing. Thin lines represent single-pair noise, thick lines for double-pair, and dots for leakage.

Figure E-14d shows that this is the case at all truncations (note the logarithmic scale). Although the double-pair configuration produces noise below 1 Sv for a wide variety of truncations, for annual and 5-year mean time series, this is somewhat academic as the leakage signal is much higher over most of this range. While the measurement noise increases towards degree 90, the leakage noise decreases, and the optimal retrievals occur where the best compromise is found. For 5-year means, this is at about degrees 75-90, and gives RMS errors of about 0.4 Sv from each source (0.6 Sv total if added in quadrature).

For detecting earthquake signals, NGGM and MAGIC perform greatly better than the polar only pair, with added value in observing the co-seismic and the post seismic signal. Figure E-15 shows the sensitivity of single- and double-pair missions regarding the detectability of the co-seismic gravity signal of selected big earthquakes.

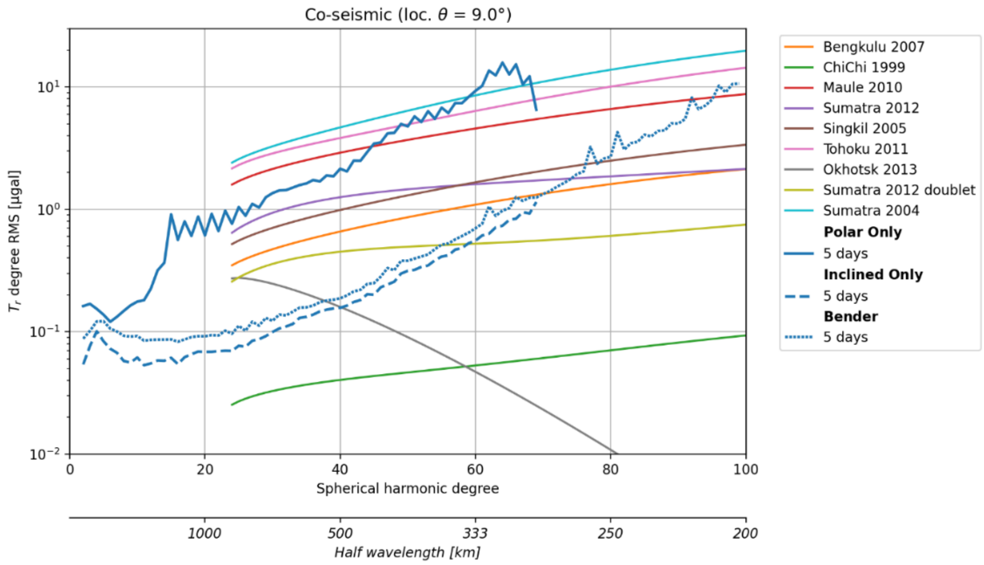

Figure E-15: Error degree amplitudes of the MAGIC mission scenarios: polar only, inclined only and Bender double-couple and the signal degree amplitudes (localized) of the coseismic signal for selected earthquakes. 5-day time integration for the gravity acquisition at the satellite.

The value of an AOHIS product that is directly estimated from the gravity observations is considered to be low for atmospheric mass estimates over the continents, whereas it is deemed potentially useful for several oceanographic analyses. For long time scales (longer than about 1-month period), the comparison of AOHIS and HIS products will enable the quantification of the dealiasing error using external dealiasing models at these long timescales. For shorter timescales, current methods use a remove-restore technique based on ocean models, with GRACE providing additional information via filters/regularizations worked out in a number of different ways by different groups. When comparing with observations, this makes it very difficult to assess how much explained variability is due to GRACE and how much due to the prior models. An independent AOHIS product is very valuable for testing and developing models of global-scale processes on such time scales, particularly around 5-day period, which, although small in amplitude (typically a few cm at most), have the potential to play an important role in storm surge predictions for flooding, and in determining the ocean's contribution to earth rotation.

Specifications of an NRT/fast-track mass change product that can satisfy a large part of related applications and services are summarized from user surveys and literature to be of 5-day temporal resolution with daily updates and a maximum latency of 2 days.

The processing of acceleration measurements to density and crosswind observations is well-established. Such observations constitute a valuable data set for use in thermospheric density and wind modeling and related applications. A roadmap has been formulated for establishing this processing and usage. This includes the generation of density and crosswind data products (Level 2). In a fast-track processing chain, where very short latencies of max. 12-14 hours are required for operational service applications. The Level 2 density data product generated with minimum latency can be assimilated into empirical and physics-driven thermosphere models (e.g., TIE-GCM; Level 3). More relaxed latency requirements apply for several scientific applications, such as the validation of thermosphere models or even the assimilation of density observations into these models, and studying dynamics during geomagnetic storms.

Based on these studies on various application fields, adaptations of the user requirements of the NGGM MRD were proposed.

6) L0-L1b inter-satellite distance algorithm development

A novel processing chain to simulate Level-0 LTI ranging data from orbit simulation inputs was implemented, and the underlying methodology was documented in detail (Figure E-16). The generated data is then further processed to Level-1a and Level-1b.

A first simple Level1a and 1b product was derived, which used a few simplifications and noise-free assumptions. Furthermore, this dataset was limited by a non-optimal interpolation method. In a more realistic dataset, the interpolation method was improved to obtain a lower noise for the orbit data and light travel times. Also different noise models, such as USO noise, POD noise and laser frequency noise, were included in the simulations.

For the next versions of the simulator, the missing parts from the flowchart will be implemented, namely:

- Light travel time calculation between TX and RX reference points
- TTL and ARC simulation (insert offset in reference points)
- consider remaining transponder laser phase noise (due to finite gain of the transponder lock)
- use attitude quaternions and corresponding orbits in inertial frame from the mission primes
- consider atmospheric and ionospheric effects in light travel time calculation
- consider a noise model for DWS closed loop
- consider noise for FSM readout when generating pointing angle products
- consider a phase readout noise (1µcycle/√Hz)

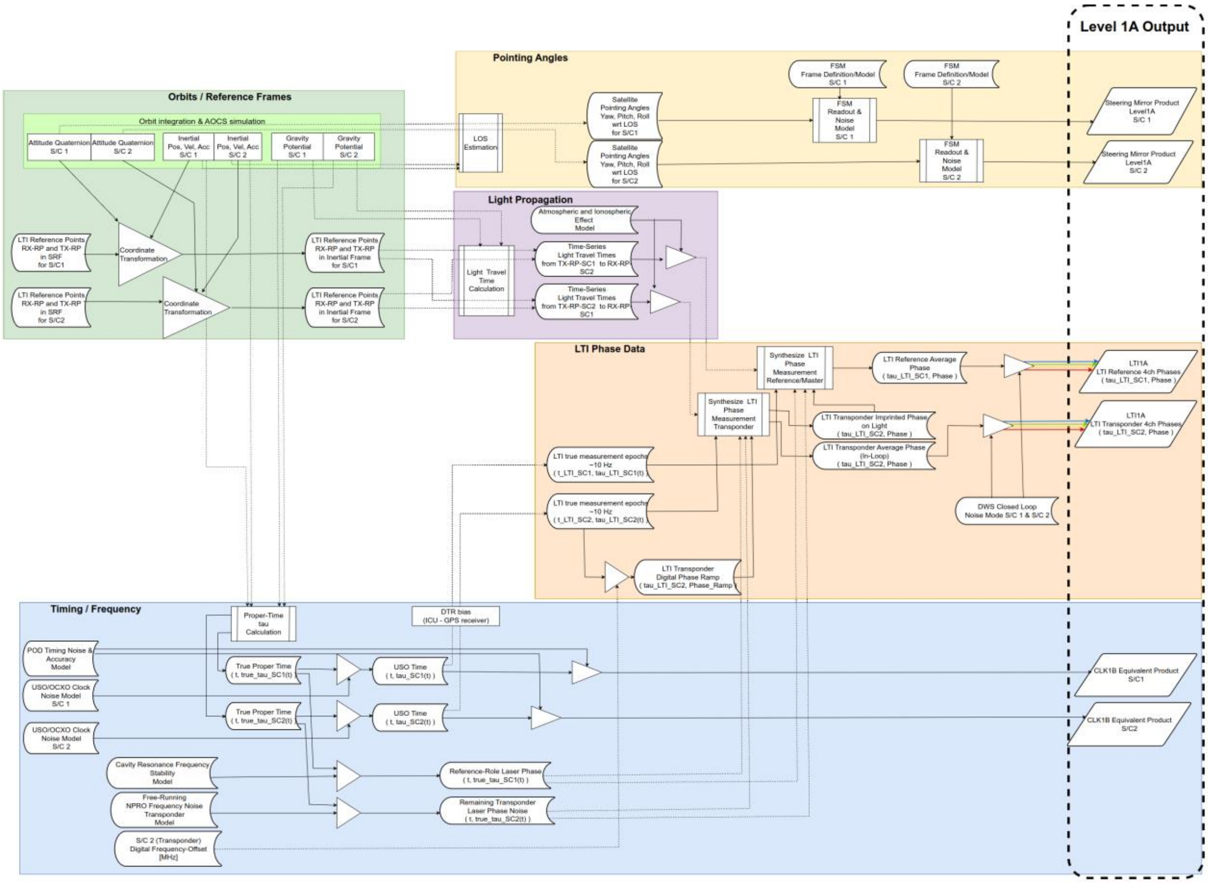

Figure E-16: Flowchart for the generation of realistic LTI Level-0/Level-1a data.

Though the simulator was intended primarily to derive LTI Level-1a data, it was already now in the early state extremely useful to better understand, validate and improve the Level-0 to Level-1b processing chain of LTI/LRI data, because this novel simulator uses a completely different approach and is not just reverting the processing steps of the existing Level-1a to Level-1b processing chain.

7) In-orbit accelerometer calibration

GNSS-based accelerometer calibration allows for a very precise determination of accelerometer biases for the X axis (predominantly the flight direction): precisions much better than 0.1 nm/s^2 are feasible when using the full error model. For the Y and Z axes (predominantly in the cross-track and height direction, respectively), these precisions are typically better than 1 and 4 nm/s^2, respectively. Of the error sources investigated, uncertainties in the tide model and uncertainties/omissions in the temporal gravity field model (e.g., errors in the de-aliasing models) are the dominant ones. The latter might be mitigated by co-estimating the gravity field.

The capability of GNSS-based accelerometer calibration for estimating accelerometer observations strongly depends on the magnitude of the (residual) non-gravitational accelerations. Four scenarios have been investigated based on the possible combinations of flying during solar minimum or maximum on the one hand and flying 1D or 3D drag free control (DFC). In case of 3D DFC, no reliable estimation of accelerometer scale factors is feasible. In case of 1D DFC, where the DFC is aligned with the X axis, only reliable scale factors for the Y and Z axes can be estimated with precisions ranging between about 0.001 and 0.18 nm/s^2 for the Y axis and 0.001 and 0.04 nm/s^2 for the Z axis. Better precisions are obtained for the solar maximum period, when the 1D DFC leaves bigger non-gravitational accelerations. During solar minimum, the uncertainty of the estimated scale factors is about 10 times worse than during solar maximum. Especially for the Y axis, the TASI simulations display a decreasing trend of the order of magnitude of the residual accelerations, leading to larger errors in the retrieved Y axis accelerometer scale factors.

Including the LRI observations in the POD-based accelerometer calibration, i.e., together with the GNSS-estimated orbit coordinates, might lead to a degraded estimation of accelerometer calibration parameters. Finding the optimal relative weight of the GNSS and LRI observations is not straightforward. Remaining gravity field modeling errors (as in, e.g., the de-aliasing products) have a relatively big impact on the LRI observations as compared to the GNSS observations. This is a contributing factor to less precise accelerometer calibration parameter estimates, despite the very high precision of the LRI observations themselves.

8) Documentation of ground processing algorithms and Science Readiness Assessment

The ground processing algorithms of the involved project partners TU Munich, GFZ and CNES were documented in an Algorithm Theoretical Basis Document (ATBD) for Level-1a to Level-3, and corresponding Science Readiness Levels (SRL) were assigned, following the criteria defined in the SRL Handbook. Since NGGM is at the end of Phase A extension, according to the SRL Handbook the SRL to be achieved is SRL-5, indicating a successful assessment of the Mission Performance with the Delta- Preliminary Requirements Review (D-PRR). SRL5 was assessed in the frame of a Science Readiness Assessment (SRA).

It could be demonstrated that the performance simulators at TUM and GFZ have reached a high degree of maturity and can provide robust and reliable results. This reliability is further strengthened by the fact that the two independent simulation environments can be used to validate each other. The involved algorithms applied for the baseline processing scheme have an SRL which is generally at least 5, but in many cases even higher than 5.

9) Evaluation of various drag-free scenarios in interaction with industry

Five product-noise scenarios representing various drag-compensation scenarios were simulated and provided by TASI. These scenarios differ by the amplitudes of assumed non-gravitational forces as well as their compensation – the ID components MIN and MAX denote the assumption of minimum or maximum level of expected drag, while the 3D and 1D components indicate whether the drag compensation is carried out in all three spatial directions or just in along-track direction.

The impact of these product noise scenarios on the performance of L2 gravity products has been investigated within a product-noise only and a full-noise (i.e. temporal gravity signal in addition to product noise) 5-day retrieval based on a stand-alone P2. The results presented in **Figure E-17** indicate that the level of drag compensation only notably affects the retrieval if the temporal gravity signal is disregarded. Once the temporal signal is added, however, it dominates the retrieval performances, while the observation errors stemming from the various drag scenarios are negligible.

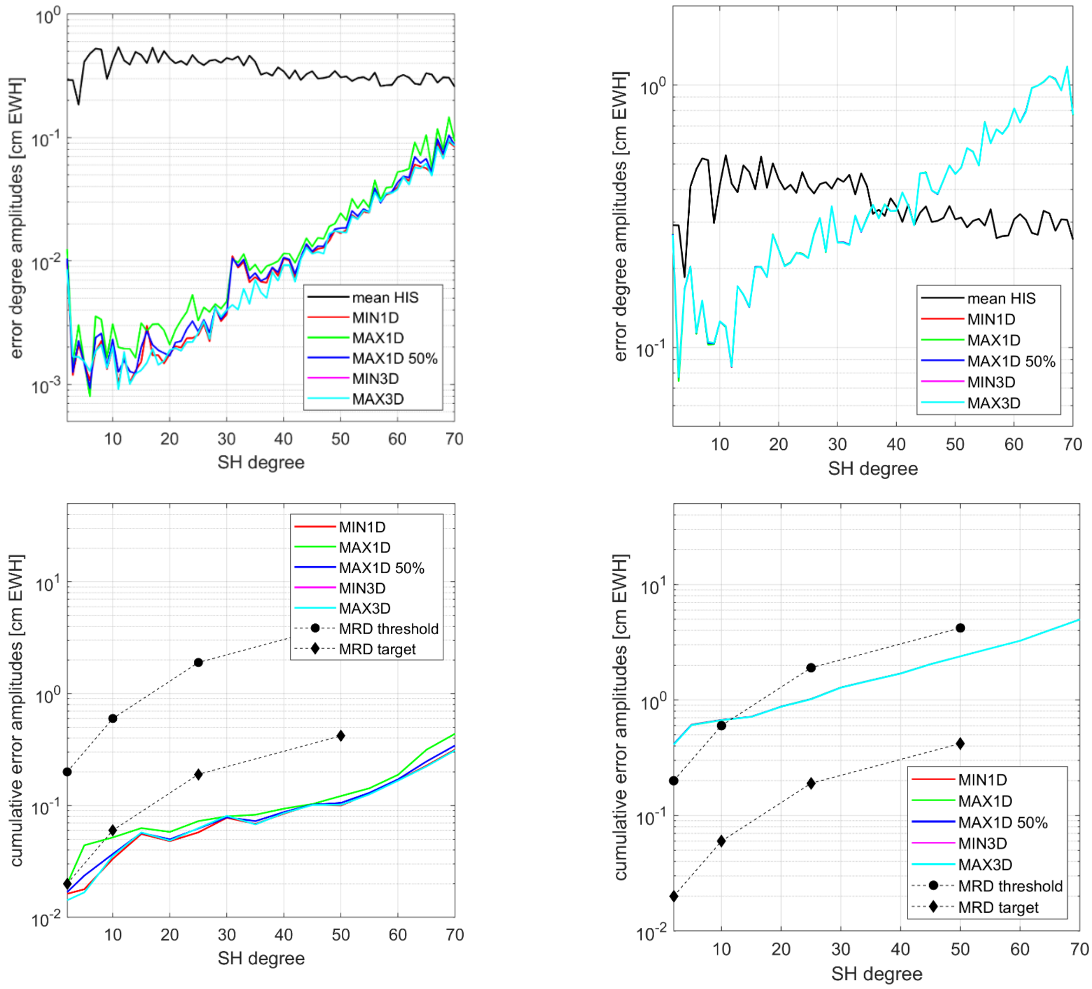

Figure E-17: Impact of drag compensation on the performance of gravity field retrieval in terms of degree ampliutudes (top row) and cumulative errors (bottom row, evaluated in the spatial domain for observation-covered regions). Note that the “polar gap wedge”, i.e. the coefficients affected by the polar gaps, have been removed in the degree amplitudes for better comparability. Left – product-noise-only simulation scenario, right – full-noise simulation scenario.

10) Outreach – scientific papers

The main results of the first phase of the MAGIC Phase A Science Support Study were documented in two scientific papers:

- Heller-Kaikov B., Pail R., Daras I. (2023), Mission design aspects for the mass change and geoscience international constellation (MAGIC). Geophys. J. Int. 235(1): 718–735, https://doi.org/10.1093/gji/ggad266.
- Daras I., March G., Pail R., Hughes C.W., Braitenberg C., Güntner A., Eicker A., Wouters B., Heller-Kaikov B., Pivetta T., Pastorutti A. (2023). Mass-change And Geosciences International Constellation (MAGIC) expected impact on science and applications. Geophys. J. Int., in review (status: October 2023).

References

Abrykosov P., Murböck M., Hauk M., Pail R., Flechtner F. (2022a): Data-driven multi-step self-de-aliasing approach for GRACE and GRACE-FO data processing, Geophysical Journal International, ggac340, doi: https://doi.org/10.1093/gji/ggac340.

Abrykosov P., Sulzbach R., Pail R., Dobslaw H., Thomas M. (2022b): Treatment of ocean tide background model errors in the context of GRACE/GRACE-FO data processing. Geophysical Journal International 228 (2022). 1850-1865, doi: https://doi.org/10.1093/gji/ggab421.

Hauk M., Pail R. (2018): Treatment of ocean tide aliasing in the context of a next generation gravity field mission. Geophysical Journal International 214, 345-365, doi: https://doi.org/10.1093/gji/ggy145.

Metzler B., Pail R. (2005): GOCE Data Processing: The Spherical Cap Regularization Approach. Studia Geophysica et Geodaetica 49(4): 441–462, doi: https://doi.org/10.1007/s11200-005-0021-5.

MRD (2020): Mission Requirements Document, Next Generation Gravity Mission as a Mass-change And Geosciences International Constellation (MAGIC) - A joint ESA/NASA double-pair mission based on NASA's MCDO and ESA's NGGM studies. ESA-EOPSM-FMCC-MRD-3785.

NGGM MRD (2023): Next Generation Gravity Mission (NGGM): Mission Requirements Document. Issue 1.0., ESA-EOPSM-NGGM-MRD-4355, ESA Earth and Mission Science Division.

Pail R., Bingham R., Braitenberg C., Dobslaw H., Eicker A., Güntner A., Horwath M., Ivins E., Longuevergne L., Panet I., Wouters B. (2015): Science and User Needs for Observing Global Mass Transport to Understand Global Change and to Benefit Society. Surveys in Geophysics, 36(6):743-772, doi: https://doi.org/10.1007/s10712-015-9348-9.

Purkhauser A.F., Pail R. (2019). Next generation gravity missions: near-real time gravity field retrieval strategy. Geophys. J. Int. 217(2), 1314–1333, https://doi.org/10.1093/gji/ggz084.

Wiese D.N., Visser P., Nerem R.S. (2011): Estimating low resolution gravity fields at short time itnervals to reduce temporal aliasing errors. Advances in Space Research 48 (2011), 1094-1107, doi: https://doi.org/10.1016/j.asr.2011.05.027.

ABBREVIATIONS AND ACRONYMS

ACC	Accelerometer
AO	Non-tidal atmosphere and Ocean
AOD	Atmosphere and ocean de-aliasing
AOerr	Atmosphere and ocean error
AOHIS	Atmosphere Ocean Hydrology Ice Solid-earth
AP	Advanced Pendulum
ASD	Amplitude Spectral Density
ATT	Attitude
BM	Background model
d/o	degree and order
DFC	Drag-Free Control
DORIS	Doppler Orbitography and Radiopositioning Integrated by Satellite
EPOS	Earth Parameter and Orbit System software
ESA	European Space Agency
ESM	Earth System Model
EWH	Equivalent Water Height
GFZ	GeoForschungZentrum Potsdam – Helmholtz Center for Geosciences
GNSS	Global Navigation Satellite Systems
GOCE	Gravity field and steady-state Ocean Circulation Explorer
GRACE	Gravity Recovery and Climate Experiment
HCU	HafenCityUniversität Hamburg
HIS	Hydrology, Ice and Solid-earth (temporal gravity)
ICGEM	International Centre for Global Earth Models
IERS	International Earth Rotation Service
ISD	Inter-satellite distance
ITRF	International Terrestrial Reference Frame
IUGG	International Union of Geodesy and Geophysics
ll-SST	low-low Satellite-to-Satellite Tracking
LRI	Laser ranging interferometer
MAGIC	Mass change And Geosciences International Constellation
NGGM	Next Generation Gravity Mission
OT	Ocean tides
PWL	Piecewise Linear
RB	Requirements Baseline
RMS	Root-Mean-Square
SDS	Science Data System
SF	Scale factor
SH	Spherical Harmonic
SST	satellite-to-satellite tracking
TUD	Delft University of Technology
TUM	Technical University of Munich
ULP	The University of Liverpool
URE	Université de Rennes
UTR	University of Trieste

WBS Work Breakdown Structure

PART 1:

ATBD OF NGGM/MAGIC L2 AND L3 PRODUCTS

1. DEFINITIONS AND ACRONYMS

1.1. Definitions

Data Level	Definition
Level 1a	Decoded and decomposed L0 data per instrument and HK data sets with original sampling converted to physical units (e.g. ACC, LRI, STR, GNSS, thrusts and other HK data).
Level 1b	Down-sampled instrument and HK data time series calibrated, preprocessed and converted to physical quantities (e.g. accelerations, biased ranges, range rates, range accelerations, quaternions, GNSS code and phase, thrust accelerations, others).
Level 2a	Precise orbits and estimated Earth gravity field SH coefficients
Level 2b	Corrected and filtered Earth gravity field SH coefficients (e.g. low degrees replaced, added back mean SH coefficients)
Level 3	Mass variations for Earth system components

1.2. Acronyms

ACC	ACCelerometer
AEI	Albert Einstein Institute for Gravitational Physics
AO	Atmosphere and Ocean
AOD	Atmosphere and Ocean Dealiasing
AOHIS	Atmosphere Ocean Hydrology Ice Solid earth
ASD	Amplitude Spectral Density
BM	Background Model
CCD	Charged-Coupled Device
CHAMP	Challenging Mini-Satellite Payload
CNR	Carrier to Noise Ratio
DMD	Data driven Multi step self De-aliasing
EGM	Earth Gravity field Model
EOP	Earth Orientation Parameters
FSR	Free Spectral Range
GFZ	GeoForschungsZentrum Potsdam – Helmholtz Center for Geosciences
GIA	Glacial Isostatic Adjustment
GNSS	Global Navigation Satellite System
GOCE	Gravity field and Ocean Circulation Explorer
GPS	Global Positioning System
GRACE	Gravity Recovery And Climate Experiment
GWS	Ground Water Storage
HIS	Hydrology Ice Solid earth
HK	Housekeeping
ICE	Ice mass Change Estimate

ICGEM	International Center for Global Earth Models
IERS	International Earth Rotation and reference Systems service
IGS	International GNSS Service
IONEX	IONosphere Exchange format
ITRF	International Terrestrial Reference Frame
JPL	Jet Propulsion Laboratory
LEO	Low Earth Orbit
LOS	Line Of Sight
LRI	Laser Ranging Instrument
LTI	Laser Tracking Instrument
MAGIC	Mass change And Geosciences International Constellation (MCM & NGGM)
MCM	Mass Change Mission
NEQ	Normal Equation System
NGGM	Next Generation Gravity Mission
NRT	Near Real Time
OBC	On Board Computer
OBP	Ocean Bottom Pressure
OT	Ocean Tides
POD	Precise Orbit Determination
PSD	Power Spectral Density
PSO	Precise Science Orbit
PVT	Position Velocity Time
RSO	Rapid Science Orbit
SAL	Self-attraction And Loading
S/C	Space Craft
SH	Spherical Harmonics
SHS	Spherical Harmonic Sereis
SMFS	Scale Factor Measurement System
SNR	Signal to Noise Ratio
SRL	Scientific Readiness Level
SST	Satellite-to-Satellite Tracking
STR	Star Tracker
TTL	Tilr-To-Length
TUD	Delft University of Technology
TUM	Technical University of Munich
TWS	Terrestrial Water Storage
USO	Ultra Stable Oscillator
UT	Universal Time
VCM	Variance Covariance Matrix

2. INTRODUCTION

The purpose of this document is to provide a consolidated description of algorithms to applied for generation of NGGM/MAGIG level 1 (L1a, L1b), level 2 (L2a, L2b) and level 3 (L3) products. While for L1a and L1b products mission specific algorithms need to be developed, algorithms for processing L2a, L2b and L3 products are well established in the geodetic gravity field community. For L1a and L1b products a distinct description of algorithms to be applied will be added after availability of the industry system study results, which shall form the baseline for further processing of instrumental and HK data to higher levels (specifically from L1a to L1b). For L2 products it is not intended to provide a full description of all algorithms as these are published in various reports and journal articles. Mainly it shall be specified what techniques are applied to estimate the Earth gravity field SH coefficients providing the relevant references. Similar for L3 products a number of published algorithms is available, which will form the baseline for mission specific algorithms to be implemented for NGGM.

The following figures provide a sketch of the processing sequence from raw data up to L3 products. They provide a rough idea how the various processing steps are interconnected and what kind of data or products are needed to generate a higher level output product. Figure 2-1 and Figure 2-2 show the data and product flow and the main processing sequence per satellite, per satellite pair and their combination.

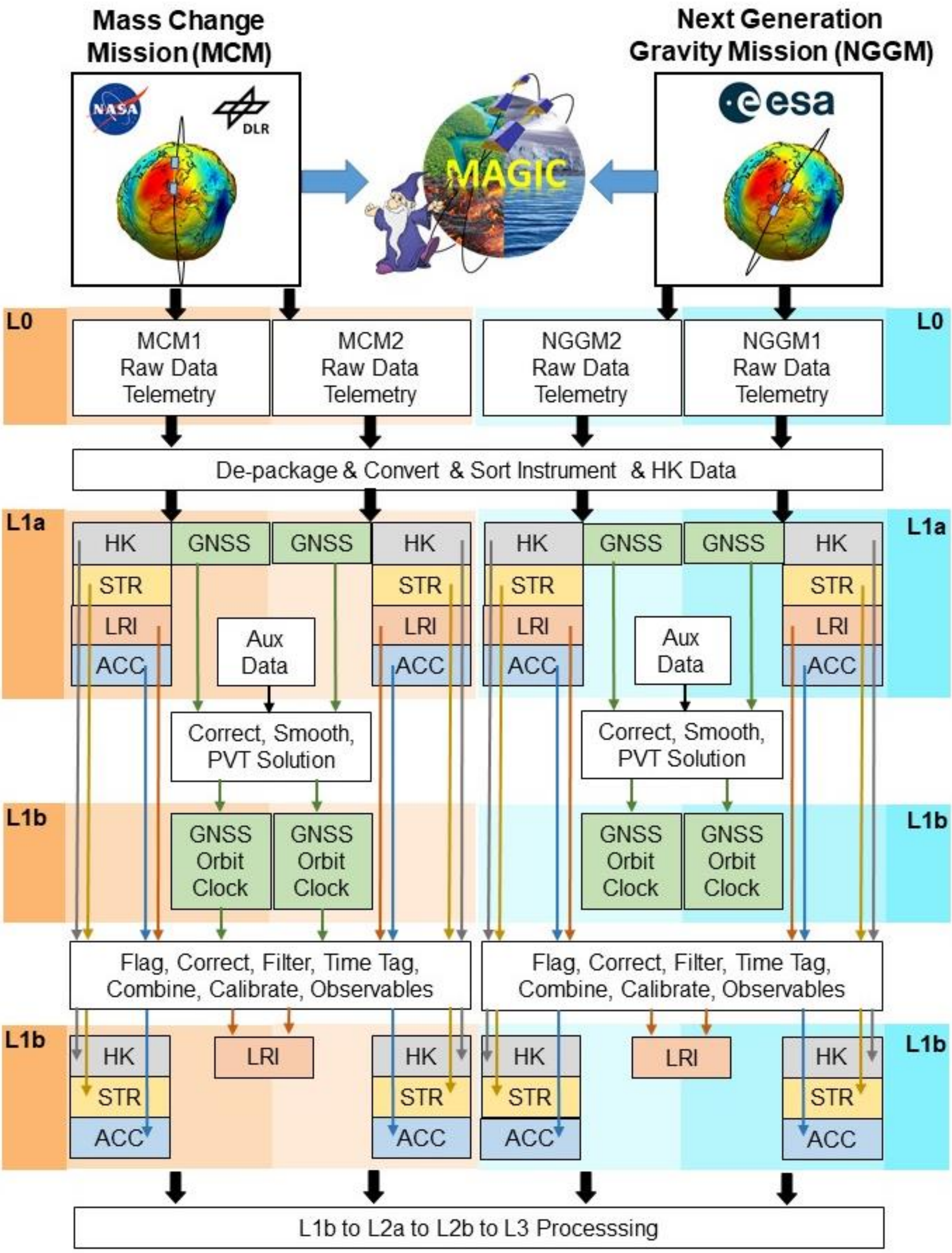

Figure 2-1: Data and product flow from L0 data to L1b products

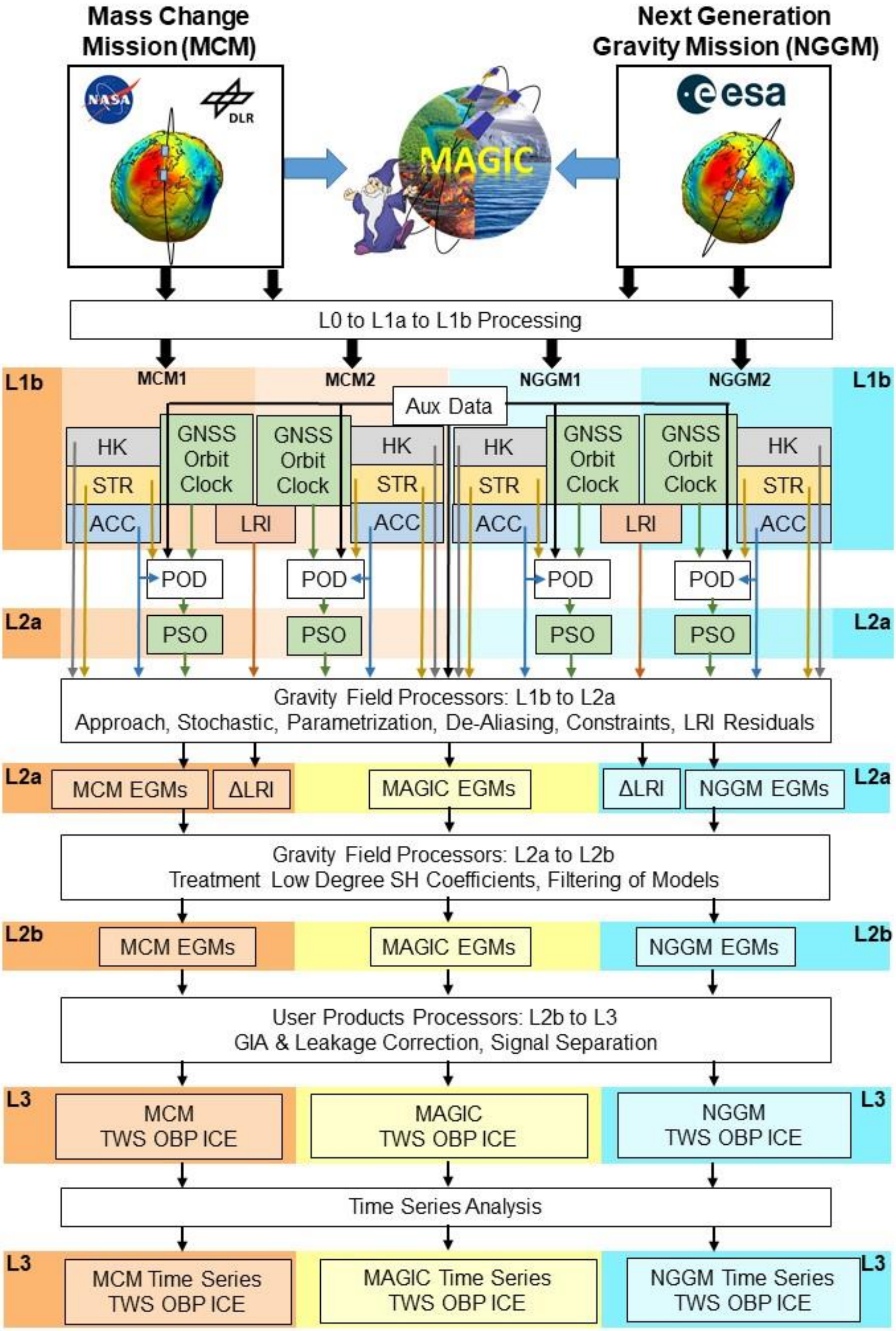

Figure 2-2: Product flow from L1b data to L3 products

3. L1A TO L1B PROCESSOR

As a starting point for processing L1b products, for each data type a sorted time series of de-packeted and converted instrumental and HK data in their original sampling rate shall be available (L1a products). Ideally these data already are checked and flagged for invalid data, such that the processing of L1b data can be done sequentially. The following sub chapters provide a sketch of the procedures to be applied per data stream and per satellite pair (NGGM or MCM). The algorithms at this point cannot be specified in detail yet and are subject to input from the industry studies, where the instrument and housekeeping data processing is to be specified in detail per instrument.

3.1. GNSS

The GNSS receiver delivers range and phase data for different satellite navigation systems and an on-board computed navigation solution with satellite positions in the observed sampling rates (L1a products). In order to determine GNSS L1b products original GNSS observations need to be corrected and smoothed and an initial solution for orbits and clocks shall be determined. The GNSS L1a and L1b data products will also be provided in RINEX format (IGS, 2023; Wen et al., 2019).

3.1.1. GNSS Range and Phase Data Correction and Smoothing

Input	Telemetry from the GNSS receiver converted to L1a products ▪ Raw carrier phase measurements ▪ Raw pseudo range measurements ▪ On-board navigation solution and clock bias ▪ Receiver time ▪ GNSS receiver housekeeping data
Procedure	(1) Correct raw phase measurements for the effect of the inter-frequency bias, (2) Correct raw pseudo range (code) measurements for the effect of the inter-channel bias, (3) Filter and smooth measurements using a suitable order polynomial for each receiver channel and each type of observable separately, (4) Estimate pseudo range noise, (5) Flag invalid data and detect cycle slips
Output	GNSS receiver L1b products ▪ Inter-frequency bias estimation results ▪ Carrier phase measurements, corrected for inter-frequency bias and cycle slips flagged ▪ Pseudo range measurements, corrected for inter-channel bias, outliers flagged ▪ Smoothed pseudo range measurements, corrected for inter-channel bias, outliers flagged ▪ Estimate of the pseudo range noise ▪ On-board navigator solution and clock bias

3.1.2. Orbit and Clock Solution

Input	GNSS receiver L1b products ▪ Pseudo range measurements, corrected for inter-channel bias, outliers flagged ▪ Smoothed pseudo range measurements, corrected for inter-channel bias, outliers flagged Raw carrier phase measurements ▪ On-board navigation solution and clock bias Auxiliary products ▪ IGS rapid clocks and orbits product ▪ Ionospheric products (IONEX data) ▪ Antenna phase center offsets ▪ Others
Procedure	(1) Apply light time correction and other relativistic effects, (2) Apply ionospheric correction either by use of simultaneous measurements on L1 and L2 or by use of IONEX global ionosphere maps, (3) Apply satellite clock corrections, (4) Consider absolute delay of receiver, (5) Consider satellite GNSS antenna offset (6) Consider satellite antenna phase centre offset and phase centre offsets for GNSS satellites, (7) Consider satellite attitude, (8) Determine position, velocity and time (PVT) of the satellite in ITRF2020 by least squares adjustment algorithm, (9) Determine stochastic uncertainty of the solution
Output	Orbit and Clocks L1b products ▪ Clock error, Position and velocity vector of satellite ▪ Sigma of Clock error, Position and Velocity of satellite from the PVT solution function ▪ Covariance matrices for position and velocity solution ▪ Position and velocity of the tracked GNSS satellites used for the derivation of the PVT solution ▪ Difference between GPS system time and on-board time

3.2. ATTITUDE (STAR CAMERAS)

Star cameras deliver attitude quaternions in the observed sampling rate (L1a products). For determining the attitude multiple star camera data are time tagged, resampled and combined (potentially involving other attitude sensor data such as the LRI pointing angles and the accelerometer angular accelerations) applying the procedures subsequently described.

3.2.1. Star Camera Time Tagging and Filtering

Input	Telemetry from star tracker instruments converted to L1a products ▪ Raw quaternions rotating inertial frame to star camera frames ▪ Star tracker house-keeping data, including CCD temperatures, big-bright object flag, and the high-rate flag

	Orbits and clocks L1b products ▪ Clock error
Procedure	(1) Flag invalid data (2) Convert raw quaternions into quaternions rotating inertial frame to satellite reference frame (3) Compute residuals of star tracker observations with respect to orbit derived orientation and flag data in case residuals exceed a predefined limit (4) Compute star tracker time tag corrections from L1b clock error product (5) Correct star tracker observations for orbital relativistic aberration (velocity of Earth about sun and inertial velocity of satellite around Earth) (6) Interpolate star camera data at integer seconds for each camera separately
Output	Star camera L1b product ▪ Resampled and flagged quaternions rotating inertial frame to satellite reference frame (per camera head, one set quaternions and house-keeping data)

3.2.2. Attitude Reconstruction

For the best attitude accuracy, data from all available attitude sensors needs to be combined. These sensors are the star cameras, the LRI pointing angles (augmented with the precise positions of both satellites from GNSS), and the accelerometer angular accelerations. The data is combined in complex fitting procedure that takes into account the particular observation geometry and sensor noise characteristics.

Input	Preprocessed and time tagged L1b ACC measurements ▪ Filtered and flagged linear and angular accelerations in satellite reference frame with designated sampling rate Star camera L1b product ▪ Resampled and flagged quaternions rotating inertial frame to satellite reference frame (per camera head, one set quaternions and house-keeping data) Preprocessed and time tagged angular measurements from the LTI (sec. 3.3.5), either pointing angles derived directly from Differential Wavefront Sensing (DWS) signals of LTI, or the data from a position sensor inside the LTI steering mirror, if closed-loop beam steering is employed or activated that zeroes the DWS. It will be likely possible to switch between both modes of operation. ▪ Filtered and flagged laser pointing angles relative to the satellite, i.e. direction of line-of-sight (connection line between the CoM of both satellite), relative to a satellite/LTI frame ▪ Filtered and flagged laser pointing angles relative to the satellite, i.e. direction of line-of-sight (connection line between the CoM of both satellite), relative to a satellite/LTI frame Precise satellite positions (both satellites)

Procedure	(1) Check flags per epoch for each attitude data set (2) Perform optimal combination of all valid star camera observations per epoch
Output	Combined attitude L1b product ▪ Optimally combined and flagged quaternions rotating inertial frame to satellite reference frame

3.3. LASER RANGING INSTRUMENT

The LRI delivers biased range observations between a spacecraft pair (L1a products). These ranges need to be corrected for a number of system related features, filtered (down sampled) and time tagged applying the procedures subsequently described. In addition, range rates and range accelerations shall be derived from the biased ranges.

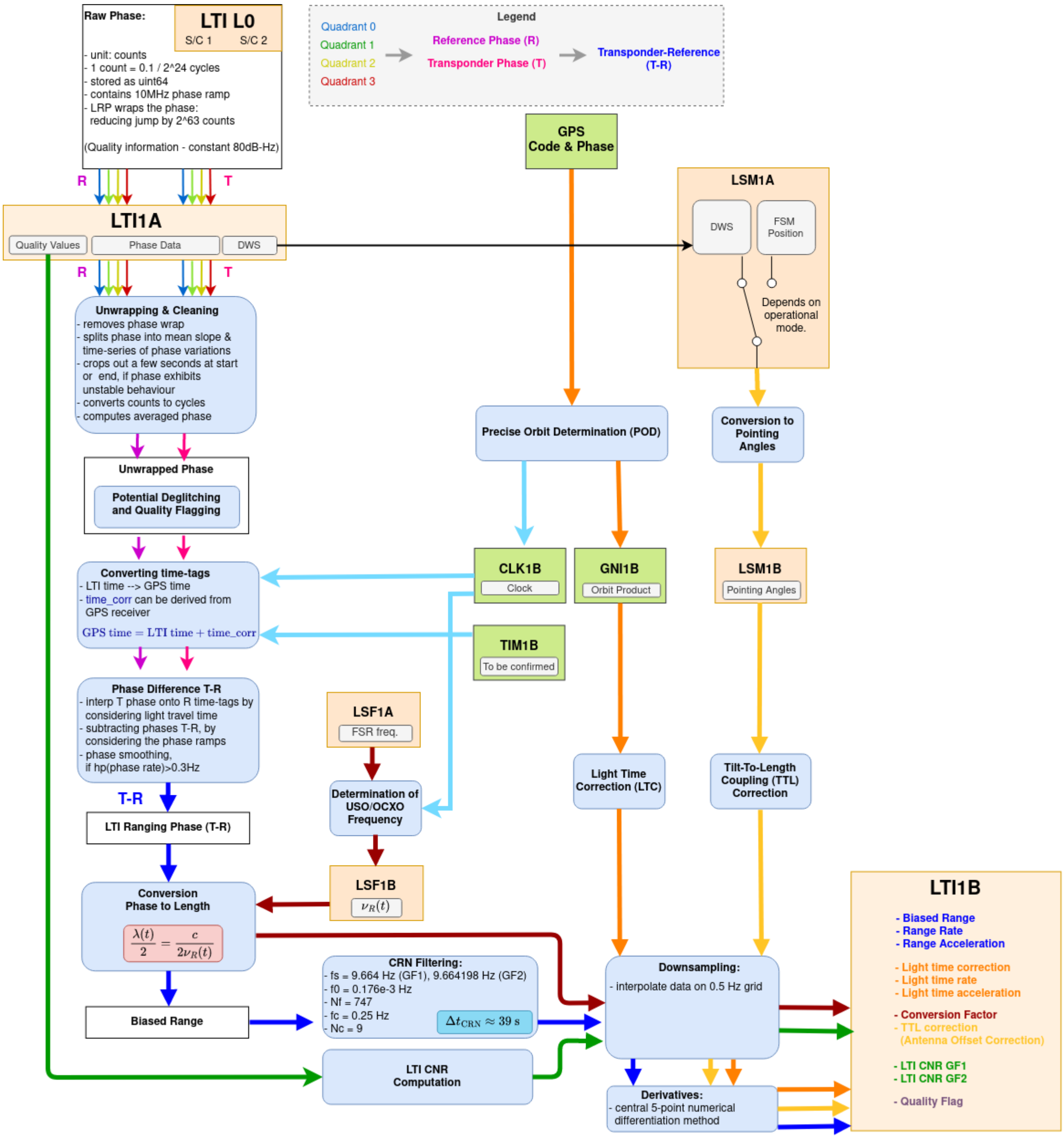

Figure 3-1: LTI Processing scheme of L0/L1A to L1B for LTI ranging data.

3.3.1. LRI Data Preprocessing

Input	Telemetry from LRI instrument converted to L1a products ▪ LRI phase measurements
Procedure	(1) Check for data breaks and set quality flag if required, (2) Phase unwrapping: remove phase reducing jumps of 2^63 counts and split phase into mean value for phase ramp (slope) and time series of smaller phase variations. This allows to convert the phase from counts to phase cycles.

	(3) Check for non-physical phase changes (unstable phase) directly after laser link was acquired or before laser link was lost, remove these segments, set quality flag if required (4) Deglitching: correct phase data for outliers, e.g. due to Single Event Upsets. Set quality flag, (5) Identify phase breaks. Set quality flag, (6) Convert LRI internal time from counts to seconds for various telemetry packets (phase, steering mirror data, house-keeping) (7) Convert the Carrier-to-noise ratio (CNR) from raw units (counts) to physical units dB-Hz, taking into account corrections from scalloping loss (8) Check CNR ratio to detect invalid measurements, set quality flag if required
Output	Preprocessed LRI measurements ▪ Edited and flagged LRI phase measurement time series

3.3.2. LRI Data Time tagging

Input	Preprocessed LRI measurements ▪ Edited and flagged LRI phase measurement time series Orbit and Clock L1b products ▪ Clock error Potentially the time-offset between on-board computer time (OBC time) and USO time. Such a product may not be present in NGGM as it depends on the details of the timing architecture.
Procedure	(1) Apply constant LTI time tag offset if required (as calibrated on-ground), (2) Fill data gaps and remove outlier in clock products if LRI measurements are continuous (in case phase break flag is not set) and if gap does not exceed a predefined length, (3) Interpolate time-tag corrections (sampled at GPS time) to LTI measurement epochs. (4) Calculate for each LTI measurement epoch the corresponding GPS time-tag, i.e. GPS-time-tag = LTI-time-tag + time-tag-correction
Output	Time tagged and corrected LRI measurements ▪ Time tagged and corrected LRI phase measurement time series

3.3.3. Auxiliary Data Generation: Light Time Correction

Input	Orbit and Clocks L1b products ▪ Products from Precise Orbit Determination: orbital states in inertial reference frame for each satellite and estimated clock offset, i.e. offset between NGGM S/C clock and GPS time.
Procedure	(1) Generate the time-series of light travel times and light time correction based on POD data. Calculation of light travel times accounts for special relativistic effects (motion of satellites during light propagation)

	and for general-relativistic effects, i.e. effect of gravity onto light propagation. A low fidelity gravity field (up to C2,0) is usually sufficient. Algorithms described in detail in Yan et al (2020). Reference: Yan et al (2021), Revisiting the light time correction in gravimetric missions like GRACE and GRACE follow-on. J Geod 95, 48 (2021). https://doi.org/10.1007/s00190-021-01498-5
Output	Intermediate LTI auxiliary product ▪ Light travel times and light time corrections.

3.3.4. Auxiliary Data Generation: Scale Factor Readout

Input	LTI telemetry (1a) of the scale-factor measurement system (SFMS) containing: ▪ NCO frequency in-loop measurements ▪ Frequency multiplier Results from on-ground calibration tables including ▪ Fractional mode number ▪ Integer mode number Orbit and Clocks L1b products ▪ Estimated clock offsets, i.e. offset between satellite clock and GPS time.
Procedure	(1) Compute the cavity free spectral range (FSR) frequency from the product of NCO in-loop frequency measurement and a frequency multiplier, (2) Cavity free spectral range (FSR) frequency from in-loop measurements at local LTI/USO time of the reference satellite needs to be converted to the absolute laser frequency in GPS time by using clock offsets, integer and fractional mode number of the cavity. $$\nu_R(\mathrm{t}) = \mathrm{f}_{\mathrm{FSR,OCXO}}(t) * \left(1 + \frac{\mathrm{d}\varepsilon_{\mathrm{time}}}{\mathrm{d}t}\right) * \left(N_{int} + N_{frac}\right) = \mathrm{f}_{\mathrm{FSR,GPS}}(t) * \left(N_{int} + N_{frac}\right)$$
Output	Intermediate LTI auxiliary product: ▪ Time-series of the absolute laser frequency, which corresponds to the resonance frequency of the cavity. Product derived only for the satellite in LTI reference role.

3.3.5. LTI Pointing Angle Product

Input	Telemetry from LRI instrument converted to L1a products ▪ Steering mirror position sensing data if closed-loop steering mirror control-loop is enabled or differential wavefront sensing (DWS) data if control-loop is disabled Dataset / Model of the offset between LTI triple mirror assembly vertex (LTI reference point) and the S/C center-of-mass position: ▪ Determined with regular center-of-mass calibration maneuvers of the satellite ▪ Time-series of offset values in Y (cross-track) and Z direction

	(radial) for the past and a prediction for near future (~6 months)
Procedure	(1) Convert pointing angles from raw units to physical angles using calibration model (coefficients) from ground measurements or in-flight calibration (2) Compute time-derivative of pointing angles (3) Compute the LTI tilt-to-length (TTL) correction given as the product of pointing angle and offset between LTI vertex and center of mass, include correction for so-called angular rate coupling. Details about the algorithms can be found in Wegener et al. (2020) and Wegener (2022). References: Wegener et al. (2020), Tilt-to-Length Coupling in the GRACE Follow-On Laser Ranging Interferometer, Journal Of Spacecraft And Rockets, https://doi.org/10.2514/1.A34790 Wegener, Henry (2022): Analysis of tilt-to-length coupling in the GRACE follow-on laser ranging interferometer. Hannover : Gottfried Wilhelm Leibniz Universität, Diss., 2022, x, 190 S. DOI: https://doi.org/10.15488/11984
Output	LTI pointing angles product for both satellites: ▪ Time-series of LTI TTL corrections for both satellites ▪ LTI pointing angles product is used in the S/C attitude reconstruction (sensor fusion with star camera and other attitude sensors, cf. sec. 3.2.2

3.3.6. LRI Data Filtering and Combination

Input	Time tagged and corrected LRI measurements ▪ Time tagged and corrected LRI phase measurement time series ▪ Carrier to Noise Ratio Auxiliary products ▪ Intermediate LTI product of Light Travel Times and Light Time Correction ▪ Intermediate LTI product of TTL correction derived ▪ Intermediate LTI product of the absolute laser frequency
Procedure	(1) Compute biased range from phase measurements: ▪ Compute phase difference of transponder minus reference by considering light travel times, ▪ Use absolute laser frequency to rescale phase to biased range [Misfeldt et al (2023), Müller et al (2022)] (2) Decimation and interpolation of ~10Hz phase data, tilt-to-length coupling correction, light time correction, carrier to noise ratio values and quality flags to time-grid with 0.5 Hz sampling. (3) Derivatives: Compute numerical derivatives to derive range rates and range accelerations, as well as for light time correction and tilt to length coupling correction quantities. References: Misfeldt et al (2023), Scale Factor Determination for the GRACE Follow-On Laser Ranging Interferometer Including Thermal Coupling. Remote Sens. 2023, 15, 570. https://doi.org/10.3390/rs15030570

	Müller et al (2022), Comparing GRACE-FO KBR and LRI Ranging Data with Focus on Carrier Frequency Variations. Remote Sens. 2022, 14, 4335. https://doi.org/10.3390/rs14174335
Output	LTI L1b product ▪ Downsampled (filtered) LRI observations as biased range, range rates and range accelerations including required corrections (tilt-to-length and light-time correction), CNR and quality flags.

3.4. ACCELEROMETER

The ACC delivers non-gravitational accelerations for each spacecraft (L1a products). These accelerations need to be corrected (calibrated), filtered (down sampled) and time tagged applying the procedures subsequently described.

3.4.1. ACC Preprocessing, Time Tagging and Filtering

Input	Telemetry from ACC instrument converted to L1a products ▪ Linear raw accelerations in original sampling rate ▪ Angular raw accelerations in original sampling rate ▪ Temperatures from several locations inside the ACC instrument Orbit and clock L1b products ▪ Clock error
Procedure	(1) Remove invalid flagged observations, (2) Apply filters and polynomials that compensate for nonlinearities (e.g., from the ADC converter) and the transfer functions of the ACC readout chain, (3) Convert on-board time to GNSS time, (4) Compute time tag correction to be added to GNSS receiver time by linear interpolation of GNSS clock corrections and resample at the corrected integer multiples of instrument sampling rate, (5) Flag and fill data gaps for a predefined maximum data gap length, (6) Apply a digital filter for down sampling and determine linear and angular accelerations for down sampled intervals (e.g. 1 second), (7) Compute fit residuals after filtering and add a quality flag if a predefined limit is exceeded, (8) Rotate linear and angular accelerations into satellite reference frame.
Output	Preprocessed and time tagged L1b ACC measurements ▪ Filtered and flagged linear accelerations in satellite reference frame with designated sampling rate

3.4.2. ACC External Calibration and Corrections

Determination of external calibration parameters and applying them to original observations using the following procedure.

Input	Preprocessed and time tagged ACC measurements ▪ Filtered and flagged linear and angular accelerations in satellite reference frame with designated sampling rate Star camera L1b product: Preprocessed and time tagged attitude measurement from the star trackers ▪ Filtered and flagged attitude quaternions from the three star camera heads LRI L1b product: Preprocessed and time tagged angular measurements from the LRI ▪ Filtered and flagged laser pointing angles relative to the satellite Orbit and Clocks L1b products ▪ Precise satellite positions (both satellites)
Procedure	Angular acceleration measurements (1) Perform a calibration of attitude sensor data (data from three camera heads of the STR, LRI with precise orbits, and angular measurements of the ACC) to correct for relative misalignments, scale factors, biases, and other calibration parameters (this will be based on science mode and calibration mode data and involve a least-square fitting approach) (2) Reconstruct attitude from the calibrated attitude sensor data Linear acceleration measurements (3) Calculate angular velocity and angular acceleration from reconstructed attitude data, and gravity gradients that apply to each of the nominal accelerometer positions (assuming a configuration of three accelerometers). (4) Perform a least-squares adjustment to determine accelerometer calibration parameters and additional parameters (this will be based on science mode and calibration mode data; this step will not provide the accelerometer biases). (5) Apply accelerometer calibration parameters to obtain calibrated accelerations (may include, e.g., linear interpolation for time). (6) Estimate biases for the accelerometers in a POD approach (7) Apply biases to calibrated accelerometer data.
Output	External calibrated ACC measurements ▪ External calibrated linear and angular accelerations in satellite reference frame with designated sampling rate

3.5. HOUSEKEEPING DATA

Different kind of spacecraft HK data are available as L1a products. If needed, a correction package needs to be prepared applying dedicated algorithms. This includes for example the timing of thruster events, thermal readings, voltages supplied to the relevant instruments or systems and any other possible information, which might disturb the instruments observations. The housekeeping L1b product needs to be defined once the required information about available housekeeping data has been specified by industry.

4. ALGORITHMS L2A PRODUCTS

L1b data as described above are the basis for computing L2a products namely precise orbits, reduced LRI observations and Earth gravity field SH coefficients estimated either from NGGM or the combined MAGIC solution.

4.1. PRECISE ORBIT DETERMINATION

4.1.1. Reduced Dynamic and Kinematic Orbit Solutions

From L1b GNSS observations and other instrument data as well as ancillary data from other sources precise orbits are computed as a L2a products. The goal is to provide best possible orbits for the MAGIC satellites, which can be used for subsequent processing tasks. Different approaches can be applied, namely a pure kinematic orbit determination by precise point positioning and a reduced dynamic processing scheme combining orbit dynamics and kinematic information. The procedures and basic algorithms are described in the subsequent chapters. It is mostly referred to reports and publications, where the algorithms are described in detail. Here mostly a description of procedures about how these algorithms are applied is provided.

Reduced-Dynamic and Kinematic Precise Orbit Determination	
Data and Products	
Input L1b Data	▪ GNSS receiver L1b product (RINEX format: IGS, 2023) ▪ Combined attitude L1b product

Input Aux. Data	▪ GNSS ephemeris products (e.g. IGS, CODE, JPL, CNES)
	▪ Earth Rotation Parameters (IERS, 2023)
	▪ Force models:
	    o Gravity field model (ICGEM, 2023)
	    o Ocean tide model (e.g. Ray, 2013; Savcenko and Bosch, 2012)
	▪ JPL planetary ephemeris (JPL, 2023)
	▪ Standards (IERS, 2023)
	▪ Satellite Laser Ranging observations (ILRS)

Output L2a Data	▪ Reduced dynamic and kinematic orbits (SP3 format: IGS, 2023), typically daily batches ▪ Quality report
Algorithms and Procedure Description	
Several operational Precise Orbit Determination (POD) are in existence for a multitude of Low Earth Orbiting missions, including GRACE-FO, Swarm and the Copernicus Sentinel missions (Fernandéz et al., 2022; Montenbruck et al., 2018; Kang et al., 2020). Each implementation has its own characteristics and processing schemes, but typically converge to solutions that are consistent at the cm-level, even for solutions with latencies as short as 1 day. The description below is based on the currently running cm-level precision reduced-dynamic and kinematic orbit determination for the ESA Swarm mission (status August 2022). The architecture of this implementation and methodology/algorithms as described and referred to in (TUD, 2012) is still relevant (see also Figure 4-1 below, note that also a so-called highly-reduced dynamic POD is included as a possible partial backup in case of accelerometer	

anomalies, see also e.g. (Van den IJssel et al., 2020).. An updated excerpt from (TUD, 2012) is included in the following paragraphs.

The GNSS receivers on board of the NGGM satellites will provide the tracking observations required for the POD. These observations have to be augmented by auxiliary and internal data that are collected and provided routinely by existing networks of ground stations and services such as the International GNSS Service (IGS) and International Earth Rotation Service (IERS, 2023). For the Swarm POD, use is made of the GHOST software (Montenbruck et al., 2005), which is developed under auspices of the DLR German Space Operations Centre with TU Delft being a co-developer. The GHOST tools can be used – or serve as example - for NGGM POD as well.

Precise orbit determination requires a very detailed and comprehensive modeling and parameter estimation (Montenbruck and Gill, 2000), but does not require extensive computer resources (a typical desk top computer with Linux operating system is sufficient, status August 2023). Precise orbit determination is an estimation process relying today on high-quality force models and tracking observations. In general, the objective of precise orbit determination is to obtain the most precise estimates for the position and velocity of the satellite as a function of time.

For NGGM, both reduced-dynamic and kinematic orbit solutions are to be produced, where the reduced-dynamic orbit solutions are anticipated to be the most precise solutions that can be used for geolocating observations and as starting point for gravity field determination. The kinematic solutions in principle do not rely on force modelling for the NGGM satellites themselves and thus provide time series of position coordinates that can be used as a condensed form of GNSS observations for gravity field estimation.

Satellite specific information (centre-off-mass, antennae and instrument locations) has to be provided as part of the calibration and characterization information and in order to refer orbit solutions to the centre-of-mass of the NGGM satellites.

For reduced-dynamic POD, typically use is made of a Bayesian batch least-squares estimation method where orbit parameters (begin position, velocity, empirical accelerations) are fit through the tracking observations (Montenbruck and Gill, 2000). The GHOST software relies on un-differenced GPS observation schemes. In the latest implementations of GHOST, a kinematic orbit solution is produced by an extension of the reduced-dynamic POD tool, where the reduced-dynamic solution serves as the reference solution and geometric corrections are estimated. Use is made of carrier-phase ambiguity fixing to arrive at the most precise solutions possible.

For POD, four sub-tasks are identified:

- Data preprocessing;
- Orbit setup definition
- Orbit computation;
- Quality assessment.

(i) The data preprocessing consists of the collection of all required observational and auxiliary data (GNSS satellite-to-satellite tracking (SST), star tracker observations, accelerometer observations, products from the IGS and IERS, JPL planetary ephemeris, gravity field and tide models, etc.). In addition, the preprocessing involves quality checking of the observations (elimination of spurious observations, reformatting, etc.).

(ii) The orbit setup definition involves the definition of the dynamic models to be used, the parameters to be estimated, definition of the arc length, etc. The setup will be consistent with the standards as specified for NGGM.

(iii) After defining the setup, the actual orbit parameter estimation will be done. For NGGM, an integrated reduced-dynamic/kinematic POD will be done.

(iv) Finally, a number of quality checks will be carried out. The correctness of the POD process is assessed by for example checking convergence and stability of the iterative estimation process (for example formal errors of, and correlations between, estimated parameters), the observation fit and overlap analysis between consecutive orbit solutions. Depending on the availability of Satellite Laser Ranging (SLR) observations, the orbit products will be confronted with these observations allowing an additional assessment of its accuracy.

The underlying mathematical concepts and algorithms for precise orbit determination (dynamic, reduced-dynamic, and kinematic) are outlined in detail in (Van Helleputte, 2004).

References

T. Van Helleputte (2004). GHOST Technical Manual, GPS High Precision Orbit Determination Software Tools, Doc. No. FDS-STM-3110, Issue 1.0, DLR

IGS (2023), https://igs.org/formats-and-standards, last accessed August 2023

IERS (2023), http://www.iers.org, last accessed August 2023

JPL (2023), https://ssd.jpl.nasa.gov/planets/eph_export.html, last accessed August 2023

ICGEM (2023), http://icgem.gfz-potsdam.de/home, last accessed August 202

R.D. Ray (2013), Precise comparisons of bottom-pressure and altimetric ocean tides, J. Geophys. Res.: Oceans, Vol. 118, pp. 4870-4584, doi: 10.1002/jgrc.20336

Savcenko, R. and Bosch, W. (2012): EOT11A - Empirical Ocean Tide Model from Multi-Mission Satellite Altimetry, München, Deutsches Geodätisches Forschungsinstitut (DGFI), hdl:10013/epic.43894

Fernandéz, Marc, Peter, H., Arnold, D., Duan, B., Simons, W., Wermuth, M., Hackel, S., Fernandéz, J., Jäggi, A., Hugentobler, U., Visser, P. and Féménias, P. (2022), Copernicus Sentinel-1 POD reprocessing campaign, Adv. Space Res., 70, 249–267, https://doi.org/10.1016/j.asr.2022.04.036

Jose van den IJssel, Eelco Doornbos, Elisabetta Iorfida, Günther March, Christian Siemes, and Oliver Montenbruck, Thermospheric densiyoes derived from Swarm GPS observations, Adv. In Space Res., 657), 1758-1771, https://doi.org/10.1016/j.asr.2020.01.004, 2020

Montenbruck, O., Hackel, S., van den Ijssel, J. and Arnold, D. (2018), Reduced dynamic and kinematic precise orbit determination for the Swarm mission from 4 years of GPS tracking, GPS solutions 22 (3), 79

Kang, Z., Bettadpur, S., Nagel, P. et al. GRACE-FO precise orbit determination and gravity recovery. J Geod 94, 85 (2020). https://doi.org/10.1007/s00190-020-01414-3

TUD (2012), SW-DD-DEOS-GS-0001, Swarm Level 2 Processing System, DEOS Sub-System Architectuarl Design Document, Rev. 4, 2012-05-15

Montenbruck O., van Helleputte T., Kroes R., Gill E. (2005), Reduced Dynamic Orbit Determination using GPS Code and Phase Measurements; Aerospace Science and Technology 9/3; 261-271

Montenbruck, O., Gill, E., Satellite Orbits – Models Methods Applications, Springer, ISBN 3-87907-106-3, 2000

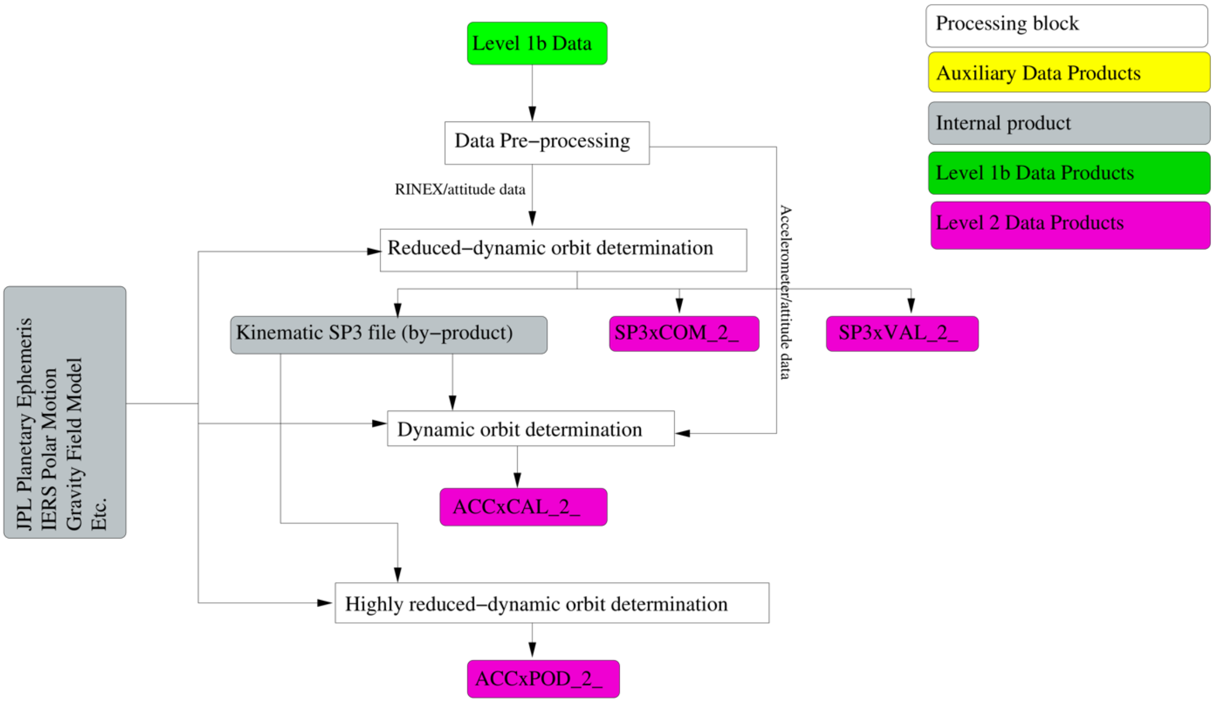

Figure 4-1 Example of flowchart for Precise Orbit Determination (POD) (TUD 2012)

4.1.2. POD-based Accelerometer Calibration

A very precise calibration of the accelerometers is a prerequisite for fully exploiting the ll-SST and GNSS observations for observing temporal gravity. The NGGM satellites will be equipped with an on-board shaking system that allows for precise determination of the accelerometer scale factors and quadratic factors. A similar system on-board ESA's first explorer GOCE allowed for a precision level of 10 ppm. The procedure based on the on-board shaking does not allow for the determination of the accelerometer biases, which are to be obtained by GNSS-based POD. Accelerometer scale factors can be determined by GNSS-based POD as well. To this aim, an additional POD implementation is to be done which aims at the best possible estimation of accelerometer biases and the best possible verification of the scale factors obtained by the on-board shaking procedure. Typically, the POD-based accelerometer calibration uses observations taken by an individual accelerometer located (nominally) in the centre-of-mass (COM) of the satellite (as is the case for missions like GRACE and GRACE-FO). However, in case of e.g. 3ACC configuration, it is possible to estimate calibration parameters for the accelerometer in the COM or for the so-called common-mode of the two eccentric accelerometers (as included in e.g. the GOCE processing chains, (Visser and van den IJssel, 2016).

POD-based Accelerometer Calibration	
Data and Products	
Input L1b Data	▪ Combined attitude L1b product ▪ Accelerometer L1b product
Input L2a Data	▪ Precise orbit solution (kinematic)
Input Aux. Data	▪ Earth Rotation Parameters (e.g. IERS) ▪ Force models: o Gravity field model (e.g. ICGEM) o Ocean tide model (e.g. FES, GOT) ▪ JPL planetary ephemeris ▪ Standards (IERS)
Output L2a Data	▪ Accelerometer External Calibration L2a Product. Accelerometer biases (typically daily), scale factors (selected depending of Drag-Free Control, typically daily) ▪ Quality report
Algorithms and Procedure Description	

Also for POD-based accelerometer calibration, use can be made of existing operational implementations. The descriptions below hold for the implementation as used in the Swarm DISC TOLEOS project, which is applied to accelerometer data of the GRACE, GRACE-FO, Champ, GOCE and Swarm satellites (Siemes et al., 2023). For this implementation can be referred to (TUD, 2012, see also Figure 4-1 above) as well (updated to stay in accordance with current standards).

In principle use is made of the same estimation methods as used for a reduced-dynamic POD. However, there are two important differences, one related to the estimated parameters, and one related to the used observations. For POD-based accelerometer calibration, use is made of a dynamic orbit determination, where only the begin state (position and velocity at epoch) and accelerometer calibration parameters (3 biases for each accelerometer axis, and possibly also scale factors for selected accelerometer axis, at most 3) are estimated on a daily biases (i.e. 24-hr arcs). Thus at most 12 parameters are estimated. The GNSS tracking observations are typically replaced by the kinematic orbit solution serving as a condensed set of the original GNSS observations. Moreover, the accelerometer observations are used to represent the non-gravitational accelerations. Thus, no non-gravitational force models (thermospheric drag, solar radiation pressure, …) are employed.

In the Swarm DISC TOLEOS implementation, use is made of the NASA/GSFC GEODYN software (Pavlis et al., 2006). Detailed descriptions of the GEODYN underlying mathematical algorithms and methods are provided in (McCarthy et al., 2015).

<u>References</u>

Siemes, C., Borries, C., Bruinsma, S., Fernandez-Gomez, I., Hladczuk, N., van den IJssel, J., Kodikara, T., Vielberg, K. and Visser, P. (2023), New thermosphere neutral mass density and crosswind datasets from CHAMP, GRACE, and GRACE-FO, J. Space Weather Space Clim., 13 (16), 1–24, https://doi.org/10.1051/swsc/2023014

TUD (2015), SW-DD-DEOS-GS-0001, Swarm Level 2 Processing System, DEOS Sub-System Architectural Design Document, Rev. 4, 2012-05-15

Pavlis, D., Poulouse, S., and McCarthy, J. (2006), GEODYN operations manual, SGT In., Greenbelt

John J. McCarthy, Shelley Rowton, Denise Moore, Despina E. Pavlis, Scott B. Luthcke, Lucia S. Tsaoussi, updated by: Jennifer W. Beall, GEODYN Systems Description Volume 1, Prepared For: Space Geodesy Branch, Code 926, NASA GSFC, Greenbelt, MD, February 23, 2015 from the original December 13, 1993 document (https://space-geodesy.nasa.gov/techniques/tools/GEODYN/GEODYN.html)

P.N.A.M. Visser and J.A.A.van den IJssel (2016) Calibration and validation of individual GOCE accelerometers by precise orbit determination, J. Geod., 90:1–13, DOI 10.1007/s00190-015-0850-0

4.2. LRI OBSERVATION RESIDUALS

From the nominal LRI/LTI L1b observations the production of the reduced LRI/LTI observations is performed in order to provide pre-fit inter-satellite ranging data after reduction of all known perturbations (Figure 4-2). This process removes (or reduces) from the LRI data those components of the inter-satellite distance variations which are associated with known gravitational variations (static gravity and long-term variations, tides, third-body perturbations), with measured non-gravitational acceleration (from accelerometers) and highly variable mass variations (atmosphere and ocean non-tidal variation).

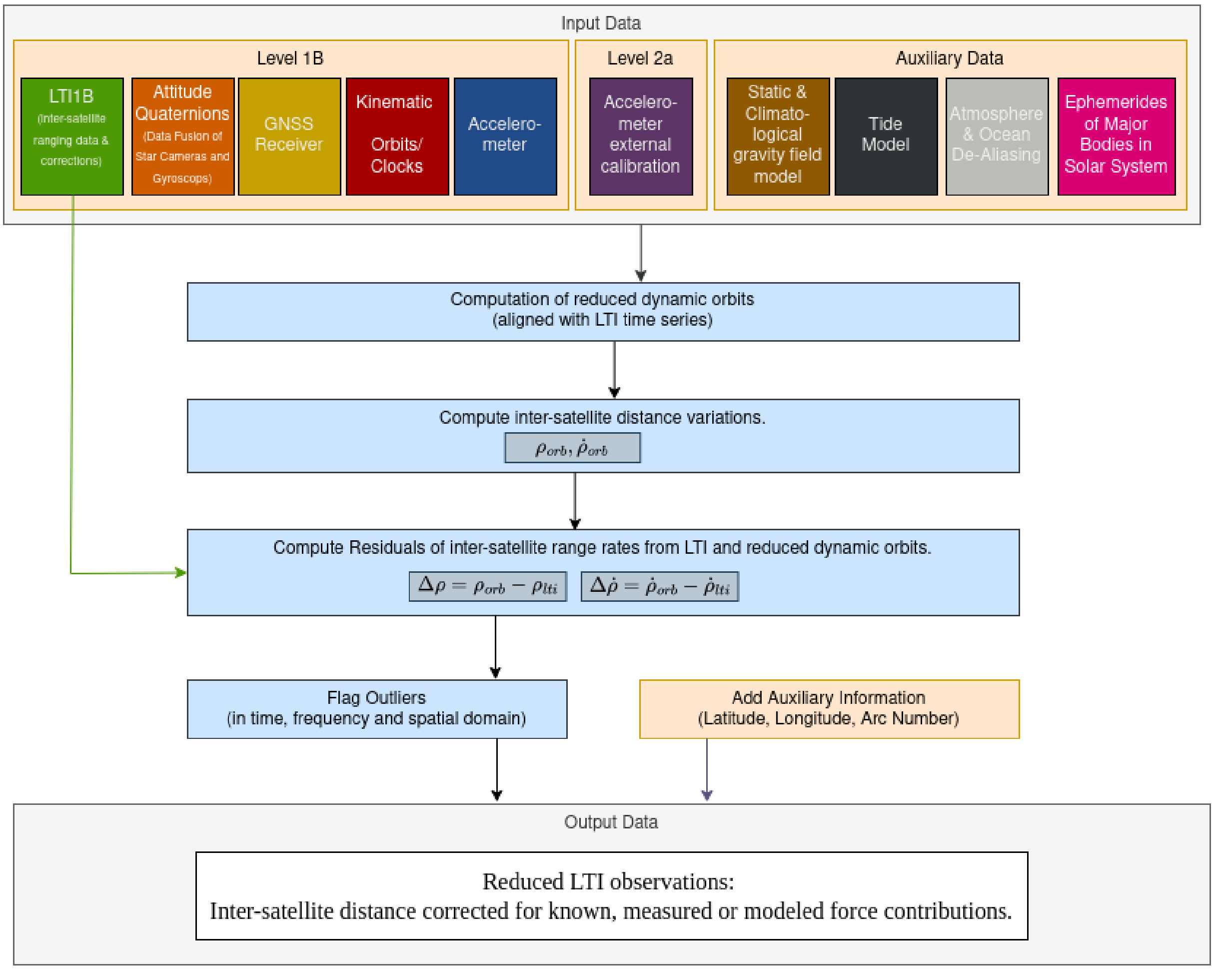

Figure 4-2 Processing scheme to derive Reduced LRI/LTI observations.

Reduced LRI Observations	
Data and Products	
Input L1b Data	▪ Orbit and Clocks L1b products ▪ Combined attitude L1b product ▪ GNSS receiver L1b product ▪ LRI L1b product ▪ Accelerometer L1b product

Input L2a Data	▪ Accelerometer External Calibration L2a Product
Input Aux. Data	▪ Static and climatological gravity field model (e.g. GOCO06S) ▪ Tide model ▪ Atmosphere & Ocean De-Aliasing Product ▪ Ephemerides of major bodies of the Solar system
Output L2a Data	▪ Reduced LRI observations: Inter-satellite distance corrected for known, measured or modelled force contributions
Algorithms and Procedure Description	
It has been recently recognized the untapped information contained in the reduced LRI data (Peidou 2023). The potential to exploit this data can only be achieved with the correct and consistent processing of the GNSS, attitude, accelerometer and LRI data, in combination with state-of-the-art models of tidal and non-tidal forces, which is already done in the context of the traditional gravity inversion process. This product is sometimes called prefit data. It is a complex data processing scheme that is generally not within reach of the general user; therefore, it is important to contemplate the production and dissemination of these data for MAGIC. Due to the high dependency of this product from other L1 products and its position at the end of the processing chain, it is suggested to refer to this product as L2a. The procedure to be applied is identified as follows: (1) Compute a reference reduced-dynamic orbit from all available measurements and models, in the time domain aligned with the LRI data, (2) Compute the difference between the inter-satellite distance derived from the reference orbit and the LRI product, (3) Flag outliers, in the time, frequency and spatial domain, (4) Append auxiliary information, namely latitude, longitude and arc number (one arc being an unbroken set of observations) References Peidou, A., Ellmer, M., Landerer, F., Wiese, D., Spero, R., Science benefits of GRACE-FO along-track data products", IUGG, Berlin 2023	

4.3. GRAVITY FIELD ESTIMATION – TUM

From L1b data sets (LRI, ACC, STR) and L2a data sets (reduced-dynamic and kinematic orbits) gravity field products are estimated, which represent the period of data coverage. Various well established and published techniques are applied and subsequently described. It is mostly referred to reports and publications, where the algorithms are described in detail. Therefore, for most of the processing tasks only procedures are described and references to published literature is provided.

4.3.1. Gravity field processor

The gravity field processor is based on a full-scale numerical mission simulator (Daras 2016; Daras et al. 2015; Hauk 2020), which has already been successfully applied in real data applications to recover satellite-only gravitational field models for CHAMP (Challenging Mini-Satellite Payload), GRACE and GOCE (Yi 2012a, 2012b). It is based on numerical orbit integration following a multistep method (Shampine and Gordon 1975), which applies a modified divided difference form of the Adams-Bashforth-Moulton Predict-Evaluate-Correct-Evaluate (PECE) formulas and local extrapolation. The adopted gravity field approach is based on a modification of the integral equation approach (Schneider 1969; Mayer-Gürr 2006) where the orbit is divided into continuous short arcs of 6 h length. The position vectors at the arc node points are set up as unknown parameters, which are estimated together with the gravity field coefficients. As stochastic observation model, spectral error models of the key instruments (ACC and LRI) are used and propagated (arc-wise) to the combined error model (in terms of full covariance matrices) of the ll-SST observations.

Figure 4-3 shows a schematic overview of the architecture of the TUM gravity field processor/simulator, which is composed of three main parts:

1. Numerical orbit integration
2. Set-up of observation equations and assembling of normal equations
3. Solution of the normal equation system

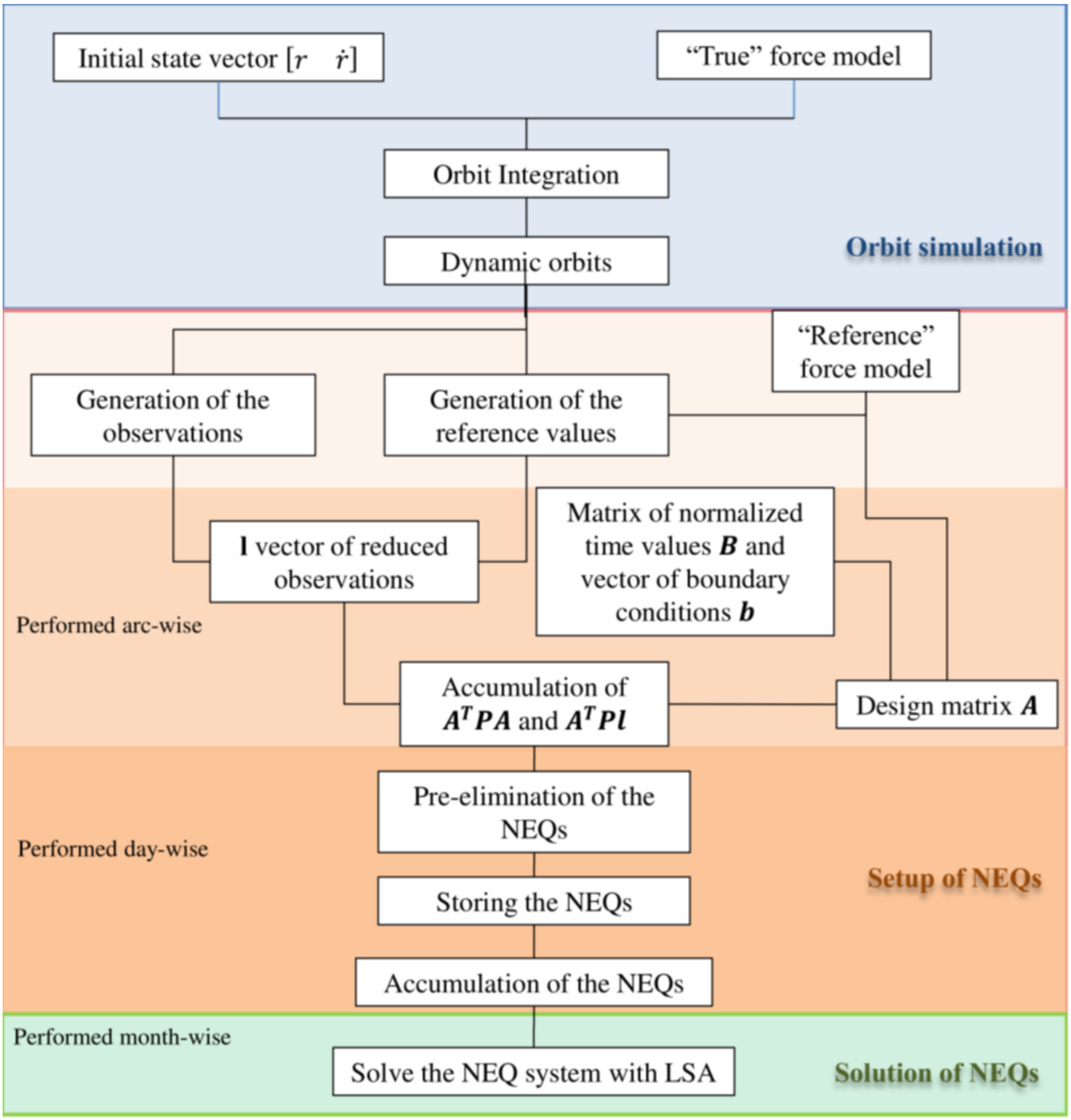

Figure 4-3: Architecture of TUM gravity field processor (from Daras, 2016)

The baseline strategy is based on the parameterization of the initial state vector (per arc), the gravity coefficients (referring to the retrieval period) and some additional conditions. It applies AO de-aliasing on the right-hand side of the NEQs to reduce temporal aliasing. As an option, advanced parameterization and processing schemes, such as the co-estimation of short-term (daily) coefficients, the DMD approach, the co-estimation of ocean tide parameters, but also the stochastic modelling of geophysical background model errors can be applied to reduce temporal aliasing. This enables to avoid a-priori de-aliasing and to estimate the full temporal gravity signal. These options are described in detail in sections 4.3.3 and 4.3.4. Figure 4-4Figure 4-4 shows an overview of the main components and the product flow of the TUM gravity processor including the several options.

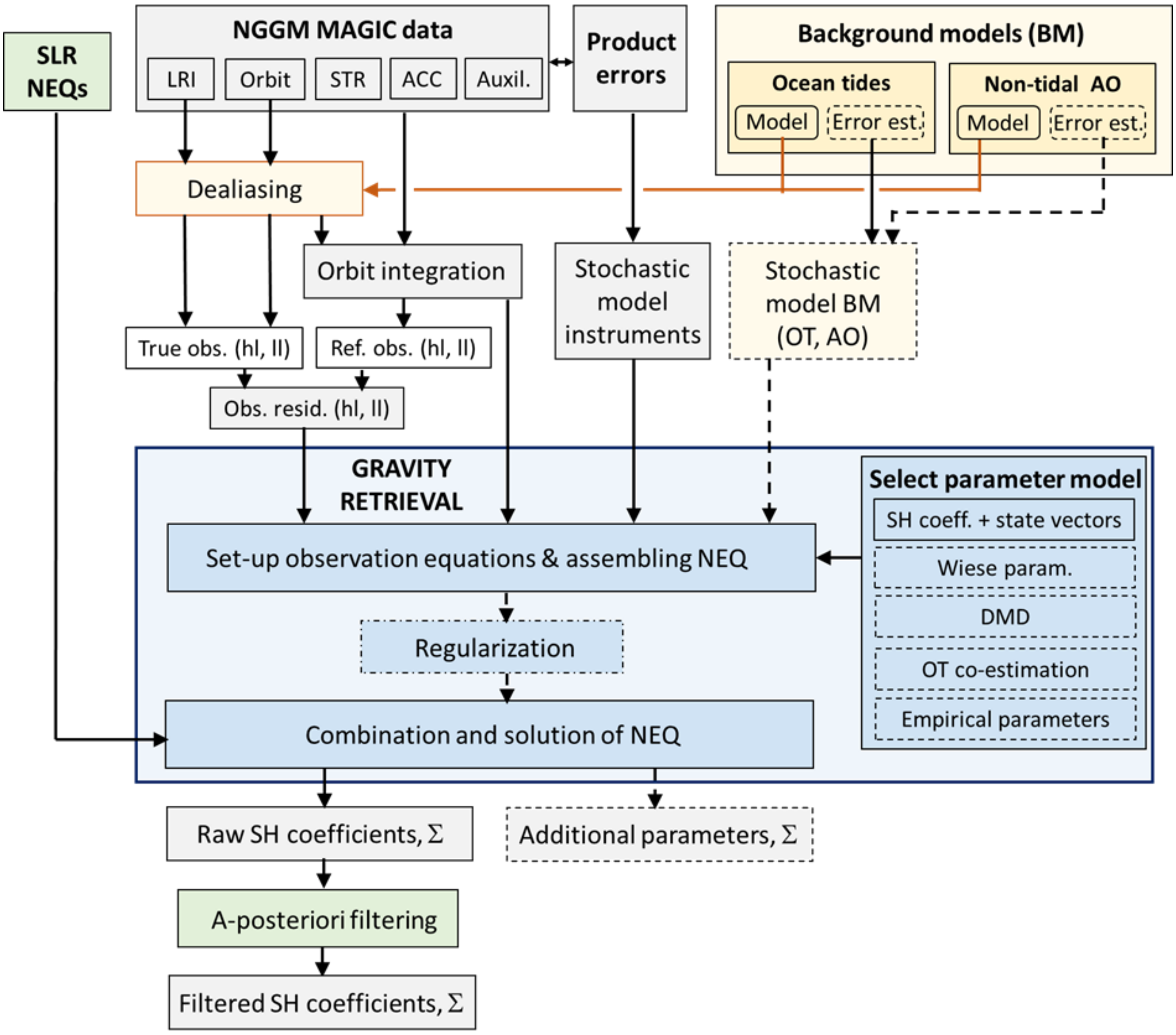

Figure 4-4: Main components and the product flow of the TUM gravity processor. Options are indicated by dashed lines.

<u>It shall be emphasized that precise orbit determination is not part of the TUM processing scheme. Level 1a POD solutions (output of 4.1.1) will be used as observations for the gravity retrieval from HL-SST.</u>

Numerical orbit integration	
Data and Products	
Input L1b Data	▪ LRI L1b product: ll-SST ranging data in terms of range, range-rate or range-acceleration ▪ ACC L1b product ▪ External calibrated ACC measurements ▪ Combined attitude L1b product
Input L2a Data	▪ Reduced-Dynamic and Kinematic Precise Orbit solution
Input Aux. Data	▪ Earth orientation parameters (EOPs) based on GNSS precise science orbit (PSO) determination. The EOPs are transformation parameters containing the nutation, sub-daily polar motion,

	mean pole, polar motion, and universal time (UT) values for the length of day ▪ Earth's static gravity field model in terms of SH ▪ Time-varying a priori gravity field model in terms of SH ▪ Ocean tide model ▪ Atmospheric tides ▪ Non-tidal atmospheric and oceanic mass variations (AOD model) in terms of SH ▪ Solid Earth and pole tides ▪ 3rd body ephemerides ▪ Non-conservative force models for atmospheric drag, solar radiation pressure, and Earth albedo and infrared radiation
Output (internal)	▪ Integrated orbits
Algorithms and Procedure Description	

The approach of gravity field processing requires precise kinematic orbits to be used in a conventional tracking analysis as observations of satellite positions. The dynamic orbits are generated at the first part of the gravity field simulation scheme (Figure 4-3).

The initial state vector defines a solution of the satellite's equation of motion at an initial epoch t_0 and refers to the satellite's center of mass in the CRF. The numerical integration of the equation of motion starting from the initial state vector, provides the position and velocity vector of the satellite at every subsequent epoch t. The orbit integrator follows a multistep method for the numerical integration according to Shampine and Gordon (1975), which applies a modified divided difference form of the Adams Predict-Evaluate-Correct-Evaluate (PECE) formulas and local extrapolation. According to this method, the order and the step size are adjusted to control the local error per unit step in a generalized sense. For detailed information refer to Yi (2012a). The local error thresholds denote the accuracy of the orbit and are selected by the user. They can reach up to 10^{-8} m in an absolute and 10^{-15} m in a relative sense when applying standard double precision processing. In order to further increase the numerical precision a quadruple precision version can be applied (Daras et al. 2015).

The usage of the dynamic orbits in a simulation environment is threefold:

- serving as computational points for the reference values of the observations (geolocation),
- explicitly computing the HL-SST and LL-SST reference values,
- implicitly computing the HL-SST and LL-SST pseudo-observations.

Set-up of observation equations and assembling of normal equations	
Data and Products	
Input L1b Data	▪ ACC L1b product ▪ Combined attitude L1b product ▪ LRI L1b product: ll-SST ranging data in terms of range, range-rate or range-acceleration
Input L2a Data	▪ Reduced-Dynamic and Kinematic Precise Orbit solution
Input Internal Data	▪ State vectors (position, velocity) from previous step (orbit integration)

Input Aux. Data	▪ Information regarding the uncertainty of instruments (ACC, ATT, ll-SST, GNSS) to be introduced in terms of variance-covariance matrices ▪ Earth orientation parameters (EOPs) based on GNSS precise science orbit (PSO) determination. The EOPs are transformation parameters containing the nutation, sub-daily polar motion, mean pole, polar motion, and universal time (UT) values for the length of day ▪ Earth's static gravity field model in terms of SH ▪ Ocean tide model ▪ Atmospheric tides ▪ Non-tidal atmospheric and oceanic mass variations (AOD model) in terms of SH ▪ Solid Earth and pole tides ▪ 3rd body ephemerides ▪ Non-conservative force models for atmospheric drag, solar radiation pressure, and Earth albedo and infrared radiation
Optional Input Aux. Data	▪ Information regarding background model errors (ocean tides, AOD) to be introduced in terms of variance-covariance matrices.
Output Internal Data	▪ Arc-wise NEQ systems for hl-SST and ll-SST observation components.
Algorithms and Procedure Description	

The approach used for gravity field recovery is based on the integral equation approach (Schneider 1969), which was later refined by Mayer-Gürr (2006) and named short-arc approach. The computation of a satellite's orbit can be formulated as a boundary value problem in the form of a Fredholm-type 2 integral equation. The orbit is divided into short arcs and the gravity field coefficients are parametrized together with the boundary point values of each arc. A modification proposed by Yi (2012a) is used, which guarantees the continuity of the orbit by setting up the position vectors at the node points as unknown parameters and estimating them together with the gravity field model. It is therefore directly based on the orbit positions and does not require solving variational equations, thus avoiding numerical errors due to differentiation.

The mathematical model implies a relationship between the orbit positions inside the arc and those at the boundary points, as well as the parameters of the force model to be estimated. The equations of motion in terms of the position of a satellite flying between the boundary points A and B of a short arc, have the form of a Fredholm integral equation of a second kind (Mayer-Gürr 2006). See a detailed description there.

The equation of motion can also be expressed in terms of position differences between two satellites:

$$\mathbf{r}^{12}(\tau) = \mathbf{r}_{A}^{12}(1-\tau) + \mathbf{r}_{B}^{12}\tau - T^2 \int_0^1 K(\tau,\tau')\mathbf{f}^{12}(\mathbf{r}(\tau'))d\tau' \tag{1}$$

where subscripts 1, 2 denote the different satellites, $\mathbf{f}^{12}$ the difference of the specific forces acting on the two satellites and $\mathbf{r}^{12}{}_{A/B}$ the position differences between the two satellites for each boundary point A and B. The velocity differences can be derived by differentiating Eq. (1):

$$\dot{\mathbf{r}}^{12}(\tau) = \frac{1}{T}(\mathbf{r}_B^{12} - \mathbf{r}_A^{12}) - T\int_0^1 \frac{\partial K(\tau,\tau')}{\partial \tau}\mathbf{f}^{12}(\mathbf{r}(\tau'))d\tau' \quad (2)$$

The functional model comprises of a hl-SST (based on kinematic precise orbits) and a ll-SST (based on LRI) component. Eq. (1) is used for the computation of the reference values for the hl-SST part of the observation system. The ll-SST part requires observations that are functionals of the LRI instrument measurements, such as the inter-satellite range, range-rate and range acceleration. The functional model may use those observables individually or totally by taking them all into account.

The reference values for the ll-SST part are derived by projecting Eqs. (1) and (2) into the line-of-sight (LOS) of the two satellites. Projecting the position vector (Eq. (1)) onto the LOS leads to the computation of the inter-satellite range:

$$\rho(\tau) = \| \mathbf{r}^2(\tau) - \mathbf{r}^1(\tau) \| = |\mathbf{e}^{12}(\tau) \cdot \mathbf{r}^{12}(\tau) \quad (3)$$

where $\mathbf{e}^{12}$ is the unit vector at the LOS direction, which is computed from the position vectors of the precise orbits. Accordingly, the projection of the velocity vector (Eq. (2)) into the LOS leads to the computation of the inter-satellite range-rate

$$\dot{\rho}(\tau) = \mathbf{e}^{12}(\tau) \cdot \dot{\mathbf{r}}^{12}(\tau) \quad (4)$$

The functional model for the equations of motion (Eq. (2)) is non-linear. A linearization can be achieved by expanding it into Taylor series and neglecting the higher order terms:

$$\bar{\mathbf{l}} = \mathbf{l}_0 + \left.\frac{\partial \mathbf{f}(\bar{\mathbf{x}}, \bar{\mathbf{y}})}{\partial \bar{\mathbf{x}}}\right|_{x_0} (\bar{\mathbf{x}} - \mathbf{x}_0) + \ldots, \quad (5)$$

resulting in a linearized least-squares adjustment problem in terms of a standard Gauss-Markov model to be solved for the unknown parameters (coefficients). The details of the adjustment system are given in Mayer-Gürr (2006), Yi (2012a) and Daras (2016). In general, the optimum estimate in least-squares sense is achieved by

$$\hat{\boldsymbol{x}} = (\boldsymbol{A}^T\boldsymbol{P}\boldsymbol{A})^{-1}\boldsymbol{A}^T\boldsymbol{P}\boldsymbol{l} \quad (6)$$

In accordance with Figure 4-4, this formulation can be extended to the specifics of the current problem:

$$\hat{\boldsymbol{x}} = \left(\boldsymbol{A}^T[\boldsymbol{\Sigma}_{prod} + \boldsymbol{\Sigma}_{AO} + \boldsymbol{\Sigma}_{OT}]^{-1}\boldsymbol{A} + \alpha\boldsymbol{R}\right)^{-1} \boldsymbol{A}^T[\boldsymbol{\Sigma}_{prod} + \boldsymbol{\Sigma}_{AO} + \boldsymbol{\Sigma}_{OT}]^{-1}(\boldsymbol{l} - \boldsymbol{l}_{REF} - \boldsymbol{l}_{AO} - \boldsymbol{l}_{OT} + \boldsymbol{l}_{reg}) + \boldsymbol{x}_{REF} + \boldsymbol{x}_{AO} + \boldsymbol{x}_{OT} \quad (7)$$

In the baseline processing, $\hat{\boldsymbol{x}}$ is composed only of the gravity field coefficients referring to the retrieval period and arc-wise initial state vectors. In order to reduce to size of the NEQs, the arc-wise parameters of the initial state vectors are pre-eliminated. In addition to the subtraction of the reference observations $\boldsymbol{l}_{REF}$ in the frame of the linearization of the observation equations, atmosphere/ocean (AO) and ocean tide (OT) signals $\boldsymbol{l}_{AO}$ and $\boldsymbol{l}_{OT}$, respectively, are reduced from the right-hand side to reduce temporal aliasing. In the end these reduced signals $\boldsymbol{x}_{REF} + \boldsymbol{x}_{AO} + \boldsymbol{x}_{OT}$ have to be restored to the estimated residual parameter vector to finally obtain $\hat{\boldsymbol{x}}$. The stochastic models in composed only of the VCM of the product errors $\boldsymbol{\Sigma}_{prod}$, while background model errors $\boldsymbol{\Sigma}_{AO}$ and $\boldsymbol{\Sigma}_{OT}$ are assumed to be zero.

Several parameter groups can be co-estimated, such as short-term (daily) gravity field solutions either as direct co-estimation ("Wiese solutions") or in a two-step DMD approach. Additional, OT parameters of selected constituents, or empirical parameters can be co-estimated in addition. These extended parameterization strategies are discussed in section 4.3.4.

Regarding stochastic modelling, in addition to the stochastic models of the instruments represented by the product error VCM $\boldsymbol{\Sigma}_{\boldsymbol{prod}}$ (section 4.3.2), also stochastic models representing errors of non-tidal $\boldsymbol{\Sigma}_{\boldsymbol{AO}}$ and tidal $\boldsymbol{\Sigma}_{\boldsymbol{OT}}$ (section 4.3.3) background models can be adopted optionally.

The normal equation systems are assembled for hl-SST and ll-SST separately for each satellite pair by means of parallel processing up to maximum SH degree n_{max}^{HL} and n_{max}^{LL}, and are stored on a daily basis.

Optionally, a penalty term $\alpha\boldsymbol{R}$ (regularization) is applied (cf. section 4.3.6).

Solution of the NEQ System	
Data and Products	
Input Internal Data	▪ Arc-wise NEQ systems for hl-SST and ll-SST observation components
Output L2a Data	▪ Estimated SH coefficients for pre-redefined retrieval period ▪ Variance-covariance matrix (VCM) of estimated SH coefficients
Optional Output	▪ Estimated short-term (daily) SH gravity field coefficients ▪ VCM of estimated short-term (daily) SH gravity field coefficients ▪ Estimated OT model updates ▪ VCM of estimated OT model updates ▪ Estimated empirical parameters ▪ VCM of estimated empirical parameters
Algorithms and Procedure Description	
Before solving the total NEQ system, the NEQs related to the two observables are summed up and combined for all satellite pairs. If in the ideal case a correct stochastic modelling of these two systems was used, the individual systems do not have to be reweighted during combination. Otherwise, empirically or statistically (variance component estimation) derived weighting factors have to be applied during the linear combination. For the sake of efficiency, the initial state vector parameters per arc are pre-eliminated from the NEQ system at daily basis after accumulation of the NEQs (but can be recovered by re-substitution in the end if needed). The dimension of the NEQ system is then reduced significantly, resulting in a more rapid inversion of the final normal matrix when solving for the gravity field parameters. This is especially true when extended parameterization schemes (section 4.3.4) are applied. As an example, for the method proposed by Wiese et al. (2011), where low resolution gravity fields are co-parameterized at short time intervals (e.g. 1 day) to reduce temporal aliasing errors, low resolution gravity field parameters to be estimated are pre-eliminated as well, which can be retrieved by means of back-substitution	

after solving the NEQ system for the longer-term gravity field parameters (Daras 2016, Hauk 2020).

In case of NGGM-only solutions based on the inclined pair, regularization (section 4.3.6) has to be applied additionally to ensure numerical stability of the following inversion. In the last step, the system is solved through Cholesky decomposition.

Due to linearization measures, eventually the 'reference' values derived from the 'reference' gravity field models have to be added to the estimated SH coefficients. The inverse of the NEQs delivers the parameter VCM.

<u>References</u>:

Daras I., Pail R., Murböck M., Yi W. (2015). Gravity field processing with enhanced numerical precision for LL-SST missions. J. Geod. 2015, 89 (2), 99-110. http://dx.doi.org/10.1007/s00190-014-0764-2

Daras, I. (2016). Gravity Field Processing Towards Future LL-SST Satellite Missions. Dissertation, Technische Universität München, Munich, Germany, 2016, DGK Series C, Dissertation No. 770, Verlag der Bayerischen Akademie der Wissenschaften, pp. 23-39. ISBN(Print) 978-3-7696-5182-9, ISSN 0065-5325. https://dgk.badw.de/fileadmin/user_upload/Files/DGK/docs/c-770.pdf

Daras I., Pail, R. (2017). Treatment of temporal aliasing effects in the context of next generation satellite gravimetry missions. J. Geophys. Res., 122(9), 7343-7362, https://doi.org/10.1002/2017JB014250

Hauk M. (2020). Simulation Studies for Gravity Field Retrieval in the context of a Next Generation Satellite Gravity Mission. Dissertation, TU München. https://mediatum.ub.tum.de/doc/1545436/1545436.pdf

Mayer-Gürr T. (2006). Gravitationsfeldbestimmung aus der Analyse kurzer Bahnbögen am Beispiel der Satellitenmissionen CHAMP und GRACE. Dissertation, Univ. Bonn. https://bonndoc.ulb.uni-bonn.de/xmlui/bitstream/handle/20.500.11811/1391/SR_09_Mayer-G%c3%bcrr.pdf?sequence=1&isAllowed=y

Schneider, M. Outline of a general orbit determination method. In Space Research IX, Proceedings of the Open Meetings of Working Groups (OMWG) on Physical Sciences of the 11th Plenary Meeting of the Committee on Space Research (COSPAR), Tokyo, Japan; Mitteilungen aus dem Institut für Astronomische und Physikalische Geodäsie, Nr. 51; Champion, K.S.W., Smith, P.A., Smith-Rose, R.L., Eds.; North Holland Publ. Company: Amsterdam, The Netherlands, 1969; pp. 37–40.

Shampine L.F., Gordon M.K. (1975). Computer solution of ordinary differential equations: the initial value problem. W.H. Freeman, San Francisco.

Wiese D.N., Visser P.N.A.M., Nerem S. (2011). Estimating low resolution gravity fields at short time intervals to reduce temporal aliasing errors. Adv. Space Res., 48(6), 1094-1107. https://doi.org/10.1016/j.asr.2011.05.027

Yi W. (2012a). The Earth's gravity field from GOCE. Dissertation, TU München. https://mediatum.ub.tum.de/doc/1091412/document.pdf

Yi W. (2012b). An alternative computation of a gravity field model from GOCE. Advances in Space Research 50(3), 371-384, https://doi.org/10.1016/j.asr.2012.04.018

4.3.2. Stochastic Modelling of Product Errors

The TUM gravity field processor presented in section 4.3.1 requires the knowledge of the covariance information Σ_{prod} for the ll-SST and hl-SST observation groups. For ll-SST, the LRI and the ACC product errors are the dominant drivers for the aggregated observation noise. It is assumed that validated spectral error information in terms of amplitude spectral densities (ASDs) or power spectral densities (PSDs) are available from these instruments (from industry and/or from in-situ validation). Based on these models, ll-SST observation covariances can be obtained by means of error propagation. For hl-SST, the accuracy information from the kinematic L2a orbits is used directly, either with covariance information (if provided) or without (if not provided).

Generation of Variance-Covariance Matrices for Product Errors (ll-SST)	
Data and Products	
Input Aux. Data	▪ Amplitude spectral densities of ll-SST and ACC
Output Internal Data	▪ Variance-covariance matrix for ll-SST observations
Algorithms and Procedure Description	

For the LRI and ACC, the individual spectral models are assumed to be provided in terms amplitude spectrum densities (ASDs). From these ASDs, individual random noise frequency series $x_i^F(f)$ can be generated by multiplying the appropriate ASD $\sqrt{S_{xx\,(i)}(f)}$ with a random normally distributed (white noise) frequency series $w_i(f)$. Applying a discrete Fourier transform A_{DFT}, these noise frequency series can eventually be transformed to a noise time series $x_i^T(t)$ of the respective instrument (in a discretized form, see, e.g., Etten 2006):

$$\underline{x_i^T} = \mathrm{A}_{DFT}\, \underline{x_i^F} \qquad (1)$$

Since the PSD $S_{xx\,(i)}(f)$ (square of ASD) represents the (co-)variance of the generated noise frequency series $x_i^F(f)$ and the Fourier transform is linear, the covariance of the noise time series can be obtained by error propagation:

$$\Sigma_{x_i^T x_i^T} = \mathrm{A}_{DFT}\, \Sigma_{x_i^F x_i^F}\, \mathrm{A}'_{DFT} = \mathrm{A}_{DFT}\, \mathrm{S}_{xx\,(i)}\, \mathrm{A}'_{DFT}. \qquad (2)$$

If the samplings are equidistant, this error propagation can be efficiently calculated through a discrete cosine transform. By making use of the functional model described in section 4.3.1, the individual covariances of the different instruments (LRI and ACC) can be combined into the final covariance (Σ_{prod}) of the line-of-sight observation (by means of another error propagation of the ACC covariances). Since the short-arc approach is used, only observations within a single arc (e.g., 6hours) need to be considered within Σ_{prod} which limits the computational effort when handling full covariance matrices.

References:

Etten, W. (2006). Introduction to Random Signals and Noise. OCLC: ocm61859925. John Wiley & Sons. 255 pp. ISBN: 978-0-470-02411-9

4.3.3. Stochastic modelling of Background Model Errors

Errors from background models are the main error contributor to the total error budget of the estimated time-varying gravity fields and are one of the main reasons for the typical striping errors. Since usually two main external geophysical models, the non-tidal atmosphere and ocean (AO) models and the ocean tide (OT) models are used for de-aliasing, i.e. application of reduction time series to the right-hand side of the NEQ according to eq. (7). These models are provided by external groups. The stochastic modelling of background model errors, and its interplay with stochastic modelling and extended parameterization schemes, is an ongoing research topic.

Stochastic modelling of Ocean Tide Background Model Errors	
Data and Products	
Input Internal Data	▪ Arc-wise NEQ systems for hl-SST and ll-SST observation components including the parameterization with respect to ocean tide parameters.
Input Aux. Data	▪ Variance-covariance matrices for tidal constituents.
Output L2a Data	▪ Estimated SH gravity field parameters. ▪ VCM of estimated gravity field parameters
Algorithms and Procedure Description	

The variance-covariance information from ocean tide models is introduced by means of explicit error VCMs for the in-phase and quadrature signal of each tidal constituent. These VCMs are assumed to be uncorrelated between different tidal constituents as well as between the in-phase and quadrature signal of any single tidal constituents. The error information is then propagated from the background model (BM) level onto the level of observations according to

$$\boldsymbol{\Sigma}_{\boldsymbol{OT}(\boldsymbol{obs})} = \boldsymbol{A}\boldsymbol{\Sigma}_{\boldsymbol{OT}(\boldsymbol{BM})}\boldsymbol{A}^{\boldsymbol{T}}. \qquad (1)$$

In the equation above, $\boldsymbol{\Sigma}_{\boldsymbol{OT}(\boldsymbol{BM})}$ denotes the combined in-phase and quadrature VCMs of the OT model's individual tidal constituents and $\boldsymbol{\Sigma}_{\boldsymbol{OT}(\boldsymbol{obs})}$ the resulting co-variance matrix of observations. $\boldsymbol{A}$ denotes the design matrix, i.e. the functionals, required to transfer the model coefficients to the hl-sst and ll-sst observations, respectively, in terms of ranges and/or range-rates. The set-up of $\boldsymbol{\Sigma}_{\boldsymbol{OT}(\boldsymbol{obs})}$ is carried out consecutively for each observation arc. Since the design matrix is given for each individual tidal constituent, all $\boldsymbol{\Sigma}_{\boldsymbol{OT}(\boldsymbol{obs})}$ related to an individual tidal constituent must be stacked together to obtain the complete co-variance matrix of hl- and ll-sst observations. Note that $\boldsymbol{\Sigma}_{\boldsymbol{OT}(\boldsymbol{BM})}$ is generally given in full form up to d/o 30 or 60, so $\boldsymbol{A}$ must be truncated to the same d/o. Alternatively, it is also possible to expand $\boldsymbol{\Sigma}_{\boldsymbol{OT}(\boldsymbol{BM})}$ by variances above this d/o.

The complete $\boldsymbol{\Sigma}_{\boldsymbol{OT}(\boldsymbol{obs})}$ is then stacked to $\boldsymbol{\Sigma}_{\boldsymbol{prod}}$, i.e. the co-variance matrix representing the stochastics of the product noise, and the resulting co-variance matrix employed in the set-up of NEQ systems, which are stacked over all processing arcs and then solved.

References:

Abrykosov P, Sulzbach R, Pail R, Dobslaw H, Thomas M (2021): Treatment of ocean tide background model errors in the context of GRACE/GRACE-FO data processing. Geophys. J. Int. 228 (3), 1850-1865, doi: https://doi.org/10.1093/gji/ggab421

Stochastic modelling of AO Background Model Errors	
Data and Products	
Input Internal Data	▪ Arc-wise NEQ systems for hl-SST and ll-SST observation components including the parameterization with respect to ocean tide parameters.
Input Aux. Data	▪ Variance-covariance matrices for the AOD error model component.
Output L2a Data	▪ Estimated SH gravity field parameters ▪ VCM of Estimated SH gravity field parameters
Algorithms and Procedure Description	

The variance-covariance information from the AOD error component is introduced in a similar fashion as the OT error VCM:

$$\boldsymbol{\Sigma}_{\boldsymbol{AOD(obs)}} = \boldsymbol{A}\boldsymbol{\Sigma}_{\boldsymbol{AOD(BM)}}\boldsymbol{A}^{\boldsymbol{T}}. \qquad (1)$$

In the equation above, $\boldsymbol{\Sigma}_{\boldsymbol{AOD(BM)}}$ denotes the co-variance information of all X-hourly (usually 6-hourly) AOD model samples within a given processing arc. No correlations are assumed between consecutive model samples. $\boldsymbol{A}$ denotes the design matrix, i.e. the functionals, required to transfer the model coefficients to the hl-sst and ll-sst observations, respectively, in terms of ranges and/or range-rates. $\boldsymbol{\Sigma}_{\boldsymbol{AOD(obs)}}$ is the resulting co-variance matrix of observations for a given processing arc. Note that $\boldsymbol{\Sigma}_{\boldsymbol{AOD(BM)}}$ is generally given in full form up to d/o 30 or 60, so $\boldsymbol{A}$ must be truncated to the same d/o. Alternatively, it is also possible to expand $\boldsymbol{\Sigma}_{\boldsymbol{AOD(BM)}}$ by variances above this d/o.

Generally, linear interpolation is used to obtain AOD model values between two neighboring model samples. In order to exploit the full benefit of stochastic modelling of the AOD errors, it is crucial to keep the interpolation functionals in the functional model, i.e. in $\boldsymbol{A}$, instead of carrying out the linear interpolation on the level of AOD model samples (as is done in GRACE/GRACE-FO data processing). This approach allows one to retain correlations between all observations of AOD sample X and X+2 in $\boldsymbol{\Sigma}_{\boldsymbol{AOD(obs)}}$, whereas the classic method would yield a strictly diagonal $\boldsymbol{\Sigma}_{\boldsymbol{AOD(obs)}}$.

The complete $\boldsymbol{\Sigma}_{\boldsymbol{AOD(obs)}}$ is then stacked to $\boldsymbol{\Sigma}_{\boldsymbol{prod}}$, i.e. the co-variance matrix representing the stochastics of the product noise, and the resulting co-variance matrix employed in the set-up of NEQ systems, which are stacked over all processing arcs and then solved.

4.3.4. Extended parameterization strategies

Extended parameterization strategies aim at a better space-time parameterization of the measured time-variable gravity field signal. The two main signals causing temporal aliasing are high-frequency atmosphere/ocean (AO) and ocean tide (OT) signals. They have a very different behavior and therefore require also a different parameterization strategy. On the one hand, due to their distinct excitation frequencies, the corresponding amplitudes and phases of OT can be parameterized directly, leading to modified OT model parameters, which can be used in a second step as improved de-aliasing model (Hauk et al. 2018). This method requires, depending on the chosen OT constituents to be parameterized the extended parameter model, a certain amount of data, in order to decorrelate OT constituents with a very similar excitation frequency. On the other hand, a whole range of excitation frequencies exists for AO signals. Therefore, by means co-estimated short-term (e.g., daily) gravity field solutions as much signal as possible shall be parameterized, in order to avoid their aliasing into the longer-term solutions. The resolvable maximum SH degree if these short-term solutions is mainly limited by the spatial ground-track coverage during this short period. The first method, also called 'Wiese parameterization', goes back to Wiese et al. (2011), and was extensively investigated, e.g., by Daras et al. (2017). The second method is denoted as 'data driven multi-step self-de-aliasing (DMD) approach' and was developed by Abrykosov et al. (2022). Both methods enable to retrieve the full AOHIS signal without the need for a priori AO dealiasing.

Extended parameter model: Wiese Parameterization	
Data and Products	
Input Internal Data	▪ Arc-wise NEQ systems for hl-SST and ll-SST observation components.
Output L2a Data	▪ Estimated SH coefficients (longer-term) ▪ VCM of estimated SH coefficients ▪ Co-estimated short-term SH coefficients ▪ VCM of co-estimated short-term SH coefficients
Algorithms and Procedure Description	
According to the Wiese method, low-resolution (e.g. up to SH d/o 15 to 25) gravity field parameters are co-estimated at short time intervals (e.g. daily) together with the higher-resolution gravity field which is sampled at a longer time interval (Wiese et al. 2011, Daras and Pail 2017). This allows the consideration of high-frequency information contained in the short-term gravity field solutions with the goal to reduce the temporal aliasing effect of those long-wavelength geophysical signals that have a period larger than twice the chosen sampling period of the short-period gravity field modelling. Starting from the arc-wise generated NEQ systems for hl-SST and ll-SST, both observation components are accumulated on an arc-wise basis for the short-term period (1 day). In the next step, the short-term (daily) parameters are pre-eliminated. This procedure is repeated for all days covering the retrieval period. By this, the pre-eliminated NEQs are accumulated to the long-term interval. Then the higher-degree system is solved in accordance with eq. (7) (see: Set-up of observation equations and assembling of normal equations), and the short-term (daily) parameters are retrieved by back re-substitution in a second step. All processes are accompanied with a rigorous error propagation in order to deliver the VCMs of the respective parameter groups. Finally, the low-degree part of the long-term field is obtained by the weighted average of all low-degree short-term parameters.	

Extended parameter model: Application of the DMD approach	
Data and Products	
Input Internal Data	▪ Arc-wise NEQ systems for hl-SST and ll-SST observation components.
Output L2a Data	▪ Step 1: Estimated SH short-term coefficients ▪ Step 1: VCM of e stimated SH short-term coefficients

	▪ Step 2: Estimated interval SH coefficients ▪ Step 2: VCM of estimated interval SH coefficients
Algorithms and Procedure Description	

Similar to the Wiese approach, the strategy of the DMD method is to capture the short-periodic long-wavelength signals, which are predominantly related to the time-variable AO component, within the interval fields and thus prevented from manifesting as temporal aliasing effects within the long-term solution (Abrykosov et al. 2022).

The gravity field observations are split into intervals of, e.g., one day for which individual low-resolution gravity fields up to a certain harmonic degree are estimated, disregarding the fact that the observations contain also high-degree signals and thus allowing for a certain amount of spectral leakage. Treating the latter prior to the estimation of the interval fields is crucial, as otherwise the entirety of the corresponding signal would be parametrized into the low-degree spectrum, thus inducing a large-scale error. Therefore, its short-wavelength components are reduced and retain the low-degree part, i.e. the estimation of the interval fields is done while fixing the high-degree spectrum to a specific gravity field. The fixing of the high-degree spectrum can be done either using the static background field model or using a post-processed time-varying gravity field model including the time period to be estimated. For the latter, a nominal gravity field solution (L2a) needs to be processed at first. The estimation of the interval fields is done by accumulating the manipulated arc-wise NEQ systems for hl-SST and ll-SST and solving the systems using the known equation (7) (see: Set-up of observation equations and assembling of normal equations). This defines the first step of the DMD approach.

In the second step, these stand-alone gravity solutions for the respective interval are further used to compute reference observations which are reduced in a subsequent step from the original ones. The introduction of these interval fields is done at the a priori orbit generation step (cf. table 'Generation of a priori orbits') serving as further de-aliasing product. Based on the 'updated' reduced observations a long-term, e.g. monthly, solution is estimated and, in a final step, restored to the mean of the interval estimates to the low degrees of the long-term solution. In fact, the latter is done in an alternative approach, where the interval fields' mean value is computed already after the estimation of the short-term interval fields and already restored to them instead of restoring the low degrees of the long-term solution, so that the reference observations used for the de-aliasing step are only comprised of variations with respect to the total signal's long-term mean.

Extended parameter model: Ocean Tides	
Data and Products	
Input Internal Data	▪ Arc-wise NEQ systems for hl-SST and ll-SST observation components.
Output L2a Data	▪ Step 1: Improved OT model coefficients ▪ Step 1: VCM of improved OT model coefficients ▪ Step 2: Estimated SH coefficients ▪ Step 2: VCM of estimated SH coefficients
Algorithms and Procedure Description	

Ocean tide models are usually represented by global in-phase grids A_ν (tidal elevations at a certain phase $\phi = 0$) and quadrature grids B_ν (tidal elevations at a certain phase $\phi = \pi/2$). The tidal height at a position $P(\theta, \lambda)$ can then be expressed as

$$\zeta(\theta,\lambda) = \sum_{\nu} f_{\nu}[A_{\nu}(\theta,\lambda)\cos(\chi_{\nu}+u_{\nu}) + B_{\nu}(\theta,\lambda)\sin(\chi_{\nu}+u_{\nu})] \quad [1]$$

where f_{ν} and u_{ν} are nodal modulation terms (for each constituent ν) stemming from the precession of the lunar node, and χ_{ν} is the astronomical argument.

The in-phase and quadrature grids can be expressed by a SH series expansion and yield

$$\begin{Bmatrix} A_{\nu}(\theta,\lambda) \\ B_{\nu}(\theta,\lambda) \end{Bmatrix} = \frac{R}{3}\frac{\rho_e}{\rho_w}\frac{2n+1}{1+k'_n}\sum_{n}\sum_{m}\left(\begin{Bmatrix} a_{nm,\nu} \\ c_{nm,\nu} \end{Bmatrix} cosm\lambda + \begin{Bmatrix} b_{nm,\nu} \\ d_{nm,\nu} \end{Bmatrix} sinm\lambda\right)\overline{P}_{nm}(cos\theta) \quad [3]$$

The advantage of this formulation is the linearity of the observation equation regarding the OT parameters, as $\{a,b,c,d\}_{\nu}$ can be transformed to Stokes' coefficients representing the Earth's gravitational potential at each epoch according to

$$\begin{Bmatrix} \Delta\overline{C}_{nm}^{OT} \\ \Delta\overline{S}_{nm}^{OT} \end{Bmatrix} = \sum_{\nu} f_{\nu}\left[\begin{Bmatrix} a_{nm,\nu} \\ b_{nm,\nu} \end{Bmatrix}\cos(\chi_{\nu}+u_{\nu}) + \begin{Bmatrix} c_{nm,\nu} \\ d_{nm,\nu} \end{Bmatrix}\sin(\chi_{\nu}+u_{\nu})\right] \quad [4]$$

The parameter vector can be extended by OT parameters $\{a,b,c,d\}_{\nu}$ of pre-defined constituents, as global parameters covering the complete analysis period. In Hauk and Pail (2018) the four principal diurnal (Q1, O1, P1, K1) and the four semi-diurnal tidal constituents (N2, M2, S2, K2) were parameterized together.

Depending on the selection of the constituents, a certain minimum time-span of data is required in order to separate individual constituents, especially those with very close excitation frequencies. Therefore, this extended parameterization is not applicable to fast-track applications.

With the inclusion of stochastic modelling of product errors, it is intended to the best possible extent to avoid the co-estimation of "empirical parameters" (Daras and Pail 2017). Still there are might be effects which cannot be adequately handled by this strategy, such as ACC biases, which therefore have to be adopted as empirical parameters.

Extended parameter model: Empirical Parameters	
Data and Products	
Input Internal Data	▪ Arc-wise NEQ systems for hl-SST and ll-SST observation components.
Output L2a Data	▪ Estimated SH coefficients (longer-term) ▪ VCM of estimated SH coefficients
Output (internal)	▪ Co-estimated empirical parameters ▪ VCM of co-estimated empirical parameters
Algorithms and Procedure Description	
Empirical parameters referring to arc-wise, daily or longer-term (global) effects are adopted and are extending the parameter model. Depending on their period of validity, parameter elimination can be applied to avoid the excessive increase in dimension of the NEQ matrix. If needed, they can be re-computed in a second step by parameter re-substitution.	

References:

Abrykosov P., Murboeck M., Hauk M., Pail R., Flechtner F. (2022). Data-driven multi-step self-de-aliasing approach for GRACE and GRACE-FO data processing. Geophys. J. Int., 232, pp. 1006-1030. https://doi.org/10.1093/gji/ggac340.

Daras I., Pail, R. (2017). Treatment of temporal aliasing effects in the context of next generation satellite gravimetry missions. J. Geophys. Res., 122(9), 7343-7362, https://doi.org/10.1002/2017JB014250.

Hauk M., Pail R. (2018). Treatment of ocean tide aliasing in the context of a next generation gravity field mission. Geophys. J. Int., 214 (1), 345-365, https://doi.org/10.1093/gji/ggy145

Wiese, D.N., Visser, P.N.A.M., Nerem, S. (2011). Estimating low resolution gravity fields at short time intervals to reduce temporal aliasing errors. Adv. Space Res., 48(6), 1094-1107. https://doi.org/10.1016/j.asr.2011.05.027.

4.3.5. De-Aliasing strategies

The de-aliasing strategies can be subdivided into four groups:

- Nominal strategy: using time varying gravity field background models for de-aliasing purposes (ocean tide model, AOD model).
- Using time varying gravity field background models (ocean tide model, AOD model) and variance-covariance information from background model errors (OTVCM, AODVCM).
- Using extended parameterization techniques without background models.
- Using extended parameterization techniques together with background models.

In the following, the processing procedure of the four different groups will be illustrated schematically.

Nominal De-Aliasing with Background Models	
Data and Products	
Input Aux. Data	▪ Ocean tide model. ▪ Non-tidal atmospheric and oceanic mass variations (AOD model) in terms of SH.
Output L2a Data	▪ Estimated SH gravity field parameters.
Algorithms and Procedure Description	
Nominally, time-varying background models representing ocean tides and non-tidal AO signals are used for de-aliasing purposes. The primary goal is to retrieve the time-varying HIS signal. Therefore, errors due to ocean tides and non-tidal AO signals shall be kept as small as possible. The processing scheme follows the description in the tables ‘NEQ system setup’ and ‘Solution of the NEQ system’. References: Dahle, C., Murboeck, M., Flechtner, F., Dobslaw, H., Michalak, G., Neumayer, K.H., et al. (2019) The GFZ GRACE RL06 Monthly Gravity Field Time Series: Processing Details and Quality Assessment. *Remote Sensing, 11(8)*, 2116. https://doi.org/10.3390/rs11182116	

De-aliasing with Variance-Covariance Information from Background Model Errors	
Data and Products	
Input Aux. Data	▪ Ocean tide model. ▪ Non-tidal atmospheric and oceanic mass variations (AOD model) in terms of SH.
Input Internal Data	▪ Variance-covariance matrices for tidal constituents. ▪ Variance-covariance matrices for the AOD error model component.
Output L2a Data	▪ Estimated SH gravity field parameters.
Output Aux. Data	▪ Co-estimated SH ocean tide parameters.
Algorithms and Procedure Description	
Next to the nominally time-varying background models representing ocean tides and non-tidal AO signals nominally used for de-aliasing purposes, variance-covariance information from background model errors is introduced in terms of constrained matrices. The processing scheme follows the description in the tables 'Application of variance-covariance matrices from ocean tide models' and 'Application of variance-covariance matrices based on the AOD error model component'.	

De-Aliasing using Extended Parameterization Techniques without Background Models	
Data and Products	
Input Aux Data	▪ Ocean tide model.
Optional Input Data	▪ Variance-covariance matrices for tidal constituents.
Output L2a Data	▪ Estimated SH gravity field parameters (L2A) including the full AOHIS signal.
Optional Output	▪ Co-estimated SH ocean tide parameters.
Algorithms and Procedure Description	
This processing scheme uses extended parameterization techniques without applying an AOD model. The introduction of an ocean tide de-aliasing model is mandatory. Therefore, variance-covariance information from ocean tide model errors can be introduced, additionally, following the procedure in the table 'Application of variance-covariance matrices from ocean tide models'. Possible extended parameterization techniques to be applied are described in the tables 'Application of the Wiese parameterization' and 'Application of the DMD approach'. These methods aim to reduce the aliasing error due to AO error signals while estimating the total AOHIS signal content.	

De-Aliasing using Extended Parameterization Techniques with Background Models	
Data and Products	
Input Aux. Data	▪ Ocean tide model. ▪ Non-tidal atmospheric and oceanic mass variations (AOD model) in terms of SH.
Optional Input Data	▪ Variance-covariance matrices for tidal constituents.
Output L2a Data	▪ Estimated SH gravity field parameters (L2A) including the HIS signal.

Optional Output	▪ Co-estimated SH ocean tide parameters.
Algorithms and Procedure Description	
This processing scheme uses extended parameterization techniques while applying an AOD model. The introduction of an ocean tide de-aliasing model is mandatory. Therefore, variance-covariance information from ocean tide model errors can be introduced, additionally, following the procedure in the table 'Application of variance-covariance matrices from ocean tide models'. Possible extended parameterization techniques to be applied are described in the tables 'Application of the Wiese parameterization' and 'Application of the DMD approach'. As already stated in the previous table, these methods aim to reduce the aliasing error due to AO error signals. The purpose of using both, an AOD model and an extended parameterization technique, is to further reduce the aliasing error due to A and O.	

4.3.6. Regularization and constraints

In general, gravity field processing schemes do not need regularization or additional constraints as long as at least one polar pair is part of the solution, i.e. global coverage which observations is given. For inclined-pair only solutions such as NGGM, regularization is needed to account for the numerical instability resulting from the missing observations in the polar cap regions, making the underlying zonal and near-zonal SH base functions strongly correlated. As developed for the case of the sun-synchronous orbit of GOCE, also for NGGM-only a dedicated "polar cap" regularization strategy (Metzler and Pail 2005) suggests itself, which puts a constraint only to those coefficients which are affected by the polar gap.

Polar Cap Regularization	
Data and Products	
Internal Input Data	▪ Arc-wise NEQ systems for hl-SST and ll-SST observation components based on inclined pair (NGGM) measurements
Output L2a Data	▪ Estimated SH coefficients (L2A) based on the applied regularization method ▪ VCM (in terms of MSE matrix) of estimated SH coefficients
Algorithms and Procedure Description	
Based on the accumulated hl-SST and ll-SST normal equations, an additional constraint in terms of a spherical cap regularization is applied. To stabilize the inversion of the ill-conditioned NEQ system, the penalty term $\alpha\boldsymbol{R}$ is applied to the NEQs (cf. eq. (7) in table 'Set-up of observation equations and assembling of normal equations'). Metzler and Pail (2005) suggests to set-up the spherical regularization matrix $\boldsymbol{R}$ by an analytical formulation in space domain via a Gram matrix or singular value decomposition. Its discrete equivalent, by means of setting up the normal equations for a certain gravity functional exclusively in the polar areas, performs in a very similar way. An alternative approach in spectral domain is based on the fact that the polar gaps affect only a group of zonal and near-zonal coefficients. Following van Gelderen and Koop (1997), the maximum affected SH order m_{max} for each SH degree n is given by $$m_{max} \approx \left\|\frac{\pi}{2} - I\right\| \cdot n, \qquad (1)$$	

with the inclination I. Based on this rule, the diagonal elements of the regularization matrix ***R*** can be defined as (Rexer M. 2012):

$$r_{ii} = \begin{cases} n^4(m_{max} - m)^p, m \leq m_{max} \\ 0, otherwise \end{cases}. \qquad (2)$$

The term $(m_{max} - m)^p$ describes an order-dependent weighting where the regularization is strongest for lower orders and reduces the regularization strength as the order increases. The optimal regularization factor α is found by setting $p = 1$.

The regularization parameter α defines the strength of the constraint. In simulation, its optimum value can be found by comparing a variety of regularized solutions against the true field, and search for the solution which minimizes the difference to the true one. Applied to real data (when the true field is not known), tuning approaches such as the L-curve method can be applied. As a side condition, the regularization shall be weak enough in order not to cause a significant alteration of the solution over the areas covered by observations. It can be shown that the approaches in spatial and spectral domain lead to very similar results. As a baseline, the approach in space domain is applied.

Usually, the right-hand side l_{reg} (Eq. (7) in table 'Set-up of observation equations and assembling of normal equations') is zero, i.e. the solution is constrained towards a zero signal over the poles. Alternatively, the solution could also be constrained against a given gravity field signal, e.g. the field of a polar-pair only solution. In this case, the regularization can be interpreted as a parameter adjustment with prior information. This strategy was also investigated to force a double-pair (MAGIC) solution towards the single-pair solution in the polar areas, in the case that there are indications that the double-pair solution performs worse there.

The solution of the total regularized NEQ system is done via equation (7) in table 'Set-up of observation equations and assembling of normal equations'.

References:

Metzler B., Pail R. (2005). GOCE data processing: the spherical cap regularization approach. Studia Geophysica et Geodaetica, 49(4):441–462, https://doi.org/10.1007/s11200-005-0021-5.

Rexer, M. (2012) Time-variable Gravity Field: contributions of GOCE Gradiometer Data to Monthly and Bi-Monthly GRACE Gravity Field Estimates. Master's Thesis. Technical University of Munich. https://mediatum.ub.tum.de/doc/1369027/622207.pdf

Van Gelderen, M., & Koop, R. (1997) The use of degree variances in satellite geometry. Journal of Geodesy, 71, pp.337-343. https://doi.org/10.1007/s001900050101

4.3.7. Fast-track processing strategies

Fast-Track Processing Strategy	
Data and Products	
Input L1b Data	24-hour quick-look data including: ▪ ACC L1b product ▪ Combined attitude L1b product ▪ LRI L1b product ▪ Orbit and Clocks L1b products ▪ Fast-track L2a orbit products
Input Aux. Data	▪ Non-tidal atmospheric and oceanic mass variations (AOD model) in terms of SH. ▪ Earth orientation parameters (EOPs) based on GPS rapid science orbit (RSO) determination.
Output L2a Data	▪ Estimated SH gravity field parameters covering the desired fast-track period, updated every day.
Algorithms and Procedure Description	

Fast-track processing strategies are applied to produce short-term gravity products with short latencies as input for operational service applications. Since short-term solutions are generally limited in spatial resolution. Either Kalman filtering (Kurtenbach et al. 2012) or averaging (sliding window) approaches (Purkhauser et al. 2019) can be applied to increase their spatial resolution (max. SH degree). We prefer a purely data-driven approach such as the sliding window technique for fast-track processing.

In order to process fast-track gravity field products, all necessary Level-1b and Level-2a data have to be provided as fast as possible. They should be available within 24 hours, and have a comparable quality as the final products. The main difference between fast-track and final products is that the fast-track data generation and distribution relies on an automated process.

For the setup of a fast-track processing chain, cronjobs would regularly check for data availability and automatically start the fast-track Level-2 processing chain for a particular day once all required input data are available. The processing scheme uses the algorithms of the baseline standard processing as described in section 4.3.1, 4.3.2, and optionally 4.3.6 (for NGGM-only solutions).

The processing logic is shown in Figure 4-5. Based on daily NEQs with a pre-defined max. SH degree, average solutions based on a certain number of days (3 – 7 days) are generated, referring to the central day of the averaging period. In a sliding window technique, this process is repeated every day once the latest NEQ is available. In contrast to daily co-estimates (“Wiese” or DMD solutions, cf. section 4.3.4), the successive “daily” estimates are not independent from each other anymore, because they are based on overlapping data periods, but have a higher spatial resolution.

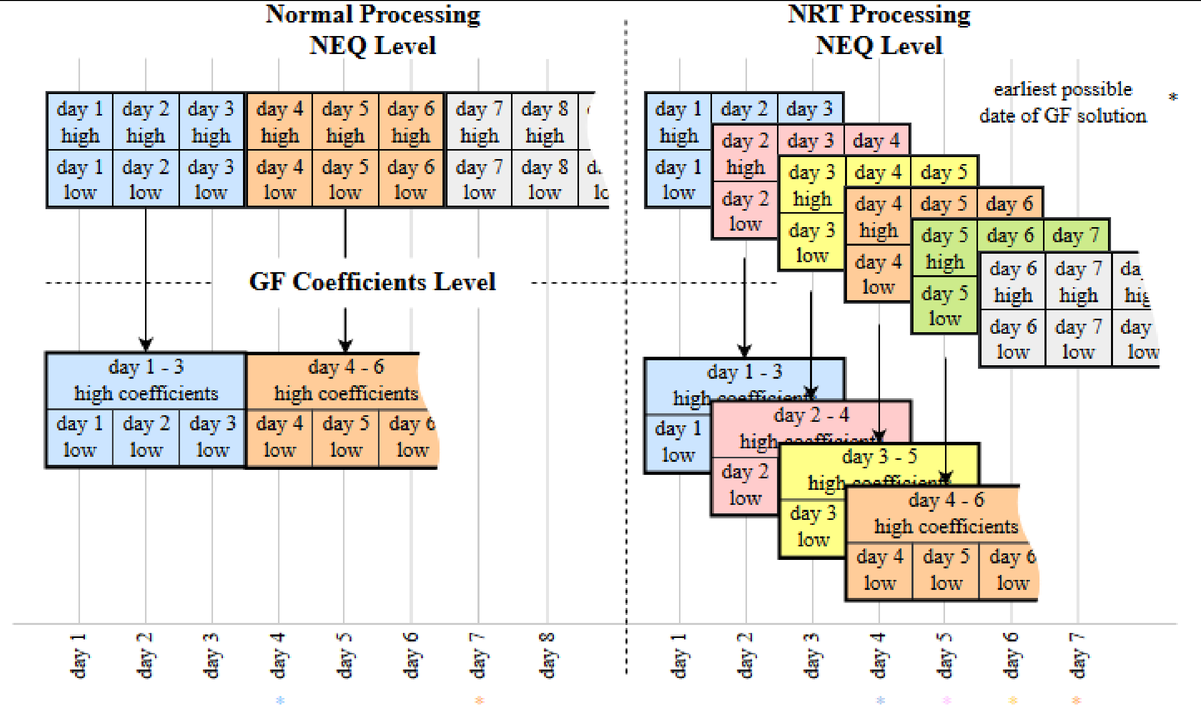

Figure 4-5: Fast-track processing scheme based on a sliding window approach (from: Purkhauser and Pail 2019).

References:
Kurtenbach E., Eicker A., Mayer-Gürr T., Holschneider M., Hayn M., Fuhrmann M., Kusche J. (2012). Improved daily GRACE gravity field solutions using a Kalman smoother, J. Geodyn. 59–60, 39-48, https://doi.org/10.1016/j.jog.2012.02.006.
Purkhauser A.F., Pail R. (2019). Next generation gravity missions: near-real time gravity field retrieval strategy. Geophys. J. Int. 217(2), 1314–1333, https://doi.org/10.1093/gji/ggz084.

4.3.8. Baseline strategy vs. options

In Table 4-1, those L1b to L2a algorithms which compose the baseline strategy, separately for NGGM-only and MAGIC, are indicated by crosses. The other algorithms are processing options, but need further investigation especially regarding their interplay.

Table 4-1: Baseline strategy and options of TUM gravity processor for NGGM and MAGIC

Algorithm	Section	NGGM	MAGIC
Numerical orbit integration	4.3.1	X	X
Set-up of observation equations and assembling of normal equations	4.3.1	X	X
Solution of the NEQ system	4.3.1	X	X
Generation of Variance-Covariance Matrices for Product Errors (ll-SST)	4.3.2	X	X
Stochastic modelling of Ocean Tide Background Model Errors	4.3.3		

Stochastic modelling of AO Background Model Errors	4.3.3		
Extended parameter model: Wiese Parameterization	4.3.4		(X)
Extended parameter model: Application of the DMD approach	4.3.4		(X)
Extended parameter model: Ocean Tides	4.3.4		
Extended parameter model: Empirical Parameters	4.3.4		
Nominal De-Aliasing with Background Models	4.3.5	X	(X)
De-aliasing with Variance-Covariance Information from Background Model Errors	4.3.5		
De-Aliasing using Extended Parameterization Techniques without Background Models	4.3.5		(X)
De-Aliasing using Extended Parameterization Techniques with Background Models	4.3.5		
Polar Cap Regularization	4.3.6	X	
Fast-Track Processing Strategy	4.3.7	X	X

4.4. GRAVITY FIELD ESTIMATION – GFZ

This section summarizes the Level-2 gravity field processing step (L1b to L2a) performed by means of the Earth Parameter and Orbit System (EPOS) software package (Neumayer et al. 2023) at GFZ. During the past decades, the software has been used to routinely process monthly gravity field models from GRACE and GRACE-FO mission data as part of the GRACE/GRACE-FO Science Data System (SDS). Different Level-2 related well established and published techniques are applied and subsequently described. In the following, the individual processing steps will be illustrated with focus on de-aliasing strategies and stochastic modelling of instrument- and background model errors.

4.4.1. Gravity field processor

The gravity field processor at GFZ is realized through the EPOS software, which has been developed and extended since decades. Actually, Level-2 gravity fields derived from the GRACE/GRACE-FO missions use the latest processing scheme GFZ RL06 (Dahle et al. 2019). In the following, the main processing steps to derive L2a data from L1b data are described. The major adaptions with respect to RL06 (preliminary RL07) are related to stochastic modelling of instrument and background model errors and will be illustrated as well in separate tables.

Gravity field processing strategy at GFZ
Underlying satellite orbit perturbations rely on a precise numerical orbit integration considering all reference system and force model related quantities (Reigber 1989). The integrated orbit is then fitted to the satellite tracking observations, i.e., GPS code and carrier phase observations, also denoted as high-low satellite-to-satellite tracking (hl-SST), and low-low satellite-to-satellite tracking (ll-SST) observations, such as K-band or LRI data. This step is done in a least-squares adjustment process solving iteratively for both satellite's state vector at the beginning of each arc, observation-specific parameters, in particular GPS receiver clock offsets, GPS carrier phase ambiguities and calibration parameters for the accelerometers (ACC), and other arc-specific parameters such as empirical accelerations. The term 'arc' refers to the time length of the integrated orbit starting with one initial state vector which is typically one day. After convergence of the initial orbit adjustment based on a priori force models, the observation equations are extended by partial derivatives for the unknown global parameters describing the gravitational potential, represented by spherical harmonic (SH) gravity field coefficients. In this way arc-by-arc normal equation (NEQ) systems are generated from the observation equations and accumulated over a dedicated time span, e.g. monthly or sub-monthly, to one overall system which is then solved by matrix inversion.

Orbit determination problem
Gravity field determination using GPS measurements on-board low Earth orbiters, such as GRACE/GRACE-FO, and inter-satellite measurements in a constellation of satellites is a generalized orbit determination problem involving all satellites of the constellation (Beutler 2005). The SST observational data are supported by the measurements in three orthogonal directions of ACCs placed in the satellite's center of mass, which give – as a function of time – biased and scaled values of the non-gravitational accelerations acting on the satellites. ACC calibration parameters have to be set up and estimated in the generalized orbit adjustment process. In order to refer the GPS- and inter-satellite measurements to the satellite's center of mass, the attitude of the satellite-fixed coordinate system has to be oriented in the inertial system (using star-tracking cameras) and the sensor offsets in the satellite-fixed coordinate system have to be known. Gravity field recovery from satellite missions can also be described in the sense

of a precise orbit determination (POD). The POD defines the central part of the gravity field processor and is executed several times during L1B to L2A processing. The procedure of POD in EPOS is described first (following two blocks) and then the individual gravity field processing steps are explained.

It is to mention that the computation of the GNSS constellation is done in house. However, precise GNSS orbits and clock information can also be obtained by the International GNSS Service (IGS).

Precise Orbit Determination – GNSS Constellation	
Data and Products	
Input GNSS Data	▪ Initial state vector (position, velocity) of the GNSS satellites. ▪ GNSS tracking data from a globally distributed ground station network necessary for the computation of the GNSS constellation.
Input Aux. Data	▪ Earth orientation parameters (EOPs) based on GNSS precise science orbit (PSO) determination. The EOPs are transformation parameters containing the nutation, sub-daily polar motion, mean pole, polar motion, and universal time (UT) values for the length of day. ▪ Earth's static gravity field model in terms of SH. ▪ Time-varying a priori gravity field model in terms of SH. ▪ Ocean tide model. ▪ Atmospheric tides. ▪ Non-tidal atmospheric and oceanic mass variations (AOD model) in terms of SH. ▪ Solid Earth and pole tides. ▪ 3^{rd} body ephemerides. ▪ Non-conservative force models for atmospheric drag, solar radiation pressure, and Earth albedo and infrared radiation.
Output GNSS Data	▪ Precise GNSS orbits and clock offsets.
Algorithms and Procedure Description	
Identical to the description in the table 'Precise orbit determination – Gravity field'. Only the orbit integration (integration of equations of motion) is performed without solving for dynamical parameters as it is done in the gravity field recovery process.	

Precise Orbit Determination – Gravity Field	
Data and Products	
Input L1b Data	▪ Orbit and Clocks L1b products: Initial state vector (position, velocity) of the spacecraft trajectory to be integrated for the orbital arcs. ▪ GNSS receiver L1b products: hl-SST code and phase measurements ▪ LRI L1b product: ll-SST ranging data in terms of range, range-rate or range-acceleration.

	▪ ACC L1b product. ▪ Combined attitude L1b product.
Input Internal Data	▪ Precise GNSS orbits and clock offsets.
Input Aux. Data	▪ Satellite laser ranging (SLR) data. ▪ Earth orientation parameters (EOPs) based on GNSS precise science orbit (PSO) determination. The EOPs are transformation parameters containing the nutation, sub-daily polar motion, mean pole, polar motion, and universal time (UT) values for the length of day. ▪ Earth's static gravity field model in terms of SH. ▪ Time-varying a priori gravity field model in terms of SH. ▪ Ocean tide model. ▪ Atmospheric tides. ▪ Non-tidal atmospheric and oceanic mass variations (AOD model) in terms of SH. ▪ Solid Earth and pole tides. ▪ 3rd body ephemerides. ▪ Antenna phase center corrections. ▪ Non-conservative force models for atmospheric drag, solar radiation pressure, and Earth albedo and infrared radiation.
Output L2a Data	▪ Estimated SH gravity field parameters. ▪ Estimated satellite state vectors per arc (position/velocity). ▪ ACC calibration parameters (biases and scale factor matrices in three directions).
Optional Output	▪ Estimated empirical (constant linear and periodic) accelerations. ▪ Estimated empirical parameters (constant linear and periodic) for ll-SST. ▪ ll-SST scale factor parameters.

Algorithms and Procedure Description

EPOS performs the integration of the orbit and the integration of the variational equations (Beutler et al. 2010) by solving the so-called equations of motion (Beutler 2005). These are usually written as second order, non-linear ordinary differential equations based on Newton's principles. The differential equation of the satellite's orbit can be written as

$$\ddot{x}(t,p) = f(t, x(t,p), \dot{x}(t,p), p), \qquad (1)$$

with the position $x(t,p)$ depending on the time t and dynamical parameters p, and with the velocity $\dot{x}(t,p)$. The initial position and velocity vectors can be written as

$$x(t_0,p) = x_0(p) \qquad (2)$$

$$\dot{x}(t_0,p) = v_0(p). \qquad (3)$$

In order to solve the parameter estimation problem, the relationship between the measurements (GPS code and phase, inter-satellite measurements, ACC measurements) and the parameters has to be linearized. Linearization implies that each orbit (arc) involved is approximated as a linear function of its defining parameters including those dynamical parameters common to several or all orbits. The linearized orbit can be written as

$$x(t) = x_0(t) + \sum_{i=1}^{n_{par}} \frac{\partial x_0(t)}{\partial p_i}(p_i - p_{0i}), \qquad (4)$$

where the a priori orbit (or initial orbit position) $x_0(t)$ is a function of time and characterized by known approximate values p_{0i} of the dynamical parameters $p_i, i = 1,2,\ldots,n_{par}$.

The right hand side of the differential equation (1) defines the disturbing accelerations yielding the satellite's trajectory and is given by

$$f(t,x,v,p) = \sum_a f_a(t,x,v,p), \qquad (5)$$

with a as the model of the forces acting on the satellite. The partial derivatives on the right hand side should be understood as the partial derivatives of the function $\ddot{x}(t,p)$ with respect to the parameters p_i and are denoted as variational equations.

By integrating the orbit, EPOS solves the six differential equations of second order per dynamical parameter for the satellite's state vectors (three for the position and three for the velocity). Therefore, the solution of the dynamical parameters, such as gravity field coefficients, requires the integration of the variational equations. The number of the differential equations depends on the number of dynamical parameters p_i to be solved for. The integration of the differential equations is realized through the Adams-Cowell approach (Hairer et al. 1993). Consequently, the POD is performed by a precise numerical orbit integration with usually 5 sec integration step size using a multistep method in terms of a symmetric, 2-times summed up Cowell approach of 8th order. The applied technique is designed for solving differential equations of second order. However, the method is not a classical Adams-approach, but is rather based on the implicit Strömer approach (Frankana 1995). The integration is implemented as an iterative fix point procedure which computes the trajectory points based on an initial state vector until the 8th order of the approach iteratively.

The POD in EPOS applies the well-known least squares adjustment method (Koch 1987). According to this method, the functional model is usually written as

$$l + \hat{v} = f(\hat{x}), \qquad (6)$$

and in terms of matrix notation

$$\boldsymbol{l} + \boldsymbol{\hat{v}} = \boldsymbol{A}\boldsymbol{\hat{x}}, \qquad (7)$$

where **l** denotes the observations from the satellites, **A** is the design matrix containing the partial derivatives ∂f(x)/∂x wrt. the unknown parameters $\mathbf{\hat{x}}$ to be estimated, and $\mathbf{\hat{v}}$ denotes the a posteriori residuals. In the sense of least squares, the a posteriori residuals $\mathbf{\hat{v}}$ should fulfil the minimum requirement $\mathbf{\hat{v}^T P \hat{v}} \rightarrow \min$ in the L_2-norm (Gauss-Markov model), with P as the weighting matrix for the observations. P can also be written as the inverse of the variance-covariance matrix (VCM) of the observations $\mathbf{Q_{ll}}$ ($\mathbf{P=Q_{ll}^{-1}}$). This matrix contains information regarding the uncertainty of observations. The ll-SST observations of the satellites can be processed in terms of ranges, range-rates, and range-accelerations. The partial derivatives of the variational equations with respect to the gravity field functional is implemented for all three observation types. NEQs are generated arc-wise and are set up separately for the hl-

SST and the ll-SST observation component. The NEQ systems are accumulated to dedicated time batches and are solved according to the method of least squares, where a best linear unbiased estimate of $\hat{x}$ is reached through

$$\hat{\boldsymbol{x}} = (\boldsymbol{A^T P A})^{-1} \boldsymbol{A^T P l}. \qquad (8)$$

The setup of the NEQ system is done with SH base functions of the first-order derivative of the Earth's disturbing potential $\partial T/\partial r$ (here given with respect to the satellite's radius vector r), also denoted as gravity disturbance, which can be expressed by a series expansion, according to Hofmann-Wellenhof & Moritz (2005)

$$\frac{\partial T}{\partial r} = \frac{GM}{a} \sum_{n=0}^{\infty} \left(-\frac{n+1}{r}\right) \left(\frac{R}{r}\right)^{n+1} \sum_{m=0}^{n} \bar{P}_{nm}(cos\theta)(\Delta\bar{C}_{nm} cos\, m\lambda + \Delta\bar{S}_{nm} sin\, m\lambda). \qquad (9)$$

In equation (9), the gravitational constant is denoted by G and M denotes the Earth's mass. The semi-major axis of the Earth is given by R, $\bar{P}_{nm}$ is the normalized Legendre polynomial of SH degree n and order m. The fully normalized SH geopotential coefficients in terms of differences to a reference potential field are denoted by $\Delta\bar{C}_{nm}$ and $\Delta\bar{S}_{nm}$, and r is the mean Earth radius plus satellite altitude. Furthermore, the geocentric co-latitude and longitude are denoted by θ and λ. Equation (9) represents the disturbing accelerations acting on the satellite due to the gravity field and causes a disturbed satellite orbit which is measured by GNSS code and carrier phase observations and ll-SST observations. From equation (9), $\Delta\bar{C}_{nm}$ and $\Delta\bar{S}_{nm}$ coefficients are solved which represent geophysical mass variations of the Earth's gravity field.

References:

Frankana, J.F. (1995) Strömer-Cowell: straight, summed and split. An overview. J Comp. and Appl. Math. 62, 129-154

Hairer, E., Noerset, P., Wanner, G. (1993) Solving Ordinary Differential Equations I: Nonstiff Problems. Second Edition, Springer Verlag

Koch, K.R. (1987) Parameterschätzung und Hypothesentests in linearen Modellen. 2., bearb. u. erw. Aufl. Bonn: Dümmler (Dümmlerbuch, 7892)

In the following, the main processing steps for Level-2A gravity field determination at GFZ are described step by step.

GNSS Data Editing	
Data and Products	
Input L1b Data	▪ Orbit and Clocks L1b products: Initial state vector (position, velocity) of the spacecraft trajectory to be integrated for the orbital arcs. ▪ GNSS receiver L1b products: hl-SST code and phase measurements ▪ LRI L1b product: ll-SST ranging data in terms of range, range-rate or range-acceleration. ▪ ACC L1b product. ▪ Combined attitude L1b product.
Input Internal Data	▪ Precise GNSS orbits and clock offsets.
Input Aux. Data	▪ Satellite laser ranging (SLR) data.

	▪ Earth orientation parameters (EOPs) based on GNSS precise science orbit (PSO) determination. The EOPs are transformation parameters containing the nutation, sub-daily polar motion, mean pole, polar motion, and universal time (UT) values for the length of day. ▪ Earth's static gravity field model in terms of SH. ▪ Time-varying a priori gravity field model in terms of SH. ▪ Ocean tide model. ▪ Atmospheric tides. ▪ Non-tidal atmospheric and oceanic mass variations (AOD model) in terms of SH. ▪ Solid Earth and pole tides. ▪ 3rd body ephemerides. ▪ Non-conservative force models for atmospheric drag, solar radiation pressure, and Earth albedo and infrared radiation.
Output Internal Data	▪ Edited hl-SST code and phase measurements. ▪ Estimated satellite state vectors per arc (position/velocity). ▪ ACC calibration parameters (biases and scale factor matrices in three directions).
Optional Output	▪ Estimated empirical (constant linear and periodic) accelerations.
Algorithms and Procedure Description	
The purpose of this step is to screen the hl-SST code and phase observations and to eliminate erroneous measurements. Editing of hl-SST data is done by automated elimination during an iterative POD. The elimination is based both on an n-sigma criterion, with varying values for n in the different iterations, and additionally an absolute threshold for the size of hl-SST residuals. The POD for the satellites is done independently from each other to obtain best possible absolute orbit accuracy for each spacecraft. In this step, no NEQ systems are set up with respect to gravity field parameters.	

ll-SST Data Editing	
Data and Products	
Input L1b Data	▪ Orbit and Clocks L1b products: Initial state vector (position, velocity) of the spacecraft trajectory to be integrated for the orbital arcs. ▪ LRI L1b product: ll-SST ranging data in terms of range, range-rate or range-acceleration. ▪ ACC L1b product. ▪ Combined attitude L1b product.
Input Internal Data	▪ Edited hl-SST code and phase measurements. ▪ Precise GNSS orbits and clock offsets.
Input Aux. Data	▪ Satellite laser ranging (SLR) data. ▪ Earth orientation parameters (EOPs) based on GNSS precise science orbit (PSO) determination. The EOPs are transformation parameters containing the nutation, sub-daily polar motion, mean pole, polar motion, and universal time (UT) values for the length of day. ▪ Earth's static gravity field model in terms of SH.

	▪ Time-varying a priori gravity field model in terms of SH. ▪ Ocean tide model. ▪ Atmospheric tides. ▪ Non-tidal atmospheric and oceanic mass variations (AOD model) in terms of SH. ▪ Solid Earth and pole tides. ▪ 3rd body ephemerides. ▪ Non-conservative force models for atmospheric drag, solar radiation pressure, and Earth albedo and infrared radiation.
Output Internal Data	▪ Edited ll-SST measurements. ▪ Estimated satellite state vectors per arc (position/velocity). ▪ ACC calibration parameters (biases and scale factor matrices in three directions).
Optional Output	▪ Estimated empirical (constant linear and periodic) accelerations.
Algorithms and Procedure Description	
The purpose of this step is to screen the ll-SST observations and to eliminate erroneous measurements. Editing of ll-SST data is done by executing an iterative POD. The elimination is based on a threshold value which needs to be chosen in accordance to the ll-SST instrument performance. In this step, no NEQ systems are set up with respect to gravity field parameters.	

Generation of a priori Orbits	
Data and Products	
Input L1b Data	▪ ACC L1b product. ▪ Combined sttitude L1b product.
Input Internal Data	▪ Precise GNSS orbits and clock offsets. ▪ Iterated state vectors (position, velocity) from previous step. ▪ Edited hl-SST code and phase measurements. ▪ Edited ll-SST measurements. ▪ Estimated ACC calibration parameters from previous step.
Optional Input Data	▪ Estimated empirical accelerations from previous step.
Input Aux. Data	▪ Satellite laser ranging (SLR) data. ▪ Earth orientation parameters (EOPs) based on GNSS precise science orbit (PSO) determination. The EOPs are transformation parameters containing the nutation, sub-daily polar motion, mean pole, polar motion, and universal time (UT) values for the length of day. ▪ Earth's static gravity field model in terms of SH. ▪ Ocean tide model. ▪ Atmospheric tides. ▪ Non-tidal atmospheric and oceanic mass variations (AOD model) in terms of SH. ▪ Solid Earth and pole tides. ▪ 3rd body ephemerides. ▪ Non-conservative force models for atmospheric drag, solar radiation pressure, and Earth albedo and infrared radiation.

Output Internal Data	▪ Estimated satellite state vectors per arc (position/velocity). ▪ ACC calibration parameters (biases and scale factor matrices in three directions). ▪ Pre-fit residuals.
Optional Output	▪ Estimated empirical (constant linear and periodic) accelerations. ▪ Estimated empirical parameters (constant linear and periodic) for ll-SST. ▪ ll-SST scale factor parameters.
Algorithms and Procedure Description	
The purpose of this step is to assure that convergence of a POD using the edited hl-SST and ll-SST observations and iterated orbit parameter estimates is reached after one iteration.	

NEQ System Setup	
Data and Products	
Input L1b Data	▪ ACC L1b product. ▪ Combined attitude L1b product.
Input Internal Data	▪ Iterated state vectors (position, velocity) from previous step. ▪ Edited hl-SST code and phase measurements. ▪ Precise GNSS orbits and clock offsets. ▪ Edited ll-SST ranging data. ▪ Estimated ACC calibration parameters from previous step.
Input Aux. Data	▪ Earth orientation parameters (EOPs) based on GNSS precise science orbit (PSO) determination. The EOPs are transformation parameters containing the nutation, sub-daily polar motion, mean pole, polar motion, and universal time (UT) values for the length of day. ▪ Earth's static gravity field model in terms of SH. ▪ Ocean tide model. ▪ Atmospheric tides. ▪ Non-tidal atmospheric and oceanic mass variations (AOD model) in terms of SH. ▪ Solid Earth and pole tides. ▪ 3^{rd} body ephemerides. ▪ Non-conservative force models for atmospheric drag, solar radiation pressure, and Earth albedo and infrared radiation.
Optional Input Aux. Data	▪ Information regarding the uncertainty of instruments (ACC, ATT, ll-SST, GNSS) to be introduced in terms of variance-covariance matrices ▪ Information regarding background model errors (ocean tides, AOD) to be introduced in terms of variance-covariance matrices.
Output Internal Data	▪ Arc-wise NEQ systems for hl-SST and ll-SST observation components.
Algorithms and Procedure Description	

The purpose of this step is to set up arc-wise NEQ systems, explicitly, for both observation components, hl-SST and ll-SST. Nominally, the NEQs represent the parameterization with respect to orbit parameters (position/velocity), ACC calibration parameters and gravity field parameters. Optionally, empirical acceleration parameters, kinematic ll-SST link parameters or ll-SST scale factor parameters can be set up. In case of applying extended parameterization techniques, such as the consideration of background model errors in terms of variance-covariance matrices, additional parameters need to be set up. In this step, the design matrices are generated including the partial derivatives with respect to the gravity field parameters to be estimated.

Solution of the NEQ System	
Data and Products	
Input Internal Data	▪ Arc-wise NEQ systems for hl-SST and ll-SST observation components.
Output L2a Data	▪ Estimated SH gravity field parameters. ▪ Estimated satellite state vectors per arc (position/velocity). ▪ ACC calibration parameters (biases and scale factor matrices in three directions).
Optional Output	▪ Estimated empirical (constant linear and periodic) accelerations. ▪ Estimated empirical parameters (constant linear and periodic) for ll-SST. ▪ ll-SST scale factor parameters.
Algorithms and Procedure Description	
Arc-wise NEQ systems are accumulated over dedicated time periods for the hl-SST and the ll-SST observation components and are combined, finally. The solution of the total NEQ system is done via least-squares adjustment using Cholesky decomposition methods. These steps are executed through separate FORTRAN routines outside the EPOS environment. Optionally, a variance component estimation (VCE), according to Koch & Kusche (2001), can be performed in order to find appropriate relative weighting factors for the individual hl-SST and ll-SST observation components. The VCE step is executed for both observation components, separately, so that next to the combined NEQ system (hl-SST + ll-SST) also the individual hl-SST or ll-SST NEQ system is required. The estimated weighting factors are applied to the corresponding NEQ systems and the weighted NEQ systems are combined and solved, finally. The VCE can be executed iteratively until the fixed threshold value, which describes the change in the weighting factors, is reached. The relative weighting step can optimize the retrieval performance and leads to more realistic formal errors. References: Koch, K.R., Kusche, J. (2001) Regularization of geopotential determination from satellite data by variance components. J. Geod. 76(5), 259–26. https://doi.org/10.1007/s00190-002-0245-x	

4.4.2. Stochastic Modelling of Product Errors

Stochastic error sources from satellite on-board sensors, also denoted as product errors, play an important role in the gravity field retrieval by influencing satellite observations due to correlated noise. The stochastic modelling of errors of the key instruments (ll-SST and ACC) is based on analytical noise models which describe the uncertainty characteristics of the instruments in the frequency domain. Such models can either be provided by industry or through science by in-orbit analysis of instrument data in an active mission and post-fit residuals. The generation of variance-covariance matrices is described in the following, separately for ll-SST and hl-SST observations.

Generation of Variance-Covariance Matrices for Product Errors (ll-SST)	
Data and Products	
Input Aux. Data	▪ Analytical noise models for the key instruments ll-SST link and ACC
Output Internal Data	▪ Variance-covariance matrix for ll-SST observations
Algorithms and Procedure Description	

Noise time series are generated by scaling the spectrum of normally distributed random time series with their individual spectral model (usually available in terms of amplitude spectrum densities) having a performance provided by industry or in-orbit behaviour analyses. The generation of noise time series is done individually for the ll-SST instrument and for the sensitive axes of the ACC instrument. Satellite gravity field missions usually measure the gravity field signals predominantly in along-track direction. Besides the radial direction, this direction is one of the two sensitive axes of the ACC instrument. In the time domain, time series are accumulated in terms of the preferred ll-SST observation type (usually range-rates). In the next step, the covariance function is computed from the combined noise time series, according to Etten (2006)

$$Cov\big(y(m+k), y(k)\big) = E[(y(m+k) - \bar{y})(y(k) - \bar{y})]. \qquad (1)$$

Let $y(k)$ with $k = 1$…nsteps be the time series, $\bar{y}$ is the averaged time series, and m defines the step size between two time epochs, then the covariance function can be calculated as a function of the autocorrelation function E. The covariance function is estimated biased, i.e. the normalization is always done with the number of all the elements in y, and not only for the part of y which is used for the corresponding time lag.

In the following step, this function fills a variance-covariance matrix where its rows and columns correspond to the computed covariance function. The variance-covariance matrix is a fully populated symmetrical matrix. The matrix is then inverted and decomposed via Cholesky and forms a triangular filter matrix **F**, covering a time span of nominally 24 hours. **F** is chosen in such a way that $F^T F$ approximates the weighting matrix **P**. It follows

$$\hat{\boldsymbol{x}} = (\boldsymbol{A^T F^T F A})^{-1} \boldsymbol{A^T F^T F l}, \qquad (2)$$

which is equivalent to equation (8) in the table 'Precise orbit determination – Gravity field'.

Some examples for the derivation of analytical noise models and the application of such weighting matrices in the scope of the GFZ gravity field software environment can be found in Murböck et al. (2023).

References:

Etten, W. (2006). Introduction to Random Signals and Noise. OCLC: ocm61859925. John Wiley & Sons. 255 pp. ISBN: 978-0-470-02411-9

Murböck, M., Abrykosov, P., Dahle, C., Hauk, M., Pail, R., & Flechtner, F. (2023) In-Orbit Performance of the GRACE Accelerometers and Microwave Ranging Instrument. *Remote Sens.* 2023, *15*(3), 563; https://doi.org/10.3390/rs15030563

Generation of Variance-Covariance Matrices for GNSS Errors (hl-SST)	
Data and Products	
Input Internal Data	▪ Analytical noise models based on pre-fit residuals of hl-SST code and phase.
Output Internal Data	▪ Variance-covariance matrices for code and phase.
Algorithms and Procedure Description	
The procedure follows the method described in the table 'Generation of variance-covariance matrices for product errors (ll-SST)'. The analytical noise models are derived from code and phase pre-fit residual analyses. Here, pre-fit residuals of dedicated GNSS satellites with respect to the low Earth orbiters are analysed in the spectral domain. Since the time span of tracking a specific GNSS satellite is about 20 min, the information contained in the variance-covariance matrices is related to this time span. The application of the variance-covariance matrices when generating the NEQ systems for hl-SST is done individually for all GNSS satellites.	

4.4.3. Stochastic modelling of Background Model Errors

Next to errors from the key instruments, errors from background models contribute significantly to the total error budget of the estimated time-varying gravity fields. The two major error sources regarding background models are related to ocean tide (OT) models and the error component of the non-tidal atmosphere and ocean de-aliasing (AOD) models. These models are provided by external groups (OT) or derived at GFZ (AOD). The stochastic modelling of background model errors is an ongoing research topic and is not yet fully documented therefore.

At GFZ, the application of variance-covariance matrices for ocean tides is based on the work of Sulzbach et al. (2023). For more information of how the variance-covariance matrices are generated, it is referred to Sulzbach et al. (2023). Fully populated variance-covariance matrices for the 8 major tidal constituents (Q1, O1, P1, K1, N2, S2, M2, K2) are publicly available under https://doi.org/10.5880/nerograv.2023.003. These matrices represent uncertainty information of ocean tide models computed from mutual differences of an ensemble of several different ocean tide models.

Application of Variance-Covariance Matrices from Ocean Tide Models	
Data and Products	
Input Internal Data	▪ Arc-wise NEQ systems for hl-SST and ll-SST observation components including the parameterization with respect to ocean tide parameters.
Input Aux. Data	▪ Variance-covariance matrices for tidal constituents.

Output L2a Data	▪ Estimated SH gravity field parameters.
Output Internal Data	▪ Co-estimated SH ocean tide parameters.

Algorithms and Procedure Description

The variance-covariance information from ocean tide models is introduced in terms of a constrained NEQ system. Extending the parameter space to include ocean tide parameters requires the setup of partial derivatives ∂f(x)/∂x with respect to the unknown ocean tide parameters. Thus, for every tidal constituent partial derivatives are formulated in terms of SH prograde and retrograde sine and cosine functions so that the vector of unknown parameters $\hat{\mathbf{x}}$ (following equations (6-8) in the table 'Precise orbit determination – Gravity field'**)** is extended by these ocean tide parameters. Analogously, the vector of observations $\mathbf{l}$ is extended by pseudo observations having zero values since the system is constraint with respect to the a priori ocean tide background model. The original stand-alone ocean tide variance-covariance matrix (OTVCM) is adapted such that it includes already both, the left-hand side $\boldsymbol{K = A^T P A}$ and the right and side $\boldsymbol{k = A^T P l}$ of the NEQ system. It contains the design matrix $\mathbf{A}$, including the partial derivatives regarding the unknown ocean tide parameters, as well as the variance-covariance matrix. Implicitly, the right-hand side of the constrained ocean tide NEQ system is zero since the system is constraint with respect to the a priori ocean tide background model. In general, the total NEQ system can be split into two groups: the first one represents the left-hand side $\mathbf{K_{SST}}$ and the right-hand side $\mathbf{k_{SST}}$ for hl-SST and ll-SST components, as denoted in equation (1), the second one defines the corresponding parts for the constrained ocean tide NEQ system $\mathbf{K_{OT}}$ and $\mathbf{k_{OT}}$, as denoted in equation (2). $\mathbf{K_{12}^{SST}}$, $\mathbf{K_{22}^{SST}}$ and $\mathbf{k_2^{SST}}$ include the extended parameterization for ocean tide constituents, the remaining parts of K_{SST} and k_{SST} contain all other parameters, e.g., the nominal gravity field parameters. $\mathbf{K_{OT}}$ and $\mathbf{k_{OT}}$ include only parameters regarding ocean tides.

$$\boldsymbol{K_{SST}}=\begin{bmatrix} \boldsymbol{K_{11}^{SST}} & \boldsymbol{K_{12}^{SST}} \\ \left(\boldsymbol{K_{12}^{SST}}\right)^{\boldsymbol{T}} & \boldsymbol{K_{22}^{SST}} \end{bmatrix}; \quad \boldsymbol{k_{SST}}=\begin{bmatrix} \boldsymbol{k_1^{SST}} \\ \boldsymbol{k_2^{SST}} \end{bmatrix} \qquad (1)$$

$$\boldsymbol{K_{OT}}=\begin{bmatrix} 0 & 0 \\ 0 & \boldsymbol{K_{constr.}^{OT}} \end{bmatrix}; \quad \boldsymbol{k_{OT}}=\begin{bmatrix} 0 \\ \boldsymbol{k_{constr.}^{OT}} \end{bmatrix} \qquad (2)$$

The three NEQ system components (hl-SST, ll-SST and ocean tides) are summed up and the total system is solved, according to equation (8) in the table 'Precise orbit determination – Gravity field'. Among the estimated gravity field coefficients and other parameters, such as accelerometer calibration parameters and satellite state vectors, $\hat{\mathbf{x}}$ contains estimates of the eight major tidal constituents in terms of SH prograde and retrograde ocean tide coefficients as well. Similar to the gravity field parameters, the ocean tide parameters are estimated in terms of a linearization process of the functional model. To obtain the full ocean tide signal, the a priori ocean tide model used for linearization purposes, is added back.

References:

Hauk, M., Wilms, J., Sulzbach, R., Panafidina, N., Hart-Davis, M., Dahle, C., et al. (2023) Satellite gravity field recovery using variance-covariance information from ocean tide models. Manuscript submitted to: Earth and Space Science. Under review.

The variance-covariance matrices for the error component of the AOD model are generated in house by the Section 1.3 working group of Henryk Dobslaw. Fully populated variance-covariance matrices are provided representing the uncertainty information of the error component of the AOD model based on the corresponding model release version.

Application of Variance-Covariance Matrices based on the AOD Error Model Component	
Data and Products	
Input Internal Data	▪ Arc-wise NEQ systems for hl-SST and ll-SST observation components including the parameterization with respect to ocean tide parameters.
Input Aux. Data	▪ Variance-covariance matrices for the AOD error model component.
Output L2a Data	▪ Estimated SH gravity field parameters
Algorithms and Procedure Description	
Similar to the application of stochastic modelling of ocean tide background model errors, the variance-covariance information from the AOD error component is introduced in terms of a constrained NEQ system. The application strategy is identical to the one described in the table "Application of variance-covariance matrices from ocean tide models'. However, the parameterization of AO parameters implicates huge NEQ systems since the information regarding non-tidal time-varying gravity field signals is usually available in a short interval step size (e.g. 6 or 3 hourly). Correspondingly, AO parameters are set up for every short interval batch so that each arc-wise NEQ includes the AO parameterization with respect to the short interval step size. The solution of the NEQ system requires some adaption in order to keep the system at a manageable size. The arc-wise NEQ systems for hl-SST and ll-SST are accumulated first, followed by the addition of the variance-covariance matrices. The latter are available in the corresponding short interval batches. In the next step, the arc-wise NEQs are reduced by the AO parameters in order to reduce the size of the systems. Then, the arc-wise NEQs are accumulated to long-term NEQs (e.g. monthly or sub-monthly) and are solved, according to equation (8) in the table 'Precise orbit determination – Gravity field'. The AO parameters are still resolved. However, they are not part of the estimated parameters since they have been previously reduced.	

4.4.4. Stochastic modelling using a-posteriori residuals

Another possibility of modelling product errors as well as background model errors stochastically, is to use the a-posteriori (or post-fit) residuals.

Generation of stochastic models from a posteriori residuals	
Data and Products	
Input Internal Data	▪ Arc-wise NEQ systems for hl-SST and ll-SST observation components. ▪ Estimated SH gravity field parameters.

Output Internal Data	▪ Arc-wise variance-covariance matrices for hl-SST and ll-SST observations.
Algorithms and Procedure Description	
The post-fit residuals can be computed from the estimated gravity field parameters and the corresponding NEQ system, according to $$\hat{\mathbf{v}}=\mathbf{A}\hat{\mathbf{x}}-\mathbf{l}, \qquad (1)$$ These residuals serve as input time series for the generation of arc-wise weighting matrices. The weighting matrices are produced and applied according to the procedure described in ‘Generation of Variance-Covariance Matrices for Product Errors (ll-SST)’ and in ‘Generation of Variance-Covariance Matrices for GNSS Errors (hl-SST)’.	

4.4.5. Extended parameterization strategies

Two so-called ‘extended parameterization strategies’ for further de-aliasing of high-frequency time-varying gravity field signals are implemented at GFZ. The first one is denoted as ‘Wiese parameterization’, the second one is denoted as ‘data driven multi-step self-de-aliasing (DMD) approach’. Both methods aim to mitigate temporal aliasing effects due to non-tidal time varying signals, mainly A and O signals. Therefore, one should ideally be able to retrieve the full AOHIS signal without the need for a priori geophysical background models (AOD models).

Application of the Wiese Parameterization	
Data and Products	
Input Internal Data	▪ Arc-wise NEQ systems for hl-SST and ll-SST observation components.
Output L2a Data	▪ Estimated SH gravity field parameters, i.e. long-term. ▪ Co-estimated short-term SH gravity field parameters.
Algorithms and Procedure Description	
According to the Wiese method, low-resolution (e.g. up to SH d/o 15) gravity field parameters are co-estimated at short time intervals (e.g. daily) together with the higher-resolution gravity field which is sampled at a longer time interval (Wiese et al. 2011). This allows the consideration of high-frequency information contained in the short-term gravity field solutions with the goal to reduce the temporal aliasing effect of those long-wavelength geophysical signals that have a period larger than twice the chosen sampling period of the short-period gravity field modelling. Starting from the arc-wise generated NEQ systems for hl-SST and ll-SST, both observation components are accumulated on an arc-wise basis. In the next step, the arc-wise NEQs are manipulated by re-naming all low-resolution gravity field parameters by adding an epoch string. After that, the NEQs are accumulated to the long-term interval (e.g. monthly or sub-monthly). The final NEQ system contains now short-term (arc-wise) and long-term gravity field parameters. Additionally, the arc-wise parameters can be accumulated to the desired short-term length (e.g. daily), if the arcs are shorter than the nominal 24 hours length due to missing measurements. The NEQ system is solved according to equation (8) in the table ‘Precise orbit determination – Gravity field’. The estimated parameters contain now low-resolution short-term parameters as well as highly resolved long-term parameters. The low-	

degree part of the long-term field is defined by the average of all low-degree short-term parameters.

References:

Wiese, D.N., Visser, P.N.A.M., Nerem, S. (2011). Estimating low resolution gravity fields at short time intervals to reduce temporal aliasing errors. Adv. Space Res., 48(6), 1094-1107. https://doi.org/10.1016/j.asr.2011.05.027

Application of the DMD Approach	
Data and Products	
Input Internal Data	▪ Arc-wise NEQ systems for hl-SST and ll-SST observation components.
Output L2a Data	▪ Step 1: Estimated SH short-term interval gravity fields. ▪ Step 2: Estimated SH gravity field parameters.
Algorithms and Procedure Description	

Similar to the Wiese approach, the strategy of the DMD method is to capture the short-periodic long-wavelength signals, which are predominantly related to the time-variable AO component, within the interval fields and thus prevented from manifesting as temporal aliasing effects within the long-term solution (Abrykosov et al. 2022).

The gravity field observations are split into intervals of, e.g., one day for which individual low-resolution gravity fields up to a certain harmonic degree are estimated, disregarding the fact that the observations contain also high-degree signals and thus allowing for a certain amount of spectral leakage. Treating the latter prior to the estimation of the interval fields is crucial, as otherwise the entirety of the corresponding signal would be parametrized into the low-degree spectrum, thus inducing a large-scale error. Therefore, its short-wavelength components are reduced and retain the low-degree part, i.e. the estimation of the interval fields is done while fixing the high-degree spectrum to a specific gravity field. The fixing of the high-degree spectrum can be done either using the static background field model or using a post-processed time-varying gravity field model including the time period to be estimated. For the latter, a nominal gravity field solution (L2a) needs to be processed at first. The estimation of the interval fields is done by accumulating the manipulated arc-wise NEQ systems for hl-SST and ll-SST and solving the systems using the known equation (8) in the table ‘Precise orbit determination – Gravity field’. This defines the first step of the DMD approach.

In the second step, these stand-alone gravity solutions for the respective interval are further used to compute reference observations which are reduced in a subsequent step from the original ones. The introduction of these interval fields is done at the a priori orbit generation step (cf. table ‘Generation of a priori orbits’) serving as further de-aliasing product. Based on the ‘updated’ reduced observations a long-term, e.g. monthly, solution is estimated and, in a final step, restored to the mean of the interval estimates to the low degrees of the long-term solution. In fact, the latter is done in an alternative approach, where the interval fields’ mean value is computed already after the estimation of the short-term interval fields and already restored to them instead of restoring the low degrees of the long-term solution, so that the reference observations used for the de-aliasing step are only comprised of variations with respect to the total signal’s long-term mean.

References:

Abrykosov P., Murboeck M., Hauk M., Pail R., Flechtner F. (2022). Data-driven multi-step self-de-aliasing approach for GRACE and GRACE-FO data processing. Geophys. J. Int., 232, pp. 1006-1030. https://doi.org/10.1093/gji/ggac340

4.4.6. De-Aliasing strategies

The de-aliasing strategies can be subdivided into four groups:

- Nominal strategy: using time varying gravity field background models for de-aliasing purposes (ocean tide model, AOD model).
- Using time varying gravity field background models (ocean tide model, AOD model) and variance-covariance information from background model errors (OTVCM, AODVCM).
- Using extended parameterization techniques without background models.
- Using extended parameterization techniques together with background models.

In the following, the processing procedure of the four different groups will be illustrated schematically. The focus lies on the treatment of the time-varying background fields.

Nominal De-Aliasing with Background Models	
Data and Products	
Input Aux. Data	▪ Ocean tide model. ▪ Non-tidal atmospheric and oceanic mass variations (AOD model) in terms of SH.
Output L2a Data	▪ Estimated SH gravity field parameters.
Algorithms and Procedure Description	
Nominally, time-varying background models representing ocean tides and non-tidal AO signals are used for de-aliasing purposes. The primary goal is to retrieve the time-varying HIS signal. Therefore, errors due to ocean tides and non-tidal AO signals shall be kept as small as possible. The processing scheme follows the description in the tables ‘NEQ system setup’ and ‘Solution of the NEQ system’. <u>References</u>: Dahle, C., Murboeck, M., Flechtner, F., Dobslaw, H., Michalak, G., Neumayer, K.H., et al. (2019) The GFZ GRACE RL06 Monthly Gravity Field Time Series: Processing Details and Quality Assessment. *Remote Sensing*, *11(8)*, 2116. https://doi.org/10.3390/rs11182116	

De-aliasing with Variance-Covariance Information from Background Model Errors	
Data and Products	
Input Aux. Data	▪ Ocean tide model. ▪ Non-tidal atmospheric and oceanic mass variations (AOD model) in terms of SH.
Input Internal Data	▪ Variance-covariance matrices for tidal constituents. ▪ Variance-covariance matrices for the AOD error model component.
Output L2a Data	▪ Estimated SH gravity field parameters.

Output Aux. Data	▪ Co-estimated SH ocean tide parameters.
Algorithms and Procedure Description	
Next to the nominally time-varying background models representing ocean tides and non-tidal AO signals nominally used for de-aliasing purposes, variance-covariance information from background model errors is introduced in terms of constrained matrices. The processing scheme follows the description in the tables ‘Application of variance-covariance matrices from ocean tide models’ and ‘Application of variance-covariance matrices based on the AOD error model component’.	

De-Aliasing using Extended Parameterization Techniques without Background Models	
Data and Products	
Input Aux Data	▪ Ocean tide model.
Optional Input Data	▪ Variance-covariance matrices for tidal constituents.
Output L2a Data	▪ Estimated SH gravity field parameters (L2A) including the full AOHIS signal.
Optional Output	▪ Co-estimated SH ocean tide parameters.
Algorithms and Procedure Description	
This processing scheme uses extended parameterization techniques without applying an AOD model. The introduction of an ocean tide de-aliasing model is mandatory. Therefore, variance-covariance information from ocean tide model errors can be introduced, additionally, following the procedure in the table ‘Application of variance-covariance matrices from ocean tide models’. Possible extended parameterization techniques to be applied are described in the tables ‘Application of the Wiese parameterization’ and ‘Application of the DMD approach’. These methods aim to reduce the aliasing error due to AO error signals while estimating the total AOHIS signal content.	

De-Aliasing using Extended Parameterization Techniques with Background Models	
Data and Products	
Input Aux. Data	▪ Ocean tide model. ▪ Non-tidal atmospheric and oceanic mass variations (AOD model) in terms of SH.
Optional Input Data	▪ Variance-covariance matrices for tidal constituents.
Output L2a Data	▪ Estimated SH gravity field parameters (L2A) including the HIS signal.
Optional Output	▪ Co-estimated SH ocean tide parameters.
Algorithms and Procedure Description	
This processing scheme uses extended parameterization techniques while applying an AOD model. The introduction of an ocean tide de-aliasing model is mandatory. Therefore, variance-covariance information from ocean tide model errors can be introduced, additionally, following the procedure in the table ‘Application of variance-covariance matrices from ocean tide models’. Possible extended parameterization techniques to be applied are described in the tables ‘Application of the Wiese parameterization’ and ‘Application of the DMD approach’. As already stated in the previous table, these methods aim to reduce the aliasing error due to AO error signals. The purpose of using both, an AOD	

model and an extended parameterization technique, is to further reduce the aliasing error due to A and O.

4.4.7. Regularization and constraints

The nominal gravity field processing scheme using measurements from satellites with polar or near-polar orbits does not require regularization techniques. However, the processing of measurements from an inclined satellite pair (NGGM), exclusively, requires certain amount of regularization so that the gravity field solutions do not suffer from missing measurements over the polar regions and resulting ill conditioned NEQs.

Regularization	
Data and Products	
Internal Input Data	▪ Arc-wise NEQ systems for hl-SST and ll-SST observation components based on inclined pair measurements.
Output L2a Data	▪ Estimated SH gravity field parameters (L2A) based on the applied regularization method.
Algorithms and Procedure Description	

Arc-wise NEQ systems are accumulated over dedicated time periods for the hl-SST and the ll-SST observation components and are combined, finally. Before solving the NEQ system, a regularization is performed. Following van Gelderen and Koop (1997), it is assumed that the maximum affected SH order m_{max} for each SH degree n is given by

$$m_{max} \approx \left|\frac{\pi}{2} - I\right| \cdot n, \qquad (1)$$

with the inclination I. To stabilize the inversion of the ill-conditioned NEQ system, Rexer (2012) suggests the regularization according to

$$\hat{x} = (A^T PA + \alpha R)^{-1} A^T Pl, \qquad (2)$$

where $A^T PA$ denotes the left-hand side of the NEQ system, α is an empirically determined regularization factor, R is the degree n dependent regularization matrix, and $A^T Pl$ denotes the right-hand side of the NEQ system. R is composed through

$$r_{ij} = \begin{cases} n^4 (m_{max} - m)^p, i = j \; and \; m \leq m_{max} \\ 0, otherwise \end{cases}. \qquad (3)$$

The term $(m_{max} - m)^p$ describes an order-dependent weighting where the regularization is strongest for lower orders and reduces the regularization strength as the order increases. The optimal regularization factor α is found by setting $p = 1$.

The solution of the total regularized NEQ system is done via equation (2).

References:

Rexer, M. (2012) Time-variable Gravity Field: contributions of GOCE Gradiometer Data to Monthly and Bi-Monthly GRACE Gravity Field Estimates. Master's Thesis. Technical University of Munich. https://mediatum.ub.tum.de/doc/1369027/622207.pdf

Van Gelderen, M., & Koop, R. (1997) The use of degree variances in satellite geometry. Journal of Geodesy, 71, pp.337-343. https://doi.org/10.1007/s001900050101

4.4.8. Fast-track processing strategies

Fast-track processing strategies are related to a Near-Real-Time (NRT) processing scheme. The idea is to set up a mostly automated processing chain for the generation of short-interval (e.g. 3 days) L2a gravity field products. These products will be updated every 24 hours by shifting the short-interval window one day further.

Fast-Track Processing Strategy	
Data and Products	
Input L1b Data	24-hour quick-look data including: ▪ Orbit and Clocks L1b products: Initial state vector (position, velocity) of the spacecraft trajectory to be integrated for the orbital arcs. ▪ GNSS receiver L1b products: hl-SST code and phase measurements ▪ LRI L1b product: ll-SST ranging data in terms of range, range-rate or range-acceleration. ▪ ACC L1b product. ▪ Combined attitude L1b product.
Input Aux. Data	▪ Non-tidal atmospheric and oceanic mass variations (AOD model) in terms of SH. ▪ Earth orientation parameters (EOPs) based on GPS rapid science orbit (RSO) determination.
Output L2a Data	▪ Estimated SH gravity field parameters covering the desired NRT period, updated every day.
Algorithms and Procedure Description	
In order to process NRT gravity field products, all necessary Level-1B data has to be provided as fast as possible. So-called quick-look Level-1B data are already available within 24 hours for most days. They have a comparable quality as the final Level-1B products. The main difference between quick-look and final products is that the quick-look data generation and distribution relies on an automated process and the products are also not validated. For the setup of a NRT processing chain, cronjobs would regularly check for data availability and automatically start the Level-2 processing chain for a particular day once all required input data are available. The processing scheme follows the description in the tables 'GNSS data editing', 'll-SST data editing', 'Generation of a priori orbits', 'NEQ system setup', and 'Solution of the NEQ system'. The already existing daily NEQ systems are updated by the latest daily NEQ and are combined to the short-interval NEQ system by shifting the short-interval window one day further. Correspondingly, the Level-2A gravity field products will be updated every day and represent a NRT solution. References: GRACE-FO Third Party Mission (TPM) Team (2023). Final Report of ESA GRACE-FO TPM – Science Phase. ESA Contract No. RFP/3-17121/21/I-DT-Ir	

4.4.9. Baseline strategy vs. options

Figure 4-6 shows an overview of the main components and the product flow of the GFZ gravity processor including the several options. The flowchart mainly illustrates the baseline processing scheme at GFZ for NGGM (inclined pair only) and for MAGIC (double pair constellation, i.e., polar pair plus inclined pair). Optional strategies are indicted in terms of dashed boxes. So far, the only difference between NGGM and MAGIC processing is the polar cap regularization for NGGM.

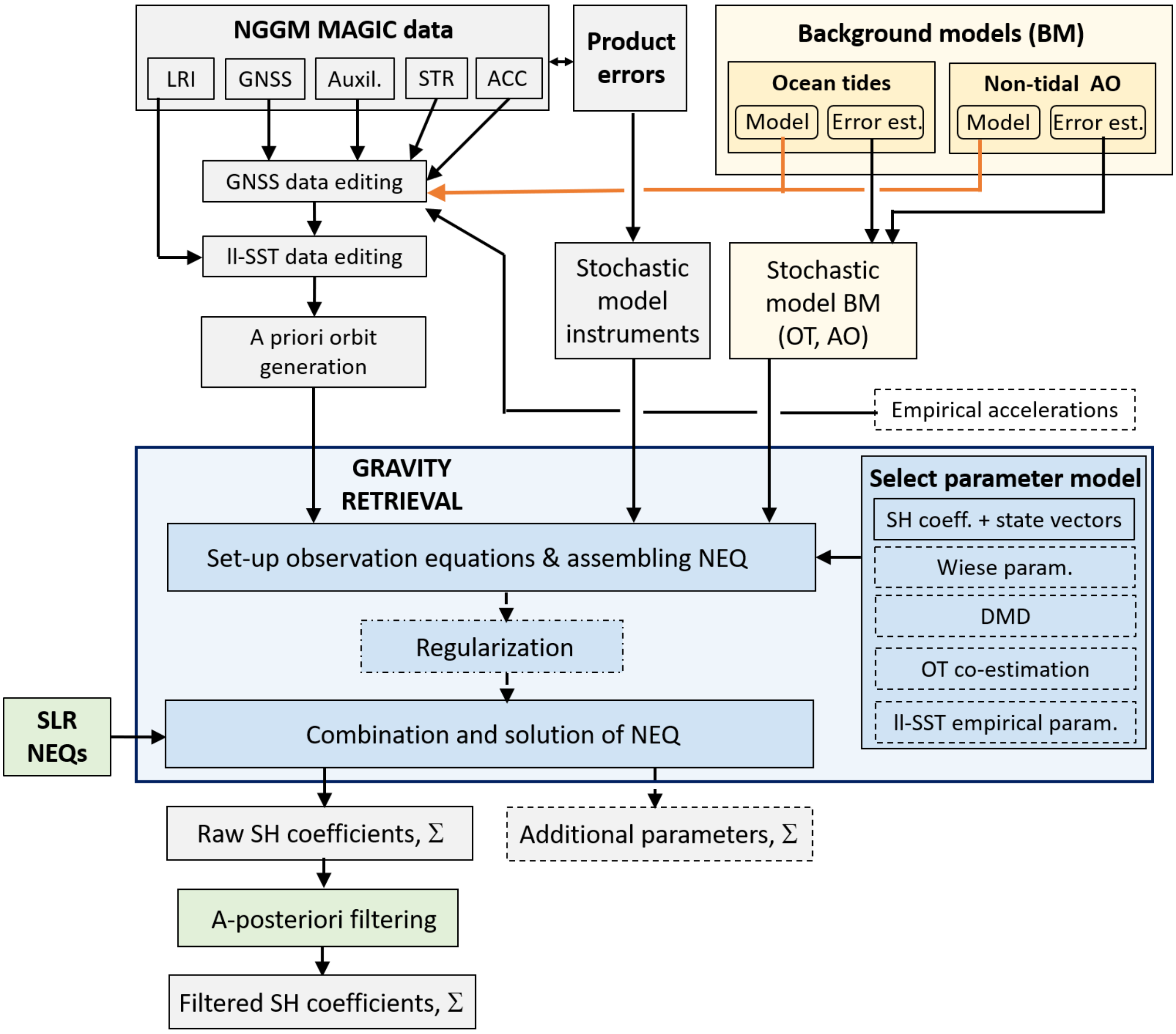

Figure 4-6: GFZ processing schemes for NGGM (inclined pair only) and for MAGIC (double pair constellation, i.e., polar pair plus inclined pair).

In Table 4-2, those L1b to L2a algorithms which compose the baseline strategy, separately for NGGM-only and MAGIC, are indicated by the letter B. The other algorithms are processing options, indicated by the letter O, but need further investigation especially regarding their interplay. Possible conflicts between optional and baseline processing strategies are indicated by parenthesis at the letter O.

Table 4-2: Baseline strategy and options of GFZ gravity processor for NGGM and MAGIC

Algorithm	**Section**	**NGGM**	**MAGIC**
GNSS data editing	4.4.1	B	B
ll-SST data editing	4.4.1	B	B
Generation of a priori orbits	4.4.1	B	B
NEQ system setup	4.4.1	B	B
Solution of the NEQ system	4.4.1	B	B
Generation of Variance-Covariance Matrices for Product Errors (ll-SST)	4.4.2	B	B
Generation of Variance-Covariance Matrices for GNSS Errors (hl-SST)	4.4.2	B	B
Application of Variance-Covariance Matrices from Ocean Tide Models	4.4.3	B	B
Application of Variance-Covariance Matrices based on the AOD Error Model Component	4.4.3	B	B
Generation of stochastic models from a posteriori residuals	4.4.4	O	O
Application of the Wiese Parameterization	4.4.5		(O)
Application of the DMD Approach	4.4.5	(O)	(O)
Nominal De-Aliasing with Background Models	4.4.6	B	B
De-aliasing with Variance-Covariance Information from Background Model Errors	4.4.6	B	B
De-Aliasing using Extended Parameterization Techniques without Background Models	4.4.6	O	O
De-Aliasing using Extended Parameterization Techniques with Background Models	4.4.6	(O)	(O)
Polar Cap regularization	4.4.7	B	
Fast-Track Processing Strategy	4.4.8	B	B

4.5. GRAVITY FIELD ESTIMATION – CNES

This section summarizes the Level-2 gravity field processing from L1b to L2a with the GINS/Dynamo software package (Marty et al, 2018) at CNES. It has been used to routinely process monthly gravity field models from GRACE and GRACE-FO mission data for almost twenty years. In the following sections, the processing steps will be described.

4.5.1. Gravity field processor

The gravity field processor at CNES consists of the GINS (POD) and Dynamo (solve) software. The Level-2 gravity fields derived from the GRACE/GRACE-FO mission data are currently according to release 5 standards (https://grace.obs-mip.fr/variable-models-grace-lageos/grace-solutions-release-05/rl05-products-description/).

Gravity field processing strategy at CNES

The basis of the procedure consists in precise numerical orbit integration employing a state-of-the-art force model and reference system (IERS). The integrated orbit is fitted to the satellite tracking observations, in this case GPS code and carrier phase observations (hl-SST), and K-band or LRI low-low satellite-to-satellite tracking (ll-SST) observations.

Observation- and arc-specific parameters (e.g. GPS receiver clock offsets, GPS carrier phase ambiguities, accelerometers calibration parameters, empirical accelerations if applicable, state vector at epoch) are estimated in an iterative least-squares adjustment process. All data are reduced in 24h arcs. After convergence of the orbit adjustment, the partial derivatives of the spherical harmonic (SH) gravity field coefficients describing the gravitational potential are calculated in addition to other geometrical and dynamical parameters and normal equation (NEQ) systems are generated per arc. The NEQs are typically accumulated per month and then solved by means of matrix inversion.

Orbit determination problem

Gravity field determination using GNSS measurements on satellites in Low Earth Orbit (LEO), such as GRACE/GRACE-FO, and inter-satellite measurements in a constellation of satellites is a generalized orbit determination problem involving all satellites of the constellation (Beutler 2005). The SST data enable estimation of positions and speeds, and changes therein, which enables estimation of orbit and geophysical parameters. The non-gravitational accelerations acting on the satellite are not precisely predicted with models, and instead an accelerometer is mounted in its center of mass that measures these accelerations very precisely in three orthogonal directions. Instrumental calibration parameters, bias and scale factor, have to be estimated in the orbit adjustment process. The GNSS- and inter-satellite measurements can be referenced to the satellite’s center of mass thanks to attitude quaternions that correctly orient the satellite-fixed coordinate system in the inertial system.

Precise orbit determination (POD) is the starting point of gravity field recovery with satellite data. The POD software constitutes the principal part of the gravity field processor. POD is performed first for the GNSS constellation, in house and contributing to IGS, and then for the LEO satellites during L1b to L2a processing. The POD and calculation of the normal equation systems, applying dynamic data editing (threshold followed by n-sigma elimination), is done in a single step, i.e., there is no specific data screening step. The orbit is fitted to the SST data until convergence is reached according to a criterion based on successive improvements in the fit, after which only the full normal equations including the gravity field coefficients are calculated.

The GPS constellation POD procedure in GINS is described first after which the individual gravity field processing steps are explained.

Precise Orbit Determination – GNSS Constellation	
Data and Products	
Input GNSS Data	▪ Initial state vector (position, velocity) of the GNSS satellites. ▪ GNSS tracking data from a globally distributed ground station network necessary for the computation of the GNSS constellation.
Input Aux. Data	▪ Earth orientation parameters (EOPs) based on GNSS precise science orbit (PSO) determination. The EOPs are transformation parameters containing the nutation, sub-daily polar motion, mean pole, polar motion, and universal time (UT) values for the length of day. ▪ Static and time-varying a priori gravity field model in terms of SH. ▪ Ocean tide model. ▪ Atmospheric tides. ▪ Non-tidal atmospheric and oceanic mass variations (AOD model) in terms of SH. ▪ Solid Earth and pole tides. ▪ 3rd body ephemerides. ▪ Non-conservative force models for solar radiation pressure, Earth albedo and infrared radiation. ▪ TEC maps, IONEX products?
Output GNSS Data	▪ Precise GNSS orbits and clock offsets.
Algorithms and Procedure Description	
Identical to the description in the table 'Precise orbit determination – Gravity field'. Only the orbit integration (integration of equations of motion) is performed without solving for dynamical parameters as it is done in the gravity field recovery process.	

Precise Orbit Determination – Gravity Field	
Data and Products	
Input L1b Data	▪ Orbit and Clocks L1b products: Initial state vectors of the spacecraft. ▪ GNSS receiver L1b products: hl-SST code and phase measurements ▪ LRI L1b product: ll-SST data in terms of range-rates. ▪ ACC L1b product. ▪ Combined star camera L1b product.
Input Internal Data	▪ Precise GNSS orbits and clock offsets ('GRG').
Input Aux. Data	▪ Earth orientation parameters (EOPs) based on GNSS precise science orbit (PSO) determination. The EOPs are transformation parameters containing the nutation, sub-daily polar motion, mean pole, polar motion, and universal time (UT) values for the length of day.

	▪ Static and time-varying a priori gravity field model in terms of SH. ▪ Ocean tide model. ▪ Atmospheric tides. ▪ Non-tidal atmospheric and oceanic mass variations (AOD model) in terms of SH. ▪ Solid Earth and pole tides. ▪ 3^{rd} body ephemerides. ▪ Antenna phase center corrections.
Optional Input Aux. Data	▪ Information regarding the uncertainty of instruments (ACC, ll-SST) to be introduced in terms of variance-covariance matrices
Output Internal Data	▪ NEQ systems per arc for hl-SST and ll-SST observations separately.
Optional Output	▪ Estimated empirical (piece-wise linear and periodic) accelerations. ▪ Estimated kinematic parameters (constant linear and periodic) for inter-satellite links.
Algorithms and Procedure Description	
GINS performs the integration of the orbit and the integration of the variational equations by solving the so-called equations of motion according to the same theory as described for EPOS in section 4.4.1. The hl-SST and ll-SST data are reduced in 24h arcs. The POD and the subsequent calculation of the NEQ systems, for hl-SST and ll-SST separately, are performed in a single process. Nominally, the NEQs represent the parameterization with respect to orbit parameters (position/velocity), ACC calibration parameters and gravity field parameters. Optionally, empirical acceleration parameters and kinematic ll-SST link parameters can be calculated too.	

Solution of the NEQ System	
Data and Products	
Input Internal Data	▪ NEQ systems per arc for hl-SST and ll-SST observations separately.
Output L2a Data	▪ Estimated SH gravity field coefficients.
Optional Output	▪ Estimated satellite state vectors per arc (position/velocity). ▪ ACC calibration parameters (biases per day, and scale factor per tbd matrices in three directions). ▪ Estimated empirical (piece-wise linear and periodic) accelerations. ▪ Estimated kinematic parameters (constant linear and periodic) for inter-satellite links.
Algorithms and Procedure Description	
The hl-SST and the ll-SST NEQ systems per arc are accumulated over specified time periods, typically one month. The solution of the monthly NEQ system is done via least-squares adjustment using Cholesky decomposition methods. The handling and solving of the NEQs is done with the Dynamo software.	

4.5.2. Stochastic Modelling of Product Errors

Stochastic error sources from satellite on-board sensors, also denoted as product errors, affect the quality of the gravity field retrieval caused by correlated noise. The stochastic modelling of errors of the key instruments (ll-SST and ACC) is based on analytical noise models which describe the uncertainty characteristics of the instruments in the frequency domain. Such models can either be provided by industry or through science by in-orbit analysis of instrument data in an active mission and post-fit residuals. The generation of variance-covariance matrices is described in the following, separately for ll-SST and hl-SST observations. It is identical to the method of GFZ.

Generation of Variance-Covariance Matrices for Product Errors (ll-SST)	
Data and Products	
Input Aux. Data	▪ Analytical noise models for the key instruments ll-SST link and ACC
Output Internal Data	▪ Variance-covariance matrix for ll-SST observations
Algorithms and Procedure Description	

Noise time series are generated by scaling the spectrum of normally distributed random time series with their individual spectral model (usually available in terms of amplitude spectrum densities) having a performance provided by industry or in-orbit behaviour analyses. The generation of noise time series is done individually for the ll-SST instrument and for the sensitive axes of the ACC instrument. Satellite gravity field missions usually measure the gravity field signals predominantly in along-track direction. Besides the radial direction, this direction is one of the two sensitive axes of the ACC instrument. In the time domain, time series are accumulated in terms of the preferred ll-SST observation type (usually range-rates). In the next step, the covariance function is computed from the combined noise time series, according to Etten (2006)

$$Cov\big(y(m+k), y(k)\big) = E[(y(m+k) - \bar{y})(y(k) - \bar{y})]. \qquad (1)$$

Let $y(k)$ with $k = 1$…nsteps be the time series, $\bar{y}$ is the averaged time series, and m defines the step size between two time epochs, then the covariance function can be calculated as a function of the autocorrelation function E. The covariance function is estimated biased, i.e. the normalization is always done with the number of all the elements in y, and not only for the part of y which is used for the corresponding time lag.

In the following step, this function fills a variance-covariance matrix where its rows and columns correspond to the computed covariance function. The variance-covariance matrix is a fully populated symmetrical matrix. The matrix is then inverted and decomposed via Cholesky and forms a triangular filter matrix **F**, covering a time span of nominally 24 hours. **F** is chosen in such a way that $F^T F$ approximates the weighting matrix **P**. It follows

$$\boldsymbol{\hat{x}} = (\boldsymbol{A^T F^T F A})^{-1} \boldsymbol{A^T F^T F l}, \qquad (2)$$

which is equivalent to equation (8) in the table ‘Precise orbit determination – Gravity field’ in the corresponding GFZ section.

Some examples for the derivation of analytical noise models and the application of such weighting matrices in the scope of the GFZ gravity field software environment can be found in Murböck et al. (2023).

References:

Etten, W. (2006). Introduction to Random Signals and Noise. OCLC: ocm61859925. John Wiley & Sons. 255 pp. ISBN: 978-0-470-02411-9

Murböck, M., Abrykosov, P., Dahle, C., Hauk, M., Pail, R., & Flechtner, F. (2023) In-Orbit Performance of the GRACE Accelerometers and Microwave Ranging Instrument. *Remote Sens.* 2023, *15*(3), 563; https://doi.org/10.3390/rs15030563

Not implemented in this phase of the project:
- Generation of Variance-Covariance Matrices for GNSS Errors (hl-SST)

4.5.3. Stochastic modelling of Background Model Errors

Not implemented in this phase of the project:
- Application of Variance-Covariance Matrices from Ocean Tide Models
- Application of Variance-Covariance Matrices based on the AOD Error Model Component

4.5.4. Extended parameterization strategies

De-aliasing of high-frequency time-varying gravity field signals according to Wiese is implemented. The method aims at mitigating temporal aliasing effects due to non-tidal time varying signals, mainly A and O signals, albeit with modest effect.

Application of the Wiese Parameterization	
Data and Products	
Input Internal Data	▪ NEQ systems per arc for hl-SST and ll-SST observations separately.
Output L2a Data	▪ Estimated SH gravity field coefficients for the full period and partial period low-degree SH gravity field coefficients.
Algorithms and Procedure Description	
According to the Wiese method (Wiese et al. 2011), low-resolution (e.g. up to SH d/o 10-15 for a single pair, 20-30 for a double pair) gravity field coefficients are co-estimated at short time periods (e.g. daily) together with the higher-resolution gravity field over the full period (e.g. one month). This partly takes into account high-frequency information contained in the short-term gravity field solutions with the goal to reduce the temporal aliasing effect of those long-wavelength geophysical signals that have at least twice longer periods than the chosen sampling period of the short-interval gravity field modelling. The NEQ systems per arc for hl-SST and ll-SST are accumulated per day. Then, the daily NEQs are manipulated by removing epoch information for degrees higher than the selected low-degrees of the short time period fields. The thus modified NEQs are accumulated for the selected full period (e.g. one month), leading to a NEQ system containing low-degree daily and full period gravity field coefficients. The NEQ system is solved with the Dynamo	

software using Cholesky decomposition. The low-degree coefficients of the full period model are calculated as the average of all low-degree short-period coefficients.

References:

Wiese, D.N., Visser, P.N.A.M., Nerem, S. (2011). Estimating low resolution gravity fields at short time intervals to reduce temporal aliasing errors. Adv. Space Res., 48(6), 1094-1107. https://doi.org/10.1016/j.asr.2011.05.027

Not implemented in this phase of the project:

- Application of the DMD Approach

4.5.5. De-Aliasing strategies

The de-aliasing strategies can be subdivided into four groups:

- Nominal strategy: using time varying gravity field background models for de-aliasing purposes (ocean tide model, AOD model).
- Using time varying gravity field background models (ocean tide model, AOD model) and variance-covariance information from background model errors (OTVCM, AODVCM) (not implemented at this stage of the project).
- Using extended parameterization techniques without background models (not implemented at this stage of the project).
- Using extended parameterization techniques together with background models.

The strategies of the two implemented methods are described below.

Nominal De-Aliasing with Background Models	
Data and Products	
Input Aux. Data	▪ Ocean tide model. ▪ Non-tidal atmospheric and oceanic mass variations (AOD model) in terms of SH.
Output L2a Data	▪ Estimated SH gravity field coefficients.
Algorithms and Procedure Description	
Time-variable background models for ocean tides and non-tidal AO signals are used in the nominal processing for de-aliasing purposes. The primary goal is to retrieve the time-varying HIS signal. Therefore, errors due to ocean tides and non-tidal AO signals should be as small as possible. The processing scheme follows the description in the tables 'Precise orbit determination – gravity field' and 'Solution of the NEQ system'. References: https://grace.obs-mip.fr/variable-models-grace-lageos/grace-solutions-release-05/rl05-products-description/	

De-Aliasing using Extended Parameterization Techniques with Background Models	
Data and Products	
Input Aux. Data	▪ Ocean tide model. ▪ Non-tidal atmospheric and oceanic mass variations (AOD model) in terms of SH.

Output L2a Data	▪ Estimated SH gravity field parameters (L2A) including the HIS signal.
Optional Output	▪ Co-estimated SH ocean tide parameters.
Algorithms and Procedure Description	
This processing scheme uses extended parameterization techniques while applying an AOD model. The extended parameterization technique to be applied is described in the table 'Application of the Wiese parameterization'. The purpose of using an AOD model in combination with an extended parameterization technique is to further reduce the aliasing error due to A and O.	

4.5.6. Regularization and constraints

The nominal gravity field processing scheme using measurements from satellites with polar or near-polar orbits does not require regularization techniques. However, only processing measurements from an inclined satellite pair (NGGM) requires regularization so that the gravity field solutions do not suffer from not having measurements over the polar regions.

Regularization	
Data and Products	
Internal Input Data	▪ NEQ systems per arc for hl-SST and ll-SST observations of the inclined pair.
Optional Internal Input Data	▪ NEQ system for the polar caps based on the mean time-variable gravity field
Output L2a Data	▪ Estimated SH gravity field parameters (L2a) based on the applied regularization method.
Algorithms and Procedure Description	

NEQ systems per arc are accumulated over selected time periods for the hl-SST and the ll-SST observations. The NEQ system is regularized mainly for the low order coefficients. Following van Gelderen and Koop (1997), it is assumed that the maximum affected SH order m_{max} for each SH degree n is given by

$$m_{max} \approx \left|\frac{\pi}{2} - I\right| \cdot n, \qquad (1)$$

with the inclination I. To stabilize the inversion of the ill-conditioned NEQ system with the Dynamo software, the coefficients to order m_{max} are constrained to their a-priori values using an input file that contains the constraints as a function of degree n and order m (decreasing from 0 to m_{max}).

NB: second method consists in accumulating the NEQ system of the inclined pair with a NEQ system for the polar caps, as was done for GOCE, and solving without regularization.

References:

Van Gelderen, M., & Koop, R. (1997) The use of degree variances in satellite geometry. Journal of Geodesy, 71, pp.337-343. https://doi.org/10.1007/s001900050101

4.5.7. Fast-track processing strategies

Not implemented at this stage of the project

4.5.8. Baseline strategy vs. options

Not yet defined at this stage of the project

5. ALGORITHMS L2B PRODUCTS

Before NGGM/MAGIC Earth gravity field models can be applied to compute L3 products they might need to be further prepared in order to be able to generate optimal higher level products. This leads to L2b Earth gravity field models. This in particular is related to replacement of low degree SH coefficients and to filtering of original models, such that they represent the "true" signal content. This needs to be done differently for NGGM only and combined solutions.

With low-low satellite gravimetry missions very low gravity field coefficients can only be determined with high uncertainties or not at all. Therefore, for generating optimal products some coefficients usually shall be replaced with information from other sources. This mainly includes degree 1 coefficients representing the geo-center and the C_{20} coefficient representing the Earth's flattening. Additionally, the models are estimated up to highest possible degree in order to avoid spatial aliasing from high frequency signals into the lower spectrum. For further use of the NGGM or MAGIC gravity field models they need to be filtered accordingly, such that they can be used for L3 product generation. Finally, a consistent mean field needs to be chosen and a GIA model needs to be agreed from which the GIA correction shall be computed.

5.1. GRAVITY FIELD MODELS – TUM

5.1.1. Treatment of Very Low Degree SH Coefficients

Not yet implemented. The intention is to perform a rigorous combination (on NEQ level) with SLR normal equations.

5.1.2. A-posteriori Filtering Gravity Field Models

A-posteriori Filtering of Gravity Field Models	
Data and Products	
Input L2a Data	▪ Spherical harmonics for dedicated time intervals (3, 5, 7 … 31 day) ▪ Normal equation of particular gravity field model to be filtered
Input L2b Data	▪ Long-term mean field
Output L2b Data	▪ Filtered spherical harmonics for dedicated time intervals (3, 5, 7 … 31 day) reduced by long-term mean field
Algorithms and Procedure Description	
For post-processing of raw NGGM and MAGIC gravity field models, the time-varying decorrelation filter technique VADER (VDK, Horvath et al. 2018) is used. It is an anisotropic filter technique that is based on the variance-covariance matrix of the respective SH model. In the course of a NGGM-only or MAGIC constellation, the error pattern of the gravity field retrieval can change. Due to the adaptability of the VADER filter, attributable to the use of full, e.g., month-to-month error covariance matrices, it can be applied for different mission concepts without major modifications. The main relation between unfiltered x and filtered x_α gravity field solutions, represented by vectors of spherical harmonic coefficients, is given by $x_\alpha = \left(N + \alpha M\right)^{-1} Nx = W_\alpha x \qquad (1)$	

with the corresponding normal equation matrix N (inverse of the error variance-covariance matrix), the inverse signal variance matrix M, and the scaling factor α. These three entities form the filter matrix W_α.

The scaling factor α tunes the strength of the filtering. Its choice shall be optimized regaring minimizing the sum of the (Figure 5-1)

- Retrieval error (commission error)
- Filter omission error
- (Residual high-degree omission error)

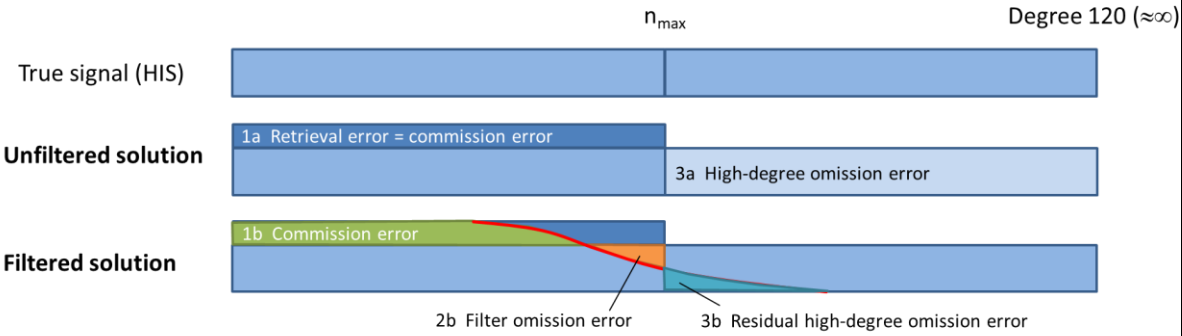

Figure 5-1: Error considerations in post-processing

References:
Horvath, A., Murböck, M., Pail, R., Horwath, M., 2018: Decorrelation of GRACE Time Variable Gravity Field Solutions Using Full Covariance Information, Geosciences, 8, 323, https://doi.org/10.3390/geosciences8090323

5.1.3. Baseline Strategy vs. Options

In Table 5-1, those L1a to L2b algorithms which compose the baseline strategy, separately for NGGM-only and MAGIC, are indicated by crosses.

Table 5-1: Baseline strategy and options of TUM gravity processor for NGGM and MAGIC

Algorithm	Section	NGGM	MAGIC
Treatment of Very Low Degree SH Coefficients	5.1.1	X	X
A-posteriori Filtering of Gravity Field Models	5.1.2	X	X

5.2. GRAVITY FIELD MODELS – GFZ

5.2.1. Mean Field

L3 products represent mass anomalies, i.e., positive or negative variations about a long-term mean gravity field of the Earth. Essentially, the choice of this mean field is arbitrary, since using a different mean field only introduces a constant bias to the time series of mass anomalies. However, when comparing these L3 products to other data or models, all-time series should refer to the same reference epoch. Therefore, the mean field has to be defined and provided to the users.

Mean Field	
Data and Products	
Input L2a Data	▪ Time series of spherical harmonics for dedicated time intervals (3, 5, 7 … 31 day).
Input Aux. Data	▪ Mean field spherical harmonics
Output L2b Data	▪ Unweighted average of input spherical harmonics for dedicated time intervals (3, 5, 7 … 31 day).
Algorithms and Procedure Description	
GRACE/GRACE-FO L2B/L3 products currently available at GFZ´s GravIS portal refer to a long-term mean field calculated as an unweighted average of 183 available GFZ RL06 Level-2 products in the period from 2002/04 through 2020/03. The choice of the mean field for NGGM/MAGIC is TBD. References: http://gravis.gfz-potsdam.de/corrections	

5.2.2. Filtering Gravity Field Models

In order to optimally separate signal and noise in the GRACE/GRACE-FO L2A data, filtering is necessary. Due to the observation geometry with its pure along-track ranging on polar orbits GRACE-like gravity fields reveal highly anisotropic error characteristics. An adequate filter technique to account for this is the decorrelation method by Kusche et al. (2009), named DDK, which is deduced from a regularization approach using signal and error information in terms of variance and covariance matrices. The filtering is applied in the spectral domain by multiplying the filter matrix to the unfiltered spherical harmonic coefficients (residuals with respect to a mean field). This method has been adapted by Horvath et al. (2018) considering the temporal variations of the error variances and co-variances, denoted by VDK filtering.

Filtering Gravity Field Models	
Data and Products	
Input L2a Data	▪ Spherical harmonics for dedicated time intervals (3, 5, 7 … 31 day) ▪ Normal equation of particular gravity field model to be filtered
Input L2b Data	▪ Long-term mean field

Output L2b Data	▪ Filtered spherical harmonics for dedicated time intervals (3, 5, 7 … 31 day) reduced by long-term mean field
Algorithms and Procedure Description	
GFZ´s monthly GRACE and GRACE-FO L2B products are optionally de-correlated and smoothed with an adaptive filter that explicitly considers the formal covariance information of the corresponding monthly GFZ RL06 L2A product. At the GravIS portal (https://gravis.gfz-potsdam.de) GFZ currently provides variants of L2B products filtered with VDK1 till VDK8 (where a larger number means weaker filtering). For NGGM and/or MAGIC the same filtering will likely be applied. Simulation studies (ESA Science Support Study and ESA TPM Science Study) have shown that for NGGM alone and for the MAGIC double pair scenario the time-varying decorrelation filter technique VADER (VDK, Horvath et al. 2018) is beneficial. According to this method, full time-varying error covariance information is used derived from the corresponding NEQ system. In the course of a NGGM-only or MAGIC constellation, the error pattern of the gravity field retrieval can change. Due to the adaptability of the VADER filter, attributable to the use of full, e.g., month-to-month error covariance matrices, it can be applied for different mission concepts without major modifications. References: Kusche, J., Schmidt, R., Petrovic, S., Rietbroek, R., 2009: Decorrelated GRACE time-variable gravity solutions by GFZ, and their validation using a hydrological model, Journal of Geodesy, 83, 10, p. 903—913, http://doi.org/10.1007/s00190-009-0308-3 Horvath, A., Murböck, M., Pail, R., Horwath, M., 2018: Decorrelation of GRACE Time Variable Gravity Field Solutions Using Full Covariance Information, Geosciences, 8, 323, https://doi.org/10.3390/geosciences8090323 http://gravis.gfz-potsdam.de/corrections	

5.2.3. Treatment of Very Low Degree SH Coefficients

The SH coefficients of degree 1 (C10, C11, S11) are related to the distance between the Earth's center of mass (CM) and center of figure (CF), which is commonly denoted as geo-center motion. However, a ll-SST gravimetry mission is not sensitive to degree 1 coefficients so that the coefficients C10, C11 and S11 are not estimated and thus set to zero in the L2a products by definition. To add information about geo-center motion, which is essential to correctly quantify both, oceanic and terrestrial mass distributions, alternative methods have to be applied.

The SH coefficient of degree 2 and order 0 (C20) is related to the flattening of the Earth. Since it is known that monthly GRACE and GRACE-FO estimates of C20 are affected by spurious systematic effects, it is recommended to replace the C20 coefficients. The same recommendation might be made for NGGM and/or NGGM/MAGIC. In addition, recent analysis from GRACE and GRACE-FO revealed that also the C30 coefficient is poorly determined when accelerometer data for one of the two spacecraft are not available or degraded and need to be transplanted from the other spacecraft. Note that due to its harmonic properties, C30 has a large impact in particular on Antarctic ice-mass change recovery. If this replacement is necessary for NGGM and/or MAGIC depends on the status of the accelerometers.

Very Low Degree SH Coefficients	
Data and Products	
Input L2b Data	▪ (optionally filtered) spherical harmonics for dedicated time intervals (3, 5, 7 … 31 day) reduced by long-term mean field
Input Aux. Data	▪ SLR normal equations from geodetic satellites
Output L2b Data	▪ (optionally filtered) spherical harmonics for dedicated time intervals (3, 5, 7 … 31 day) reduced by long-term mean field and corrected for dedicated low degree spherical harmonic coefficients
Algorithms and Procedure Description	
To add information about geo-center motion we approximate those coefficients according to the method of Swenson et al. (2008) and insert them into the L2b products. Apart from the effect of self-attraction and loading (SAL), which is not implemented in our approximation, the recommended setup as outlined by Sun et al. (2016) is used. As replacement time series for degree 2 and 3, GFZ applies a combination of SLR and low-low SST gravimetry missions on the level of normal equations. The SLR part includes the six geodetic satellites LAGEOS-1 and -2, AJISAI, Stella, Starlette, and LARES and shall be based on the same background models and standards as applied during NGGM/MAGIC processing. Relative weighting of the individual SLR normal equations is done by means of variance component estimation whereas relative weighting of the SLR-combined and NGGM/MAGIC normal equations is based on empirical weights. Gravity field coefficients up to degree/order 6 are estimated independently for each time interval. From these estimates, the low degree coefficients as well as their formal standard deviations are used to replace the L2a low degree NGGM/MAGIC solutions. References: Swenson, S., Chambers, D., Wahr, J., 2008: Estimating geocenter variations from a combination of GRACE and ocean model output, Journal of Geophysical Research: Solid Earth, 113, B08410, https://doi.org/10.1029/2007JB005338 Sun, Y., Riva, R., Ditmar, P., 2016: Optimizing estimates of annual variations and trends in geocenter motion and J2 from a combination of GRACE data and geophysical models, Journal of Geophysical Research: Solid Earth, 121, p. 8352—8370, https://doi.org/10.1002/2016JB013073 http://gravis.gfz-potsdam.de/corrections	

5.2.4. GIA Correction

Glacial Isostatic Adjustment (GIA) denotes the deformation of the solid Earth (lithosphere and upper mantle in particular) caused by ice-mass redistribution over the last 100,000 years, dominated by the termination of the last glacial cycle. Due to the Earth's viscoelastic response to mass redistribution between the ice sheets and the ocean, the Earth's gravity field is affected by long term secular trends mainly in previously glaciated regions such as North America, Fennoscandia, and Antarctica. Moreover, also coefficients of low degrees and orders are affected. A GIA model will not be applied during L2A processing due to still existing large uncertainties of these models.

GIA Corrections	
Data and Products	
Input L2b Data	▪ (optionally filtered) spherical harmonics for dedicated time intervals (3, 5, 7 … 31 day) reduced by long-term mean field and corrected for dedicated low degree spherical harmonic coefficients
Input Aux. Data	▪ GIA model providing long term secular trends for SH coefficients
Output L2b Data	▪ (optionally filtered) spherical harmonics for dedicated time intervals (3, 5, 7 … 31 day) reduced by long-term mean field and corrected for dedicated low degree spherical harmonic coefficients and GIA
Algorithms and Procedure Description	
To add information about GIA the L2A coefficients have to be corrected for trend signals provided by a suitable GIA model. At GFZ´s GravIS portal (http://gravis.gfz-potsdam.de/home) the model ICE-6G_D (VM5a) (Peltier et al., 2018) is used. Since GIA is a topic of active research, revised GIA models will certainly become available well before the launch of NGGM. References: Peltier, W.R., Argus, D.F., Drummond, R., 2018: Comment on 'An Assessment of the ICE-6G_C (VM5a) Glacial Isostatic Adjustment Model' by Purcell et al., Journal of Geophysical Research: Solid Earth, 123, p. 2019—2028, https://doi.org/10.1002/2016JB013844 http://gravis.gfz-potsdam.de/corrections	

5.2.5. Aliased Signal of the S2 Tide

A global ocean tide model is used as background model within NGGM/MAGIC L2a gravity field processing to remove ocean tide signals. However, it is well known that errors are present in ocean tide models and these errors are known to be amongst the largest error sources in GRACE-like gravity field recovery. A prominent alias frequency in GRACE-like gravity fields has a period of 161 days which is likely caused by model errors of the semi-diurnal solar tide S2 present in both ocean and atmosphere.

Aliased Signal of the S2 Tide	
Data and Products	
Input L2b Data	▪ (optionally filtered) spherical harmonics for dedicated time intervals (3, 5, 7 … 31 day) reduced by long-term mean field and corrected for dedicated low degree spherical harmonic coefficients and GIA.
Output L2b Data	▪ (optionally filtered spherical harmonics for dedicated time intervals (3, 5, 7 … 31 day) reduced by long-term mean field and corrected for dedicated low degree spherical harmonic coefficients, GIA and aliased signal of the S2 tide.
Algorithms and Procedure Description	
For GRACE and GRACE-FO a harmonic signal at this 161-day frequency is fitted (together with bias, linear trend, annual, and semi-annual components) to the time series and subtracted	

from each monthly GFZ RL06 Level-2B product. Note that when fitting the S2 tidal alias frequency to a combined GRACE and GRACE-FO time series, a phase offset of 100 degrees should be applied between the two missions as the nodal planes of both are not specifically aligned to each other (Landerer et al., 2020).

It has to be investigated if a similar correction will have to be applied for NGGM and/or MAGIC, as improved ocean tide modelling techniques and co-estimation of ocean tides are expected to be implemented in future L2A processing.

References:

Landerer, F., Flechtner, F., Save, H., Webb, F., et al. (2020): Extending the global mass change data record: GRACE Follow-On instrument and science data performance, Geophysical Research Letters, 47, e2020GL088306, https://doi.org/10.1029/2020GL088306

http://gravis.gfz-potsdam.de/corrections

5.3. GRAVITY FIELD MODELS – CNES

5.3.1. Mean Field

L3 products represent mass anomalies, i.e., positive or negative variations about a long-term mean gravity field of the Earth. Essentially, the choice of this mean field is arbitrary, since using a different mean field only introduces a constant bias to the time series of mass anomalies. However, when comparing these L3 products to other data or models, all-time series should refer to the same reference epoch. Therefore, the mean field has to be defined and provided to the users.

GRACE/GRACE-FO L2A CNES products are available on the GRGS portal, together with the long-term static mean field to be used as reference as well as the monthly gravity field solutions. The static field chosen by CNES for its RL04 and RL05 Releases corresponds to the unweighted average of the monthly GRACE solutions at roughly the middle of the data span, i.e. August 2008.

The choice of the mean field for NGGM/MAGIC is TBD.

References:
https://grace.obs-mip.fr/variable-models-grace-lageos/grace-solutions-release-05/rl05-download-products

5.3.2. Filtering Gravity Field Models

Presently, the DDK filter is implemented to filter solutions that can be interactively displayed and compared pointwise, per hydrological basin, or for a polygon.

Reference:
https://thegraceplotter.com

5.3.3. Treatment of Very Low Degree SH Coefficients

The SH coefficients of degree 1 (C10, C11, S11) are related to the distance between the Earth's center of mass (CM) and center of figure (CF), which is commonly denoted as geo-center motion. However, a ll-SST gravimetry mission is not sensitive to degree 1 coefficients and partials for the coefficients C10, C11 and S11 are not calculated. Information about geo-center motion is essential to correctly quantify oceanic and terrestrial mass distributions.

The SH coefficient of degree 2 and order 0 (C20) is related to the flattening of the Earth. The monthly GRACE and GRACE-FO estimates of C20 are affected by spurious systematic effects, The holds for NGGM and/or NGGM/MAGIC. In addition, recent analysis from GRACE and GRACE-FO revealed that also the C30 coefficient is poorly determined when accelerometer data for one of the two spacecraft is not available or degraded and needs to be transplanted from the other spacecraft. Note that C30 has a large impact in particular on Antarctic ice-mass change estimates.

Both issues are solved through the addition of geodetic SLR satellite NEQs, after which degree 1 can be estimated, and degrees 2/3 accurately estimated.

Very Low Degree SH Coefficients	
Data and Products	
Input Internal Data	Monthly (weekly etc) accumulated NEQ systems
Input Aux. Data	SLR normal equations from geodetic satellites
Output L2a Data	Estimated SH gravity field coefficients including degree 1
Algorithms and Procedure Description	
The SLR NEQ (degrees 1-30) and the monthly NEQ (deg 2-120) are accumulated, and then solved via Cholesky decomposition. Degree 1 is estimated based on the SLR data (i.e. via the SLR NEQ) only, whereas degrees 2 and higher are estimated based on both SLR and hl-SST data. In practice, although the partial derivatives of the gravity field are present up to degree 30 in the SLR NEQs, only degree 1, 2 and 3 of the SLR NEQs actively participate in the combined SLR/NGGM/MAGIC solutions. The information from NGGM/MAGIC completely dominates the information from SLR for degrees higher than 3. The SLR NEQ contains data from the geodetic satellites LAGEOS-1 and -2, AJISAI, Stella, Starlette, and LARES and shall be based on the same background models and standards as applied during NGGM/MAGIC processing. Relative weighting of the SLR-combined and NGGM/MAGIC normal equations is based on empirical weights. References: https://grace.obs-mip.fr/variable-models-grace-lageos/grgs-slr-only-solutions/	

6. ALGORITHMS L3 PRODUCTS

From the gravity field models (L2B products in spherical harmonics) gridded mass variations for Earth system components are further derived. This requires further post-processing of NGGM and/or MAGIC solutions and its time series. In particular, this addresses specific corrections to be applied to compute mass variation products (e.g. spatial leakage correction) and algorithms for signal separation and time series analyses. As an example, L3 GRACE and GRACE-FO products at GFZ´s GravIS portal (http://gravis.gfz-potsdam.de/) comprise gridded mass anomalies as well as basin average time series and are available for Terrestrial Water Storage (TWS) over non-glaciated regions, Ocean Bottom Pressure (OBP) variations in the oceans, and ice-mass changes in both Antarctica and Greenland ice sheets (AIS and GIS).

The following L3 product descriptions and algorithms are closely related to the GravIS portal operated at GFZ for GRACE and GRACE-FO data. If and how this needs to be updated for NGGM/MAGIC is TBD.

6.1. SIGNAL SEPARATION

For identifying mass distribution and mass transport for different Earth system components it is essential to separate the signal under investigation from the total signal, which is delivered by the NGGM/MAGIC gravity field models. This specifically applies to hydrology, oceanography and glaciology.

6.1.1. Terrestrial Water Storage

Level-3 TWS over non-glaciated regions as observed by NGGM and/or MAGIC is an integrated signal from all water storage compartments including snow, surface water, soil moisture, and deep groundwater. It represents anomalies relative to a long-term mean as described in Section 5.2.1 and are provided in terms of cm of equivalent water height.

TWS estimates and additional information such as TWS uncertainty, spatial leakage contained in TWS or the atmospheric mass of the background model applied during L2 processing (AOD1B) are provided either at 1° latitude-longitude grids as defined over all land regions except Greenland and Antarctica or as averaged anomalies for certain predefined regions such as river basins or climatically similar regions (i.e., regions with similar precipitation regimes). The reference surface for the spherical harmonic synthesis to the 1° grid is the reference ellipsoid as defined in the IERS Conventions (2010), Table 1.1.

Terrestrial Water Storage	
Data and Products	
Input L2b Data	▪ Filtered spherical harmonics for dedicated time intervals (3, 5, 7 … 31 day) corrected for dedicated low degree spherical harmonic coefficients, GIA and aliased signal of the S2 tide.
Input Aux. Data	▪ VDK filter matrices.
Output L3 Data	▪ TWS estimates and additional information such as TWS uncertainty, spatial leakage contained in TWS or the atmospheric mass of the background model applied during L2 processing (AOD1B) as gridded data defined

	over all land regions except Greenland and Antarctica or averaged anomalies for certain predefined regions.

Algorithms and Procedure Description

Gridded Products

a) TWS: The L2b coefficients are filtered with VDK5 and VDK3 and the trend as well as annual and semi-annual harmonics for both filter versions are estimated. In view of the lower noise level of the seasonal components, the deterministic components from VDK5 are subsequently combined with the residual month-to-month and inter-annual variations from VDK3. In months, where the standard deviation of the residuals is larger than two times the mean of the monthly standard deviation, the residual variations are taken from VDK2 filtered fields. As an additional correction, which is not part of the L2b processing, co- and post-seismic deformations from megathrust earthquakes (magnitude > 8.8 for GRACE/GRACE-FO) are removed. We expect this threshold to be much lower for NGGM/MAGIC, which aims at observing earthquakes down to magnitude 7 according to the MAGIC MRD. The empirical correction is based on a step function which is fitted to all available monthly solutions in a spherical cap with a radius of 1000 km centered at the epicenter and an exponential decay function which is fitted over two years following the main event (note that solutions from subsequent epochs are no longer statistically independent as soon as earthquake signals were empirically estimated and removed). Mass anomalies are unambiguously inverted from the Stokes coefficients by utilizing the thin layer approximation (Wahr et al., 1998). The TWS data is not corrected for spatial leakage. In the future, signal separation of earthquake signals might be further augmented by numerical forward modelling.
b) TWS uncertainty: The TWS signal estimates are accompanied by associated uncertainties that take into account the varying noise level from month-to-month (or other sub-monthly periods) associated with (i) the amount of available sensor data in a certain month which might be limited due to, e.g., satellite manoeuvers; (ii) the actual ground track pattern which might be sparse during periods of occasional short repeat orbits; and (iii) the condition of the satellites' on-board batteries which impacts the maintenance of thermal stability and thereby the noise level of the science instruments. For each monthly TWS field this information consists of the standard deviation of the TWS residuals (after removal of trend, annual and semi-annual signal) over the open ocean, i.e. all ocean points with a distance of at least 1000 km to the coast. These standard deviations are further used in the uncertainty modeling provided for the basins. The uncertainty modeling is based on a spatial covariance model which takes the non-homogeneous and anisotropic structure of spatial correlations as well as non-stationarity into account. The uncertainties are not based on formal uncertainties provided with the Stokes coefficients, but are estimated from empirical co-variances of the TWS fields. Further details can be found in Boergens et al. (2020) and Boergens et al. (2022).
c) TWS leakage: This additional information is provided to enable the correction for spatial leakage of the TWS data, if needed. The spatial leakage is estimated from differences of a combination of VDK filters with different filter strengths. The spatial leakage estimation is separated into spatial leakage of the deterministic signals (VDK5) and interannual variability (VDK3). The spatial leakage of VDK5 is estimated from scaled differences between VDK6 and VDK4, likewise for VDK3 the

differences between VDK4 and VDK2 are used. Further details are reported in Dobslaw et al. (2020).

d) TWS atmospheric mass: A certain fraction of the time-variable gravity signal picked up by a satellite gravimetry mission is caused by atmospheric mass variability. The non-tidal de-aliasing product AOD1B can be used to subtract the atmospheric contribution already during the processing of the Level-2 monthly gravity fields. In order to provide users with some flexibility to restore these atmospheric signals, the monthly mean estimate of the atmospheric background model is provided as well.

Regional Products

Time series of regional average (mean) estimates for predefined such as for the world's largest river basins, or for climatically similar regions (i.e., regions with similar precipitation properties) are provided as well. Also, for these regional average products the four different data sets TWS, TWS uncertainty, TWS leakage and TWS atmospheric mass as provided for the gridded products are calculated.

References:

Boergens, E., Dobslaw, H., Dill, R., Thomas, M., Dahle, C., Murböck, M., Flechtner, F. (2020): Modelling spatial covariances for terrestrial water storage variations verified with synthetic GRACE-FO data. International Journal on Geomathematics, 11, 24. https://doi.org/10.1007/s13137-020-00160-0

Boergens, E., Kvas, A., Eicker, A., Dobslaw, H., Schawohl, L., Dahle, C., Murböck, M., Flechtner, F. (2022): Uncertainties of GRACE-Based Terrestrial Water Storage Anomalies for Arbitrary Averaging Regions. J. Geophys. Res.: Solid Earth, 127, 2, e2021JB022081. https://doi.org/10.1029/2021JB022081

Dobslaw, H., Dill, R., Bagge, M., Klemann, V., Boergens, E., Thomas, M., Dahle, C., Flechtner, F. (2020): Gravitationally Consistent Mean Barystatic Sea Level Rise From Leakage-Corrected Monthly GRACE Data. J. Geophys. Res.: Solid Earth, 125, e2020JB020923. https://doi.org/10.1029/2020JB020923

IERS Conventions (2010). Gérard Petit and Brian Luzum (eds.). (IERS Technical Note ; 36) Frankfurt am Main: Verlag des Bundesamts für Kartographie und Geodäsie, 2010. 179 pp., ISBN 3-89888-989-6

Wahr, J. M., Molenaar, M., & Bryan, F. (1998): Time variability of the Earth's gravity field: Hydrological and oceanic effects and their possible detection using GRACE. J. Geophys. Res., 103, 30205-30229. http://doi.org/10.1029/98JB02844

http://gravis.gfz-potsdam.de/tws

6.1.2. Ocean Bottom Pressure

Satellite gravimetry as realized with NGGM and/or MAGIC is sensitive to all mass variations in the ocean basins that are proportional to a change in hydrostatic pressure at the sea floor. Ocean Bottom Pressure (OBP) variations are caused by three distinctly different dynamic processes: (i) air masses as represented by variations in atmospheric surface pressure; (ii) changes in ocean mass due to an inflow of water from the continents into the ocean basin and regional re-distribution due to attraction effects of external masses located at the continents and in the atmosphere; and (iii) the re-distribution of water within the ocean basins in response to atmospheric surface winds, atmospheric surface pressure gradients, and ocean thermohaline effects (i.e., the general ocean circulation). OBP variations are relative to a long-term mean as described in Section 5.2.1 and are provided in terms of cm of equivalent water height.

OBP estimates and additional information such as gravity-based barystatic sea-level pressure (barslv), gravity-based barystatic sea-level pressure uncertainties (std_barslv), gravity-based residual ocean circulation pressure (resobp), gravity-based residual ocean circulation pressure uncertainties (std_resobp), gravity-based bottom pressure variations likely caused by spatial leakage (leakage), background-model ocean circulation pressure (model_ocean) and background-model atmospheric surface pressure (model_atmosphere) as applied during L2 processing (AOD1B) are provided either as 1° latitude-longitude grids as defined over the world's ocean basins or as regional average (mean) estimates for predefined ocean regions (layers 'barslv', 'resobp', 'leakage', 'model_ocean', and 'model_atmosphere'). The reference surface for the spherical harmonic synthesis to the 1° grid is the reference ellipsoid as defined in the IERS Conventions (2010) Tab 1.1.

Ocean Bottom Pressure	
Data and Products	
Input L2b Data	▪ Filtered spherical harmonics for dedicated time intervals (3, 5, 7 … 31 day) corrected for dedicated low degree spherical harmonic coefficients, GIA and aliased signal of the S2 tide.
Input Aux. Data	▪ VDK filter matrices.
Output L3 Data	▪ OBP estimates and additional information such as gravity-based barystatic sea-level pressure, gravity-based barystatic sea-level pressure uncertainties, gravity-based residual ocean circulation pressure, gravity-based residual ocean circulation pressure uncertainties, gravity-based bottom pressure variations likely caused by spatial leakage, background-model ocean circulation pressure and background-model atmospheric surface pressure as applied during L2 processing (AOD1B) as gridded data defined over the world's ocean basins or as regional average (mean) estimates for predefined ocean regions
Algorithms and Procedure Description	
Gridded Products a) Gravity-based barystatic sea-level pressure (barslv): NGGM and/or MAGIC-based TWS estimates and the associated atmospheric mass distributions as given by AOD1B are used to calculate a gravitationally consistent sea-level anomaly for each month based on the theory of Tamisiea et al. (2010). The resulting sea-level variations contain both a distinct annual variation of the global mean sea-level, a pronounced positive trend, and additional strong seasonal pattern in regions characterized by Monsoon circulations in the atmosphere. b) Gravity-based barystatic sea-level pressure uncertainties (std_barslv): This information is provided as the temporal standard deviation at each grid point. c) Gravity-based residual ocean circulation pressure (resobp): The Level-2B coefficients are filtered with VDK5 and VDK2 and the trend as well as annual and semi-annual harmonics for both filter versions are estimated. In view of the less dominant annual and semi-annual signals over the ocean compared to the trend, the trend component from VDK5 is combined with the annual and semi-annual	

components and the remaining month-to-month and inter-annual variations from VDK2. As an additional correction which is not part of the Level-2B processing, co- and post-seismic deformations from megathrust earthquakes (magnitude > 8.8 for GRACE/GRACE-FO) are removed. We expect this threshold to be much lower for NGGM/MAGIC, which aims at observing earthquakes down to magnitude 7 according to the MAGIC MRD. The empirical correction is based on a step function which is fitted to all available monthly solutions in a spherical cap with a radius of 1000 km centered at the epicenter and an exponential decay function which is fitted over two years following the main event (note that solutions from subsequent epochs are no longer statistically independent as soon as earthquake signals were empirically estimated and removed). Differences between this data-set and the gravity-based barystatic sea-level pressure (barslv) are interpreted as residual ocean circulation signals (resobp).

d) Gravity-based residual ocean circulation pressure uncertainties (std_resobp): The uncertainty of the residual OBP data is spatially constant for each time step and is calculated as the standard deviation of the VDK2 filtered OBP grids reduced by the deterministic signals.
e) Gravity-based bottom pressure variations likely caused by spatial leakage (leakage): This additional layer is provided to enable a spatial leakage correction of the residual ocean circulation data if needed. The spatial leakage is estimated from differences of a combination of VDK filters with different filter strengths. The spatial leakage estimation is separated into spatial leakage of the deterministic signals (VDK5) and interannual variability (VDK3). The spatial leakage of VDK5 is estimated from scaled differences between VDK6 and VDK4, likewise for VDK3 the differences between VDK4 and VDK2 are used. Further details are reported in Dobslaw et al. (2020).
f) Background-model ocean circulation pressure (model_ocean) and atmospheric surface pressure (model_atmosphere): A certain fraction of the time-variable gravity signal picked up by a satellite gravimetry mission is caused by atmospheric mass variability and the corresponding oceanic response to changes in, e.g., surface winds. The non-tidal de-aliasing product AOD1B can be used to subtract the atmospheric contribution -- and to a large extent also the ocean contribution except for the barystatic sea-level variations -- already during the processing of the Level-2 monthly gravity fields. In order to provide users with some flexibility to restore those signals, the monthly mean estimates of both the atmospheric and the oceanic background models are provided as well.

Regional Products

Time series of regional average (mean) estimates for predefined ocean regions are provided as well for the layers ‘barslv’, ‘resobp’, ‘leakage’, ‘model_ocean’, and ‘model_atmosphere’. In case of the layer ‘barslv’, each value is accompanied by its uncertainty which is variance-propagated from the point standard deviations in layer “std_barslv” of the gridded products. In case of the layer ‘resobp’, each value is accompanied by the same (spatially constant) uncertainty value taken from the layer “std_resobp” of the gridded products.

References:

Dobslaw, H., Dill, R., Bagge, M., Klemann, V., Boergens, E., Thomas, M., Dahle, C., Flechtner, F. (2020): Gravitationally Consistent Mean Barystatic Sea Level Rise From Leakage-Corrected Monthly GRACE Data. J. Geophys. Res.: Solid Earth, 125, e2020JB020923. https://doi.org/10.1029/2020JB020923
IERS Conventions (2010). Gérard Petit and Brian Luzum (eds.). (IERS Technical Note ; 36) Frankfurt am Main: Verlag des Bundesamts für Kartographie und Geodäsie, 2010. 179 pp., ISBN 3-89888-989-6
Tamisiea, M., Hill, E., Ponte, R., Davis, J., Velicogna, I., Vinogradova, N. (2010): Impact of self-attraction and loading on the annual cycle in sea level. J. Geophys. Res., 115, C07004. http://doi.org/10.1029/2009JC005687
http://gravis.gfz-potsdam.de/obp

6.1.3. Ice Mass Change

Mass changes of the Greenland Ice Sheet (GIS) and Antarctica Ice Sheet (AIS) as observed by NGGM and/or MAGIC are calculated relative to a long-term mean as described in Section 5.2.1 and are provided in terms of Gigatons for gridded ice-mass changes or basin-averaged ice-mass changes.

Ice Mass Change	
Data and Products	
Input L2b Data	▪ Filtered spherical harmonics for dedicated time intervals (3, 5, 7 … 31 day) corrected for dedicated low degree spherical harmonic coefficients, GIA and aliased signal of the S2 tide.
Input Aux. Data	▪ Wiener filter matrices.
Output L3 Data	▪ GIS and AIS estimates for gridded ice-mass changes or basin-averaged ice-mass changes.
Algorithms and Procedure Description	
Gridded Products Gridded ice mass variations for the AIS and GIS obtained from unfiltered NGGM and/or Level-2B coefficients are provided at polar-stereographic grids with a grid spacing of 50km x 50km. The applied algorithm has been successfully used to generate gravimetric mass balance products within the ESA Climate Change Initiative (CCI) projects for the AIS and the GIS. A more comprehensive description of the algorithm and the error assessment of the products is given in Nagler et al. (2017a, b). Tailored sensitivity kernels (Groh & Horwath, 2016) resembling averaging kernels used in the regional integration approach of Swenson & Wahr (2002) are derived for each grid cell covering the entire AIS/GIS. Each kernel realizes a trade-off between the following conflicting conditions, which are to minimize leakage effects (I+II) as well as NGGM and/or MAGIC error effects (III): I. Mass changes inside the cell will be correctly recovered II. Mass changes outside the cell will have no impact on the grid cell III. Propagated errors of the NGGM and/or MAGIC solutions have minimum influence on the mass change estimate of the cell To solve for the spherical harmonic coefficients of each sensitivity kernel, a large number of condition equations, accounting for mass changes of the ice sheet as well as of the	

surrounding far-field regions, needs to be established. To control the propagation of the NGGM/MAGIC error effects, an error variance/covariance model for the monthly solutions is required. This model is expressed as an empirical variance/covariance matrix derived from the short-term month-to-month scatter of the monthly Level-2B products. The optimal weights for the conflicting conditions are chosen from a set of plausible combinations by assessing the noise level and leakage errors in the corresponding surface mass estimates. Leakage errors are derived from a range of synthetic data sets with a priori known true mass changes, mimicking mass variations in different compartments of the Earth system.

Regional Products

Basin-average ice mass variations for the AIS and GIS are obtained from unfiltered Level-2B coefficients. The definition of 25 major drainage basins for the AIS and 7 drainage basins for the GIS, as well as the inversion procedure based on a forward modelling approach follows Sasgen et al. (2013) and Sasgen et al. (2012), respectively. The inversion procedure uses predefined spatial patterns of surface-mass change of known magnitude to calculate their regional imprint in the gravity field. In a second step, the regional patterns are filtered identically to NGGM and/or MAGIC observations and least-squares adjusted (scaled) to fit the observations in the spatial domain. Using the forward model localizes the mass change more towards the coast, leading to a more realistic mass distribution with each basin compared to assuming uniform mass distribution. The inversion results are weakly dependent on the choice of the mass distribution (< 10 %), however, less prone to biases as the forward model and the GRACE data are subjected to the same post-processing procedure. For the time series the following processing steps are applied:

I. Spectral masking of region of interest
II. Low-pass filtering using a Wiener optimal filter (Sasgen et al. 2006) constant in time
III. Conversion from gravity field to surface-mass changes using elastic compressible surface-load Love numbers
IV. Least-squares adjustment

The spectral mask is 1 until 200 km outside the grounding line of the ice sheet, following a smooth transition to 0 reached at 1000 km (AIS) or 600 km (GIS). The Wiener filter is approximately equivalent to a Gaussian filter of 4° spatial half-width.

<u>References</u>:

Groh, A., Horwath, M. (2016): The method of tailored sensitivity kernels for GRACE mass change estimates. Geophysical Research Abstracts, 18, EGU2016-12065

Nagler, T., et al. (2017a): Algorithm Theoretical Basis Document (ATBD) for the Antarctic_Ice_Sheet_cci project of ESA's Climate Change Initiative, version 2.1. Available from: http://www.esa-icesheets-antarctica-cci.org/

Nagler, T., et al. (2017b): Comprehensive Error Characterisation Report (CECR) for the Antarctic_Ice_Sheet_cci project of ESA's Climate Change Initiative, version 2.1. Available from: http://www.esa-icesheets-antarctica-cci.org/

Sasgen, I., Martinec, Z., Fleming, K. (2006): Wiener optimal filtering of GRACE data. Studia Geophysica et Geodaetica, 50, 4, p. 499-508. http://doi.org/10.1007/s11200-006-0031-y

Sasgen, I., van den Broeke, M., Bamber, J., Rignot, E., Sørensen, L., Wouters, B., Martinec, Z., Velicogna, I., Simonsen, S. (2012): Timing and origin of recent regional ice-mass loss in Greenland. Earth and Planetary Science Letters, 333-334, p. 293-303. https://doi.org/10.1016/j.epsl.2012.03.033

Sasgen, I., Konrad, H., Ivins, E., Van den Broeke, M., Bamber, J., Martinec, Z., Klemann, V. (2013): Antarctic ice-mass balance 2003 to 2012: regional reanalysis of GRACE satellite gravimetry measurements with improved estimate of glacial-isostatic adjustment based on GPS uplift rates. The Cryosphere, 7, p. 1499-1512. https://doi.org/10.5194/tc-7-1499-2013

http://gravis.gfz-potsdam.de/ais

http://gravis.gfz-potsdam.de/gis

7. ALGORITHMS' SRL

Most of the algorithms described in the previous chapters are mature and used in operational environment. Some algorithms were developed and used in simulations in order to identify the optimal setup for using them. In order to estimate the maturity of algorithms the scientific readiness level is classified according to the scheme shown in Table 7-1 [AD-1]:

Table 7-1: Definition of scientific readiness levels [AD-1]

SRL	Definition
1	Initial Scientific Idea Formulated
2	Scientific Idea Consolidated
3	Requirements Drafted
4	Feasibility Shown
5	Mission Performance Assessed
6	Mission Concept Validated
7	Science Demonstrated
8	Science Validated and Matured
9	Science Impact Quantified

Table 7-2 provides an estimate about the SRL of the algorithms defined in this document. Note: Here only algorithms from L1b to L2a and higher levels are considered as algorithms from L1a to L1b are subject to input from the industry studies. De-Aliasing strategies as described in sections 4.3.5, 4.4.6 and 4.5.5 are not included as they represent strategies and not algorithms. The strategies defined there apply algorithms explained in the previous chapters of each section.

Many algorithms included in Table 7-2 have already been applied successfully in GRACE/GRACE-FO real data processing. An SRL of 8 has been assigned to them consistently, because of the assumption that they can be further optimized and tuned for the processing of NGGM and MAGIC towards SRL 9.

Table 7-2: Estimate of SRL of NGGM/MAGIC algorithms

Level	Algorithm	Institute	SRL
L1b to L2a	Reduced-Dynamic and Kinematic Precise Orbit Determination	TUD	8
	POD-based Accelerometer Calibration	TUD	8
	POD-based Accelerometer Calibration	CNES	8
	Reduced LRI Observations	TUD	5
	Numerical orbit integration	TUM	8
	Set-up of observation equations and assembling of normal equations	TUM	8
	Solution of the NEQ system	TUM	8
	Generation of Variance-Covariance Matrices for Product Errors (ll-SST)	TUM	8

	Stochastic modelling of Ocean Tide Background Model Errors	TUM	5
	Stochastic modelling of AO Background Model Errors	TUM	4
	Extended parameter model: Wiese Parameterization	TUM	7
	Extended parameter model: Application of the DMD approach	TUM	7
	Extended parameter model: Ocean Tides	TUM	5
	Extended parameter model: Empirical Parameters	TUM	5
	Polar Cap Regularization	TUM	8
	Fast-Track Processing Strategy	TUM	5
	Precise Orbit Determination – GNSS Constellation	GFZ	8
	Precise Orbit Determination – Gravity Field	GFZ	8
	GNSS Data Editing	GFZ	8
	ll-SST Data Editing	GFZ	8
	Generation of a priori Orbits	GFZ	8
	NEQ System Setup	GFZ	8
	Solution of the NEQ System	GFZ	8
	Generation of Variance-Covariance Matrices for Product Errors (ll-SST)	GFZ	8
	Generation of Variance-Covariance Matrices for GNSS Errors (hl-SST)	GFZ	8
	Application of Variance-Covariance Matrices from Ocean Tide Models	GFZ	6
	Application of Variance-Covariance Matrices based on the AOD Error Model Component	GFZ	6
	Stochastic modelling using a posteriori residuals	GFZ	8
	Application of the Wiese Parameterization	GFZ	7
	Application of the DMD Approach	GFZ	7
	Regularization	GFZ	8
	Fast-Track Processing Strategy	GFZ	4
	Precise Orbit Determination – GNSS Constellation	CNES	8
	Precise Orbit Determination – Gravity Field	CNES	8
	Solution of the NEQ System	CNES	8
	Generation of Variance-Covariance Matrices for Product Errors (ll-SST)	CNES	4
	Generation of Variance-Covariance Matrices for GNSS Errors (hl-SST)	CNES	1
	Application of Variance-Covariance Matrices from Ocean Tide Models	CNES	1
	Application of Variance-Covariance Matrices based on the AOD Error Model Component	CNES	1
	Application of the Wiese Parameterization	CNES	4
	Application of the DMD Approach	CNES	1
	Regularization	CNES	4
	Fast-Track Processing Strategy	CNES	1
L2a to L2b	Treatment of Very Low Degree SH Coefficients	TUM	2

	A-posteriori Filtering of Gravity Field Models	TUM	8
	Mean Field	GFZ	8
	Filtering Gravity Field Models	GFZ	8
	Treatment of Very Low Degree SH Coefficients	GFZ	8
	GIA Correction	GFZ	8
	Aliased Signal of the S2 Tide	GFZ	8
	Mean Field	CNES	8
	Filtering Gravity Field Models	CNES	8
	Treatment of Very Low Degree SH Coefficients	CNES	8
L2b to L3	Terrestrial Water Storage	GFZ	8
	Ocean Bottom Pressure	GFZ	8
	Ice Mass Change	GFZ	8

8. REFERENCES OF PART 1

8.1. APPLICABLE DOCUMENTS

[AD-1] Scientific Readiness Levels (SRL) Handbook, ESA-EOPSM-SRL-MA-4267, Issue 2.0, Date: 10.02.2023

8.2. REFERENCE DOCUMENTS

Algorithm Theoretical Basis Document for GRACE Level 1B Data Processing, GRACE 327-741, Revision: 1.2, Authors: S.C. Wu, G. Kruizinga, W. Bertiger, Date: 09.05.2006

GOCE Ground Segment Instrument Processing Facility 1, Proposed Algorithms for the SSTI Processor, GO-TN-IAPG-GS-0003, Issue 1, Revision 1, Date: 29.03.2004

GOCE Ground Segment Instrument Processing Facility 1, Detailed Processing Model for SSTI [DPM-SSTI], GO-TN-IAPG-GS-0002, Issue 4, Revision 2, Date: 05.02.2006

GOCE Ground Segment Instrument Processing Facility 1, Detailed Processing Model for EGG [DPM-EGG], GO-TN-IAPG-GS-0001, Issue 4, Revision 8, Date: 14.09.2009

GOCE High Level Processing Facility, GOCE Level 2 Product Data Handbook, GO-MA-HPF-GS-0110, Issue 5, Revision 0, Date: 04.08.2014

IGS, IGS Formats and Standards, https://igs.org/formats-and-standards, 2023

Optimal combination of quaternions from multiple star cameras, JPL Internal Memorandum, Author: L.J. Romans, Date: May 2003

Wen, H.Y., Kruizinga, G., Paik, M., Landerer, F., Bertiger, W., Sakumura, C., Bandikova, T. and Mccullough, C., Gravity Recovery and Climate Experiment Follow-On (GRACE-FO) Level-1 Data Product User Handbook, JPL D-56935 (URS270772), NASA Jet Propulsion Laboratory, California Institute of Technology, September 11, 2019

8.3. SCIENTIFIC REFERENCES

Beutler, G. (2005) Methods of celestial mechanics. Springer, Berlin

Beutler, G., Jäggi, A., Mervart, L., Meyer, U. (2010) The celestial mechanics approach: theoretical foundations. J. Geod. Vol. 84, pp. 605-624, https://doi.org/10.1007/s00190-010-0401-7

Dahle, C., Murboeck, M., Flechtner, F., Dobslaw, H., Michalak, G., Neumayer, K.H., et al. (2019) The GFZ GRACE RL06 Monthly Gravity Field Time Series: Processing Details and Quality Assessment. Remote Sensing, 11(8), 2116. https://doi.org/10.3390/rs11182116

Frommknecht, B., Integrated Sensor Analysis of the GRACE Mission, Dissertation Technical University of Munich, 2007, https://nbn-resolving.de/urn/resolver.pl?urn:nbn:de:bvb:91-diss-20071009-630607-1-0

Frommknecht, B., Lamarre, D., Meloni, M. et al., GOCE level 1b data processing. J Geod 85, 759–775 (2011). https://doi.org/10.1007/s00190-011-0497-4

Hofmann-Wellenhof, B., & Moritz, H. (2005) Physical Geodesy. Springer Vienna, ISBN 3-211-23584-1

Marty, JC, Loyer S., Algoritmic documentation of the GINS software, (2018) , https://www5.obs-mip.fr/wp-content-omp/uploads/sites/28/2020/05/GINS_Algo.pdf

Neumayer, KH., Schreiner, P., König, R., Dahle, C., Mammadalayiev, N., Glaser, S., Flechtner, F. (2023). EPOS-OC, A universal software tool for satellite geodesy at GFZ. Poster presentation at international Union of Geodesy and Geophysics (IUGG) 2023 symposium Berlin, Germany, 11-20 July. Abstract number IUGG23-4363

Reigber, C. (1989) Gravity field recovery from satellite tracking data. In Theory of Satellite Geodesy and Gravity Field Determination; Lecture Notes in Earth Sciences; Sanso, F., Rummel, R., Eds.; Springer: Berlin/Heidelberg, Germany, 1989; Volume 25, pp. 197-234, ISBN 3-540-51528-3

Siemes, C., Rexer, M., Schlicht, A. et al. GOCE gradiometer data calibration. J Geod 93, 1603–1630 (2019). https://doi.org/10.1007/s00190-019-01271-9

Stummer, C., Gradiometer Data Processing and Analysis for the GOCE Mission, Dissertation Technical University of Munich, 2012, https://nbn-resolving.de/urn/resolver.pl?urn:nbn:de:bvb:91-diss-20121123-1111698-0-3

Sulzbach, R., Hart-Davis, M., Dettmering, D., & Thomas, M. (2023): Regularized Empirical Variance-Covariance-Matrices for stochastic gravity modeling of 8 major ocean tides. GFZ Data Services. https://doi.org/10.5880/NEROGRAV.2023.003

PART 2:

SCIENTIFIC READINESS ASSESSMENT (SRA) REPORT

9. INTRODUCTION

The purpose of this document is to describe the self-assessment procedure in accordance with [RD-1] and based on the ESA SRL Handbook [AD-1]. In this document the SRA aim, objectives, and organisation to follow to conduct self-assessed SRA to be agreed by the Agency based on advice provided in the ESA SRL Handbook are described. Criteria to be used to define when an SRL level has been met (i.e. what evidence needs to be available in the peer review literature or other ESA-endorsed Technical notes, software, data etc) are defined, and the corresponding evidence base to support SRL claims according to the criteria and process set out are collected. The underlying algorithms are defined in the document D1-CCN1, "ATBD of NGGM/MAGIC L2 and L3 products" [RD-1]. The document also reports on the review process conducted with ESA Technical Officer and the SRA panel, and the its results and conclusions.

The main goal is to

- demonstrate SRL 5 according to the ESA SRL handbook at the end of Phase A extension for the numerical simulators at TUM and GFZ.

Due to the fact that development of the CNES simulation environment has been started only during the extension of this Phase A study, it is not yet at a stage to demonstrate an SRL of 5.

10. DEFINITION OF SRL5

In the following the definition of the requirements of SRL5 according to [1] are repeated. Criteria that seem to be most important for the assessment are highlighted in the text.

"The key modules of an end-to-end performance simulator are available. This comprises as a minimum a scene generator providing the stimuli entering an instrument module, and a processing chain generating measurement data and observation data. All modules represent critical elements in the development of the mission which also pose a scientific risk.

The E2E simulator retrieval capability is developed, tested and validated using realistic simulations and / or proxy data from actual measurement data. These measurement data could for example be provided through targeted campaigns or existing observing systems approximating the mission. The performance evaluation is applied to a predefined range of conditions (including representative variabilities of natural and observational origins) and can be used to address the needs originating from the science/user requirements in an end-to-end manner.

Performance simulations applicable for a realistic range of uncertainties (both geophysical and technical) are traced through the system and are compared against a pre-defined performance metric (or set of metrics) reflecting observation and measurement requirements. The objective is to quantify performance and to verify the mission concept rather than delivering a software tool. Ideally, modules are chained resulting in a first version of the end-to-end performance simulator."

11. GUIDING HIGH-LEVEL QUESTIONS

In [AD-1] guiding high-level questions are provided. In the following sections, they will be answered by the contributing processing centers TUM, GFZ and CNES individually.

11.1. ANSWER TO HIGH-LEVEL QUESTIONS – PERFORMANCE SIMULATOR TUM

Is a performance simulator in place and are the most important and significant processes and input parameters (including sources of uncertainty) properly represented?

- YES. A performance simulator for the realistic simulation of NGGM and MAGIC scenarios, including all relevant error sources (product errors, background model errors) is available. It was further developed and applied for numerous numerical studies of various scenarios in the ESA projects SC4MVG ([RD-17]), ADDCON ([RD-18]), ADDCON Extended Phase ([RD-19]), and the current MAGIC Science Support Study (incl. CCN1) ().
- The main components of the numerical simulator are: orbit integrator, gravity retrieval (including all relevant gravitational signals, stochastic modelling of instrument/product errors, standard parameterization + co-estimation of short-term solutions, numerically stable inversion), assessment and validation tools in time and frequency domain.
- The processor is described in several journal publications, e.g. [RD-2], [RD-3], [RD-4], [RD-5], [RD-6], [RD-7].

- The capability and performance of this simulator will be evaluated by means of realistic test scenarios (cf. Chapter 13).

Is an error propagation model in place allowing the rigorous computation of uncertainties (e.g. accounting for co-variant error effects) for measurement and observation data?

- YES, an error propagator is in place, which performs the rigorous propagation of uncertainties starting from error models of the key payload through the whole system.
- As the current baseline, realistic error models of the key payload (= pre-fit residuals of product-only noise scenario) are used as stochastic model of observation errors introduced in terms of a weighting matrix in the gravity retrieval.
- Optionally and existing, stochastic models based on post-fit residuals of full-noise case to accommodate temporal aliasing errors could be used as an alternative.
- Optionally (not fully implemented yet): Stochastic modelling of background model errors in addition to product-errors. These methods are going to be further developed during Phase B. [RD-8], [RD-9]

Has a set of realistic and representative test scenarios and input scenes been established and are they scientifically justified?

- YES, a multitude of product-noise only and full noise scenarios has been established. The test scenario used in the frame of this review will be based on the current 5d_397_i70. It is described in detail in Chapter 13.
- The scientific analysis and assessment of the results is performed by a science expert group as part of the project.
- A set of previous test scenarios was also analyzed by user representatives in the frame of JMCMEG.

Is the simulator tested, verified / validated and applied for the predefined set of scenarios?

- YES. The results of the simulator tests are presented in Chapter 15 and matched against the test criteria specified in Chapter 14.
- In the past, the TUM simulator was tested in the course of the MAGIC Science Support Study, Phase A, against a second simulator implementation based on EPOS software at GFZ: Detailed comparison of intermediate and final products for test scenario 3d_H in product-noise only and full noise case: difference in results <5% of the error level in full-noise case (see MAGIC/Science Phase 1 Final Report)
- Simulator comparison with 5 Chinese gravity processing centers showed good agreement (performed in the frame of ESA ADDCON ([RD-19]), extended phase; [RD-4]).

Are all assumptions of the performance simulator documented and critically discussed?

- The components of the simulator are described in the ATBD [AD-1].
- The performance simulator documented in several scientific publications, e.g. [RD-2], [RD-3], [RD-4], [RD-5], [RD-6], [RD-7].
- The results of a multitude of simulation scenarios are documented in the Deliverables of the SV4EMG ([RD-17]), ADDCON ([RD-18], [RD-19]) and MAGIC/Science Phase A projects ([RD-20]).

11.2. ANSWER TO HIGH-LEVEL QUESTIONS – PERFORMANCE SIMULATOR GFZ

Is a performance simulator in place and are the most important and significant processes and input parameters (including sources of uncertainty) properly represented?

- Yes
- In-house developed EPOS (Earth Parameter and Orbit System) software available
- Used for GRACE/GRACE-FO real data analysis and was further developed and applied for numerical studies of various scenarios in the ESA projects MAGIC Science Support Study (incl. CCN1) and TPM Science Study
- Includes forward simulation (generation of realistic ll-SST and hl-SST observations based on orbit scenarios and background models) and backward simulation (a priori orbit generation using POD which includes all relevant gravitational signals, NEQ generation, stochastic modelling of instrument/product errors, de-aliasing by background models and stochastic modelling of background model errors, numerically stable inversion). More detailed information on the individual processing steps can be found in the ATBD [AD-1]
- Assessment and validation tools available in time and frequency domain

Is an error propagation model in place allowing the rigorous computation of uncertainties (e.g. accounting for co-variant error effects) for measurement and observation data?

- Yes, an error propagator is in place, which performs the rigorous propagation of uncertainties starting from error models of the key payload through the whole system.
- As the current baseline, the generation of uncertainties is done by scaling the spectrum of normally distributed random time-series with their individual spectral error model. The noise time-series generated in this way contain correlated noise characteristics and are added to the simulated observations in terms of range-rates for the ll-SST link and in terms of accelerations in three directions for the accelerometer. The error models for the key payload are provided by ESA and/or industry as long as error models based on in-orbit performance analyses are not available yet (e.g. LRI performance from GRACE-FO). The characteristics of the observation error model, which is introduced in order to generate realistic measurements, are reflected in the pre-fit residuals of product-only simulations proving that the processing software is capable to numerically propagate the introduced noise characteristics in a rigorous way. GRACE/GRACE-FO-like noise free simulations have shown that the system is capable to propagate noise with an accuracy of less than 1 nm/sec (based on pre-fit residuals) having a noise floor of less than 10^{-11} m/s/sqrt(Hz) for frequencies smaller than 10^{-2} Hz. The accuracy of the error propagation of individual error sources of the key payload can be evaluated by computing pre-fit residuals which contain the error component of interest, exclusively. Given the numerical accuracy of the processor, the error propagation of the noise models for the key payload can be assumed as correctly
- The stochastic model of observation errors is introduced in terms of variance-covariance matrices (VCMs) in the gravity retrieval. For ll-SST, the error information is derived from the error models (baseline). The stochastic modelling of the GPS code and phase

components is based on pre-fit residuals. The procedure of the generation of the VCMs for observations is described in the ATBD [AD-1]

- Optional and existing: stochastic modelling based on error assumptions by means of pre-fit residuals of product-only noise scenario
- Optional and existing: stochastic modelling based on post-fit residuals of full-noise case to accommodate temporal aliasing errors
- Optionally and existing: static ocean tide VCM
- Optionally (not fully tested yet): AOD VCM information
- Optionally (not yet implemented): time-variable AOD VCM (will be implemented within NEROGRAV)

Has a set of realistic and representative test scenarios and input scenes been established and are they scientifically justified?

- Yes
- EPOS has been used to simulate realistic single and double pair scenarios in the frame of MAGIC/TPM
- Product-noise only and full noise scenarios
- Current baseline scenario 5d_397_i70 plus previous baseline/experimental (e.g., 3d_H, 5d_Ma or 5d_Mb)
- Retrieval of gravity fields from 1 day to multiple years
- Scientific analysis and assessment of results by science expert group as part of both projects

Is the simulator tested, verified / validated and applied for the predefined set of scenarios?

- Yes
- Simulator tested against a second simulator implementation at TUM: Detailed comparison of intermediate and final products for test scenario 3d_H in product-noise only and full noise case: difference in results <5% of the error level in full-noise case (see MAGIC/Science Phase 1 Final Report)
- GRACE-FO simulations have been verified against GRACE real data (Flechtner et al. (2016), https://doi.org/10.1007/s10712-015-9338-y)
- GRACE-I simulations have been validated against GRACE real data (Flechtner (2022), Phase-A Final Report, not public)
- Background model implementation has been successfully tested against orbit and gravity field determination software of other GRACE/GRACE-FO ACs (Lasser et al. (2020), https://doi.org/10.5194/adgeo-55-1-2020)
- Simulator can be used to address the needs originating from the science/user requirements in an end-to-end manner.

Are all assumptions of the performance simulator documented and critically discussed?

- The components of the simulator are described in the ATBD [AD-1].

- The performance simulator is documented in the following scientific publications: [RD-21]and [RD-22]. Further, a paper by Neumayer et al., EPOS-OC, a universal software tool for satellite geodesy at GFZ, will be submitted to Iternational Association of Geodesy Symposia – IUGG Berlin volume
- Documentation in Deliverables of MAGIC/Science Phase 1 + CCN1 and TPM

11.3. ANSWER TO HIGH-LEVEL QUESTIONS – PERFORMANCE SIMULATOR CNES

Is a performance simulator in place and are the most important and significant processes and input parameters (including sources of uncertainty) properly represented?

- Yes
- In-house developed GINS and Dynamo software available
- Used for GOCE, GRACE/GRACE-FO real data analysis as well as for various simulation studies (e.g. GOCE, MARVEL, e-GRASP)
- GINS can perform forward simulation: generation of position, DORIS, SLR, accelerometer observations based on orbit scenarios and background models. In GINS, only white noise can be added to the observations. Colored noise (e.g. accelerometer noise for MAGIC) is generated with specific software, or read from file, and then added to perfect observations.
- GINS can perform backward simulation: the orbits are fitted to the simulated observations until convergence is reached, then normal equations pertaining notably to gravity field parameters and accelerometer calibration parameters are calculated in an additional step with the fitted orbit parameters fixed. Instrument noise models can be taken into account via VCM applied to the LRI residuals. Empirical parameterization schemes (e.g. hourly bias estimation in the RTN frame, 1/2/n-CPR estimation) can be used with position observations. Bias, slope and 1/2/n-CPR parameters can also be estimated for KBR or LRI range-rate or range observations. The normal equations are manipulated (stack, re-order, etc) and solved with the Dynamo software.
- Assessment and validation tools available in time and frequency domain

Is an error propagation model in place allowing the rigorous computation of uncertainties (e.g. accounting for co-variant error effects) for measurement and observation data?

- No (work in progress)
- Started implementation of stochastic modelling based on realistic error assumptions of the key payload by means of analytical noise models for KBR/LRI and ACC

Has a set of realistic and representative test scenarios and input scenes been established and are they scientifically justified?

- No

Is the simulator tested, verified / validated and applied for the predefined set of scenarios?

- No

- MARVEL simulations have been verified against GRACE real data (cnes internal report)

Are all assumptions of the performance simulator documented and critically discussed?

- No

11.4. ANSWER TO HIGH-LEVEL QUESTIONS – ACCELEROMETER CALIBRATION (TUD, CNES)

Is a draft mission calibration and product validation strategy available and properly described?

- Regarding a calibration and product validation strategy based on GNSS Precise Orbit Determination (POD), the answer is YES: such strategies are available.
- Regarding a proper description, it can be stated that descriptions exist based on, e.g., GRACE, GRACE-FO, and Swarm heritage (e.g., also current Swarm DISC TOLEOS project;, [RD-11]). These descriptions have not yet been explicitly tailored for NGGM.
- Both at CNES and TU Delft, operational software is available for GNSS-based accelerometer calibration (estimation of biases and scale factors). The associated software packages have been extensively used - and tested with - real data from several missions, including CHAMP, GRACE, GOCE-FO, Swarm and GOCE (the latter flying drag-free).
- The same software packages have been - and are being – used for End-to-End simulations for defined NGGM scenarios, which is (being) documented in Technical Notes.

11.5. ANSWER TO HIGH-LEVEL QUESTIONS – LRI CALIBRATION (AEI)

Is a draft mission calibration and product validation strategy available and properly described?

- The mission primes have a technical note TN36 “calibration plan”, where LTI calibrations are described. These include the on-ground calibrations, e.g. for the laser frequency model, LTI processing delays w.r.t. GNSS receiver, LTI pointing angles & Differential Wavefront Sensing and others, as well as the in-flight calibrations comprising the absolute laser frequency (LTI scale factor), tilt-to-length coupling calibrations, LTI pointing angles, LTI retro-reflector unit & transmit beam calibrations and some other non-regular calibrations.
- A dedicated description for the validation of the level1b LTI data products has not been set up to our knowledge. Such a validation should cover at least the LTI ranging data product and the LTI pointing angles.
- Validation of the LTI ranging data product can be achieved by

  - so-called Himalaya plots at a qualitative level indicating the range-variation when satellites pass a certain mass concentration like the Himalaya region
  - evaluating the spectrum of LTI range at frequencies above 200 mHz, which should contain only LTI instrument noise as the gravitational and non-gravitational signals decay below the LTI noise at these frequencies. It is expected that the LTI ranging spectrum is limited by laser/cavity frequency noise above 200 mHz, as shown in the plot from GRACE-FO below (yellow trace indicates predication of frequency noise). The LTI range rms variations in particular frequency bands can also be plotted geographically or on argument of latitude plots to identify particular features.

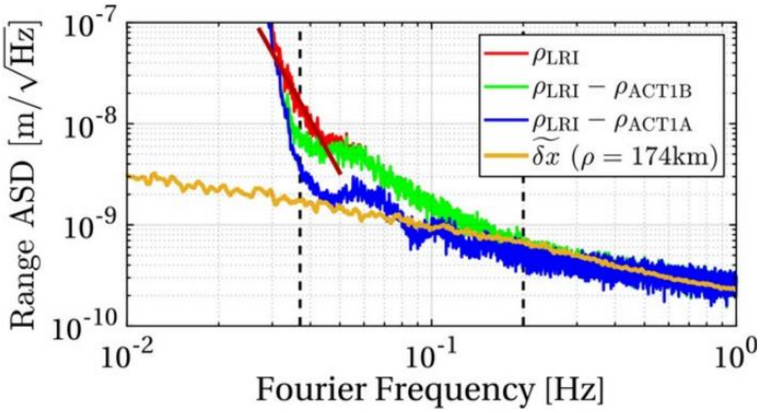

  - analyzing the pre-fit and post-fit residuals during gravity field recovery. However, the level of these residuals is typically significantly higher than the LRI noise at low frequencies. At high frequency, where the LTI range variations are caused by the static gravity field, the pre-fit residual level should be reduced to a level caused by instrument noise or background model errors.
  - comparison of LTI range with GNSS-derived range, which should be limited by GNSS precision
  - correlating the LTI range (acceleration) data with the ACC data, in particular in the frequency band between 35 and 200 mHz, as here the LTI ranging data is typically dominated by non-gravitational signals. This validation is only feasible, if drag compensation/drag free is disabled, e.g. during calibration or commissioning activities, because otherwise the drag-compensation would remove the non-gravitational accelerations (in ACC and LTI). Also, transient events like impacts of micrometeorites or thruster activations of non-continuous on/off thruster (if present) could be resolved both by LTI and ACC. They can be useful in validating the LTI datasets, e.g. to determine potential time-shifts.
  - during the generation of the LTI level1b datasets, consecutive runs of data processing produce typically overlapping segments, which are usually truncated in the public data to, e.g., day bounds. Evaluating the differences in the LTI range on these overlapping segments, e.g. for day N and day N+1, can reveal information on the quality of data products.
- The LTI pointing information data products can be validated using

- post-fit residuals during the TTL calibrations.
- Inter-comparison of different attitude sensors like ACC, star cameras, inertial measurement unit with the LTI dataset.

11.6. ANSWER TO HIGH-LEVEL QUESTIONS – USERS & EVALUATION OF APPLICATIONS

Is there a demonstrated interest of users?

- YES. A summary is given in the IUGG study ([RD-10]), expressed also in the IUGG 2015 Resolution No. 2. It is also demonstrated by a huge number of scientific publications in high-level journals.
- IUGG 2015 resolution on the need of future gravity and magnetic field missions (Resolution No. 2), IUGG Resolution 2023 on Terrestrial Water Storage (Resolution No. 2)
- MAGIC MRD/NGGM MRD
- The current user needs are also reflected in the result of the user questionnaire performed in the course of this project.

Is there a first evaluation of (simulated or measured data) in applications?

- YES
- Work by Uni Stuttgart and Uni Luxembourg during ADDCON ([RD-18], [RD-19])
- See, e.g., MAGIC science paper (GJI, in review)
- Evaluation by user expert group in the frame of MAGIC Science Support Study (Phase 1 and Phase 2), TPM (WP400) and experts of JMCMEG

11.7. ANSWER TO HIGH-LEVEL QUESTIONS – ROBUSTNESS AGAINST EXTERNAL DATA

Has the robustness of the simulator been demonstrated against independent observations (e.g. campaign data)?

- There has been only a limited degree of demonstration yet. However, this is also true for the GRACE/GRACE-FO mission, especially regarding the low-degree spectral range where temporal gravity signals have their largest amplitude. The main problem is that these gravity missions achieve unprecedented accuracies in the low-degree range. and therefore independent data with a comparable accuracy simply does not exist.
- To validate the quality of results of GRACE and GRACE-FO, frequently one uses large-scale regions where no big temporal gravity signals are expected, such as big deserts or the ocean areas. However, also here remaining signals cannot be automatically interpreted as noise in the gravity field solutions, but could also be newly detected signal.

- A certain kind of validation can also be achieved by inter-comparison with other missions. As an example, the inter-comparison of GRACE and GOCE (based on static gravity field) in the spectral region where both missions have comparable performance indicated a very good consistency among these two missions. This can also be analyzed in combined gravity solutions such as GOCO and EIGEN.
- An indirect validation can be achieved on product level, when comparing, e.g., gravimetric ice mass balance estimates with those based on altimetry or the input/output method. Inter-comparison exercises such as, e.g., the IMBIE studies demonstrated a good consistency of gravity field mission results with complementary techniques.
- In will be very difficult also in the future to design campaigns to solve to problem. The accuracy needed for complementary data is on the microGal level, which is currently only achievable for terrestrial gravity meters, while the achievable accuracy of airborne and shipborne gravimetry is on the milliGal level. Therefore, they are not sensitive to large-scale gravity changes even in repeat campaigns. On the other hand, the results of a potential field (gravity) mission is very difficult to compare against very localized measurements of terrestrial gravimetry, which can be additionally influenced by very local phenomena. The requirements for such a campaign would be an accuracy on the microGal level for a rather big regions of at least 200-300 km, without any significant systematic effects.
- The capabilities to independently validate the results of temporal gravity missions have been discussed since the launch of GRACE, but there is hardly any complementary technique that can come close to the unprecedented accuracy of gravity missions to monitor large-scale mass transport processes.

12. E2E PERFORMANCE SIMULATORS

The E2E performance simulator implementations of TUM, GFZ and CNES are based on the algorithms described in the ATBD [RD-1]. In the case of GFZ and CNES, they have been derived from real-data processors.

The underlying assumption of the E2E performance simulations is that they try to mimic reality as realistically as possible, by including realistic static and temporal gravity field signals and realistic assumptions for the instruments and their coupling. The degree of realism can be demonstrated by the heritage from GRACE and GRACE-FO. From these missions, together with the mission design of NGGM/MAGIC, realistic error trees for both the satellite/measurement system and the environmental effect can be derived, and thus the main error sources to be included in the performance simulation can be identified. The simulator outputs when simulating GRACE/GRACE-FO-like missions can be directly compared with the results obtained from the real data, indicating potential inconsistencies between the simulation and real world.

The main simplifications of the simulation world is that currently uninterrupted observation time series are assumed. Therefore, issues of incomplete data, outliers and other data deficiencies that are not described by the performance assumptions of the key payload is not yet taken into account in the simulations.

The evaluation scenario (chapter 13) and the evaluation criteria (chapter 14) are formulated to both, make a consistency check of the simulator outputs (product-noise only scenario), and to validate the simulator results against mission requirements (full-noise scenario).

13. EVALUATION SCENARIO

The retrieval performance shall be evaluated on the basis of full-fledged numerical closed-loop simulations of constellation scenario 5d_397_70, i.e. the current MAGIC baseline scenario, for the test month of January 2002. The orbital parameters are provided in Table 13-1. Both the polar (P1) and the inclined satellite pair (P2) feature a 5-daily sub-cycle. This means that the ground track pattern reoccurs in an identical manner after every five days, but with a longitudinal shift.

Table 13-1: Orbital parameters of scenario 5d_397_70.

	Semi-major axis [m]	eccentricity	incl. [°]	asc. node [°]	argument of perigee [°]	mean anomaly [°]
P1-A	6871210.979	0.0016	89	359.98	27.78	331.51
P1-B	6871208.124	0.0016	89	359.98	29.17	331.95
P2-A	6780418.955	0.0008	70	2.34	5.46	353.82
P2-B	6780416.219	0.0008	70	2.34	8.46	352.68

The gravity retrieval shall be carried out for the case of a double-pair scenario (in chapters 14 and 15 referred to as MAGIC) as well as for the case of a stand-alone P2 (in chapters 14 and 15 referred to as NGGM).

Two noise scenarios shall be investigated in either scenario – product-noise-only (PO) and full-noise (FN). In case of PO, all time-variable gravity signal components are disregarded, and only the LOS-projected noise of individual instruments is considered as an error contributor to the low-low observations. Here, we consider only the two most dominant instruments – the ACC (SuperSTAR-type for P1, MicroSTAR-type for P2) and the LRI (for P1), or LTI (for P2), respectively. Further, tone errors, i.e. sinusoidal errors occurring at multiples of the orbital frequency, shall be considered here. Their specifications – valid both for P1 and P2 – are given in Table 13-2.

For the high-low observations carried out by means of GPS, white noise is assumed. All noise specifications denoted above are given in Eq. 1 to Eq. 5 and are furthermore visualized in Figure 13-1. Note that the term L in Eq. 4 denotes the inter-satellite distance in meters.

In case of FN, also the temporal variations of the gravity field are considered in addition to the instrument noise, thus constituting a realistic time-variable gravity retrieval scheme. Regarding tidal variations, the de-aliasing is simulated by forward-modelling of the ocean tide model EOT11a ([RD-12]), while the reference observations are set up on the basis of GOT4.7 ([RD-13]). Regarding non-tidal variations, the full AOHIS taken from the updated ESA ESM ([RD-14]) is used as the true signal, while the reference observations for the de-aliasing are set up as the difference between the (true) AO signal and the sum of the DEAL and AOerr components from the updated ESA ESM. For the static gravity signal in both PO and FN the model GOCO05s ([RD-15]) is used. In case of FN, the target signal is HIS, while in case of PO, considering that the temporal variations of the gravity field are disregarded, the target signal is zero.

Table 13-2: Tone errors

multiple of orbital frequency	amplitude [μm]
1	100
2	20
3	4

$$acc_{P1} = \sqrt{2}\cdot 10^{-10}\sqrt{1+\frac{0.005\ Hz}{f}}\left[\frac{m}{s^2\sqrt{Hz}}\right] \quad \text{Eq. 1}$$

$$acc_{P2} = 10^{-11}\sqrt{\frac{\left(\frac{10^{-3}\ Hz}{f}\right)^2}{\left(\left(\frac{10^{-5}\ Hz}{f}\right)^2+1\right)}+1+\left(\frac{f}{10^{-1}Hz}\right)^4}\left[\frac{m}{s^2\sqrt{Hz}}\right] \quad \text{Eq. 2}$$

$$lri_{P1} = \sqrt{\left(L\cdot\frac{10^{-15}}{\sqrt{f}}\right)^2+\left(\frac{10^{-12}}{f^2}\right)^2}\left[\frac{m}{\sqrt{Hz}}\right] \quad \text{Eq. 3}$$

$$lti_{P2} = L\cdot 2\cdot 10^{-13}\sqrt{1+\left(\frac{10\ mHz}{f}\right)^2}\sqrt{1+\left(\frac{1\ mHz}{f}\right)^2}\left[\frac{m}{\sqrt{Hz}}\right] \quad \text{Eq. 4}$$

$$GPS_{P1} = GPS_{P2} = 10^{-2}\frac{f}{f}\left[\frac{m}{\sqrt{Hz}}\right] \quad \text{Eq. 5}$$

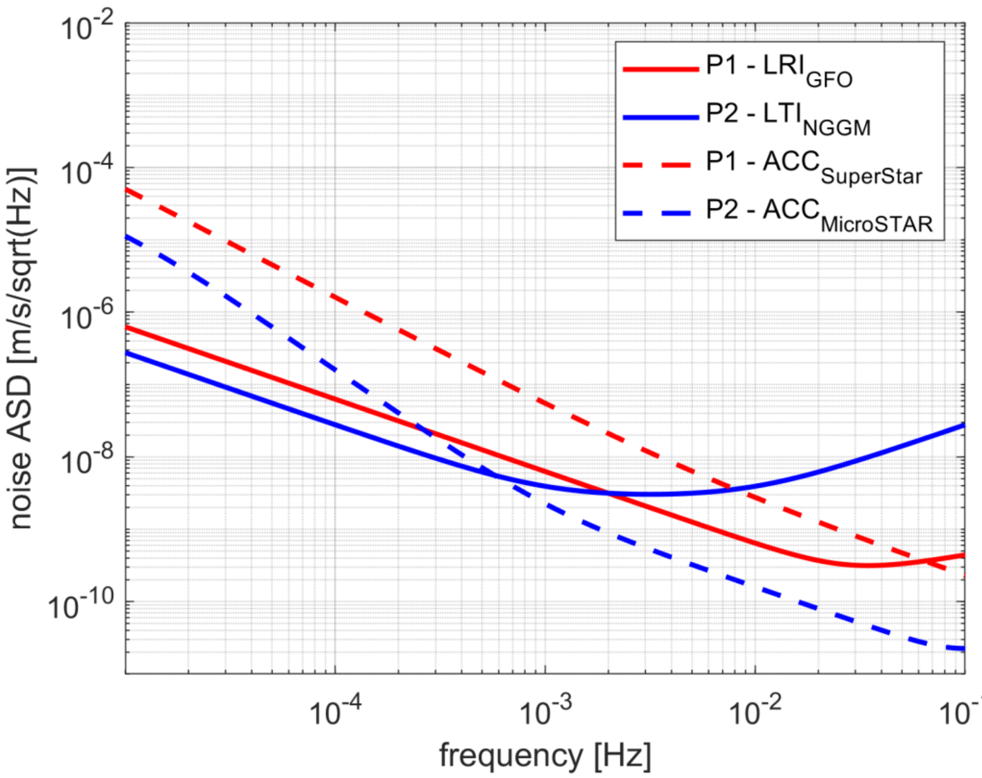

Figure 13-1 Instrument noise specification (in terms of LOS projection) for 5d_397_70.

The retrieval period is 5 days (sub-cycle), in order to demonstrate the capability of NGGM and MAGIC to generate high-quality short(er)-term gravity products. The gravity retrieval shall be carried out for January 2002, resulting in six consecutive 5-day solutions.

Further, it is noted that the nominal parametrization scheme is applied for all retrieval scenarios and periods, i.e. a single set of spherical harmonic coefficients is estimated by means of least squares adjustment to represent the mean target signal of the respective period as closely as possible. The maximum degree used for the evaluation is d/o 70 for NGGM and d/o 80 for MAGIC.

Stochastic modelling tailored to the respective instrument noise shall be applied in either simulation scenario. I.e., the normal equations set up for each satellite pair shall include information on the stochastic behaviour of the instrument noise in terms of a full co-variance matrix. Note that tailored stochastic modelling of tone errors shall be applied for PO scenarios, but not for FN scenarios.

In case of NGGM, a regularization is required to mitigate the impact of the large polar gaps, as they would otherwise greatly deteriorate the gravity solution (0).

The algorithms applied by the processing centers TUM and GFZ are documented in [RD-1]. The estimated SLRs of these algorithms are given in Table 7.3 therein.

The simulation scenarios are summarized in Table 13-3.

Uncertainty budget estimates for the NGGM Level-2b products are not part of this SRA for SRL5, but will be addressed in future B1 studies.

Table 13-3: Overview of simulation scenarios.

constellation	noise scenario	retrieval period	True observations	Reference observations	resolution of solution
MAGIC	PO	5 days	instruments + tone errors + GOCO05s	GOCO05s (d/o 100)	d/o 80
	FN	5 days	instruments + tone errors + AOHIS + EOT11a + GOCO05s	[DEAL + AOerr] + GOT4.7 + GOCO05s (d/o 100)	d/o 80
NGGM	PO	5 days	instruments + tone errors + GOCO05s	GOCO05s (d/o 70)	d/o 70
	FN	5 days	instruments + tone errors + AOHIS + EOT11a + GOCO05s	[DEAL + AOerr] + GOT4.7 + GOCO05s (d/o 70)	d/o 70

14. EVALUATION CRITERIA AND PERFORMANCE REQUIREMENTS

PR-001	**Consistency of product-only (PO) scenario (NGGM)**
Description	Based on P2 of the test scenario 5d_397_70 (product-only), compare the coefficient differences of the resulting gravity field retrieval to the true solution and the formal errors. If coefficient differences and formal errors match, this demonstrates that the software works consistently.* EWH grid differences between the retrieved and the true solution shall be evaluated in the region $\lvert\varphi\rvert < 70°$. They shall be compared with the covariance propagation of the formal errors (either rigorously or via “Monte-Carlo”-technique).
Requirement	The mean RMS of EWH grid differences and propagated formal errors at max. degree 70 averaged over the six 5-day solutions shall agree within 10%.
Center	This requirement has to be fulfilled by TUM (PR-001-TUM) and GFZ (PR-001-GFZ) individually.

* The underlying reasoning is that according to basic adjustment theory, in the case of consistent system, i.e. the observation errors are correctly described by the stochastic model used as the metric in the frame of the least squares adjustment, the differences of the estimated parameters should be reflected in a statistical sense by their formal errors. In this case, the post-fit residuals correspond to the (negative) true errors applied on the right-hand side of the normal equation system. In the case that these errors are even correctly scaled, i.e. the amplitude spectral density of the true errors matches the instrument (product) error specifications used to set-up the stochastic model, the a-posteriori variance estimated from the post-fit residuals under the used metric is ‘1’.

PR-002	**Consistency of product-only (PO) scenario (MAGIC)**
Description	Based on P1+P2 of the test scenario 5d_397_70 (product-only), compare the coefficient differences of the resulting gravity field retrieval to the true solution and the formal errors. If coefficient differences and formal errors match, this demonstrates that the software works consistently. EWH grid differences between the retrieved and the true solution shall be evaluated in the region $\lvert\varphi\rvert < 90°$. They shall be compared with the covariance propagation of the formal errors (either rigorously or via “Monte-Carlo”-technique).
Requirement	The mean RMS of EWH grid differences and propagated formal errors at max. degree 80 averaged over six 5-day solutions shall agree within 10%.
Center	This requirement has to be fulfilled by TUM (PR-002-TUM) and GFZ (PR-002-GFZ) individually.

PR-003	**Consistency of full-noise (FN) scenario within processing centers (NGGM)**
Description	Based on P2 of the test scenario 5d_397_70 (full-noise scenario), compare the coefficient differences of the resulting gravity field retrieval to the true solution among the processing centers TUM and GFZ. EWH grid differences of the retrieved solutions shall be evaluated in the region $\lvert\varphi\rvert < 70°$ at max. degree 80 for the processing centers TUM and GFZ. They shall be compared between each other.
Requirement	RMS of EWH grid differences between the solutions of TUM and GFZ shall be lower than 10% of the true EWH signal.
Center	This requirement has to be fulfilled by TUM and GFZ jointly.

PR-004	**Consistency of full-noise (FN) scenario (NGGM)**
Description	Based on P2 of the test scenario 5d_397_70, compare the coefficient differences of the resulting gravity field retrieval to the true solution and the NGGM MRD requirements for 5 days. If coefficient differences and MRD requirements match, this demonstrates that the functionality of the software to process realistic constellations. Cumulative degree error amplitudes shall be computed from EWH grid differences between the retrieved and the true solutions for varying SH degree, and evaluated in the region $\lvert\varphi\rvert < 70°$. The resulting cumulative EWH error curve shall be compared against the NGGM MRD requirements.
Requirement	The mean cumulative EWH error curve averaged over six 5-day solutions shall stay below the NGGM MRD requirements for 5-day solutions at the SH degrees for which the requirements are given (MRD 210 and corresponding Table 11).
Center	This requirement has to be fulfilled by TUM (PR-004-TUM) and GFZ (PR-004-GFZ) individually.

PR-005	**Consistency of full-noise (FN) scenario (MAGIC)**
Description	Based on P1+P2 of the test scenario 5d_397_70, compare the coefficient differences of the resulting gravity field retrieval to the true solution and the MAGIC MRD requirements. If coefficient differences and MAGIC MRD requirements match, this demonstrates that the functionality of the software to process realistic constellations. Cumulative degree error amplitudes shall be computed from EWH grid differences between the retrieved and the true solutions for varying SH degree, and evaluated in the region $\lvert\varphi\rvert < 90°$. The resulting cumulative EWH error curve shall be compared against the NGGM MRD requirements.

Requirement	The mean cumulative EWH error curve averaged over six 5-day solutions shall stay below the MAGIC MRD requirements for 5-day solutions at the SH degrees for which the requirements are given.
Center	This requirement has to be fulfilled by TUM (PR-005-TUM) and GFZ (PR-005-GFZ) individually.

PR-006	**Long-term stability of full-noise (FN) solutions (NGGM)**
Description	Based on P2 of the test scenario 5d_397_70 (full noise), compare the coefficient differences of the resulting gravity field retrievals for five 5-day solutions (January 2002) to the corresponding true solutions. Five instead of six solutions are used for the realization of the median value. Cumulative degree error amplitudes shall be computed from EWH grid differences between the retrieved and the true solutions for varying SH degree, and evaluated in the region $\lvert\varphi\rvert < 70°$ for all five individual 5-day retrievals. They shall be compared to the median of these solutions.
Requirement	The RMS of the individual 5-day solutions up to max. degree 80 shall deviate less than 20% from the median (in accordance with the respective NGM MRD requirement MRD 180).
Center	This requirement has to be fulfilled by TUM (PR-006-TUM) and GFZ (PR-006-GFZ) individually.

PR-007	**Long-term stability of full-noise (FN) solutions (MAGIC)**
Description	Based on P1+P2 of the test scenario 5d_397_70 (full noise), compare the coefficient differences of the resulting gravity field retrievals for five 5-day solutions (January 2002) to the corresponding true solutions. Five instead of six solutions are used for the realization of the median value. Cumulative degree error amplitudes shall be computed from EWH grid differences between the retrieved and the true solutions for varying SH degree, and evaluated in the region $\lvert\varphi\rvert < 90°$ for all five individual 5-day retrievals. They shall be compared to the median of these solutions.
Requirement	The RMS of the individual 5-day solutions up to max. degree 80 shall deviate less than 20% from the median.
Center	This requirement has to be fulfilled by TUM (PR-007-TUM) and GFZ (PR-007-GFZ) individually.

15. EVALUATION RESULTS

15.1. PR-001

15.1.1. PR-001-TUM

The results presented in Figure 15-1 suggest that the treatment, i.e. stochastic modelling, of tone errors is still suboptimal. The effect of the tone errors manifests primarily, but not exclusively, in the very low degrees (up to d/o 5) with a very high amplitude, thus greatly affecting the quality of the gravity estimate up to the medium degree range. In this case, the requirement is only fulfilled above d/o 65.

Once the coefficients up to d/o 4 are omitted from this evaluation, the fit improves drastically, and the requirement is fulfilled between d/o 30 and 50 as well as above d/o 65.

In case the tone errors are removed from the simulation environment, the requirement can be upheld for all d/o except 2.

The impact of tone errors is further shown in Figure 15-2 in terms of degree amplitudes. The optimal stochastic modelling of tone errors shall be subject to further investigation.

The cumulative spatial errors are also summarized in Table 15-1.

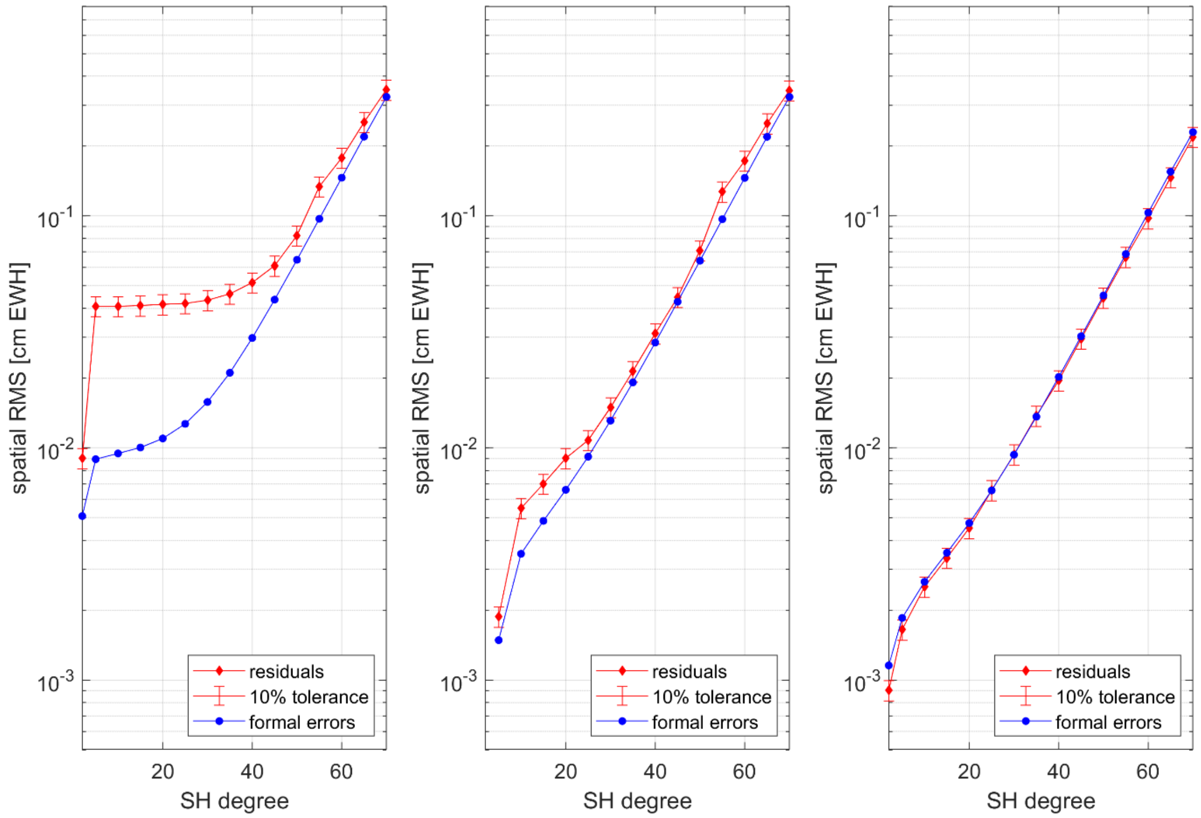

Figure 15-1: Mean spatial RMS of error grids and the corresponding propagated from six product-noise-only 5-day solutions. Left: Tone Errors included, evaluation from minimum d/o 2. Center: Tone Errors included, evaluation from minimum d/o 5. Right: No Tone Errors, evaluation from d/o 2.

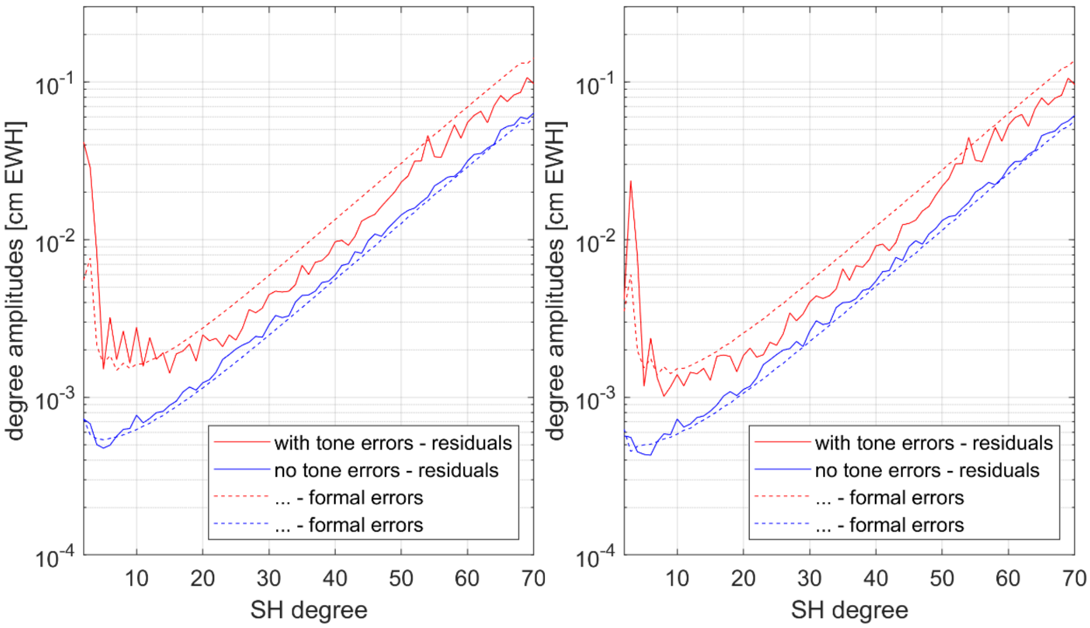

Figure 15-2: Degree amplitudes of P2-only solutions showcasing the impact of tone errors on the retrieval performance. Left: full set of coefficients used. Right: near-zonal coefficients affected by polar gap issue omitted from evaluation.

Table 15-1: mean spatial RMS of error grids and the corresponding propagated from six product-noise-only 5-day solutions.

max. d/o	scenario: tone errors included, min. d/o 2		scenario: tone errors included, min. d/o 5		scenario: no tone errors, min. d/o 2	
	RMS of residuals	RMS of propagated uncertainties	RMS of residuals	RMS of propagated uncertainties	RMS of residuals	RMS of propagated uncertainties
2	0.009	0.005	-	-	0.001	0.001
5	0.041	0.009	0.002	0.001	0.002	0.002
10	0.041	0.009	0.005	0.003	0.003	0.003
15	0.041	0.010	0.007	0.005	0.003	0.004
20	0.042	0.011	0.009	0.007	0.005	0.005
25	0.042	0.013	0.011	0.009	0.007	0.007
30	0.043	0.016	0.015	0.013	0.009	0.009
35	0.046	0.021	0.021	0.019	0.014	0.014
40	0.052	0.030	0.031	0.028	0.020	0.020
45	0.061	0.044	0.045	0.043	0.030	0.030
50	0.082	0.065	0.071	0.064	0.044	0.045
55	0.134	0.097	0.127	0.097	0.066	0.068
60	0.178	0.146	0.173	0.146	0.098	0.103
65	0.254	0.219	0.250	0.219	0.147	0.155
70	0.350	0.326	0.347	0.326	0.219	0.230

15.1.2. PR-001-GFZ

Since GFZ simulations were done mostly without tone errors, we have, initially, excluded tone errors from our results. However, tone errors are now included, and we show both the tone-free and toned results. In Figure 15-3, we compare the tone-free coefficient differences of the gravity field retrieval for a product-only P2-only simulation up to D/O 70 to the true solution.

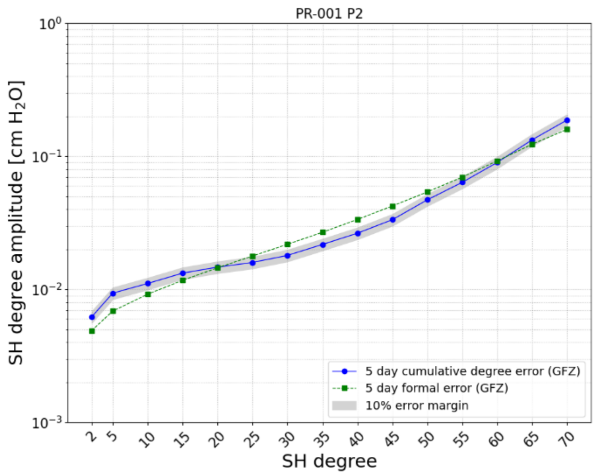

Figure 15-3 Consistency of product-only scenario (NGGM): Tone-free EWH grid differences between the retrieved and the true solution for an NGGM product-only scenario, evaluated in the region |rho|<70.

The mean cumulative retrieval errors, shown in blue in Figure 15-3, and the corresponding formal errors, shown in green, were calculated from six 5-day solutions for January 2002.

Results that include tone-errors are shown in Figure 15-4. Since tone-errors have a significant impact on the lower degrees and order, we show results for accumulated errors that include C_{20}, accumulated errors in which we have omitted C_{20}, and accumulated errors in which we omit all degrees and orders smaller than 5. Due to the regularization, the impact of C_{20} is relatively small when investigating P2 alone.

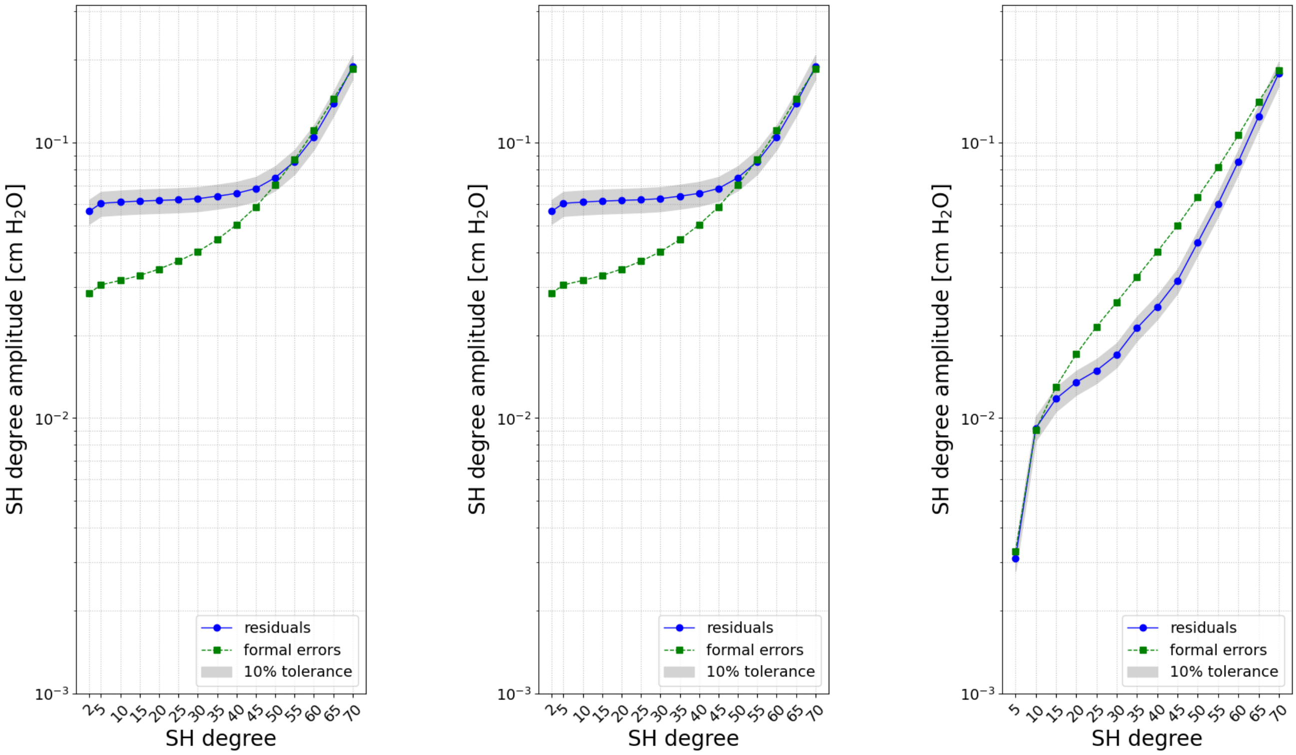

Figure 15-4 Accumulated errors, including tone errors. Left: Results including C20. Middle: Results excluding C20. Right: Results excluding degrees and orders smaller than 5.

The requirement, that the formal and retrieval errors shall match within a 10% range, shown as the shaded grey area around the blue curve, is only met for degrees 15, 20, and degrees larger than 50 when tone errors are omitted. When tone errors are included, the requirement is only met for degrees and orders larger than 50 if degrees smaller than 5 are considered.

The cumulative retrieval errors are compared to the formal errors in Table 15-2.

Table 15-2 Cumulative retrieval errors and formal error comparison.

max. d/o	scenario: no tone errors, min. d/o 2		scenario: tone errors, min. d/o 2		scenario: tone errors, min. d/o 5	
	RMS of residuals	RMS of propagated uncertainties	RMS of residuals	RMS of propagated uncertainties	RMS of residuals	RMS of propagated uncertainties
2	0.006221	0.004912	0.056393	0.028402	--	--
5	0.009381	0.006879	0.060217	0.030467	0.003095	0.003279
10	0.011092	0.009215	0.060896	0.031612	0.009189	0.009044
15	0.013274	0.011718	0.061375	0.032961	0.011751	0.012996
20	0.014726	0.014554	0.061726	0.034765	0.01349	0.017061
25	0.015962	0.017841	0.062063	0.037127	0.014875	0.021469
30	0.018035	0.021866	0.062634	0.04017	0.017002	0.026383
35	0.0218	0.0269	0.063936	0.044457	0.021234	0.032539
40	0.026478	0.033597	0.065473	0.050334	0.025376	0.040198
45	0.033457	0.04241	0.068201	0.058496	0.031582	0.050041
50	0.047191	0.054093	0.074623	0.070376	0.043467	0.063523
55	0.063941	0.070004	0.085467	0.086763	0.059976	0.081304
60	0.090207	0.092547	0.105039	0.110649	0.085347	0.106421
65	0.133533	0.123602	0.138734	0.144273	0.124329	0.141057
70	0.18809	0.159892	0.188942	0.185251	0.178602	0.182757

15.2. PR-002

15.2.1. PR-002-TUM

The results obtained in this evaluation scenario are presented in Figure 15-5 and show a nearly identical behavior as the results shown in section 15.1.1. The imperfect stochastic modelling of the tone errors is once again predominantly present in the spectral range up to d/o 5 and thus dominates the cumulative retrieval errors up to d/o ~50. In this case, the requirement is met from d/o 60 upwards.

Once the affected coefficients are removed from the evaluation, the fit improves greatly, and the requirement can be met for all d/o except d/o 10 to 15 as well as 45.

In case the tone errors are removed from the simulation environment, the requirement is met for all d/o.

The impact of tone errors is further shown in Figure 15-6 in terms of degree amplitudes. The optimal stochastic modelling of tone errors shall be subject to further investigation.

The cumulative spatial errors are also summarized in Table 15-3.

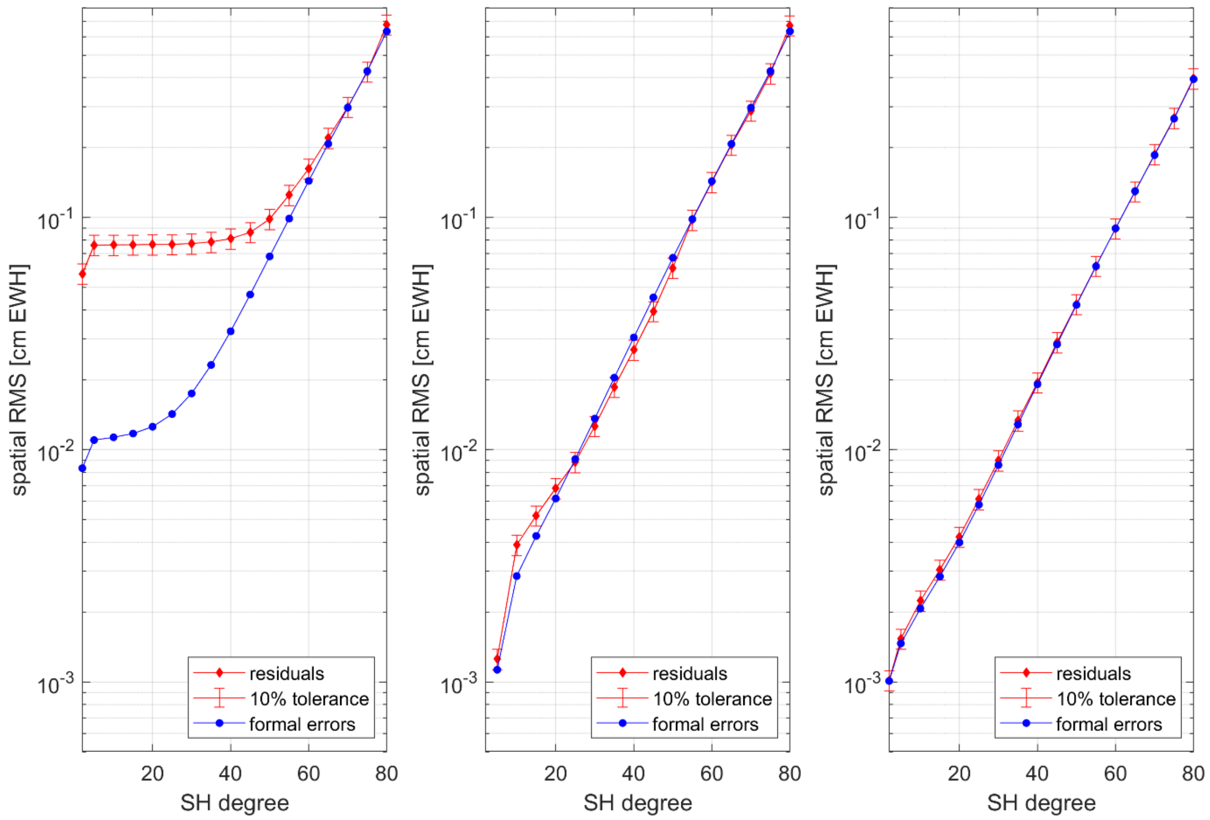

Figure 15-5: Mean spatial RMS of error grids and the corresponding propagated from six product-noise-only 5-day solutions. Left: Tone Errors included, evaluation from minimum d/o 2. Center: Tone Errors included, evaluation from minimum d/o 5. Right: No Tone Errors, evaluation from d/o 2.

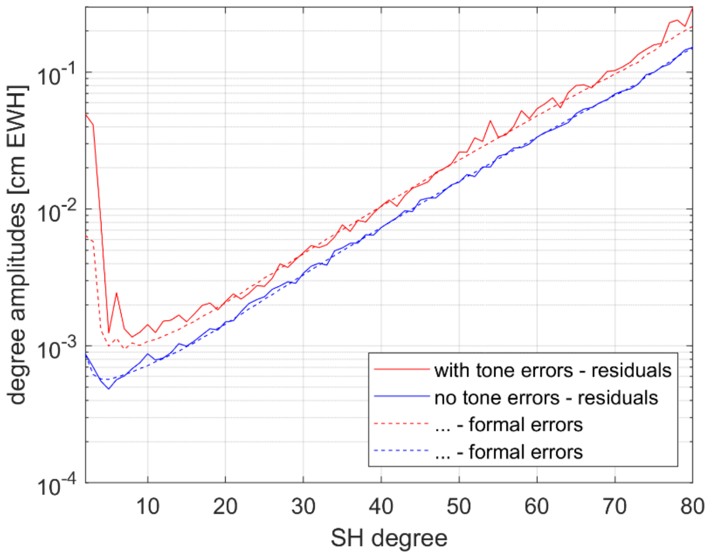

Figure 15-6: Degree amplitudes of P2-only solutions showcasing the impact of tone errors on the retrieval performance. Left: full set of coefficients used. Right: near-zonal coefficients affected by polar gap issue omitted from evaluation.

Table 15-3: mean spatial RMS of error grids and the corresponding propagated from six product-noise-only 5-day solutions

max. d/o	scenario: tone errors included, min. d/o 2		scenario: tone errors included, min. d/o 5		scenario: no tone errors, min. d/o 2	
	RMS of residuals	RMS of propagated uncertainties	RMS of residuals	RMS of propagated uncertainties	RMS of residuals	RMS of propagated uncertainties
2	0.057	0.008	-	-	0.001	0.001
5	0.076	0.011	0.001	0.001	0.002	0.001
10	0.076	0.011	0.004	0.003	0.002	0.002
15	0.076	0.012	0.005	0.004	0.003	0.003
20	0.076	0.013	0.007	0.006	0.004	0.004
25	0.077	0.014	0.009	0.009	0.006	0.006
30	0.077	0.017	0.013	0.014	0.009	0.009
35	0.079	0.023	0.019	0.020	0.013	0.013
40	0.081	0.032	0.027	0.030	0.020	0.019
45	0.086	0.047	0.039	0.045	0.029	0.028
50	0.098	0.068	0.061	0.067	0.042	0.042
55	0.125	0.099	0.098	0.098	0.062	0.062
60	0.162	0.144	0.142	0.143	0.090	0.090
65	0.220	0.208	0.206	0.207	0.129	0.130
70	0.299	0.297	0.288	0.297	0.187	0.186
75	0.425	0.427	0.417	0.427	0.268	0.267
80	0.677	0.634	0.672	0.634	0.397	0.395

15.2.2. PR-002-GFZ

In Figure 15-7, we compare the coefficient differences of the gravity field retrieval for a double pair scenario to the true solution where the tone errors are omitted.

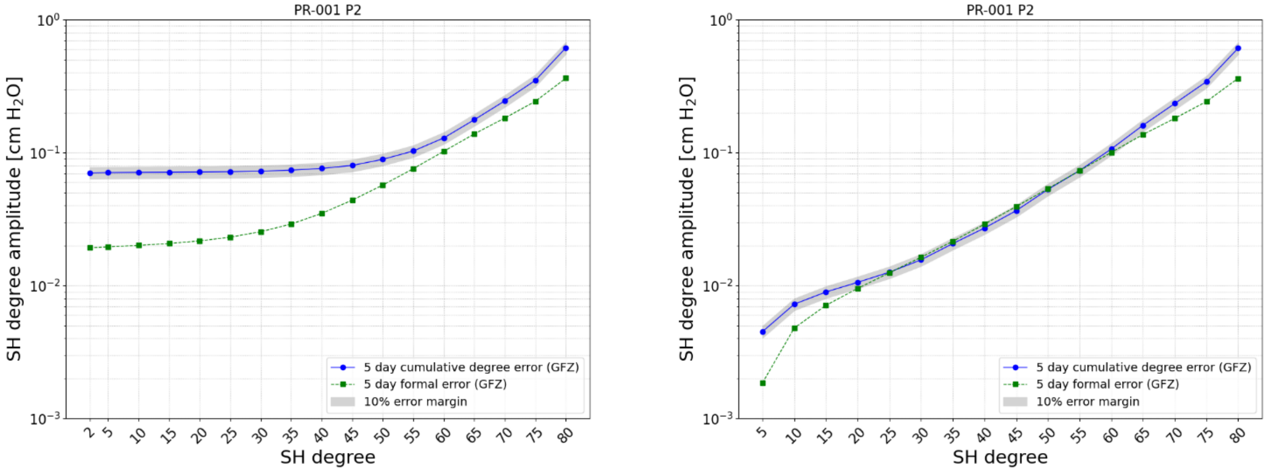

Figure 15-7 Consistency of product-only scenario (NGGM): EWH grid differences between the retrieved and the true solution for a MAGIC product-only scenario, evaluated in the region |rho|<90. On the left, errors have been accumulated from D/O 2. On the right the accumulation was done from D/O 5.

From Figure 15-7 we conclude, the 10% requirement is only met when degrees and orders below 5 are omitted. In this case, the 10% criterium is met for degrees larger than 15 and smaller than 60.

The cumulative retrieval and formal errors are listed in Table 15-4 for the tone-free results.

Table 15-4 Cumulative tone-free retrieval and formal errors for a product-only MAGIC scenario.

max. d/o	scenario: no tone errors, min. d/o 2		scenario: no tone errors, min. d/o 5	
	RMS of residuals	RMS of propagated uncertainties	RMS of residuals	RMS of propagated uncertainties
2	0.070676	0.019279	--	--
5	0.070963	0.019594	0.00451	0.001857
10	0.071209	0.020091	0.007256	0.004797
15	0.071422	0.020769	0.008964	0.00711
20	0.071661	0.021719	0.010595	0.009532
25	0.072014	0.023182	0.012622	0.01251
30	0.072647	0.025471	0.015652	0.016365

35	0.074024	0.029087	0.020721	0.021562
40	0.076233	0.034997	0.027135	0.02904
45	0.080317	0.043997	0.036682	0.039415
50	0.089242	0.057137	0.052977	0.05368
55	0.103078	0.075924	0.073502	0.073352
60	0.129388	0.102605	0.106858	0.100714
65	0.177252	0.138604	0.161175	0.137211
70	0.246136	0.182666	0.234733	0.181614
75	0.350968	0.243734	0.343157	0.242948
80	0.617138	0.363965	0.612697	0.363438

Results that include tone-errors are shown in Figure 15-8. Again, we show results for accumulated errors that include C_{20}, accumulated errors in which we have omitted C_{20}, and accumulated errors in which we omit all degrees and orders smaller than 5.

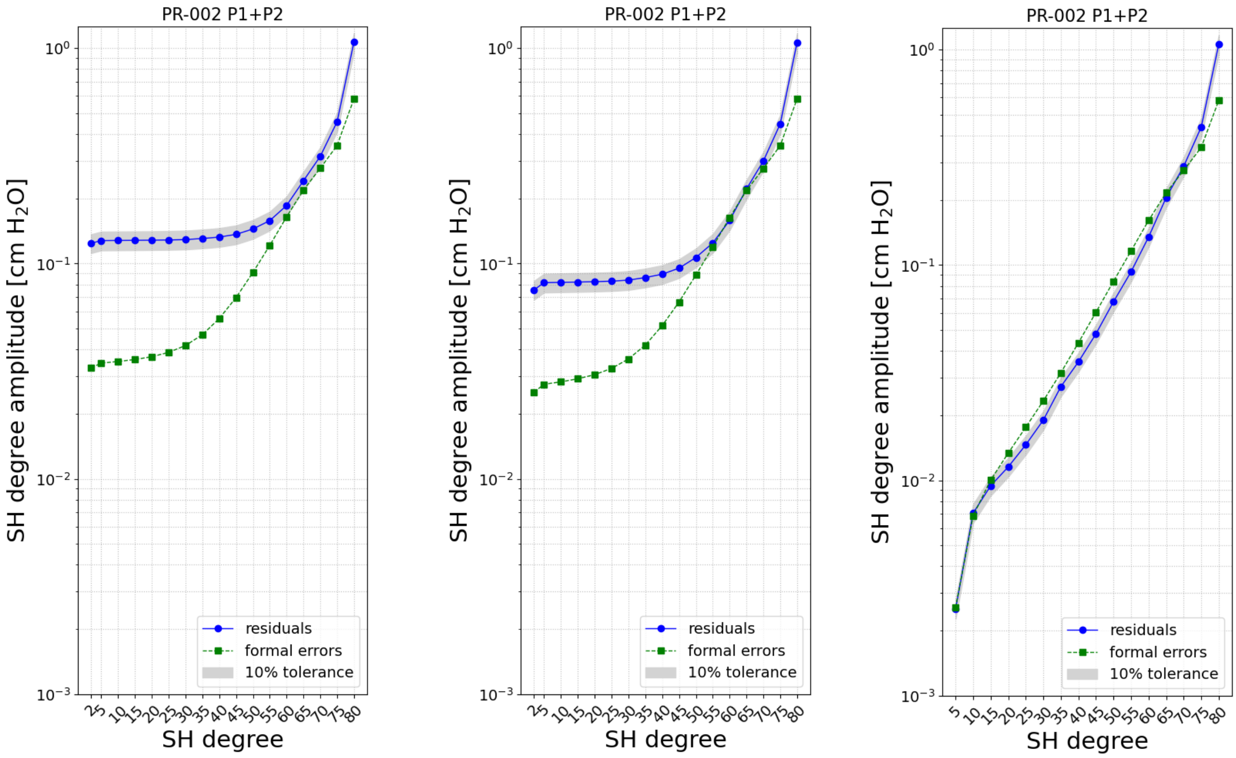

Figure 15-8 Accumulated errors, including tone errors. Left: Results including C20. Middle: Results excluding C20. Right: Results excluding degrees and orders smaller than 5.

Even when accumulation is done for degrees and orders equal to and larger than 5, the GFZ formal errors remain farther away from the residuals than allowed by the 10% tolerance when tone errors are considered. The values for the scenario in which C_{20} is included and the scenario that only accumulates degrees-and orders larger than 5, are listed in Table 15-5.

Table 15-5 Cumulative toned retrieval and formal errors for a product-only MAGIC scenario.

max. d/o	scenario: tone errors, min. d/o 2		scenario: tone errors, min. d/o 5	
	RMS of residuals	RMS of propagated uncertainties	RMS of residuals	RMS of propagated uncertainties
2	0.124313	0.032763	--	--
5	0.12789	0.034514	0.002529	0.002562
10	0.128066	0.035095	0.007047	0.006857
15	0.128225	0.03585	0.009439	0.010029
20	0.128399	0.036934	0.011555	0.013397
25	0.12871	0.038686	0.014631	0.01766
30	0.129285	0.041628	0.019058	0.023413
35	0.130764	0.04673	0.02725	0.031604
40	0.132766	0.055535	0.035519	0.043581
45	0.136661	0.069482	0.047934	0.060355
50	0.144765	0.090886	0.067581	0.084114
55	0.158279	0.121344	0.09308	0.116358
60	0.186107	0.164837	0.135046	0.161202
65	0.242417	0.219503	0.205801	0.216787
70	0.314943	0.277335	0.287638	0.27519
75	0.456127	0.353827	0.437679	0.352149
80	1.070598	0.583302	1.062782	0.582285

15.3. PR-003 (TUM, GFZ)

Based on a P2 scenario, the full-noise coefficient differences of the resulting gravity field retrieval to the true solution was tested among the processing centers TUM and GFZ. For the first test results, shown in Figure 15-9, GFZ omitted tone-errors. TUM included tone errors.

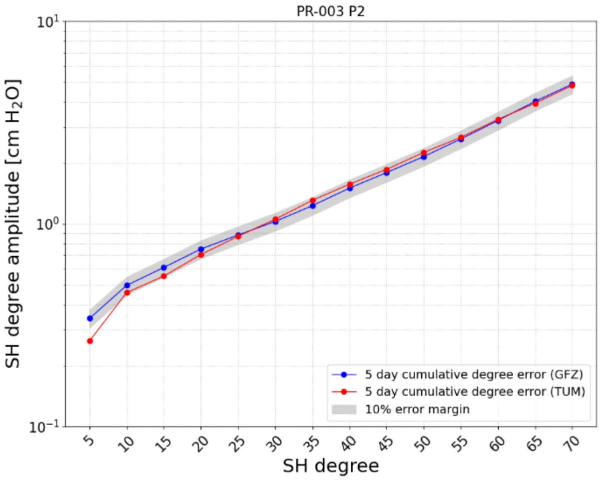

Figure 15-9 Consistency of full-noise scenario within processing centres: EWH grid differences between the retrieved and the true solution for an NGGM full-noise scenario, evaluated in the region |φ|<70. Note that GFZ omitted tone-errors for the results shown here.

From the results shown in Figure 15-9 it can be concluded that GFZ and TUM results deviate to an extent in the low-degree spectrum, but are highly consistent from d/o 15 to 20 upwards. It is noted that since C_{20} features significant uncertainties, the cumulative errors have been computed from d/o 5 upwards. Table 15-6 shows the corresponding numbers.

Table 15-6 Comparison between TUM and GFZ of mean spatial RMS of error grids from six full-noise 5-day solutions

max. d/o	scenario: Full noise, min. d/o 5	
	RMS of residuals (GFZ no tones)	RMS of residuals (TUM inc. tones)
5	0.341818	0.264928
10	0.497736	0.458496
15	0.609797	0.552639
20	0.752094	0.706681
25	0.881823	0.869022
30	1.02895	1.055372

35	1.230301	1.30743
40	1.501864	1.570757
45	1.792098	1.859548
50	2.150116	2.252457
55	2.624914	2.675454
60	3.240649	3.279314
65	4.024219	3.938309
70	4.893202	4.822207

A comparison that includes tone-errors is shown in Figure 15-10.

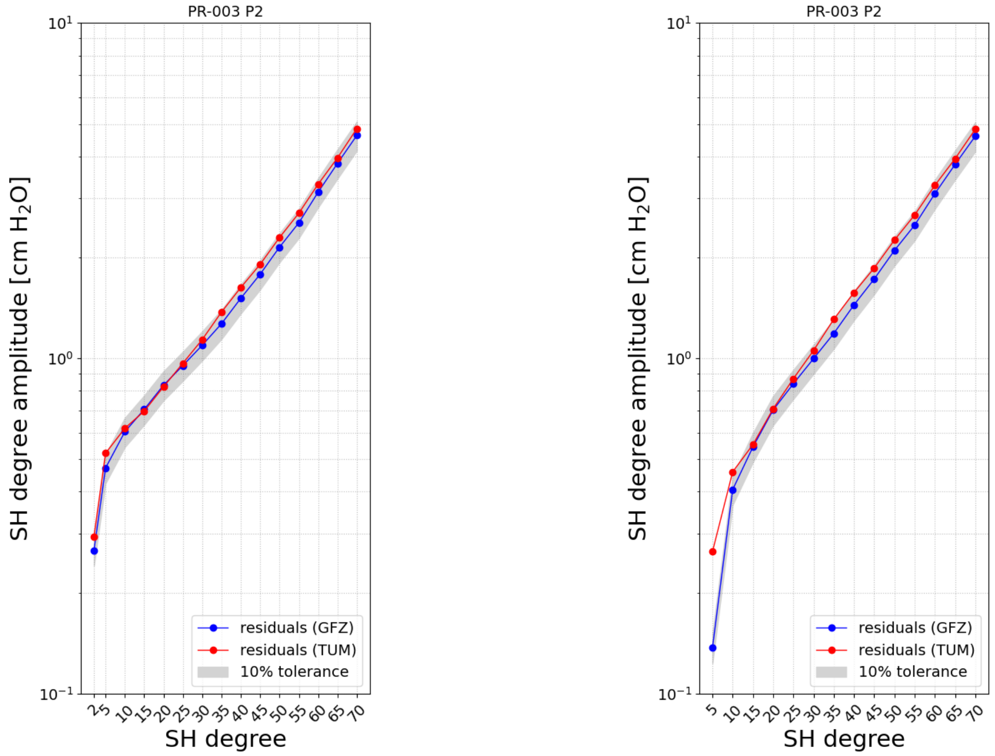

Figure 15-10 Consistency of full-noise scenario within processing centres: EWH grid differences between the retrieved and the true solution for an NGGM full-noise scenario, evaluated in the region |lat|<70 in which tone-errors are included by both GFZ and TUM. Left: accumulation done from d/o=2. Right: accumulation done only for d/o >4.

The values for the two plots shown in Figure 15-10, are listed in Table 15-7.

Table 15-7 Comparison between TUM and GFZ of mean spatial RMS of error grids from six full-noise 5-day solutions

max. d/o	scenario: Full noise, min. d/o 2		scenario: Full noise, min. d/o 5	
	RMS of residuals (GFZ)	RMS of residuals (TUM)	RMS of residuals (GFZ)	RMS of residuals (TUM)
2	0.267347	0.294227	--	--
5	0.47074	0.521036	0.13691	0.264928
10	0.603954	0.618575	0.40582	0.458496
15	0.704065	0.695509	0.543825	0.552639
20	0.831484	0.822322	0.701059	0.706681
25	0.951327	0.966334	0.839493	0.869022
30	1.093755	1.136988	0.997786	1.055372
35	1.26816	1.374274	1.186123	1.307430
40	1.510998	1.626792	1.442771	1.570757
45	1.781785	1.906971	1.723995	1.859548
50	2.145188	2.291811	2.097301	2.252457
55	2.535588	2.708798	2.495062	2.675454
60	3.130365	3.306506	3.097608	3.279314
65	3.813837	3.960618	3.786933	3.938309
70	4.620582	4.840573	4.59844	4.822207

When both GFZ and TUM include tone errors, results match well when the accumulation is done from d/o=2. Note that both processing centers included C_{20}.

15.4. PR-004

15.4.1. PR-004-TUM

The NGGM MRD threshold requirement are met above d/o 10, as is shown in Figure 15-11. Removing the coefficients below d/o 5 from the evaluation allows to meet the threshold requirements at d/o 10, which indicated that comparatively high error amplitudes are present in the respective spectral bands.

In real-data processing, the low degree coefficients will be significantly stabilized by the inclusion of information from SLR, which is currently not part of the simulation.

Thus, the requirement of this evaluation scenario can be considered as fulfilled.

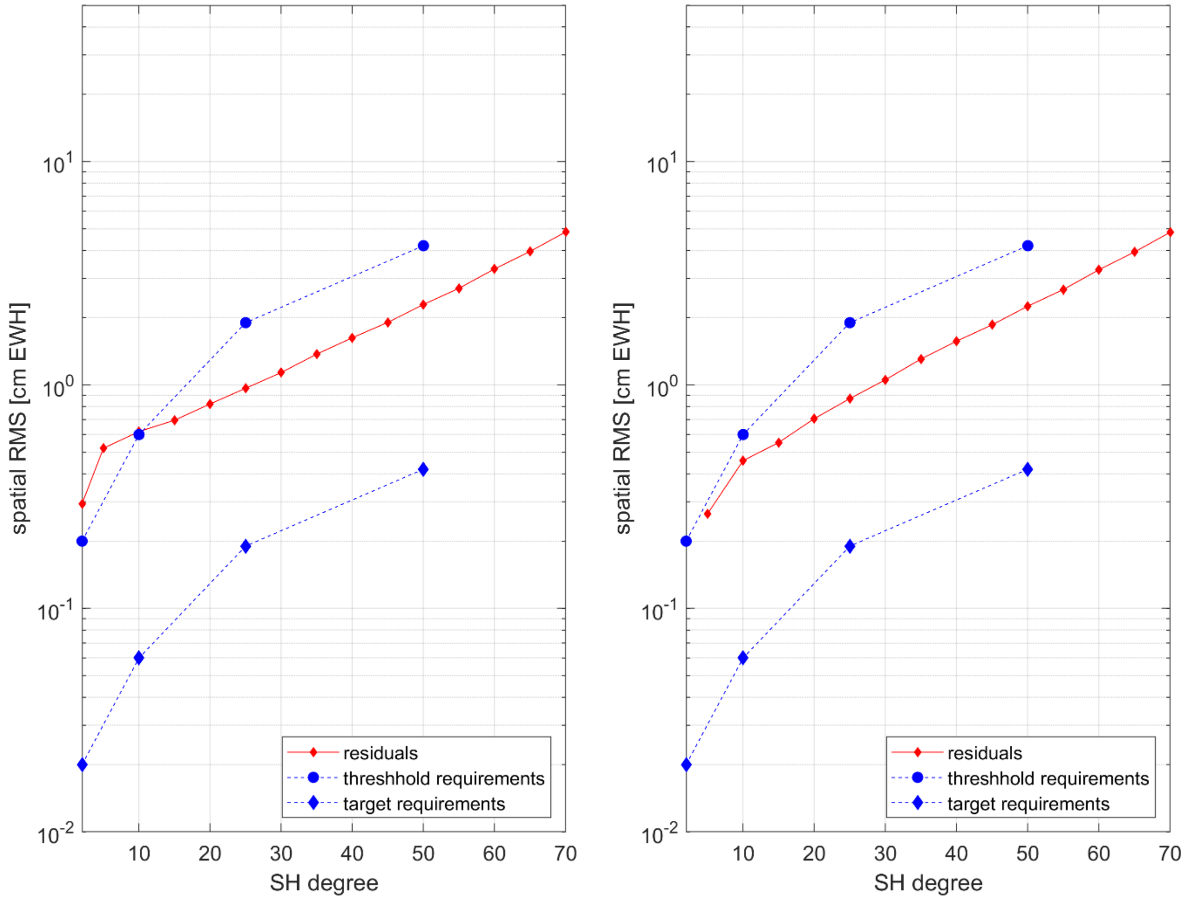

Figure 15-11: Mean spatial RMS of error grids from six full-noise 5-day solutions compared to MRD requirements. Left: evaluation from minimum d/o 2. Right: evaluation from minimum d/o 5

15.4.2. PR-004-GFZ

The P2 tone-free coefficient differences of the resulting gravity field retrieval to the true solution and the NGGM MRD requirements are shown in Figure 15-12.

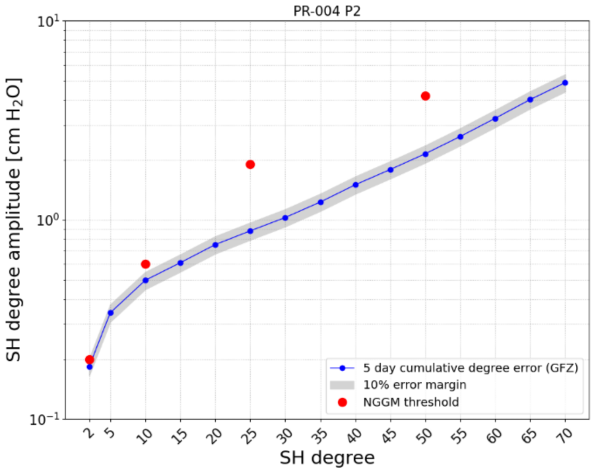

Figure 15-12 Comparison of NGGM thresholds to cumulative degree error amplitudes, computed from EWH grid differences between the retrieved and the true solutions for varying SH degree and evaluated in the region |lat|<70.

From Figure 15-9 it can be concluded that GFZ meets all requirements when tone errors are omitted.

The results for simulations that include tone errors are shown in Figure 15-13.

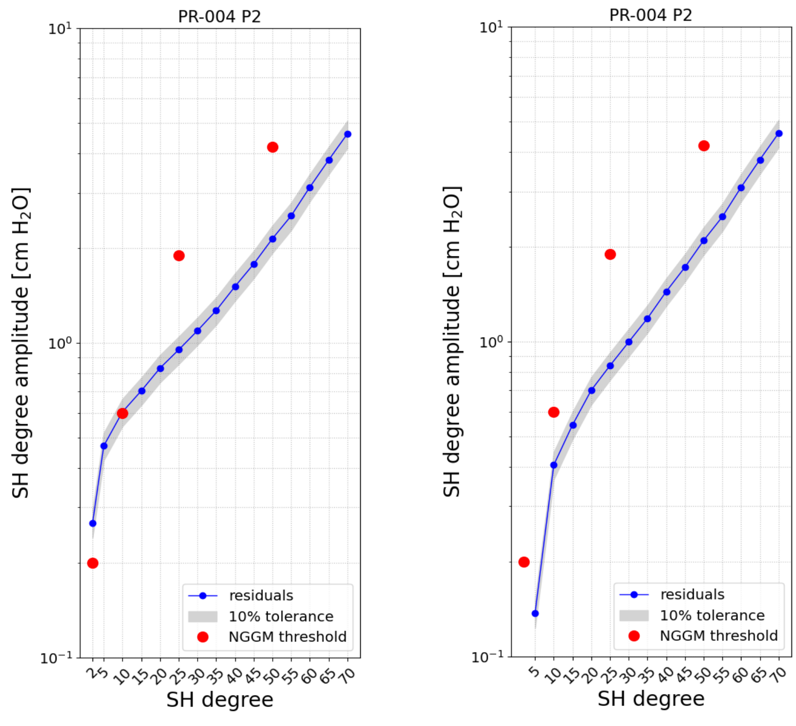

Figure 15-13 Comparison of NGGM thresholds to cumulative degree error amplitudes, computed from EWH grid differences between the retrieved and the true solutions for varying SH degree and evaluated in the region |lat|<70. Left: Accumulation done from d/o=2. Right: Accumulation done from d/o 5.

When tone errors are included into the GFZ simulations, the requirement is not met for d/o=2.

15.5. PR-005

15.5.1. PR-005-TUM

As can be seen in Figure 15-14, the threshold requirements are met for all d/o except 10 and below. Removing the coefficients below d/o 5 from the evaluation allows to meet the threshold requirements at d/o 10, which indicated that comparatively high error amplitudes are present in the respective spectral bands.

In real-data processing, the low degree coefficients will be significantly stabilized by the inclusion of information from SLR, which is currently not part of the simulation.

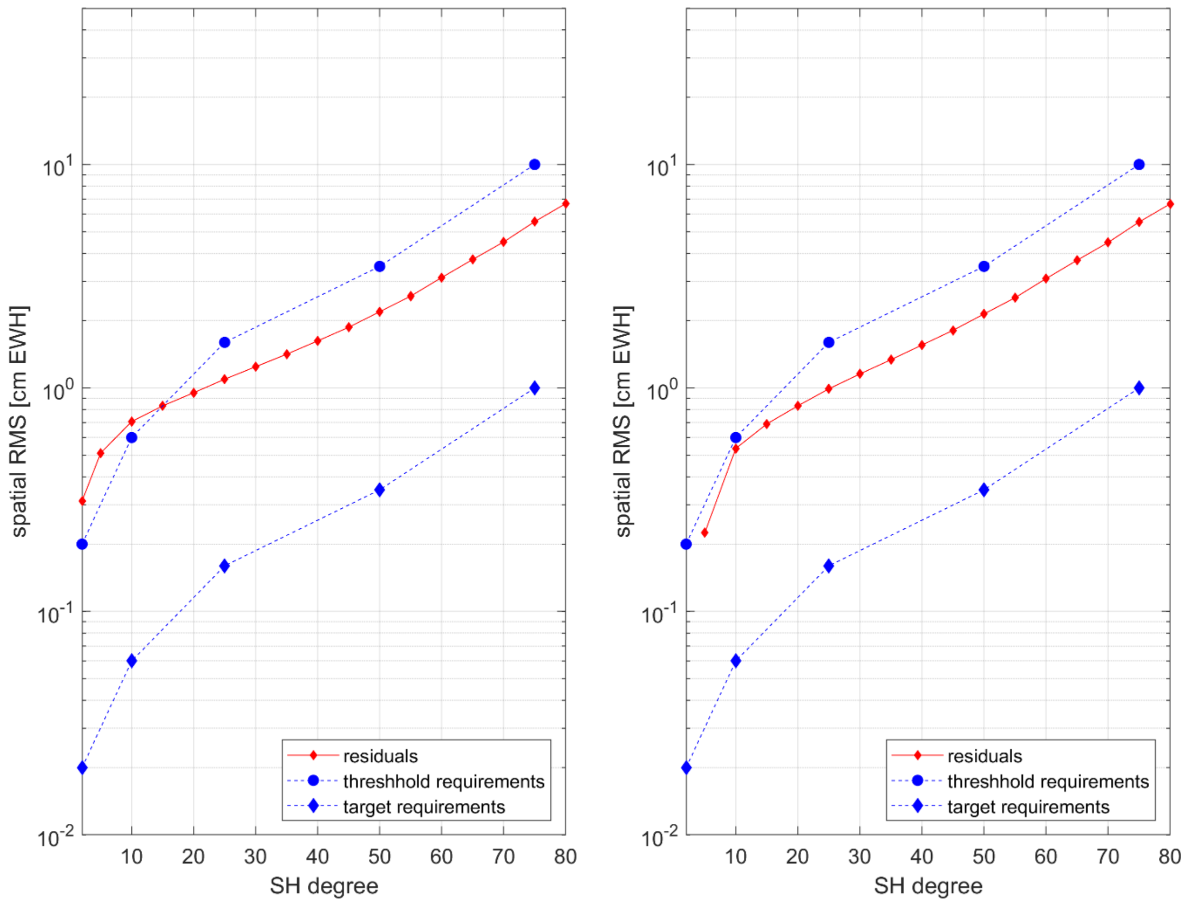

Figure 15-14: Mean spatial RMS of error grids from six full-noise 5-day solutions compared to MRD requirements. Left: evaluation from minimum d/o 2. Right: evaluation from minimum d/o 5

15.5.2. PR-005-GFZ

The P1+P2 tone-free coefficient differences of the resulting gravity field retrieval to the true solution and the MAGIC MRD requirements are shown in Figure 15-15.

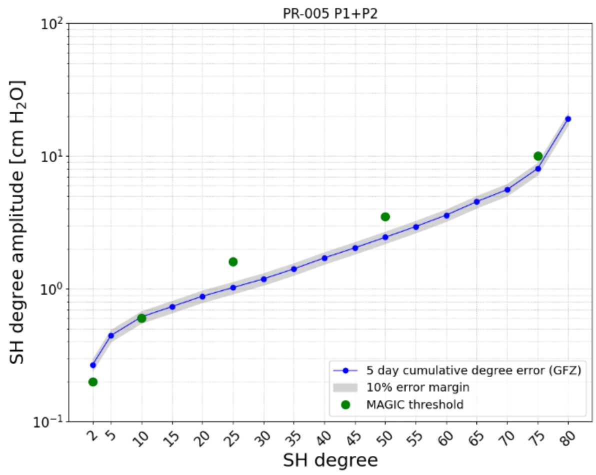

Figure 15-15 Comparison of MAGIC threshold requirements to cumulative degree error amplitudes, computed from EWH grid differences between the retrieved and the true solutions for varying SH degree and evaluated in the region |lat|<90.

From Figure 15-15, GFZ does not meet the requirement for degree 2 when tone-errors are omitted.

Results that include tone-errors are shown in Figure 15-16. Again, results are shown for a scenario that includes C_{20}, one that does not include C_{20}, and another for which errors are only accumulated for degrees and orders larger than 4. From Figure 8-16, the significance of C_{20} is seen when comparing the figure on the left to that in the middle.

When tone errors are included, GFZ fulfils the set requirement only for degrees and orders larger than 25 when all coefficients are considered. Omission of C20 improves results (middle plot) but, again, the requirement is only clearly met for degrees and orders larger than 25. However, the threshold values are nearly met for degrees and orders 10 and above. Once all degrees and orders below 5 are omitted, the requirement is met for degrees and orders larger than 10.

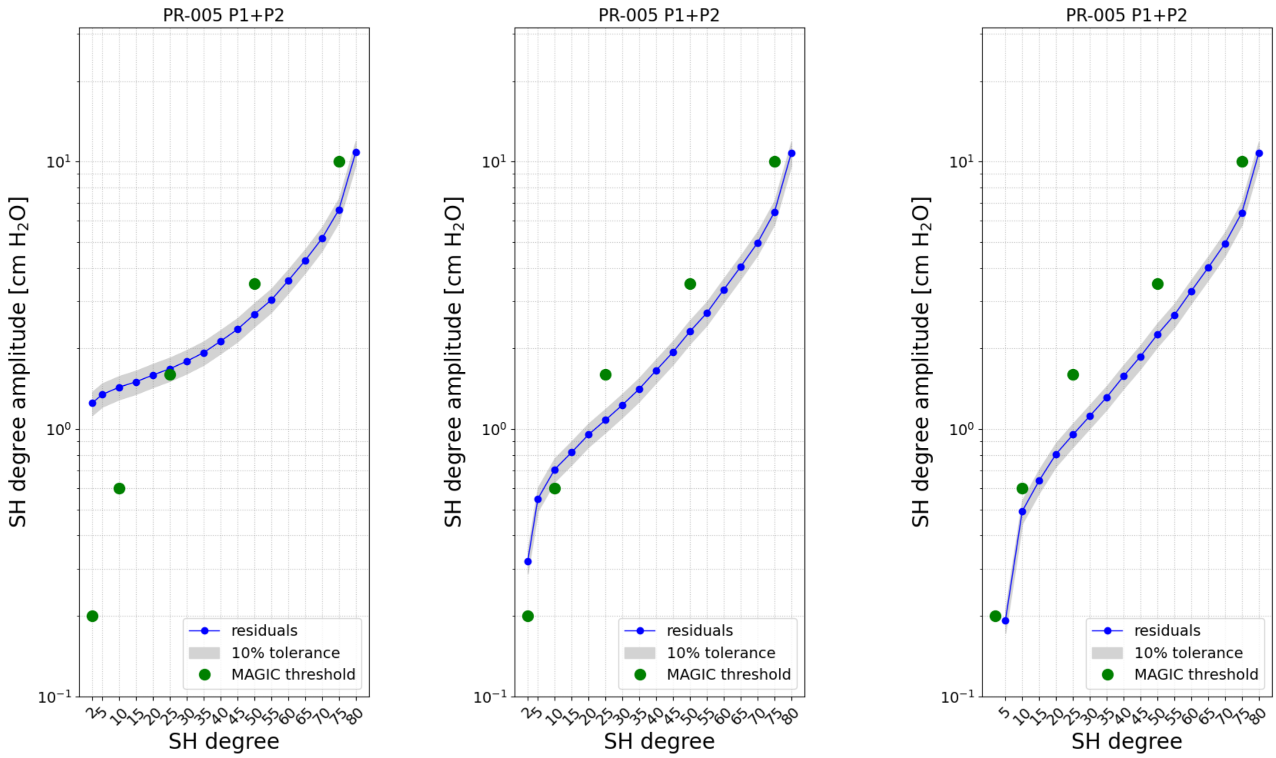

Figure 15-16 Comparison of MAGIC threshold requirements to cumulative degree error amplitudes, computed from EWH grid differences between the retrieved and the true solutions for varying SH degree and evaluated in the region |lat|<90. Results include tone errors. . Left: Accumulation done from d/o=2 and C_{20} is considered. Middle: Accumulation done from d/o=2 but C_{20} is omitted. Right: Accumulation done from d/o 5.

15.6. PR-006

15.6.1. PR-006-TUM

As can be seen in Figure 15-17, the requirement of 20% deviation from the median can be met for all d/o except 2 and 60.

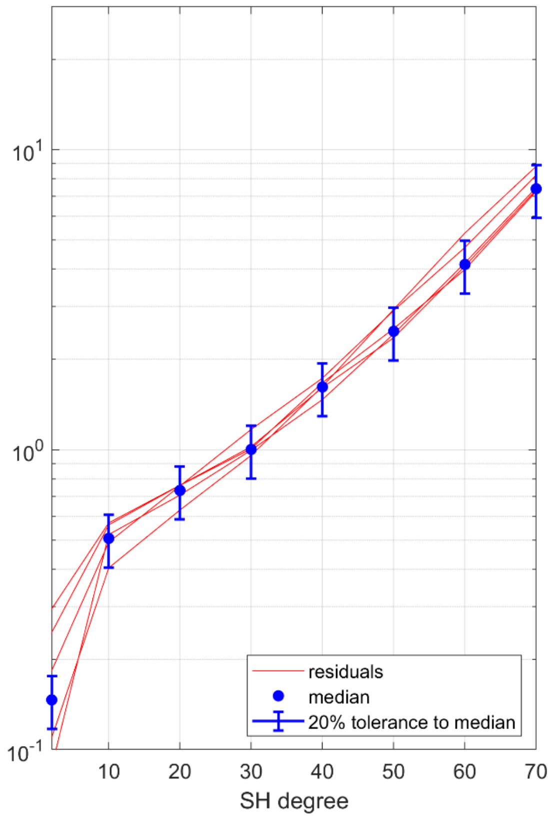

Figure 15-17: Spatial RMS of error grids from six full-noise 5-day solutions.

15.6.2. PR-006-GFZ

The tone-free coefficient difference of five 5-day P2 solutions (January 2002) along with their median, is shown in Figure 15-18.

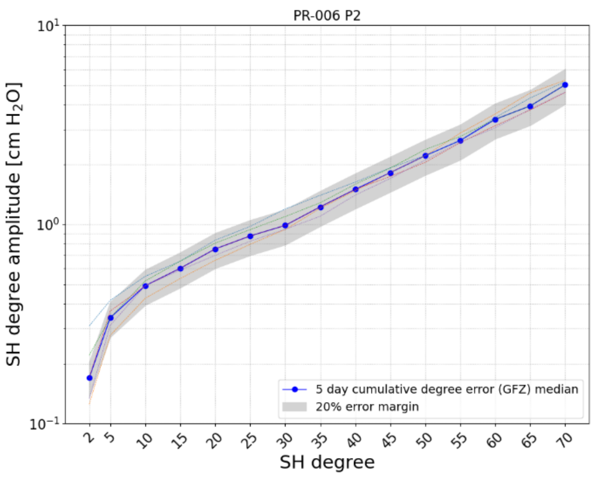

Figure 15-18 Cumulative degree error amplitudes, computed from EWH grid differences for P2 evaluated for |lat|<70.

From Figure 15-18, the individual 5-day solutions do not deviate more than 20% from their median and the requirement is therefore met when tone errors are omitted.

Results that include tone-errors are shown in Figure 15-19. Again, results are shown for a scenario that includes C_{20}, one that does not include C_{20}, and another for which errors are only accumulated for degrees and orders larger than 4. From Figure 15-19, the significance of C_{20} is seen when comparing the figure on the left to that in the middle.

When tone errors are included, GFZ fulfils the set requirement only for degrees and orders larger than 25 when all coefficients are considered. Omission of C_{20} improves results (middle plot) but, again, the requirement is only clearly met for degrees and orders larger than 25. However, the threshold values are nearly met for degrees and orders 10 and above. Once all degrees and orders below 5 are omitted, the requirement is met for degrees and orders larger than 10.

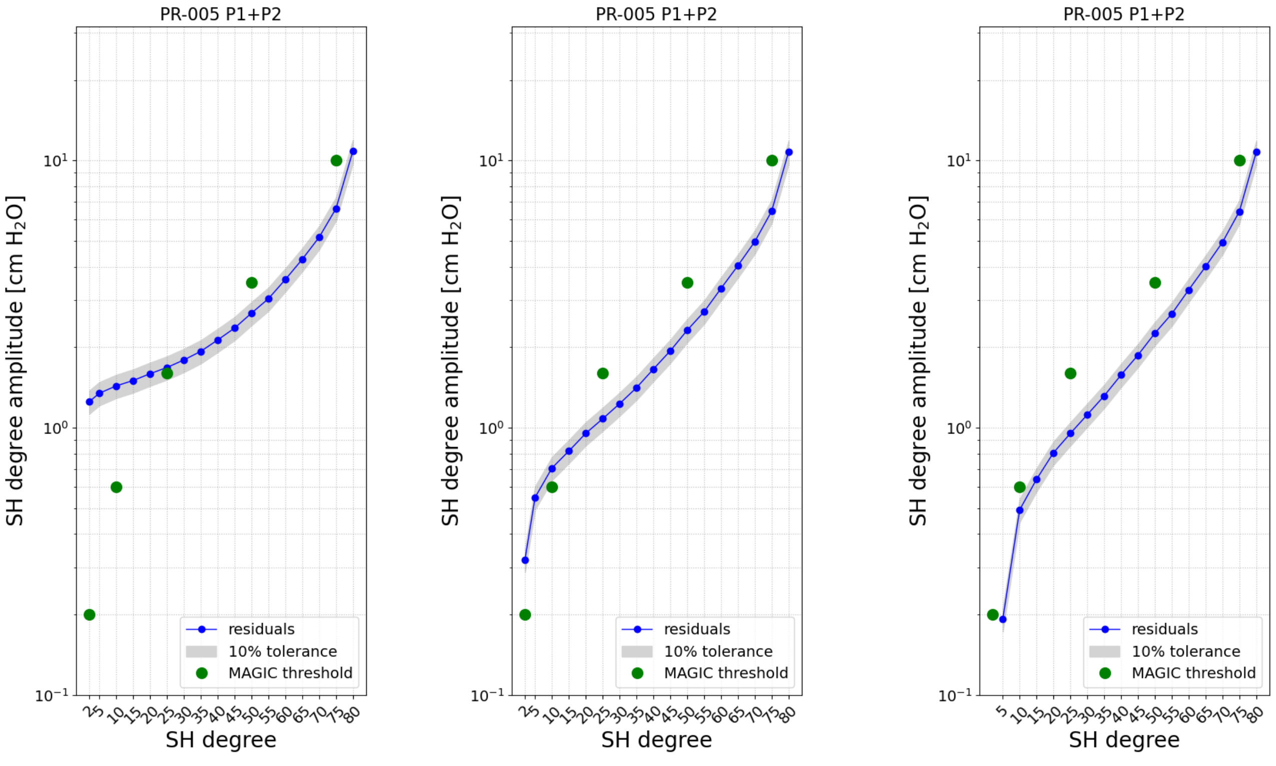

Figure 15-19 Comparison of MAGIC threshold requirements to cumulative degree error amplitudes, computed from EWH grid differences between the retrieved and the true solutions for varying SH degree and evaluated in the region |lat|<90. Results include tone errors. . Left: Accumulation done from d/o=2 and C_{20} is considered. Middle: Accumulation done from d/o=2 but C_{20} is omitted. Right: Accumulation done from d/o 5.

15.7. PR-007

15.7.1. PR-007-TUM

As can be seen in Figure 15-20, the requirement of 15% deviation from the median can be met for all d/o except 2, 10 and 60.

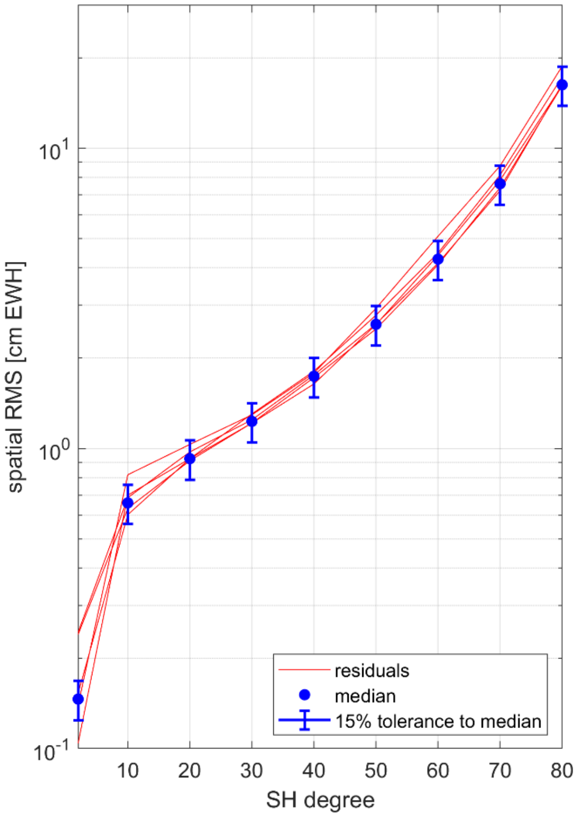

Figure 15-20: Spatial RMS of error grids from six full-noise 5-day solutions.

15.7.2. PR-007-GFZ

Tone-free cumulative degree error amplitudes are shown for the MAGIC scenario in Figure 15-21.

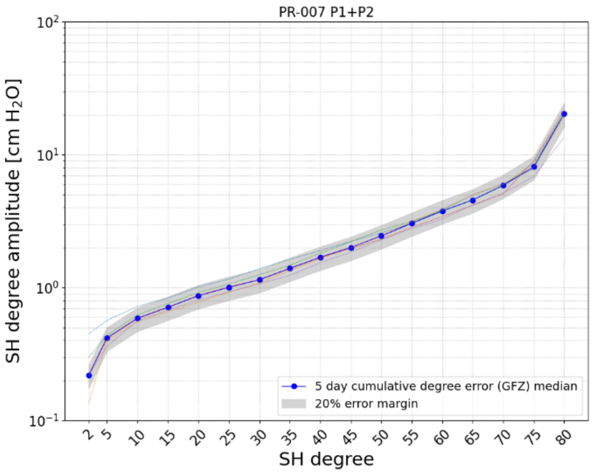

Figure 15-21 Cumulative degree error amplitudes, computed from EWH grid differences for P1+P2 evaluated for |lat|<90. These results were calculated without tone errors.

From Figure 15-21 , the individual 5-day solutions do not deviate more than 20% from their median for degrees and orders larger than 5 when tone errors are omitted. However, this criterium is not met for degrees and orders smaller than 5.

Results that include tone errors are shown in Figure 15-22. Three scenarios were investigated. First, the median was calculated with all the retrieval periods except days 26-30 (left). The procedure was then repeated but days 6-10 was omitted instead (middle). Finally, the median was calculated with the omission of C_{20} (right).

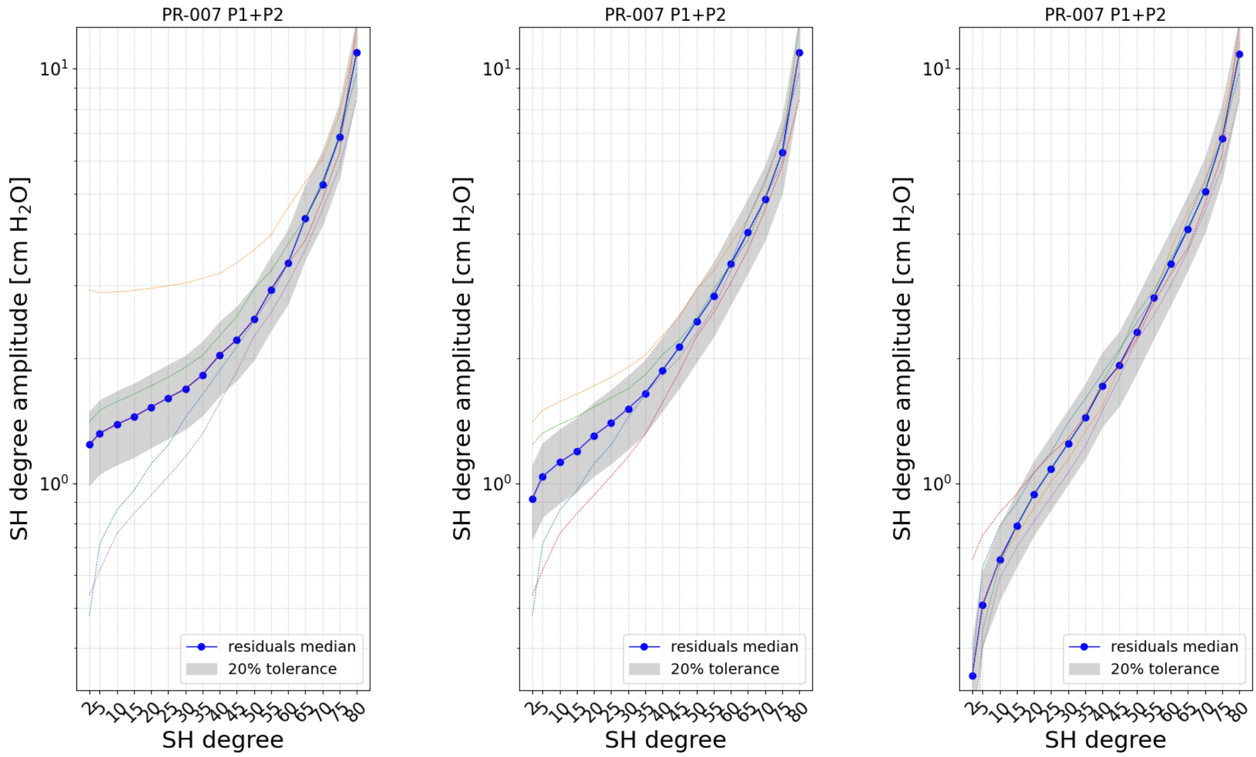

Figure 15-22 Cumulative degree error amplitudes, computed from EWH grid differences for P1+P2 evaluated for |lat|<90. These results were calculated with tone errors. Left: Accumulation from d/o=2 and the median is calculated with all retrieval periods but days 26-30. Middle: Accumulation from d/o=2 and the median is calculated with all retrieval periods but days 06-10. Right: Accumulation is done from d/o 2, but C20 is omitted.

When tone errors are included the GFZ solutions adhere to the criterium for d/o > 40 if C_{20} is considered. However, once C_{20} is excluded from the calculation, the 20% criterium is met for d/o > 15.

16. CONCLUSIONS

The evaluation reported in chapter 15 demonstrates that not all the criteria defined in chapter 14 could be met. To a large extent, this related to the fact that the definition of these was very ambitious.

Regarding product noise-only scenarios, the main issue is the adequate stochastic modeling of tone errors, which were included in the product error assumptions only in the course of the CCN1 phase of this project. It turned out that modelling these tone errors by means of notch filters, the main driver is the width of the notch filters. Very sharp filters reflect best the true noise used for superimposing the signal on the right-hand side of the NEQ system, but can cause numerical instabilities of the NEQ matrix. Therefore, a compromise has been found, which, however, means a deviation from the theoretically best consistency. It was also found during this project that the stochastic modelling of tone errors has a negative effect on full-noise solutions, because important frequencies inherent in the temporal gravity signal are down-weighted. As a main conclusion from this evaluation, it can be stated that the software and algorithms are in place and working as expected, but the optimal tuning has to investigated further.

Regarding the full-noise solutions, it can be concluded that the NGGM MRD threshold requirements are formulated in such a way that, based on the current quite pessimistic error assumptions for AO and OT background model errors, they are at the edge to be reachable. Again, the very low degrees are mainly hampered by the treatment of tone errors. Improved strategies of tone error handling as well as complementary information from SLR have to be investigated in the next project phases to stabilize to solutions in the very low degrees.

The TUM and GFZ full-noise results show very good consistency, with the exception of the very low degrees. The deviations in the low degrees can be largely explained with the different processing arc lengths as well as different methods of applying stochastic modelling of observations.

The currently formulated NGGM MRD requirement regarding the long-term stability of full-noise solutions of 20% deviation from the median is very ambitious, alone due to the varying signal structure and amplitudes of the underlying temporal gravity signals, and the stochasticity of the product noise. Still, this criterium could be met in most of the cases.

In conclusion, it could be demonstrated that the performance simulators at TUM and GFZ have reached a high degree of maturity and can provide robust and reliable results. This reliability is further strengthened by the fact that they can be used to validate each other. The involved algorithms applied for the baseline processing scheme have an SRL which is at least 5, but in many cases even higher than 5.

17. REFERENCES TO PART 2

17.1. APPLICABLE DOCUMENTS

[AD-1] Scientific Readiness Levels (SRL) Handbook, Issue/Revision 2.0, ESA-EOPSM-SRL-MA-4267

[AD-2] NGGM Science Readiness Assessment (SRA) Procedure for SRL 5. Version 1.0, Draft.

17.2. REFERENCE DOCUMENTS

[RD-1] ATBD of NGGM/MAGIC L2 and L3 products, Technical Report of the MAGIC Science Support Study, CCN1, doc. no. MAGIC_TR_D1-CCN1.

[RD-2] Daras, I.; Pail, R.; Murböck, M.; Yi, W.: Gravity field processing with enhanced numerical precision for LL-SST missions. Journal of Geodesy **2015** (89), 2015, 99-110

[RD-3] Daras, Ilias; Pail, Roland: Treatment of temporal aliasing effects in the context of next generation satellite gravimetry missions. Journal of Geophysical Research: Solid Earth **122** (9), 2017, 7343—7362

[RD-4] Pail, Roland; Yeh, Hsien-Chi; Feng, Wei; Hauk, Markus; Purkhauser, Anna; Wang, Changqing; Zhong, Min; Shen, Yunzhong; Chen, Qiujie; Luo, Zhicai; Zhou, Hao; Liu, Bingshi; Zhao, Yongqi; Zou, Xiancai; Xu, Xinyu; Zhong, Bo; Haagmans, Roger; Xu, Houze: Next-Generation Gravity Missions: Sino-European Numerical Simulation Comparison Exercise. Remote Sensing **11** (22), 2019, 2654

[RD-5] Hauk, Markus; Pail, Roland: Gravity Field Recovery Using High-Precision, High–Low Inter-Satellite Links. Remote Sensing **11** (5), 2019

[RD-6] Purkhauser, Anna F; Siemes, Christian; Pail, Roland: Consistent quantification of the impact of key mission design parameters on the performance of next-generation gravity missions. Geophysical Journal International **221** (2), 2020, 1190-1210

[RD-7] Purkhauser, Anna F.; Pail, Roland: Triple-Pair Constellation Configurations for Temporal Gravity Field Retrieval. Remote Sensing **12** (5), 2020

[RD-8] Abrykosov, Petro; Sulzbach, Roman; Pail, Roland; Dobslaw, Henryk; Thomas, Maik: Treatment of ocean tide background model errors in the context of GRACE/GRACE-FO data processing. Geophysical Journal International **228** (3), 2021, 1850-1865

[RD-9] Abrykosov, Petro; Murböck, Michael; Hauk, Markus; Pail, Roland; Flechtner, Frank: Data-driven multi-step self-de-aliasing approach for GRACE and GRACE-FO data processing. Geophysical Journal International **232** (2), 2022, 1006-1030.

[RD-10] Pail, R.; Bingham, R.; Braitenberg, C.; Dobslaw, H.; Eicker, A.; Güntner, A.; Horwath, M.; Ivins, E.; Longuevergne, L.; Panet, I.; Wouters, B.: Science and User Needs for Observing Global Mass Transport to Understand Global Change and to Benefit Society. Surveys in Geophysics **36** (6), 2015, 743-772

[RD-11] Siemes, Christian, Claudia Borries, Sean Bruinsma, Isabel Fernandez-Gomez, Natalia Hladczuk, Jose van den IJssel, Timothy Kodikara, Kristin Vielberg, and Pieter Visser (2023), New thermosphere neutral mass density and crosswind datasets from CHAMP, GRACE, and GRACE-FO, J. Space Weather Space Clim., 13 (16), 1–24, doi: 10.1051/swsc/2023014.

[RD-12] Savcenko, R., Bosch, W. (2012). EOT11a - empirical ocean tide model from multi-mission satellite altimetry. DGFI-Report No.89.

[RD-13] Ray, R. (2008). GOT4.7. Extension of Ray R (1999) A global ocean tide model from Topex/Poseidon altimetry GOT99.2. NASA Tech Memo 209478.

[RD-14] Dobslaw, H., Bergmann-Wolf, I., Dill, R., Forootan, E., Klemann, V., Kusche, J. \& Sasgen, I. (2015). The updated ESA Earth System Model for future gravity mission simulation studies. J. Geod. 89(5): 505–513, doi: 10.1007/s00190-014-0787-8.

[RD-15] Mayer-Gürr, T., Pail, R., Gruber, T., Fecher, T., Rexer, M., Schuh, W.-D., Kusche, J., Brockmann, J.-M., Rieser, D., Zehentner, N., Kvas, A., Klinger, B., Baur, O., Höck, E., Krauss, S., Jäggi, A. (2015). The combined satellite gravity field model GOCO05s. Geophys. Res. Abstracts, 17, EGU2015-12364, European Geosciences Union General Assembly 2015 (Vienna, Austria), doi: 10.13140/RG.2.1.4688.6807.

[RD-16] Metzler, B., Pail, R. (2005). GOCE Data Processing: The Spherical Cap Regularization Approach. Studia Geophysica et Geodaetica 49(4): 441–462, doi: 10.1007/s11200-005-0021-5.

[RD-17] Sneeuw, N. et al. (2015). Assessment of Satellite Constellations for Monitoring the Variations in Earth Gravity Field (SC4MGV). Final Report, v1.0.

[RD-18] Pail, R., et al. (2018). Additional Constellation and Scientific Analysis Studies of the Next Generation Gravity Mission (ADDCON). Final Report (D6), v3.1, ESA Contract No. 4000118480/16/NL/FF/gp.

[RD-19] Pail, R. et al. (2019). Additional Constellation and Scientific Analysis Studies of the Next Generation Gravity Mission (ADDCON), Extended Phase (CCN1). Final Report (D10), v1.4. ESA Contract No. 4000118480/16/NL/FF/gp.

[RD-20] Pail R. et al. (2022). NGGM/MAGIC – Science Support Study During Phase A (MAGIC). Final Report, v1.0, ESA Contract No. RFP/3-17035/20/NL/FF/tfd.

[RD-21] Flechtner, F., Neumayer, K.H., Dahle, C., Dobslaw, H., Fagiolini, E., Raimondo, J.C., et al. (2015) What can be Expected from the GRACE-FO Laser Ranging Interferometer for Earth Science Applications? *Surv. Geophys. 37*, 453-470. DOI 10.1007/s10712-015-9338-y

[RD-22] Hauk, M., Wilms, J., Sulzbach, R., Panafidina, N., Hart-Davis, M., Dahle, C., et al. (2023). Satellite gravity field recovery using variance-covariance information from ocean tide models. *Earth and Space Science, 10*, e2023EA003098

PART 3:

MRTD CRITICAL ASSESSMENT AND COMPLIANCE REPORT

18. INTRODUCTION

The purpose of this document is to provide a critical assessment of the draft of the MRTD with respect to MAGIC and NGGM mission requirements and to give feedback on science questions and objectives as a basis for future updates of the MRTD. The contributions to this document are based on the activities in WP1200 of CCN1 and partly based on analyses results for different fields of applications in WP1600.

Suggested modifications as well as comments are visible in track-change mode in the MRTD draft in a separate file and summarized below in Chapter 19.1. For selected suggestions, ore detailed explanations are given in Chapter 19.2.

19. ESA MRDT CRITICAL ASSESSMENT (WP1200)

19.1. OVERVIEW ON SUGGESTED MRTD MODIFICATIONS AND OF COMMENTS

#	Chapter, Figure, Table, etc.	Current draft	Suggested modification	Comment
1	Throughout document	ground-water	groundwater	Change spelling to the more common form in hydrology
2	Table 1 and several instances throughout document	Extreme events warning (e.g., drought, flood)	Extreme events (droughts, floods)	The relevant signal in the thematic field of hydrology is not ‘warning’ but the extremes themselves. Also, as there are hardly any other hydrological extremes of relevance for NGGM, ‘e.g.’ can be deleted
3	Chapter 3.1, list of research fields that are expected to benefit from the NGGM mission	• Extreme events warning (e.g., drought, flood) • • Water cycle separation of contributions	• Extreme events forecast and monitoring (droughts, floods) • new entry: ‘Earth’s crustal studies and dynamics;’ • Attribution of hydrological change	• Extreme events warning (e.g., drought, flood) • • ‘Separation of contributions’ is not clear. What is meant here? 1) Separation of the dynamics and trends of different storage compartments in the water cycle

				or 2) Attribution of change in the regional to global water cycle
4	Table 2 – Updated IUGG mission scenarios and performances			How do the numbers in Table 2 relate to the numbers in the thematic sub-fields and in the SATM tables (Tables 4 and following) below? There are partly different / inconsistent numbers in these tables.
5	Chapter 3.2.1 Science objective H1-a	‘confined to scales larger or equal than 250x250 km2’	delete	The limit of size of river basins is not that clearly traceable from the evaluation results and based on Table 2 and Table 4? The limit also changes with the time scale under consideration.
6	Chapter 3.2.1 Science objective H4-a	Improve drought and flood monitoring to forecast short-term (3-5 days) impacts more accurately and to assess potential mitigations based on fast-track observations.	Improve drought and flood forecasting and monitoring, including short-term (3-5 days) impacts, and assess potential mitigations based on fast-track observations.	The original formulation missed / didn’t adequately enough consider three issues: - for forecasting, also/in particular the monitoring before the actual event is important - impacts are not necessarily only short-term - the goal of forecasting is not only the short-term impact The new formulation is broader and tries to incorporate these issues.
7	Chapter 3.2.2 Table 6 NGGM user requirements for Cryosphere			The numbers given in Table 6 are identical to those for MAGIC. Given that most of the ice sheet area is located >65-70 latitude, it seems unlikely that we can expect even a similar performance as we now have for GRACE/GRACE-FO and we probably should hold it against the same standards as MAGIC.
8	Chapter 3.2.2 Table 6 NGGM user	Time scale M; Threshold-b: 150 km @ 50.0 cm		based on the earlier MAGIC results, tis can probably be lowered

	requirements for Cryosphere			
9	Chapter 3.2.2 Table 6 NGGM user requirements for Cryosphere	Time scale L; Threshold-b: 130 km @ 15.0 cm/yr		not sure how we can evaluate this as it would require d/o ~150
10	Chapter 3.2.4 Table 10. NGGM user requirements for Solid Earth	Solid Earth Time scale L; Threshold-a: 250 km @ 0.6 cm/yr; Threshold-b: 150 km @ 4.6 cm/yr Solid Earth Target-a: 250 km @ 0.06 cm/yr; Target-b: 150 km @ 0.46 cm/yr	Time scale L; Threshold-a: 250 km @ 1.2 cm/yr; Threshold-b: 150 km @ 14 cm/yr Target-a: 250 km @ 0.12 cm/yr; Target-b: 150 km @ 1.4 cm/yr	Comparing with the MAGIC error curves, the values seem too low, see graphs in Chapter 3.2.1 below, in which the values are compared to the cumulative error curve.
11	Chapter 3.2.4 Table 10. NGGM user requirements for Solid Earth	Geohazards Time scale M; Threshold: 300 km @ 1 cm (Mw 8 earthquakes) Target: 200 km @ 1.0 cm (Mw > 7.4 earthquakes)	Geohazards Time scale M; Threshold: 300 km @ 2 cm (Mw 8 earthquakes) Target: 200 km @ 0.2 cm (Mw > 7.4 earthquakes)	
12	Chapter 3.2.4 Table 10. NGGM user requirements for Solid Earth	Geohazards Time scale M; Threshold: 200 km @ 1 cm/yr	Geohazards Time scale M; Threshold: 200 km @ 3 cm/yr	
13	Chapter 3.2.4 Table 10. NGGM user requirements for Solid Earth	Geohazards Time scale L; Target: 100 km @ 1.0 cm/yr		This value seems much too low compared to the MAGIC cumulated error
14	Chapter 3.2.4 Table 10. NGGM user requirements for Solid Earth	Natural Resources Exploitation Time scale S; Target: <250 km @ 10.0-1.0 cm	Natural Resources Exploitation Time scale S; Target: <250 km @ 5 cm	
15	Chapter 3.2.4 Table 10. NGGM user requirements for Solid Earth	Crustal properties Time scale M; Target: <200 km @ 10.0-1.0 cm	Crustal properties Time scale M; Target: <200 km @ 1.0 cm	10 cm is like the threshold, so take 1 cm
16	Chapter 3.2.4 Table 10. NGGM user requirements for Solid Earth	Crustal properties Time scale L; Target: <220 km @ 1.0 cm/yr		Vvalue is the same as threshold- should be lowered, or is the wavelength lowered?

Further minor suggestions of wording, corrections of typos, etc. can be found throughout the MRTD draft in track-change mode but are not listed here in detail.

19.2. DETAILED EXPLANATIONS

19.2.1 User requirements for Solid Earth

Modifications to NGGM requirements for Solid Earth applications are suggested, see Figure 19-1 and Table 10 in the MRTD draft.

Thematic field	Time scale S: Short-term (3-5 days); **M**: Monthly; L: Long-term trend	**Threshold: Resolution & Accuracy [EWH]**	**Target: Resolution & Accuracy [EWH]**
Solid Earth	**S** *Latency: 3-5 days*	Threshold: 400 km @ 4.2 cm	Target: 400 km @ 0.42 cm
	M *Latency: 1 month*	Threshold-a: 350 km @ 2.8 cm; Threshold-b: 180 km @ 20 cm.	Target-a: 350 km @ 0.28 cm; Target-b: 180 km @ 2.0 cm.
	L	Threshold-a: 250 km @ ~~0.6~~1.2 cm/yr; Threshold-b: 150 km @ ~~4.6~~14 cm/yr	Target-a: 250 km @ 0.~~06~~12 cm/yr; Target-b: 150 km @ ~~0.46~~1.4 cm/yr
Thematic sub-field			
Geohazards	**S** *Latency: 3-5 days*	Threshold: 300 km @ <10.0 cm (Mw 8 earthquakes)	Target: <250 km @ 10.0-1.0 cm
	M *Latency: 1 month*	Threshold: 300 km @ ~~1~~2 cm (Mw 8 earthquakes)	Target: 200 km @ ~~1.0~~0.2 cm (Mw > 7.4 earthquakes)
	L	Threshold: 200 km @ ~~1~~3 cm/yr	Target: 100 km @ 1.0 cm/yr
SE response to earlier Ice load forcing	**L**	See Solid Earth	Target-2c: <100 km @ 10 cm/yr
Natural resources exploitation	**S** *Latency: 3-5 days*	Threshold: 300 km @ 10.0 cm	Target: <250 km @ ~~10.0-1.0~~5 cm
Deep interior properties and dynamics	**S** *Latency: 3-5 days*	See Solid Earth	Target: 6000 km @ 0.15 mm (Body tides)
	L	See Solid Earth	Target-a: 2000-6000 km @ 0.05-0.1 mm in 10 yr; Target-b: 230-330 km @ 1 mm in 10 yr
Crustal properties and dynamics associated with the terrestrial water cycle	**S** *Latency: 3-5 days*	See Solid Earth	<250km @ 10.0-1.0 cm
	M *Latency: 1 month*	Threshold: 200 km @ 10 cm	Target: <200 km @ ~~10.0~~ 1.0 cm
	L	Threshold: 220 km @ 1 cm/yr	Target: <220 km @ 1.0 cm/yr

BC **BRAITENBERG CARLA**
Comparing with the magic error curves the values as they are seem too low- see the attached graphs, in which the values are compared to the cumulative error curve.

BC **BRAITENBERG CARLA**
This value seems much too low compared to the magic cumulated error

BC **BRAITENBERG CARLA**
10 cm is like the threshold, so leave 1 cm

BC **BRAITENBERG CARLA**
Attention, value is the same as threshold- should be lowered, or the wavelength lowered?

Figure 19-1: Suggested corrections for NGGM MRTD Table 10 (NGGM user requirements for Solid Earth (Geohazards, Solid Earth's response to the forcing of earlier ice loads, Natural resources exploitation, Deep interior properties and dynamics, Crustal properties and dynamics associated with the terrestrial water cycle).

We propose these changes based on the following figures (Figure 19-2 to Figure 19-6), in which the plotted target and threshold values are those of the updated table shown in Figure 19-1.

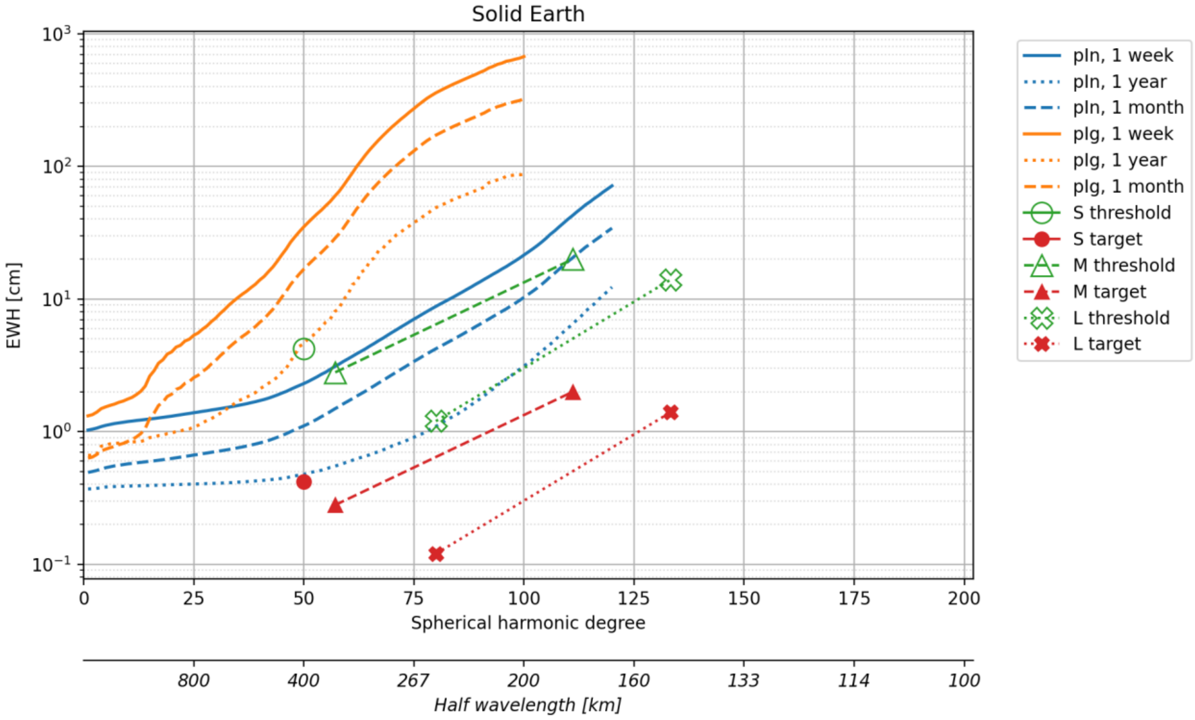

Figure 19-2: Target and threshold values of the Table 10 in the MRD document for the subject Solid Earth.

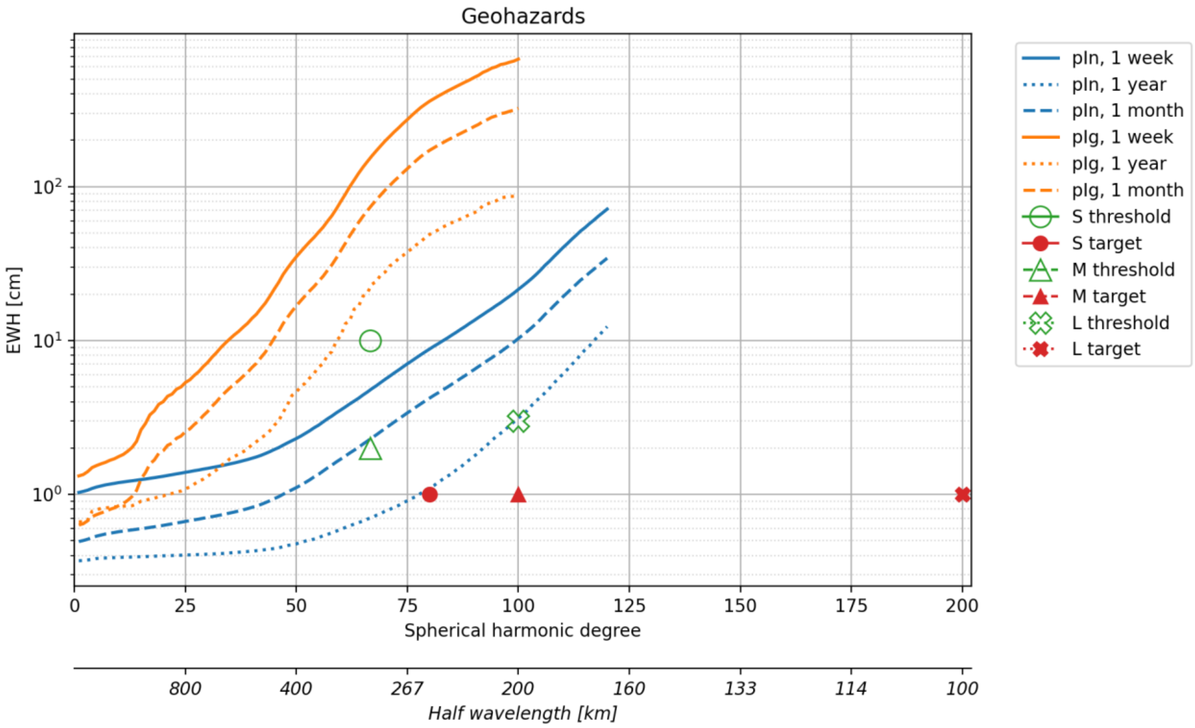

Figure 19-3: Target and threshold values of the Table 10 in the MRD document for the subject Geohazards.

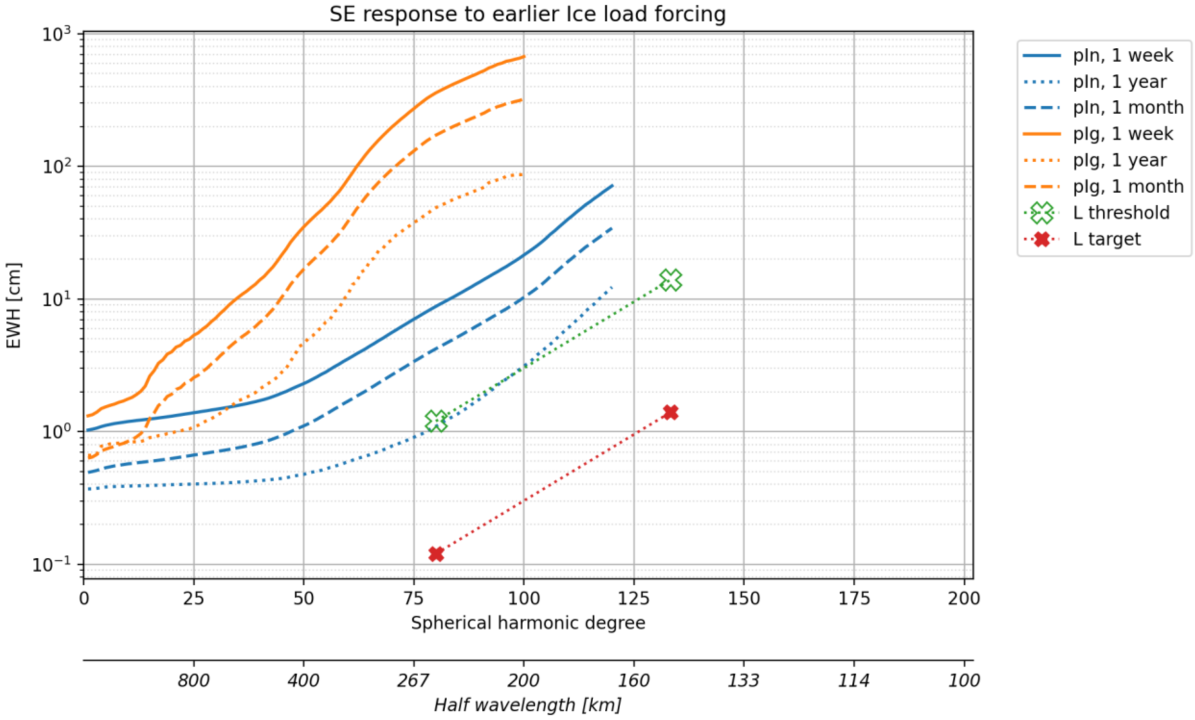

Figure 19-4: Target and threshold values of the Table 10 in the MRD document for the subject Solid Earth response to earlier ice load forcing.

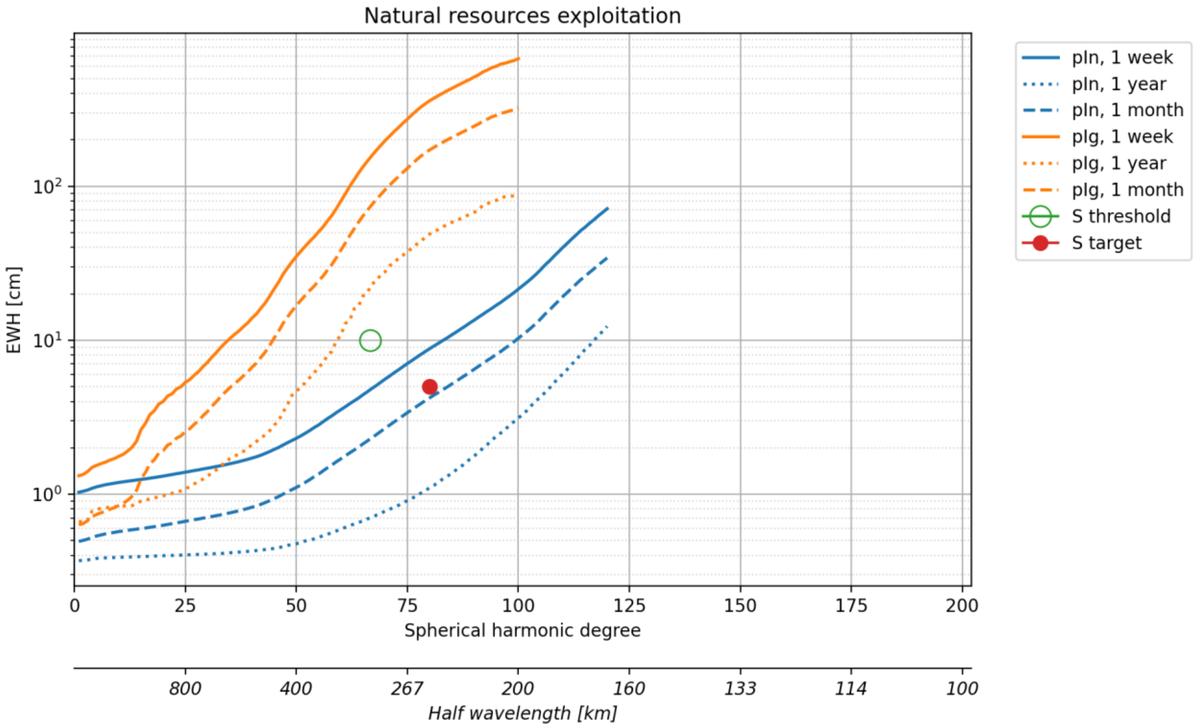

Figure 19-5: Target and threshold values of the Table 10 in the MRD document for the subject Natural resources exploitation.

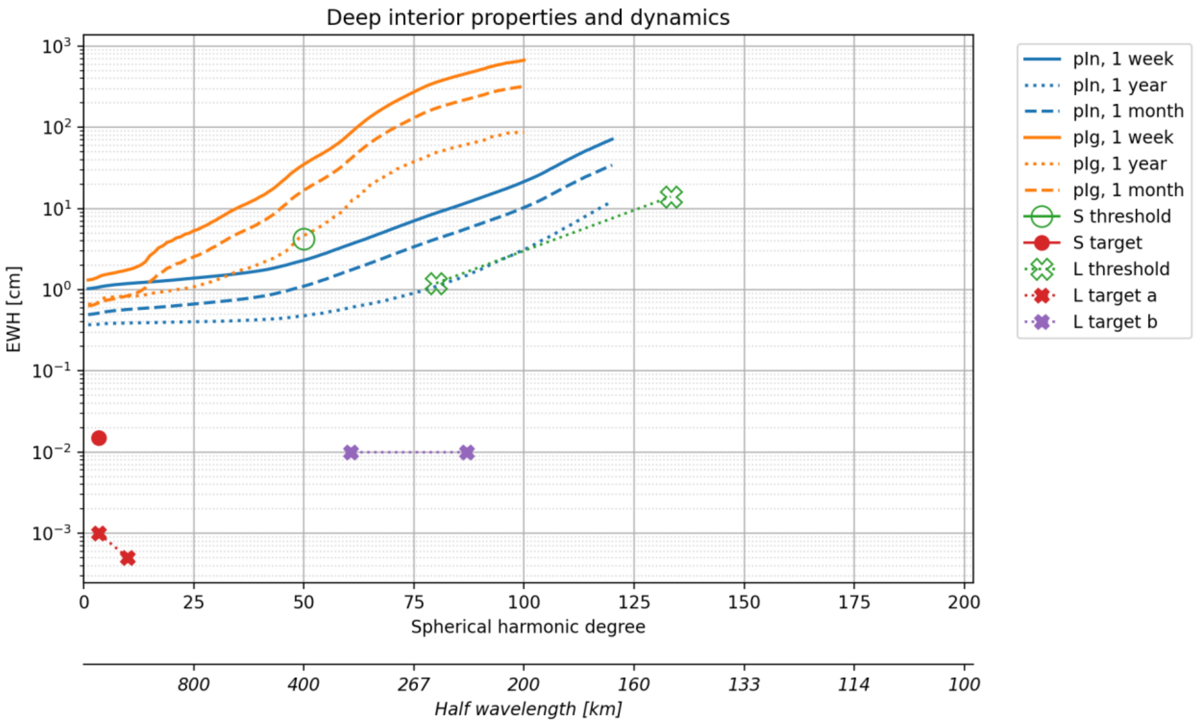

Figure 19-6: Target and threshold values of the Table 10 in the MRD document for the subject Deep interior properties and dynamics.

19.2.2 Cryosphere applications

The cryosphere part of the MRD was adjusted regarding the adaptation to NGGM considering the impact of the polar gap of an inclined-only pair on mass balance estimates of Greenland and Antarctica.

20. APPLICABLE DOCUMENTS, REFERENCE DOCUMENTS, AND PUBLICATIONS TO PART 3

20.1. APPLICABLE DOCUMENTS

[AD-1] Mission Requirements Document, Next Generation Gravity Mission as a Mass-change And Geosciences International Constellation (MAGIC) - A joint ESA/NASA double-pair mission based on NASA's MCDO and ESA's NGGM studies (2020). ESA-EOPSM-FMCC-MRD-3785

[AD-2] Scientific Readiness Levels (SRL) Handbook, Issue 1, Revision 0, 05-08-2015

[AD-3] Statement of Work - ESA Express Procurement - EXPRO NGGM/MAGIC science support study during Phase A, Issue 1, Revision 0, 18/01/2021 Ref ESA-EOPSM-FUTM-SOW-3813

20.2. REFERENCE DOCUMENTS

[RD-1] Getirana, A., M. Rodell, S. Kumar, H.K. Beaudoing, K. Arsenault, B. Zaitchik, H. Save, and S. Bettadpur, GRACE improves seasonal groundwater forecast initialization over the U.S., J. Hydrometeor., 21 (1), 59-71, doi:10.1175/JHM-D-19-0096.1, 2020.

PART 4:

E2E SIMULATIONS: DESCRIPTION, RESULTS AND ANALYSIS

21. INTRODUCTION

The purpose of this document is to describe the further development of L2 algorithm, of L0 to L1b inter-satellite ranging algorithms, and refined results of E2E simulations and their analysis performed during this CCN1. This refers to WP 1300, 1400 and 1500 of the WBS.

22. L2 ALGORITHM DEVELOPMENT (WP1300)

22.1. DMD APPROACH WITH BASELINE MAGIC SCENARIO (WP1310)

The goal of this section is to understand the performance of the DMD approach (Abrykosov et al. 2022) in the frame of a double-pair-based gravity retrieval, exemplarily carried out on the basis of the baseline scenario's observation geometry (orbital parameters cf. Table 13-1). The DMD approach primarily aims to reduce temporal aliasing stemming from non-tidal mass variations and was originally envisioned application to GRACE/GRACE-FO, i.e. single-pair, gravity retrieval. However, it has also shown indications of being beneficial for Bender-type constellations. It is noted that all simulations presented in this section have been carried out with the reduced-scale simulation software.

“Wiese bumps”

The processing approach denoted in this document as “Wiese approach” or “Wiese parametrization” has been presented in Wiese et al. (2011) as a self-de-aliasing approach applicable in Bender-type-based (Bender et al., 2008) gravity processing. It consists of the co-estimation of short-interval (typically daily) low-resolution gravity field parameters in addition to the high degrees which are estimated once over the full retrieval period (typically one month). The goal of this approach is to capture short-term long-wavelength temporal variations of the gravity field in the daily estimates and hereby prevent them from manifesting as temporal aliasing in the higher degrees of the full (monthly) estimate. However, it has been shown that the Wiese parametrization may degrade the monthly retrieval in certain spectral bands. These degradations could be attributed to an instable inversion of the NEQ matrix which in turn is related to an interplay between large differences in the weight of the observations of the polar and inclined satellite pairs and the underlying parametrization scheme. It is noted that the differences in observation weights may stem on one hand from the applied stochastic model and on the other hand from the observation geometry, i.e. from the satellite pairs' respective orbital altitude (Pail et al. 2022).

In the following, we investigate whether the DMD approach suffers from similar artefacts, in the following referred to as “(Wiese) bumps”. For this, we simulate a 30-day gravity retrieval based on the Wiese parametrization as well as on DMD, both approaches respectively employing the estimation of daily fields up to d/o 15. In addition, DMD scenarios where in addition to daily fields up to d/o 15 also two-daily fields up to d/o 30 as well as three-daily fields up to d/o 45 are estimated subsequently are investigated.

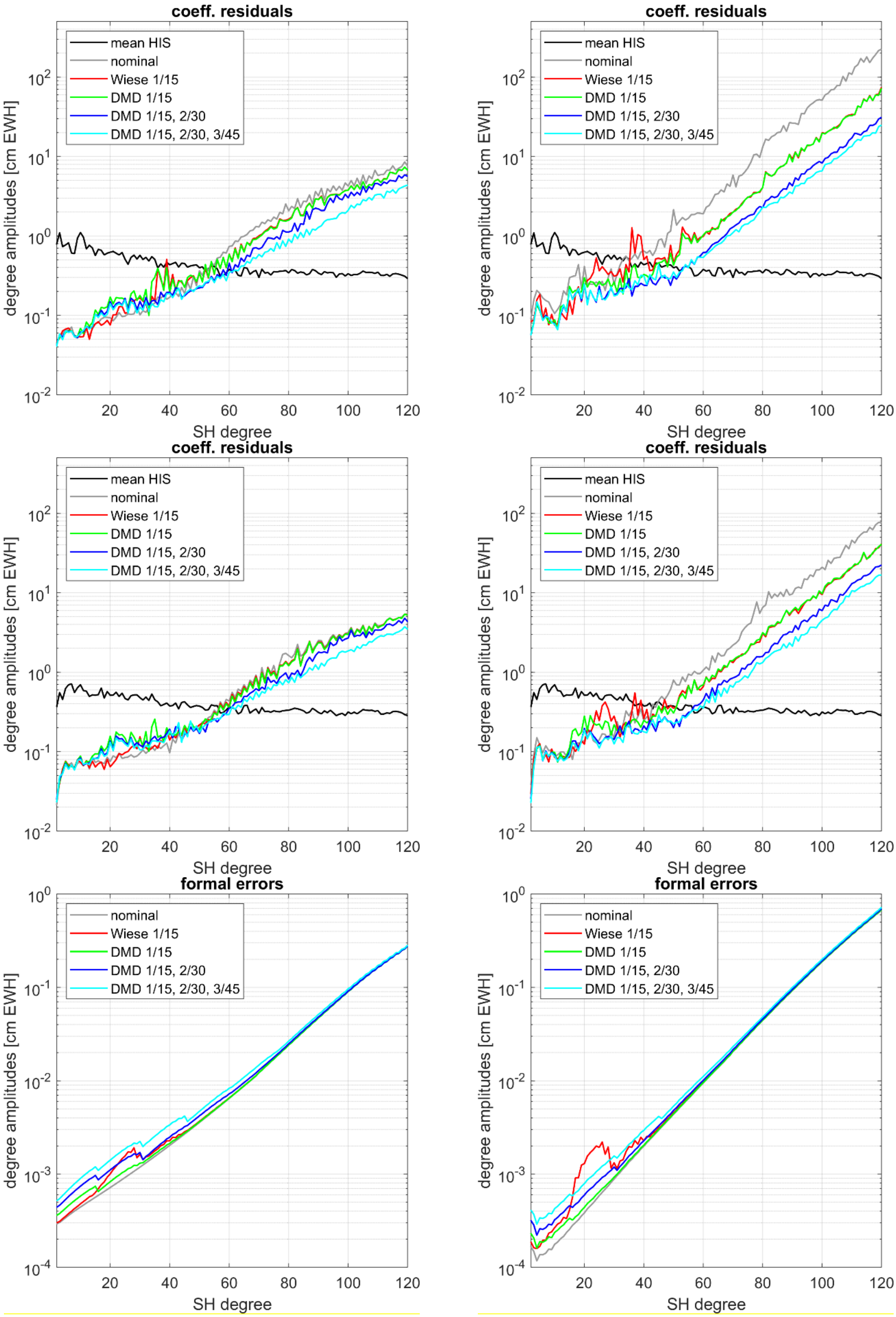

Figure 22-1 Coefficient residuals and formal errors (bottom row) of a 30-day gravity retrieval. Top row: no a priori BM-based AO de-aliasing, i.e. target signal is AOHIS; centre row: with a priori BM-based AO

de-aliasing, i.e. target signal is HIS. Results are shown with application of stochastic modelling based on product noise specifications (right column) and without stochastic modelling (left column).

The simulation results are presented in Figure 22-1 for a simulation scenario with AOHIS as well as HIS as the target signal (no BM-based a priori de-aliasing in the former scenario). Additionally, the formal errors are shown. Both sets of simulations are repeated with and without stochastic modelling of instrument noise.

The formal errors confirm that that the Wiese approach suffers from an instable inversion of the underlying NEQ system, i.e. the bump is clearly present. This effect is further amplified when stochastic modelling is applied, as the superior noise performance of the instruments used for P2 increases the disparity between the individual weights of P1 and P2 observations. The DMD, on the other hand, does not suffer from this specific behaviour. However, it can be seen that the DMD features its own individual “jumps” in the formal errors, which occur precisely at the maximum d/o of the interval estimates. This behaviour is not unexpected, since error propagation is continuously applied at each interval step. In other words, the first step of the DMD, i.e. the estimation of the interval fields, considers the nominal VCM of observations. These short-term fields consequently obtain individual VCMs. Once these fields are reduced from the full observations in preparation of the second step, the contribution of their individual errors must be considered, and thus, their error VCMs are propagated onto the level of observations and the resulting VCM of observations are stacked with the original VCM of observations. This procedure is repeated at each estimation step until the final long-term field is obtained. We note that while this is – from a mathematical perspective – the correct strategy, one may also consider neglecting the error propagation and instead process each interval step with the original VCM of observations. In this case, the formal errors of all three presented DMD schemes would correspond to those of the nominal scenario.
The Wiese bumps can also be seen to some extent in the coefficient residuals. It can be seen, however, that they do not only depend on the individual weighting of P1 and P2 observations, but also on the sampled signal. In this way, the Wiese-based results with a priori AO de-aliasing feature a comparatively small bump at d/o ~30, while the scenario without a priori de-aliasing features an additional, significantly larger bump around d/o ~40. Once stochastic modelling is added to the processing scheme, the bumps greatly increase in amplitude. Bumps can also be found in the DMD-based results. In case of DMD 1/15, the bumps behave quite similarly to those of the Wiese approach, but can for a large part be negated by introducing additional intermediate de-aliasing steps. Thus, the bump amplitudes are greatly reduced in amplitude in the multi-step DMD scenarios.

In conclusion, it can be stated that the Wiese bumps occur due to an interplay of the disparity between the individual weight of P1 and P2 observations, introduced through large differences in orbital altitude as well as stochastic modelling, and the observed signal. These weights, or rather weight differences, play no role in the DMD processing, as the inversion of the underlying NEQ system is more stable than in the Wiese approach. Bumps may still occur in the formal errors as well as in the coefficients of the retrieved signal here, but they are exclusively related to the employed error propagation for the former and to the sampled signal for the latter. In this regard, therefore, the DMD can be regarded as superior to the standard Wiese approach.

DMD with multiple sequential short-term estimates

In this subchapter, we evaluate whether a DMD scheme where multiple interval solutions of increasing spatial resolution over longer periods are estimated subsequently before solving for final, e.g. monthly, gravity product. The investigation is based on three DMD scenarios – DMD 1/15 (estimation of daily fields up to d/o 15), DMD 3/45 (estimation of 3-daily fields up to d/o 45) and DMD 1/15, 2/30, 3/45 (subsequent estimation of daily fields up to d/o 15, 2-daily fields up to d/o 30 and 3-daily fields up to d/o 45) which are applied in a full-noise, 30-day simulation. Here, we consider two full-noise scenarios – in the first, we attempt to retrieve the full AOHIS signal, whereas in the second the target signal is HIS, i.e. a priori AO de-aliasing based on geophysical BMs is applied.

The retrieval errors of the 30-day estimate are depicted in Figure 22-2. It is evident that the best retrieval performance can be reached when applying the multi-step DMD. This scheme allows to increase the reliable estimation of the target signal to d/o 62 from d/o 52 in case of AOHIS and d/o 57 in case of HIS, respectively. Evidently, the additional de-aliasing resulting from multiple estimation steps significantly outweighs potential misparametriaztion errors. It is also notable that “bumps” occur both in DMD 1/15 and DMD 1/15, 2/30, 3/45, whose origin is not yet determined with absolute certainty. Regardless, it becomes clear that the bumps occurring in the DMD 1/15 scenario are far less pronounced that in case of DMD 1/15, 2/30, 3/45, thus further advocating the application of the multi-step processing.

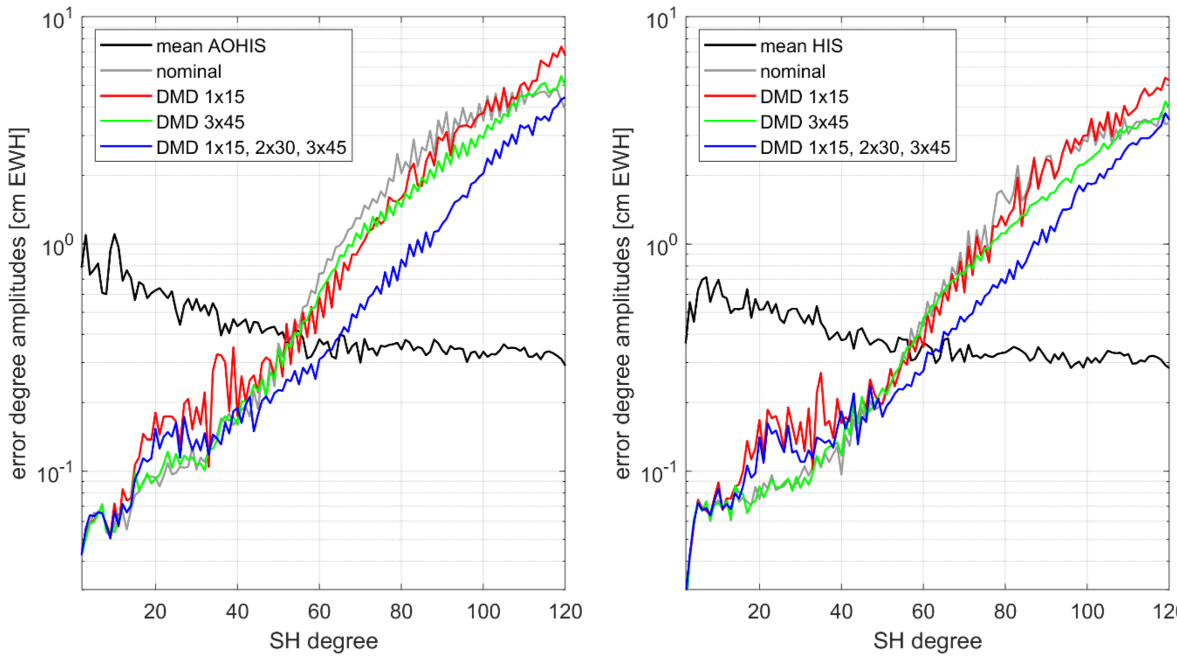

Figure 22-2: Retrieval errors of the 30-day estimate obtained with various DMD parametrization schemes. Left: retrieval of the full AOHIS; right: retrieval of HIS (i.e. a priori BM-based AO de-aliasing is applied).

In addition to the monthly estimate, we also evaluate the 3-daily fields retrieved with DMD 1/15, 2/30, 3/45 and DMD 3/45. The results are shown in Figure 22-3, and clearly indicate a better performance of the multi-step approach. Evidently, the additional de-aliasing capabilities come into play here as well and allow for an increase in performance of up to 30% in case of AOHIS and 20% in case of HIS retrieval.

It can be concluded that a DMD parametrization featuring multiple de-aliasing steps enhances both the retrieval of the short-term as well as that of the long-term estimate. It is thus shown to be all-around superior as compared to its single-step counterparts, and is thus recommended for application in data processing.

Additional studies should be directed towards finding an "optimal" parametrization scheme (though, effectively, only an approximation of such can be reached), as well as towards determining the origin of the "bumps" (which, however, are not related to the multi-step parametrization in itself).

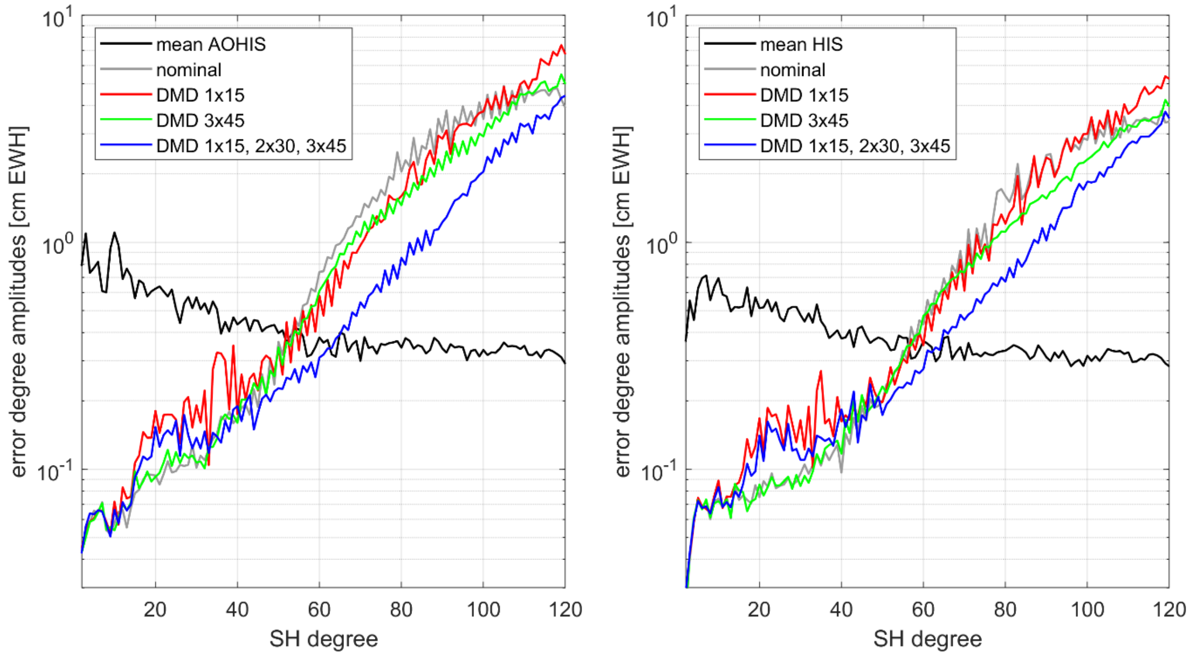

Figure 22-3: Retrieval errors of the 3-daily estimate obtained with a single- and multi-step DMD. Left: retrieval of the full AOHIS; right: retrieval of HIS (i.e. a priori BM-based AO de-aliasing is applied).

Impact of static background model

In the following, we discuss the impact of the chosen static background gravity model. As discussed in Abrykosov et al (2022), the DMD approach poses a trade-off between reduction of temporal aliasing at the cost of misparametrization of signal components (leakage). I.e., when short-term low-resolution fields are estimated in the first step, high-degree signal is allowed to leak into the low frequencies. This trade-off has been proven to be fully acceptable in case of time-variable signal components. The high-degree static gravity signal, however, must be reduced a priori, as it features significantly higher magnitudes which would otherwise severely hamper the DMD method. In order to minimize the misparametrization error, the static background model used for the reduction must be of the highest-possible quality.

A static gravity model generally features two sources of uncertainty. Firstly, a gravity field model is based on a set of observations that are not error-free. The observation errors are propagated through the least-squares adjustment onto the level of the final model, so each coefficient can be estimated with a certain level of uncertainty. Secondly, the observations are accumulated over a long period of time during which periodic as well as secular signal components occur (e.g. seasonal variations in hydrology, negative trends in polar regions due to ice melting). Thus, a trend parameter as well as amplitudes of an annual signal are additionally estimated for every coefficient, and a reference epoch is defined for the static model. Consequently, the static model must be adjusted accordingly with regard to the epoch of the "currently" evaluated observation period.

In addition to these intrinsic error sources, truncation errors may arise in data processing. Per definition, gravity signal is not spectrally limited, but is treated as such in data processing due to computational demands. Thus, omitted gravity signal will manifest below the degree at which the reduction model is truncated.

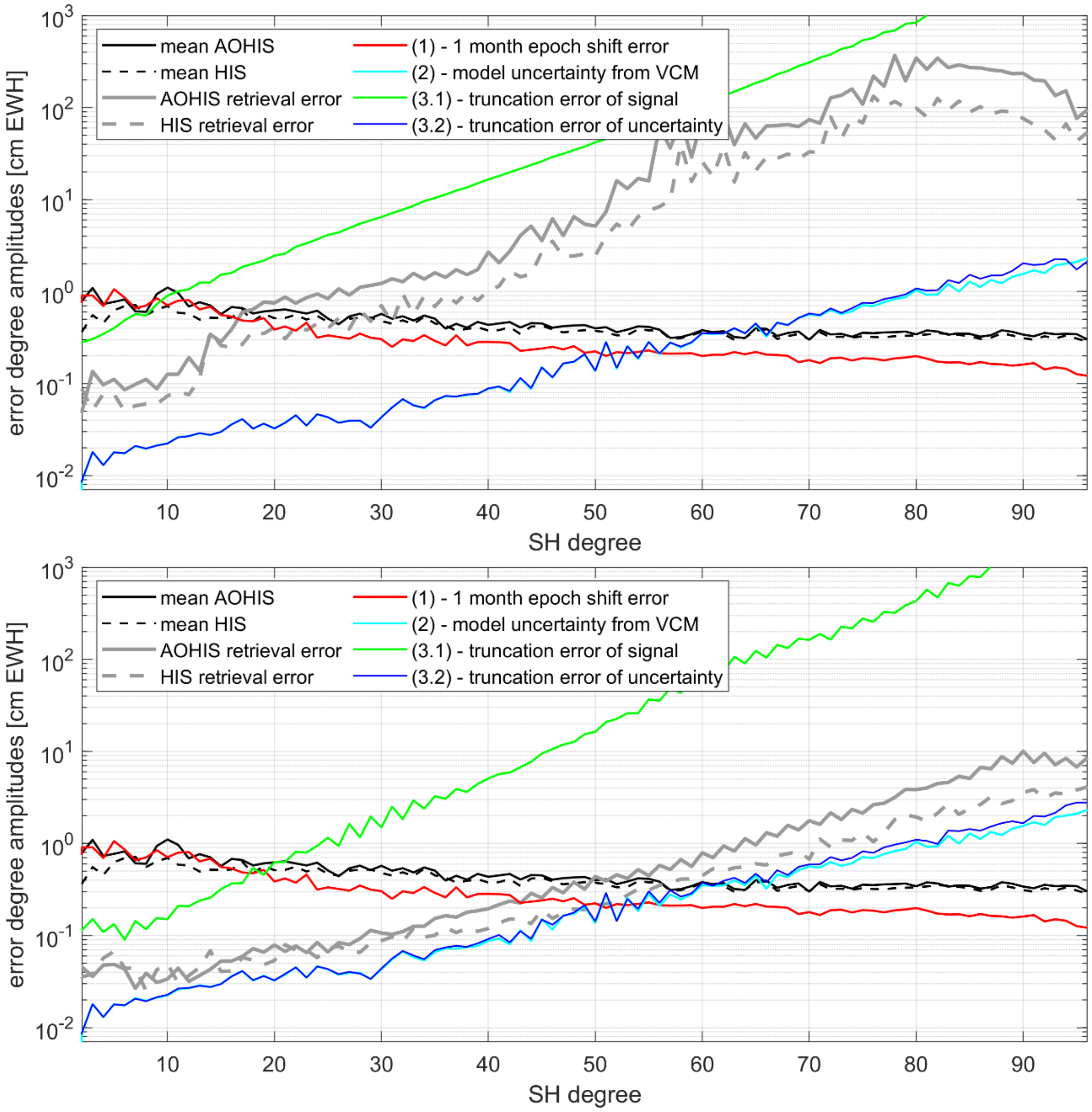

Figure 22-4: Potential error contributors of the static background model in a 30-day single-polar-pair (top) and double-pair (bottom) gravity retrieval scenario. Note that no DMD is applied here.

The error contributions of each of the issues described above are depicted individually in Figure 22-4 and compared against the retrieval error induced by temporal aliasing for a single-polar-pair and a double-pair scenario in case of a nominal processing. In this set of simulations, GOCO06s (Kvas et al. 2021) is used as the true static model. Note that the time-variable signal was truncated to d/o 96 for the purpose at hand, thus representing a best-case scenario, as a higher resolution would allow for more, or rather stronger, aliasing effects. We note that we attempt to retrieve on one hand the full AOHIS signal and on the other hand only the HIS component. In the latter case, a priori AO de-aliasing is applied. To simulate the epoch error (1), the retrieval is carried out with GOCO06s whose reference epoch is shifted by one month. For the issue of estimation accuracy (2), the VCM of GOCO06s is used to obtain realistic (error) coefficients to be used in the simulation. Finally, the truncation error (3.1) is simulated by introducing the true static up to d/o 190, while the retrieval is only carried out up to d/o 96. This simulation is repeated for the model's uncertainty as well (3.2).

First, it is evident that an error in the static field's reference epoch has a severe impact on the low-degree spectrum. By inducing an epoch shift of just one month, the low degrees up to d/o 10 of the time-variable signal are covered entirely which effectively makes their recovery impossible. If the DMD was to be applied with this model, leakage from the spectrum above the interval estimates' maximum degree into the interval fields can be expected. Further, the impact of the model uncertainty is fully negligible in case of the single-pair retrieval, as it is fully covered by the aliasing errors. In case of the double-pair, however, the intrinsic de-aliasing almost reduces the aliasing errors to the level of those of the static model's uncertainty in case a priori AO de-aliasing is applied. Depending on the part of the spectrum, the difference between the two effects ranges from a factor 2 to 0 (around d/o 50). The truncation error poses the largest contribution to the error budget from around d/o 10 (single-pair) and 20 (double-pair) upwards. It is also notable that the truncation errors related to the model uncertainty are near-identical to those when no truncation error is assumed at all, which can be attributed to the model uncertainty's white-noise nature.

Evidently, neither the DMD approach nor the nominal processing can be reasonably applied if such errors are present. Error (3.1) can be almost fully reduced by simply applying the static background model to an as high as possible resolution, i.e.by aiming to omit as little signal as possible. Since the model uncertainties are of near-white-noise nature, (3.2) is on the same level as (2), thus both can be regarded as equivalent. Error (1) can be reduced by adjusting the reference epoch as precisely as possible. In consequence, error (2) and any residuals of error (1) would be of concern. However, both can be circumvented by estimating a static field a priori on the basis of the underlying data in an a priori step. This could be done iteratively, e.g. by first estimating weekly or monthly fields over a long time period (multiple years) with the nominal processing scheme under application of any static BM, and then using their mean as the new static BM within data reprocessing (respectively, this can also be done on the basis of residuals). This mean field would then display a perfect fit to the true static signal, and using it either in the nominal or a DMD-type processing would fully negate the effect of (1) and (2), and, by extension, that of (3.2).

As a final point, we investigate the impact of the DMD approach on error (2) and, for the sake of completeness, also on error (1), in order to understand whether the interaction between the error contributors changes with respect to the nominal processing. For the single-pair processing, a multi-step DMD scheme is chosen where daily fields are estimated up to d/o 12 and two-daily fields are estimated up to d/o 20. For the double-pair processing, daily fields are resolved up to d/o 20 and two-daily field up to d/o 40.

The results are depicted in Figure 22-5. In case of the single-pair retrieval, the aliasing reduction is not hampered by misparametrization of the static field's errors. However, it is notable that while error (2) remains practically unaffected by the DMD, most likely due to its white-noise behaviour, the error related to the epoch shifting increases significantly above d/o 40. This behaviour is not present in the double-pair case – an increase of error (1) can only be observed above d/o 80. While the impact of error (2) is slightly reduced by the DMD in the medium- to high degrees, it nevertheless becomes the dominant error contributor above d/o 70. However, this does not severely impact the retrieval of the time-variable signal, as its SNR becomes 1 around d/o 67 for both HIS and AOHIS. This poses an improvement to the nominal retrieval scenario where the retrieval of AOHIS is achievable up to d/o 50 and that of HIS up to d/o 55. Thus, the aliasing reduction by means of the DMD can still be fully exploited independently of error (2).

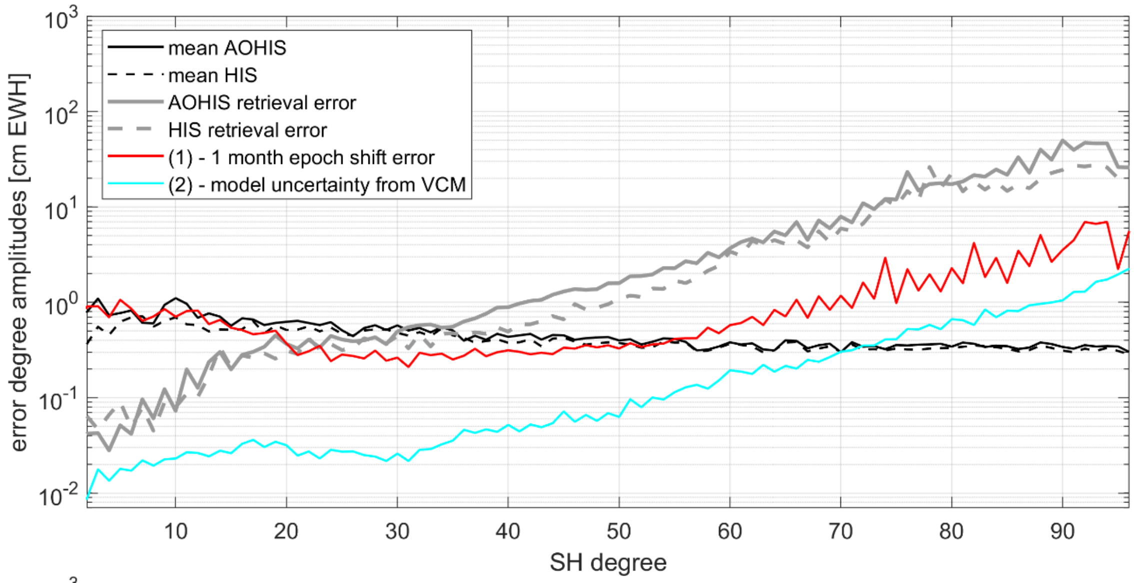

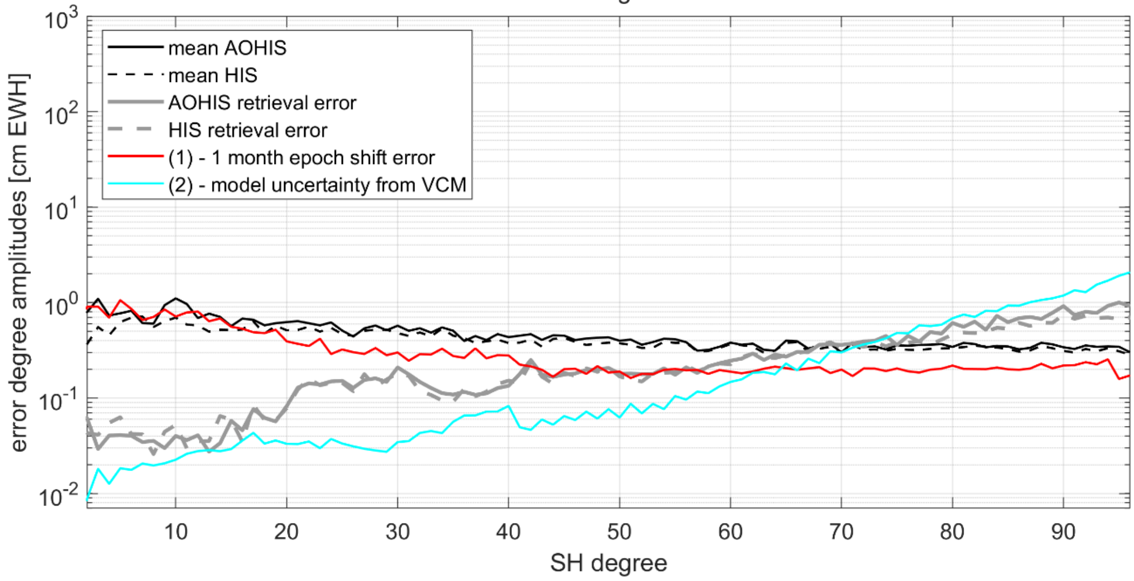

Figure 22-5: Impact of the DMD on potential error contributors of the static background model in a 30-day single-polar-pair (top) and double-pair (bottom) gravity retrieval scenario.

In conclusion, it can be stated that the DMD offers great potential for both the single- and double-pair-based gravity retrieval as long as a good-quality static background model is applied. This means on one hand that as much of high-degree static signal as possible must be taken into account to avoid truncation errors, as it would otherwise leak into the daily estimates and thus heavily degrade the DMD performance. On the other hand, the epoch of the static reference field must be adjusted as closely as possible to maximize the gain in the low- to medium-degree spectrum. While in the single-polar-pair case the static model's estimation uncertainty plays practically no role, its effect is much more pronounced in the double-pair-based retrieval due to the enhanced intrinsic de-aliasing of its observation geometry, and becomes the dominant error contributor in the high degrees in case the DMD is applied. Though technically of secondary relevance because the effect occurs beyond the degree up to which the temporal variations can be derived reliably, it is nevertheless undesirable.

In order to circumvent the error contributors of the static background model, one may consider to estimate a new static BM model in a preliminary step if the DMD is to be applied in the data processing. However, in order to generate such a model, long-term observations would have to be available. Therefore, this approach can only realistically be considered for the reprocessing of data, but not for an "on-the-fly" generation of e.g. (sub-)monthly data products as e.g. done in case of GRACE/GFO.

Interaction of DMD with stochastic modelling of OT BM errors

It was shown in previous studies that while the uncertainty of the OT BM model is significantly more pronounced in the double-pair- than in the single-polar-pair case. This holds true independently of whether the full AO signal is considered, or a priori AO de-aliasing is applied (c.f. Figure 22-6). Therefore, the stochastic modelling of OT background model errors according to the approach shown in Abrykosov et al. (2021) can be expected to be beneficial. A further logical question is then whether this methodology can be combined with the DMD processing scheme to maximize the de-aliasing performance.

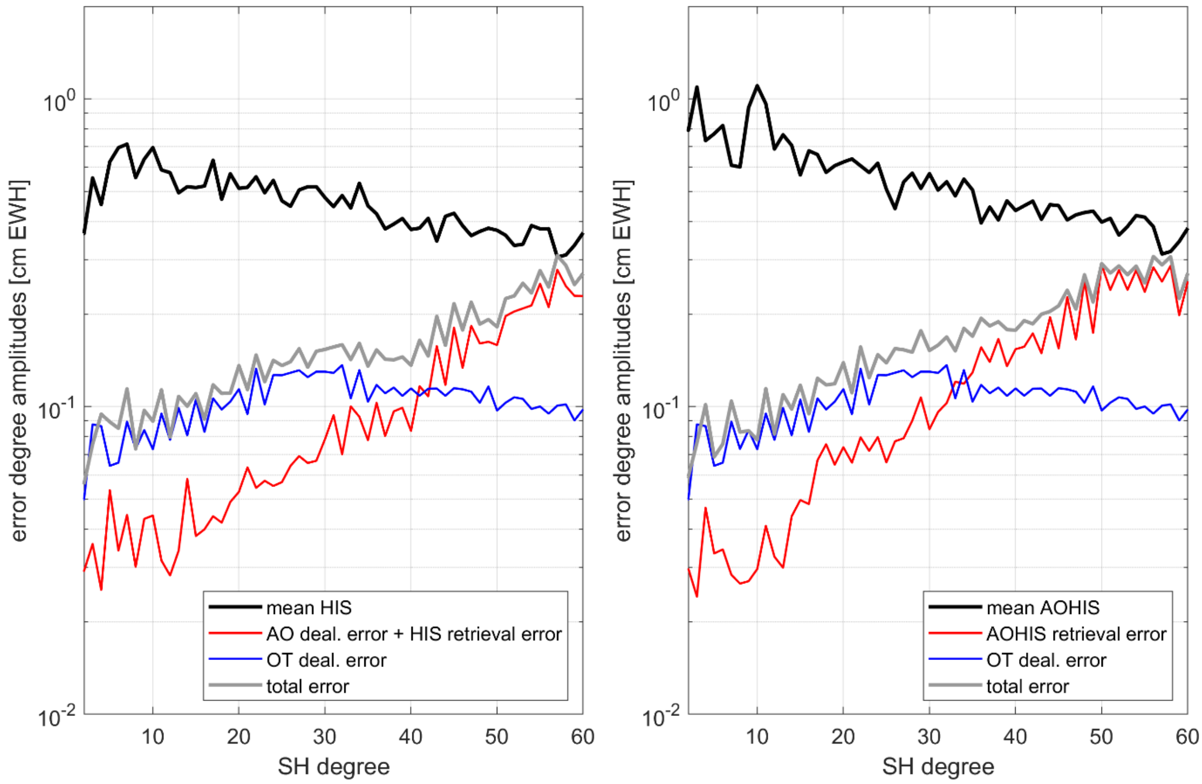

Figure 22-6: Contributions to the total retrieval errors in case of the full AOHIS signal (right) and HIS with a priori AO de-aliasing (left).

To validate this, we simulate a 30-day gravity retrieval on the basis of the double-pair baseline scenario. In terms of observations, we consider the OT de-aliasing error as the difference between the eight principal tidal constituents of the models TPX09 (Egbert and Erofeeva, 2002) and DTU10 (Cheng and Andersen, 2011), as well as non-tidal temporal variations. Here, we differentiate between a scenario with a priori AO de-aliasing (in this case, the target signal is HIS) and a scenario without (in this case, the target signal is AOHIS). We then apply OT error weighting and the DMD separately as well as in combination. For the DMD, we investigate two schemes which are named DMD1 and DMD2. In DMD1, daily fields are estimated up to d/o 20 and two-daily fields are estimated up to d/o 40, whereas in DMD2 we estimate daily, two-daily and three-daily fields up to d/o 15, 30 and 45, respectively. , c.f. Table 22-1.

Table 22-1: DMD parametrization scenarios for combination with stochastic modelling of OT errors

	1-day estimates	2-day estimates	3-day estimates
DMD1	d/o 20	d/o 40	-
DMD2	d/o 15	d/o 30	d/o 45

As reference, we use a scenario which employs the nominal processing scheme, i.e. where no OT error weighting or DMD is applied. The maximum resolution of the input gravity signal as well as that of the retrieved 30-day mean field is set to d/o 60, as this is also the degree up to which the OT error VCMs are provided.

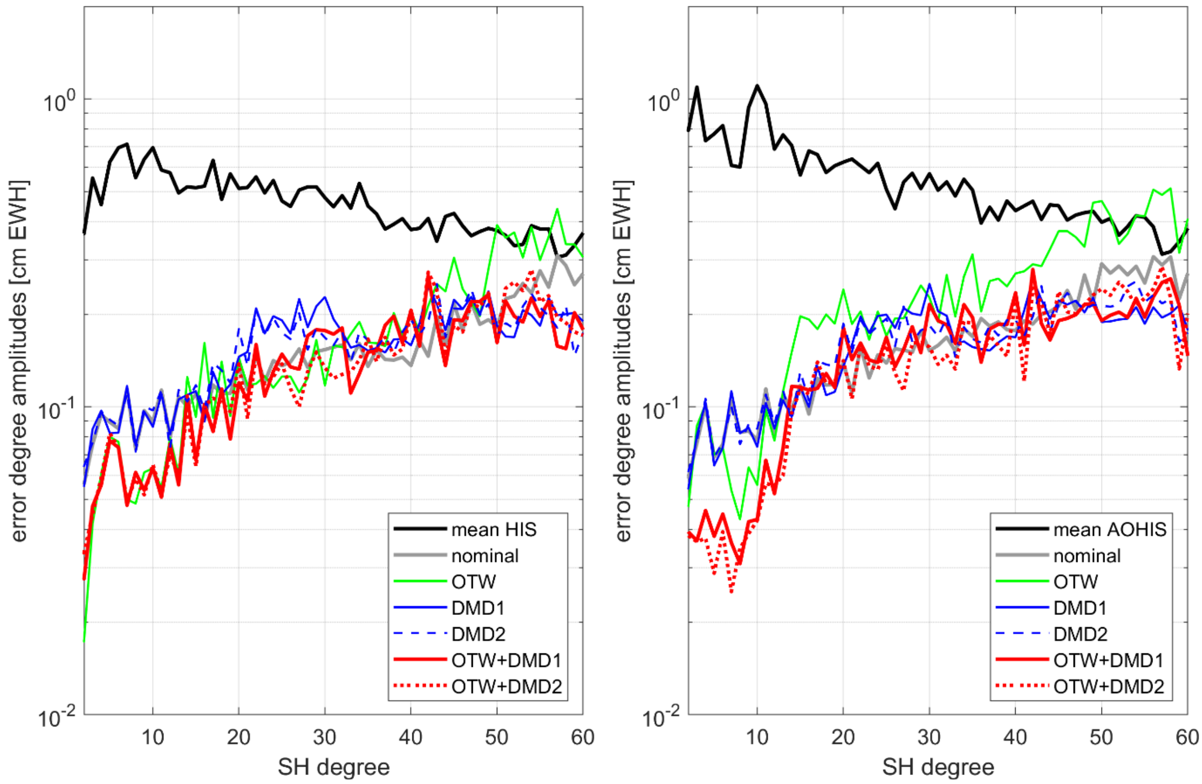

Figure 22-7: Retrieval performance with application of stochastic modelling of OT errors (OTW) and DMD as well as their combination in case of the full AOHIS signal (right) and HIS with a priori AO de-aliasing (left).

The retrieval errors of the respective scenarios are shown in Figure 22-7. As a first aspect, it becomes notable that applying OT error weighting alone indeed enhances the retrieval performance in the low degrees, but may degrade the quality in the medium- to high degree spectrum in comparison to the reference scenario. This holds both for the scenario with and without a priori AO de-aliasing, though the effect is much more pronounced in the latter case. The reason for this are inevitable interactions between the non-tidal signals and the OT error weighting.

The stand-alone DMD schemes show a comparable performance between each other and offer some added value in the high degrees with respect to the nominal processing, but somewhat degrade the retrieval quality in the spectral range around d/o 25. The low degrees remain unaffected.

A combination of OT error weighting and DMD on one hand allows to retain and even enhance the gains in the low-degree spectrum (which seemingly stem from the OT error weighting) as well in the high degrees (attributed to the DMD). On the other hand, the spectral range around d/o 25 which was shown to feature a low performance in the DMD-only case now showcases an improvement and does not perform notably worse than the nominal scenario. This is somewhat surprising, since at least in the full-AOHIS scenario the stand-alone OT error weighting doesn't contribute to an enhancement in this spectral range either.

It can thus be concluded that a combination of DMD and the stochastic modelling of OT BM errors indeed offers an added value, as it seemingly allows to utilize the benefit of both methodologies, and is therefore recommended for application in double-pair-based gravity processing. However, there are also effects that – while beneficial – cannot be entirely explained and should be studied in further detail. At this point, the most reasonable explanation is the induction of interactions between the OT stochastic model and non-tidal signals. One should thus aim to stochastically model the non-tidal components as well, as this would mitigate such interactions while (most likely) allowing one to retain the benefits and even further enhance them.

22.2. STOCHASTIC MODELLING OF DE-ALIASING MODEL ERRORS – TUM (WP1320)

In Abrykosov et al. (2021) it was shown that stochastically modelling OT BM errors positively affects gravity retrieval in spectral bands dominated by aliasing stemming from insufficiently compensated OT signal. It was also shown that aliasing effects stemming from non-tidal variations of the gravity field pose a limitation to the maximum gain achievable through the stochastic modelling of OT BM errors. Hence, it is logical to attempt the reduction of aliasing related to the AO signal components in the same manner. This WP therefore aims to develop such a methodology for the stochastic modelling of AO BM errors and to quantify the related gains for gravity retrieval in a simulation environment.

Methodology

A major difference between OT and AO BM errors is the fact that OT BM errors depend on geolocation, but not on time (largest errors occur in high latitudes and shallow waters due to poor altimetry performance), whereas AO BM errors feature a time-variable component (uncertainty can be considered proportional to pressure gradient), meaning that AO BM errors are largest wherever changes in pressure occur. Considering that such changes are related e.g. to the evolution of weather fronts, it is obvious that they may occur on quite small temporal and spatial scales. Consequently, a representation by means of a single, i.e. static, error VCM of the AO background model can be seen as insufficient, and should be replaced (or at least refined) with a time-variable one. Preferably, since the AOD product is generally given in 6-hourly samples (Dobslaw et al. 2015), individual error VCMs should also be derived for each sample and used accordingly in the data processing.

Nevertheless, a static error VCM can be used as a first approximation. Such a VCM has been generated in the scope of the NEROGRAV project (DFG Research Unit) on the basis of the 11-year time series of the AOerr product (zero-mean large- and small-scale errors of the AO BM which have been shown to be relatively realistic in previous studies) by computing the co-variance between any given pair of SH coefficients up to d/o 30 (and in the frame of this project, extended to d/o 60 based on the same methodology) over the entire 11-year period for which the model is given. Effectively, such an error VCM exclusively represents a spatial pattern where high error values are assigned to geolocations with high signal variability (assumed to represent high model uncertainty) and vice-versa. Therefore, propagating such an error VCM onto the level of observations will lead to a down-weighting of observations in high-variability regions within the gravity adjustment, which in turn should reduce the level of aliasing in the final gravity product.

It is also attempted to derive time-variable VCMs for the AO BMs. As basis, once again the AOerr product is used and the approach is as follows. In the simulation environment, AOerr serves as the discrepancy between the "true" AO signal and the BM used for its de-aliasing according to

$$AO = DEAL - AOerr.$$

The goal is evidently to have $AOerr = 0$, which would correspond to a perfect de-aliasing model. However, AOerr deviates from the optimal zero-signal case by a Δ according to

$$0 + \Delta = AOerr$$

Thus, Δ can be regarded as an error measure for AOerr itself, as the expression above can be rewritten to $\Delta = AOerr$, and one can attempt to introduce it as such in the data processing scheme. To do this, the SH coefficients of each 6-hourly AOerr field are first projected onto a global grid in terms of a dimensionless quantity by means of a SH synthesis according to

$$\Delta_{grid}(\theta, \lambda, T) = \sum_{n=0}^{n_{max}} \sum_{m=0}^{n} \overline{P}_{nm}(\cos\theta)\left(\overline{C}_{nm}(T)\cos m\lambda + \overline{S}_{nm}(T)\sin m\lambda\right)$$

In a following step, a SH analysis is carried out to estimate a set of SH coefficients X representing each Δ_{grid} with Δ_{grid} serving both as observation and observation weight according to

$$\underline{X}(T) = (A^T P A)^{-1} A^T P \Delta_{grid}(T)$$

with A as the functionals connecting the spectral and spatial domain and

$$P = diag\left(\Delta_{grid}^{-2}(T)\right).$$

Here, we are not interested in the coefficients $\underline{X}(T)$, but rather in each set's $VCM(T) = (A^T P A)^{-1}$, because since every grid point has been weighted with its deviation from the desired "zero-case", this spatial signal distribution is now contained in the VCM. If each such VCM is then connected with its corresponding 6-hourly BM coefficients and the temporal evolution of the BM is represented correctly within the functional model, the observations will receive a weight according to the amplitude of the underlying AOerr signal at the point in space at the time they are taken (low weight when taken over region featuring low AOerr amplitude at the respective epoch and vice-versa). Such a tailored weighting can reasonably be expected to lower the level of temporal aliasing stemming from AOerr.

Next, the definition of the functional model mentioned above is discussed. As the de-aliasing model is generally given in terms of 6-hourly samples, the model values for the epochs between two consecutive samples are obtained by means of linear interpolation. The linear interpolation can be carried out either on the level of model coefficients (approach 1) or it can be explicitly integrated into the functional model (approach 2). For an observation at an arbitrary epoch t located between the consecutive 6-hourly samples T_0 and T_1, approach 1 reads

$$obs(t) = \underline{a}(t) \cdot \left[w(t)X(T_0) + \left(1 - w(t)\right)X(T_1)\right],$$

whereas approach 2 reads

$$obs(t) = \left[w(t)\underline{a}(t), \left(1 - w(t)\right)\underline{a}(t)\right] \cdot [X(T_0), X(T_1)].$$

In the equations above, the $[m\ x\ 1]$-sized vector $\underline{a}$ contains the functionals connecting the BM coefficients X with the observation of the current epoch t, $w(t)$ denotes the interpolation weight at a given t and m is the number of BM coefficients. Note that the values of $\underline{a}$ depend on t, as the satellite pair's position changes with time.

Exemplary transferring the above relations to a full day of n observations which contains 5 BM samples T (00h, 06h, 12h, 18h and 00h of the next day) yields

$$obs = A_1\tilde{X}$$
$$= \begin{bmatrix} \underline{a}(0) & 0 & & & & & \\ 0 & \underline{a}(1) & & & 0 & & \\ & & \cdots & & & & \\ & & & \underline{a}(t) & & & \\ & & & & \underline{a}(t+1) & & \\ & 0 & & & & \cdots & \\ & & & & & & \underline{a}(n) \end{bmatrix} \begin{bmatrix} w(0)X(T_0) + \left(1 - w(0)\right)X(T_1) \\ w(1)X(T_0) + \left(1 - w(1)\right)X(T_1) \\ \cdots \\ w(t)X(T_1) + \left(1 - w(t)\right)X(T_2) \\ w(t+1)X(T_1) + \left(1 - w(t+1)\right)X(T_2) \\ \cdots \\ w(n)X(T_4) + \left(1 - w(n)\right)X(T_5) \end{bmatrix}$$

for approach 1 and

$$obs = \tilde{A}_2 X$$
$$= \begin{bmatrix} w(0)\underline{a}(T_0+0) & \left(1 - w(0)\right)\underline{a}(T_0+0) & 0 & 0 & \cdots \\ w(1)\underline{a}(T_0+1) & \left(1 - w(1)\right)\underline{a}(T_0+1) & 0 & 0 & \cdots \\ \cdots & \cdots & 0 & 0 & \cdots \\ 0 & w(0)\underline{a}(T_1+0) & \left(1 - w(0)\right)\underline{a}(T_1+0) & 0 & \cdots \\ 0 & \cdots & \cdots & 0 & \cdots \\ 0 & 0 & w(0)\underline{a}(T_2+0) & \left(1 - w(0)\right)\underline{a}(T_2+0) & \cdots \\ \cdots & 0 & \cdots & \cdots & \end{bmatrix} \begin{bmatrix} X(T_0) \\ X(T_1) \\ X(T_2) \\ \cdots \end{bmatrix}$$

for approach 2.

It is clear that both approaches yield identical results in terms of observations. However, even if one assigns an error VCM Σ_{xx} to the BM error at each observation epoch, an error propagation onto the level of observations according to

$$\Sigma_{obs} = A\Sigma_{xx}A^T,$$

will only yield a diagonal Σ_{obs} in case of approach 1. Approach 2, however, would result in a Σ_{obs} with a block-banded structure, i.e.

$$\Sigma_{obs} = \begin{bmatrix} \Sigma_{00h-06h,00h-06h} & & & sym \\ \Sigma_{00h-06h,06h-12h} & \Sigma_{06h-12h,06h-12h} & \Sigma_{06-12,12-18} & \Sigma_{06-12,12-18} \\ \Sigma_{06h-12h,12h-18h} & \Sigma_{06h-12h,12h-18h} & \Sigma_{12h-18h,12h-18h} & \\ 0 & & \Sigma_{12h-18h,18h-00h} & \Sigma_{18h-00h,18h-00h} \end{bmatrix}$$

due to the “forced” correlation of each 6-hour sample with its direct neighbours, and, thus, of any two epochs in within such three samples. In the expression above, each $\Sigma_{XX-YY,YY-ZZ}$ is a full matrix.

Validation in AOerr-only simulations

The approaches described above have been implemented into the reduced-scale simulator and the performances are validated in a single-polar- and a double-pair-based retrieval on the basis of the MAGIC baseline scenario (c.f. section 22.1). For sake of simplicity, it is assumed that the true (static) signal is strictly zero, and the recovered signal is zero perturbed by AOerr. No further signal or noise component are added in the simulation. It is hypothesized that if AOerr is correctly stochastically modelled, the amplitudes of residuals in such a simulation scenario should be reduced in comparison to the nominal case (i.e. one without stochastic modelling).

First, the performance of the static and time-variable error VCMs is validated in a single-polar and double-pair based 30-day retrieval. It is noted than in case of the static error, the same error information is introduced at each epoch. The results are presented in Figure 22-8. In case of the static error VCMs, the relative retrieval performance is very similar between the single- and the double-pair scenario. In both scenarios, the reduction of the VCM of observations to a diagonal structure (approach 1) is proven to have little value, as in this case the improvements are limited exclusively to the high degrees and are overall quite small. Taking into account additional co-variances, in turn, is clearly beneficial. Here, the improvements manifest predominantly in the medium to high degrees and constitute up to a factor of 2 in the single-pair- and up to a factor of 3 in the double-pair scenario. The length of the processing arc seems to be of secondary importance, especially in the double-pair scenario.

The situation is very different in case of the time-variable error VCMs. In the single-pair scenario, the relative performance between approaches 1 and 2 is similar to the simulations with static error VCMs. However, the largest improvements can be established already around d/o 15-20 in case of approach 2 and then diminish until d/o 30, upward from which the nominal scenario performs better. Approach 1, on the other hand, shows an overall degraded performance in comparison to the nominal case. However, once an inclined satellite pair is added to the observation geometry, the behaviour between approach 1 and 2 reverses. Now, approach 1 outperforms approach 2 from around d/o 15 onwards, although both approaches feature severe degradations compared to the nominal case.

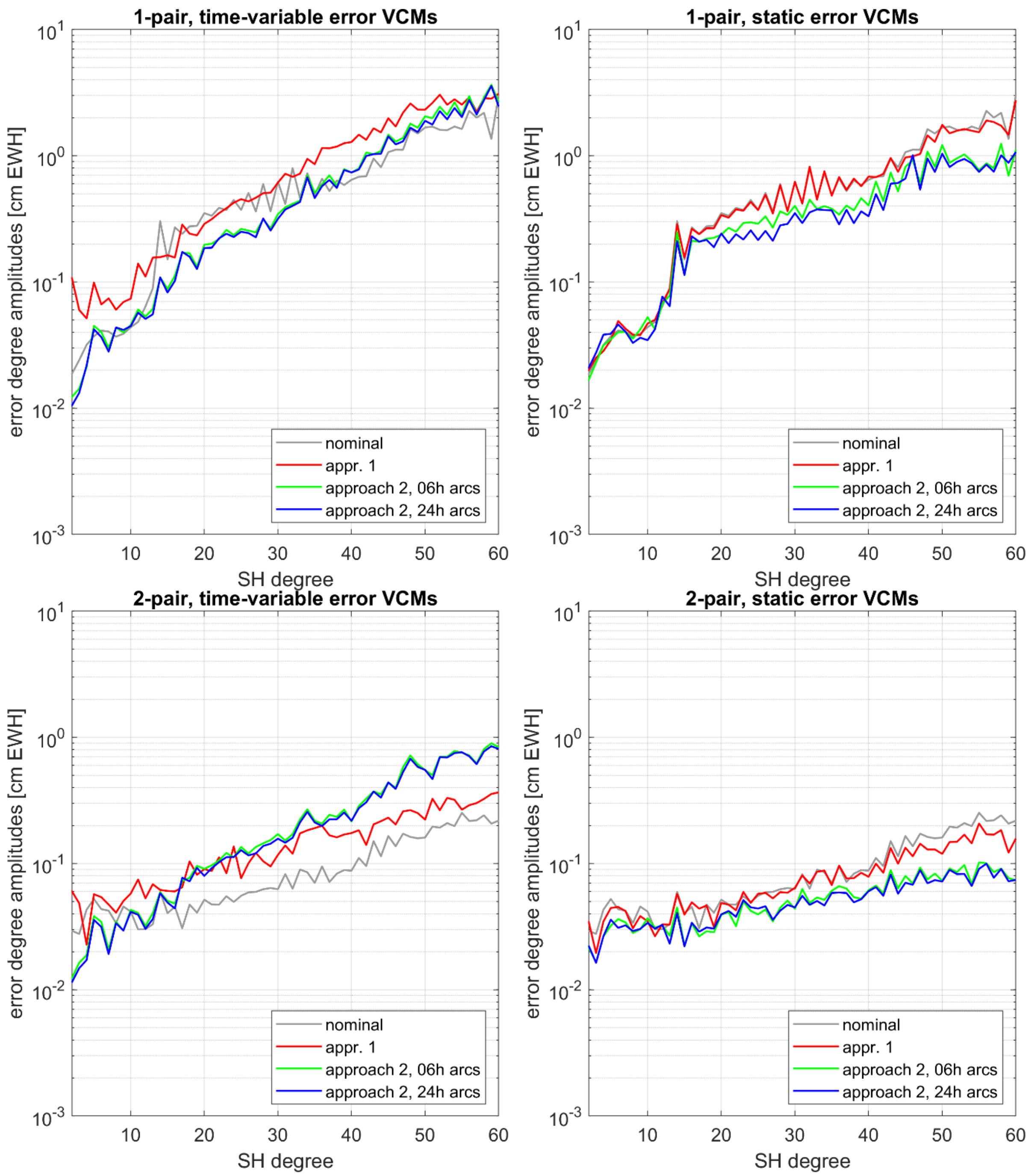

Figure 22-8: Retrieval error with and without applying stochastic modelling of AOerr for a single-polar- and double-pair scenario.

This behaviour is not understood and cannot be explained at the given moment. In order to rule out an erroneous set-up of the time variable error VCMs, i.e. to validate that they indeed contain the desired spatial patterns, they can be propagated into the spatial domain and compared with the true AOerr fields. For this test, we choose to propagate the error VCM of 01.01.2002, 00:00 and that of 15.01.2002, 12:00 (dates selected randomly) onto a global dimensionless grid according to

$$\Sigma_{grid} = A\Sigma_{xx}A^T,$$

where A denotes the functionals of the SH synthesis. The main diagonal of Σ_{grid} is then plotted onto the grid and compared to the true AOerr of the respective epochs in Figure 22-9.

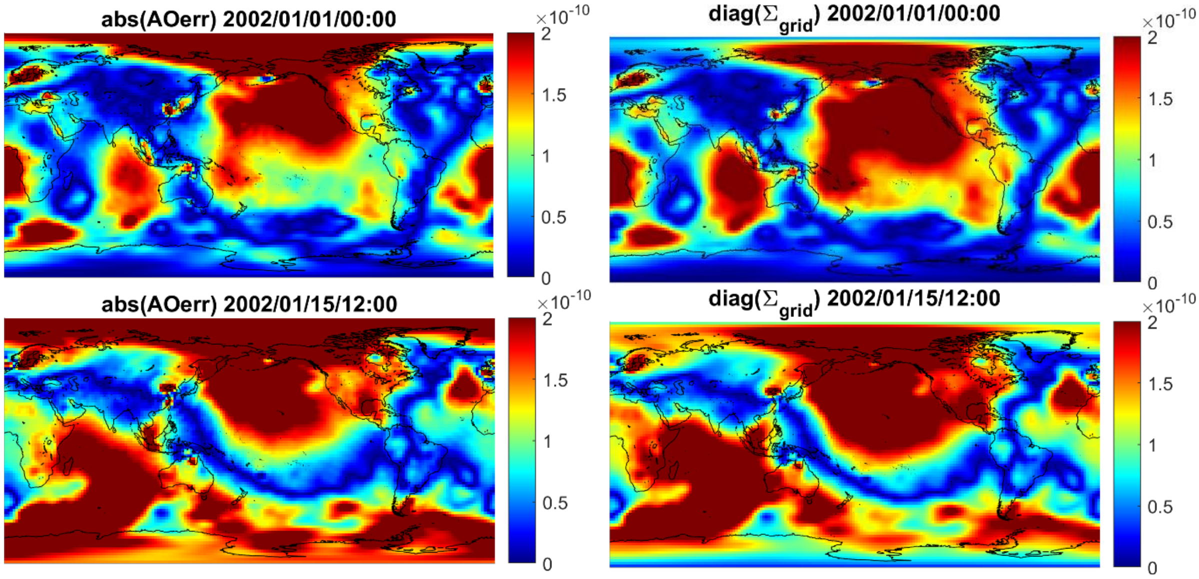

Figure 22-9: absolute of true AOerr signal (left) and square root of the diagonal of Σ_{grid} obtained through error propagation of time-variable Σ_{xx} (right)

It is evident that while a majority of the desired spatial signal has indeed been correctly mapped into the error VCMs, it can also be seen that especially polar regions feature significant discrepancies. It is not yet understood why this behaviour occurs, but it may well be the reason for the issues shown in Figure 22-8.

The static error VCM is also projected into the spatial domain, and, for comparison purposes, the grid-wise RMS is computed over all 6-hourly samples of the 11-year AOerr time series (17532 samples in total) in oder to understand the static error VCM's connection to signal variability. The graphical representations can be found in Figure 22-10. It is evident that the standard deviations of Σ_{grid} and the gird-point-wise RMS are near-identical in terms of spatial distribution. It is thus proven that the propagation of the static error VCM to the observation domain (or, in general, the spatial domain) results in a down-weighting of observations carried out over regions with high variability of AOerr. Because AOerr is a zero-mean signal, high-variability is equivalent to high deviation from zero (which is the sought AOerr signal!), and, therefore, the improvements shown in Figure 22-8 are a reasonable consequence.

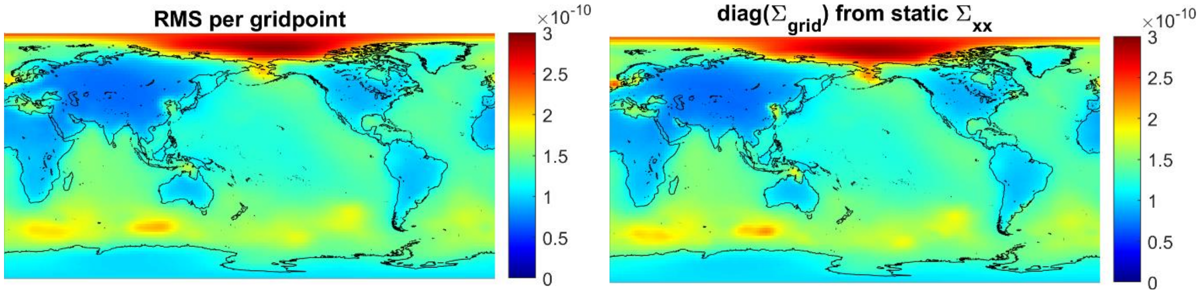

Figure 22-10: grid-point-wise RMS of true AOerr signal (left) and the square root of the diagonal of $\mathbf{\Sigma}_{grid}$ obtained through error propagation of the static $\mathbf{\Sigma}_{xx}$ (right)

From the results presented above, it can be concluded that the application of the static error VCM is beneficial for the reduction of aliasing stemming from AOerr. Moreover, it can be stated that this approach only shows notable benefits with the developed error propagation methodology, i.e. but shifting the interpolation between neighbouring 6-hourly samples into the functional model rather than carrying it out the level of coefficients. In this way, temporal as well as spatial correlations overarching three consecutive 6-hourly samples are explicitly introduced.

An aspect that requires further thought is whether similar improvements can be expected with a static error VCM in case of a non-zero-mean AOerr. Further research shall also be carried out towards the correct implementation and propagation of time-variable stochastic information of the BM error, as it can still be reasonably expected to yield a great added value in the data processing.

Combination with stochastic modelling of OT BM error

In the following, we attempt to combine the stochastic modelling of AO BM errors with the stochastic modelling of OT BM errors. For the AO BM errors, the static error VCM is used and applied as described above. On the side of OT BM errors, we use the error VCM derived in Abrykosov et al. (2021) and propagate it according to the methodology described there. The value of the joint stochastic modelling is assessed in a 30-day retrieval of a full-noise double-pair scenario processed in the reduced-scale simulator. To represent the AO BM error the AOerr product is used, whereas for the AO BM error we use the difference between the models TPX09 and DTU10 as was done in Abrykosov et al. (2021). The instruments, i.e. the ACC and LRI/LTI, are disregarded, since their impact is negligible next to the amplitudes of the time-variable gravity signal (c.f. e.g. Figure 24-3). Since the respective error VCMs are given in full form up to d/o 60, the input signal is also truncated to d/o 60 and the gravity estimation is analogously also carried out up to the same d/o.

The results are presented in Figure 22-11 in terms of error degree amplitudes. The left-hand side of the figure shows the individual contributors to the total retrieval error. It is evident that both the AO and the OT BM error can be significantly reduced by means of stochastic modelling. However, it is also likely that that the limiting factor of this approach shall to some extent be the intrinsic aliasing of the HIS signal, as it gains strength within the short-wavelengths spectrum and partially overtakes the retrieval error of the error induced by AOerr with stochastic modelling applied (red curve) in some spectral bands. This expectation is to awide extent confirmed in the right-hand side of the figure, which shows the combined retrieval error with and without applying stochastic modelling. In comparison to the scenario which only incorporates AO and OT error (i.e. best-case scenario, c.f. light-red curve), the retrieval error of the realistic scenario, i.e. the one with HIS included, increases wherever the HIS-induced error features high amplitudes. These deteriorations, however, lie within the range of around 5%, and still yield an average improvement of ca. 60% towards the nominal scenario (i.e. without any stochastic modelling).

Additionally, the comparison of the nominal full-noise scenario and the full-noise scenario where stochastic modelling is applied for the tidal and non-tidal components is given in the spatial domain (Figure 22-12). Also here the added value of the stochastic modelling is unequivocally proven, as the error magnitudes are greatly decreased primarily in regions featuring little (or, in general, low-amplitude) HIS-related signals.

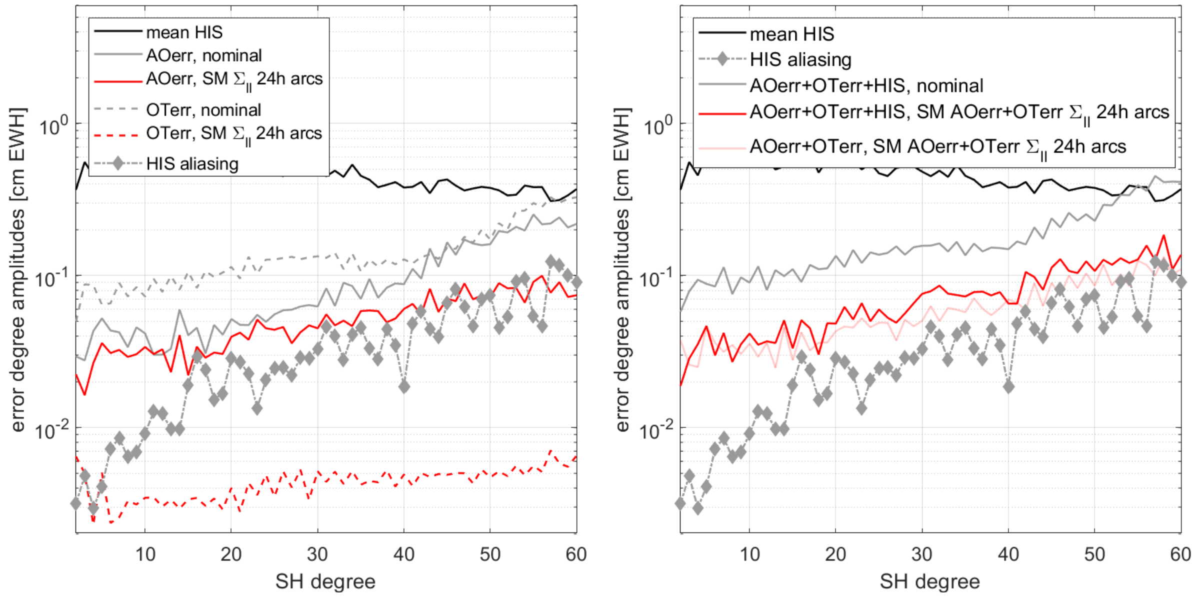

Figure 22-11: Retrieval error of individual error contributors (left) as well as the combined retrieval error (right) with and without applying stochastic modelling (SM).

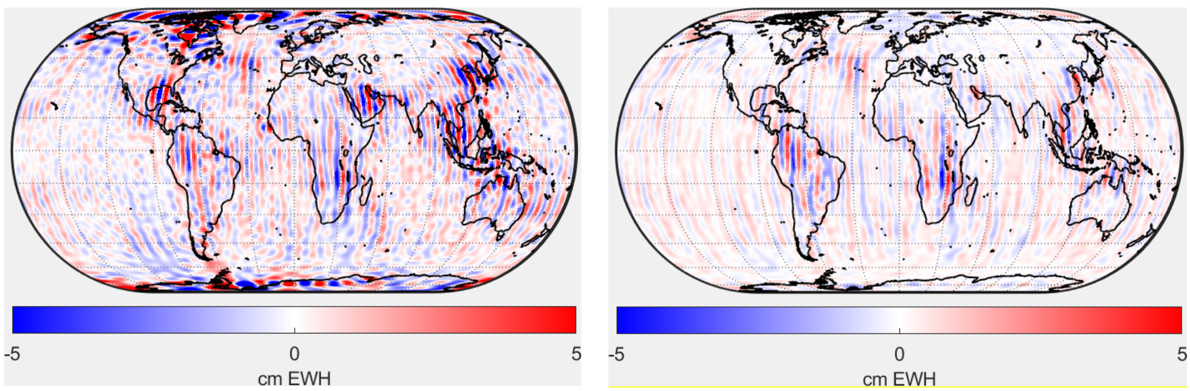

Figure 22-12: Combined retrieval error with (right) and without (left) applying stochastic modelling for AO and OT BM error presented in the spatial domain

As a final aspect, we briefly discuss the importance of applying stochastic modelling to both time-variable components. Figure 22-13 shows the retrieval error of full-noise simulation scenarios which contain both the AO as well as the OT BM error, but stochastic modelling is applied for only one of the two. It is evident that weighting only one of the two components not only doesn't allow to exploit the full potential of the processing strategy at hand, but in large parts also greatly deteriorates the retrieval performance. Thus, it can be concluded that stochastic modelling should always be used for each component that features stochastic properties in order to maximize the gains in solution quality.

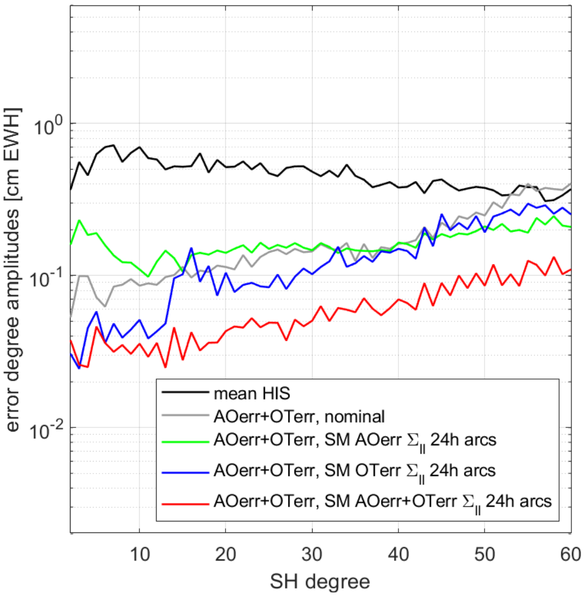

Figure 22-13: Combined retrieval error with application of stochastic modelling for either the AO or the OT BM error as well as to both components.

22.3. STOCHASTIC MODELLING OF DE-ALIASING MODEL ERRORS – GFZ (WP1321)

The EPOS software has been updated to include Atmosphere-ocean variance-covariance information. Real data for 2009 and 2014 have been processed and simulations have been performed for the polar pair of the baseline scenario for January 2002

Mean degree amplitude residuals, relative to climatology, for 2009 and 2014 are shown on the left- and right sides of Figure 22-14, respectively.

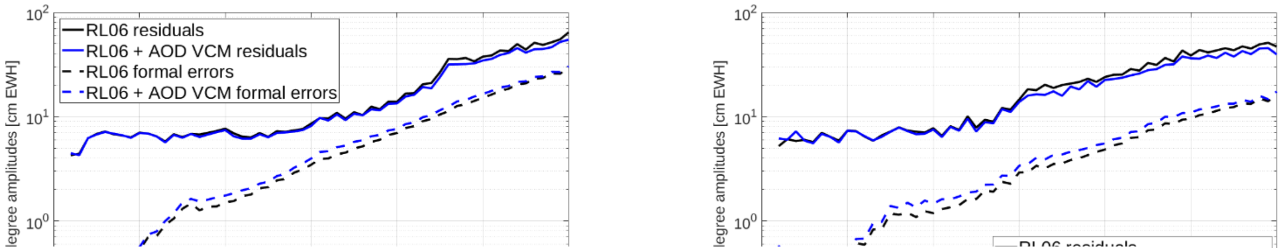

Figure 22-14 Mean degree amplitudes for 2009 (left) and 2014 (right). Black curves are results for RL06 processing and blue curves denote results for processing that includes stochastic modelling of de-aliasing model errors.

Monthly latitude-weighted ocean RMS values for 2009 and 2014, are shown on the left- and right side of Figure 22-15, respectively.

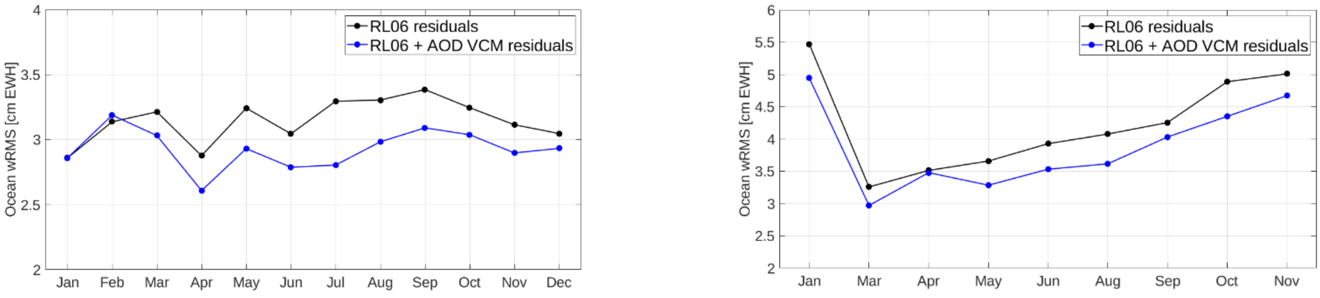

Figure 22-15 Monthly mean ocean wRMS, relative to climatology, for 2009 (left) and 2014 (right). Black curves denote results for RL06 processing. Blue curves denote results for processing that includes stochastic modelling of de-aliasing model errors.

Simulations that include the stochastic modelling of de-aliasing errors were performed for the polar pair of the baseline scenario. Two scenarios were investigated.

- An AO-error only scenario that only includes Atmosphere-Ocean model errors.
- A full noise scenario that includes all model errors, instrument noise, and stochastic modelling of the instrument errors.

Results for January 2002 for the full noise and the AO-error only scenario for the polar pair of the baseline scenario are shown on the left- and right sides of Figure 22-16, respectively.

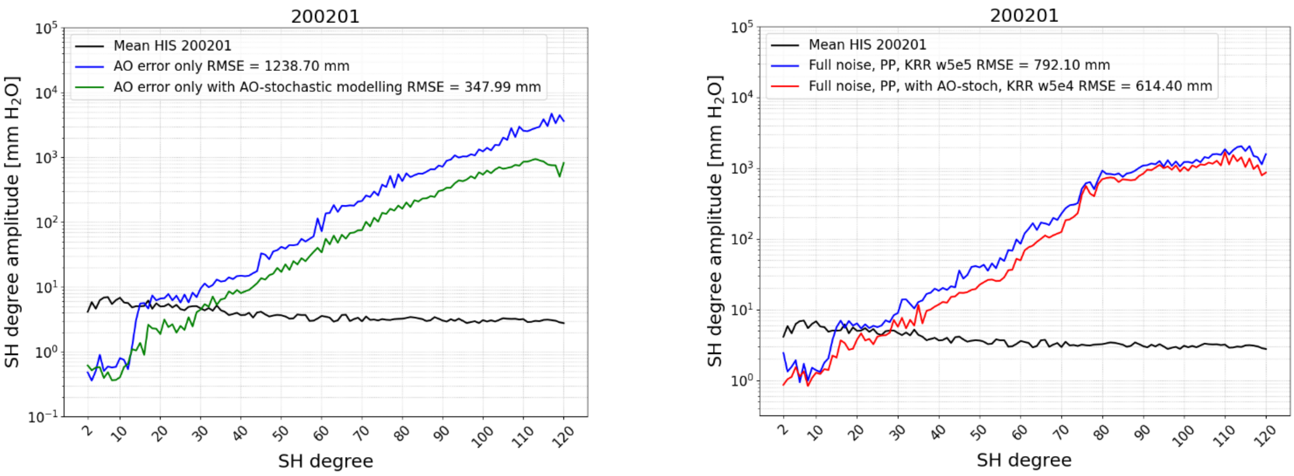

Figure 22-16 Residuals in terms of degree variances for an AO-error only scenario (left) and a full noise scenario (right).

Residuals obtained for a double pair solution for AO-error only and full noise are shown on the right and left of Figure 22-17, respectively. Here the blue curve indicates processing done without the AOD VCM and red indicates processing that includes AOD VCM information.

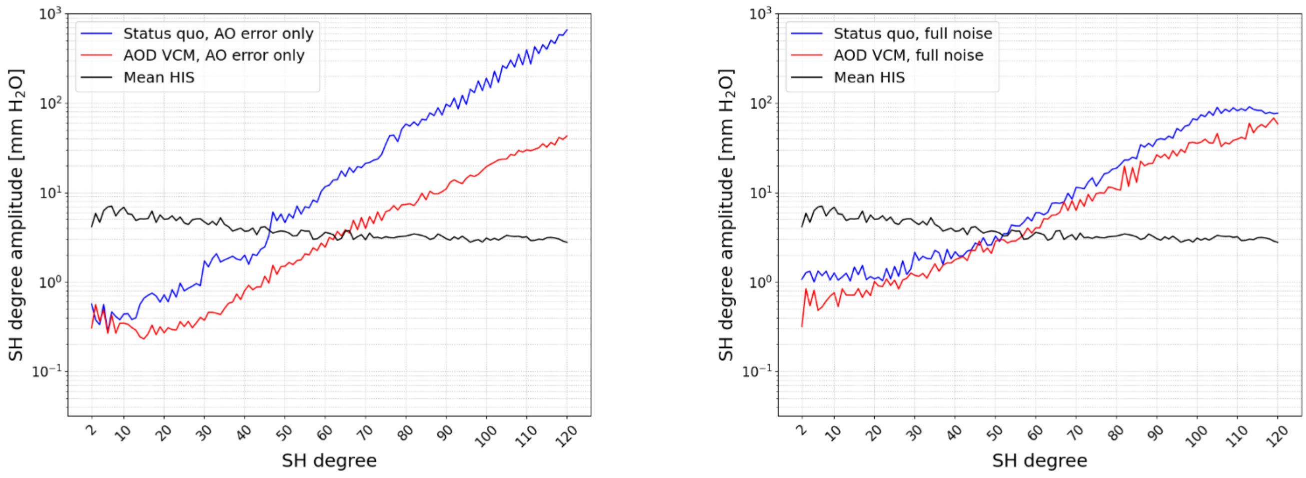

Figure 22-17 Residuals in terms of degree variances for a double pair AO-error only scenario (left) and a full noise scenario (right).

Residuals obtained for a double pair solution for AO-error only and full noise are shown on the right and left of Figure 22-17, respectively. Here the blue curve indicates processing done without the AOD VCM and red indicates processing that includes AOD VCM information.

For both real data processing and simulations, the inclusion of stochastic modelling of de-aliasing model errors yield reduced gravity field retrieval errors.

22.4. TREATMENT OF P1-P2 TRANSITION ZONE ARTEFACTS (WP1330)

This WP was triggered by an open issue of the first phase: It was identified that in the double-pair solutions, the polar regions which are only covered by the polar pair (P1) are sometimes degraded compared to the polar single-pair solutions. A tailored spherical cap regularization strategy was developed, which constrains the double-pair solutions towards to P1-solution in the polar cap areas, without changing the solution in the regions covered by both pairs (|φ| < 70°) significantly. This strategy was tested for the 3d_H scenario, which represented the baseline at this time. It was found out that the method worked very well for most of the configurations, but not for the monthly solution up to max. degree/order 120.

In the frame of this WP, the method shall be applied for the new baseline scenario 5d_397_70, and adapted to solve the problem identified above.

Figure 22-18 shows the original situation based on the 31-day solution up to d/o 120 for the 3d_H scenario in terms of RMS deviations from the true values, averaged per latitude. Evidently, with the optimized parameters for the regularization, i.e. polar cap size of $|\varphi| = 78°$ and an regularization parameter, $\alpha = 10^{24}$, the double-pair (DP) solution is only slightly improved by regularization, but the single-pair (SP) performance is not reached over the poles. In this case, the polar cap regularization was realized by constraining all polar and near-polar coefficients that are affect by the polar gap of the inclined pair using the formula by Sneeuw and van Gelderen (1997)

$$m_{max}(n) = \left|\frac{\pi}{2} - \boldsymbol{\varphi}\right| \cdot n$$

towards the SP solution.

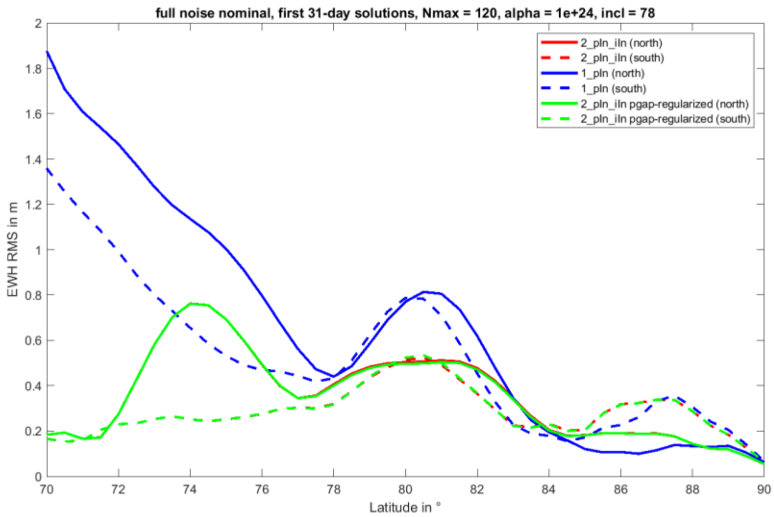

Figure 22-18: EWH RMS per latitude for scenario 3d_H

This regularization strategy was applied to the 31-days normal equation system of the baseline scenario 5d_397_70, using the same polar cap size $|\varphi| = 78°$, but applying a larger regularization parameter $\alpha = 10^{26}$. Figure 22-19 shows the results, again separated for the northern and southern regions.

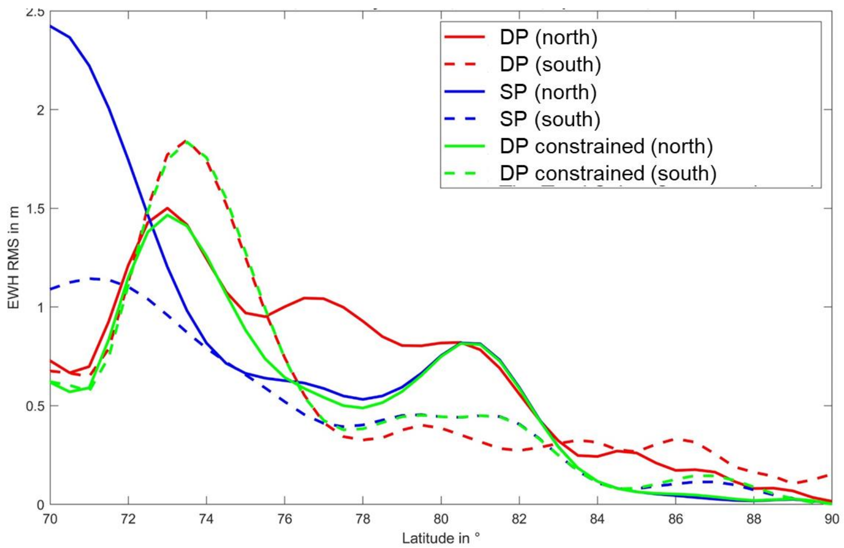

Figure 22-19: EWH RMS per latitude for baseline scenario 5d_397_70: unconstrained and constrained (polar cap size $|\varphi| = 78°$) solutions

Evidently, with this setting the constrained DP solution follows very nicely the SP solution for the latitude range $|\varphi| > 78°$, However, in this specific case the SP solution by itself is slightly worse than the DP solution in the south pole region in the range -83° < φ < -77°, and thus also the constrained DP solution.

For this case, obviously the latitude range was chosen with $|\varphi| > 78°$ too high, because the constrained solution follows the worse DP solution in the range of 72° < φ < 75°. The performance cross-over of SP and DP solution is approximately at $|\varphi| = 72.5°$. Therefore, this value was chosen in a second attempt for the definition of the spherical cap. It should be emphasized that this kind of optimization can only be done in simulation, where the true world is known.

Figure 22-20 shows the results in green the results of the constrained DP solution for a cap definition of $|\varphi| > 72.5°$. Evidently, it is even below the SP and DP solutions. This behaviour is even continued down to lower latitudes of about $|\varphi| > 60°$. This behaviour is demonstrated in Figure 22-21, which is the same as Figure 22-20, but with a larger latitude range.

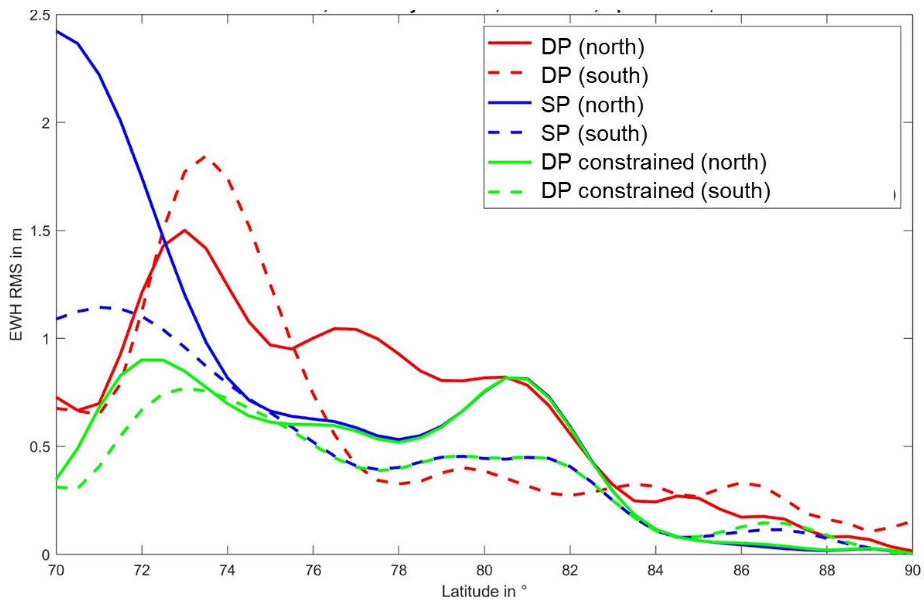

Figure 22-20: EWH RMS per latitude for baseline scenario 5d_397_70: unconstrained and constrained (polar cap size $|\varphi| = 72.5°$) solutions

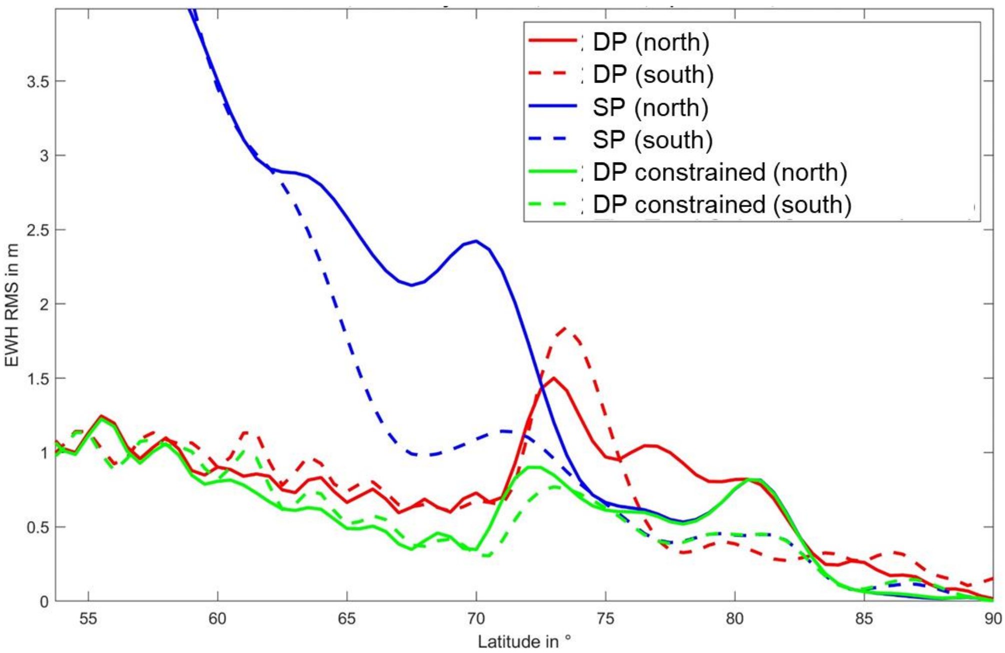

Figure 22-21: EWH RMS per latitude for baseline scenario 5d_397_70: unconstrained and constrained (polar cap size $|\varphi| = 72.5°$) solutions (zoom-out)

The reason for this improved performance can be easily seen when analysing the performance in the spatial domain. At first, Figure 22-22 (top row) shows the input SP and DP solution in terms of EWH error grids up to max. d/o 120, clearly reflecting the typical striping behaviour of the SP solution, but also its partly superior behaviour in the polar areas. Figure 22-22 (bottom left) shows the constrained DP solution corresponding to the green curves in Figure 22-21. As to be expected, it shows the error pattern of the SP solution in the polar areas, but hardly any change w.r.t. the DP solution in the areas covered by the inclined pair. However, investigating the difference between the unconstrained and the constrained DP solution in Figure 22-22 (bottom right), beyond the significant changes in the polar regions, also a positive effect of damping of high-frequency noise in the transition zone becomes evident, which explains the slightly improved performance of the constrained DP solution own to latitudes of about $|\varphi| > 60°$.

In order to validate the regularization approach, an alternative implementation in space domain was performed. Instead of constraining zonal and near-zonal coefficients, the normal equations for the polar caps were set up explicitly, with a right-hand side containing the information of the polar pair. These normal equations were used as regularization matrix to constrain the DP solution. In order to be consistent with the previous simulation, also here a limiting latitude of $|\varphi| = 72.5°$ was selected. Figure 22-23 shows the results as magenta curves.

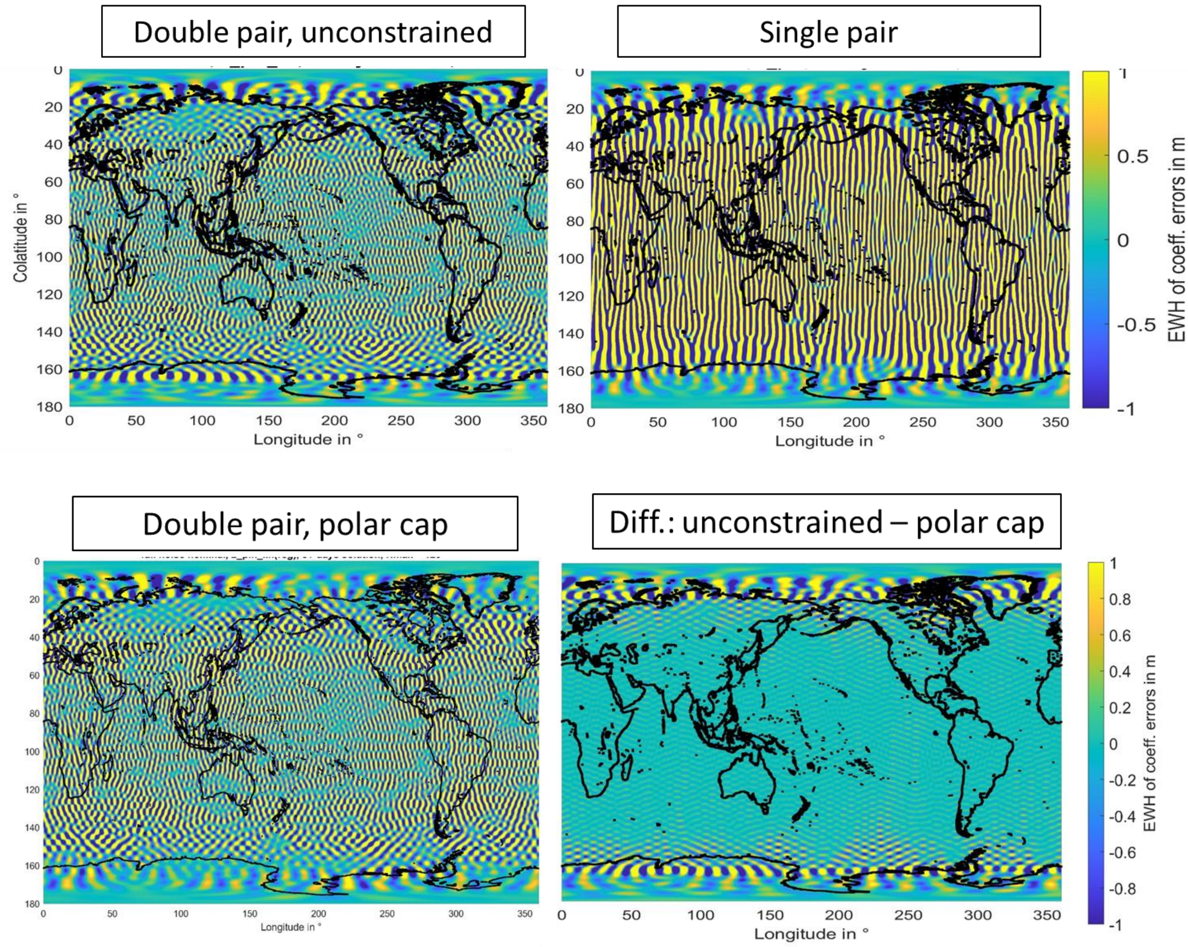

Figure 22-22 EWH grids: deviations from true signal [m]

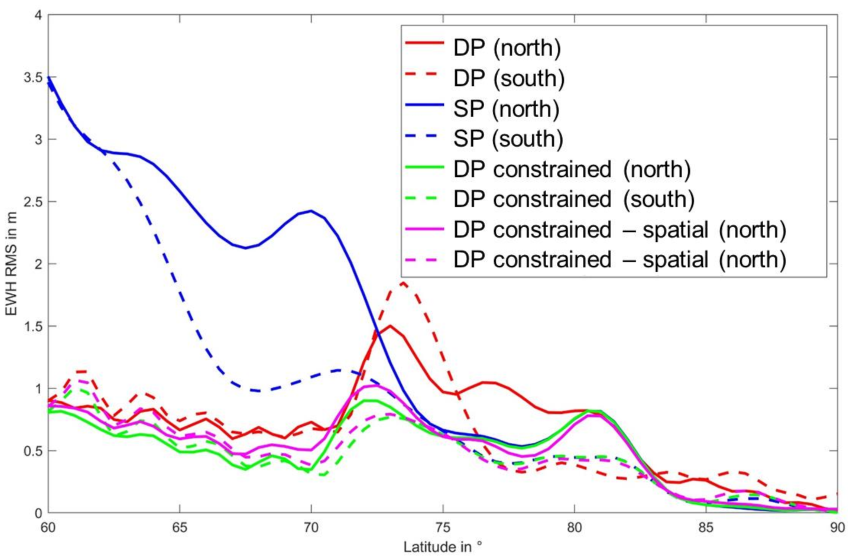

Figure 22-23: EWH RMS per latitude for baseline scenario 5d_397_70: constraints applied in spectral and spatial domain

22.5. AOHIS VS. HIS PROCESSING SCHEMES (WP1340)

Simulations were performed for the 3dH (polar pair at 463 km and inclined pair at 432 km) and HIS solutions were obtained with four approaches for 30, 7, and 3-day retrieval periods. In addition, simulations for a 31-day retrieval period were performed for the Baseline scenario (polar pair at 488 km and inclined pair at 397 km). The four approaches are:

1) The nominal method with on-the-fly AOD1B de-aliasing
2) The nominal method without de-aliasing, followed by a posteriori subtraction of AO+AOerr
3) The DMD method with on-the-fly AOD1B de-aliasing
4) The DMD method without de-aliasing, followed by posteriori subtraction of AO+AOerr

A comparison of the gravity field retrieval error of all four approaches, using a 30-day retrieval period, is shown in Figure 22-24.

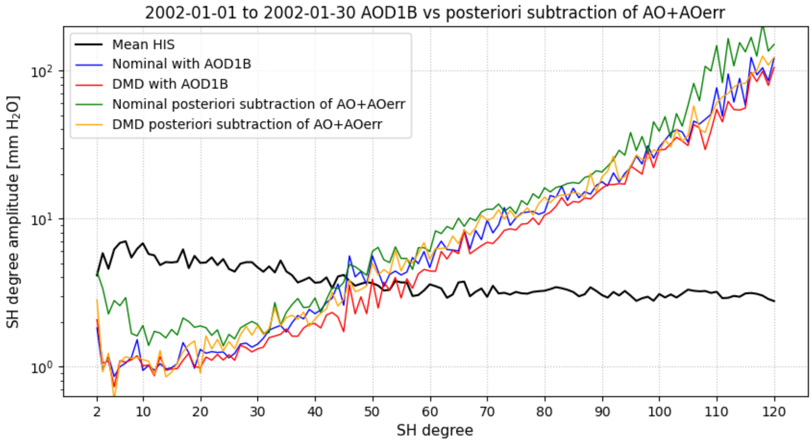

Figure 22-24 Comparison of gravity field retrieval error for on-the-fly de-aliasing and posteriori subtraction of AO+AOerr.

From Figure 22-24, the DMD approach with on-the-fly de-aliasing (in red) shows the smallest gravity field retrieval error. The second-best performance is shown by both the nominal on-the-fly de-aliasing (blue) and the DMD approach with posteriori subtraction of AO+AOerr (yellow). The largest error is obtained when the nominal method is performed without on-the-fly de-aliasing and posteriori subtraction of AO+AOerr.

A similar trend is shown for the sub-monthly 7- and 3-day retrieval periods on the left- and right-hand-sides of Figure 22-25, respectively.

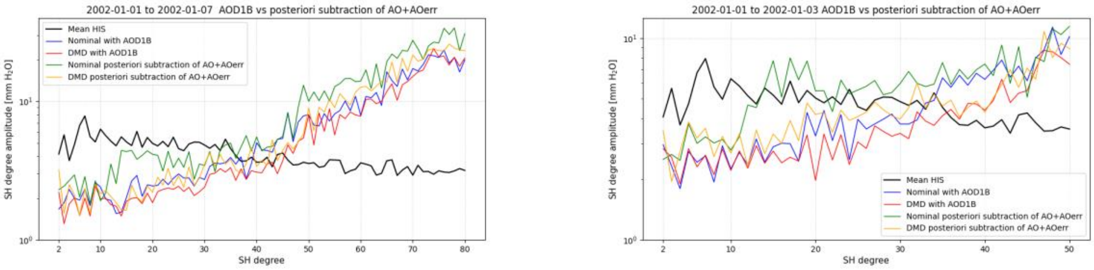

Figure 22-25 Comparison of on-the-fly de-aliasing with posteriori subtraction of AO+AOerr for 7- and 3-day retrieval periods, shown on the left- and right-hand-side, respectively.

Analysis of the gravity field retrieval error shows that DMD with posteriori subtraction of AO+AOerr and the nominal method with on-the-fly de-aliasing, perform similarly (see 30-, 7-, and 3-day retrieval periods in Figure 22-26).

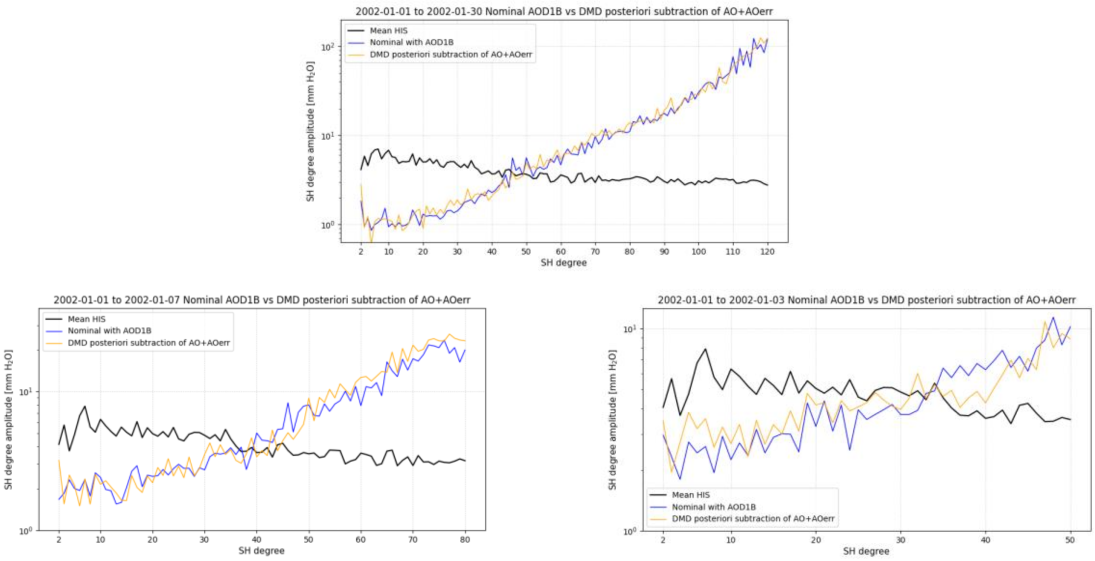

Figure 22-26 Comparison of nominal approach with on-the-fly de-aliasing with DMD and posteriori subtraction of AO+AOerr.

The nominal method with on-the-fly de-aliasing shows smaller errors than Nominal with posteriori subtraction of AO+AOerr as shown in Figure 22-27.

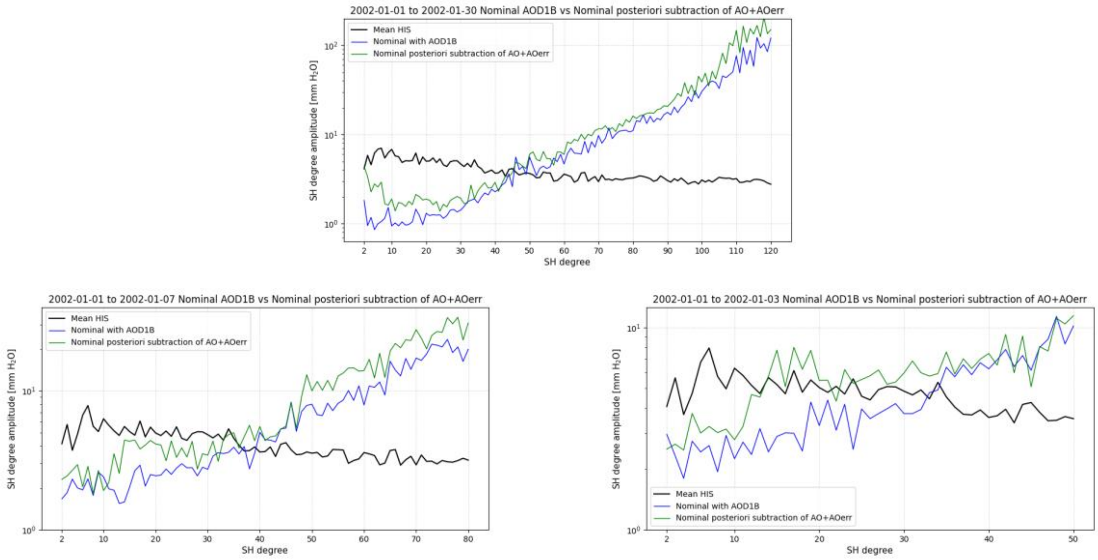

Figure 22-27 Comparison of on-the-fly de-aliasing and posteriori subtraction of AO+AOerr for the nominal method.

The DMD method with on-the-fly de-aliasing outperforms DMD with posteriori subtraction of AO+AOerr as shown in Figure 22-28.

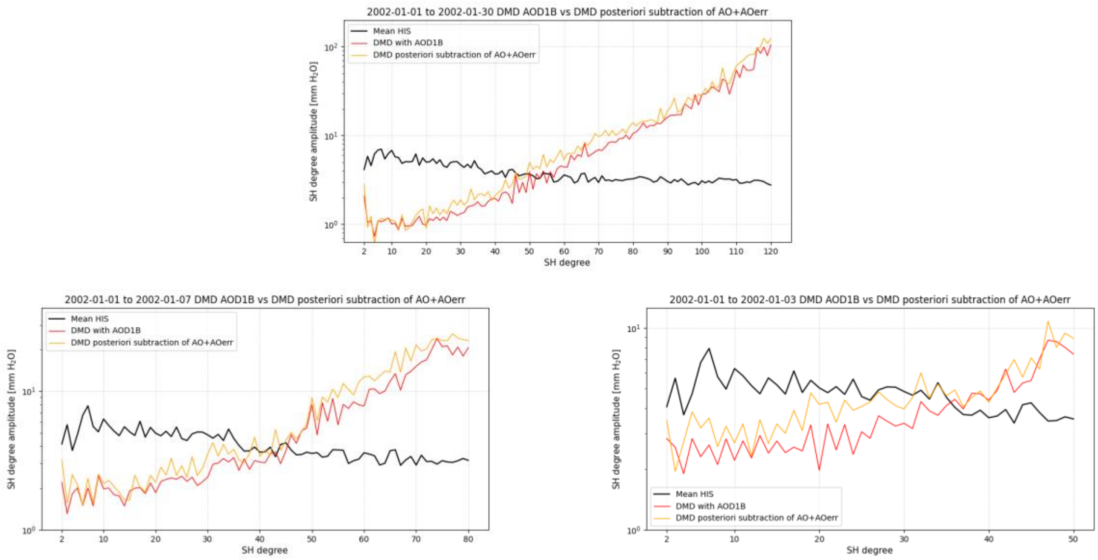

Figure 22-28 Comparison of on-the-fly de-aliasing and posteriori subtraction of AO+AOerr for the DMD approach.

From Figure 22-28 it can be concluded that the DMD approach with on-the-fly de-aliasing shows the smallest errors. However, since there is still ongoing debate if these solutions are biased, the nominal method with on-the-fly de-aliasing is proposed as the baseline strategy.

The four approaches were also investigated for the Baseline scenario. Here we only investigated a 31-day retrieval period. The conclusions drawn are in line with that drawn from the 3dH scenario analysis. In Figure 22-29 a combined comparison is shown.

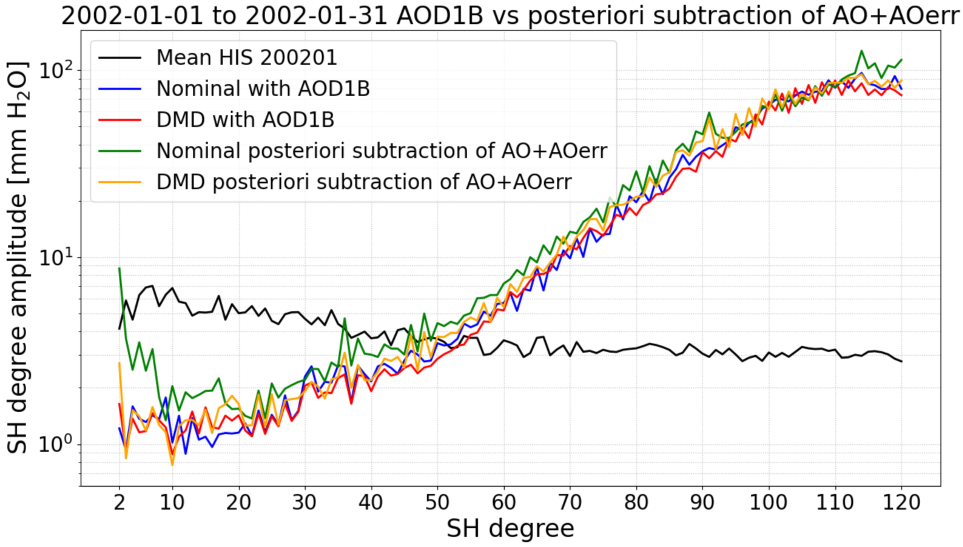

Figure 22-29 Combined comparison for the Baseline scenario.

Individual comparisons are shown in Figure 22-30, Figure 22-31, and Figure 22-32. In Figure 22-30 a comparison is shown between nominal with on-the-fly and nominal with a posteriori subtraction. In Figure 22-31 we see the comparison of DMD with on-the-fly and DMD with a posteriori subtraction and, in Figure 22-32, the comparison between nominal with on-the-fly de-aliasing and DMD with a posteriori subtraction is shown.

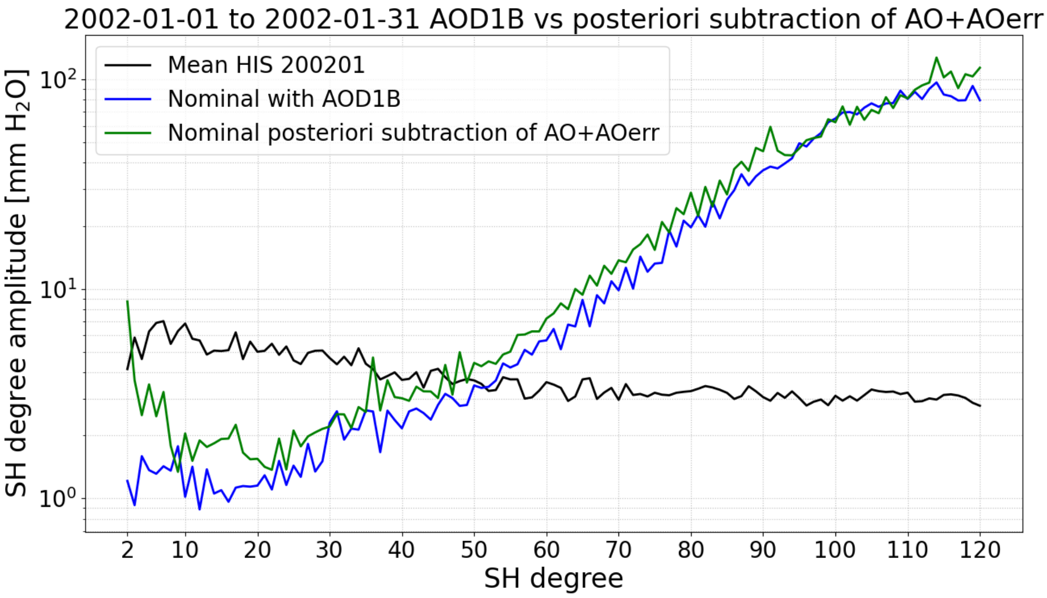

Figure 22-30 Nominal with on-the-fly de-aliasing vs nominal with a posteriori subtraction of AO+AOerr for the Baseline scenario.

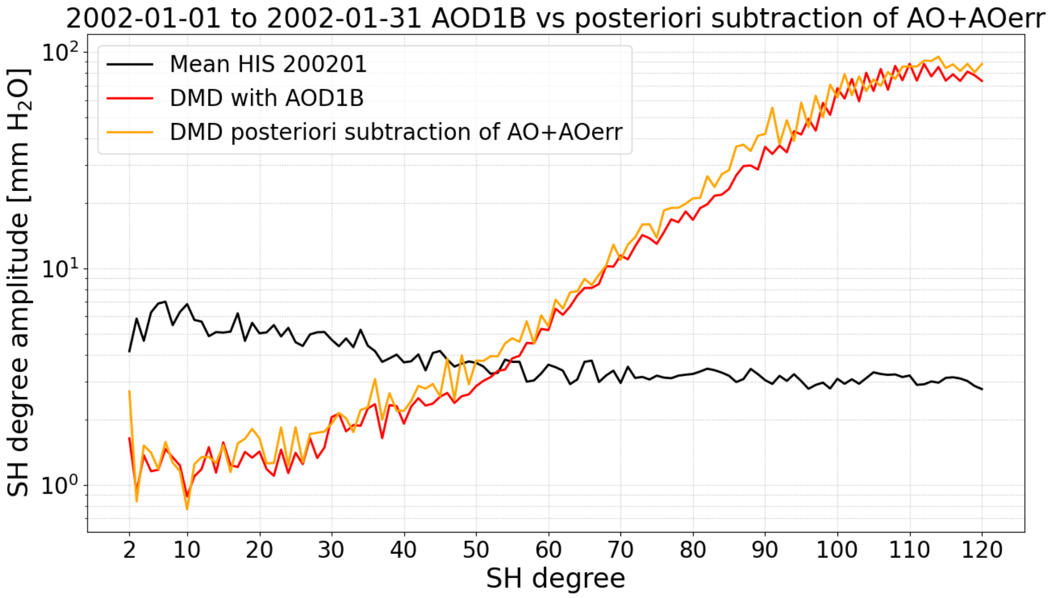

Figure 22-31 DMD with on-the-fly vs DMD with a posteriori subtraction of AO+AOerr for the Baseline scenario.

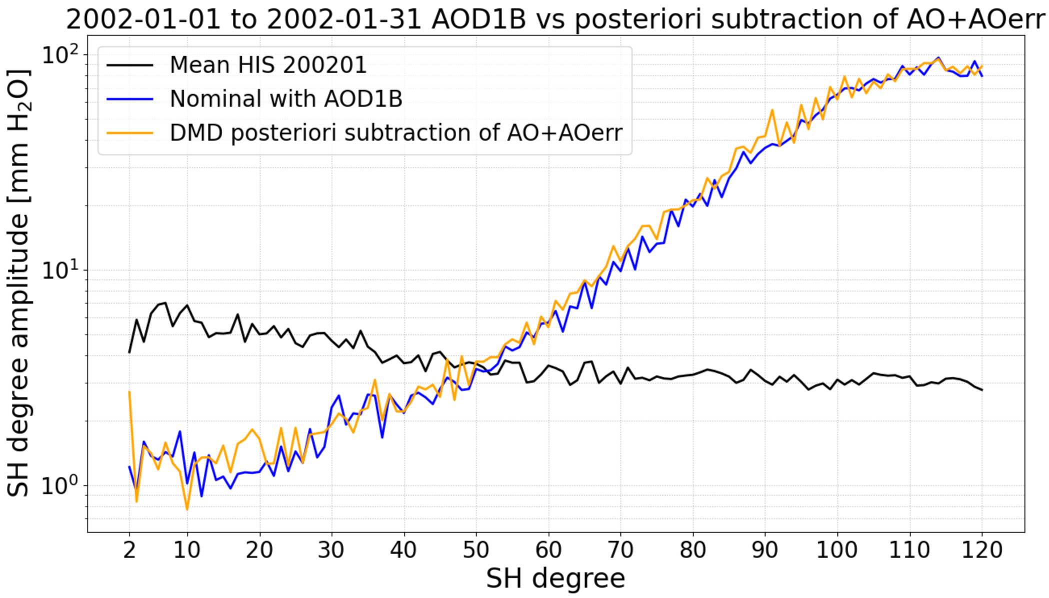

Figure 22-32 Nominal with on-the-fly de-aliasing vs DMD with a posteriori subtraction of AO+AOerr for the Baseline scenario.

From the results obtained for the 31-day gravity retrieval for the Baseline scenario, the conclusion still remains that the baseline strategy will be to apply the nominal approach which includes on-the-fly de-aliasing.

23. L0-L1B INTER-SATELLITE DISTANCE ALGORITHMIC DEVELOPMENT (WP1400)

23.1. REFINEMENT OF L0-L1B ALGORITHMS FOR LTI (WP1410)

The algorithms to transform level0 laser ranging telemetry to a level1b product can be split into the conversion of level0 data to level1a data, and further into level1a to level1b. A processing chain for both conversion steps is available at AEI Hannover for the GRACE Follow-On Laser Ranging Instrument, and based on the telemetry from JPL's Laser Ranging Processor (LRP).

The conversion from level0 to level1a is a rather trivial step, where the instrument-internal telemetry files are first converted from binary to a text format called GISL file. These GISL files contain all the telemetry received, even pure binary information is transformed to hexadecimal text in the GISL file. Then, the relevant information from the GISL files is parsed and saved as level1A information. Binary files like diagnostic scan data are made only available to the instrument team and is not distributed as public level1A file. Also some very few telemetry packets, that represent diagnostic information, may not be converted to level1A files. Conversion means here non-destructive and reversible conversion, which may or may not include conversion from digital counts to physical units (e.g. Temperature in degree C). The data might be edited, i.e. bad data packets are removed and quality control flags are derived and added to the level1a. Some time-tags for telemetry packets (e.g. directly after instrument reboot) might need some processing to resolve the correct integer second, which is then provided in the level1a data (instead of the incorrect unresolved time-tag). All time-tags in level1A refer to the instrument (receiver) clock time, not GPS time.

The GRACE-FO LRI level1A data comprises the following files [RD-1400]

- LHK1A: LRI housekeeping data
- LLG1A: LRI log messages
- LLT1A: LRI light travel times used to compute the light time correction in LRI1B
- LRI1A: LRI phase measurements containing the phase for all four channels and quality figures (beat note amplitude and noise in the vicinity of the 10 MHz beatnote frequency)
- LSM1A: LRI steering mirror data in yaw and pitch with units of digital counts

In general, we can expect a very similar procedure and data products for NGGM. Currently, NGGM baselines a Laser Tracking Instrument with a European Instrument Control Unit instead of the US Laser Ranging Processing (LRP). The European ICU is developed to have very similar interfaces as the US LRP, which extends also to the telemetry structure. Due to the LTI scale factor measurement system foreseen for pair 1 (MCM) and pair 2 (NGGM), we would propose to introduce or would expect an additional data product

- LSF1A: LRI scale factor product, containing the on-board measured time-series of cavity free spectral range (FSR) frequency with unit of Hz and with a data rate 0.1 Hz, the FSR frequency is referred/relative to the nominal master oscillator frequency of the satellite (USO/OCXO).

The conversion from level1a to level1b is in general a non-reversible process and generates in case of GRACE-FO the following data-sets:

- LHK1B: LRI housekeeping data
- LLK1B: clock offset values to convert LRI time-tags to GPS time
- LRI1B: LRI biased range with 0.5 Hz rate including corrections to convert quantity to an instantaneous biased range, contains quality flags
- LSM1B: LRI steering mirror data at 10 Hz rate as yaw and pitch pointing angles in unit of microradian

In order to have a high compatibility between GRACE-FO, pair 1 (MCM) and pair 2 (NGGM), we would also expect a similar level1b file set in NGGM. Again, due to the additional scale factor measurement system, we would expect to have additional files for

- LSF1B: LRI scale factor product containing a time-series of the cavity resonance frequency with unit of Hz, i.e. the laser frequency of the reference satellite. The value is approximately 281 THz. The data rate could be 0.1 Hz or even lower. The values in this file refer to GNSS-referenced frequencies, which means the values in LSF1A are rescaled from the nominal USO/OCXO master frequency to the refined actual USO/OCXO frequency available after precise-orbit-determination (POD).

Moreover, for NGGM we propose to rename the LRI1A/B product to LTI1A/B in case of NGGM.

23.1.1. OVERVIEW OF LTI1B GENERATION

Figure 23-1 visualizes the anticipated processing steps to derive LTI1B data from level 0 or level1A. It is a refined version for NGGM based on the L0-L1B processing available at AEI for GRACE-FO [RD-1401, RD-1402a, RD-1402b] and with publicly available LRI1B products (and documentation) at [RD-1403].

The LTI level0 phase measurements are basically 1:1 written into the LTI1A in Figure 23-1. They contain phase measurements for the four channels, which are derived from the in total 8 segments of the two quadrant photodiodes. The average of the four channels contains the ranging information (sometimes called longitudinal phase, (A+B+C+D)/4), while the differential combinations (A+B-C-D or A-B+C-D or A-B-C+D) represent the so-called differential wavefront sensing (DWS) signal. Two of linear combinations represent DWS yaw and pitch, meaning that they describe the differential angle between the two interfering light beams and these DWS signals are an error signal and typically zeroed by an automatic beam alignment controller in the instrument using the steering mirror as actuator. The third linear combination (A-B-C+D) is often called DWS cross or ellipticity, and is non-zero only when the beams are not rotational symmetric.

In order to ensure the numerical precision, the phase data in level0 and level1a, the phase values are stored and telemetered as unsigned integer with 64 bit width, where the least significant bit represents ~6 nanocycles, or ~6 femtometer. Since the phase data is a monotonically increasing ramp, it is wrapped before exceeding 2^64 counts using a well-defined step of 2^63 counts by the on-board processing unit of the ranging instrument. The phase time-series for the four individual channels (A,B,C,D) are provided in separately in LTI1A for the reference and transponder spacecraft or spacecraft 1 and 2.

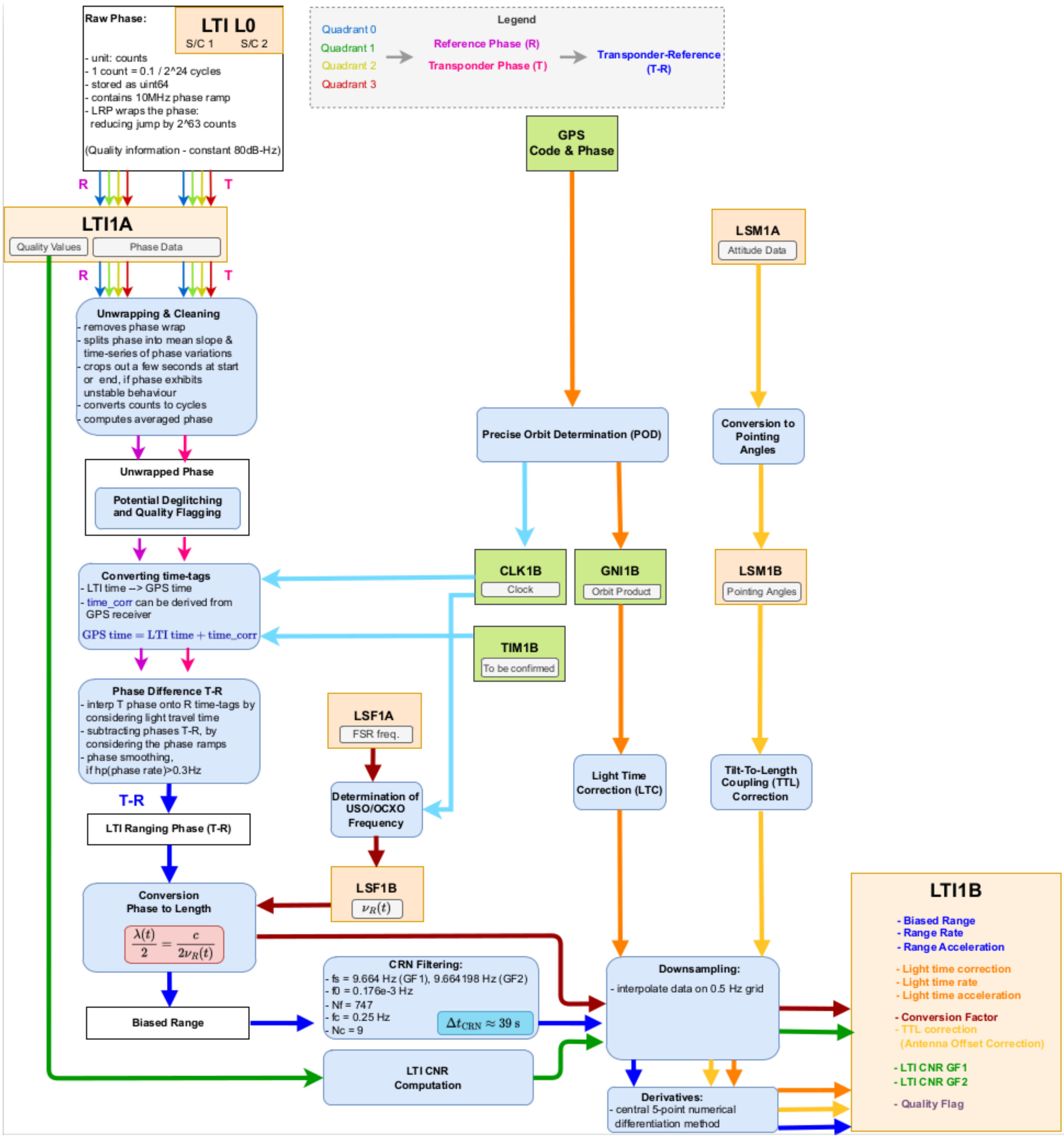

Figure 23-1: LTI data flow-chart from level0/level1a to level1b

For further conversion from LTI1A to LTI1B, the phase time-series of all four channels needs to be unwrapped, i.e. the steps with 2^63 counts are removed. However, in order to preserve the numerical precision, the phase is also decomposed into a constant frequency value, a scalar value representing the monotonically increasing phase ramp, and a time-series of phase variations around the ramp with constant slope. Both parts, the scalar frequency and the phase variations time-series flow down into the LTI1B product.

Once the phase of the four channels is unwrapped, outliers and transient disturbances at the beginning or end of the time-series, i.e. directly before or after laser link acquisition, are detected and removed. This procedure is denoted as "cleaning" in Figure 23-1. Finally, the four channels on each satellite are averaged into a single clean time-series of phase variations and single scalar frequency, representing the longitudinal phase information with units of phase cycles.

In case of GRACE Follow-On an additional "deglitching" algorithm is applied afterwards, to remove undesired phase disturbances like phase jumps and single event upsets. Although the removal of phase jumps induced by thruster activation in GRACE-FO is conceptually simple, it required significant effort to cover all sorts of edge-cases. Even though AEI expects that the disturbances from phase jumps by thruster activations [RD-1404] as well as single-event upsets in the filters [RD-1405] can be mitigated for pair 1 and NGGM, there might be still some other or new disturbances, e.g. during sun-blinding periods when light enters the LTI baffles, which needs to be identified in data screening, marked with a quality flag and potentially be removed. This process is indicated by the box "potential deglitching and quality flagging" in Figure 23-1.

Afterwards LTI time-tags, given first only as a local receiver/LTI time, are converted to GPS time. In GRACE-FO, the proper conversion of LTI time-tags covering all edge-cases was a major effort for AEI. One difficulty was that the so-called datation reports, representing the time-offset between OBC time and LRI time, were sparsely recorded in the beginning (first few months of the mission). Moreover, the GPS receiver (called IPU in GRACE-FO) is frequently rebooting (approx. every week), which changes the time offsets between LRI and GPS. In summary, the time-tag conversion in GRACE-FO is based in the combination of three products: CLK1B, TIM1B and datation reports. The first contains the clock offset between GPS receiver time and actual GPS time as derived during Precise Orbit Determination (POD). The second (TIM1B) describes the offset from GPS receiver time to OBC time, while the third (Datation report) yields the offset from OBC time to LRI time.
The timing architecture for the pair 1 (MCM) and pair 2 (NGGM) is not settled yet. We may expect that there will be less reboots of the GPS receiver in the future, simplifying the data processing, but that the datation reports of LTI and the CLK1B product are still needed and used. The necessity for TIM1B product depends on the actual implementation of the timing architecture, i.e. which unit provides the PPS signal to the LTI processor. As such, we cannot really assess at the current stage the algorithms needed for NGGM, but we provide a review of the timing requirements in the SRD further below, as they should ensure that the LTI can meet its ranging requirements.

Afterwards the phase difference of reference and transponder phase is formed yielding the so-called LTI ranging phase (see corresponding box in Figure 23-1). Forming the phase difference utilizes the time-series of phase variations and the scalar frequency value from both satellites (as introduced above) and it requires that the data of both satellites is interpolated onto the same time-grid. As described in [RD-1401, sec. 6.5], it is recommended to interpolate the data from the transponder LTI onto the time-grid of the reference LTI. The ranging phase time-series contains no phase ramp, because it is removed by the difference, meaning that no scalar frequency component is required any more. At this stage, the phase information is also converted from an integer quantity with 64-bit width to a floating-point quantity with double precision.

This LTI ranging phase, denoted in the following as φ_{TWR}, is then converted from cycles to a biased (half-round-trip) range ρ_{TWR} in units of meter. The abbreviation TWR stands for two-way ranging phase and describes the transponder-based laser ranging quantities, while microwave ranging quantities use a so-called dual-one-way-ranging (DOWR) approach. This re-scaling requires the absolute laser frequency ν_R(t) of the reference LTI/spacecraft, which will be measured by a dedicated measurement system or unit in pair 1 and pair 2.

The current processing from GRACE-FO employed by the Science Data System (SDS) utilizes to our knowledge simple equations that assume a (piecewise) constant laser frequency ν_R:

$$\rho_{\mathrm{TWR}}(t) = \frac{c_0}{2*\nu_R}\varphi_{\mathrm{TWR}}(t) + \mathrm{const.}$$

(Eq. 23-1)

where ν_R is constant over one day, i.e. over the data file that is being produced. As discussed in [RD-1406], this approach has some drawbacks like potential discontinuities in the range-rate at day bounds. [RD-1406] presented novel formulas to convert the phase φ_{TWR} to range ρ_{TWR}, accounting for variations in ν_R(t):

$$\rho_{\mathrm{TWR}}(t) = \frac{c_0}{2}\int_0^t \frac{\mathrm{d}\varphi_{\mathrm{TWR}}/\mathrm{d}t'}{\nu_R(t'-\Delta t_{\mathrm{RTR}}(t'))} - \left(\frac{\nu_R(t')}{\nu_R(t'-\Delta t_{\mathrm{RTR}}(t'))} - 1\right)\mathrm{d}t'$$

(Eq. 23-2)

where Δt_{RTR} is the round-trip light propagation time (from reference to transponder and back to reference), which can be estimated from precise orbit determination as centimeter accuracy is sufficient for this quantity. The second term in the integral is the novelty of this approach, as it accounts properly for the variations in laser frequency. This second term can be approximated as

$$\frac{c_0}{2}\int_0^t \frac{\nu_R(t')}{\nu_R\big(t'-\Delta t_{\mathrm{RTR}}(t')\big)} - 1\,\mathrm{d}t' \approx \frac{c_0}{2}\int_0^t \frac{\dot{\nu_R}(t')}{\nu_R(t')}\Delta t_{\mathrm{RTR}}(t')\,\mathrm{d}t'$$
$$\approx \frac{c_0}{2}\langle\Delta t_{\mathrm{RTR}}\rangle \frac{\log\big(\nu_R(t)\big)}{\log\big(\nu_R(0)\big)} \approx \langle \mathrm{L}\rangle * \frac{\nu_R(0)-\nu_R(t)}{\nu_R(0)}$$

(Eq. 23-3)

which shows that the fractional laser frequency variations couple with the mean satellite separation ⟨L⟩, a common knowledge in laser interferometry. Eq. 23-2 represents to our knowledge the currently most accurate way to convert phase to range. It is being employed in the LRI1B data products by AEI, but not in the SDS-released LRI1B data products of GRACE-FO.

The resulting biased range is finally low-pass filtered with a CRN filter and down-sampled from 10 Hz to 0.5 Hz. This biased range and its first- and second-time derivatives are provided in LTI1B. In addition, LTI1B contains the light time correction calculated from GNI1B orbits and the tilt-to-length coupling correction calculated from inter-satellite pointing angles, both further described below.

In summary, the NGGM LTI level0/level1A to level1b processing is expected to be similar to GRACE-FO, with minor differences related to the deglitching of data, potentially some changes in time-tag conversion and an enhanced method to convert phase to range that is currently not employed by SDS but by AEI for GRACE-FO.

23.1.2. LTI SCALE FACTOR LSF1A TO LSF1B CONVERSION

The absolute laser frequency ν_R(t) is needed to convert the LTI ranging phase to a biased range. Any error or uncertainty in ν_R(t) can be understood as a scale factor error in the range measurement. An in-depth analysis of the GRACE-FO LRI scale factor and of different methods to determine it was presented in [RD-1407]. For pair 1 (MCM) and pair 2 (NGGM), a novel technique [RD-1408, RD-1409] is foreseen that will determine the free spectral range (FSR) of the cavity. In pair 1 (MCM), a dedicated unit called Scale Factor Unit (SFU) is foreseen to provide measurements, while in pair 2 (NGGM), the ICU that is currently being designed should implement the functionality internally in the Scale Factor Measurement (Sub)System (SFMS).

In the beginning of this section 23.1, we proposed novel data products denoted as LSF for LTI scale factor. The LSF level1A data product (LSF1A) is supposed to contain the raw observation of the SFMS, which is the frequency $\mathrm{f}_{\mathrm{FSR,OCXO}}$ representing the free spectral range of the cavity w.r.t. the on-board master clock (OCXO). A low data rate of 0.1 Hz is sufficient, as the scale factor or ν_R(t) is supposed to change only very slowly on daily or even monthly scales.

For the LSF level-1b product, the FSR measurement is finally converted to the absolute laser frequency ν_R(t) in the GPS time system and on the LTI in reference-role, where the laser is locked to the cavity, using the following formula

$$\nu_R(\mathrm{t}) = \mathrm{f}_{\mathrm{FSR,OCXO}}(t) * \left(1 + \frac{\mathrm{d}\varepsilon_{\mathrm{time}}}{\mathrm{d}t}\right) * \left(N_{int} + N_{frac}\right) = \mathrm{f}_{\mathrm{FSR,GPS}}(t) * (N_{int} + N_{frac})$$

(Eq. 24-4)

where $\frac{\mathrm{d}\varepsilon_{\mathrm{time}}}{\mathrm{d}t}$ is obtained from the CLK1B data product and corrects the measured frequency from the nominal OCXO frequency to the actual OCXO frequency that is determined by precise orbit determination. N_{int} is the integer mode that, describing which resonance number is used and that is not expected to change from ground-measurements. N_{frac} describes a fractional offset, that arises from specifics of the optical coatings and mirror curvatures.

The FSR for NGGM is expected to be around 3 GHz, while the pair 1 cavity is expected to have an FSR around 1.5 GHz based on the US cavity.

Although the FSR readout technique will provide the absolute laser frequency with a few MHz accuracy, the so-called telemetry-based method described in [RD-1407] should still be employed as a sanity check as it does not require additional hardware is expected to reach an accuracy of a few ten MHz.

23.1.3. REVIEW OF SRD TIMING REQUIREMENTS

As discussed above, at the current stage it is difficult to assess the algorithms for time-tag conversion from LTI receiver time to GPS time, because the timing architectures for NGGM and MCM are not yet defined and AEI has no experience with the GNSS receiver that will be used in these missions. We review the SRD timing requirements, as they are supposed to ensure proper timing for the mission and the LTI ranging observable.

The timing requirements are shown in Figure 23-2.

Requirement SYS-320 specifies an Ultra Stable Oscillator (USO), which could be interpreted as science-grade USO as flown in GRACE and GRACE-FO. We would propose to re-phase the requirement as
"All science related telemetry shall be time-stamped with a timestamp derived from a single reference clock oscillator (e.g. USO or OCXO) on the satellite, which also drives a high-resolution SCET (spacecraft elapsed time)". We added the word "single" to highlight the importance of a single clock.

Requirement SYS-330 is difficult to understand. The USO is in our understanding a unit that provide just a sine or rectangular oscillation, and which has as such no timer or counter, which counts the oscillation cycles. A clock offset can only be determined between two timers. Since the most relevant timing is between LTI and GNSS, we would propose to state the requirement as "The offset between LTI receiver time and GNSS receiver time shall be measured with an accuracy if 1 µsec (knowledge)".

Requirement SYS-340 seems appropriate and sufficient as it is now.

SYS-320 Time-stamped of science related telemetry

All science related telemetry shall be time-stamped with a timestamp derived from a reference Ultra Stable Oscillator (USO), which also drives a high-resolution SCET (Spacecraft Event Time).

DOORS unique identifier : SRD-883

SYS-330 USO and GNSS Offset Knowledge

The offset between the USO and the GNSS shall be measured with a knowledge of 1usec.

DOORS unique identifier : SRD-1029

SYS-340 Reference Clock and POD Timeing Precision

The reference clock and POD timing precision at the LTI ICU clock sync interface, shall have a stability better than LC{ `$\displaystyle 5\times 10^{-11} \sqrt{1+\left(\frac{0.01Hz}{f}\right)^{2}} \sqrt{1+\left(\frac{0.001Hz}{f}\right)^{2}} $` \EOLC for f greater than 0.0001Hz. As depicted in the figure below.

Note 1: This requirement is equivalent to the phase noise and clock error jitter.
Note 2: For low freqencies this requirement is applicable to the POD precision and for high frequencies it applies to the intrinsic stability of the reference clock oscillator.

DOORS unique identifier : SRD-1030

Figure 23-2: Timing requirements from SRD v.1.4.

23.1.4. TILT TO LENGTH CORRECTION

Tilt-to-length errors arise from the offset between the virtual TMA vertex point VP and the true center of mass (CM) of the spacecraft. Such an offset induces a range change under spacecraft rotations, since the projection of the VP position onto the line-of-sight is altered, as indicated in by the green and purple lines in Figure 23-3. Since this error is hidden below the ranging signal of the gravity field, it can only be determined by satellite rotation manoeuvres, like the center-of-mass calibration manoeuvres (CMcal or CMC). During a CMC, the spacecraft attitude is excited at a fixed frequency of 83.3 mHz using the magneto-torque rods in a sinusoidal shape with magnitudes below 50 µrad, one angle after the other. Through data analysis, one can derive coupling factors between the spacecraft attitude angles and the variations in the range measured by the LRI.

According to Wegener et al ([RD-1410]), the effect of TTL can be linearised as

$$\delta_{TTL,i} \approx c_y c_z \Delta x + \left(s_x s_y c_z - c_x s_z\right)\Delta y + \left(c_x s_y c_z + s_x s_z\right)\Delta z \tag{Eq. 23-5}$$

where $c_x = \cos(\theta_x)$, $s_x = \sin(\theta_x)$ and accordingly for y- and z-directions. θ_x denotes the roll angle, while θ_y is pitch and θ_z is the yaw angle. The second order approximation for small angles reads

$$\delta_{TTL,i} \approx \left(1 - \frac{1}{2}\theta_y^2 - \frac{1}{2}\theta_z^2\right) \cdot \Delta x + \left(\theta_x \theta_y - \theta_z\right) \cdot \Delta y + \left(\theta_y + \theta_x \theta_z\right) \cdot \Delta z \tag{Eq. 23-6}$$

Any constant term can be omitted, as the LRI measures the biased range.

An additional coupling arises from the angular rate (ARC) of the satellite in LTI reference role, which can be described by [RD-1411]

$$\delta_{TTL,ARC} = \frac{L}{c} * \ c_{ARC,yaw} * \frac{d\theta_{y,ref}}{dt} - \frac{L}{c} * c_{ARC,pitch} * \frac{d\theta_{z,ref}}{dt}$$

(Eq. 23-7)

where the coupling factors $c_{ARC,yaw}$ and $c_{ARC,pitch}$ with units of mm/rad are given by the coordinates of the OBA w.r.t. the CM position, L is the absolute satellite separation and c is the speed of light. The angular rate coupling is insignificant during nominal science mode, because the angular rates are small, however, it becomes relevant during CMC where rates are higher.

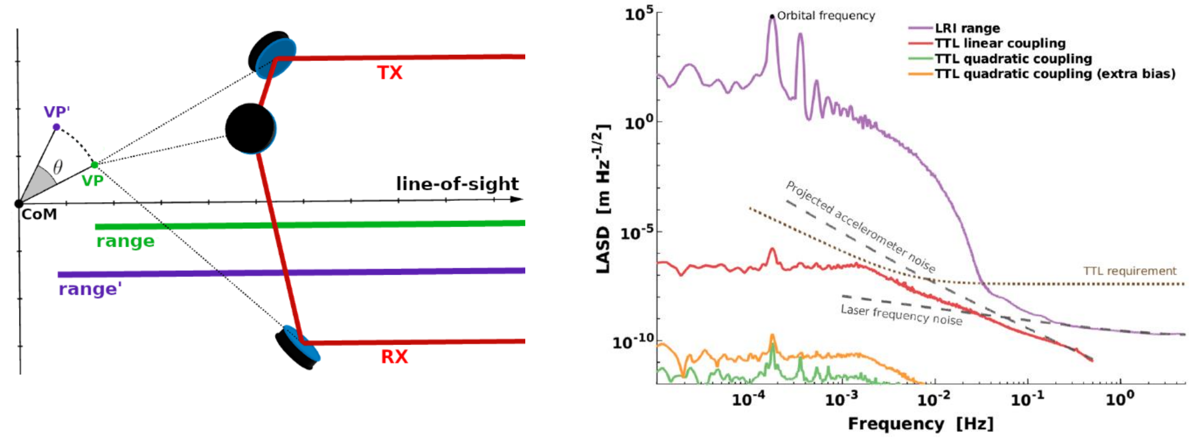

Figure 23-3: (left) TTL coupling schematic showing the projection of the vertex position change upon rotation, (right) Amplitude spectral density of LRI range, measured linear TTL coupling, and expected quadratic TTL coupling [RD-03]

The TTL for a combination of both spacecraft reads

$\delta\rho_{TTL}(t) = \delta_{TTL,1} + \delta_{TTL,2} + \delta_{TTL,ARC}$

$$\approx \Delta z_1 \theta_{y.1} - \Delta y_1 \theta_{z,1} + \Delta z_2 \theta_{y,2} - \Delta y_2 \theta_{z,2} + \frac{L}{c} * \ c_{ARC,yaw} * \frac{d\theta_{y,ref}}{dt} - \frac{L}{c} * c_{ARC,pitch} * \frac{d\theta_{z,ref}}{dt}$$

(Eq. 23-8)

where $\theta_{y,i}$ and $\theta_{z,i}$ denote pitch and yaw angles for spacecraft i. Δy_i and Δz_i denote the y and z components of the vector pointing from the TMA VP to the CM of S/C i, expressed in the satellite frame SF. Δy_i and Δz_i are determined by means of the CMC.

The TTL correction foreseen for NGGM LTI, and already employed in GRACE-FO LRI in the AEI-derived datasets, is based on the above Eq. 23-8. The satellite pointing angles in yaw, pitch, roll with respect to the line-of-sight are derived either from star-camera or steering mirror, while the angular-rate coupling factors (ARC) are known from the CAD layout of the satellite. The TTL coupling factors Δz and Δy need to be measured using TTL calibration maneuvers.

For the simulation aspects of WP-1420, we will employ above linearized formula only for the backword modelling (level1a to level1b), but the forward modelling (i.e. orbit simulations to level1a) will rely on non-linearized formulas.

23.1.5. TRANSFER FUNCTIONS OF SATELLITE MOTION TO LRI/LTI MEASUREMENT FOR REFERENCE ROLE AND TRANSPONDER ROLE

In this section we analyse and document a property of the transponder-based ranging that was to our knowledge so far not described. This property is a slight difference in the transfer function how motion of the reference (master) satellite changes the non-instantaneous range observable compared to motion of the transponder satellite (satellite where LRI/LTI is in transponder role). This property is a consequence of the fact that the non-instantaneous biased range measurement is proportional to the round-trip light propagation time, i.e. the time the light needs to travel from the reference satellite to the transponder and back to the reference. As such, the proper relativistic description of the LTI/LRI quantities presented by Yan et al. (2021) [RD-1412] contains already this effect, but it was not emphasized so far.

The LRI/LTI shall measure instantaneous biased range variations between satellites,

$$\rho_{inst}(t) = |\,\overrightarrow{r_R}\,(t) - \overrightarrow{r_T}\,(t)| + \text{const.} \tag{Eq. 23-9}$$

where $\overrightarrow{r_R}\,(t)$ is the trajectory of the reference (master) satellite in a quasi-inertial frame (ECI / GCRS) and $\overrightarrow{r_T}$(t) is the transponder satellite trajectory, both evaluated at the same coordinate (GPS) time t. The instantaneous biased range is the input to gravity field recovery and provided in the LRI1B/LTI1B data product. The instantaneous biased range is derived from a laser-interferometric phase measurement, where the (longitudinal) phase measurement on the reference satellite can be approximated as

$$\varphi_R(t) \approx \varphi_{R,laser}(t) - \varphi_{R,laser}\big(t - \Delta t_{RTR}(t)\big) + f_{T,off}(t - \Delta t_{TR}) * t + \text{const.} \tag{Eq. 23-10}$$

where $\varphi_{R,laser}(t)$ is the laser's optical phase at coordinate (GPS) time t. $f_{T,off}$ is the transponder offset frequency, typically close to 10 MHz and constant in the local Lorentz frame of the transponder satellite, but slightly time-dependent in the quasi-inertial (ECI/GCRS) frame due to relativistic effects. The phase ramp arising from the offset frequency is usually removed in the ranging phase by forming the transponder minus reference combination:

$$\varphi_{TWR}(t) \coloneqq \varphi_T(t - \Delta t_{TR}) - \varphi_R(t) \approx \varphi_{R,laser}(t) - \varphi_{R,laser}\big(t - \Delta t_{RTR}(t)\big) \tag{Eq. 23-11}$$

where the longitudinal phase observable from transponder is given by

$$\varphi_T(t) \approx f_{T,off}(t) * t + \text{const.} \tag{Eq. 23-12}$$

We may consider the following simple model for the laser phase

$$\varphi_{R,laser}(t) = \nu_0 * t + \delta\varphi_{R,laser}(t)$$
(Eq. 23-13)

where ν_0 is the mean laser frequency in Hz and $\delta\varphi_{R,laser}$ are the laser phase variations arising from the frequency stability of the laser (and cavity) in units of phase cycles. This allows to approximate the LTI two-way ranging phase as

$$\varphi_{TWR}(t) \approx -\nu_0 * \Delta t_{RTR}(t) + [\delta\varphi_{R,laser}(t) - \delta\varphi_{R,laser}\big(t - \Delta t_{RTR}(t)\big)]$$
(Eq. 23-14)

where the first term contains the ranging information and the second term describes the laser phase noise in the range observation. The noise term shows that the laser phase variations are reduced at low frequencies, since the laser phase noise is reduced by a slightly delayed instance of itself (with delay time $\Delta t_{RTR} \approx 2 * \frac{L}{c_0} \approx 1.4$ millisecond). This relation can easily be expressed in the spectral domain as

$$\delta\varphi_{R,laser}(t) - \delta\varphi_{R,laser}(t - \Delta t_{RTR}) \overset{FFT}{\leftrightarrows} \delta\varphi_{R,laser}(f) * (1 - e^{i2\pi * f * \Delta t_{RTR}})$$
(Eq. 23-15)

which exhibits a transfer function term of $(1 - e^{i2\pi * f * \Delta t_{RTR}})$. This transfer function acts as a derivative for low frequencies (f << 1/Δt_{RTR} ≈ 681 Hz), meaning that the laser phase noise appears as laser frequency noise in the interesting science measurement band. This behaviour is well understood and known for a long time. The transfer function will be revisited and plotted further below.

The round-trip light propagation time Δt_{RTR}, cf. eq. 23-14, contains the actual ranging information and is usually defined as the sum of the two individual light travel times from reference to transponder, and from transponder to reference, properly delayed by the corresponding light travel times, i.e.

$$\Delta t_{RTR}(t) \coloneqq \Delta t_{R''T'R}(t) \coloneqq \Delta t_{R''T'}(t) + \Delta t_{T'R}(t)$$
(Eq. 23-16)

where we used single-primed quantities to refer to delayed instances by approx. L/c_0 of the satellite position and double-prime indicates delayed quantities by approx. 2*L/c_0.

The light propagation time from transponder to reference can be obtained by solving the implicit equation

$$\Delta t_{T'R}(t) = \frac{\left|\,\overrightarrow{r_R}\,(t) - \overrightarrow{r_T}\,\big(t - \Delta t_{T'R}(t)\big)\right|}{c_0}$$
(Eq. 23-17)

where c_0 is the speed of light and where we consider only the motion of the satellites (special-relativistic effects) but neglect effects from the gravitation potential (general relativistic effects) as described in [RD-1412, eq. 31].
A similar implicit equation defines the propagation time from reference to transponder satellite:

$$\Delta t_{R''T'}(t) = \frac{\left|\overrightarrow{r_R}\left(t - \Delta t_{T'R}(t) - \Delta t_{R''T'}(t)\right) - \overrightarrow{r_T}\left(t - \Delta t_{T'R}(t)\right)\right|}{c_0}$$

(Eq. 23-18)

Combining both equations and considering that the light propagation time in the argument is approximately given by $L/c_0 \approx 220\,\text{km}/c_0 \approx 0.7$ millisecond yields the following approximation for the round-trip propagation time:

$$\Delta t_{R''T'R}(t) \approx \frac{\left|\overrightarrow{r_R}\left(t - 2 * \frac{L}{c_0}\right) - \overrightarrow{r_T}\left(t - \frac{L}{c_0}\right)\right|}{c_0} + \frac{\left|\overrightarrow{r_R}(t) - \overrightarrow{r_T}\left(t - \frac{L}{c_0}\right)\right|}{c_0}$$

(Eq. 23-19)

This simplified equation suggests that there is an asymmetric response to motion of transponder or reference satellite. The situation is further visualized in the Figure 23-4, where the impact of a step response in either reference or transponder satellite is sketched. A step response or any other stimulus in the position of the transponder satellite becomes apparent in the LTI range with twice the amplitude after a delay of L/c_0. A step response in the reference satellite is seen instantaneously in the LTI range with single amplitude, however, another step with single amplitude appears after $2*L/c_0$ when the information propagated around the round-trip distance. The round-trip observation has always twice the amplitude of the physical motion.

Using the simplification of a one-dimension motion of the satellites, we can approximate the round-trip propagation time or ranging observable as

$$\Delta t_{R''T'R}(t) * c_0 \approx r_R\left(t - 2 * \frac{L}{c_0}\right) + r_R(t) - 2 * r_T\left(t - \frac{L}{c_0}\right)$$

(Eq. 23-20)

which shows that the transponder motion is appears just delayed, while the reference motion appears staggered.

Thus, the relation between motion of satellites in the frequency domain in transponder-based laser ranging and ranging signal, i.e. light propagation time, can be understood as a transfer function (TF) with the following form

TF-Transponder: $e^{-i2\pi * f * \Delta t_{RTR}/2}$ (Eq. 23-21)
TF-Reference: $(1 + e^{-i2\pi * f * \Delta t_{RTR}})/2$ (Eq. 23-22)

While for the laser phase noise the following transfer function was derived in eq. 23-15

TF-Laser Phase Noise: $(1 - e^{-i2\pi * f * \Delta t_{RTR}})/2$ (Eq. 23-23)

The three transfer functions are plotted in Figure 23-5 and were all re-scaled to half round-trip quantities, i.e. proper range and not twice the range. It is apparent that periodic satellite motion of the reference satellite along the line-of-sight with a frequency of ~342 Hz, or an uneven integer multiple (3,5,7,…) of it, cannot be resolved by the LRI/LTI.

The transfer function for satellite motion might be of relevance for diagnostic scans, e.g. when one attempts to analyse thruster signature in the LTI and attempts to resolve high frequency signals. In such analysis, the raging signatures from thruster activations on the reference satellite will appear filtered compared to the thruster impulses on the satellite in transponder role, because some particular frequency components are removed.

However, at low frequencies below 1 Hz, the reference transfer function is close to unity. When evaluating the deviation of the “TF-Reference” from unity one obtains

$$1-(1+e^{-i2\pi*f*\Delta t_{RTR}})/2 = (1-e^{-i2\pi*f*\Delta t_{RTR}})/2 \qquad \text{(Eq. 23-24)}$$

which is actually the identical to the transfer function for the laser phase noise suppression (shown as black trace in Figure 23-5). The black trace indicates that at 342 Hz, the laser phase noise is not suppressed in the LRI/LTI.

These transfer functions for the motion describe the output in the raw range measurement, i.e. the non-instantaneous range. However, when evaluating the instantaneous biased range that is actually used for gravity field recovery, the effect of the above transfer functions is reverted at low frequencies by the light time correction that is applied to the data. The purpose of the light time correction [RD-1412] is account for effects from the light propagation time. However, the correction can usually not be derived at high frequencies, because the orbit products cannot resolve the satellite motion at such high frequencies.

In summary, the discussed effect of the transfer functions and difference in how motion of transponder and reference satellite appear in the LRI/LTI observables is mainly relevant for diagnostic purposes like analysis of high frequency disturbances, but the effect is properly accounted for und removed by the light time correction and therefore not critical for gravity field recovery aspects.

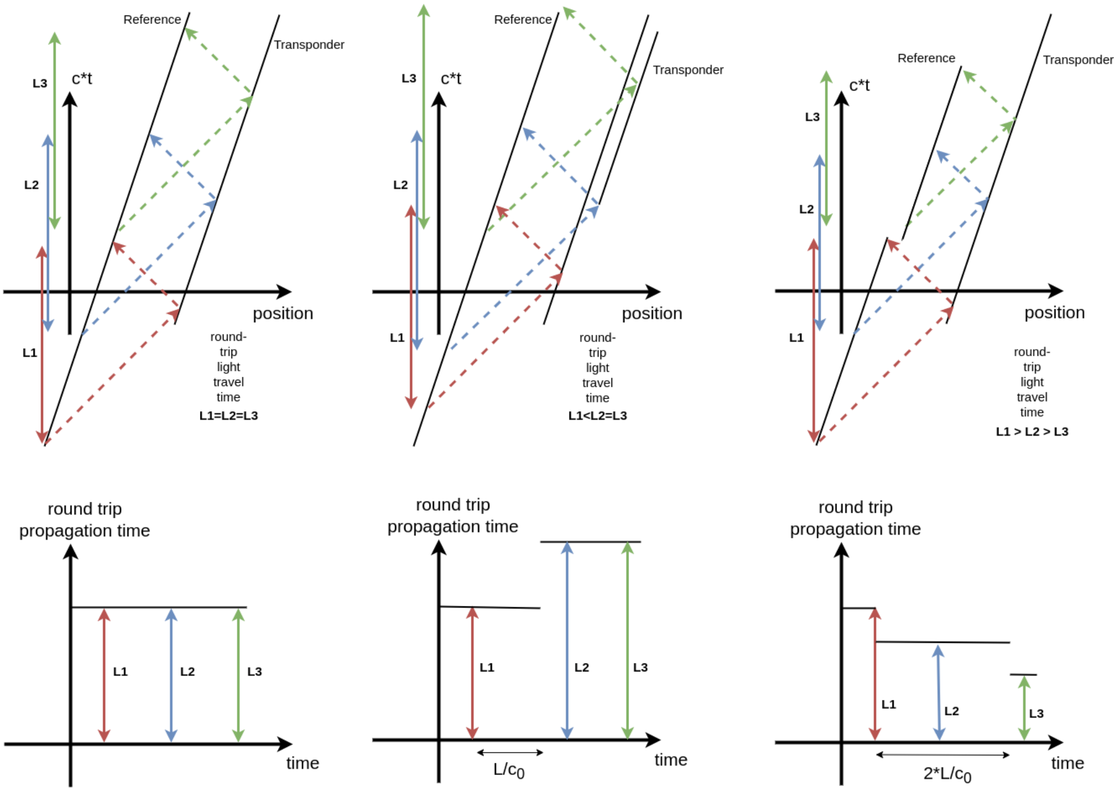

Figure 23-4: **Upper plots: Minkowski diagrams; lower plots: time-series of round-trip propagation time; left plots: satellite separation is static; central plots: step response of the transponder satellite; right plots: step response of reference satellite. Step response occurs when red light path is received on reference satellite.**

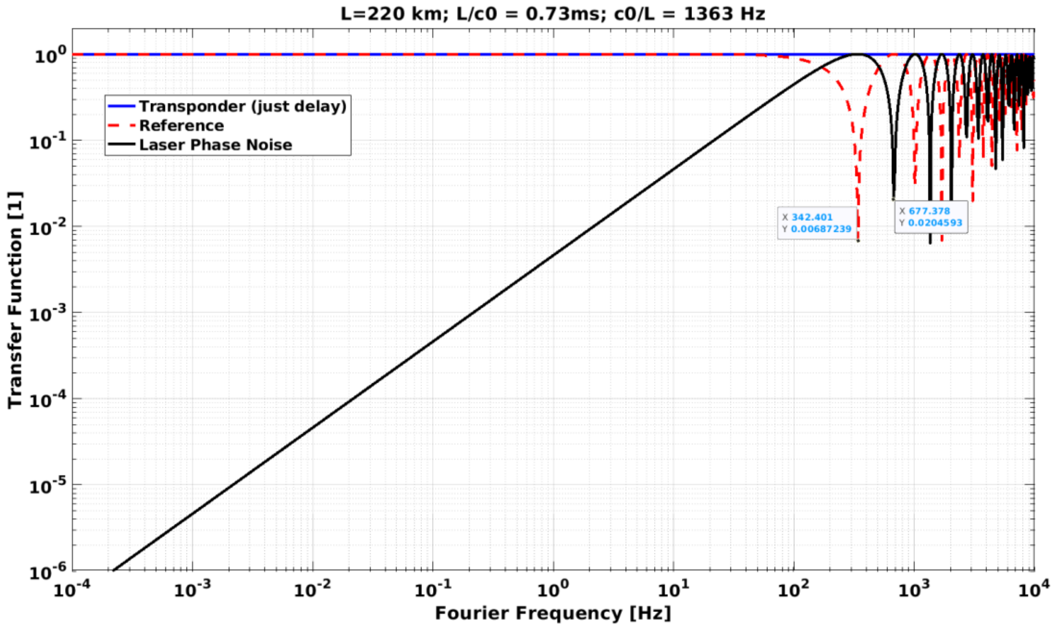

Figure 23-5: **DC-normalized magnitude of transfer functions showing the LTI ranging phase response to motion of the transponder satellite (blue), reference satellite (red) and how laser phase noise is suppressed at low frequencies.**

23.1.6. UPDATE TO LSM1A TO LSM1B CONVERSION

The meaning of the steering mirror level1b data product is not properly documented in GRACE-FO, as has been initially pointed out by Chr. Siemes from TU Delft. The documentation [RD-1400] states that the LSM1B product provides satellite pointing angles, however, there is no convention given how exactly the pointing angles are derived or how they should be interpreted. The pointing angles of the satellite w.r.t. the line of sight depend on the convention, i.e. the order of rotations.

We reviewed the issue and agree that the documentation and algorithms should be updated in the future.

Currently in GRACE-FO, the conversion of steering mirror pointing angles from digital counts to physical angles is performed using a simple linear transformation, where the offsets and scale factors were derived in on-ground calibrations. One important aspect is that these calibrations rely on a small angle approximation based on measurement by an autocollimator. Under a small angle approximation, all conventions yield the same result and are not distinguishable.

If the conversion formulas from raw steering mirror telemetry (LSM1A) to pointing angles (LSM1B) are refined using in-flight calibrations, the LSM1B pointing angles become dependent on the rotation convention used to derive the refined conversion formulas. Hence, the documentation for the LSM1B product would need to state the used convention.

With regard to the ground-calibrations, one needs to properly derive the conversion formulas, which is attempted in the following.

The mentioned GRACE-FO LRI ground-calibrations of the steering mirror relied mainly on the direction of the transmit beam and aimed to establish a relation between the transmit beam (TXB) direction and the sensor readings of the steering mirror using the so-called Position Sensing System (PSS).
The transmit beam direction in the satellite's Science Reference Frame (SRF) can be parametrized as

$$\mathrm{TXB\_DIR\_SRF} = \begin{pmatrix} \sqrt{1 - \sin^2\theta - \sin^2\phi} \\ -\sin\phi \\ -\sin\theta \end{pmatrix}$$

(Eq. 23-25)

where θ and ϕ are the TXB's pitch and yaw angle, respectively, which are directly computed from the PSS values using:

$$\begin{pmatrix} \phi \\ \theta \end{pmatrix} \approx \begin{pmatrix} 4.5 & 0 \\ 0 & 4.5 \end{pmatrix} * \begin{pmatrix} -1 & 1 \\ 1/\sqrt{2} & 1/\sqrt{2} \end{pmatrix} * \begin{pmatrix} PSS_0 - 1830 \\ PSS_1 - 1830 \end{pmatrix}$$

(Eq. 23-26)

However, we aim to find the relation between these TXB angles (θ, ϕ) and the usually used inter-satellite pointing angles roll (ψ), pitch (Θ) and yaw (Φ), which describes satellite rotations around the x-,y- and z-axis respectively. There are many different conventions for the satellite pointing angles, which depend on the matrix rotation order. Two conventions are shown here:

$$R_{conv1} = R_x(\Psi) * R_y(\Theta) * R_z(\Phi)$$
$$R_{conv2} = R_z(\Phi) * R_y(\Theta) * R_x(\Psi)$$

(Eq. 23-27)

where the $R_{x/y/z}$ represent rotation matrices around the three different axes:

$$R_x(\Psi) = \begin{pmatrix} 1 & 0 & 0 \\ 0 & \cos\Psi & -\sin\Psi \\ 0 & \sin\Psi & \cos\Psi \end{pmatrix}$$
$$R_y(\Theta) = \begin{pmatrix} \cos\Theta & 0 & \sin\Theta \\ 0 & 1 & 0 \\ -\sin\Theta & 0 & \cos\Theta \end{pmatrix}$$
$$R_z(\Phi) = \begin{pmatrix} \cos\Phi & -\sin\Phi & 0 \\ \sin\Phi & \cos\Phi & 0 \\ 0 & 0 & 1 \end{pmatrix}$$

(Eq. 23-28)

The rotation matrices R_{conv1} and R_{conv2} describe the rotation of a vector in the SRF into the line-of-sight frame, when the vector is multiplied from the right side to the matrix.

The usual implementation for satellite control is the 3-2-1 rotation, which is given by convention 1 [RD-1415]. We know that the incoming light beam of the LRI is fixed to the LOSF along the x-axis. Therefore, we can define the received beam (RXB) with [-1, 0, 0] in the LOSF. Due to the DWS control loop and special properties of the Triple Mirror Assembly, the transmitted beam to the distance spacecraft is anti-parallel to the RXB direction. Therefore, the outgoing TXB is here defined with [1, 0, 0].

Again we are interested in the beam direction of the TX beam in SRF, which can be derived by rotating [1, 0, 0] with the rotation matrix for convention 1 or 2 as:

$$\text{BEAM\_DIR\_SRF\_CONV1} = R_{conv1}^{-1} * \begin{pmatrix} 1 \\ 0 \\ 0 \end{pmatrix} = \begin{pmatrix} \cos\Theta\cos\Phi \\ -\cos\Theta\sin\Phi \\ \sin\Theta \end{pmatrix} \qquad \text{(Eq. 23-29)}$$

$$\text{BEAM\_DIR\_SRF\_CONV2} = R_{conv2}^{-1} * \begin{pmatrix} 1 \\ 0 \\ 0 \end{pmatrix} = \begin{pmatrix} \cos\Theta\cos\Phi \\ \cos\Phi\sin\Theta\sin\Psi - \cos\Psi\sin\Phi \\ \cos\Psi\cos\Phi\sin\Theta + \sin\Psi\ \sin\Phi \end{pmatrix}$$

(Eq. 23-30)

By comparing the second and third vector element of TXB_DIR_SRF with BEAM_DIR_SRF_Conv1, one can establish the relation between the TXB angles (pitch θ and yaw ϕ) and the satellite pointing angles yaw Φ and pitch Θ. For convention 1 exist four possible solutions, but we chose the one where TXB angles and pointing angles do not have a π shift. This yields

$$\begin{pmatrix}\Phi_{\text{conv1}}\\ \Theta_{\text{conv1}}\end{pmatrix}=\begin{pmatrix}\arcsin\left(\tan(\phi)\,/\sqrt{1-\tan(\phi)^2}\right)\\ \arctan\left(-\sin(\theta)\,/\sqrt{1-\sin(\theta)^2}\right)\end{pmatrix}\approx\begin{pmatrix}\phi\\ -\theta\end{pmatrix}$$

(Eq. 23-31)

For the approximation, the result was Taylor expanded up to second order in the angles.

Using the same approach for TXB_DIR_SRF with BEAM_DIR_SRF_Conv2 yields a more complicated result and is also not easy to simplify by using a Taylor expansion. In that case we applied the approximation first and then solved for the pointing angles, which results in

$$\begin{pmatrix}\Phi_{\text{conv2}}\\ \Theta_{\text{conv2}}\end{pmatrix}=\begin{pmatrix}-\frac{\Psi*\theta+\phi}{1+\Psi^2}\\ -\frac{\Psi*\phi+\theta}{1+\Psi^2}\end{pmatrix}$$

(Eq. 23-32)

This solution is not the preferred one, because it shows a cross-coupling between the two TXB angles and the pointing angle roll. Also we needed to apply approximations to end at a useful formula.

Using the results from convention 1 and assuming TXB angle variations of 1 mrad in yaw and pitch, which is larger than usual pointing variations on GRACE-FO, we can compute the actual inter-satellite pointing angles to

$$\begin{pmatrix}\Phi_{\text{conv1}}\\ \Theta_{\text{conv1}}\end{pmatrix}=\begin{pmatrix}\arcsin\left(\tan(1\text{ mrad})\,/\sqrt{1-\tan(1\text{ mrad})^2}\right)\\ \arctan\left(-\sin(1\text{ mrad})\,/\sqrt{1-\sin(1\text{ mrad})^2}\right)\end{pmatrix}\approx\begin{pmatrix}1.000001\\ -1\end{pmatrix}\text{ mrad}$$

(Eq. 23-33)

This result show, that the error introduced by the small angle approximation in (Eq. 23-31) is usually smaller than 1 nrad and it is safe to assume that the TXB pointing angles are equivalent to the satellite pointing angles up to a sign change.

In summary, we derived the relation between the LRI/LTI pointing angles, derived from the steering mirror PSS readout, to the transmit beam (TXB) pointing and further to the inter-satellite pointing angles yaw, pitch and roll, that depend on particular conventions of the rotation matrix order. We have shown that the convention 1, which is often employed in GRACE context, has a simple relation to the PSS-derived angles.

23.2. L0-L1B SIMULATIONS AND ASSESSMENT (WP1420)

Orbit integration, as usually employed in simulation studies for gravimetric missions like NGGM, provides satellite state time-series, which can be used to compute the inter-satellite range. As such, the simulated inter-satellite range is already the “true” range and is the ideal LTI/LRI level1b dataset. In order to assess the quality of the L0/L1A to L1B processing chain, one first has to develop a processing chain that can generate realistic L0 or L1A data. Such a processing chain to generate realistic L1A data from simulated data does not exist so far, but was developed within this study. The challenge to simulate and assess the quality of performance of the L0-L1B chain lies in the generation of realistic level0/level1a data.

One way to obtain level0 data is to start with the true satellite range and apply all processing steps in reverse order (reverse operation) that are usually being applied in the L0-L1B chain. However, the L0 to L1B chain contains typically some approximations and assumptions and it is doubtful that such a level0 product is really helpful.

Hence, we derived from scratch the processing steps that would provide high-fidelity level0 data from simulation – not considering what is so far being implement in the currently available L0-L1B chain. The processing steps are shown in the flowchart in Figure 23-6.

We use these processing steps to arrive at realistic level0/level1A data set from simulated data (forward processing), and in a next step the well-established and with GRACE-FO data validated level1A to level1B processing (backward processing) is used to obtain the final level1b product.

23.2.1. PROCESSING STEPS FOR GENERATING LEVEL0 LTI DATA

Orbits and Reference Frames (green box Figure 23-6):

The most important quantity, i.e. the instantaneous range or distance between the two satellites, can directly be obtained from orbit data in an inertial frame and serves as the starting point to calculate the inter-satellite distance variations. The latest processing chain at AEI interpolates low-rate orbit data to an equally spaced time-grid of 10 Hz, which we label as GPS time (see explanation for blue box below).

The generation of orbit data by means of numerical integration takes a certain gravity potential into account, which should ideally be used in later processing steps of the LTI ranging data. Furthermore, corresponding satellite attitude data has to be simulated in the same process and should be provided together with the positions and velocities in the inertial frame, since both quantities, attitude and position, are required to transform between Earth's centered inertial frame (ECI) and the satellite reference frame (SRF). This coordinate transformation is applied for the LTI's reference points, which are defined in SRF, but need to be obtained in the ECI frame.

In general, the reference points describe between which two points the inter-satellite distance is measured. There are two points per satellite, the receive (RX) reference point and the transmit (TX) reference point [RD-1413]. However, these may under some simplifications be combined into a total reference point, given by the centroid of RX and TX-RP. The total reference points are often referred to the vertex-points of the triple mirror assemblies, which are co-located with the satellites' center of mass (CoM). However, due to small inaccuracies in the mounting and the movement of the CoM, there always exists an offset of the order of 100 µm between the vertex and the COM. When satellite attitude jitters around with respect to the line-of-sight, this leads to apparent range changes called Tilt-to-Length (TTL) coupling. This TTL coupling can be well described by the total reference point (TMA vertex). However, during the operation of the LRI aboard GRACE-FO, an additional effect was observed that can only be explained using the TX- and RX reference points: the so-called Angular Rate Coupling (ARC) [RD-1410],[RD-1411]. The TTL and ARC effect can be corrected in data processing using an empirical model with linearized coupling factors, which is done in the regular level0 to level1b processing at AEI. However, to achieve a precise simulation that can also account for non-linear terms in the ARC, we switched in the forward-processing (simulated data to level1a) to the approach with the transmitted (TX) and received (RX) reference points.

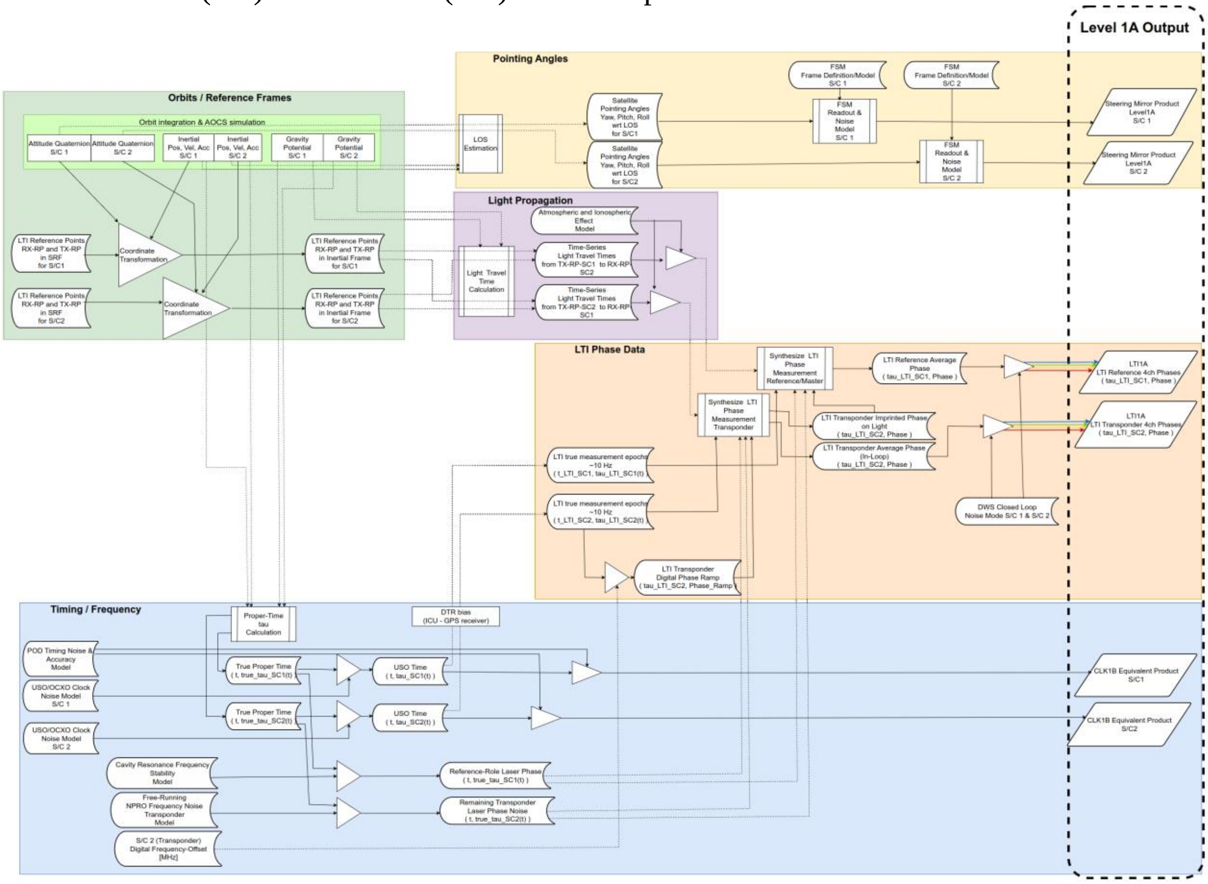

Figure 23-6: Flowchart for the generation of realistic LTI level0/level1a data.

Figure 23-7 shows the locations of the different reference points, while Figure 23-8 illustrates the arrangement of TX and RX in more detail. The distance between TX and RX is equal to the distance between CoM and CoM, if both satellite's point perfectly along the line-of-sight.

In the simulations we define the two nominal reference points in the SRF coordinates as TX= [-1000, 300, 24] mm and RX = [1000, -300, -24] mm. In order to simulate the effect of TTL we add offsets in the order of 100 µm, corresponding to 100 µm/rad in yaw and pitch, to the y- and z-axes (forward-processing). In the backward processing we remove most of the TTL effect up to some simulated uncertainties arising from the fact that the TTL coupling and the satellite attitude are not perfectly known (measurement errors). The ARC coupling depends only on the RX reference point and is even present, when the TMA vertex is perfectly co-located with the CoM (zero TTL). It should be noted that TTL and ARC can only be simulated when a time-series or a model of the attitude data product is available.

At the time of writing (2023-09-11), we are still validating and finalizing the implementation of TTL and ARC computation, e.g. by using a time series of GRACE-FO pointing variations. However, it is foreseen to switch to simulated attitude quaternions from the mission primes, when this data will be provided together with the corresponding orbits in inertial frame.

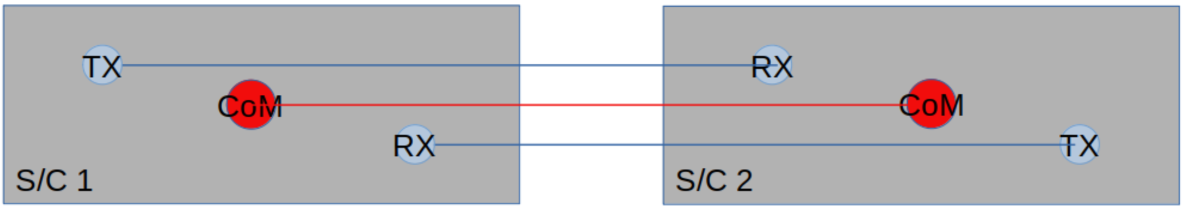

Figure 23-7: The distance between the satellites' reference points TX and RX are equal to the distance between the two center of mass (CoM), only in the ideal case when the satellites have no pointing error and no offsets from the nominal TX and RX reference point position is introduced. The sum of the length of both blue paths (between the RP) is twice the CoM-CoM distance. If one of the satellite has a pointing error, i.e. rotates around the CoM, one of the blue paths contracts, while the other expands. However, the sum of the length of both paths remains as twice the CoM-CoM distance (no TTL effect as the nominal RX and TX RP are symmetric around the CoM.

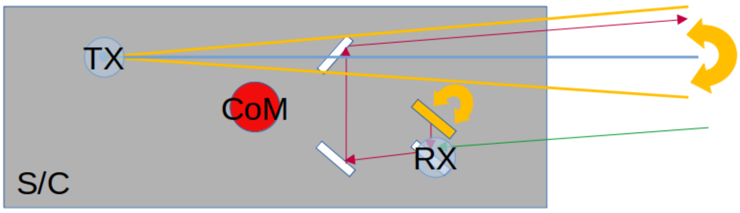

Figure 23-8: The RX reference point is co-located with the receiving aperture on the optical bench, which is imaged onto the photodetector. The TX point can be imagined in the point, where a distant observer would assume to find the origin of the transmitted beam when the steering mirror rotates, see [RD-1413] for details. The two mirrors represent the triple mirror assembly.

Pointing Angle Generation (yellow box Figure 23-6):
Satellite inertial positions as well as attitude quaternions are needed to calculate the line of sight (LOS), given as the vector between the satellites' CoM, and to derive the satellite pointing angles roll, pitch and yaw. These angles describe the orientation of the SRF w.r.t. the LOS frame. In order to generate a LTI pointing data product based on the steering mirror information, such as LSM1A, we need to make some assumptions for the readout system and on the noise model of the steering mirror. Currently, we are using the inverted transformation of GRACE-FO to convert the yaw and pitch physical angles into digital counts of the readout system. In GRACE-FO, the steering mirror orientation is measured by a PSS (Position Sensing System), and the reading of the PSS and COM (commanded positions from DWS) values are reported as telemetry. To transform LSM1A into LSM1B (backward processing), the same transformation is used as in the forward processing, i.e. currently no noise model for the readout system is considered. More details on the PSS conversion can be found in [RD-1414, slide 25].

Light Travel Time Calculation (purple box Figure 23-6):

The LTI range is to first order proportional to the phase of the light exchanged between the satellites. This phase is proportional to the light travel time (LTT) between the RX- and TX reference points. The LTT is usually computed in the inertial frame, because the equations are simpler. The special-relativistic components of the LTT use only the kinematic orbit information, i.e. position, velocity and acceleration of each RX- and TX reference point. The general-relativistic effects account also for the gravitational potential and Earth's rotation (spin for gravito-magnetic effect), which affects the light propagation. Details about the calculation can be found in Yan et al. [RD-1412].

Furthermore, effects of atmosphere and ionosphere might be added in the future to the simulations, but are not yet part of it, as their effect is expected to be extremely small for the LTI. Remark: When orbit data is not on a rate of 10 Hz, the LTT needs to be interpolated to an equally spaced GPS time grid with that sampling.

Timing and Frequency (blue box Figure 23-6):
Timing:
Different time systems need to be involved in the generation of realistic level1a data. As a starting point for the simulation, we define a GPS time grid with equal spacing of 0.1s (=10 Hz sampling), which we regard as error free and which is in a relativistic context often called coordinate time as it parameterizes the simulation. In order to preserve numerical precision, we usually split the time variables into integer seconds and fractional seconds. However, any ideal clock or ideal oscillator on the satellite will track or display not the GPS time but the true proper time (τ), which can be computed from the following model [RD-1401]:

$$\frac{d\tau}{dt} - 1 = -\frac{GM}{|\vec{r}_{S/C}|\cdot c_0^2} + \frac{GM}{|\vec{r}_{S/C}|\cdot c_0^2}\cdot J_2\left(\frac{a_e}{|\vec{r}_{S/C}|}\right)^2 \frac{3\cdot z^2 - \vec{r}_{S/C}^{\,2}}{2\cdot|\vec{r}_{S/C}|} - \frac{\vec{v}_{S/C}^{\,2}}{2\cdot c_0^2} - \frac{\phi_0}{c_0^2} \tag{Eq. 23-34}$$

This model uses the orbit positions ($\vec{r}_{S/C}$) and velocities ($\vec{v}_{S/C}$) as input data and also takes the geoid gravity potential (ϕ_0) into account, while c_0 is the speed of light, z is the z component of the position vector in ECI; J_2, a_e and GM are the Earth flattening parameter, the mean Earth radius and Earth's standard gravitational parameter, respectively.

The above equation can be numerically integrated to obtain the proper time τ for each satellite. The proper time represents an ideal USO/OCXO (Ultra Stable Oscillator or Oven-Controlled Oscillator) measurement, and by adding a noise model to the proper time, we obtain a more realistic USO/OCXO observation in the simulation. At the moment, we use a noise model based on the GRACE-FO USO stability, shown in [RD-1406, eq. 59]. The USO clock signal is used to drive the GNSS receiver and the LTI Instrument Control Unit (ICU). Hence, GNSS receiver time and the ICU time are equivalent to the USO time up to some biases.

At the current stage, since the timing architecture for NGGM is not defined yet, we assume for the moment no additional time offset or timing uncertainty between the GNSS receiver and the LTI Instrument Control Unit (ICU). It is reasonable to consider that there will be a synchronization of the timers in the ICU and in the GNSS receiver, similar to what is done in GRACE-FO with the so-called datation reports. In the future, we may add additional noise to the time-tags in that regard.

For the later backward-processing from level1a to level1b, we store the time difference between USO time (=GNSS receiver time) and coordinate GPS time in a CLK1B equivalent format. For real GRACE-FO data-processing this eps_time is usually determined by means of precise orbit determination (POD), where also the precise orbit products of GNI1B/GNV1B emerge from. Therefore, we can consider a noise model for the POD timing solution given by [RD-1406, eq. 60].

This POD timing noise is added to the CLK1B eps_time estimate, such that the total time difference inside CKL1B results in

$$\begin{aligned} CLK(eps\ time) &= \text{ coordinate GPS time } - \text{ GNSS receiver time } + \text{ POD timing noise} \\ &= \text{ coordinate GPS time } - \text{ Proper time } - \text{ USO noise } + \text{ POD timing noise } , \end{aligned} \quad \text{(Eq. 23-35)}$$

which can be used to correct the LTI time tags to GPS time in the LTI1A to 1B chain as:
LTI time + eps_time = coordinate GPS time. Again, here we assume that the LTI time is the same as the GNSS receiver time, i.e. we omit offsets between the two instruments. The USO noise model and POD noise model, as well as the proper time effect are shown in Figure 23-9.

As stated above, we start the simulation with an equally spaced 10 Hz coordinate GPS time-grid. For this time-grid, we calculate the corresponding LTI observables and LTI time-tags based on the proper time for both satellites, which are not equally spaced in the time-frame of the coordinate GPS time. However, in the end, the observations are performed locally on the satellite and on an equally-spaced LTI (or USO) time-grid.

For simulating the equally-spaced LTI time, a sampling frequency of 9.664 Hz for the reference S/C and 9.664198 for the transponder S/C, is used, based on GRACE-FO USO frequencies. The actual NGGM LTI values are still under discussion. To synthesize the LTI phase later (see description for orange box in Figure 23-6), all important quantities like the LTI phase are interpolated from their equally-spaced coordinate GPS time-tags with 10 Hz rate (which correspond to unequally spaced LTI time) to the equally-spaced LTI time grid with a rate of ~9.66 Hz.

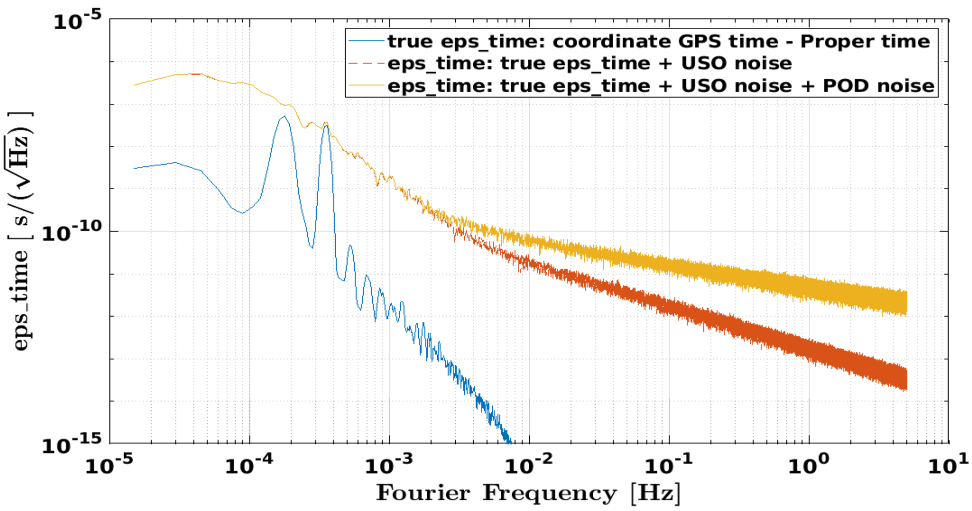

Figure 23-9: Time difference between coordinate GPS time and GNSS receiver/USO time is visualised by the parameter eps_time, as it is usually called in the GRACE-FO context (cf. CLK1B product). The blue curve is derived from a relativistic model for the proper time, while for the red one USO stability noise was included, and for the yellow curve the consideration of POD noise as well.

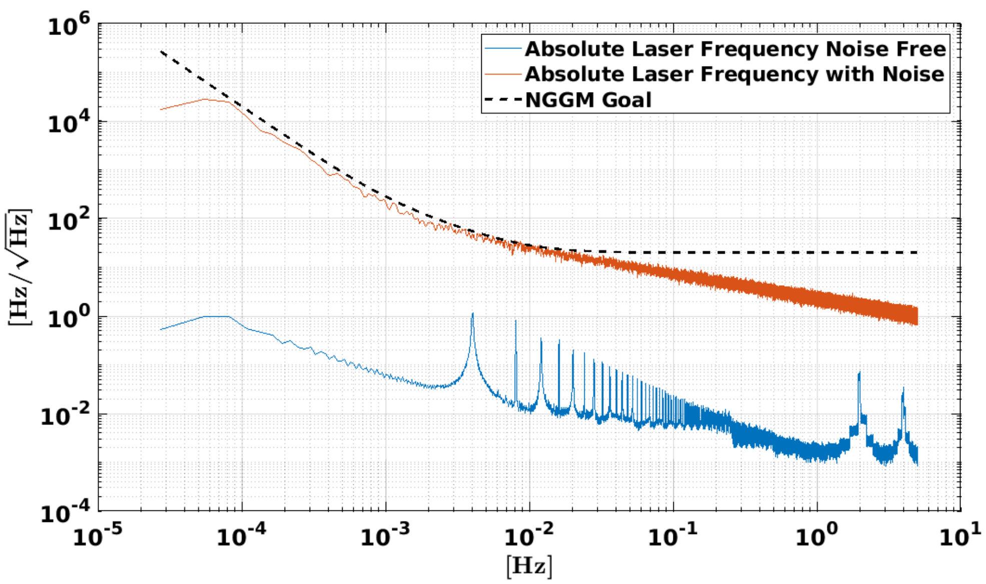

Figure 23-10: Absolute laser frequency from exponential cavity decay model in local satellite frame. The blue curve shows the noise-free case, which might be limited by numerical noise of the model. The red trace contains assumptions for a laser frequency noise, based on the NGGM noise goal.

Laser/Cavity Frequencies: The LTI laser frequency of the reference S/C is locked to an optical cavity. The stability of the cavities' resonance frequency is usually specified for frequencies in the measurement band (0.18 mHz to 0.1 Hz) and in terms of long-term drifts (well below 0.18 mHz). In our current processing chain for the level1a data generation, we can switch between a constant absolute laser frequency, or use an exponential cavity decay model as long-term drift, which was derived for the GRACE-FO mission [RD-1407].

The latter one is a more realistic description of physical changes over time inside the cavity. In the beginning of the GRACE-FO mission, the frequency changed faster, but converged to a certain value after some years. For the generation of level1a data, we used the frequency drift of GRACE-FO from January 2019, which is a drift of approximately 0.5 Hz/s. Additionally, laser frequency noise in the measurement band (>0.18 mHz) can be added to that model. The noise was adjusted to be aligned with the NGGM LTI frequency-noise goal in lower frequencies (f < 20 mHz) and a slightly lower noise towards higher frequencies as shown in Figure 23-10.

$$ASD[\nu]_{NGGM}^{goal}(f) = 20\frac{Hz}{\sqrt{Hz}}\sqrt{1+\left(\frac{0.01Hz}{f}\right)^2}\cdot\sqrt{1+\left(\frac{0.001Hz}{f}\right)^2}$$
$$ASD[\delta\rho_{error}^{goal}](f) = 20\frac{nm}{\sqrt{Hz}}\sqrt{1+\left(\frac{0.01Hz}{f}\right)^2}\cdot\sqrt{1+\left(\frac{0.001Hz}{f}\right)^2}$$
(Eq. 23-36)

The generated absolute laser frequency for the reference S/C is initially defined locally on the satellite, but it is transformed to the Earth's inertial frame and the coordinate GPS time by multiplying with (1 + dτR/dt), where dτR/dt is the first time-derivative of the reference satellite's true proper time w.r.t. coordinate GPS time, i.e. proper time without noise of USO or POD.

For the LTI in the transponder role, the laser frequency is locked to the incoming light field. The transponder laser is offset by 10 MHz from the received light field in order to produce a detectable beatnote frequency on the photodiodes of both S/C.
The phase of the photodiode signals on the transponder side can be approximated as

$$\varphi_T(\tau_{T,LTI}) \approx \int_0^{\tau_{T,LTI}} 10\text{ MHz }\, d\tau + \text{TLPN}(\tau_{T,LTI})$$
(Eq. 23-37)

where the remaining transponder-lock phase noise (TLPN) was introduced. The TLPN arises from the finite gain and bandwidth of the laser lock. The measurement of the phase on the reference satellite can be approximated as

$$\varphi_R(\tau_{R,LTI}) \approx \text{ranging signal} + \varphi_T(\tau_{R,LTI})$$
(Eq. 23-38)

By forming the phase difference of transponder and reference in the L1A to L1B chain, the ramp arising from the 10 MHz offset and the TLPN cancels out and only the ranging information remains. At the current stage, the TLPN is not yet implemented in our level1a generation.

LTI Phase Generation (orange box in Figure 23-6):

Synthesize Transponder Phase: The transponder-lock ensures that the photodetector on the transponder satellite measures a constant 10 MHz frequency, which yields after integration a phase ramp. The transponder phase reads

$$\varphi_T(\tau_{T,LTI}) \approx \int_0^{\tau_{T,LTI}} 10\ \text{MHz}\ d\tau + \text{TLPN}(\tau_{T,LTI}) \approx\ 10\ \text{MHz} * \tau_{T,LTI} + TLPN(\tau_T)$$

(Eq. 23-39)

where $\tau_{T,LTI}$ is the LTI time of the transponder. The phase ramp φ_T is in general monotonically increasing, which may cause a loss in precision as the numerical values grow. In our implementation, we first rewrite the 10 MHz physical frequency, which corresponds to 10 million cycles per second, into a phase change in units of cycles per measurement sample by considering the sampling rate of the ICU. Using the resolution of the phase accumulator in the phasemeter, we further convert it to a phase change in counts per sample. Finally, we perform a discrete integration to obtain the phase values in counts. The phase data is typically stored as an unsigned integer with 64 bit depth. Hence, whenever the phase value approaches the 64th bit, a deliberate and well-defined phase-wrapping step is introduced, as in GRACE-FO data processing. In the end, the phase data is split from 64 bit into 2x32 bit and provided as the LTI1A dataset.

Synthesize Reference Phase: As explained in the section on timing, each GPS time-tag is related to one USO time-tag by GPS time = USO time + eps_time. That means, all previously mentioned quantities, like the light travel time LTT, the absolute laser frequency, and eps_time are computed on a regularly 10 Hz sampled coordinate GPS time grid, but their corresponding local USO/LTI time is known as well, but it is irregularly sampled. To compute the LTI phase measurement, all these quantities are interpolated from their irregularly sampled LTI/USO time-tags to the equally sampled LTI time grid of the corresponding S/C at a rate of about 9.6 Hz.

The phase measurement on the reference S/C consists of two main contributors:

$$\Phi_R(\tau_R) = -\nu(\tau_R) \cdot \Delta t_{RTR}(\tau_R) - \frac{1}{2}\frac{d\nu}{d\tau_R} \cdot \Delta t_{RTR}^2 + \Phi_R^{ramp}(\tau_R) \cdot \tau_R + TLPN$$

(Eq. 23-40)

The first part is the ranging information, which can be extracted from the first two terms in the equation (23-40) above. The third term contains the received transponder phase ramp as it appears on the reference side. The fourth term is the residual transponder-lock phase noise, which is at the moment set to zero.

1) Ranging Information: To compute the first and second term we need the absolute laser frequency ν, its first time derivative, and the light travel time ΔtRTR for the photon path of

reference to transponder and back to reference (RTR). To get more accurate results we recommend to split the laser frequency ν and light travel time ΔtRTR into a constant and time-variable part, by subtracting the mean of ν and ΔtRTR and handling the means separately. The second term proportional to the squared ΔtRTR is a second-order term that is often omitted, as it is in general very small.

2) Phase Ramp: The transponder phase ramp (Φ_T^{ramp}) needs to be transformed into the system of the reference satellite by taking into account the ratio of transponder and reference clock rates, containing the difference between 9.664 Hz and 9.664198 Hz as well as the Doppler effect. To avoid the numerically unstable and monotonically increasing phase ramp, the calculation is performed on the first-derivative, i.e. the phase change per sample (indicated by δ-symbol). The relation of the phase ramp slopes ($\delta\Phi_R^{ramp}$ and Φ_T^{ramp}) between both satellites is given by

$$\begin{aligned}\delta\Phi_R^{ramp}(\tau_R) &= \delta\Phi_T^{ramp} \cdot \left[\frac{d\tau_T^{USO}}{dt^{GPS}} \cdot \left(\frac{d\tau_R^{USO}}{dt^{GPS}}\right)^{-1}\right]_{interp2\tau_R^{LTI}=\tau_R} \\ &= \delta\Phi_T^{ramp} \cdot \left[\frac{\Delta\tau_T^{USO}}{\Delta\tau_R^{USO}}\right]_{interp2\tau_R^{LTI}=\tau_R}\end{aligned}$$

(Eq. 23-41)

where the interpolation is needed to transform the quantities from the GPS time to the local LTI time on the reference.
Finally, we get the reference phase rate by adding ranging information and phase ramp terms together, δΦRvar(τR)+δΦRramp(τR). As explained for the transponder, the phase rate is integrated sample wise as uint64, phase wraps are applied, and finally split into two uint32 numbers, which are saved in the LTI1A product.

LTI1A remarks: LTI1A datasets contain four channels of phase data. At the current state, the generated level1a data uses the same phase value in all four channels, meaning that there is an ideal zero DWS signal. It is planned for future releases to include also some DWS noise.

23.2.2. VERSION 00 OF LTI LEVEL1A

For the milestone meeting 1 (2023-05-31), a first preliminary LTI dataset named v00 was provided. The simulated level1a data, which was processed further to level1b, was supposed to be a noise-free case. Other specialities and assumptions were:

- Noise-free orbits in the inertial frame with a sampling rate of 0.2 Hz were generated by AEI. This orbit data was upsampled to 1 Hz using matlab's spline interpolation method, to generate equivalent orbit data, as usually provided in GNI1B.
- From this orbit data the light travel times were computed between the satellites' TX and RX reference points and interpolated to a 10 Hz GPS time-grid. Angular rate or tilt-to-length coupling was not considered, which would occur from an offset in the reference

point location in combination with attitude jitter. For v00, we started with the simplification of perfect satellite alignment, i.e. no pointing jitter and roll = yaw = pitch = 0°.

- The LTI time was assumed to be identical to GPS time.
- The absolute laser frequency is the same for satellite frame and inertial frame, i.e. no modulation with proper time.
- A constant value for the absolute laser frequency was chosen: 281616393 MHz.
- No laser frequency noise was considered.
- The LTI1A data was generated for 30 days and provided in a file format similar to the GRACE-FO data.
- Simplified formulas for phase computation were employed:
  $\Phi_R(t) = -\nu(t) \cdot \Delta t_{RTR}(t) + 10MHz \cdot t, \qquad and \quad \Phi_T(t) = 10MHz \cdot t$
  Remark: The v00 dataset had a sign error as the minus in the first term was missing in the processing. When using the ranging data of v00, just flip the sign.

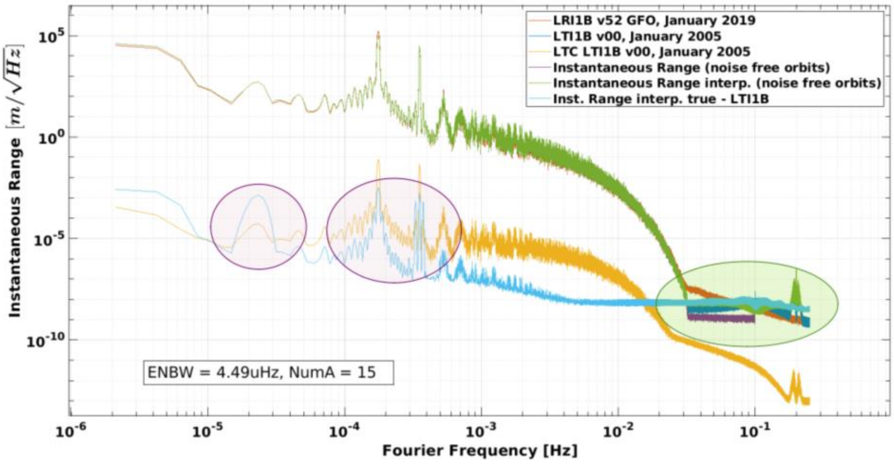

Figure 23-11: LTI1B v00 instantaneous range for January 2005 (dark blue) in comparison to GRACE-FO (orange) and geometric satellite distance from orbit data (purple). The difference of the range from interpolated orbit data (i.e. true range) and LTI1B range (obtained from forward and backward processing) is shown in light which blue, is the most interesting curve.

Figure 23-11 shows the amplitude spectral density (ASD) of the instantaneous range of LTI1B v00, i.e. the result after forward and backward processing, in dark blue. It can be compared with the instantaneous range from orbit data shown in purple. To form their difference, it was necessary to interpolate the orbit data to LTI1B time-tags (green curve). We used the matlab interpolation method spline. The resulting difference curve is shown in light blue. In principle the data set should have the same noise level as the orbit data, because we did not consider any noise sources. However, LTI1B v00 exhibits errors in frequencies > 50 mHz due to a non-optimal interpolation method of orbit data and light travel times, and furthermore additional signals at 2/day, 1/rev and 2/rev can be observed. They might be related to other initial issues in the processing chain of the v00 data generation, or also to the interpolation issue. However, with the second LTI1B version (v01) all these problems were eliminated, so we did not attempt to further understand their origin.

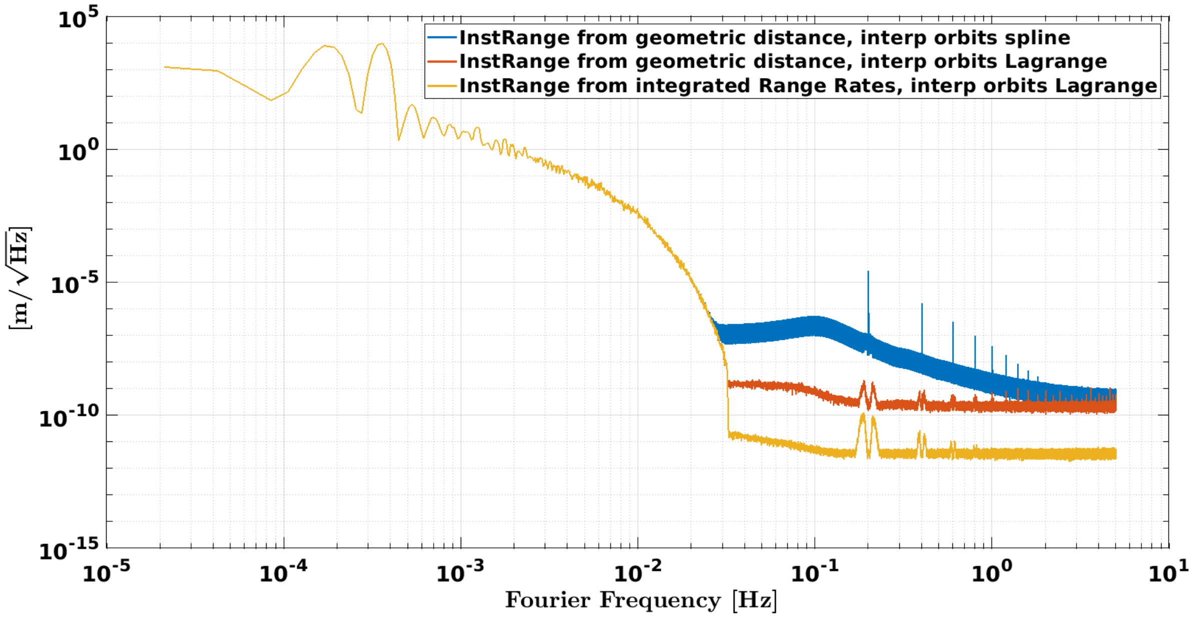

Figure 23-12: LTI1B v01 and future products, use Lagrange interpolation (order 7) to upsample the orbit data to a 10Hz rate. Furthermore, the instantaneous range in the light travel time calculation is now derived from integrated range rates in the forward processing. This allows to handle the 200km bias separately, which preserves the numerical precision (yellow trace).

23.2.3. INTERPOLATION METHODS

LTI1B v00 is limited by a non-optimal interpolation method for orbits and light travel times. In order to upsample the orbit data from 0.2 Hz to 10 Hz, we investigated different strategies. The plot in Figure 22-12 shows different attempts to further reduce the noise level for the instantaneous range from orbit data.

Exchanging matlab's spline interpolation by Lagrange interpolation of order 7 already reduces the noise in higher frequencies from the blue to the red level. Furthermore, different methods to compute the instantaneous range from orbit data can reduce the noise even further.
The first option to compute the instantaneous range, as shown by the blue and red curve, is just the geometrical distance from the orbit positions of the two S/C: $\rho_{geo} = |\vec{r}_{SC1} - \vec{r}_{SC2}|$.
However, the second option uses the range-rate, as obtained from the velocity of the satellites, which is numerically integrated to a biased range. It is called biased range, because it does not contain the ~200 km, which is beneficial to preserve numerical precision (yellow tace in Figure 22-12). Nevertheless, we compute the missing bias from the orbit positions and store it separately, in order to use it whenever needed.
The separation of a large static bias from small time-varying components is also employed for the light travel times, as it otherwise spoils the precision of simulation results.

23.2.4. VERSION 01 OF LTI LEVEL1A: V01

At the progress meeting 2 (2023-09-04), the version 01 of the LTI level1a data was presented. In comparison to v00, the following changes were applied:

- AEI noise-free orbits in the inertial frame with a sampling rate of 0.2 Hz were upsampled to 10 Hz data by using Lagrange interpolation.
- From this orbit data the light travel times are computed between the satellites' CoM.
- The simplification of LTI time = GPS time was removed, LTI time is properly calculated from the proper time and an USO noise model.
- USO & POD noise were considered (cf. Figure 23-9).
- The absolute laser frequency (defined in the LTI time frame) is transformed to the inertial frame and modulated by the proper time.
- An exponential cavity decay model was chosen for the absolute laser frequency: drift ~0.5Hz/sec.
- Laser frequency noise is considered (cf. Figure 23-10).
- Phase computation considers also second order term:

$$\Phi_R(\tau_R) = -\nu(\tau_R) \cdot \Delta t_{RTR}(\tau_R) - \frac{1}{2}\frac{d\nu}{d\tau_R} \cdot \Delta t_{RTR}^2 + \Phi_R^{ramp}(\tau_R) \cdot \tau_R$$

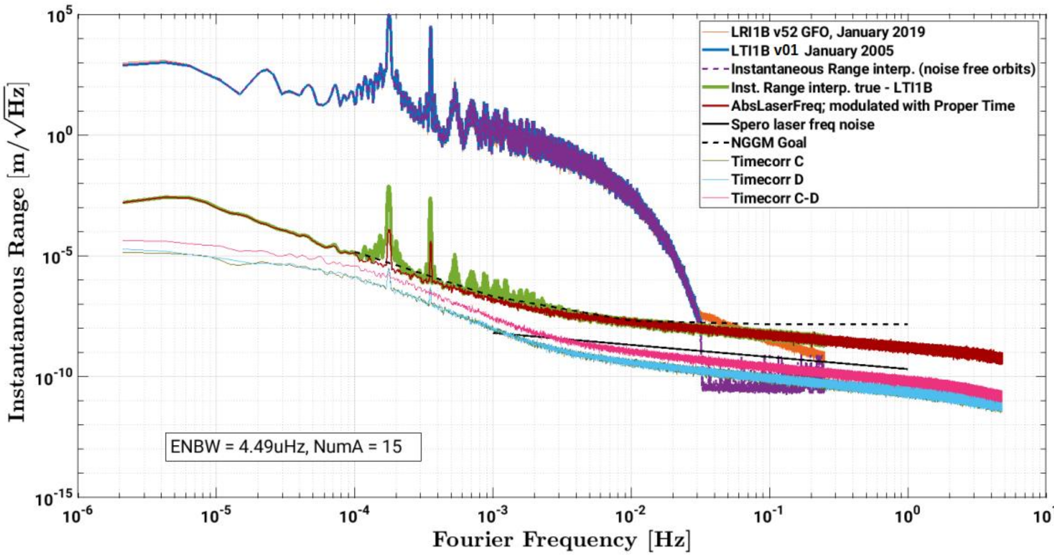

Figure 23-13: The difference between LTI1B v01, obtained from forward- and backward processing, and the orbit instantaneous range, representing the true range, is given by the green curve. As expected, this dataset is limited by the laser frequency noise at all frequencies.

Figure 23-13 shows the amplitude spectral density (ASD) for the instantaneous range of LTI1B v01 in dark blue, obtained after calculating LTI level1a and converting that to level1b using AEI GRACE-FO processing chain. As for v00, the result can be compared against the instantaneous range from orbit data (purple curve), representing the true range. The difference of both data streams is shown by the green trace. LTI1B v01 is limited by the laser frequency noise, as we can observe from the overlap with the dark red curve. This is expected, because the laser frequency noise is one of the limiting noise sources for the LTI or LRI instrument in the high frequencies (f > 30 mHz).

The green difference trace exhibits some signals at integer multiples of the orbital frequencies. Which part of the processing chain might be responsible for these features is still under investigation.

23.2.5. SUMMARY AND OUTLOOK

Within this work package we implemented a novel processing chain to simulate level0 LTI ranging data from orbit simulation inputs. The methodology was shown and explained in detail with the flowchart in Figure 23-6. The generated data is then further processed to level1a and level1b. We derived a first simple level1a and 1b product, called v00, which used a few simplifications and noise-free assumptions. Furthermore, this dataset was limited by a non-optimal interpolation method.
A more realistic dataset, v01 was provided for the progress meeting 2. We improved our interpolation method to obtain a lower noise for the orbit data and light travel times. Also, different noise models, such as USO noise, POD noise and laser frequency noise were included in the simulations.
For the next versions of the simulator, we plan to implement the missing parts from the flowchart, namely:

- Light travel time calculation between TX and RX reference points
- TTL and ARC simulation (insert offset in reference points)
- consider remaining transponder laser phase noise (due to finite gain of the transponder lock)
- use attitude quaternions and corresponding orbits in inertial frame from the mission primes
- consider atmospheric and ionospheric effects in light travel time calculation
- consider a noise model for DWS closed loop
- consider noise for FSM readout when generating pointing angle products
- consider a phase readout noise (1µcycle/√Hz)

Though the simulator was intended primarily to derive LTI level1a data, but it was already now in the early state extremely useful to better understand, validate and improve the level1 to level1b processing chain of LTI/LRI data, because this novel simulator uses a completely different approach and is not just reverting the processing steps of the existing level1a to level1b processing chain.

23.3. POINTING ANGLES FROM SYSTEM SIMULATOR

The LTI level0/l1a simulation requires satellite attitude data and corresponding orbits in Earth's cantered inertial (ECI) frame to rotate different quantities between the satellites' science reference frame (SRF) and the ECI frame. Both data streams are also necessary to compute the inter-satellite pointing angles w.r.t. the Line of Sight (LOS).

ECI orbits and attitude quaternions should come from the system simulator and be provided by the mission primes.

AEI received a first dataset from ESA generated with the system simulator of Thales Alenia Space, Italy (TASI) in May 2023, however, the attitude quaternions were not suitable for the purpose of computing inter-satellite pointing angles, since the orbit data was provided in the Earth-centered-Earth-fixed (ECF) coordinate system.

For that reason, ESA requested a second dataset from TASI, which contains attitude data and orbits in ECI frame. Finally, this data was provided for the time span of January 1st to 8th, 2002.

The new dataset was used to derive and analyse the satellites' pointing jitter. The results were presented at the Final Meeting (2023-09-27).

TASI File Versions:
TASI provided five different versions for attitude and orbit data, where they used the following abbreviations:

- MAX_397km_1D_50th: 50th percentile of atmospheric density, drag-compensation in one axis (1D)
- MAX_397km_1D: Maximal atmospheric density (MAX), drag-compensation in one axis (1D)
- MIN_397km_1D: Minimal atmospheric density (MIN), drag-compensation in one axis (1D)
- MAX_397km_3D: Maximal atmospheric density (MAX), drag-compensation in three axes (3D)
- MIN_397km_3D: Minimal atmospheric density (MIN), drag-compensation in three axes (3D)

TASI Orbit Product Structure:
The datasets included ECF and ECI orbit positions and velocities in file4_1 and file4_2 for S/C1 and S/C2, respectively. The orbit data of interest (ECI) can be extracted from column 8-13, with corresponding GPS time-tags in column 1.

TASI Attitude Product Structure:
True attitude quaternions and reconstructed (PostFacto) quaternions can be extracted from column 2-5 or 6-9 respectively, from the file3_1 or file3_2 depending on S/C1 or S/C2. GPS time-tags are available in column 1.
It should be noted that the scalar quaternion is provided in the last place (column 5 or 9), which is different to the GRACE-FO SCA1A or SCA1B files, where the scalar quaternion is provided in the first place.

AEI Data Preparation:
To use existing algorithms at AEI, the orbit data of the five different versions for S/C1 and S/C2 are re-organized into equivalent (GRACE-FO) GNI1B orbit datasets. Nominally GNI1B contains GRACE-FO CoM positions and velocities in Earth-Inertial-Frame.
Moreover, for each of the five TASI versions for S/C1 and SC2, and the provided true and reconstructed quaternions, equivalent GRACE-FO attitude datasets (SCA1B) were generated. That means, in total 20 different attitude datasets can be used to compute and analyse inter-satellite pointing angles from TASI.

Each of the 20 files show a jump in the time tags between the samples 604801 and 604802. In order to not falsify the computation of inter-satellite pointing angles, the last 60 samples (604802 to 604860) were removed, which only correspond to 1 minute of data in the 1-week long data set.

Pointing Angle Results in in Time Domain:
The results for all five TASI versions are very similar in the time domain. One example for the MAX_397_3D case of S/C1 for true and reconstructed quaternions is shown in Figure 23-14.

Yaw and pitch variations from true quaternions show a jitter of 2 µrad at an offset of 1 µrad. Reconstructed quaternions exhibit a yaw-jitter of +/- 50 µrad around zero, while pitch has an offset of 75µrad and jitters by +/-25 µrad. This pitch offset might be related to some assumptions for the orientation (consideration of camera head mounting errors) of the star cameras in TASI simulations.

Further validation and investigation of the offset is recommended in order to understand the effect.

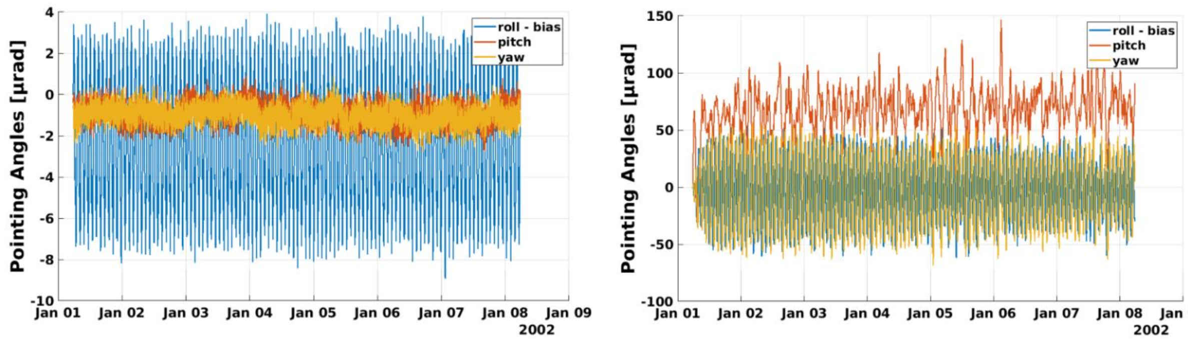

Figure 23-14: Inter-satellite pointing angles roll, pitch and yaw w.r.t. the LOS, derived from true (left) and reconstructed (right) quaternions of S/C1, version MAX_397_3D.

Pointing Angle Results in in Frequency Domain:
The three plots in Figure 23-15 show roll, pitch and yaw angles derived from the true quaternions of the version MIN_397_1D of S/C1 in blue, while other traces are the differences with all other TASI versions. The pitch variations in all versions exhibit a very similar spectrum, where differences between versions are of the order of 10%, i.e. one order of magnitude lower than the original signal for frequencies above 1e-4 Hz. The differences between the versions for roll and yaw are also minor, however, comparing MAX and MIN versions with each other show some additional tone signals in the frequency band of 1e-4 < f < 1e-3 Hz (see first and third panel in Figure 23-15). For yaw, the differences are well below the actual signal levels, while for roll the differences have a similar magnitude as the signal.

The results of reconstructed (PostFacto) quaternions in Figure 23-16 show again the signals of roll, pitch and yaw variations are higher than all the difference curves, which means all reconstructed quaternions of the different versions are very similar.

We plotted the pointing angle variations from true and reconstructed TASI quaternions together with pointing angles from GRACE-FO in Figure 23-17. These were derived from the SCA1B

dataset for the period of 1st to 8th of January 2019. The SCA1B product is a based-on sensor fusion of star camera and IMU data.
The colour scheme was chosen similarly for roll, pitch and yaw, while the darker colours show the TASI angles and the lighter colours GRACE-FO.

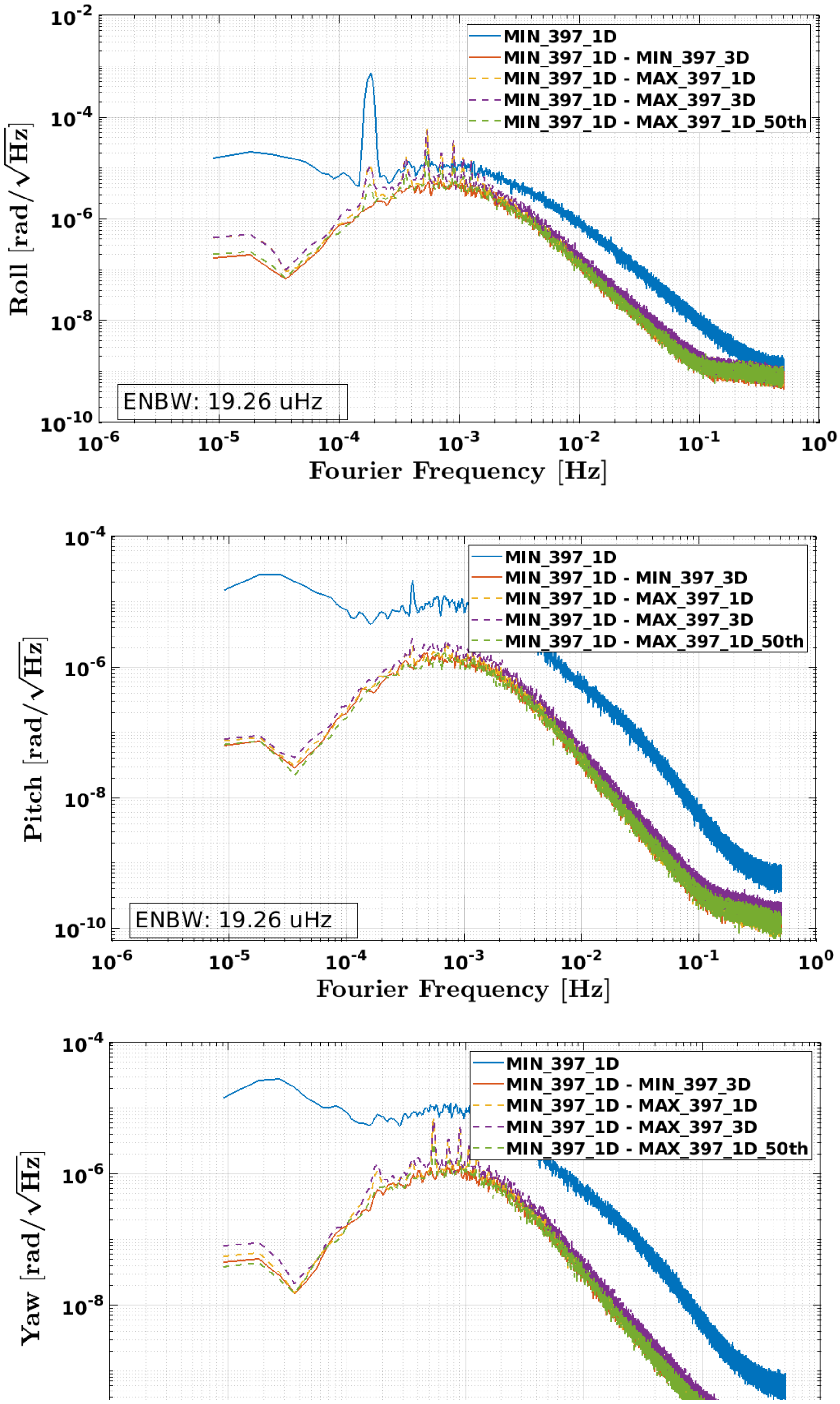

Figure 23-15: Amplitude spectral densities for roll, pitch and yaw derived from the true quaternions, and their differences between different TASI versions.

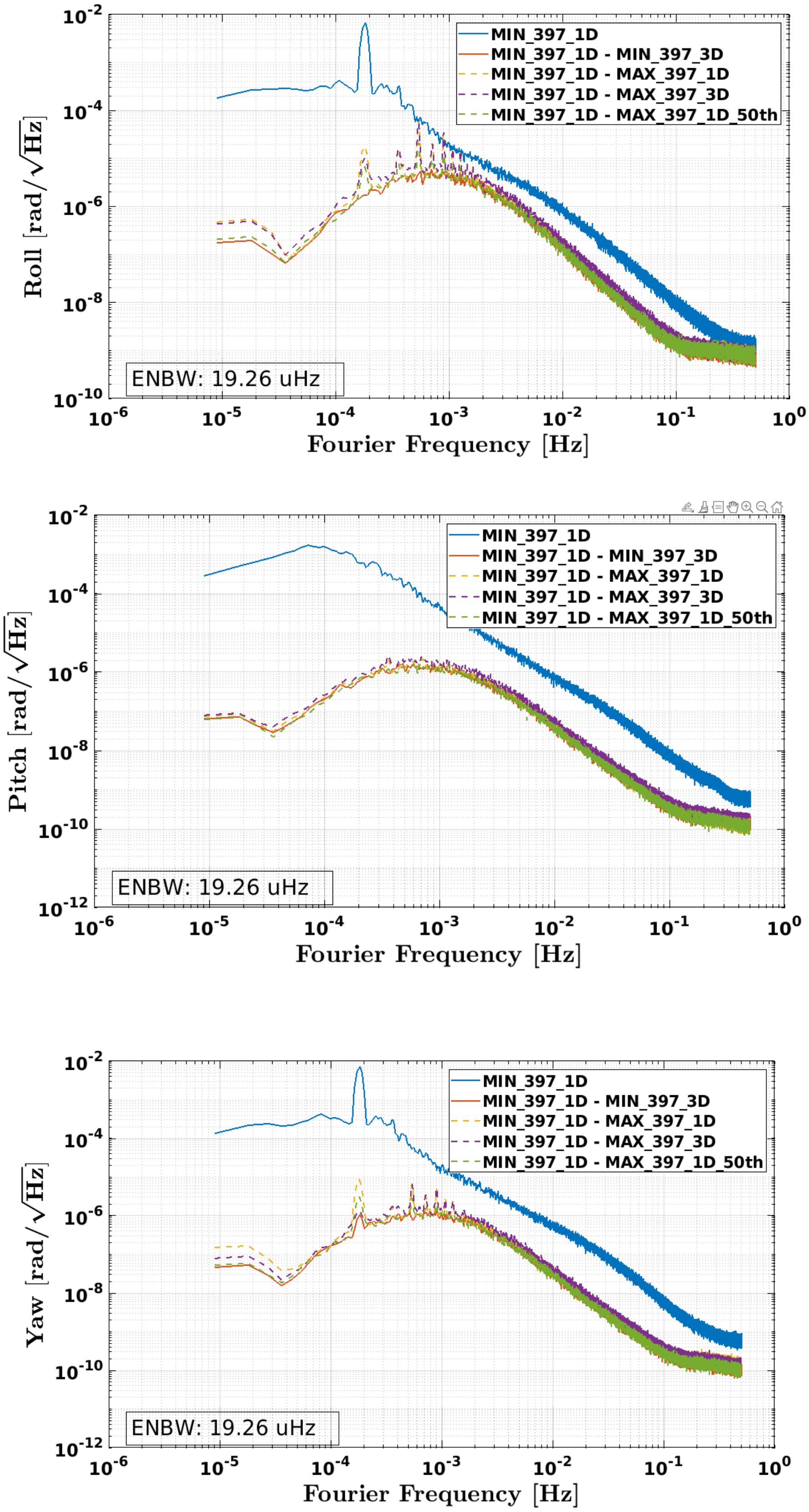

Figure 23-16: Amplitude spectral densities for roll, pitch and yaw derived from the reconstructed quaternions, and their differences between different TASI versions.

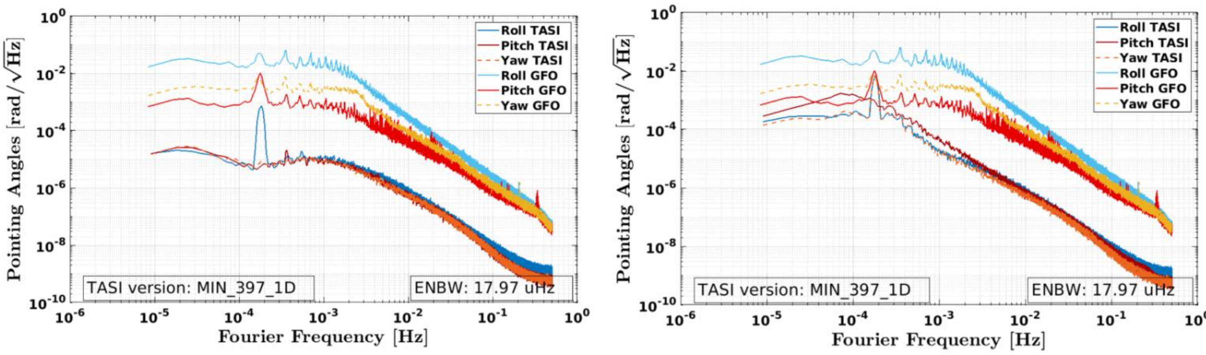

Figure 23-17: Amplitude spectral densities for roll, pitch and yaw (dark colours) derived from the true quaternions (left plot), and from reconstructed quaternions (right plot) in comparison to GRACE-FO inter-satellite pointing angles, derived from the SCA1B attitude data product for 1st to 8th of January 2019.

One can observe that the pointing angle variations from true quaternions are 2-3 orders of magnitude smaller in comparison to GRACE-FO. Also yaw and pitch angles from TASI data lack signal at 1/rev frequency.

The right panel of Figure 22-18 shows the comparison of the reconstructed quaternions with GRACE-FO results. Here the roll and pitch angle at 1/rev are only ~1 order of magnitude smaller. However, for frequencies above 1/rev, the TASI angles are two or three orders of magnitude smaller, as it is the case for the true quaternions.

Summary:
The attitude quaternions and orbits in inertial frame provided by TASI can be used to compute inter-satellite pointing angles. As expected, the reconstructed quaternions are more similar to GRACE-FO in-flight values than the true quaternions. However, for frequencies above 1/rev, the TASI pointing variations are 2-3 orders of magnitude smaller than GRACE-FO values. This might be related to an improved AOCS system or might be caused by too optimistic assumptions.

In the future, the TASI data sets might be used within the algorithm to generate LTI1B datasets. For that purpose, it would be desired to get one month +/- 1 day of attitude and orbit data in earth inertial frame. An alternative might be to estimate a model for the pointing angle variations from the spectra above and extrapolate the data to a longer span.

24. REFINED NGGM/MAGIC E2E L2 SIMULATIONS (WP1500)

24.1. SIMULATION OF 3 REFERENCE SCENARIOS AND CHECK AGAINST MRD AND MRTD REQUIREMENTS (WP1510)

In the following we investigate the retrieval performance of the double-pair scenarios 3d_409_70 (in the following denoted as sc1), 5d_397_70 (baseline scenario, in the following denoted as sc2) and 3d_402_65 (in the following denoted as sc3). Their orbital parameters are provided in Table 13-1. Note that MRTD requirements are not valid anymore, and are replaced by NGGM MRD requirements. These relate to the performance of a stand-alone NGGM satellite pair (inclined pair), whereas the MAGIC MRD requirements relate to the double-pair performance.

Table 24-1: Orbital parameters of the three reference scenarios. Note that these scenarios share the same polar pair (P1) and differ in the inclined pair (P2).

	Semi-major axis [m]	eccentricity	incl. [°]	asc. node [°]	arg.of perigee [°]	mean anomaly [°]
P1-A	6871210.979	0.0016	89	359.98	27.78	331.51
P1-B	6871208.124	0.0016	89	359.98	29.17	331.95
P2-A sc1 (3d_409_70)	6791878.839	0.0008	70	3.97	5.10	354.17
P2-B sc1 (3d_409_70)	6791876.502	0.0008	70	3.97	8.12	353.02
P2-A sc2 (5d_397_70)	6780418.955	0.0008	70	2.34	5.46	353.82
P2-B sc2 (5d_397_70)	6780416.219	0.0008	70	2.34	8.46	352.68
P2-A sc3 (3d_402_65)	6785066.223	0.0005	65	2.36	358.13	1.15
P2-B sc3 (3d_402_65)	6785063.648	0.0005	65	2.36	3.14	358.00

Simulation setup

The total simulation period is set to 01.01.-03.09.2002, for which we derive two consecutive 31-day, 9 consecutive 7-day, 13 consecutive 5-day and 22 consecutive 3-day solutions. The maximum resolution of the 31- and 7-day solutions is set to 120, while the 5- and 3-day solutions are resolved up to d/o 100 and 70, respectively, due to sparse spatial coverage.

We differentiate between full-noise and product-noise (resp. instruments-only) scenarios which differ by the inclusion of the time-variable components of the Earth’s gravity field (not present in product-noise scenario). In terms of instruments, we consider the two most dominant error contributors – the ACC and the LRI. The respective noise specifications for the polar pair in terms of product noise are as follows:

$$acc_{polar} = \sqrt{2} \cdot 10^{-10} \sqrt{1 + \frac{0.005\ Hz}{f}} \left[\frac{m}{s^2\sqrt{Hz}}\right]$$

$$lri_{polar} = \sqrt{\left(L \cdot \frac{10^{-15}}{\sqrt{f}}\right)^2 + \left(\frac{10^{-12}}{f^2}\right)^2} \left[\frac{m}{\sqrt{Hz}}\right]$$

The respective noise specifications for the inclined pair in terms of product noise are as follows:

$$acc_{inclined} = 10^{-11} \sqrt{\left(\frac{10^{-3}\ Hz}{f}\right)^2 \Big/ \left(\left(\frac{10^{-5}\ Hz}{f}\right)^2 + 1\right) + 1 + \left(\frac{f}{10^{-1} Hz}\right)^4} \left[\frac{m}{s^2\sqrt{Hz}}\right]$$

$$lti_{inclined} = L \cdot 2 \cdot 10^{-13} \sqrt{1 + \left(\frac{10\ mHz}{f}\right)^2} \sqrt{1 + \left(\frac{1\ mHz}{f}\right)^2} \left[\frac{m}{\sqrt{Hz}}\right]$$

Note that the term L in the equations above denotes the inter-satellite distance in meters.
We also consider tone errors based on version 1.4 of the SRD in both the full-noise as well as in the product-noise scenarios. The applied specifications are given Table 13-2. Note that they are given as combination of the LRI and ACC components. The tone errors are introduced into the simulation environment as described in the e2.motion study. It is noted that tailored stochastic modelling is applied in order to mitigate the impact of the tone errors as far as possible.

Table 24-2: Tone errors

multiple of orbital frequency	amplitude [μm]
1	100
2	20
3	4

In terms of time-variable gravity signal, we consider tidal and non-tidal mass variations. For the tidal signal, the eight principal tidal constituents of the GOT4.7 model (Ray 2013) are used as the true signal and the corresponding de-aliasing error is simulated by setting up reference observations based on EOT11a (Savchenko and Bosch 2012). For the non-tidal signal, the Updated ESA Earth System Model (Dobslaw et al. 2014) consisting of the AOHIS components is used, and the AO de-aliasing error is simulated by setting up reference observations based on the DEAL product superimposed with AOerr. For the representation of the static gravity field GOCO05s (Mayer-Gürr et al., 2015) is used both for the true as well as for the reference observations.

Impact and treatment of tone errors

First, we investigate the impact of the tone errors on the performance of the performance of gravity retrieval. For this matter, we consider three different approaches. In the first, denoted as no, no tone errors are considered. In the second, denoted as w0, tone errors are considered as given in Table 13-2, but are not explicitly stochastically modelled. The third approach (w1) is equivalent to w0, but this time the tone errors are explicitly considered in the stochastic modelling. Note that tone errors are considered for both satellite pairs in the same manner.

Stochastic modelling is introduced on the basis of digital filters (Siemes 2008) both for the “regular” instrument noise as well as for the instrument noise combined with tone errors. In this approach, a cascade of digital filters is fitted in such a way that its frequency response matches the noise ASD as closely as possible. In a following step, the filter coefficients are transformed to arc-wise VCMs (or, respectively, their inverse), which are then used in the gravity field adjustment. While fitting a filter cascade to the respective combined ACC and LRI is comparatively simple, the task becomes more complicated when tone errors come into play. To treat them, notch filters are applied which should ideally fully negate the noise contribution at exclusively the frequencies in question. However, in practice a trade-off must be made between the magnitude and the “sharpness” of the notch filter, as either the filter or the derived VCM (or weighting matrix, respectively) may quickly become numerically unstable and thus degrade the gravity retrieval performance. To illustrate this issue, we examine an additional weighting scenario, w2, as shown in Figure 24-1. The scenario w2 features a near-optimal (i.e. narrow, high-amplitude) frequency response, while w1 seemingly features broader peaks.

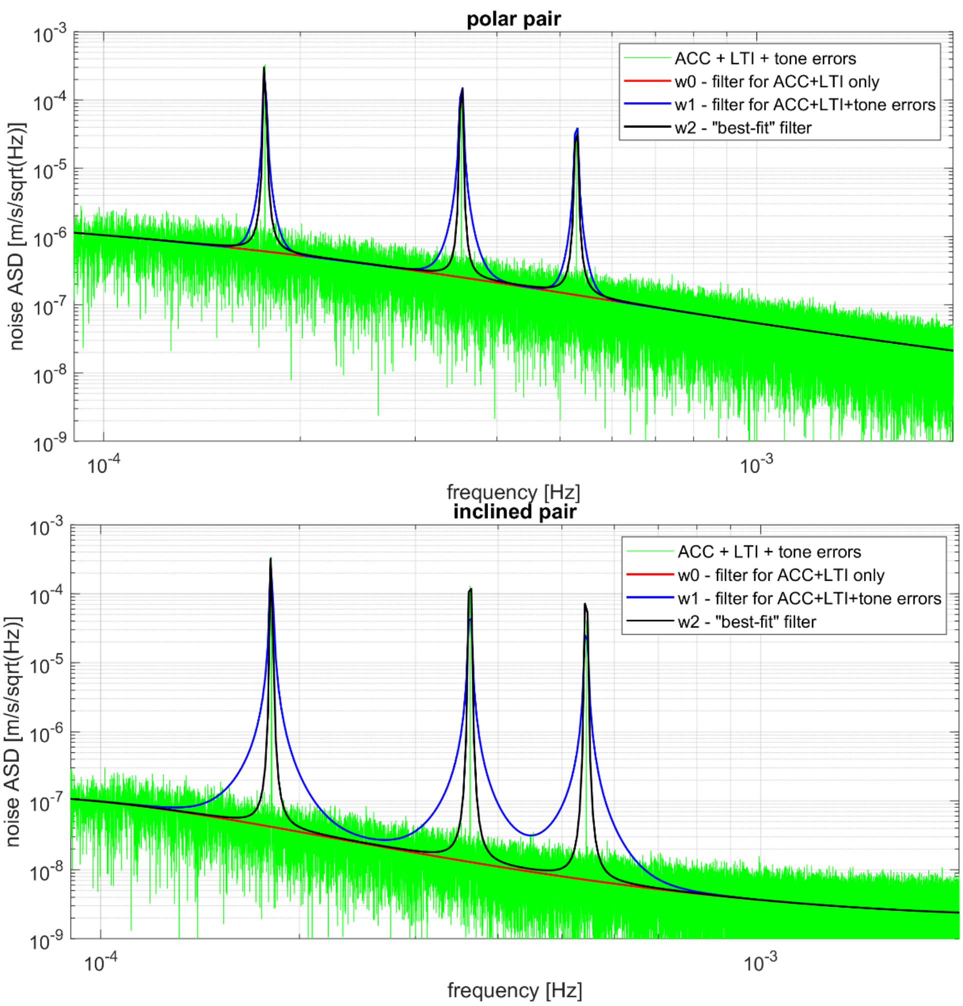

Figure 24-1: Frequency responses of two investigated filter cascades including various notch filters for polar-pair (top) and inclined-pair (bottom) product noise.

Figure 24-2 representatively shows the retrieval performance of the four above described processing approaches for a 31-day full-noise and product-noise case based on sc2 (the relative behaviour remains unaffected when altering retrieval period and observation).

It is evident that the largest variations are found in the product-noise case. The best performance is reached with scenario no, whereas w0 results in a major degradation of the retrieval performance. The difference between these two scenarios represents the impact of tone errors when left untreated. On the other hand, w1 yields a performance which is only slightly degraded in comparison to no, thus clearly demonstrating the added value of tone error weighting. The performance of w2, however, is of greatest interest. While the underlying stochastic modelling initially seemed to be suited best (as demonstrated in Figure 24-1), it evidently yields a worse performance than w1, hereby indicating the numerical instability of the weighting matrices derived from the underlying very narrow, high-amplitude notch filters.

In case of a full-noise-based retrieval scenario, the differences between the weighting scenarios are much smaller, albeit still notable in the low-degree spectrum (below d/o ~10). Here, no and w0 perform close to identically. The reason for this can be found in the way the tone errors and the temporal gravity signal map into the observations. As can be seen in Figure 24-3, the temporal signal fully covers the regular instrument noise in the pre-fit residuals. The tone errors at 2 and 3 cpr are superimposed in the same manner, and the only remaining tone error contribution stems from 1 cpr. Evidently, this component's overall amplitude is reduced to that of the time-variable signal (in a relative sense) and its contribution to the following gravity field adjustment is minor. Adversely, the worst retrieval performance in the full-noise case is reached when applying w1. The main deterioration can be found below d/o 4 and constitutes up to a factor of 2. While w2 does indeed perform better than no and w0, some minor degradations below d/o 4 can nevertheless be seen. This behaviour can be explained with the fact that w1 doesn't exclusively "hit" the frequencies at which the tone errors occur, but also affects some of the nearby frequencies containing temporal signal, thus resulting in undesirable interactions. In w2, although proven unstable, this interaction seems to be reduced.

For the sake of completeness, the impact of the different weighting strategies is also depicted in Figure 24-4. In the ideal case of a filter that exclusively eliminates signal at x/rev, only the zonals should be affected. Here, it is evident that the notch filters affect the entire spectrum up to d/o 3 in case of w1, while the impact of w2 to non-zonals is reduced, thus demonstrating the impact of the underling notch filter "width".

In light of the fact that a product-noise-only retrieval is merely a hypothetical scenario for the time being and a missions' true observations correspond to the full-noise scenario, it is imperative to focus on obtaining the best-possible performance for the latter. Here, it is clearly demonstrated that for the most part the tone errors are superimposed by the temporal gravity signal, and the remaining contribution barely affects the adjustment process and the resulting gravity solution. Attempting to further minimize the already nearly non-existent impact by stochastically modelling the tone errors, however, degrades the low degrees of the solutions. It is therefore recommended to proceed with the w0 approach for the full-noise cases, and, since only one version of stochastic modelling is forseen for the L2 processing chain, by extension also for the product-noise cases. The approaches w1 and w2 shall be retained as back-up scheme for the case that significantly improved de-aliasing models should become available at some point, as this would in turn make the tone errors more prominent. Consequently, the product noise cases are additionally also processed on the basis of the w1 approach.

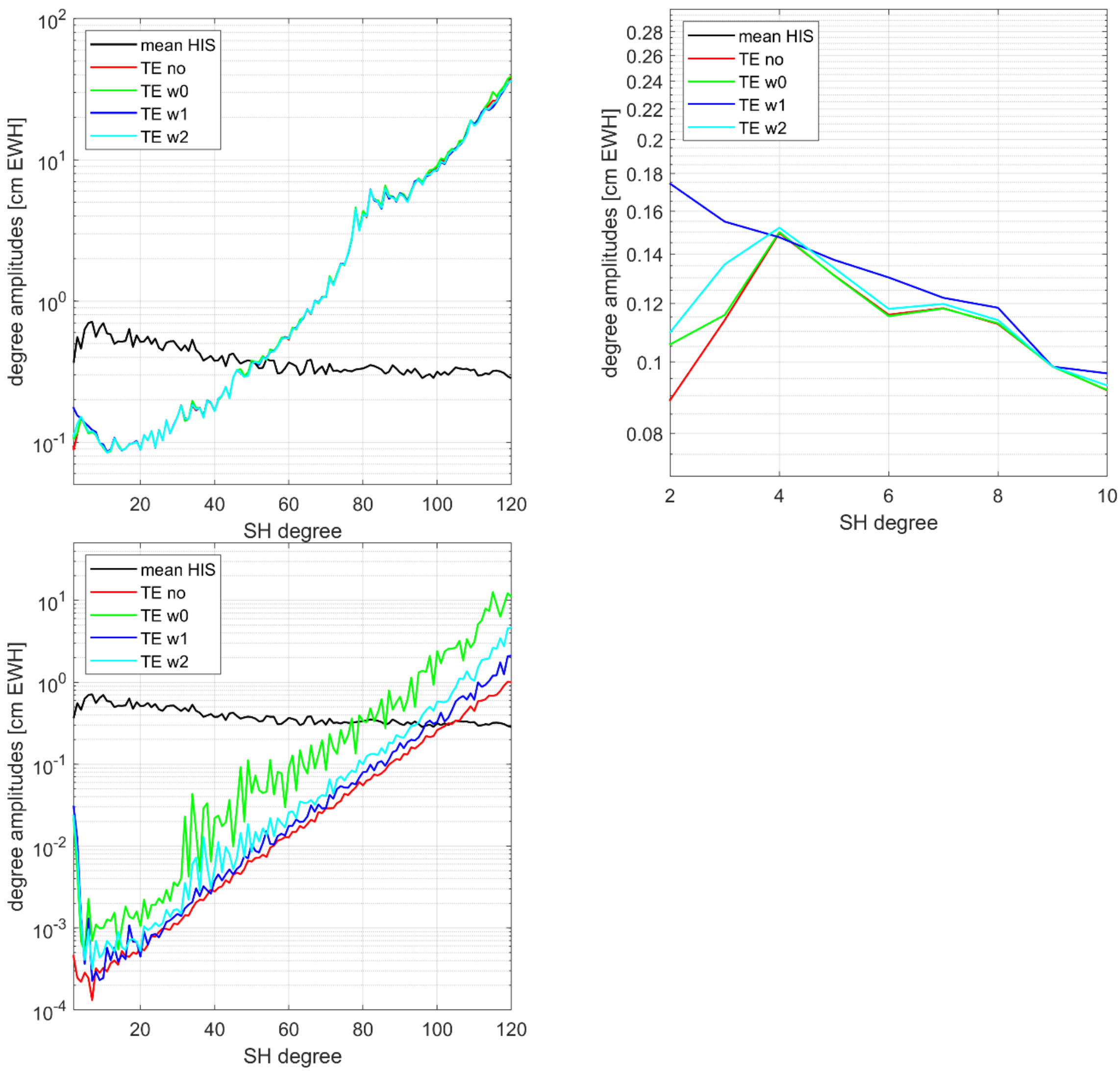

Figure 24-2: Comparison between the performance of tone error weighting scenarios *no*, *w0*, *w1* and *w2* for *sc2* considering full-noise (top) and product noise (bottom) in terms of error degree amplitudes. The plot on the right is a zoom-in to the low degrees of the full-noise error degree amplitudes.

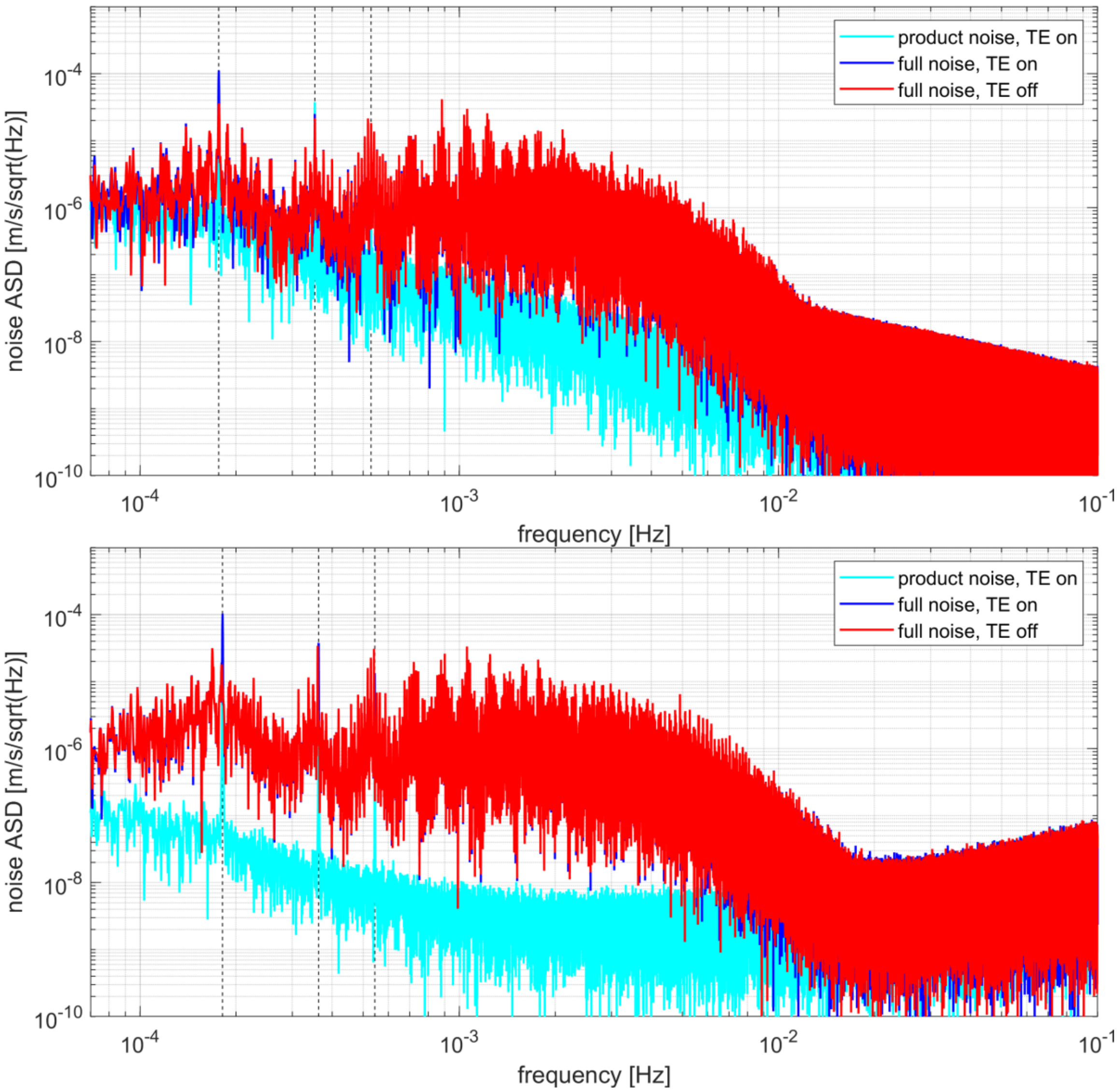

Figure 24-3: Pre-fit residuals for sc2 (top – polar pair, bottom – inclined pair) accumulated over 31 days of observations. The vertical dashed lines represent multiples of the orbital frequency at which the tone errors occur.

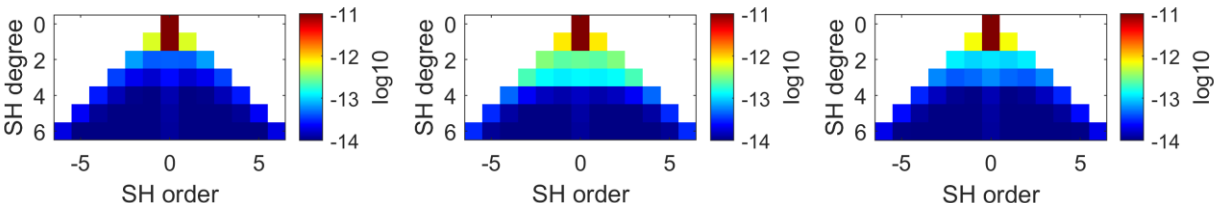

Figure 24-4: Formal errors of the weighting scenarios *no* (left), *w1* (centre) and *w2* (right) discussed in Figure 24-2, zoomed in to the spectrum up to d/o 6.

Impact of spectral leakage

In the following, we quantify the impact of the spectral leakage in short-term solutions. This effect arises predominantly in the short-term solutions, as these are generally estimated to a lower maximum d/o than the monthly solution in order to prevent spatial aliasing, while the input signal is always taken up to d/o 120. In Figure 24-5 we present a 3-day full-noise retrieval scenario on the basis of *sc2*, where the input signal is taken either up to d/o 120 or to the maximum of the solution. It is evident that the effects of spectral leakage are to a wide extent covered by temporal aliasing errors. They only become notable once the spatial resolution of the retrieved gravity product is reduced substantially, e.g. to d/o 15 in the shown example. They are, however, limited to the highest degrees of the solution. Also, it should be stated that such a retrieval is purely artificial, as in reality the solution will always be parametrized up to a significantly higher d/o (e.g., 3-day double-pair solutions are solved up to d/o 70, see red curve in Figure 24-5), and the issue is thus of no further concern.

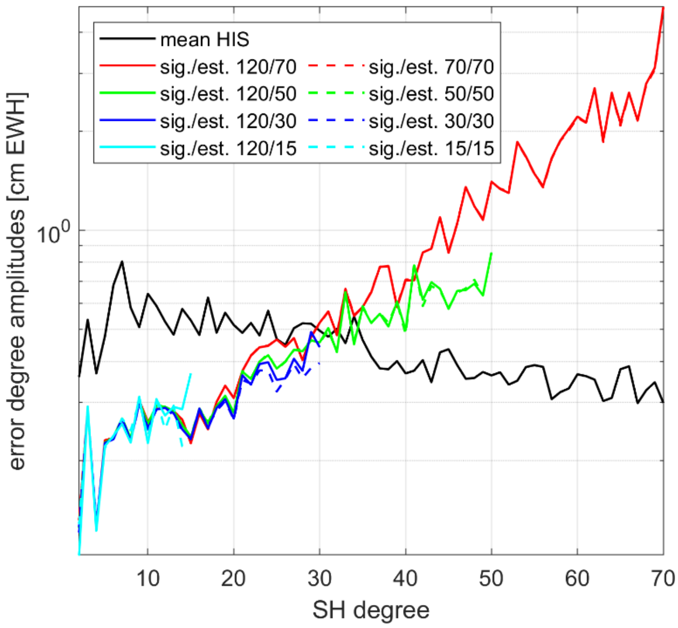

Figure 24-5: Impact of spectral leakage in a 3-day full-noise retrieval scenario. The results represented by the solid lines denote scenarios which include input signal up to d/o 120 and are parametrized up to a lower d/o, while in the scenarios denoted with the dashed lines the d/o of input and parametrized signal is equal.

Simulation results

The simulation results for sc1, sc2 and sc3 are provided in terms of the mean of degree amplitudes of the retrieval errors of each retrieval period. The results of the full-noise scenarios are given in Figure 24-6 and those of the product-noise scenarios in Figure 24-7. As discussed in the previous subsection, no explicit stochastic modelling of tone errors is applied.

In case of full-noise it is evident that sc2 shows the worst performance for a 3-day retrieval, but conversely the best one in case of the 5-day solutions (albeit the gain over the other two scenarios is minimal). The performance of the three scenarios is near-identical in the 7-day case. Lastly, the 31-day retrieval reveals that sc2 suffers a degradation around d/o 80. This behaviour is not present in either sc1 or sc3, nor can it be observed for any other retrieval interval. However, it should be noted that the SNR is 1 around d/o 50 for all three scenarios, and thus, considering that post-processing, i.e. filtering, shall be applied, this issue is of minor concern.

The increased variations between the scenarios over short retrieval intervals can be attributed to the underlying spatio-temporal sampling of the time-variable gravity signal. Due to the short time scales and, consequently, the sparser ground track coverage, fewer of the disturbing signal components, i.e. de-aliasing errors, are averaged out than in longer-term solutions. Evidently, the observation geometry of sc3 is best suited for the recovery of three-daily gravity fields and has less of an impact the longer observations are accumulated.

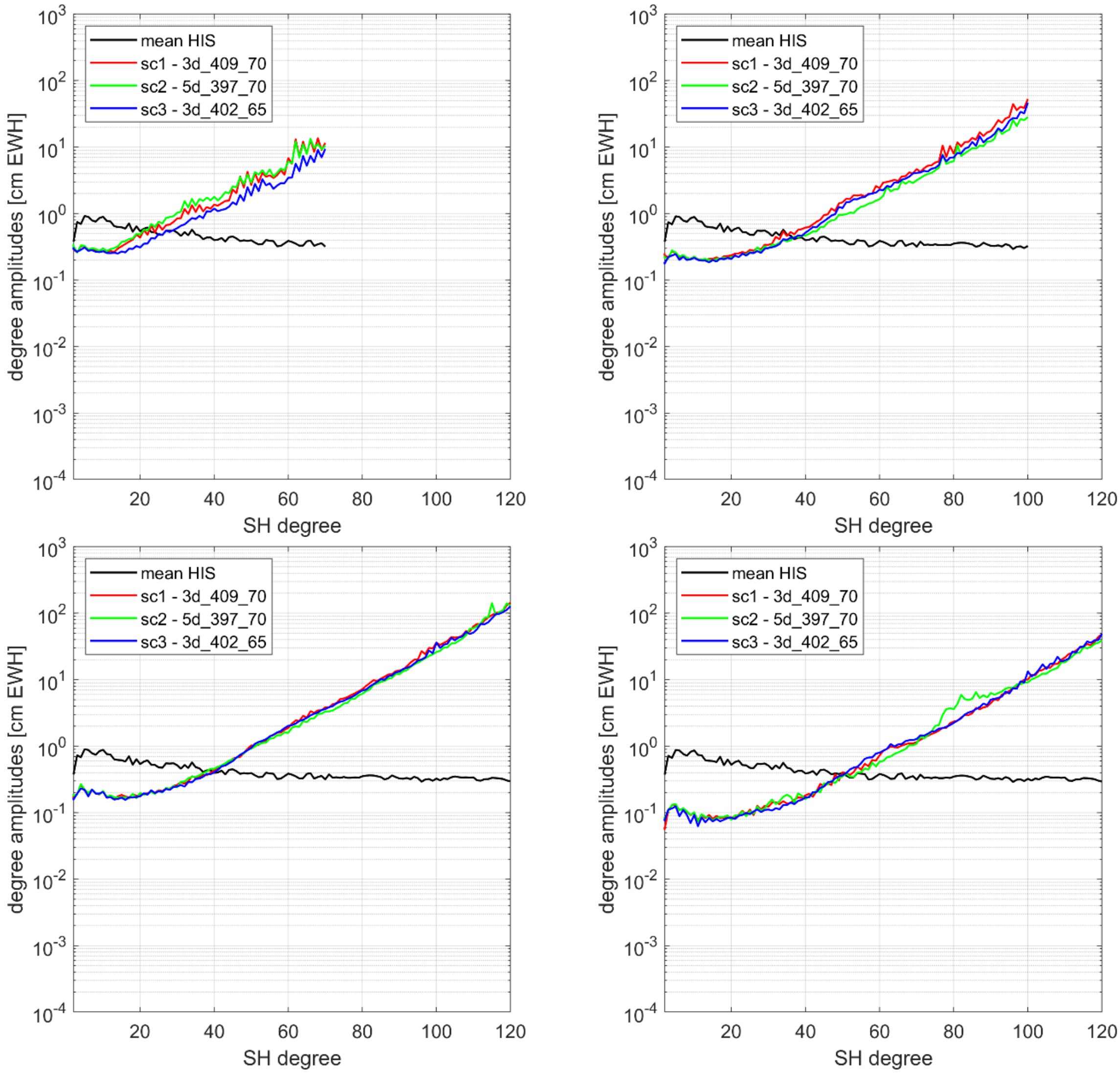

Figure 24-6: Full-noise simulations with *w0*-type stochastic modelling; mean of degree amplitudes of the retrieval errors of sc1-3 for a 3- (top left), 5- (top right), 7- (bottom left) and 31-day (bottom right) retrieval.

In case of product-noise simulations the presented mean error degree amplitudes feature major fluctuations between subsequent spectral bands. This issue can be attributed entirely to the impact of tone errors, which show their full impact with the w0 processing approach (c.f. previous subsection). Thus, a detailed interpretation with respect to the impact of observation geometry of either scenario proves difficult, though in general it can be stated that the retrieval performance of 3-, 5- and 7-day solutions is very similar in all cases. On the other hand, the 31-day solutions might indicate that sc2 is more strongly subjected to tone-error-induced fluctuations in the medium degree range than sc1 and sc2.

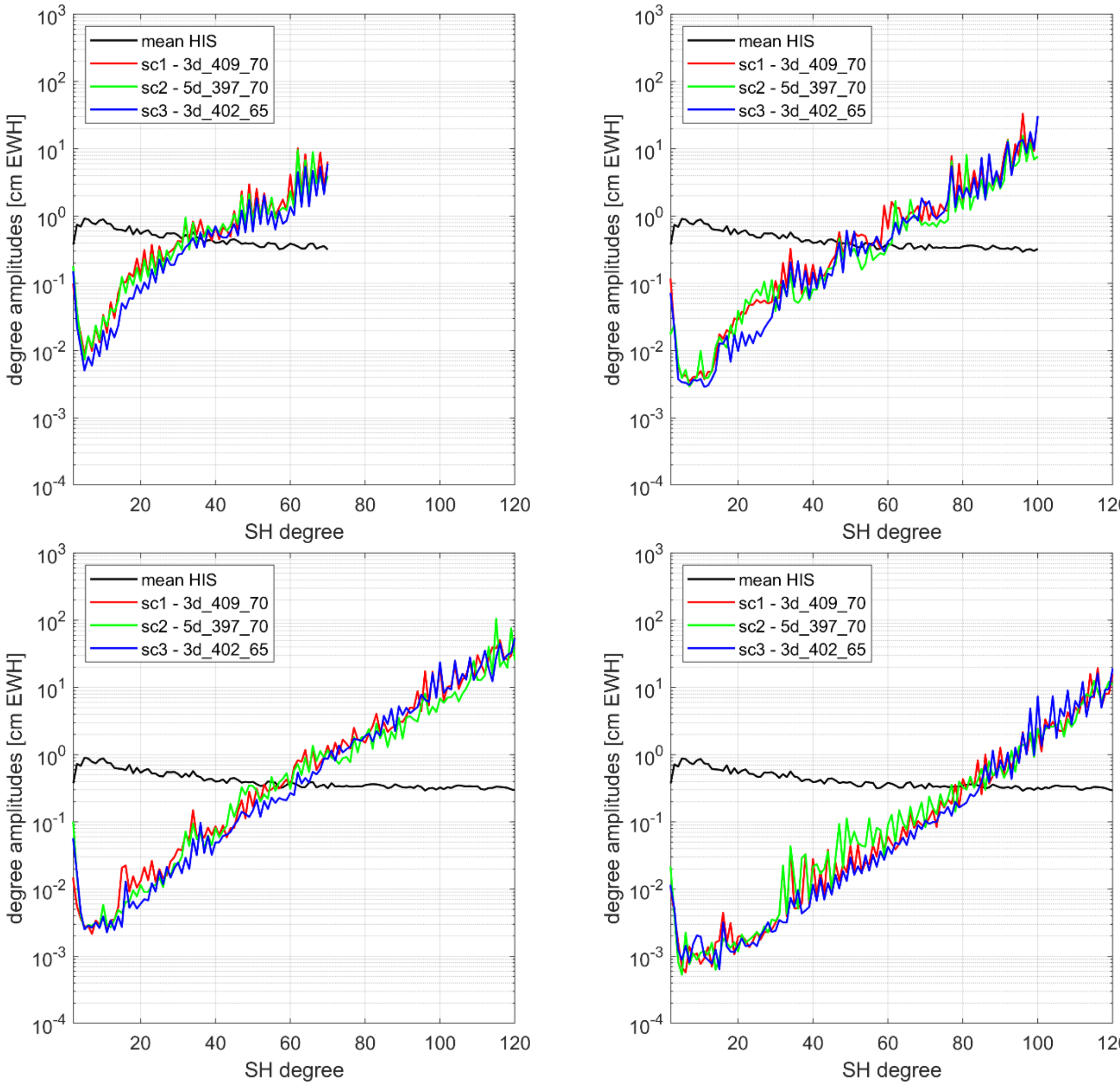

Figure 24-7: Product-noise-only simulations with *w0*-type stochastic modelling; mean of degree amplitudes of the retrieval errors of sc1-3 for a 3- (top left), 5- (top right), 7- (bottom left) and 31-day (bottom right) retrieval.

Furthermore, the error degree amplitudes discussed above are shown in a cumulative representation in Figure 24-8 and Figure 24-9 and compared to the requirements defined in the MRD. We note that since these requirements are only given for 31-day solutions, they are adjusted for an n-day retrieval through scaling with sqrt(31/n).

With regard to the full-noise scenario it is evident that the threshold requirements and, by extension, also the target requirements are missed by all scenarios over any given retrieval period length.

In case of product-noise retrieval, all threshold requirements, and by extension also all target requirements, are missed by either scenario except by sc3 at d/o 25 in case of w0-type processing. In case of the 5-day retrieval, all target requirements are missed by either scenario, but the threshold requirements for d/o 25 and 50 are fulfilled. The same is true for the 7-day retrieval, with the exception that sc2 now also fulfils the threshold requirement for d/o 100.

Lastly, the 31-day retrieval seems to satisfy the threshold requirements for all scenarios, while sc3 even fulfils the target requirements for d/o 25 and 50. It is once again emphasized that these results aren't fully representative and the performance can be expected to improve drastically if w1-type processing is applied. This is also clearly demonstrated in Figure 24-10 and Figure 24-11 Here, the MRD threshold requirements are satisfied independently of the retrieval period, and in case of 31-day retrieval even the MRD target requirements at d/o 50 are satisfied. These results clearly suggest the application of w1 over w0 should the tone errors become more prominent, i.e. if greatly improved de-aliasing models should become available in the future.

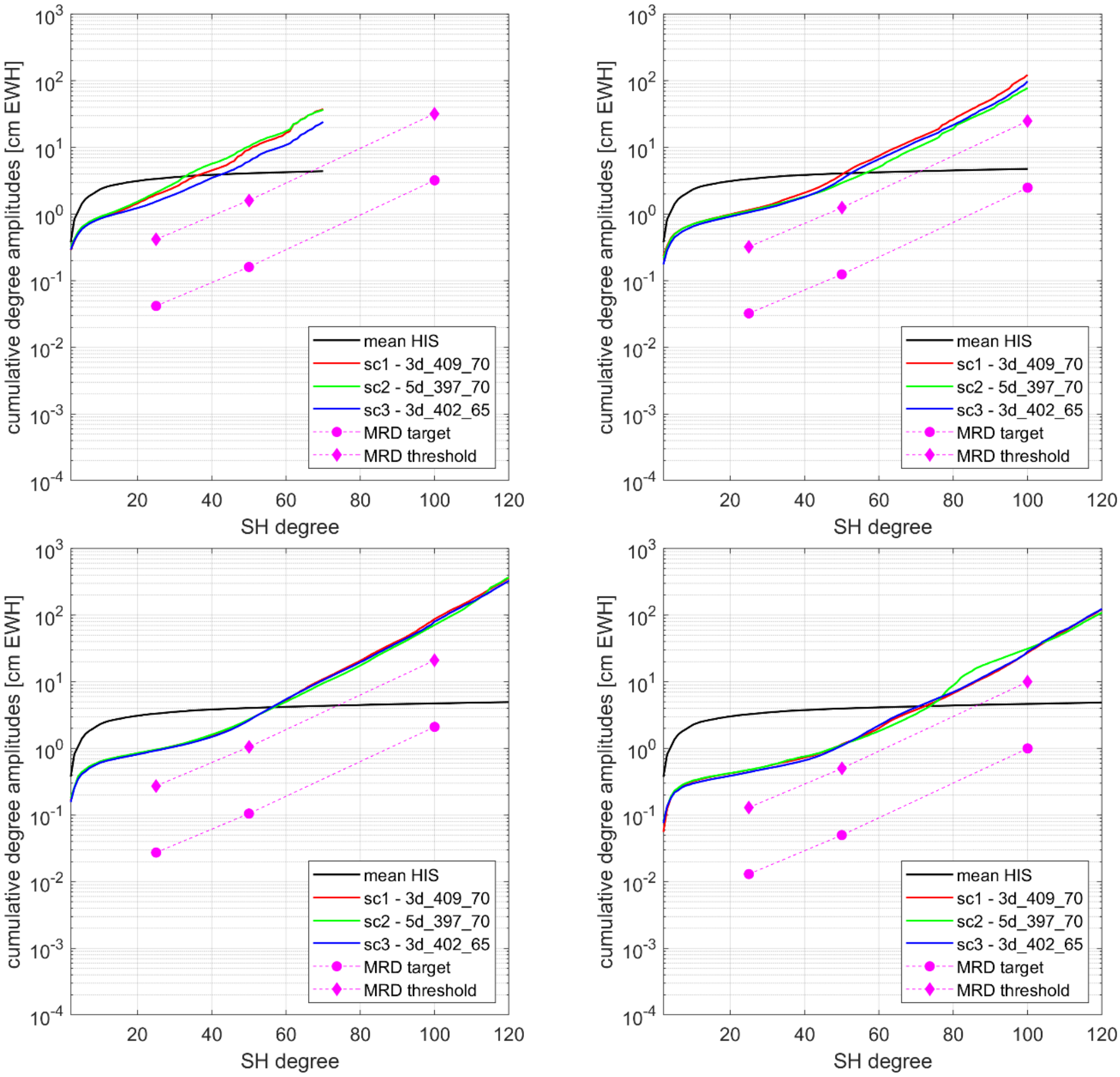

Figure 24-8: Full-noise simulations with *w0*-type stochastic modelling; mean of cumulative degree amplitudes of the retrieval errors of sc1-3 for a 3- (top left), 5- (top right), 7- (bottom left) and 31-day (bottom right) retrieval compared to MAGIC MRD requirements (note that the short-term requirements, i.e. for 3-5 days, are plotted in the 7d-case)

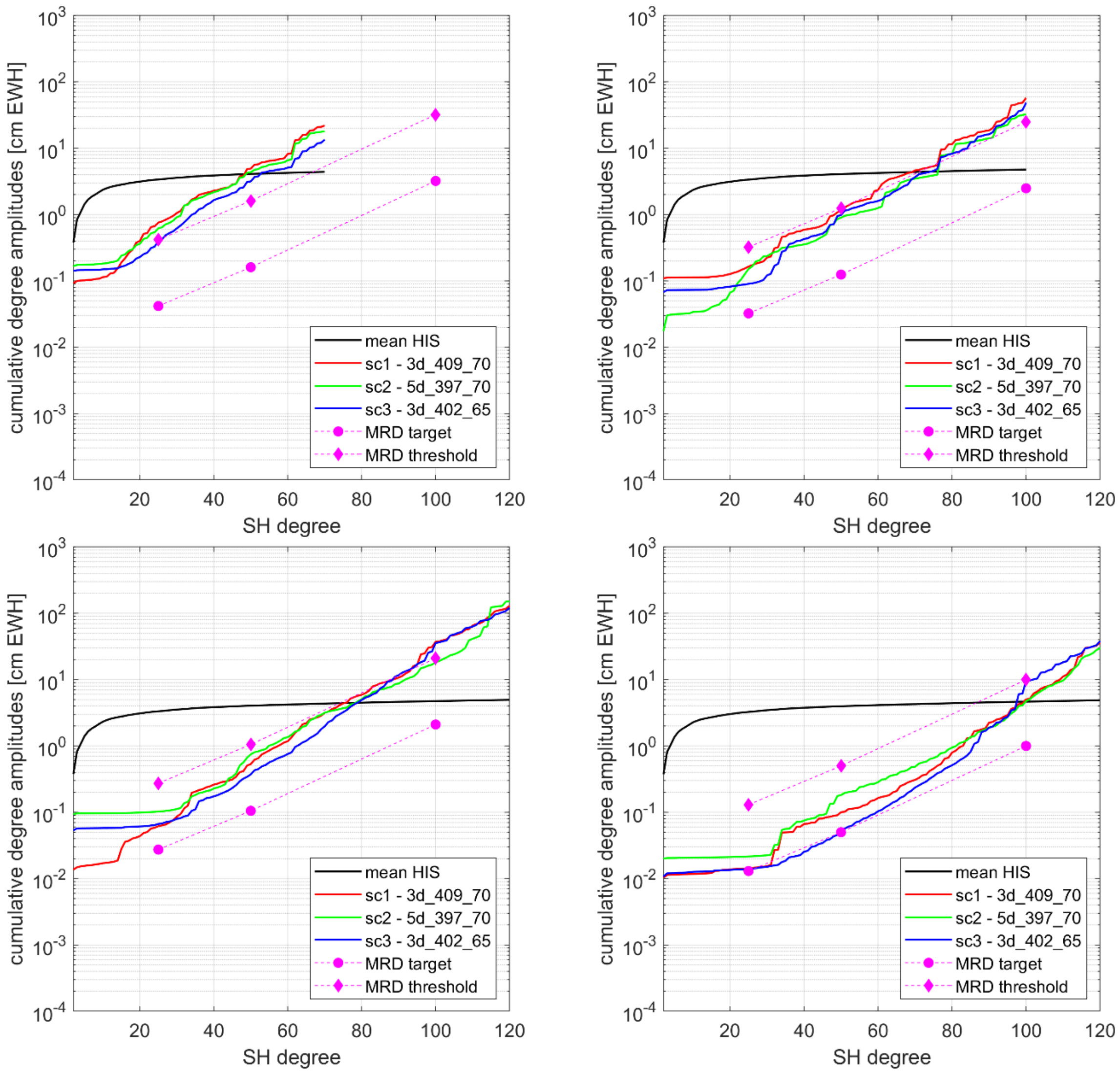

Figure 24-9: Product-noise-only simulations with *w0*-type stochastic modelling; mean of cumulative degree amplitudes of the retrieval errors of sc1-3 for a 3- (top left), 5- (top right), 7- (bottom left) and 31-day (bottom right) retrieval compared to MAGIC MRD requirements (note that the short-term requirements, i.e. for 3-5 days, are plotted in the 7d-case)

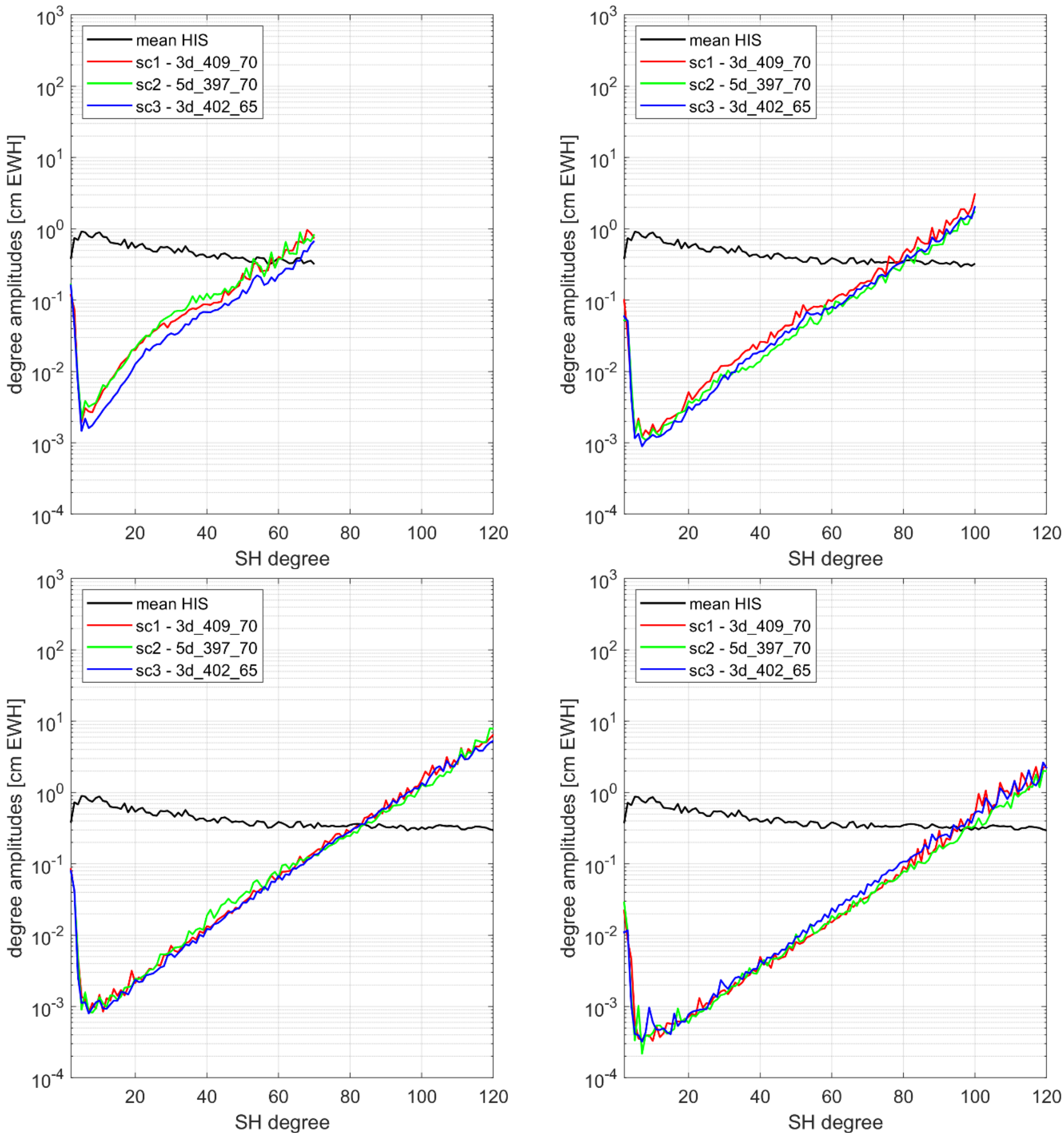

Figure 24-10: Product-noise-only simulations with *w1*-type stochastic modelling; mean of degree amplitudes of the retrieval errors of sc1-3 for a 3- (top left), 5- (top right), 7- (bottom left) and 31-day (bottom right) retrieval.

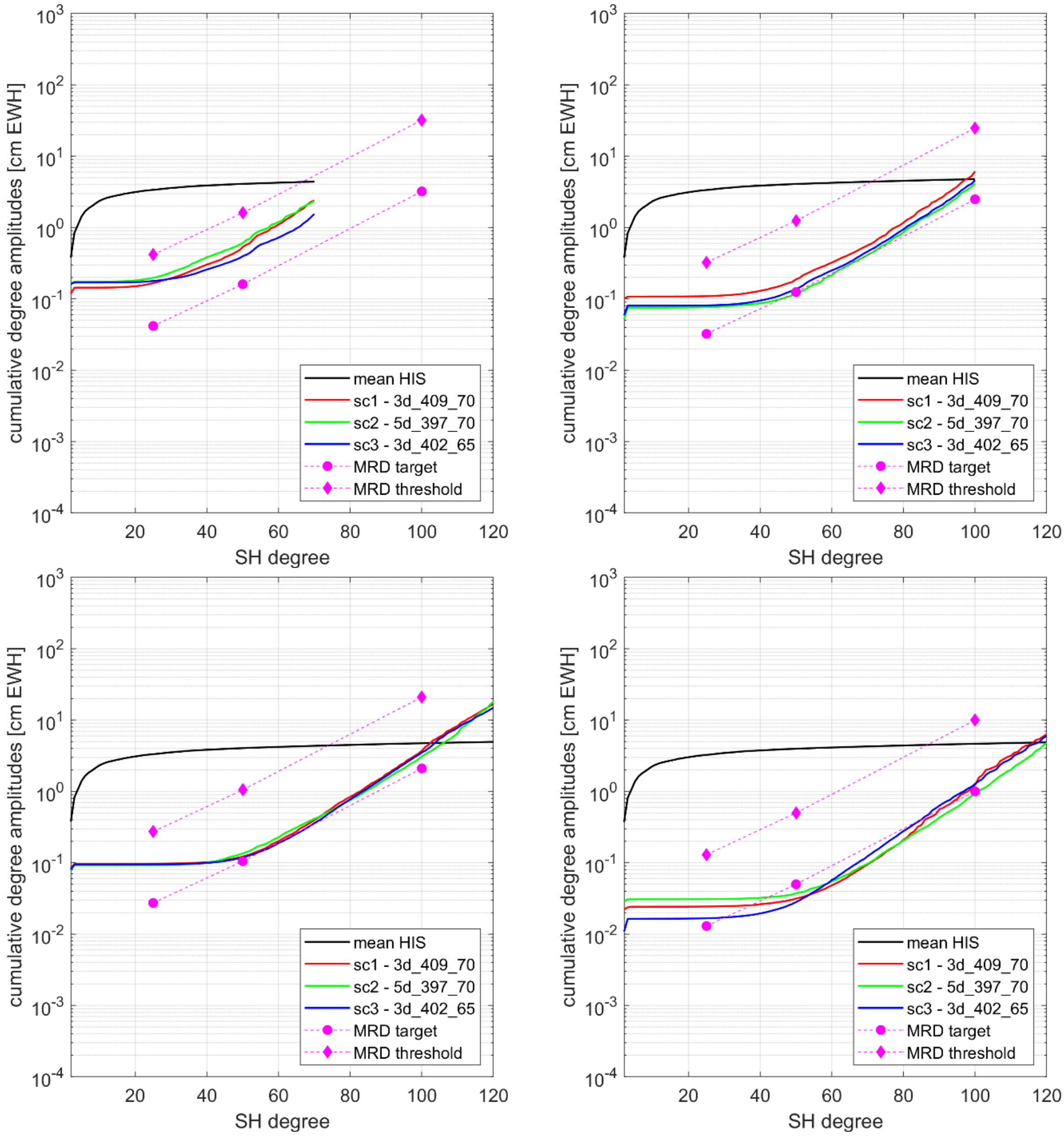

Figure 24-11: Product-noise-only simulations with *w1*-type stochastic modelling; mean of cumulative degree amplitudes of the retrieval errors of sc1-3 for a 3- (top left), 5- (top right), 7- (bottom left) and 31-day (bottom right) retrieval compared to MAGIC MRD requirements (note that the short-term requirements, i.e. for 3-5 days, are plotted in the 7d-case)

24.1.1. INFLUENCE OF TONE ERRORS (GFZ)

As part of the tone-error analysis, GFZ was requested to investigate the influence of tone errors. This investigation was done for the double-pair baseline scenario. Full-noise simulations were carried out for scenarios with and without tone-errors included in the instrument noise and for each scenario we performed the simulations with and without stochastic modelling. The tone-errors have been described by TUM in Section 24.1 and these same tone errors were used by GFZ.

The four scenarios include:

- 'tone, no stoch': Tone errors are applied but stochastic modelling, tailored to the instrument, is not done. A single RMS value is calculated by an orbital fit, and this value is placed on the main diagonal of the weighting matrix. For the polar pair with tone errors, this value is: 0.171. For the inclined pair with tone errors, this value is: 0.178.
- 'no tone, no stoch': Tone errors are not applied and, similar to 'tone, no stoch', stochastic modelling, tailored to the instrument, is not done and a single RMS value is calculated via orbital fit which is then placed on the main diagonal of the weighting matrix. For the polar pair without tone errors, this value is 0.166. For the inclined pair without tone errors, this value is 0.174.
- 'tone, stoch': Tone errors are applied and stochastic modelling, tailored to the instruments, is done. A full (and not just diagonal) weighting matrix, fitted to the noise specifications of the instrument, is applied.
- 'no tone, stoch': Tone errors are not applied and stochastic modelling, tailored to the instruments are done. A full (and not just diagonal) weighting matrix, fitted to the noise specifications of the instrument, is applied.

The degree variance residuals for these four scenarios are shown in Figure 24-12.

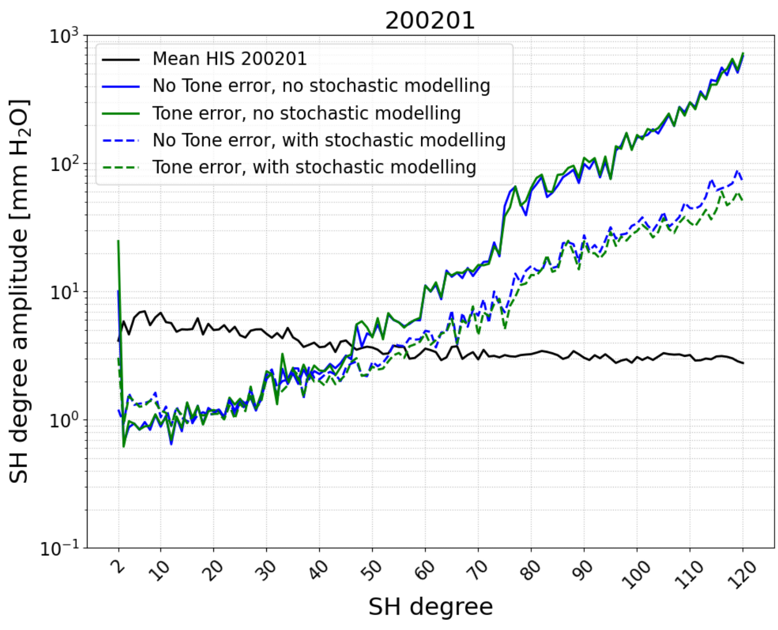

Figure 24-12 Full noise simulations for scenarios with and without tone-errors and with and without stochastic modelling.

For those scenarios in which stochastic modelling was not done, the effect of the tone errors can only be seen for degree-2 amplitudes (i.e., errors are larger for degree 2 when comparing tone errors (solid green) to no-tone error scenarios (solid blue)).

For scenarios in which stochastic modelling was done, the overall differences are still small, and only degree-2 amplitudes differ significantly. As in the no-stochastic modelling scenario, tone-errors seem to produce larger residuals for degree 2.

To investigate the increased errors for d/o 2, the effect of weighting the individual components of the double pair solution was investigated. The low-low satellite component's relative weight was increased from 5e5 to 5e6 and also decreased from 5e5 to 5e4. In addition, the relative weight of the polar component of the bender normal equation solution was increased by factors of 2 and 4. Results are shown in Figure 24-12 from which the following can be concluded:

Errors decrease when the low-low observation weight is increased from 5e5 to 5e6 (solid green line in Figure 24-13). Decreasing to low-low observation component's weight, however, yields larger errors.

When, in addition to the increased low-low observation weighting, the relative weight of the polar pair component is increased by a factor of 2, the error decreases further. Increasing the polar pair component by a factor of 4, however, does not further reduce errors for d/o 2 (refer to the right of Figure 24-13)

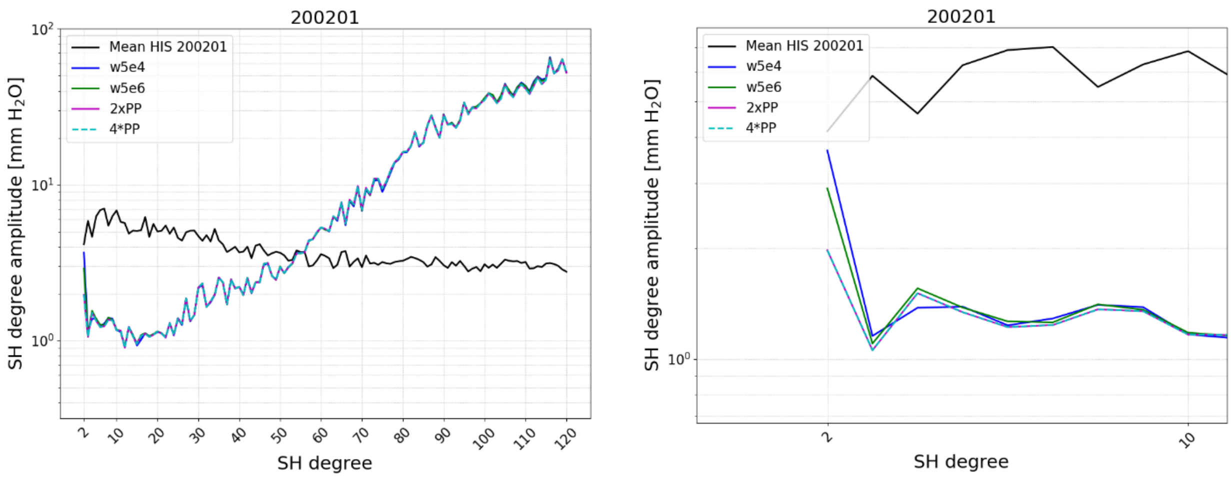

Figure 24-13 Right: Error degree variances for relative low-low satellite weightings of 5e4 and 5e6 and polar pair relative weightings of 2 and 4. Left: Zoomed in view of lower degree value range.

At request, the tone-error simulations were also performed for the inclined pair alone. In Figure 24-14 a comparison is shown between the double pair and the inclined-only solutions.

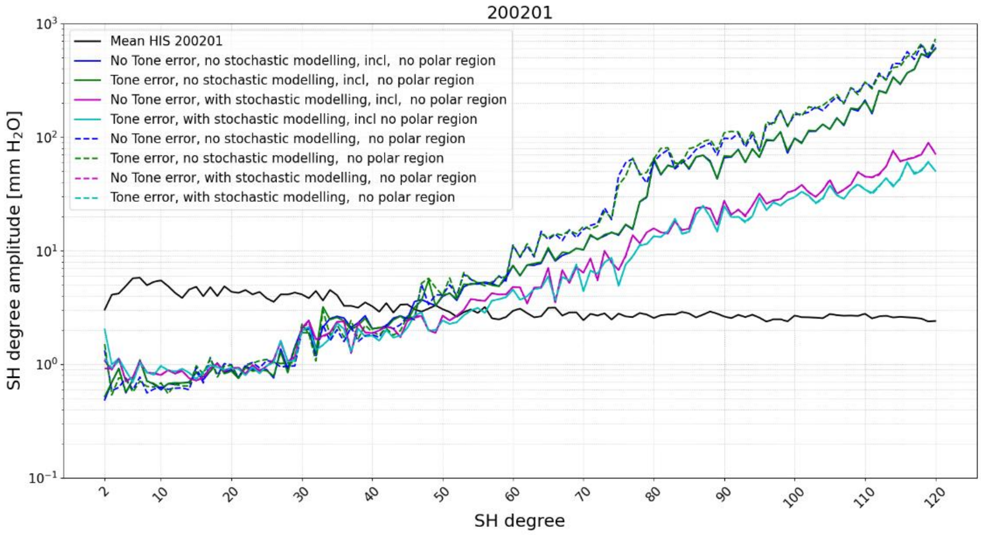

Figure 24-14 Inclined-only vs double pair solutions where the polar cap has been excluded

In Figure 24-14, solutions for the double pair scenario are given by the dashed lines and solutions for the inclined-only scenario are given by the solid lines. All solutions exclude the polar cap and the inclined pair only solutions have been regularised by a factor of 1e22. For a detailed description of the regularisation procedure and how the polar caps are excluded, the reader is referred to Section 24.4 (i.e., WP 1531).

Due to the exclusion of the polar caps, lower orders have been omitted and the error residuals for d/o are therefore reduced when comparing the double pair solutions, shown in Figure 24-14, with those shown in Figure 24-12.

Inclined-only results, in which stochastic modelling was applied, agree with the double pair solutions: The dashed and solid curves for both magenta (no tone error with stochastic modelling) and cyan (tone error with stochastic modelling) are similar. The triangle plots for the inclined-only C/S coefficient errors, are shown in Figure 24-15.

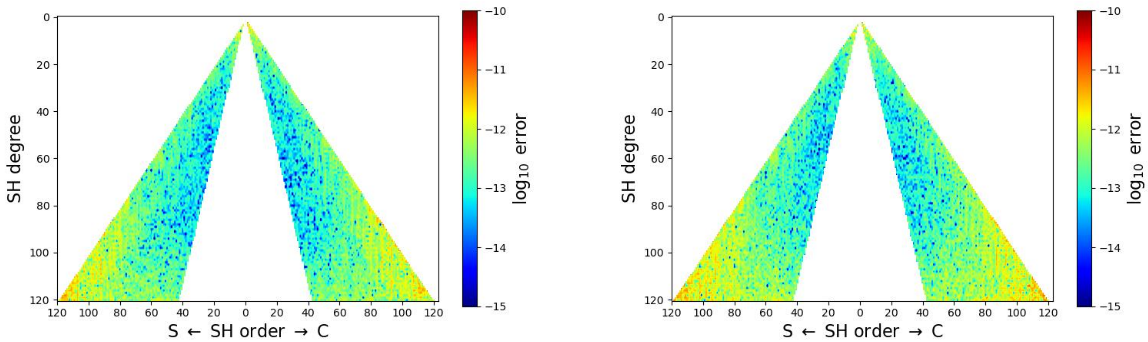

Figure 24-15 Left: No Tone errors and stochastic modelling. Right: Solutions including tone errors with stochastic modelling.

The left triangle shows slightly smaller errors for the scenario in which tone-errors were included. This is most likely due to stochastic modelling that could be improved for the scenario that does not include tone errors.

24.2. REFINED ANALYSIS OF PRR BASELINE SCENARIO AND GENERATION OF L2 AND L3 PRODUCTS (WP1520)

In the following, simulation results obtained on the basis of product-noise time series provided by TASI are presented for a 5-day P2-only retrieval. The retrieval is carried out for a product-noise-only and full-noise case. The product noise time series represent various levels of assumed drag compensation (either in 1D or 3D) under assumption of minimum and maximum level of atmospheric drag. The corresponding ASDs are presented in Figure 24-16. The figure also shows the ADS of the observed time-variable gravity signal used in full-noise simulations. It is clear that the time-variable gravity signal fully superimposes the product noise. The results of the full-noise simulations can therefore be expected to feature a near-identical performance.

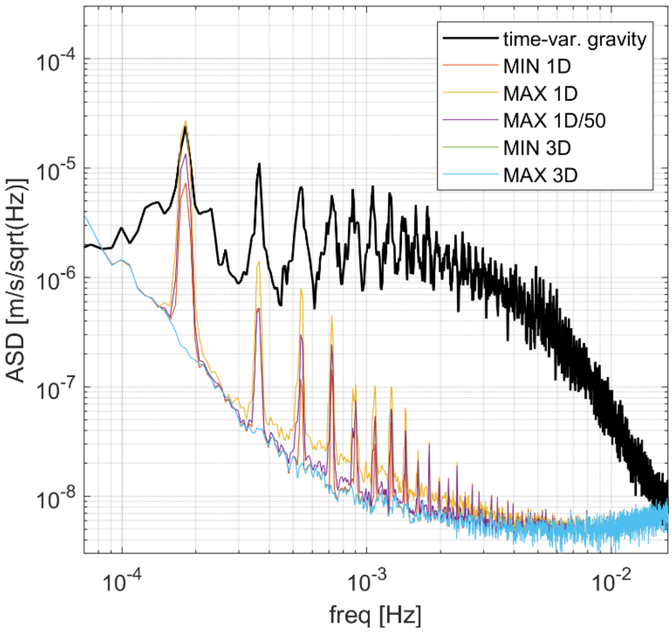

Figure 24-16 Left: ASDs of PRR noise scenarios.

The retrieval errors are presented in Figure 24-17. As expected, the level of drag compensation only notably affects the retrieval performance once temporal gravity signal is disregarded. Here, the induced tone errors in case of the 1D-compensation lead to a degradation of certain spectral bands. Once the temporal gravity signal is present, however, the retrieval performance is dictated by temporal aliasing errors, and the observation errors stemming the drag are of no further importance.

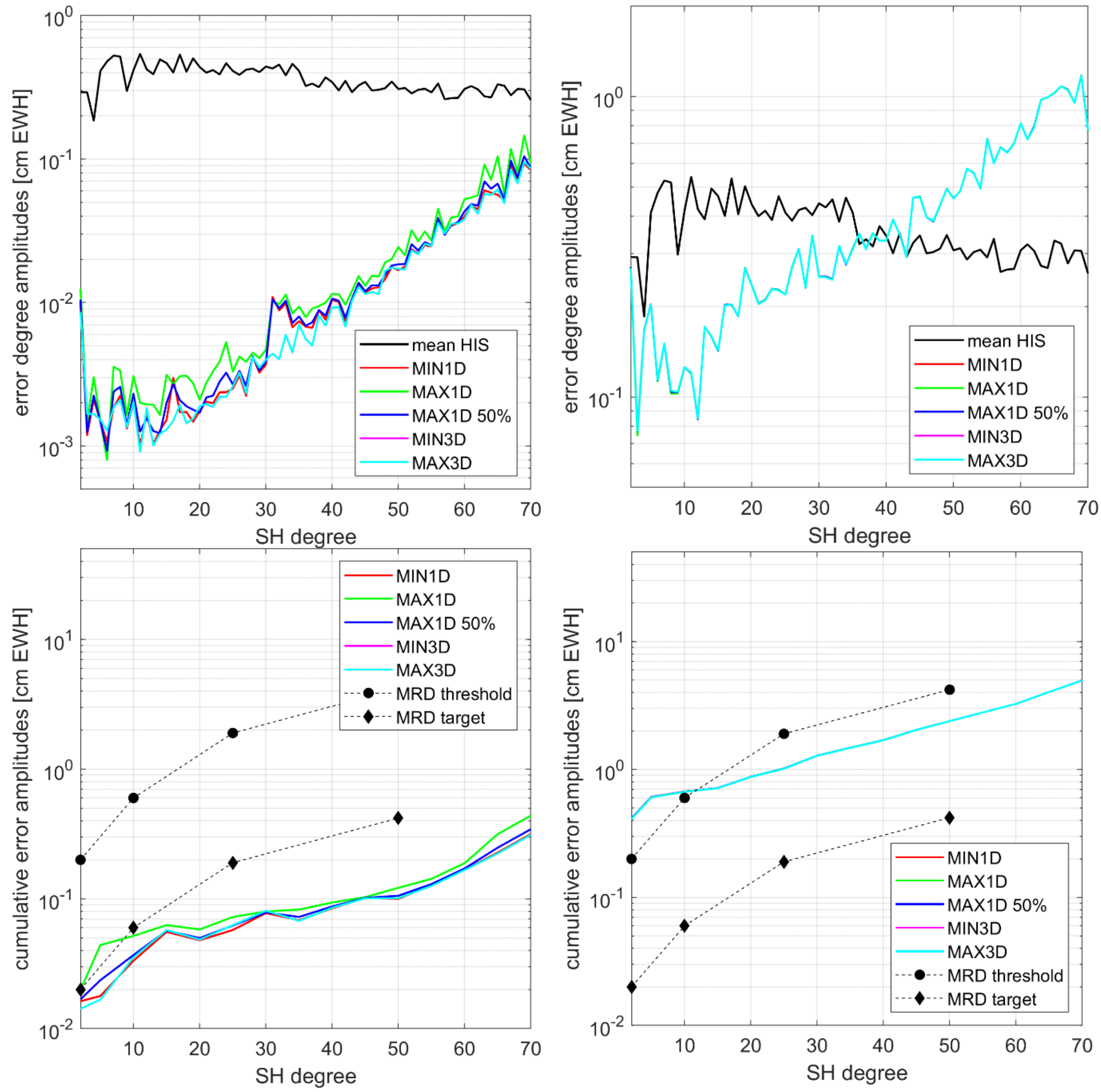

Figure 24-17 Left: Retrieval errors of product-noise-only (left) and full-noise simulation scenarios (right) in terms of degree amplitudes (top row) and cumulative errors calculated within observation-covered regions (bottom row). The cumulative errors are compared with MRD target and threshold requirements.

24.3. INCLINED-PAIR ANALYSIS OF BASELINE SCENARIO - TUM (WP1530)

In the following we investigate the performance of solutions based on the stand-alone inclined pair (p2) of the baseline scenario (sc2). The simulation setup here is analogous to the double-pair setup described in section 24.1. However, 3-day solutions are not computed due to severely lacking global observation coverage, and the resolution of the 5-day and 7-day solutions is set to d/o 70 and d/o 100 for the same reason. In order to account for the lack of observations in the polar regions, a spherical cap regularization (Metzler and Pail 2005) is applied with a regularization factor (i.e. weight) of 0.01cm geoid, as it has been determined to perform optimally during Phase A.

Impact and treatment of tone errors

Analogously to the double-pair case, we first investigate the impact of tone errors. Note that the w2 approach is disregarded this time, and evaluations are only carried out for the approaches no (no tone errors considered), w0 (tone errors considered without explicit stochastic modelling) and w1 (tone errors considered with explicit stochastic modelling). Looking at the pre-fit residuals in Figure 24-3, it can be expected that the three approaches will behave in a similar manner for the double-pair.

This expectation is confirmed by the results depicted in Figure 24-18. Once again, a near-identical performance of no and w0 can be observed independently of the underlying retrieval interval in full-noise simulations. Deviations of the w1 approach to the other two of up to a factor 2 can also be observed in the lowest degrees here. It is further notable that the retrieval performance of p2-based solutions is extremely similar to their double-pair based counterparts. This is in line with the findings of the Phase A study where it was shown that the inclined pair provides the major contribution to the double-pair solutions in the areas that it covers.

Also in the product-noise simulations the same relative behaviour can be observed as in case of the double pair. A severe performance degradation can be established in w0 with regard to the nominal no scenario. Again, the deteriorations can to a wide extend be remedied with the w1 approach.

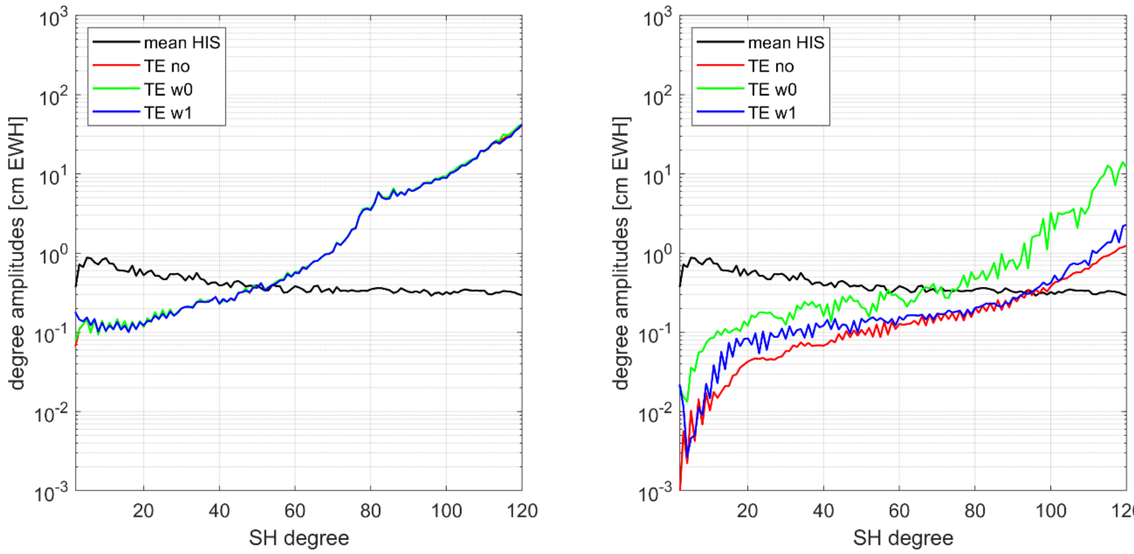

Figure 24-18: Performance comparison of tone error weighting scenarios *no*, *w0*, *w1* and *w2* for a stand-alone p2 solution considering full-noise (left) and product-noise (right) in terms of error degree amplitudes.

Simulation results

The simulation results for the p2-based retrieval scenarios are shown in Figure 24-19. For the processing of the p2-based gravity retrieval, the w0 approach is chosen with the same reasoning as for the double-pair constellation.
As already discussed in the previous subchapter, the depicted error degree amplitudes are very similar to the ones obtained on the basis of double-pair observations, as the inclined pair is the main driver of the double pair's performance.

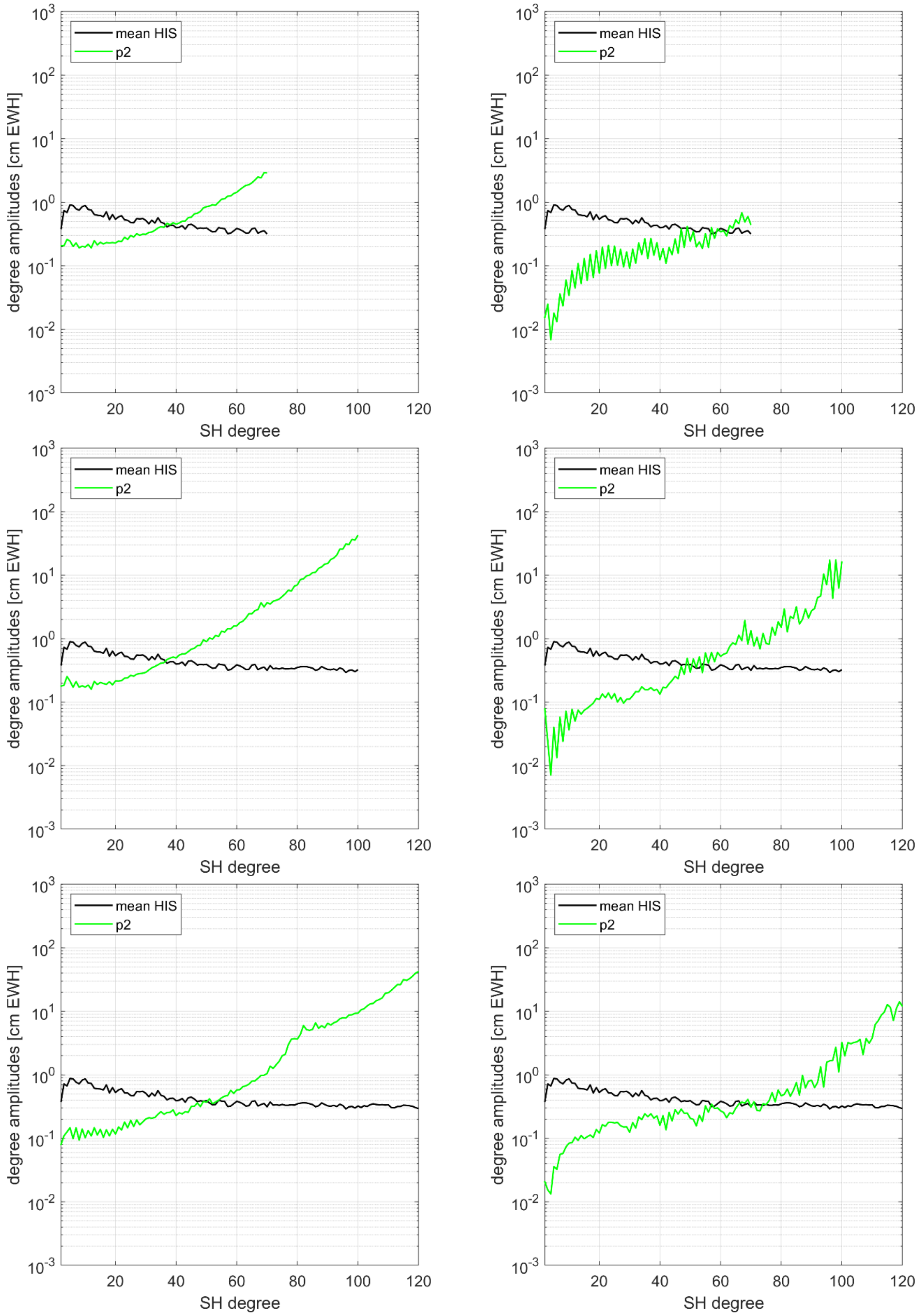

Figure 24-19: Full-noise (left) and product-noise simulations (right); mean of degree amplitudes of the retrieval errors based on stand-alone p2 for a 5- (top row), 7- (centre row) and 31-day (bottom row) retrieval.

However, a notable difference with respect to the double-pair sc2 can be found in the absolute values of the product noise error degree amplitudes. Here, a strong increase of the error curve can be observed in the low-degree range, followed by a flattening in the medium-degree spectrum. This behaviour can be attributed to the impact of the so-called polar gap wedge, which arises from the lack of observations in the polar regions and the resulting degradation of (near-)zonal coefficients (c.f. Figure 24-20). In order to circumvent the impact of the wedge, the maximum affected SH order m_{max} (per degree n) can be determined by applying the rule-of-thumb formula derived in v Gelderen and Koop (1997):

$$m_{max} = \left|\frac{\pi}{2} - i\right| n,$$

with i being the inclination of p2. All coefficients of the order below or equal m_{max} rounded to the nearest higher integer can then be removed and the amplitudes recomputed. However, in order to allow for a fair comparison, a degree-wise normalization with $\sqrt{1/(2n - 2m_{max})}$ must then be applied to account for the missing coefficients, thus converting degree amplitudes to degree RMS. The results provided exemplarily for the 31-day product-noise retrieval in Figure 24-20 show a drastic increase in solution quality up to d/o 80 where evidently the polar gap wedge was the main driving force. Nevertheless, the large fluctuations between subsequent SH degrees confirm that also here the impact of the tone errors is predominant. Overall, it can be concluded that in the produt-noise case the retrieval performance in the low- to medium degree range is significantly better than may be initially assumed. In case a fair comparison to a single-polar- or double-pair-based retrieval is desired, the existence of the polar gap wedge should always be taken into account and treated accordingly.

Finally, the stand-alone p2 simulation results are evaluated on the basis of cumulative degree amplitudes which are compared to the NGGM MRD requirements. As opposed to the MAGIC MRD requirements, these requirements are adjusted to the presence of a single inclined satellite pair and consider the lack of observations in high latitudes. Note that the 7-day solutions are compared against the short-term time scale requirements.

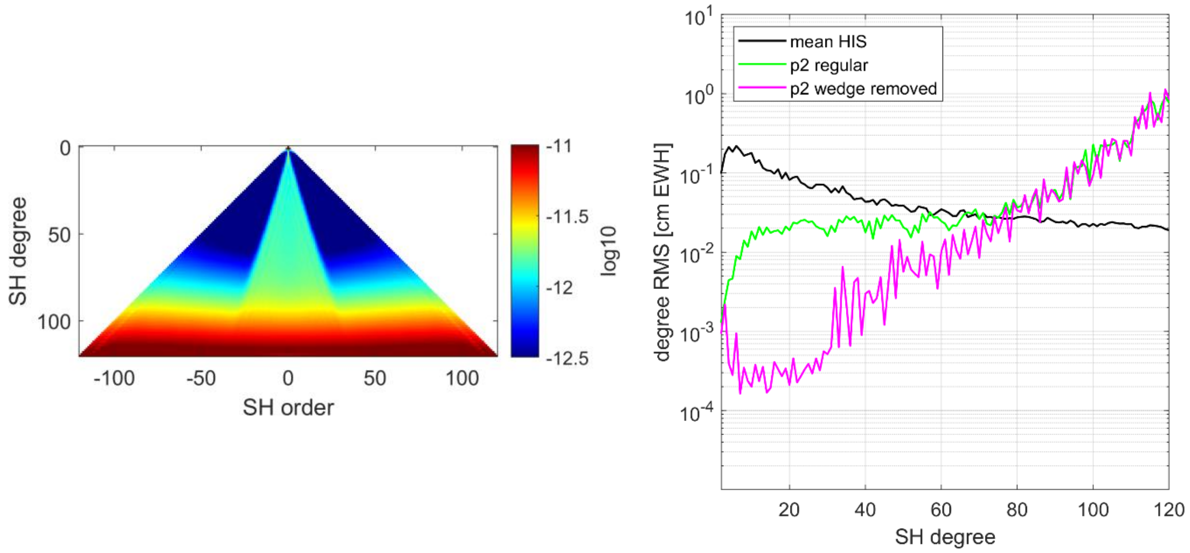

Figure 24-20: Left: Formal errors of a stand-alone 31-day retrieval based on *w0*. Right: Mean of degree RMS of the retrieval errors based on stand-alone *p2* for a 31-day retrieval with and without considering the polar gap wedge in the product-noise case.

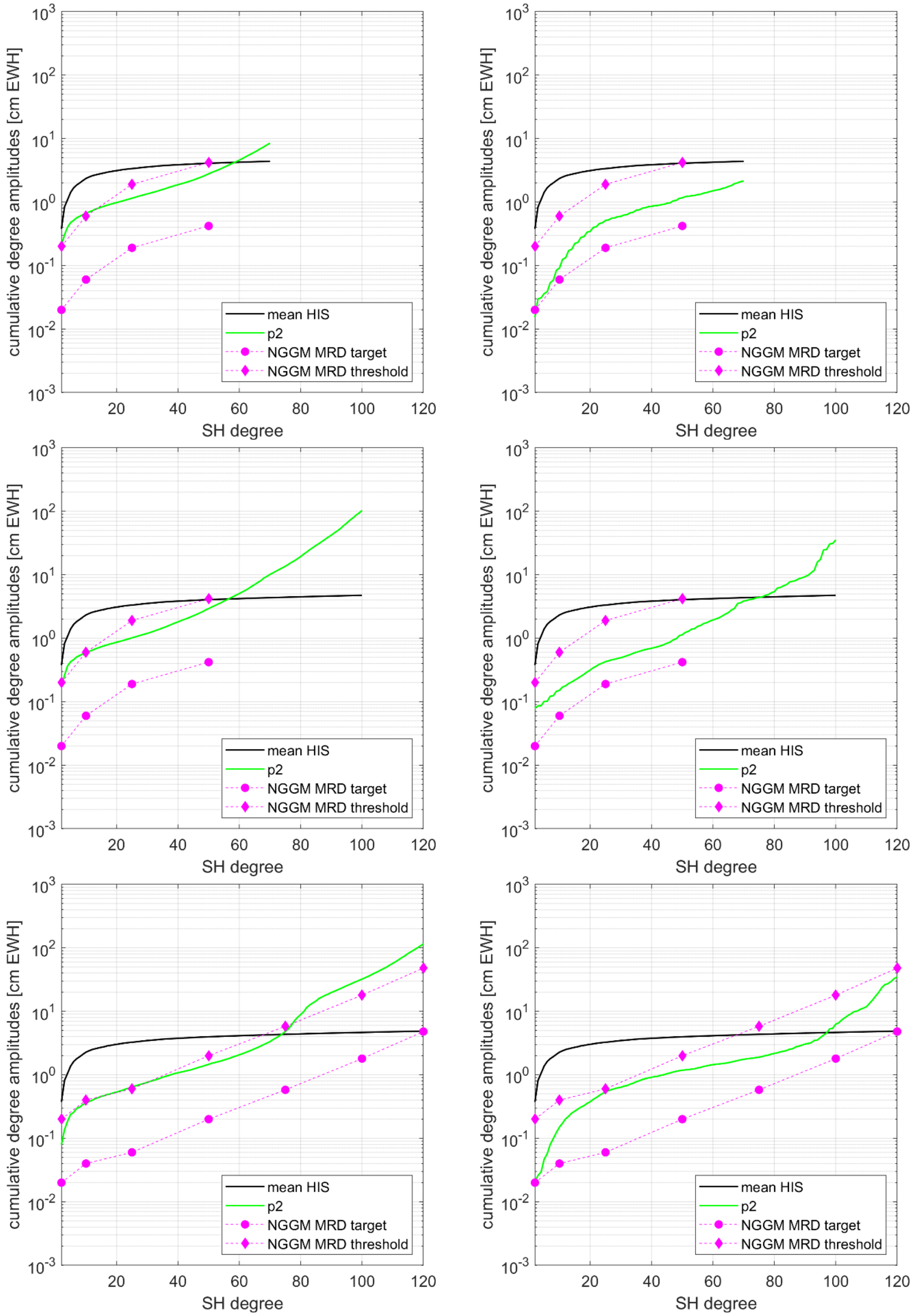

Figure 24-21 Full-noise (left) and product-noise simulations (right); mean of cumulative degree amplitudes of the retrieval errors based on stand-alone p2 for a 5- (top row), 7- (centre row) and 31-day (bottom row) retrieval compared against NGGM MRD requirements.

The cumulative degree amplitudes are presented in Figure 24-21. In case of the 5- and 7-day solutions, all threshold requirements are satisfied both in full-noise as well as product-noise scenarios, whereas the target requirements are missed. In case of the 31-day full-noise-based retrieval the threshold requirements are met up until d/o 75. Conversely, in the product-noise case the all given threshold requirements are met, but the target requirements cannot be satisfied. As discussed beforehand, the degree amplitudes presented for the product-noise case pose a very conservative estimate of the true retrieval performance due to the influence of the degraded near-zonals. In order to obtain a realistic error quantification, it is proposed to compute the retrieval error in the spatial domain and disregard the polar caps not observed by P2 in the future. It can be shown that this spatial representation is equivalent to the spectral one where the polar gap wedge (i.e. affected near-zonals) have been removed.

Wiese parametrization with stand-alone P2

Further, we investigate the value of stand-alone P2 within the scope of Wiese parametrization. For this, we conduct six subsequent 5-day retrievals of the HIS signal (i.e., a priori AO de-aliasing is applied) which includes a co-estimation of daily fields up to d/o 10, 12 and 15 and compare their performance to those of the baseline scenario with the same parametrization scheme. For the sake of completeness, we also simulate stand-alone P1 retrieval with the Wiese approach. Note that for the sake of consistency, the maximum degree of resolution was limited to 70 for the double-pair simulations.

The results are presented in Figure 24-22. It is evident that main limitation of the P2 solutions is its spatial resolution. In this way, the performance of single-inclined-pair and double-pair Wiese 1/10 is close to identical, both with respect to the daily as well was the 5d-solutions. Once the resolution of daily fields is increased to d/o 12 and 15 and the inclined pair “runs out” of spatial coverage, its performance deteriorates accordingly, as can be seen both in the daily and the 5d-estimates. It is interesting to see that the “Wiese bumps” (c.f. section 27.1) occur in P2 as well as P1+P2 in a similar fashion. For P2, however, they are significantly increased once spatial resolution becomes an issue, which can easily be related to the even further reduced stability of the underlying NEQ systems. Overall, though, also in case of the Wiese approach it is evident that P2 dictates the overall performance of the double-pair retrieval.

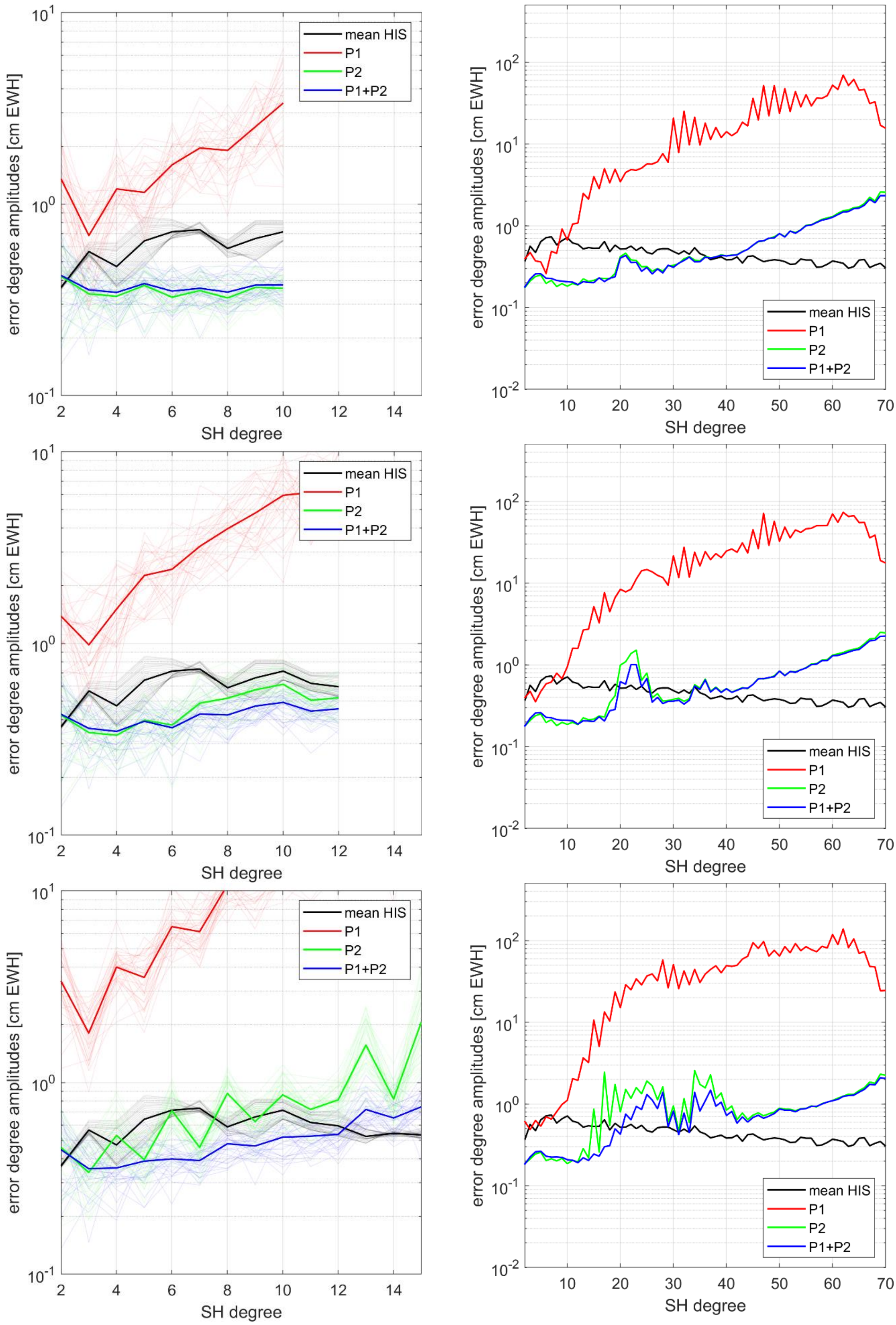

Figure 24-22: mean retrieval error of daily fields (left) and the 5d-solutions (right) obtained with Wiese parametrization where daily fields are co-estimated up to d/o 10 (top), 12 (centre) and 15 (bottom).

DMD with stand-alone P2

In the following we investigate the performance of the DMD approach (c.f. section 22.1) in the context of a gravity retrieval based on a stand-alone P2. In this study we use the inclined pair of the baseline scenario, c.f. Table 13-1, and apply a spherical caps regularization in the same manner as described above. Note that the regularization must be applied both to the interval fields obtained with DMD and the full solution alike.

For the DMD scheme itself, we use two different parametrization schemes, in the following denoted as DMD1 and DMD2 (c.f. Table 24-3). As described in Abrykosov et al. (2022), DMD1 shows an optimal performance for a stand-alone P1, whereas DMD2 shows a good performance for a double-pair constellation. Both parametrization schemes are applied within a 31-day full-noise scenario with the full AOHIS as the target signal (i.e. without a priori AO de-aliasing) as well as HIS as the target signal (i.e. with application of a priori AO de-aliasing). In addition, in each scenario the DMD scheme is applied with (c1) as well as without constraining the interval fields to the nominal solution (c0). It is noted that in case of c1 the constrained nominal solution is used.

It is further noted that the simulations shown in this subchapter have been obtained through reduced-scale simulations, since the DMD has not yet been implemented in the full-scale simulation software.

Table 24-3: DMD scenarios for stand-alone P2

	1-day estimates	2-day estimates	3-day estimates
DMD1	d/o 12	d/o 20	-
DMD2	d/o 15	d/o 30	d/o 45

The retrieval errors of the 31-day solutions based on stand-alone P1, stand-alone P2 and a combination of P1 and P2 with and without the application of DMD is shown in Figure 24-23. These plots show error degree amplitudes on the basis of the full set of coefficients, while Figure 24-24 shows the same results, but with the polar gap wedge removed (c.f. previous sub-chapter) in order to reveal the true performance of P2 in the observation-covered regions. In order to allow for proper comparability between all scenarios, the polar gap wedge has been removed from all solutions as well as from the reference signal.

It can be seen in Figure 24-23 that the DMD approach overall improves the stand-alone P2 retrieval in the medium- to high-degree spectrum, while the low-degree spectrum remains either unaffected (if full AOHIS is retrieved), or is slightly degraded in certain frequency bands (if HIS is retrieved). It can also be established that DMD2 shows an overall better performance that DMD1, which only yields minor gains in comparison to the nominal retrieval. Further, it seems that the impact of the low-degree constraint is negligible.

Once the polar gap wedge is removed (c.f. Figure 24-24), the impact of DMD becomes more pronounced. In case of DMD1 the improvement towards the nominal solution in the high degrees is increased, although it is overall still minor. For DMD2 the gain towards the nominal solution is increased as well – in case of the HIS retrieval primarily notable above d/o 60, whereas in case of the AOHIS retrieval the major improvements can be found around d/o 50 to 90. However, it can also be seen that by removing the polar gap wedge the degradations in the low-degree spectrum become more prominent. It can thus be concluded that the DMD scheme increases the errors in higher-order coefficients of the low- to medium-degree spectrum if applied to stand-alone P2 data. This behaviour is on one hand related to the DMD's intrinsic property of increasing the errors in near-sectrorial coefficients, but seems to also be significantly enhanced in case of P2-only. To further solidify this finding, the error coefficients are explicitly presented for the P2-only and double-pair scenarios in Figure 24-25.

Now, the DMD-based interval solutions are analysed. The corresponding retrieval errors for the retrieval of the full AOHIS are depicted in Figure 24-26 and Figure 24-27 and in Figure 24-28 and Figure 24-29 for HIS, respectively. Overall, it is clear that a stand-alone P2 outperforms a stand-alone P1 in terms of short-term solution performance. In comparison to a double-pair scenario, however, P2 shows a slightly worse performance, provided that the same parametrization scheme is applied. In total, though, the performance degradation due to an insufficient spatial resolution is significantly smaller than in case of the Wiese parametrization, c.f. Figure 24-22. Additionally, it can be seen that constraining the interval solution to the nominal reference is beneficial for the enhancement of their retrieval performance. This is in particular the case when DMD2 is used, or, in general, interval fields of higher resolution are estimated over shorter time spans, as it helps mitigate the effects of spatial leakage.

In conclusion, it can be stated the application of DMD for the processing of stand-alone P2 solutions poses a viable strategy, as it allows to retain all the benefits of this processing scheme, i.e. obtaining short-interval gravity products while reducing aliasing effects in the medium to high degrees. The interval fields feature a significantly enhanced retrieval performance in comparison to those obtained with a stand-alone P1 with an identical parametrization. As expected, the performance of the P2-based interval fields is slightly reduced in comparison to a double-pair due to the less favourable observation coverage. Regarding the long-term, i.e. monthly, stand-alone P2 solution the DMD yields similar gains in the shorter spatial frequencies as in case of the double pair. In the low-degrees, however, the DMD induced higher errors in the near-sectorials than in case of a stand-alone P1 or the double-pair.

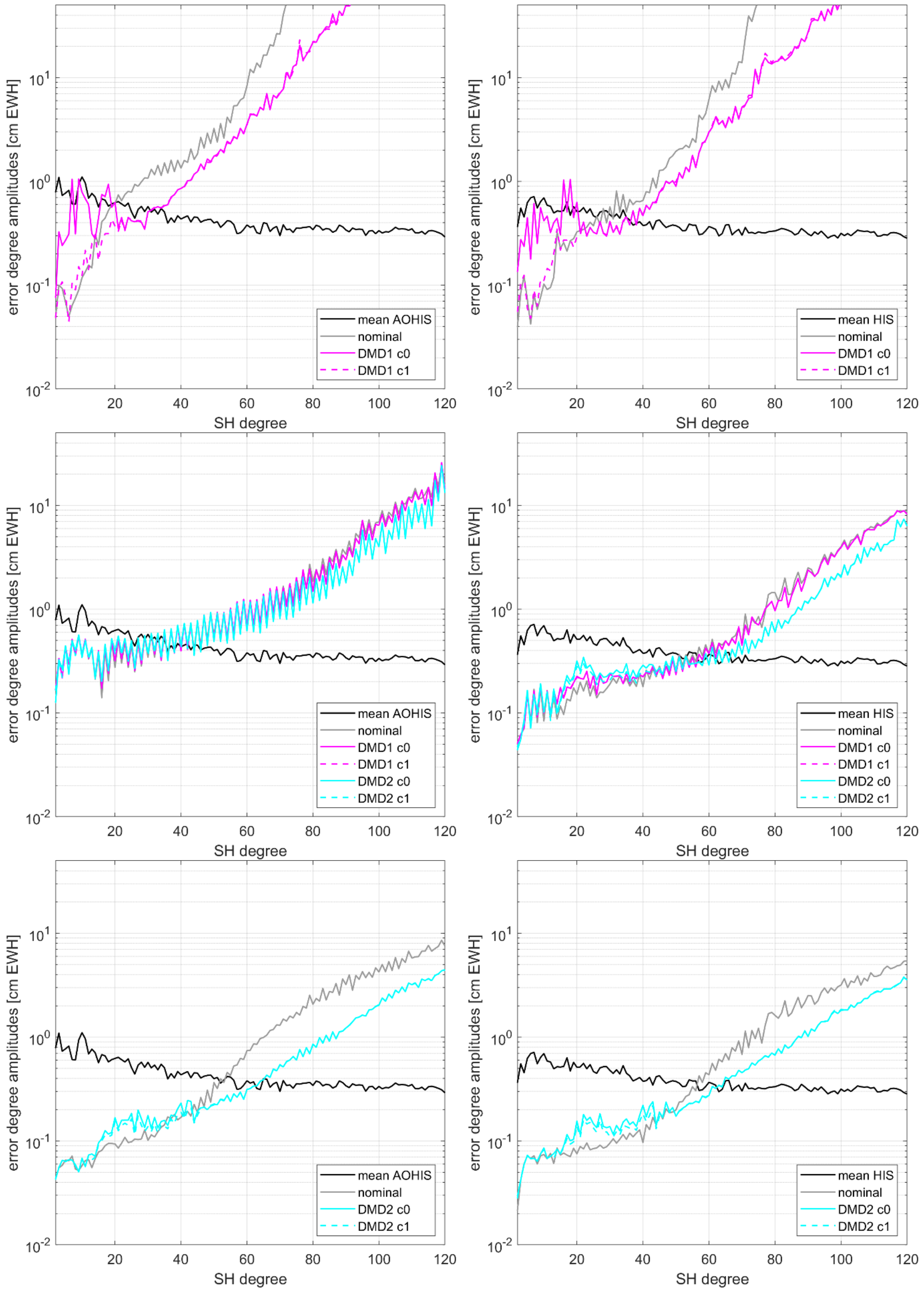

Figure 24-23: Retrieval error of a 30-day full-noise scenario (left column: retrieval of full AOHIS, right column: retrieval of HIS, i.e. with a priori AO de-aliasing) based on stand-alone P1 (top), stand-alone P2 (center) and a double-pair case with and without applying DMD.

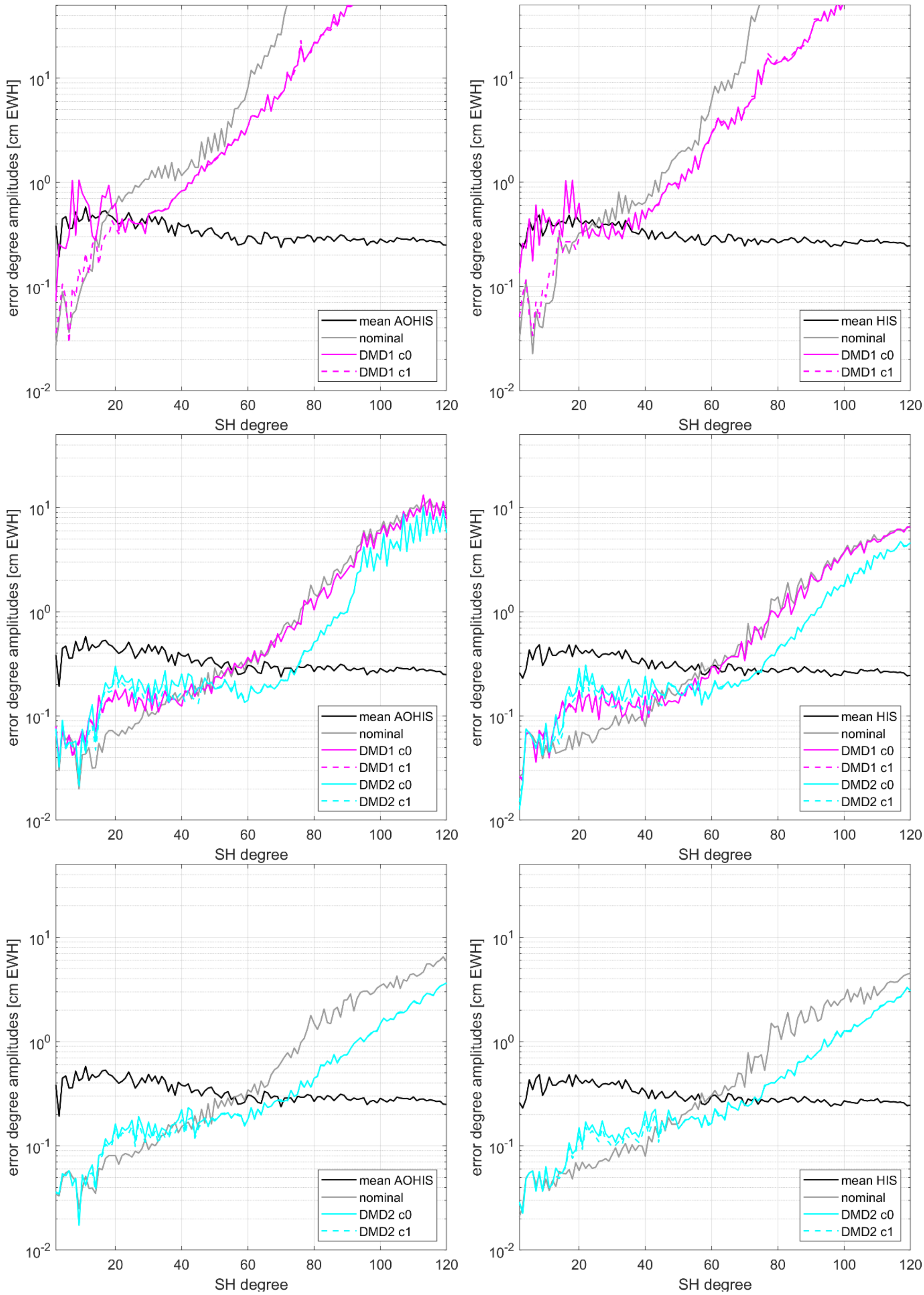

Figure 24-24: Retrieval error of a 30-day full-noise scenario (left column: retrieval of full AOHIS, right column: retrieval of HIS, i.e. with a priori AO de-aliasing) based on stand-alone P1 (top), stand-alone P2 (center) and a double-pair case with and without applying DMD. Only coefficients outside of the polar gap wedge are considered.

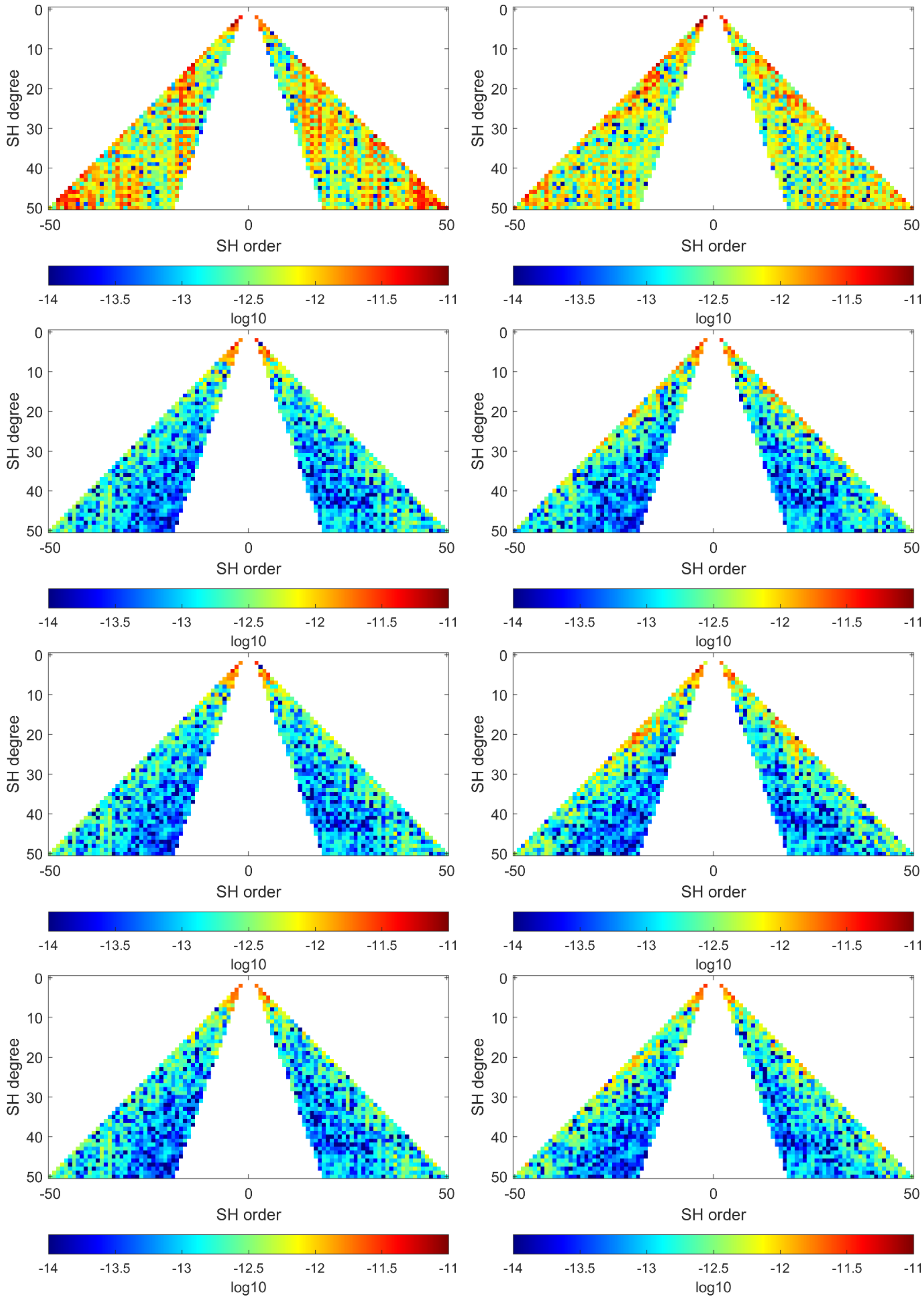

Figure 24-25: Error coefficients of the 30-day solution based on stand-alone P2 obtained with DMD (right column) and with the nominal processing (left column). Row 1: stand-alone P1 (DMD1 and nominal); Row 2: stand-alone P2 (DMD1 and nominal); Row 3: stand-alone P2 (DMD2 and nominal); Row 4: double-pair (DMD2 and nominal).

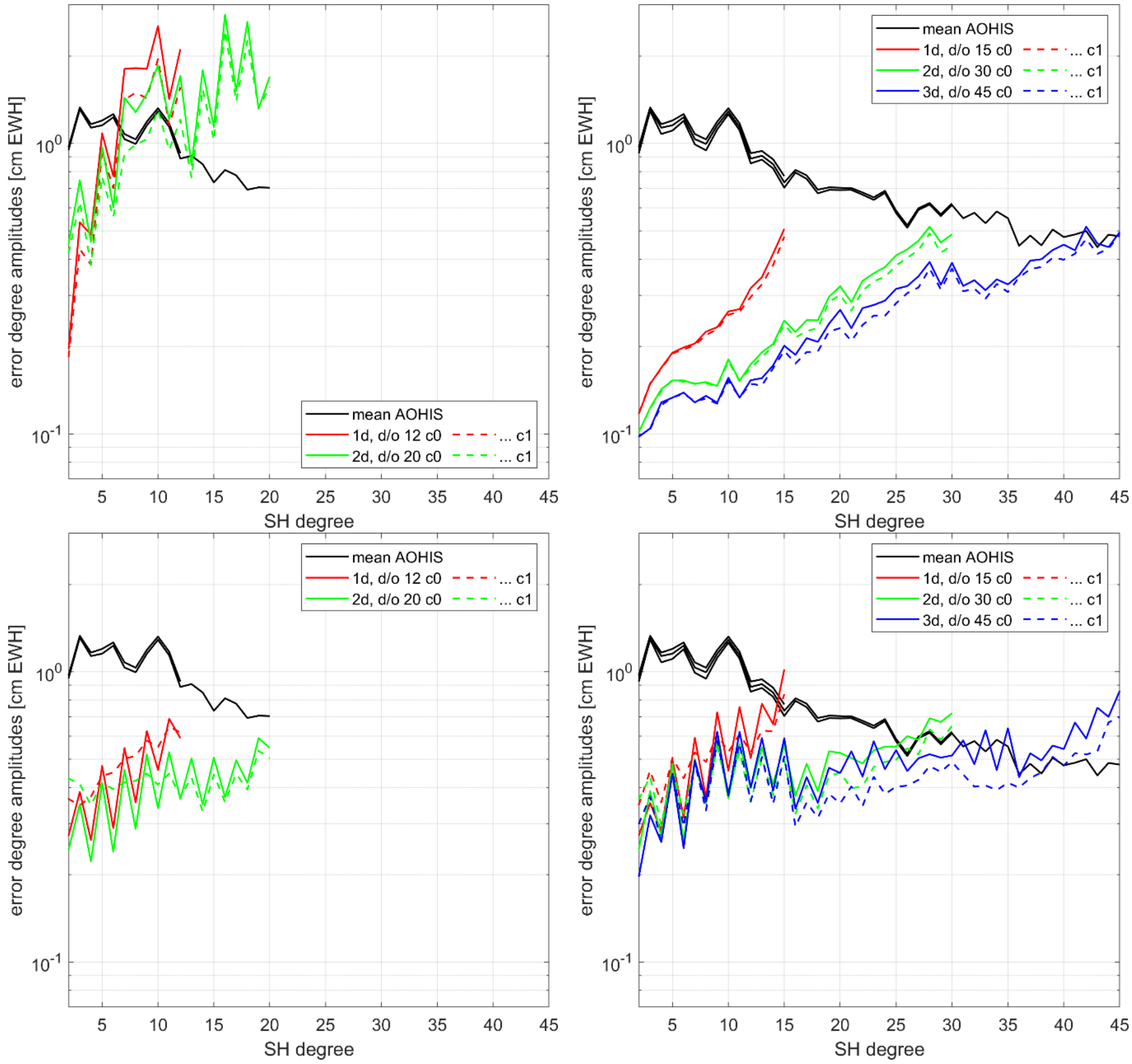

Figure 24-26: Mean AOHIS retrieval error of DMD-derived interval solutions for stand-alone P1 (DMD1, top left), double-pair (DMD2, top right), stand-alone P2 (DMD1 and DMD2, bottom left and bottom right, respectively).

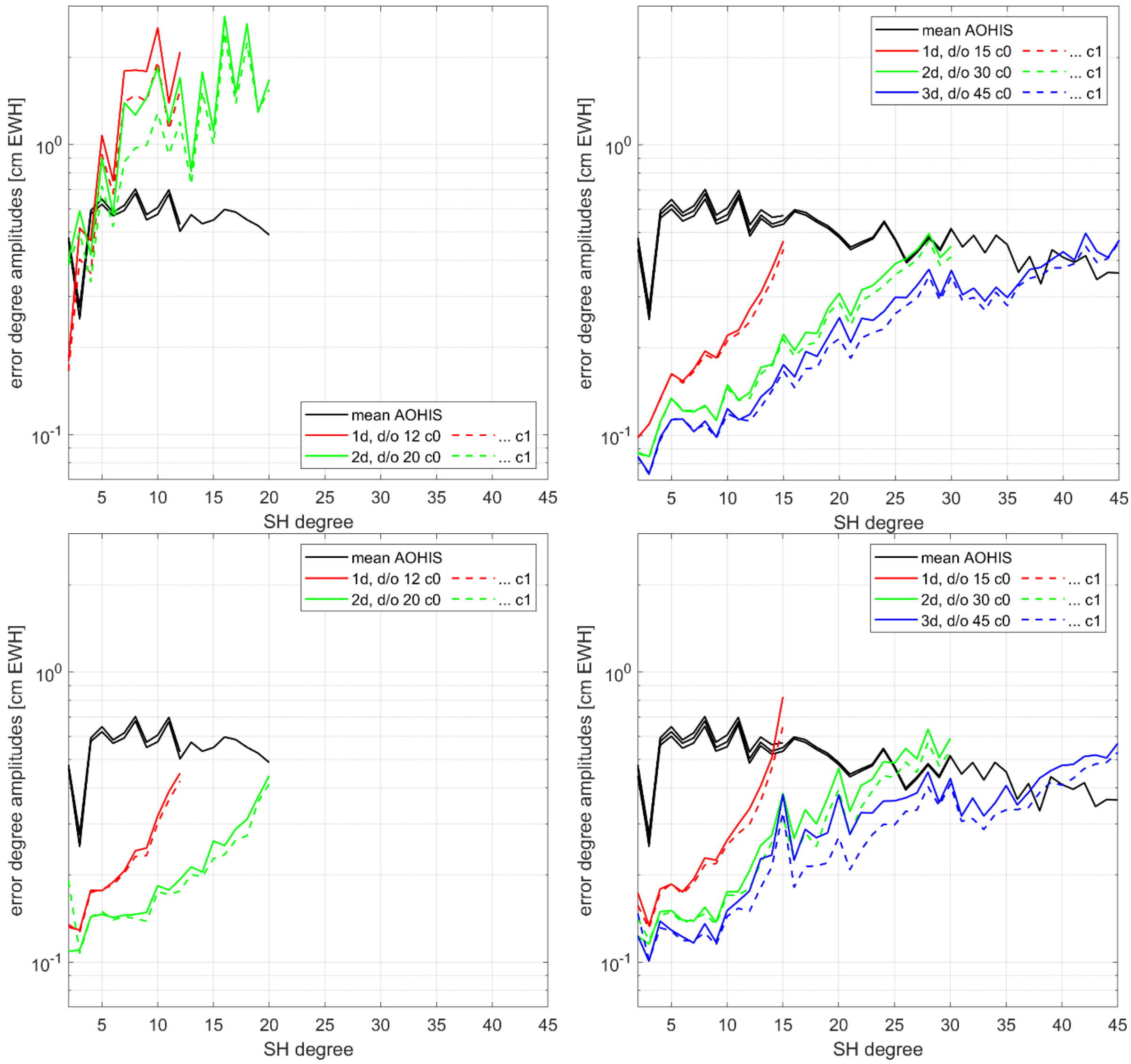

Figure 24-27: Mean AOHIS retrieval error of DMD-derived interval solutions for stand-alone P1 (DMD1, top left), double-pair (DMD2, top right), stand-alone P2 (DMD1 and DMD2, bottom left and bottom right, respectively). Only coefficients outside of the polar gap wedge are considered.

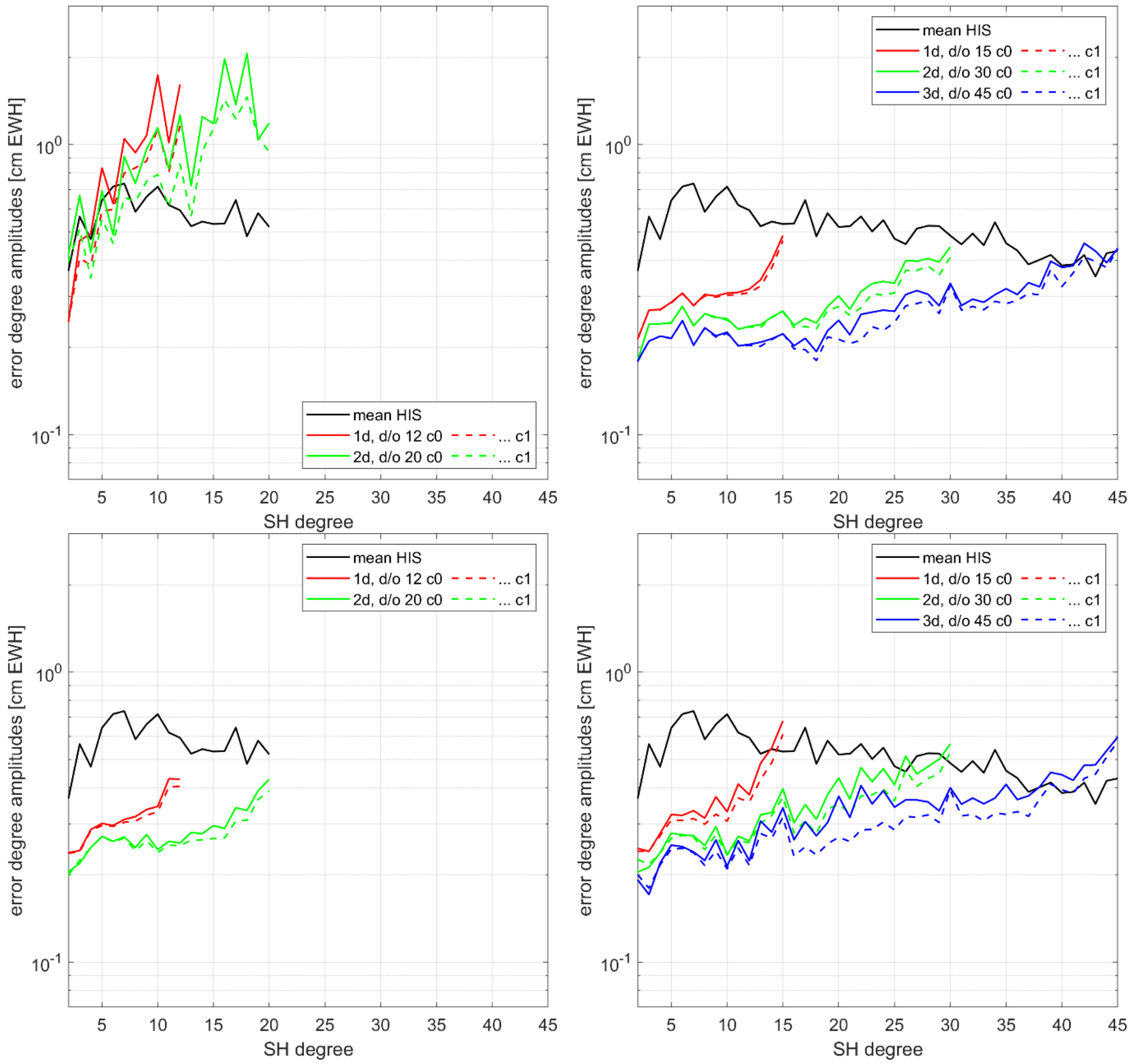

Figure 24-28: Mean HIS retrieval error of DMD-derived interval solutions for stand-alone P1 (DMD1, top left), double-pair (DMD2, top right), stand-alone P2 (DMD1 and DMD2, bottom left and bottom right, respectively).

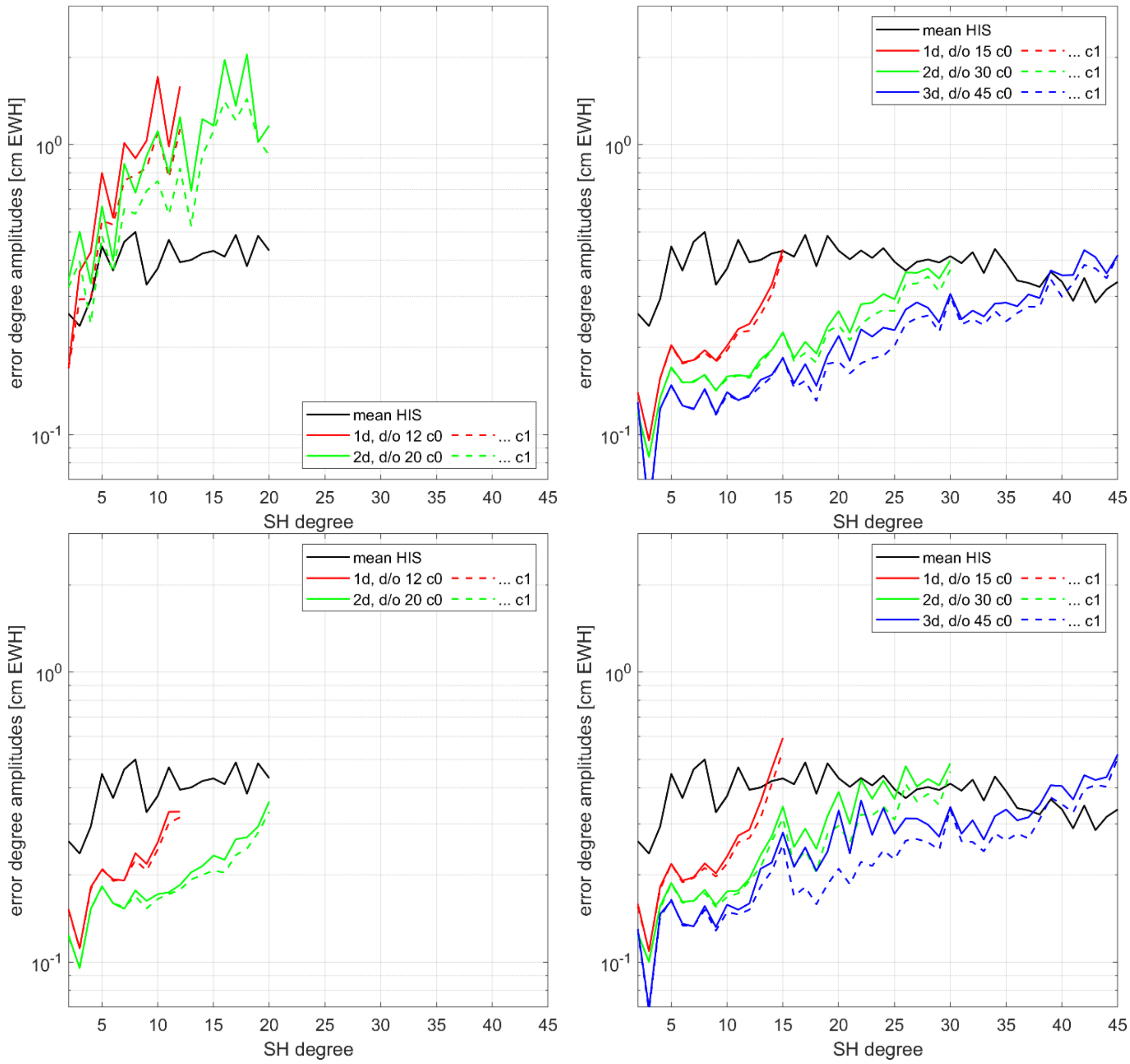

Figure 24-29: Mean AOHIS retrieval error of DMD-derived interval solutions for stand-alone P1 (DMD1, top left), double-pair (DMD2, top right), stand-alone P2 (DMD1 and DMD2, bottom left and bottom right, respectively). Only coefficients outside of the polar gap wedge are considered.

"Bump" in P2-based solutions

As a final aspect, we investigate the "bump" around d/o 80 in the nominal full-noise 31-day solutions obtained with full-scale simulations. These are of special interest, since nothing similar occurs in the shorter-term retrieval, and they are also not present in the solutions obtained by GFZ (c.f. section 24.4).

To understand this behaviour, we first cross-check the pre-fit residuals with those of GFZ in order to uncover potential differences which may cause such bumps. The spectral comparison can be found in Figure 24-30, and the spatial comparison is shown in Figure 24-31. It can be stated that both pre-fit residuals time series are highly consistent, and only notably differ in the long-wavelength spectrum (around and below the orbital frequency). This behaviour has already been verified in the simulation software cross-comparison carried out in the previous phase of the science study, and is attributed to the difference in processing arc length (6h for TUM, 24h for GFZ).

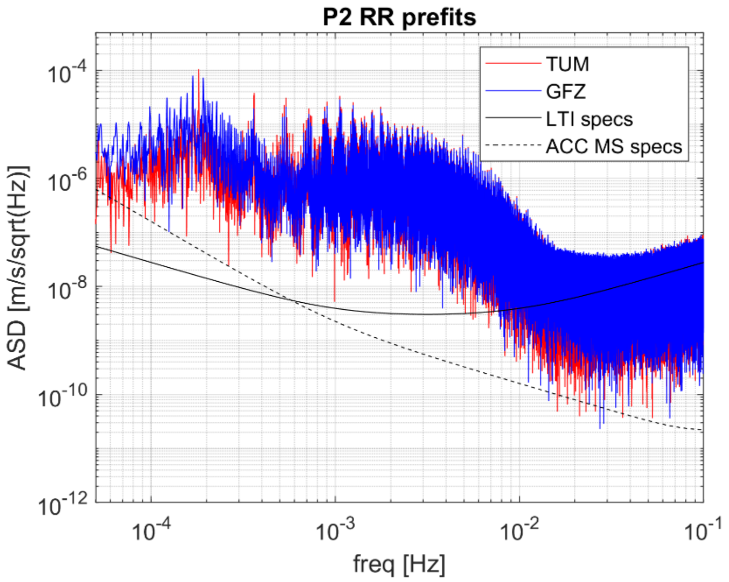

Figure 24-30: Comparison of pre-fit residuals time series for 01.01.-31.01.2002 in the spectral domain

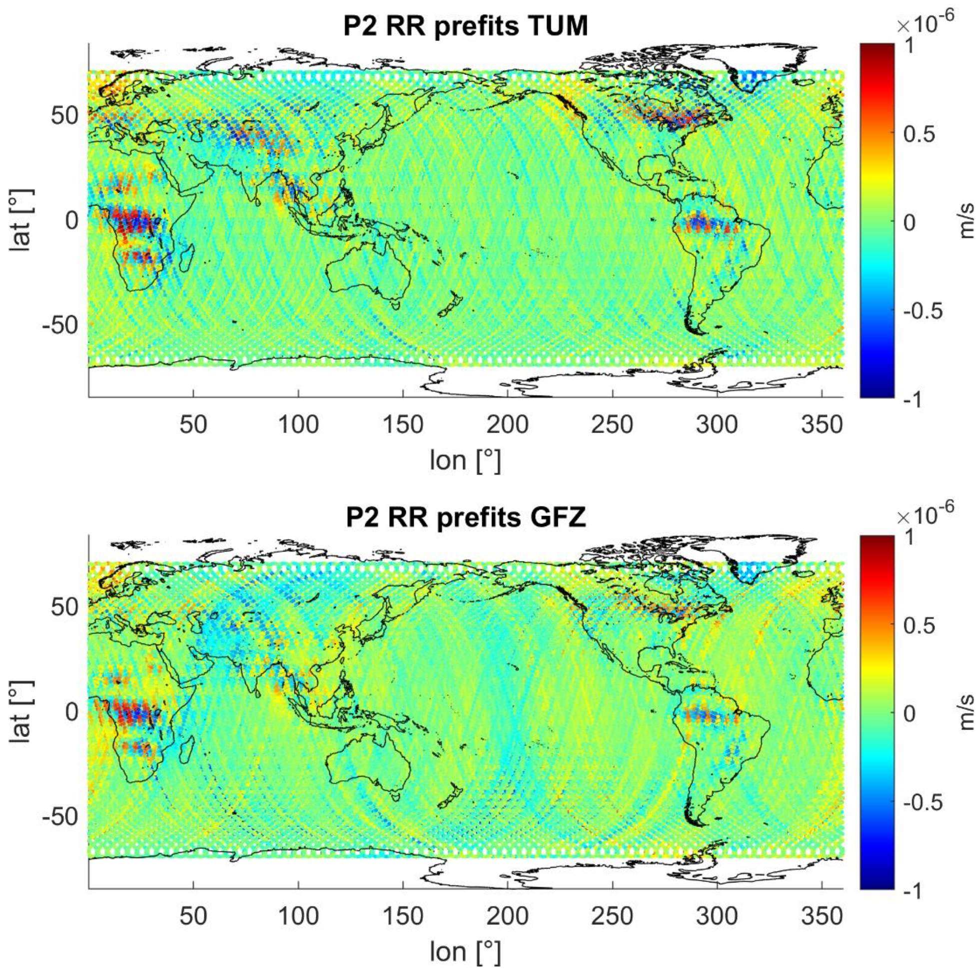

Figure 24-31 Comparison of pre-fit residuals time series for 01.01.-31.01.2002 in the spatial domain

Further, we vary the parametrization scheme of the bump-affected retrieval scenario. From the initial 31-day d/o 120 solution, we reduce the retrieval period to 25, 20, 15 and 10 days, and, additionally, we also compute a 31-day retrieval up to d/o 100. The respective results are shown in Figure 24-32. It is evident that the bump does not occur in the sc1-based solutions no matter the parametrization. On the other hand, the sc2-based solutions all feature the bump to various extents except for the 10-day solution, whose intrinsic noise level is high enough to cover the bump.

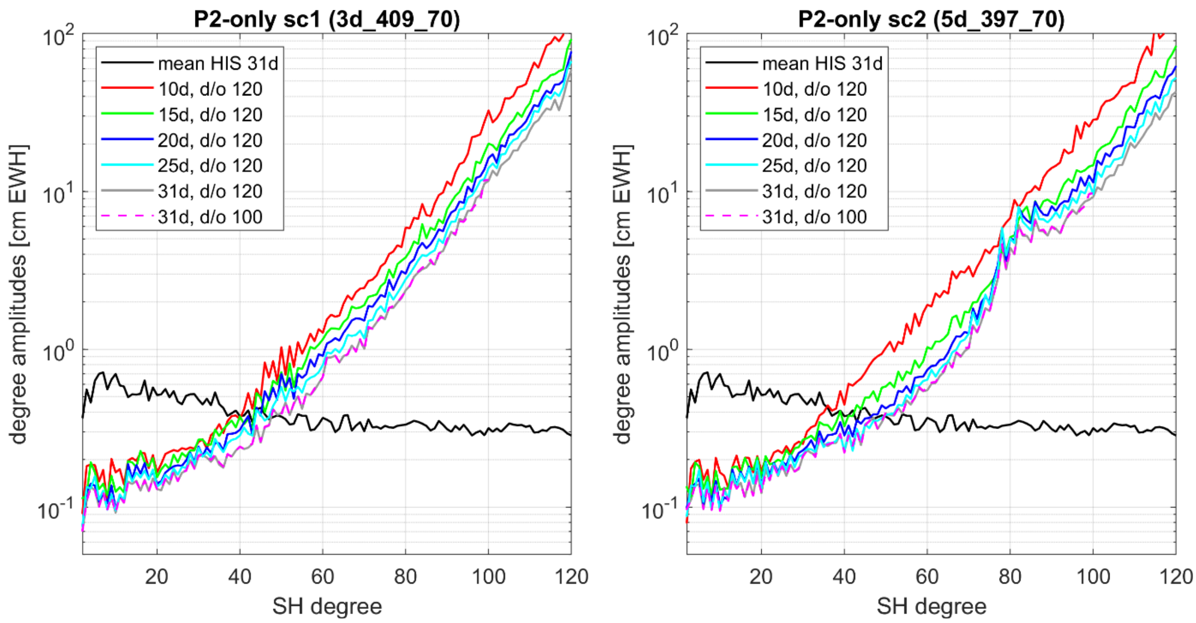

Figure 24-32: Mean degree amplitudes of full-noise stand-alone P2 retrieval errors for *sc1* (left) and *sc2* (right) with tweaked retrieval parameters.

In a next investigation step, the full-noise scenario is split up into individual error contributors, i.e. AOD as well as OTD error and HIS, in order to understand whether all of them feature the bump in the same manner. The results in Figure 24-33 clearly show that HIS is the component that is predominantly responsible for the bump, while in case of the AOD error the bump is not present at all. In case of the OTD error the bump is present in a very reduced form.

In order to understand whether the stochastic modelling plays a role within the shown behaviour, we investigate two additional scenarios. In the first scenario, the weighting matrix is assumed to be a scaled unity matrix according to

$$P = \frac{1}{\alpha^2} I$$

with $\alpha = 10^{-11} \frac{m}{s}$ in order to maintain a similar relative weighting of the ll-SST to the hl-SST observations as in the nominal case. In this way, the observation noise is treated as if it had white-noise properties. In the second scenario, we apply the weighting matrix tailored to the product noise of the polar pair. The impact on the individual contributors of the full-nosie scenario is depicted in Figure 24-34. It becomes evident that in case of the white-noise-type weighting all three contributors feature the bump in the same manner. In case of the second weighting scenario, on the other hand, the bump disappears in AOD and OTD errors, and remains to some extent present in the HIS component, although in a significantly reduced manner in comparison to the nominal weighting scenario. Additionally, it seems that the application of the P1 weighting matrix leads to a significant decrease of retrieval errors within the medium- to high-degree spectrum. For better comparability, the retrieval errors of the full-noise scenarios obtained with the three weighting approaches are jointly presented in Figure 24-35.

These findings lead to the conclusion that the bump is not induced by the stochastic model, but rather through the interplay of the observation geometry and the sampled observations (as expected, since the same nominal weighting is applied in all investigated orbital scenarios), though the exact reason can still not be pinpointed. The fact that the bump is present in all error contributors in the same manner when white-noise-type weighting is applied further suggests that the bump is not simply a bug within the processing software. In combination with the consistent pre-fit residuals' behaviour, it is much rather an indication that the gravity adjustment works as intended, and that signals are misparametrized due to potentially "unfortunate" ground track spacing.

The stochastic modelling can be regarded as a way of "regulating" the bump. In principle, the weighting scenario that yields the best result can be used without any issue, since it is not more or less correct in the full-noise case than the stochastic modelling that is specifically tailored to the respective product noise. One should keep in mind that due to the mismatch of the parametrization (i.e. one static set of coefficients for the entire observation period) and the input signal (varying at very short time scales) the stochastic model does not explicitly target the product noise, but much rather affects the combined observations containing the time-variable signal and thus leading to undesirable effects. However, the cleanest approach with regard to stochastic modelling would be to base the observation weighting on the stochastic properties of all individual error contributors, i.e. product noise as well as AOD and OTD BM errors (and potentially others), c.f. section 22.2 and Abrykosov et al. 2021. This can be expected to greatly mitigate the impact of the mismatch of input signal and parametrization scheme and, in case of a multi-pair constellation, also to allow for a realistic relative weighting of the observations of the different satellite pairs.

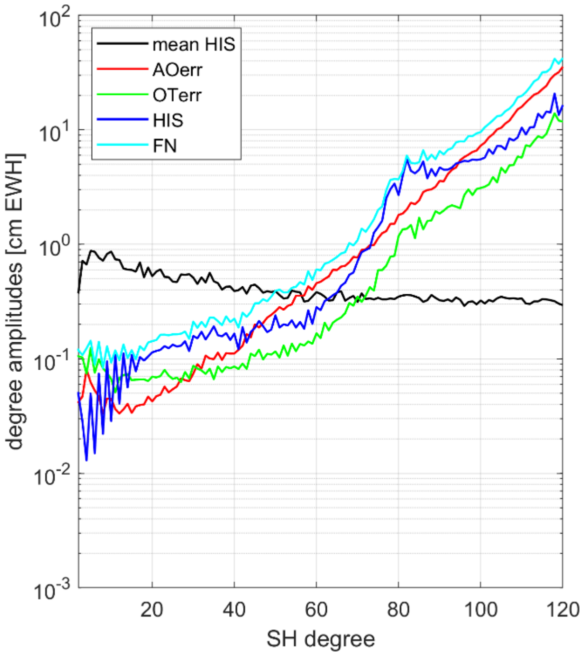

Figure 24-33: Retrieval error induced through individual error components of the full-noise scenario excluding the product noise (stand-alone P2 of baseline scenario, 31-day retrieval).

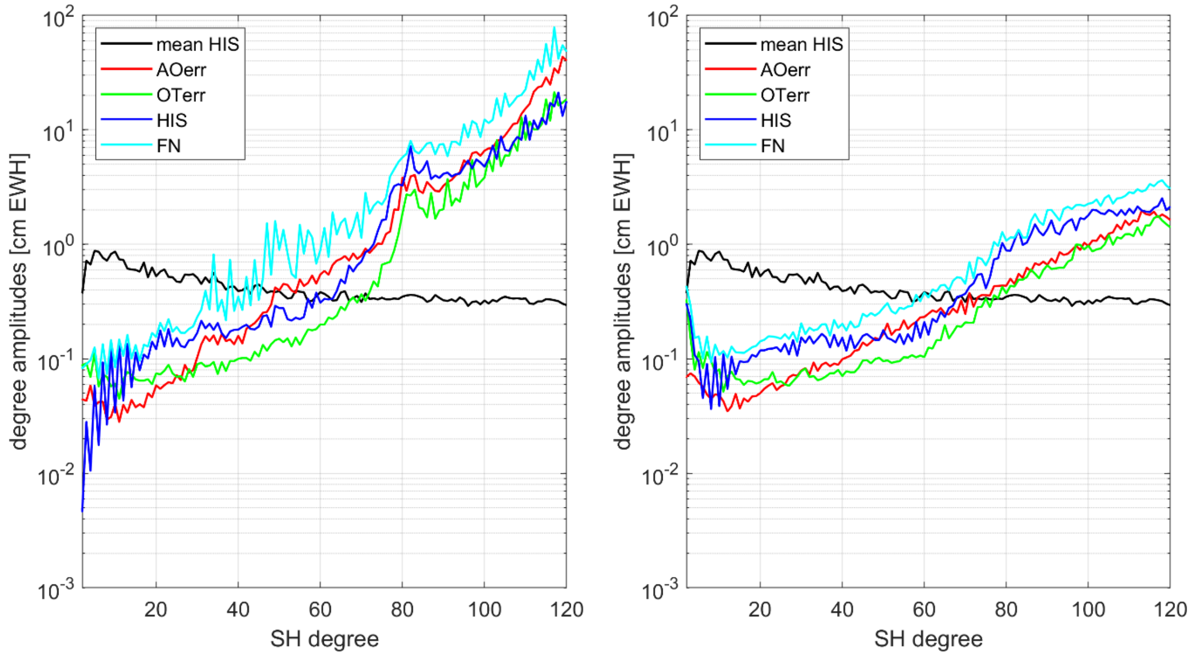

Figure 24-34: Retrieval error induced through individual error components of the full-noise scenario (excluding the product noise) under application of white-noise-type stochastic modelling (left) and the stochastic modelling tailored to the product noise of the polar pair (right). (stand-alone P2 of baseline scenario, 31-day retrieval).

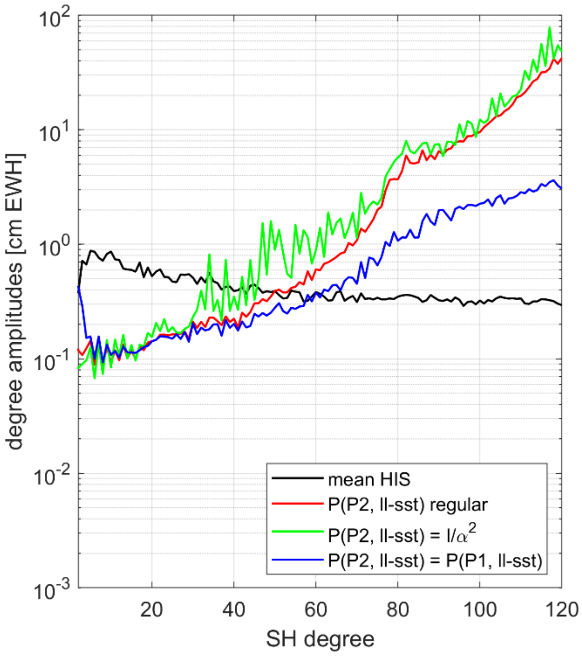

Figure 24-35: Retrieval error of the full-noise scenarios obtained with the three different stochastic modelling approaches. (stand-alone P2 of baseline scenario, 31-day retrieval).

24.4. INCLINED-PAIR ANALYSIS OF BASELINE SCENARIO - GFZ (WP1531)

In this work package, we investigate solving only for the inclined pair of the baseline scenario, 5d_397_70. Due to the missing polar region information, the inclined-pair-only normal equations are ill conditioned and require regularization in order to obtain a sensible solution up to degree and order 120. Especially the low-order coefficients are not well determined. Dimensionless gravity field coefficients, obtained without regularization, are shown in Figure 24-36.

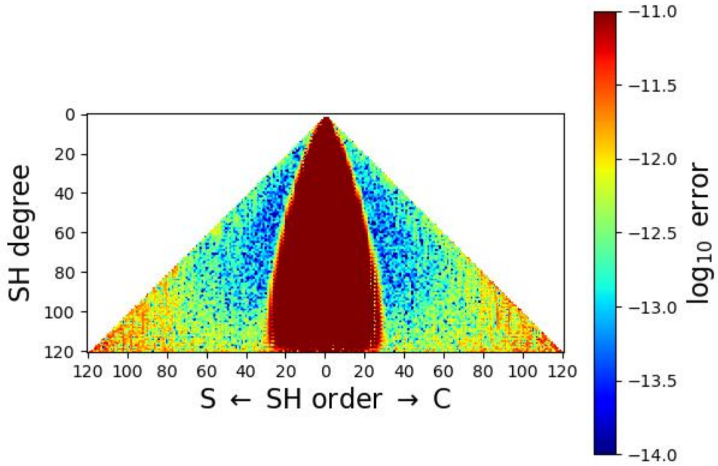

Figure 24-36 Dimensionless C- and S-coefficient values for a non-regularized inclined-pair only scenario.

Following van Gelderen and Koop (1996), we assume that the coefficients affected by the polar gaps are located in the red, sharply defined wedge-shaped area, shown in Figure 24-36 and that the maximum affected order, m_{max}, for each degree, n, is given by

$$m_{max} \approx \left|\frac{\pi}{2} - I\right| * n,$$

where I is the inclination of the inclined pair in radians.

In Figure 24-37, the degree variances for the inclined-only and the double-pair scenario are compared for those coefficients that are not influenced by the polar gaps.

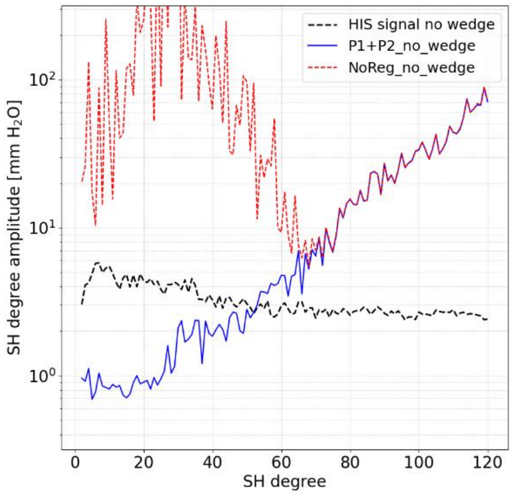

Figure 24-37 Degree variance residuals, in terms of EWH, for a double pair (in blue) and a non-regularized inclined-only-scenario (in red) over areas not affected by the missing polar cap information.

Note that no regularization has been applied to the inclined-only scenario shown in Figure 24-37.

Following Rexer (2012), regularization is applied to stabilize the inversion of this ill-conditioned, inclined-pair-only normal equation matrix. The regularization method is given by

$$x = (A^T PA + \alpha R)^{-1} A^T Pl,$$

where $A^T PA$ denotes the normal equation matrix, α is an empirically determined regularization factor, l is a vector of observations, and P is a weighting matrix that contains stochastic modelling parameters. The degree, n, dependent terms of the diagonal regularization matrix, R, are denoted by

$$r_{ij} = \begin{cases} n^4 (m_{max} - m)^p, i = j \; and \; m \leq m_{max} \\ 0, \quad otherwise. \end{cases}$$

In this equation, the $(m_{max} - m)^p$ term enables an order-dependent weighting: The regularization is strongest for the lower orders and reduces as the order increases.

The optimal regularization factor, α, is found by setting $p = 1$. Four regularization factors, ranging from 1e22 to 1e25, were tested and the results obtained for the gravity retrieval residuals are shown in Figure 24-38.

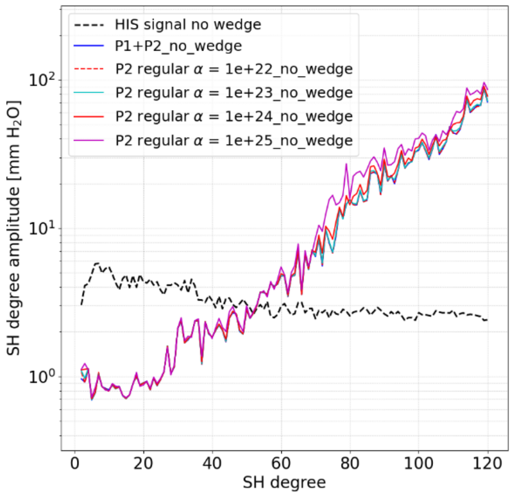

Figure 24-38 Degree variance residuals in terms of EWH for various alpha values for regions not affected by the missing polar-cap information.

The latitude-weighted global RMSE for these alpha values are shown in Figure 24-39.

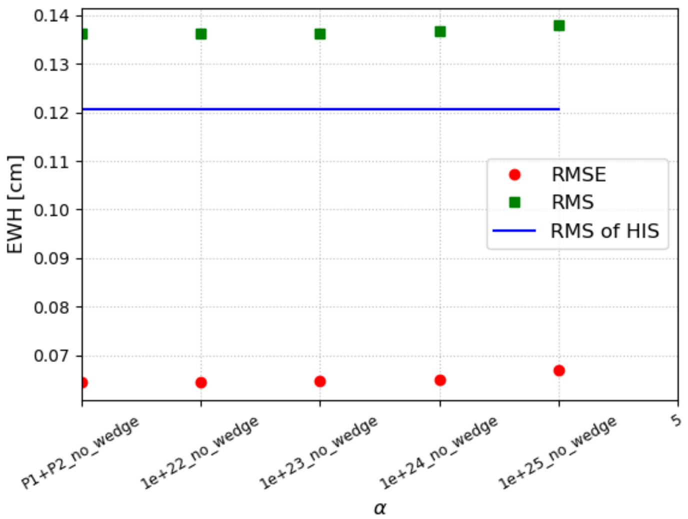

Figure 24-39 Global (excluding polar-cap) signal strength (RMS in green), signal error (RMSE in red), and signal strength of the ground truth HIS.

In Figure 24-39, the error and signal obtained for a double-pair are given by the red and green dots, respectively, and are denoted by P1+P1_no_wedge on the x-axis. The overall accuracy for alpha values 1e+22 to 1e+24 are similar if the RMSE values are compared and accuracy seems to deteriorate slightly for an alpha of 1e+25. This is also verified by the degree variance residuals, shown in Figure 24-38 where the purple curve (for alpha=1e+25) shows increase residuals.

The influence of the alpha parameter was also investigated by comparing the dimensionless gravity field coefficient triangles. In Figure 24-40 the left-most figure shows the gravity field coefficients for a non-regularized inclined-only scenario. The centre figure shows the coefficients for the double-pair scenario and the right-most figure shows the coefficients for the regularized inclined-pair-only scenario for alpha=1e+22.

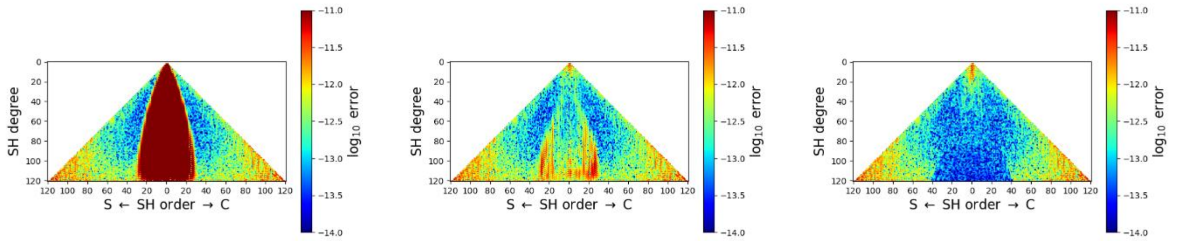

Figure 24-40 Dimensionless gravity field coefficients. Left: non-regularized inclined-only scenario. Middle: double pair scenario. Right, regularized inclined-only scenario with alpha=1e+22.

From Figure 24-40, it can be seen that the influence of the regularization is strongest in the polar gap wedge and that coefficients outside of the wedge remain similar for all three scenarios (i.e. non-regularized inclined-only, double-pair, and regularized inclined-only scenarios).

A comparison between the double pair and the regularized inclined-only scenario, that does not take the polar gap into account, is shown in Figure 5-38. The retrieval error per degree and the cumulative retrieval error are shown on the left- and right of Figure 24-41, respectively.

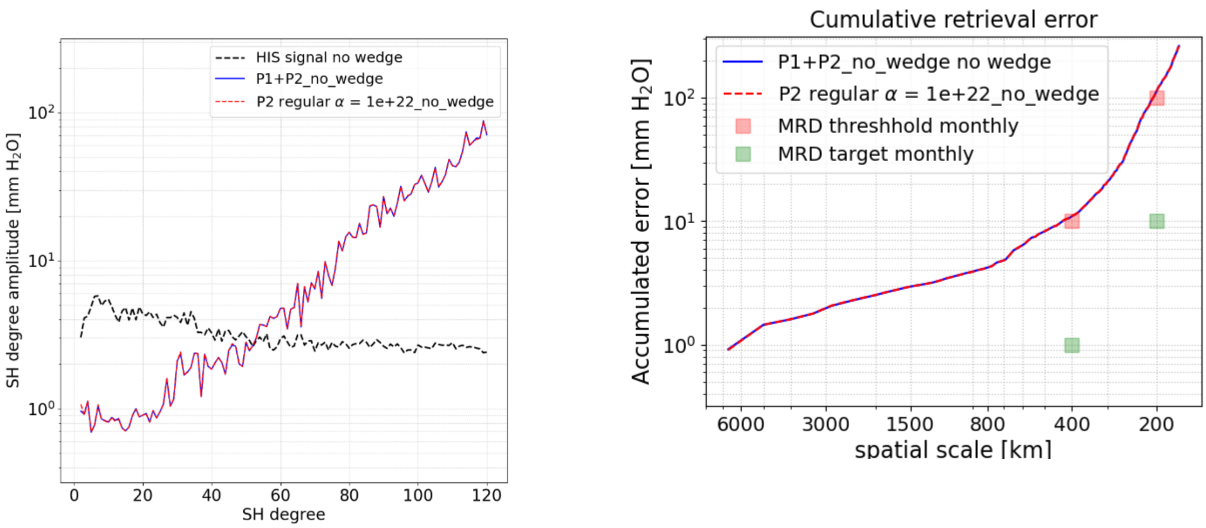

Figure 24-41 Degree variance residuals (left) and cumulative degree variance residuals (right) in terms of EWH for a double pair scenario (blue) and a regularized inclined-only scenario. This comparison is done for coefficients that were not influenced by the polar gap regions.

From Figure 24-41, it can be concluded that the double-pair scenario yields similar accuracy for those regions not affected by the polar gaps.

This is verified by spatial comparisons of the residuals up to degree and order 60 which are shown in Figure 24-42.

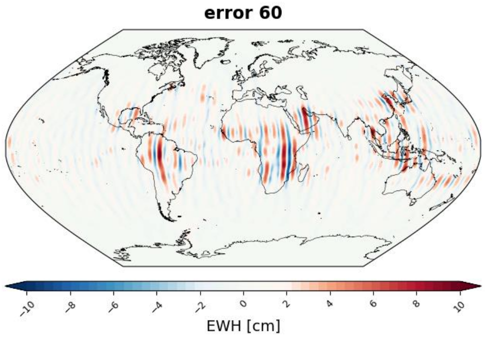

Double-pair

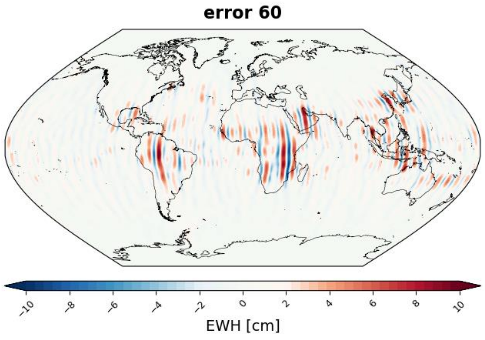

Regularized inclined-only

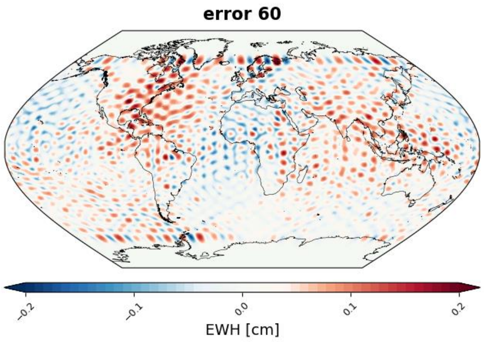

Inclined-only – Double-pair

Figure 24-42 Spatial comparison of the double-pair and the inclined-only scenario for a regularization factor of alpha=1e22. Note that the scale for the difference plot ranges from -0.2 to 0.2.

For non-polar regions, an optimally regularized inclined-pair-only solution is on par with that of a double pair scenario for regions not affected by the polar gap.

Three- and Five-day sub-monthly retrieval periods were also investigated and the coefficient errors are shown in the form of triangle plots for a 5-day and 3-day retrieval period in Figure 24-43 and Figure 24-44, respectively.

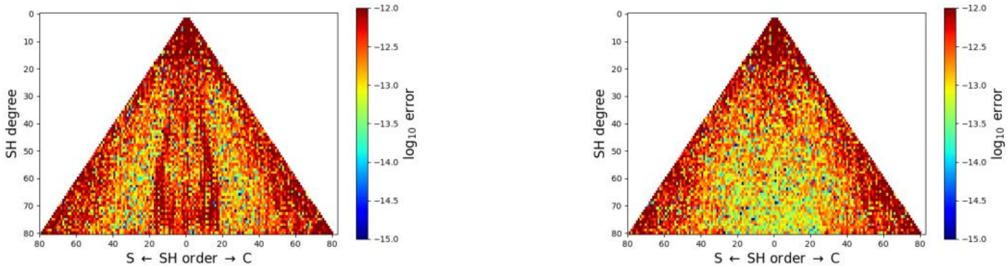

Figure 24-43 5-day retrieval period (day 01-05) coefficient errors. Left triangle is for a double pair scenario. The right triangle is for a regularized, inclined-only scenario.

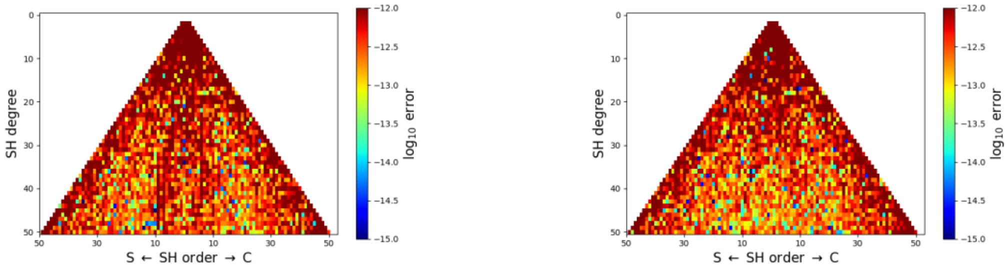

Figure 24-44 3-day retrieval period (day 01-03) coefficient errors. Left triangle is for a double pair scenario. The right triangle is for a regularized inclined-only scenario.

The degree variance errors for the 3- and 5-day retrieval periods are shown on the left and right of Figure 24-45, respectively.

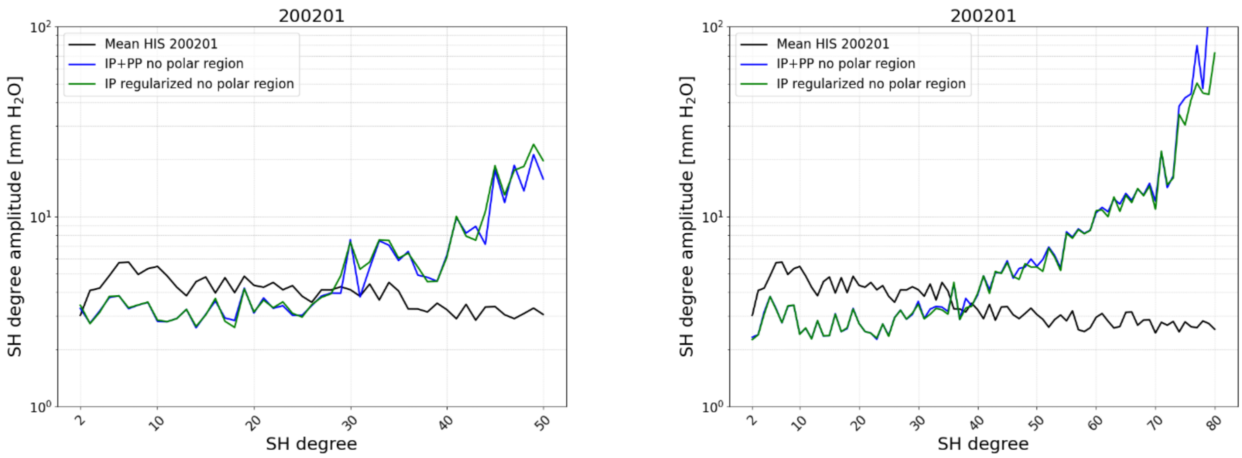

Figure 24-45 Retrieval errors in terms of degree variances for days 01 to 03 (left) and days 01 to 05 (right).

For the sub-monthly investigation, the conclusion remains the same as it was for the monthly retrieval period: Retrieval errors are similar for regions that exclude latitudes larger than 70 degrees when a double pair solution is compared to that of a regularized single inclined pair.

25. APPLICABLE DOCUMENTS, REFERENCE DOCUMENTS, AND PUBLICATIONS

25.1. APPLICABLE DOCUMENTS

[AD-1] Mission Requirements Document, Next Generation Gravity Mission as a Mass-change And Geosciences International Constellation (MAGIC) - A joint ESA/NASA double-pair mission based on NASA's MCDO and ESA's NGGM studies (2020). ESA-EOPSM-FMCC-MRD-3785

[AD-2] Scientific Readiness Levels (SRL) Handbook, Issue 1, Revision 0, 05-08-2015

[AD-3] Statement of Work - ESA Express Procurement - EXPRO NGGM/MAGIC science support study during Phase A, Issue 1, Revision 0, 18/01/2021 Ref ESA-EOPSM-FUTM-SOW-3813

25.2. REFERENCE DOCUMENTS

Abrykosov P, Sulzbach R, Pail R, Dobslaw H, Thomas M (2021) Treatment of ocean tide background model errors in the context of GRACE/GRACE-FO data processing. Geophysial Journal International 228, 1850-1865, https://doi.org/10.1093/gji/ggab421

Abrykosov P, Murböck M, Hauk M, Pail R, Flechtner F (2022) Data-driven multi-step self-de-aliasing approach for GRACE and GRACE-FP data proessing. Geophyiscal Journal International 232, 1006-1030, https://doi.org/10.1093/gji/ggac340

Kvas A, Brockmann JM, Krauss S, Schubert T, Gruber T, Meyer U, Mayer-Gürr T, Schuh WD, Jäggi A, Pail R. (2021) GOCO06s - a satellite-only global gravity field model, Earth System Science Data, 13(1), 99–118. https://doi.org/10.5194/essd-13-99-2021

Egbert GD, Erofeeva SY (2002) Efficient inverse modelling of barotropic ocean tides, J. Atmos. Ocean. Technol. 19 (2), 183-204

Cheng Y, Andersen OB (2011) Multimission empirical ocean tide modelling fior shallow waters and polar seas. J. geophys. Res. 116 (C11), https://doi.org/10.1029/2011JC007172

Ray R (2013) Precise comparisons of bottom-pressure and altimetric ocean tides, J. geophys. Res. 118 (9), 4570-4584

Savchenko R, Bosch W (2012) EOT11a – Global Empirical Ocean Tide model from multimission satellite altimetry, DGFI Report No. 89, München: Deutsches Geodätisches Forschungsinstitut

Dobslaw H, Bergmann-Wolf I, Dill R, Forootan E, Klemann V, Kusche J, Sasgen I (2014) Updating ESA’s Earth System Model for Gravity Mission Simulation Studies: 1. Model Description and Validation, (Scientific Technical Report; 14/07), Potsdam: Deutsches GeoFOrschungsZentrum GFZ, 69p.

Mayer-Gürr, T., Pail, R., Gruber, T., Fecher, T., Rexer, M., Schuh, W.-D., Kusche, J., Brockmann, J.-M., Rieser, D., Zehentner, N., Kvas, A., Klinger, B., Baur, O., Höck, E., Krauss, S., Jäggi, A. (2015): The combined satellite gravity field model GOCO05s, (Geophysical Research Abstracts, 17, EGU2015-12364, 2015), European Geosciences Union General Assembly 2015 (Vienna, Austria).

Siemes C (2008) Digital Filtering Algorithms for Decorrelation within Large Least Square Problems. Bonn: Rheinische Friedrich-Wilhelms-Universität, Hohe Landwirtschaftliche Fakultät, Dissertation

Metzler B, Pail R (2005) GOCE Data Processing: The spherical cap regularization approach, Studia Geophysica et Geodaetica 49, 441-462, https://doi.org/10.1007/s11200-005-0021-5

Rexer M, Pail R (2012) Time-variable Gravity Field: Contributions of GOCE Gradiometer Data to Monthly and Bi-monthly GRACE Gravity Field Estimates, Master's Thesis, https://mediatum.ub.tum.de/doc/1369027/622207.pdf

Pail R, Abrykosov P, Heller-Kaikov B, Visser P, Hauk M, Flechtner F, Wilms J, Bruinsma S, Marty J, Güntner A, Eicker A, Wouters B, Braitenberg C, Hughes C, Lnguevergne L (2022) NGGM/MAGIC – Science Support Study During Phase A "MAGIC". ESA Contract No. RFP/3-17035/20/NL/FF/tfd, Final Report.

van Gelderen M, Koop R (1997) The use of degree variances in satellite gradiometry. Journal of Geodesy 71, 337-343, https://doi.org/10.1007/s001900050101

[RD-1400] Wen, H. Y., Kruizinga, G., Paik, M., Landerer, F., Bertiger, W., Sakumura, C., ... & Mccullough, C. (2019). Gravity recovery and climate experiment follow-on (GRACE-FO) level-1 data product user handbook. JPL D-56935 (URS270772), 11. https://archive.podaac.earthdata.nasa.gov/podaac-ops-cumulus-docs/gracefo/open/docs/GRACE-FO_L1_Handbook.pdf

[RD-1401] Laura Müller, Master Thesis, "Generation of Level 1 Data Products and Validating the Correctness of Currently Available Release 04 Data for the GRACE Follow-On Laser Ranging Interferometer", Leibniz Universität Hannover, http://doi.org/10.15488/11818

[RD-1402a] Müller, L., Müller, V., Misfeldt, M., Wegener, H., Yan, Y., Hauk, M., ... & Heinzel, G. (2022). New Versions of the AEI-derived LRI1B dataset (No. GSTM2022-38). Copernicus Meetings.
https://presentations.copernicus.org/GSTM2022/GSTM2022-38_presentation-h400506.pdf

[RD-1402b] Müller, L., Müller, V., Misfeldt, M., Wegener, H., Hauk, M., & Heinzel, G. (2022, May). Derivation of an alternative GRACE Follow-On LRI1B data product. In EGU General Assembly Conference Abstracts (pp. EGU22-6109).
https://meetingorganizer.copernicus.org/EGU22/EGU22-6109.html

[RD-1403] https://www.aei.mpg.de/grace-fo-ranging-datasets

[RD-1404] Abich, Klaus, et al. "In-orbit performance of the GRACE follow-on laser ranging interferometer." Physical review letters 123.3 (2019): 031101.
https://doi.org/10.1103/PhysRevLett.123.031101

[RD-1405] Misfeldt, Malte, et al. "Disturbances from Single Event Upsets in the GRACE Follow-On Laser Ranging Interferometer." under review (2023).
https://doi.org/10.48550/arXiv.2302.07681

[RD-1406] Müller, Vitali, et al. "Comparing GRACE-FO KBR and LRI ranging data with focus on carrier frequency variations." Remote Sensing 14.17 (2022): 4335.
https://doi.org/10.3390/rs14174335

[RD-1407] Misfeldt, Malte, et al. "Scale Factor Determination for the GRACE Follow-On Laser Ranging Interferometer Including Thermal Coupling." Remote Sensing 15.3 (2023): 570.
https://doi.org/10.3390/rs15030570

[RD-1408] Emily Rose Rees, Andrew R. Wade, Andrew J. Sutton, Robert E. Spero, Daniel A. Shaddock, and Kirk Mckenzie, Absolute frequency readout derived from ULE cavity for next generation geodesy missions https://doi.org/10.1364/OE.434483

[RD-1409] Rees, Emily Rose, et al. "Absolute Frequency Readout of Cavity against Atomic Reference." Remote Sensing 14.11 (2022): 2689.
https://doi.org/10.3390/rs14112689

[RD-1410] Wegener, Henry, et al. "Tilt-to-length coupling in the grace follow-on laser ranging interferometer." Journal of spacecraft and rockets 57.6 (2020): 1362-1372. https://doi.org/10.2514/1.A34790

[RD-1411] Wegener, Henry: Analysis of tilt-to-length coupling in the GRACE follow-on laser ranging interferometer. Hannover : Gottfried Wilhelm Leibniz Universität, Diss., 2022, x, 190 S. DOI: https://doi.org/10.15488/11984

[RD-1412] Yan, Y., Müller, V., Heinzel, G., & Zhong, M. (2021). Revisiting the light time correction in gravimetric missions like GRACE and GRACE follow-on. Journal of Geodesy, 95, 1-19. https://doi.org/10.1007/s00190-021-01498-5

[RD-1413] Vitali Müller (2017), Design Considerations for Future Geodesy Missions and for Space Laser Interferometry, https://doi.org/10.15488/9029

[RD-1414] Laura Müller et al, (2023), Comparing GRACE Follow-On Inter-Satellite Pointing Angles from Star Camera and LRI Fast Steering Mirror, Presentation at IUGG Berlin 2023
https://doi.org/10.15488/14306

[RD-1415] Tamara Bandikova (2005), PhD Thesis: The role of attitude determination for inter-satellite ranging,

PART 5:

NGGM/MAGIC SCIENCE IMPACT ANALYSIS

26. INTRODUCTION

The purpose of this document is to describe the science impact analyses of the relevant mission scenarios performed during CCN1 in WP1600 in different fields of applications of the mass change data in geosciences, in particular in the fields of hydrology, ocean science, cryosphere, solid Earth science and climate change. The goal is to provide an assessment of their science value with respect to the selected applications and thus also providing additional grounds for updating or rephrasing of science questions and objectives and mission requirements (WP1200).

27. SCIENCE IMPACT ANALYSIS (WP1600)

27.1. IMPACT ANALYSIS OF SIMULATION RESULTS (WP1610)

Analysis of 5-days simulations for terrestrial water storage variations in river basins

We evaluate 5-days simulation results for a double-pair mission (5d_397_70, in the following denoted as MAGIC), and the respective results for a polar-pair-only and an inclined-pair-only (NGGM) scenario. Similar to the assessment carried out for earlier 7-days simulations, time series of equivalent water heights were derived for basin averages of 405 individual river basins defined by the Global Runoff Data Center (GRDC), representing the largest river basins worldwide. The temporal root-mean-square difference (RMSD) between the reference and the simulation time series was computed for each river basin to assess the accuracy of the simulation results.

The NGGM MRD lists target and threshold numbers to specify the envisaged accuracies for specific spatial resolutions, e.g. 600km and 400km for the “3-5 days” time scale in the thematic field of hydrology. As before, unfiltered solutions are used to mark the worst-case-scenario and the series expansions are truncated at the degree corresponding to the desired spatial resolution, i.e. 600km ≙ Nmax=33 and 400km ≙ Nmax=50, starting at degree 2. Figure 27-1 shows the RMSD for the 405 river basins for the lower resolution (600km) and Figure 27-2 the respective results for the higher resolution (400km). It can be concluded that for hydrological applications, which mostly take place in the lower to mid latitudes (almost all basins are below +/-70° degree latitude) the inclined pair represents a significant improvement above using the polar pair only. To better assess the difference between the double-pair and the NGGM scenario, the difference between both (MAGIC minus NGGM, lower right of Figure 27-1 and Figure 27-2 is plotted additionally. While these results might even suggest that with the exception of some basins in the higher latitudes the NGGM scenario fits better to the reference than the MAGIC solution, this is not a conclusion regarding the actual mission performance, but an indication of the potential for improvement in the processing choices. The regularization necessary for the NGGM pair might have a strong influence on the results and the relative weighting of the two MAGIC pairs has so far only been determined based on instrument performance while neglecting the improved self-dealiasing capabilities of the inclined pair. This might have led to possibly overestimating the weight of the polar pair in the MAGIC results. Figure 27-3 shows a summary of the basin averages in terms of a scatter plot of RMSD vs. basin size. Again, the strong improvement achieved by launching the NGGM pair can be observed and it becomes evident that the MAGIC and the NGGM scenarios perform very similarly with a small advantage for the NGGM simulations due to the processing choices outlined above. The horizontal blue lines indicate the threshold requirements listed in the NGGM MRD for the 3-5 days short-term variations in the thematic field of hydrology (i.e. 4.2 cm for 400km and 2.5 cm for 600km). The statistics of these plots are summarized in Table 27-1, which shows the number and percentage of river basins for each resolution that are below the respective threshold. While for the polar-only scenario only very few basins (4-5%) fulfill the requirement, for both MAGIC and the NGGM scenario the requirement is fulfilled for the large majority of basins (93-97%) confirming the added benefit of NGGM for hydrological applications. However, it should be kept in mind that the threshold was defined for 3-5 days and the simulation period of 5 days is at the upper (i.e. most optimistic) end of this range, for 3 days the numbers will likely be lower. Nevertheless, from the 5-days simulation results it can be concluded that simulations are very consistent with the envisaged mission performance for short-term mass variations.

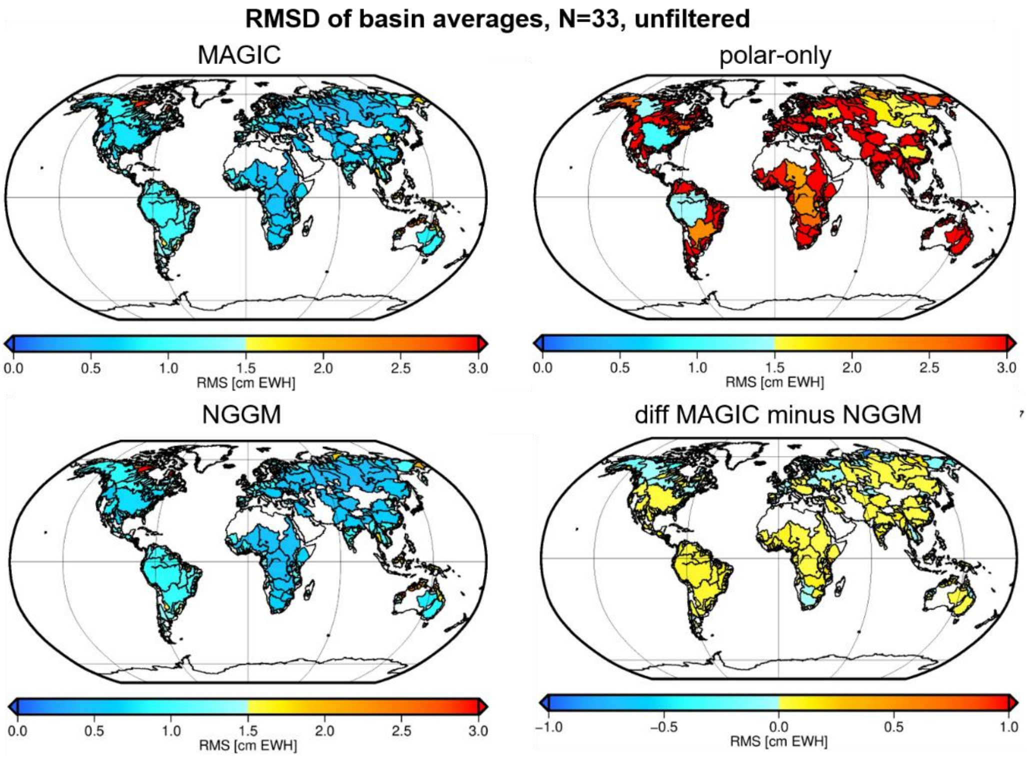

Figure 27-1: Temporal RMSD of 5-days simulation output and reference solution truncated at N=33 for basin averaged time series of 405 river basins defined by the Global Runoff Data Center (GRDC): double-pair MAGIC mission (top left), polar-pair-only (top right) and NGGM (bottom left). The figure on the bottom right shows the difference between the MAGIC and the NGGM result.

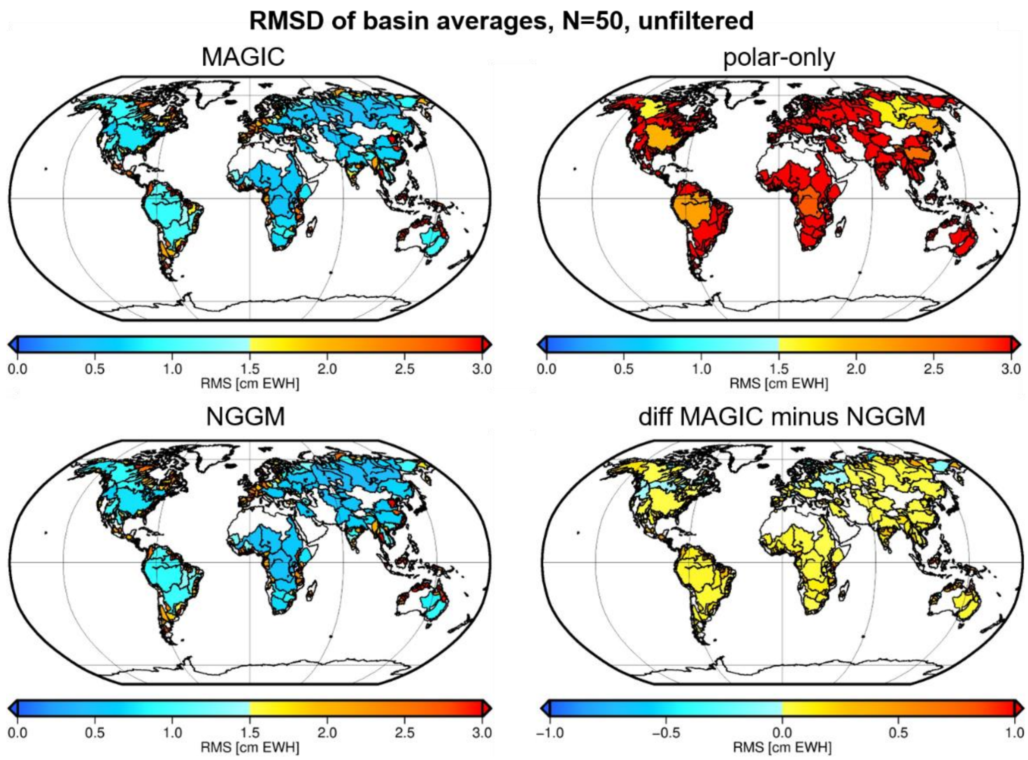

Figure 27-2: Temporal RMSD of 5-days simulation output and reference solution truncated at N=50 for basin averaged time series of 405 river basins defined by the Global Runoff Data Center (GRDC): double-pair MAGIC mission (top left), polar-pair-only (top right) and NGGM (bottom left). The figure on the bottom right shows the difference between the MAGIC and the NGGM result.

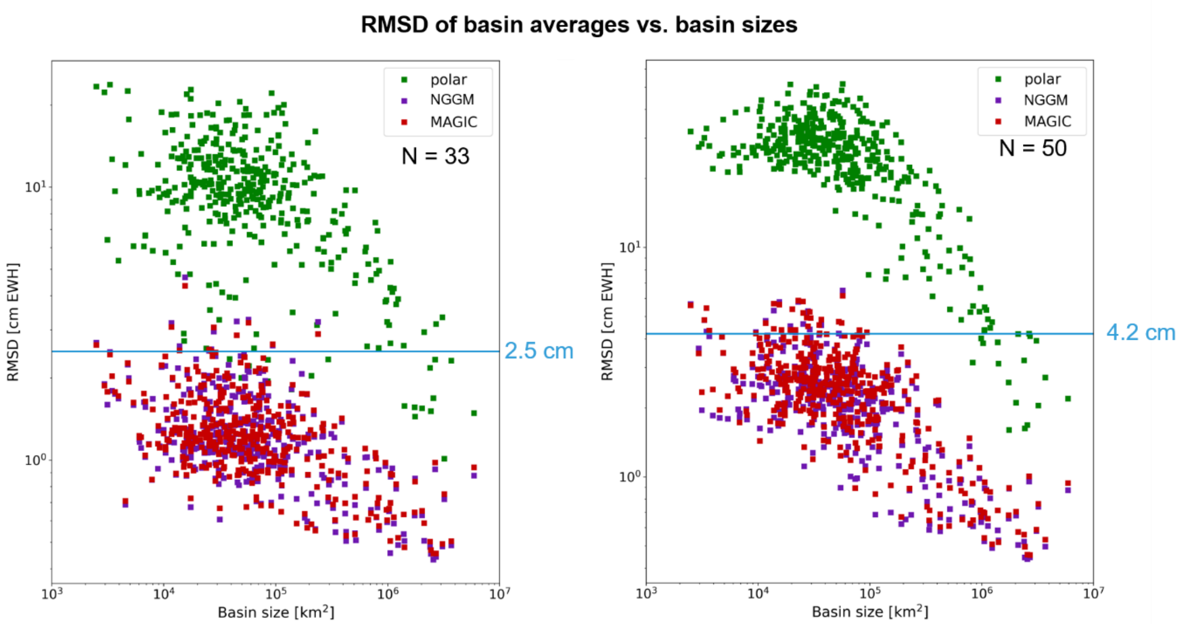

Figure 27-3: Scatter plot of RMSD of basin average time series vs. size of the river basin for different mission scenarios and spatial resolutions for N=33 (left) and N=50 (right). The blue line shows the threshold requirement listed in the NGGM MRD for 3-5 days solutions of the respective spatial resolutions.

Table 27-1: Number of river basins that meet the threshold requirements for the two spatial resolutions and the 5-days temporal resolution.

	N = 33 [600km], threshold: 2.5cm		N = 50 [400km], threshold: 4.2 cm	
	# basins	percent	# basins	percent
polar-only	19	5%	17	4%
NGGM	394	97%	386	95%
MAGIC	394	97%	377	93%

27.2. IMPACT ANALYSIS ON PROVISION OF AOHIS VS. HIS L2 PRODUCT (WP1620)

In the following, it is assessed if and for which applications the user community may benefit from a MAGIC AOHIS product in which all AOHIS components are estimated directly from the NGGM observations, without prior de-aliasing of AO. The assessment is provided separately for potential applications over the continental areas and for ocean areas.

Continents

For applications on the continental areas, the mass variations in the terrestrial hydrosphere and cryosphere as well as solid Earth-related signal have typically been regarded as target variables of satellite gravimetry. However, the satellite observations are additionally influenced by atmospheric mass variations. This influence has been studied in detail in ESA's GRACE-FO TPM project and a manuscript on the findings has been submitted to Surveys in Geophysics (Balidakis et al., submitted). The total change of atmospheric mass (dry and wet parts) represented by the barometric surface pressure is already very well constrained by barometric observations. Related uncertainties in numerical weather prediction models or atmospheric reanalyses are small. Therefore, the total mass change of the atmosphere cannot be regarded as a profitable target of satellite gravimetry missions. In contrast to this, the water vapour mass change would in general be an interesting target of geodetic observations. However, it represents only a small portion (~4%) of the mass variations in the atmosphere, and its uncertainties are at the sensitivity level of current and future satellite gravimetry missions (Balidakis et al., submitted). A reliable signal separation is, therefore, most likely not feasible in the foreseeable future. Thus, in conclusion we see little benefit of an improved atmospheric mass estimate derived from NGGM/MAGIC over the continents. Other geodetic observation techniques, such as GNSS tomography are much more promising in this regard.

Oceans

For ocean applications, the provision of a new AOHIS product in which the high frequency content is based on gravity observations rather than a dealiasing model, is of value to the oceanographic community in a number of ways:

For long time scales (longer than about 1-month period), since the difference between the two products (i.e., the new AOHIS product and the nominal product with a-priori dealising of atmosphere and oceans and subsequent re-adding of these components) is in their handling of higher frequencies, the main interest would be to see how (if at all) this "leaks" via the dealiasing calculations into the longer time scales. It would help to provide a quantification of the dealiasing error at these long timescales, based on the results from two completely different approaches – something which has hitherto not been possible. For this purpose, it would be helpful for the AOHIS product itself to be made available for researchers who wish to dig more deeply into any differences, but the primary information would be the long-period dealiased fields themselves.

For shorter timescales, current methods use a remove-restore technique based on ocean models, with GRACE providing additional information via filters/regularisations worked out in a number of different ways by different groups. When comparing with observations, this makes it very difficult to assess how much explained variability is due to GRACE and how much due to the prior models (see, e.g. Schindelegger et al. (2021) and Ponte and Schindelegger (2022) for examples where care has been taken to disentangle the causes). There are important global-scale processes on such time scales, particularly around 5-day period, which, although small in amplitude (typically a few cm at most), have the potential to play an important role in storm surge predictions for flooding, and in determining the ocean's contribution to earth rotation. A truly independent AOHIS product would be very valuable for testing and developing models of these processes, which are presently only assessed very sporadically, and mostly by comparison with a poorly distributed network of ocean bottom pressure recorders (e.g. Thompson and Fine, 2021).

Interest in the shorter timescales for such ocean applications has a particular focus at an around 5-days period, although other periods (both longer and shorter) are also of interest. The 5-day mode represents a basin-scale mass exchange between the Pacific and mainly the Atlantic, driven predominantly by atmospheric pressure fluctuations due to a normal mode of the atmosphere (Ponte and Schindelegger 2022). It is a valuable probe to test global ocean models in a non-tidal regime in which loading and self-attraction are important processes, which is relevant for development of the next generation of storm surge models for coastal flood warning. For this reason, a 3-days sampling period would be more appropriate than 5-days or longer.

27.3. DEFINITION OF IMPACT ANALYSIS ON NEUTRAL DENSITY AND WIND PRODUCTS, AND SPACE WEATHER (WP1630)

The task of this work package is to design a road map for an E2E impact study from level 0 (accelerometer observations) to level 3 (SSA).

Processing from Level 0 to Level 3

Level 0 processing often involves converting the telemetry packets into level 0 data products, typically sorted per instrument. The next processing from level 0 to level 1a selects relevant parameters from the level 0 data products and converts from engineering units to physical units, potentially requiring a database with auxiliary data for conversion. The Level 1b processing can then involve more complex processing to transform the raw measurements (Level 1a) into scientifically usable measurements (Level 1b). The exact content of the level 1b processing will depend on the instruments, their characteristics, and the needs of subsequent level 2 processing. Thus, we cannot anticipate this now in detail. Level 1b data products serve as input for deriving density and crosswind data products, for which we outline the processing below.

The processing of acceleration measurements to density and crosswind observations is well-established. An instructive and complete description is available in Doornbos (2011) and Siemes et al. (2023), and an overview is provided in Figure 27-4. Starting from the measured acceleration, the first step is the preprocessing that reduces any kind of undesired signal and noise to obtain a “clean” acceleration. These accelerations are still scaled and biased. Therefore, the next step is the estimation of the scale and bias parameters in a precise orbit determination approach using GNSS receiver data and, subsequently, applying these parameters to obtain the calibrated acceleration. The aerodynamic acceleration $\boldsymbol{a}_{aero}$ is obtained by subtracting the radiation pressure acceleration from the calibrated one. The radiation pressure is modeled based on solar and Earth radiation flux data in combination with a satellite model for radiation pressure. The latter is determined via a ray tracing simulation. In a similar way, we obtain an aerodynamic satellite model via a DSMC simulation of aerodynamic forces. This model is essentially a lookup table for the aerodynamic coefficient vector $\boldsymbol{C}_{aero}$. Once the aerodynamic acceleration and the aerodynamic satellite model are available, the density and crosswind observations are derived via direct and iterative algorithms as described in Doornbos (2011). The following sections provide further details on these processing steps.

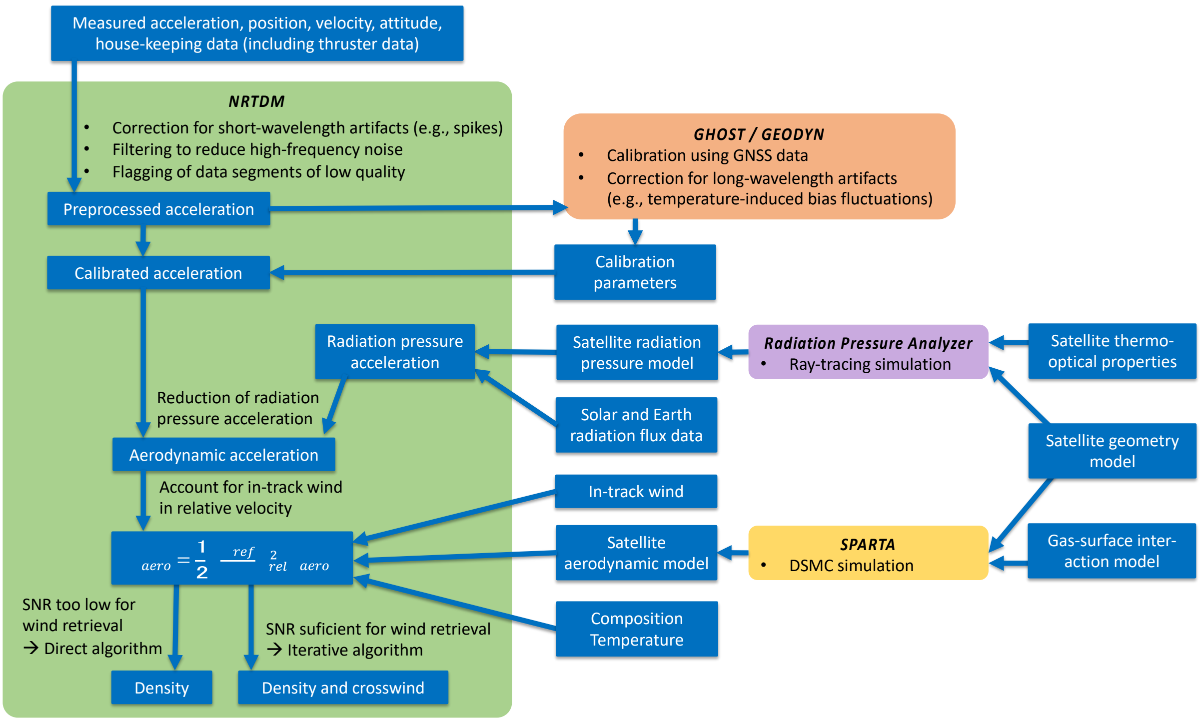

Figure 27-4: Processing of measured accelerations to density and crosswind.

Accelerometer data preprocessing

The accelerometer data preprocessing aims at reducing all kinds of undesired signals and noise. This includes, in particular, artificial spikes and accelerations due to thruster activations. Spikes are typically detected by applying a moving-median filter to the accelerometer measurements and detecting outliers in the residuals. In addition, housekeeping data from the AOCS is used to identify thruster activations in case of impulsive thrusts or the thrust force in case of continuous thrust.

Accelerometer data calibration

The estimation of calibration parameters is described in detail in van Helleputte et al. (2009), Visser and van den IJssel (2016), and Siemes et al. (2023). In short, the calibrated accelerations are expressed as a linear function of the preprocessed acceleration, where a scale factor and a bias are the parameters of the linear function. In the case of NGGM/MAGIC, more complex calibration models could be applied (e.g., including quadratic factors). The bias is adjusted within a precise orbit determination procedure, where the sum of gravitational and non-gravitational accelerations is integrated twice and fitted to a precise orbit derived from the GNSS receiver data.

High-fidelity satellite geometry model

The satellite geometry models form the basis for radiation pressure and aerodynamic modeling. High-fidelity geometry models were already available for the CHAMP and GRACE satellites as described in March et al. (2019a). For the GRACE-FO satellites, we derived the high-fidelity geometry model directly from the CAD model of the satellites using the Blender software. The derivation requires reducing the CAD model to the outer surface, which must be “water-tight”. Further, the surface is simplified to some extent to reduce the number of facets, which facilitates a reasonable run-time of the radiation pressure and aerodynamic simulations. For NGGM/MAGIC, it would be very beneficial to access the CAD model of the satellites, noting that the interior is not required.

Satellite radiation pressure model

The satellite radiation pressure model has two components. The first is the radiation pressure force coefficient vector determined within a ray tracing simulation. In short, simulated light rays are traced to surface elements of the satellite geometry, where they create a pressure on the surface that depends on the absorptive and reflective properties of the surface. This allows us to account for shadowing and multiple reflections. The second component of the radiation pressure model is a thermal model of the satellite (Siemes et al., 2023). The advantage of this model is that we can integrate the absorbed radiation along the orbit and, thus, account for the thermal inertia of the satellite. It will be very beneficial to access the thermo-mathematical model available from the industry, and to have data from thermistors on all major outer panels of the satellite, noting that the thermistors might need to be calibrated.

Satellite aerodynamic model

The satellite aerodynamic model is described in depth in March et al. (2021), and Mehta et al. (2022). It is obtained via a DSMC simulation where the gas-surface interaction is assumed to be diffuse with incomplete energy accommodation. For example, the aerodynamic models for the CHAMP and GRACE satellites are described in detail in March et al. (2019b).

Density and crosswind retrieval

The density and crosswind observations are derived by the direct and iterative algorithms described in detail in Doornbos (2011). For the density observations, we always use the direct algorithm where the acceleration is projected onto the x-axis of the satellite reference frame, which is approximately aligned with the flight direction. This guarantees a large aerodynamic signal in the nominal flight orientation and guarantees that only the sensitive accelerometer axis is used, which is also the most accurate in terms of calibration. The crosswind observations are obtained using the iterative algorithm.

In the following, we distinguish between space weather applications, for which timely provision of observations is paramount, and scientific applications that do not require low latency.

Space weather applications

The thermosphere is a highly driven system, externally forced by solar radiation, solar wind (stream of charged particles), coronal mass ejections, and their interaction with Earth's magnetic field, often called geomagnetic activity. Also, gravity waves generated in the lower layers of the atmosphere propagate upward as secondary and tertiary waves and deposit energy into the thermosphere. In the context of space weather, neutral density and wind should be considered as two out of many different types of relevant observations.

The connection between the external forcing and the thermosphere's response is complex, and observations of the external forcing are far from complete. This makes accurately now- and forecasting the thermosphere's state a challenging task. Models employed for this purpose are often subject to biases of several tens of percent in neutral density, hampering their use for orbit predictions. In this context, we highlight that the low-Earth orbit environment gets evermore crowded as new space companies deploy their mega-constellations of satellites, drastically increasing the chance of collisions and, therefore, the need for more accurate orbit predictions for conjunction analysis and collision risk assessment.

Neutral density and wind observations reflect the state of the thermosphere and, therefore, can be used to correct thermosphere model biases. Methods to do so range from simple adjustments of the reduced-order models (ROM) to full-fledged data assimilation into complex models replicating first-order principles of atmosphere physics. While ROMs are the simplest type of model, their potential rests in the fact that a large fraction of the thermosphere variability can be expressed with a very limited number of parameters (Licata et al., 2022; Mehta and Linares, 2017; Licata and Mehta, 2023), enabling straight forward data assimilation schemes (Callejón et al., 2023).

1. ***We identify using neutral density observations to correct thermosphere models as the single, most important space weather application, which is highly relevant for conjunction analysis and collision risk assessment.***

Since the thermosphere is highly driven and conditions may change fast, the timeliness of observations is paramount. Observations that are several days old are practically useless for correcting model biases. The 'age' of the observations is the time from the measurement to the moment the observation is used to correct a model. This includes the time between measurement on board the satellite and the downlink of telemetry to the ground station, the time needed to process the telemetry and send the output data to a processing center, the processing time, and the time needed to send the processed data to a user.

2. ***In the context of space weather, providing neutral density observations with the lowest possible latency is paramount.***

Neutral density observations that are derived from accelerometer measurements provide the highest possible resolution along the orbit, allowing us to interpret the observations as in situ. However, when certain prerequisites are met, we can also derive neutral density observations from the measurements of GNSS receivers, albeit at a lower resolution along the orbit. How much lower depends on the accuracy of the GNSS receiver measurements. As a rough guideline, GNSS receivers that provide positioning at meter-level accuracy allow for deriving neutral density observations with a resolution of only several orbits, i.e., global mean density. In contrast, GNSS receivers that enable positioning with cm-level accuracy allow for deriving neutral density observations with a resolution of about 20 minutes, enabling the detection of, e.g., day-nightside differences. The latter can only be achieved when dual frequency carrier phase observations are processed on the ground, using accurate GNSS position and clock data from, e.g., the IGS. This should be judged against current practice, where radar tracking with an accuracy of hundreds of meters is used in space operational awareness.

Nowadays, many satellites are equipped with capable GNSS receivers, e.g., the fleet of Lemur satellites of Spire Global. However, we are unaware that any satellite constellation provides the required GNSS receiver data free of charge, with sufficiently low latency, and all required auxiliary data (satellite attitude, mass, geometry, surface properties, etc.). ESA's Swarm mission is the best constellation for this purpose, with three satellites in two distinct orbits and two downlinks of telemetry daily. Nevertheless, GNSS receiver measurements bear great potential due to their superior accuracy compared to radar tracking and, in theory, their abundance. More data becoming available will diminish the importance of individual data sets. Accelerometer-derived neutral density data sets will play an important role because of their unmatched along-track resolution, making them the only in situ observations.

3. ***Accelerometer measurements are not the only data source for deriving neutral density observations. However, their high resolution along the orbit makes them unique.***

Scientific applications

Other accelerometer-derived density data sets exist from the CHAMP, GRACE, GOCE, Swarm, and GRACE-FO missions. In some use cases, it is important that they are collected during the same period as other thermosphere/ionosphere/magnetosphere (MIT) observations because of the dynamic nature of the MIT system. The scientific value of the density and crosswind observations should therefore be evaluated not only in self-standing but also in view of synergies with other missions collecting observations of the MIT system. In the following, we collect and briefly explain various scientific use cases of density and crosswind observations.

Assimilation of density observations in thermosphere models

Thermosphere observations can serve as the primary data source for constructing thermosphere models (Bruinsma and Boniface, 2021; Boniface and Bruinsma, 2021), be used for model evaluation (Sutton et al. ,2021; Bruinsma et al., 2021), be assimilated in reduced-order models (Callejón et al., 2023; Mehta and Linares, 2017; Licata and Mehta, 2023), semi-empirical models (Forootan et al., 2021; Forootan et al., 2022) and physics-based model (Fernandez-Gomez, 2022; Kodikara, 2022).

Comparison to different observation types

In-situ observations of neutral density are often used as ground truth compared to other, more indirect observation types. For instance, SABER (Sounding of the Atmosphere using Broadband Emission Radiometry) remote sensing observations have been compared with in situ Swarm observations of neutral density (Weimer et al., 2018). Another example is the comparison of the exospheric temperature measured by NASA's Global-scale Observations of the Limb and Disk (GOLD) mission with density observations (Park et al., 2022). These randomly selected examples indicate the value of in situ neutral mass observations compared to completely different observation types.

Validation of other observation types

Closely related to the comparison to different observation types, neutral density observations can also be compared to other observation types that directly relate to neutral density, albeit at a lower resolution along the orbit. In this case, too, in situ observations of thermosphere density are often treated as the ground truth so that we may speak of validating other observation types. This includes the validation of density derived from radar tracking observations, which are the most abundant data source, yet provide the lowest accuracy (tracking errors are hundreds of meters or even kilometers) and spatial resolution (Gondelach et al., 2021; Gondelach and Linares, 2021; Brandt et al., 2020; Riviere-Casanova and Collins, 2021).

GNSS tracking is already far more accurate than radar tracking and can be subdivided into tracking based on code measurements and dual-frequency carrier phase measurements. The first provides meter-level and the latter centimeter-level accuracy. Examples are provided by Bussy-Virat and Ridley (2021), Sutton et al. (2021) and van den IJssel et al. (2020). Depending on the processing of the GNSS data, accelerometer-derived densities either serve to validate the GNSS-derived density observations or merely add spatial resolution.

Validation of thermosphere models

In situ thermosphere observations are also frequently used for the validation of thermosphere models. For instance, Manzi et al. (2020) use neutral density observations to validate an empirical model that is based on the assimilation of two-line element (TLE) data (derived from radar tracking). Another example is provided by Calabia et al. (2020), who use neutral density observations to assess the NRLMSISE-00 model. Kalafatoglu Eyiguler et al. (2019) evaluate the performance of thermosphere models during geomagnetic storms, and Kodikara et al. (2018) compare neutral density observations to empirical and physics-driven models. The performance of thermosphere models during geomagnetic storms is reviewed by Oliveira et al. (2021). There are many more examples, but it is already clear from the selection in this paragraph that in situ neutral density observations play a major role for the validation of thermosphere models.

Studying dynamics during geomagnetic storms

In situ neutral density observations are often used to study the dynamics of the ionosphere-thermosphere systems during geomagnetic storms via multi-parameter analysis. Examples of geomagnetic storms analyzed in this way are the ones that occurred on 7-8 September 2017 (Zhang et al., 2017; Yuan et al., 2019; Wang et al., 2019) and 21-23 June 2015 (Astafyeva et al., 2017).

Neutral wind observations

A peculiarity about crosswind observations derived from accelerometer measurements is that they represent not the full wind vector but its projection onto the cross-track direction. In other words, crosswind observations are scalars that apply in a certain direction. Nevertheless, neutral winds can be used to study the dynamics of the thermosphere. For instance, Förster et al. (2011) estimate the mean polar wind field from CHAMP crosswind observations. Further, Drob et al. include GOCE crosswind observations in constructing the Horizontal Wind Model 2014. Crosswind observations can also be used to study atmospheric dynamics during geomagnetic storms (Sutton et al., 2005).

Roadmap

Density and crosswind data products (Level 2)

The first, most obvious steps will be establishing processing chains for the density and crosswind observations, one aiming at low latency and another for scientific applications. The main differences between the processing chains will be related to the accelerometer data calibration, particularly the bias estimation via precise orbit determination based on GNSS receiver data. Aiming for low latency means using the most recently available satellite data, which requires a lot of adaptions to detect new data, select an appropriate time window for processing, fetch all required auxiliary data from the IERS and IGS, etc., and do all of that automated in a robust way. In other words, it will take a substantial effort to establish this processing chain. The scientific processing chain may be operated with a latency of about a month, so all input and auxiliary data is available in its final form in daily batches. Such a processing chain is similar to the existing processing chain for CHAMP, GRACE, GOCE, and GRACE-FO and will require less effort to implement. The two processing chains will enable more direct use of the accelerometer and GNSS data than any lower-level accelerometer data product.

To maximize the usefulness of the density and crosswind observations, they should be augmented with an uncertainty quantification, which is presently not done for any available dataset. Such an uncertainty quantification is currently under development and requires a quantification of the uncertainty of input parameters, including the satellite geometry, thermos-optical surface properties (reflection and absorption coefficients, heat capacitances, etc.), atmospheric temperature, composition, and in-track wind, and the gas-surface interaction.

More details on the near-real-time aspects of the processing will be provided in WP1720.

Assimilation of density data products for space weather applications (Level 3)

The Level 2 density data product generated with minimum latency can be assimilated into ROM, empirical, and physics-driven thermosphere models (e.g., TIE-GCM). Because no near-real-time in situ density data exists presently, such approaches are still in their infancy. We have several proof-of-concept studies, as described in the previous paragraphs, which can serve as a starting point for further study. An important point that still needs to be studied is the spatiotemporal distribution of the observations, and how that influences what parameters can be estimated, particularly in the case of ROM.

Fortunately, such density observation assimilation methods can be tested based on existing density data. The first activity should focus on comparing existing methods and assessing their skill based on existing density observations. A second, later activity should demonstrate the use of these models within the context of orbit prediction in as realistic as possible settings, to prove that the assimilation schemes ultimately lead to improved orbit predictions. Uncertainty quantification in the assimilation method and the propagation of uncertainty to orbit prediction will be relevant for collision risk assessment.

Assimilation of density and crosswind data products for scientific applications (Level 3)

Density and crosswind can be used to construct or update thermosphere models. For instance, the DTM2020 model (Bruinsma and Boniface, 2021) is heavily based on accelerometer-derived density observations. Similarly, crosswind observations could be used to create a model of polar wind fields. However, the exact usage of density and wind observations in scientific contexts is more difficult to prepare due to the diversity of application cases and, often, the fact that density and wind observations of a particular mission play only a supporting role. Therefore, we do not need to prepare a particular scientific use case based on NGGM/MAGIC-derived density and crosswind observations. The support of scientific use cases should be considered while the mission is operational.

27.4. IMPACT ANALYSIS OF NRT APPLICATIONS INCLUDING EXTREME WEATHER EVENTS (FLOODS, DROUGHTS) (WP1640)

Here we evaluate the performance of the 5-days simulation to represent extreme hydrological events. We compare the double-pair mission (5d_397_70, in the following denoted as MAGIC), the polar-pair-only and the inclined-pair-only (NGGM) scenario. Similar to previous analyses and the river basin analysis in Chapter 27.1, we use unfiltered solutions and the series expansions are truncated at the degree corresponding to the desired spatial resolution of 400km ≙ Nmax=50, starting at degree 2, stated in the NGGM MRD for the “3-5 days” time scale in the thematic field of hydrology.

We define hydrological extremes directly from the mass change time series of the ESM reference model. To this end, we take the full available ESM time series from 1995 to 2006 that - similar to the simulation data – is aggregated to a 5-days resolution, truncated at Nmax=50, and converted to a 1-degree geographical grid. At the grid cell scale, we then remove the 12-year linear trend to minimize the possible disturbing effect of long-term processes such as glacier melt or groundwater depletion on the analysis of the short-term hydro-meteorological extremes of interest here. For the 474 largest river basins worldwide based on the Global Runoff Data Center (GRDC) basin delineation, basin-average time series of 5-day mass anomalies of terrestrial water storage (TWS) in equivalent water heights were then derived for the full ESM period from 1995 to 2006. A percentile approach was then used to define threshold values for wet and dry extremes in this period: we used the 1%, 2% and 5% percentiles to define dry extremes. This means, for instance, that the threshold for a dry extreme at the 1% level represents a TWS anomaly value that is fallen short at only 1% of all timesteps in the analysis period (12 years with 73 5-day intervals = 876 timesteps in total). Similarly, we use the 99%, 98% and 95% percentiles to define wet extremes in the 12-year time series. As the MAGIC and NGGM simulations cover the year 2002 only, we then identify the river basins that exhibit wet and dry events for the different thresholds in the ESM data of 2002. These events are subsequently used as test cases to analyze the performance of the simulations to represent hydrological extremes. To assure the same level of TWS anomalies, the simulated time series of 2002 are shifted so that their mean in 2002 is identical to the mean TWS anomaly of 2002 given in the ESM reference data.

In a first analysis step, we look at the single 5-days interval at which the maximum value of a wet extreme (or the minimum value of a dry extreme) occurs in ESM and check whether the simulations surpass the threshold for an extreme event of a certain percentile at this timestep. Evaluation score A reports the fraction of extreme events that are captured by the simulations over all river basins worldwide and over all extremes at the respective percentiles. Additionally, we calculate the difference of the TWS anomaly of the scenario (in equivalent water height) to the ESM reference on that 5-day interval where the extreme event occurs. Averaging these differences over all the basins with extremes in 2002 worldwide allows to calculate an average performance measure on how closely the simulations match observed extremes (score B).

Table 27-2 and Table 27-3 summarize this evaluation of the simulations in representing extreme events. It is obvious that the number of river basins with extremes in 2002 in ESM decreases with taking more extreme percentiles (from 95% to 98% to 99% in the case of wet extremes, from 5% to 2% to 1% in the case of dry extremes). The fraction of these extremes that are captured by the simulations tends to decrease for the more extreme extremes, for example for the NGGM simulation from a percentage of 64.9% to a percentage of 53.8% for the 5% and 1% percentile dry extremes, respectively. This indicates that it is more difficult for the simulations to represent the rarer events.

Table 27-2: Evaluation of simulations to represent 5-day dry hydrological (TWS) extremes for the 474 largest river basins worldwide. n: number of river basins (out of the 474 basins) with an extreme below the 1, 2 and 5% percentile in 2002. Score A: fraction of river basins in the simulations that match the extremes in ESM (in %). Score B: Mean deviation of the simulated TWS anomaly from the TWS anomaly value of the ESM reference on the 5-day interval with an extreme event (in cm EWH).

	Dry extremes								
	1%			2%			5%		
	n	A	B	n	A	B	n	A	B
		%	cm		%	cm		%	cm
ESM	80			116			202		
polar-pair	38	47.5	21.0	64	55.2	22.6	103	51.0	21.5
NGGM	43	53.8	1.9	66	56.9	2.0	131	64.9	1.8
MAGIC	46	57.5	1.7	65	56.0	1.9	120	59.4	1.8

Table 27-3: Evaluation of simulations to represent 5-day wet hydrological (TWS) extremes for the 474 largest river basins worldwide. n: number of river basins (out of the 474 in total) with an extreme exceeding the 95, 98 and 99% percentile in 2002. Score A: fraction of river basins in the simulations that match the extremes in ESM (in %). Score B: Mean deviation of the simulated TWS anomaly from the TWS anomaly value of the ESM reference on the 5-day interval with an extreme event (in cm EWH).

	Wet extremes								
	99%			98%			95%		
	n	A	B	n	A	B	n	A	B
		%	cm		%	cm		%	cm
ESM	63			102			173		
polar-pair	28	44.4	16.9	53	52.0	18.8	92	53.2	20.5
NGGM	42	66.7	1.8	71	69.6	2.1	131	75.7	2.0
MAGIC	41	65.1	1.9	70	68.6	2.2	130	75.1	2.2

For both dry and wet extremes at all percentiles, the fractions of extremes that are captured by NGGM or MAGIC are larger (with fractions in the range of 54% to 76%) than the fractions for the polar-pair (44% to 55%) (Score A in Table 27-2 and Table 27-3). This better performance of NGGM and MAGIC over the polar-pair is more pronounced for the wet extremes than for the dry extremes. For all extremes, the error in quantifying the size of the event in EWH (Score B in Table 27-2 and Table 27-3) is about one order of magnitude larger for the polar-pair simulation (in the range of 17 to 23 cm EWH) than for NGGM or MAGIC. The latter two perform almost identically well with an error of about 2 cm EWH.

The global distribution of the errors in representing the extreme TWS anomalies is shown for the example of the 5% percentile dry extremes (Figure 27-5) and the 95% percentile wet extremes (Figure 27-6). The similar performance of NGGM and MAGIC is obvious also on these plots. Only for a few high-latitude river basins in northern Siberia the performance of MAGIC is better than for NGGM, as MAGIC either captures extremes at all or with smaller error. The polar-pair scenario exhibits more basins than NGGM or MAGIC where the extreme event by surpassing the respective TWS anomaly threshold is not represented at all (in grey in Figure 27-5 and Figure 27-6). There are no clear patterns of those basins in terms their geographical distribution or size.

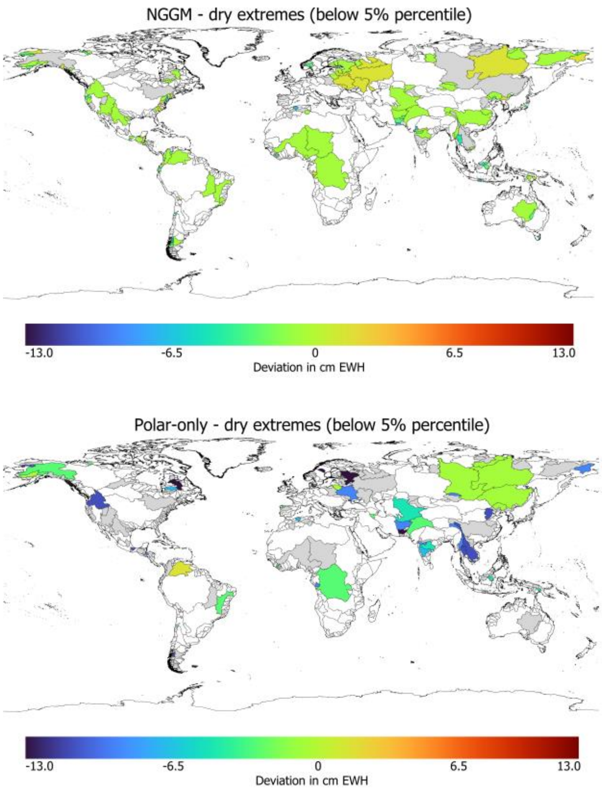

Figure 27-5: Dry extremes (below the 5% percentile) for 5-day data (with Nmax=50) in large river basins worldwide in the year 2002 that are captured by the simulations of the NGGM inclined-pair only (upper left plot), the MAGIC double-pair (upper right plot) and the polar-pair only (lower plot). The colours give the deviation of the simulated mass anomaly of the extreme from the reference mass anomaly of the extreme given in the ESM reference (all values in cm EWH). River basins filled in white do not exhibit a dry extreme event below the 5% percentile in the ESM data in 2002; in river basins filled with grey colour there was an extreme event in 2002 but it was not captured by the scenario.

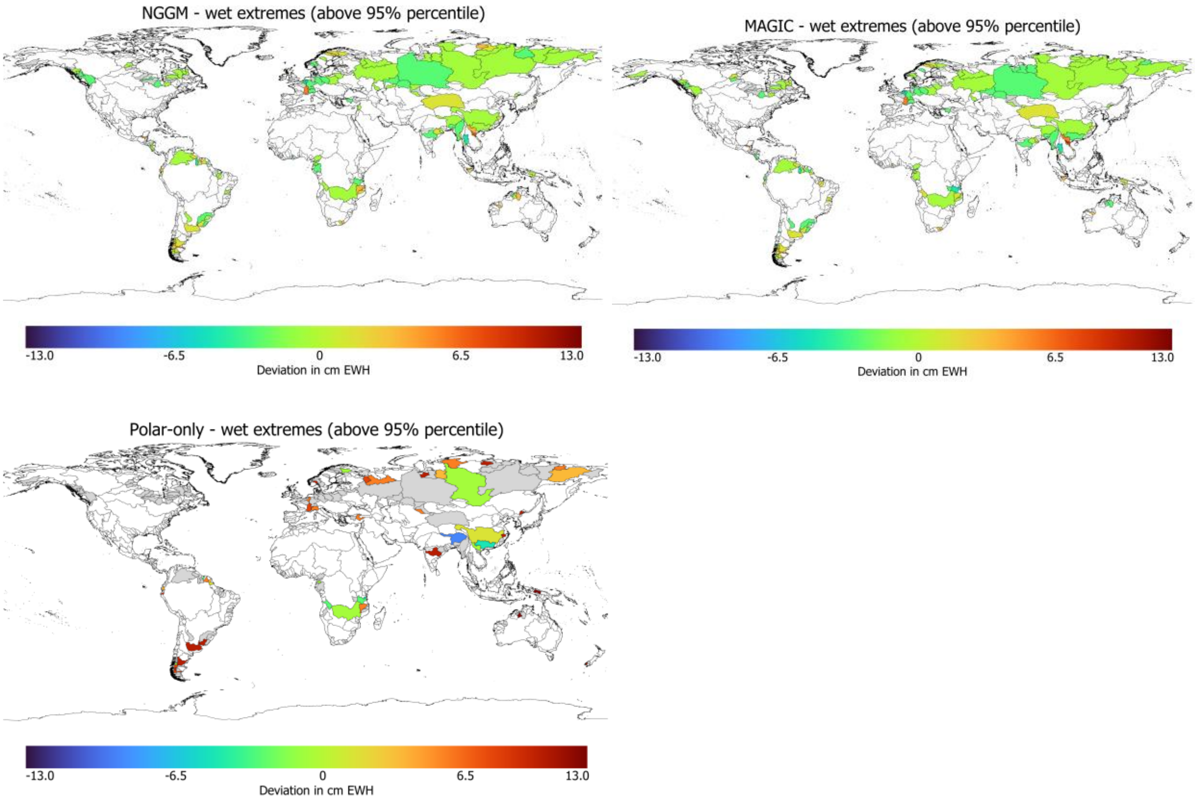

Figure 27-6: Similar to Figure 27-5 but for wet extremes (above the 95% percentile. River basins filled in white do not exhibit a wet extreme event above the 95% percentile in the ESM data in 2002; in river basins filled with grey colour there was an extreme event in 2002 but it was not captured by the scenario.

The aforementioned results on the accuracy with which extreme values can be detected (score B) are in line with observations of the hydrological evaluation of the entire simulation time series in Chapter 27.1. The results indicate that at the selected resolution of 400 km (Nmax=50), the threshold requirement of 4.2 cm can be reached by NGGM and MAGIC even at the level of individual 5-day time steps of extreme TWS anomaly values, whereas the polar-only pair largely fails in reaching this requirement.

For the polar-pair simulations, the comparatively high percentage of extremes matched in time (score A, in the range of 44% to 55%) but with high absolute deviations in EWH (score B) can be explained by the high noise of the polar-pair simulation. This spuriously causes frequent extreme values in the simulation time series, including the possibility that several real extremes given by the ESM reference are captured by chance by the polar-pair simulation only. This is illustrated by time series examples for an individual river basin, here the Mekong basin (Figure 27-7), and can similarly be observed in all other basins.

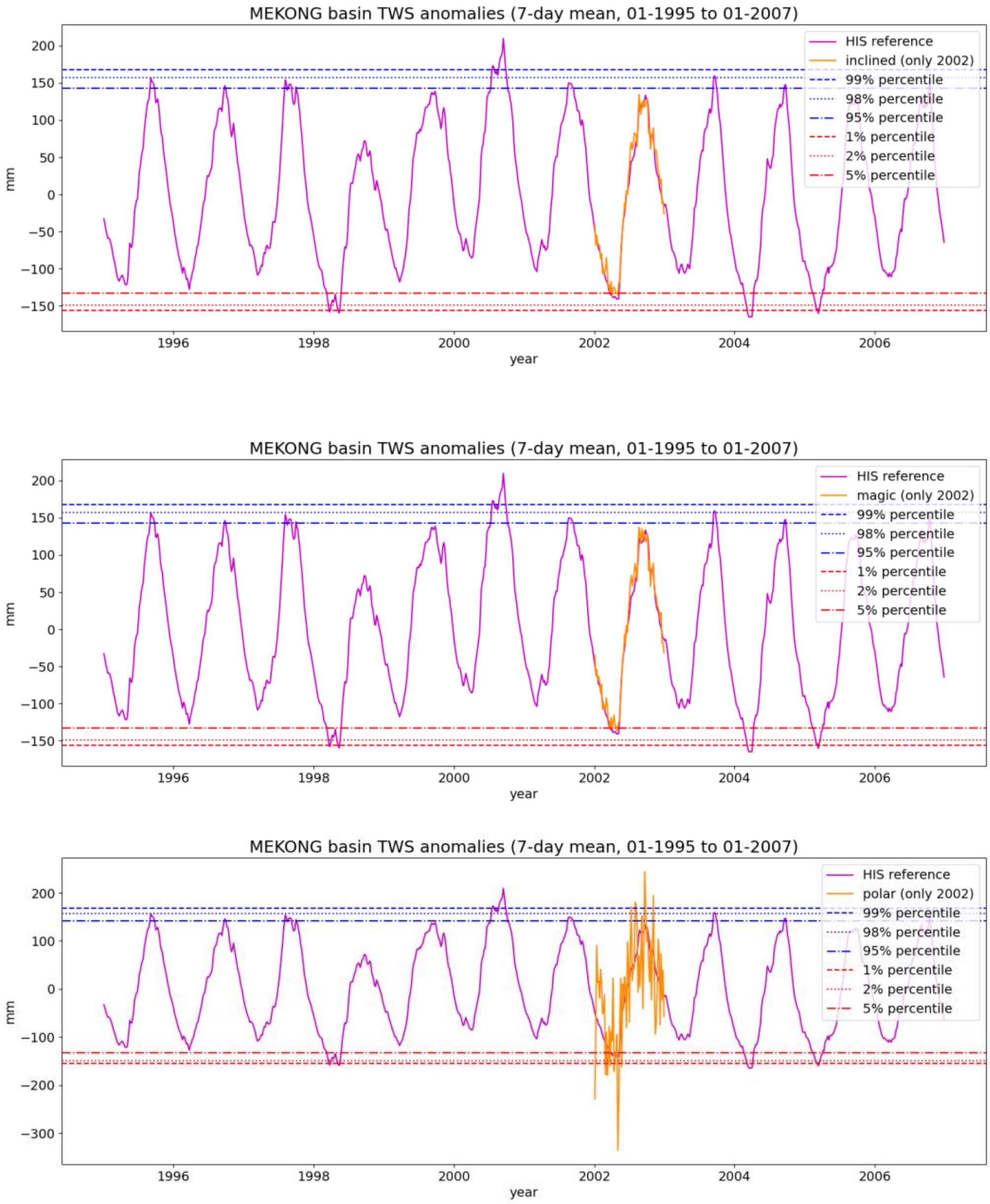

Figure 27-7: Example of 5-day TWS time series for the Mekong river basin. The different percentile thresholds for wet and dry extremes derived from the ESM HIS reference time series of 1995-2006 are indicated. The orange line represents the 5-day simulation results of the NGGM inclined-pair only (top plot), the MAGIC double-pair (centre plot) and the polar-only pair (lower plot).

To consider this issue of noisy data in a quantitative way in the evaluation of the simulations, an analysis of false positives was carried out. With a false positive, we refer to a 5-day interval in 2002 that is a wet or dry extreme (i.e., that surpasses the threshold of an extreme TWS anomaly) in the simulation but not in the ESM reference data. We compare the number of the false positives (FP) to the number of correct hits (CH), i.e., 5-day intervals where the simulation shows an extreme that matches with an extreme in the ESM reference at the same time interval. Additionally, quantitative performance scores are defined as follows:

$$Score\ 1 = \frac{CH}{N_{ref}}$$

$$Score\ 2 = 1 - \frac{FP}{N_{ref}}$$

$$Score\ 3 = \frac{CH - FP}{N_{ref}}$$

In the above scores, N_{ref} is the total number of extreme intervals in the ESM reference data in 2002 for a certain river basin. Score 1 thus describes the performance of the scenario in representing extremes at the correct time intervals, Score 2 is a measure of false positives in the simulation, and Score 3 is a combined index that balances between correctly and incorrectly simulated extreme intervals. All three scores have an optimum value of 1. A negative value of score 3 indicates that the simulation resulted in more false positive extreme intervals than correctly simulated extreme intervals in the respective river basin. The scores were derived for each of the 474 river basins and then averaged over all basins worldwide to give global performance metrices of the simulations. The results are presented here for the 95% percentile wet extremes and the 5% percentile dry extremes as an example, and similarly apply to the other percentile thresholds used for defining the TWS extremes.

Table 27-4: Performance of the simulations in representing dry extremes (5% percentile threshold). Metrics are an average over 202 river basins with dry TWS extremes in 2002 in the ESM reference data. CH: correct hits; FP: false positives; scores 1-3 see main text; FP basins (last column) denotes the number of false positive basins with extremes in the simulation but none in reference data.

5% percentile **dry extremes** (in 202 of 474 basins, with 9.2 intervals on average per basin)						
	CH	FP	Score 1	Score 2	Score 3	FP basins
polar-pair only	5.2	23.5	0.51	-4.68	-5.17	269
NGGM	6.1	7.1	0.55	-0.13	-0.58	156
MAGIC	6.0	7.3	0.56	-0.21	-0.65	161

Table 27-5: Performance of the simulations in representing wet extremes (95% percentile threshold). Metrics are an average over 173 river basins with wet TWS extremes in 2002 in the ESM reference data. CH: correct hits; FP: false positives; scores 1-3 see main text; FP basins (last column) denotes the number of false positive basins with extremes in the simulation but none in reference data.

95% percentile **wet extremes** (in 173 of 474 basins, with 9.2 intervals on average per basin)						
	CH	FP	Score 1	Score 2	Score 3	FP basins
polar-pair only	3.9	22.3	0.51	-4.32	-4.81	297
NGGM	5.8	4.8	0.64	0.04	-0.32	106
MAGIC	5.9	4.9	0.63	-0.03	-0.41	110

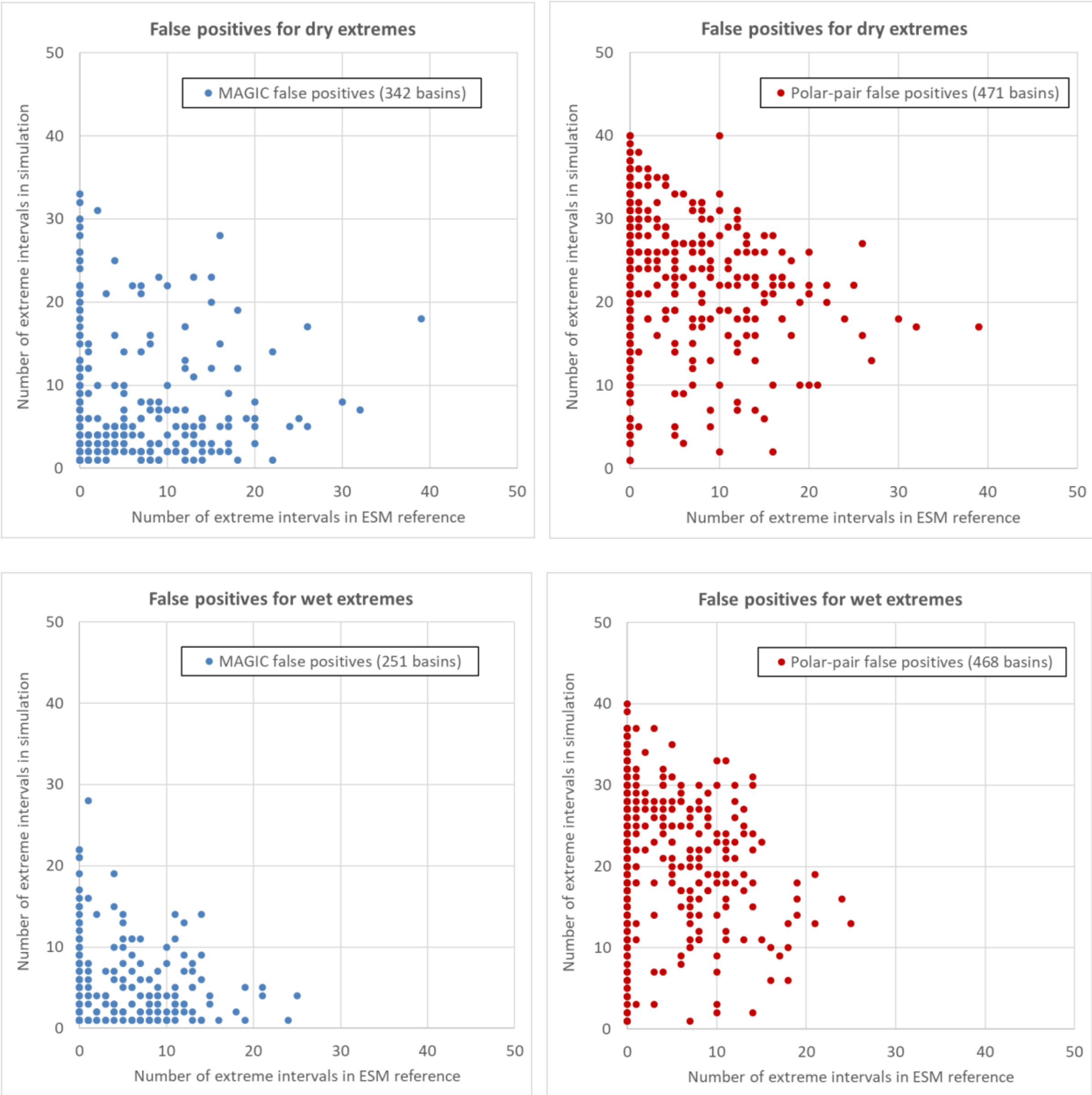

Figure 27-8: Number of false positive 5-day intervals of TWS extremes in river basins in 2002 for dry extremes (5% percentile) (upper row) and wet extremes (95% percentile) (lower row) for the MAGIC simulations (left column) and the polar-pair simulation (right column).

Overall, the results show that the polar-pair simulation is characterized by a very high number of false positives whereas for both NGGM and MAGIC the number of false positives is much lower (Table 27-4, Table 27-5 and Figure 27-8). The ESM reference data exhibit about 9 timesteps with wet or dry extremes in 2002 and the polar-pair simulation results in more than twice that number of false positives. This confirms that also several of the correct hits of extremes that lead to a comparatively high score A in Table 27-2 and Table 27-3 and here in Score 1 are by chance. For the NGGM and MAGIC simulations, in contrast, the number of false positive intervals is only about 5 and 7 for wet and dry extremes, respectively. This is similar to the number of correct hits and results in only slightly negative values of Score 3 on average over all basins, with again somewhat better results for the wet than for the dry extremes. There are about 160 and 110 river basins for dry and wet extremes, respectively, where the simulations of NGGM and MAGIC result in 5-day intervals with extreme TWS values although there is no extreme in the ESM reference data (last column of Table 27-4 and Table 27-5).

The spatial distribution of the overall Score 3 that balances the correct hits with the false positives is shown for the three scenarios in Figure 27-9 and Figure 27-10. The poorer performance of the polar-pair scenario is clearly visible. The patterns show no clear geographical distribution of better or worse performing basins for the dry extremes. For the wet extremes, the good representation by MAGIC and NGGM in all Russian/Siberian river basins stands out. Furthermore, the patterns indicate that smaller river basins tend to have a lower performance, indicated by reddish colors or dark grey (the letter marks basins that have extremes in the scenario but none in the reference data). As the signal to noise ratio tends to increase when averaging over larger areas, this expected behavior is further illustrated in Figure 27-11. The number of false positives decreases with basin size.

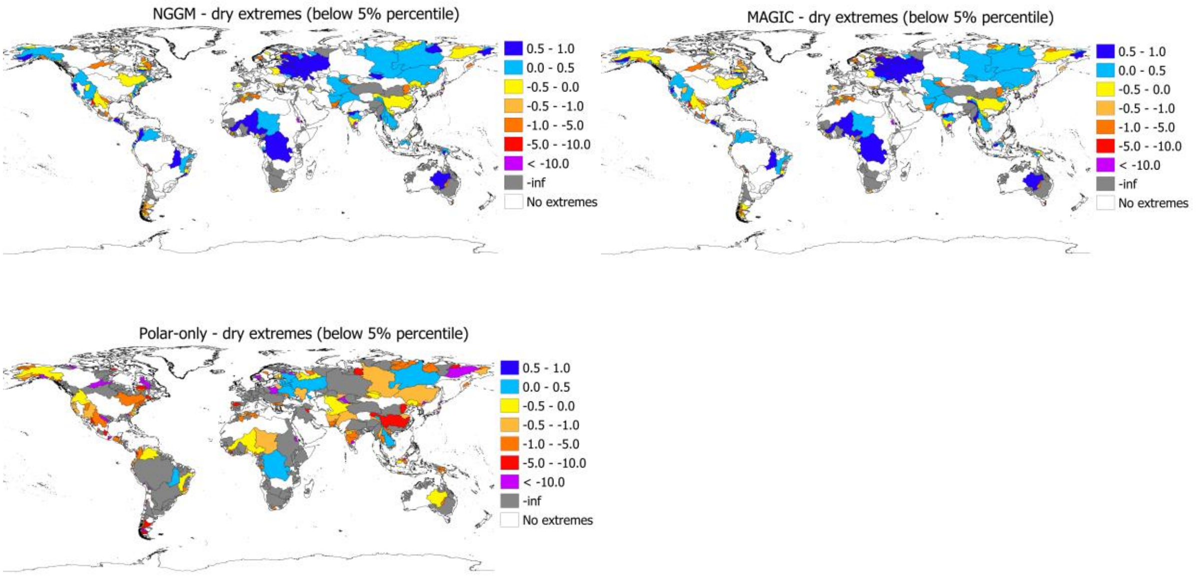

Figure 27-9: Score 3 on the performance of representing dry extremes for all river basins with dry extreme TWS anomalies (5% percentile) in 2002 in the ESM reference data, for NGGM, MGIC and the polar-only simulation. False positive basins (with extreme values in the simulation but not in the reference) are given in dark grey (Score 3 is not defined in this case).

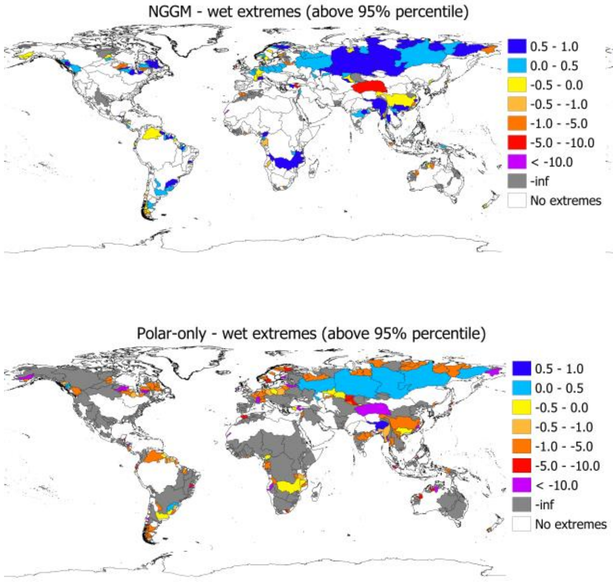

Figure 27-10: Score 3 on the performance of representing wet extremes for all river basins with wet extreme TWS anomalies (95% percentile) in 2002 in the ESM reference data, for NGGM, MGIC and the polar-only simulation. False positive basins (with extreme values in the simulation but not in the reference) are given in dark grey (Score 3 is not defined in this case).

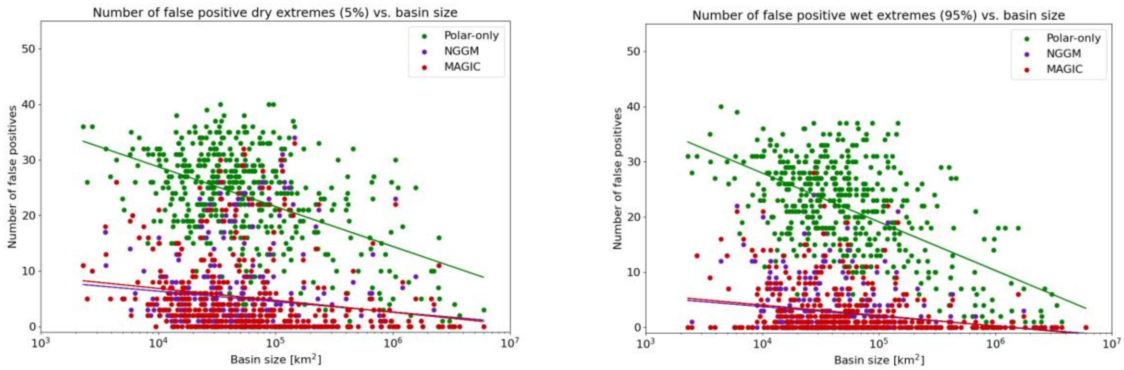

Figure 27-11: Number of false positives for dry (left) and wet (right) extremes versus river basin size, for the three scenarios.

In summary, the results of the impact analysis for hydrological extremes shows marked improvements in detecting wet and dry TWS extremes by NGGM and MAGIC over the polar-only scenario. The results are based on the analysis of basin-average TWS time series with 5-day resolution in 2002 for time intervals that have been classified as extremes based on a percentile threshold derived from the 12-year ESM reference data set. The benefit of MAGIC and NGGM is clearly shown in all performance criteria considered here, including a score that balances the number of correct hits of extremes with false positives, i.e., simulations of extremes for timesteps where there was no extreme in the reference data. Additionally, the accuracy with which extreme TWS values are represented by the MAGIC or NGGM simulations is largely superior to the polar-pair simulation. With an accuracy of about 2 cm EWH for detecting the extreme values, the threshold requirement of 4.2 cm @ 400 km

(Nmax=50) of NGGM is met even at the level of individual 5-day intervals. The performance of the NGGM and MAGIC simulations is slightly better for wet than for dry extremes. A possible reason is that wet extremes often are more pronounced in time and magnitude when triggered by clearly defined extreme precipitation events, whereas dry extremes evolve gradually. Thus, dry extremes might be more difficult to be correctly located in time.

NGGM and MAGIC perform very similar, with marginally better results for NGGM. However, as also stated in Chapter 3.1, this cannot be taken as a conclusion on the actual performance of the two missions relative to each other, as the potential for improvements in the respective processing choices by regularization and by relative weighting of the pairs has not yet been fully implemented in this study. Furthermore, it should be noted that the analysis presented her evaluates the scenario performance for hydrological extremes directly at their time of occurrence only, using independent 5-day timesteps. An extended analysis may also consider the persistence of extremes over longer time periods, i.e., consecutive 5-day intervals. Future analysis for hydro-meteorological extremes may also assess the predictive skill of improved satellite gravity data in a forecasting setup, e.g., to which extent flood/drought forecasting systems benefit in the skill of their forecasts when improved TWS anomalies derived from NGGM/MAGIC are incorporated into these systems by data assimilation, for instance.

27.5. NRT CONCEPT NEEDS FROM SCIENCE APPLICATIONS (WP1650)

Operational science and service applications in the field of hydrology and water resources that use GRACE/GRACE-FO-based products of terrestrial water storage (TWS) anomalies in their modelling or analysis setup are rarely established at the moment. This currently limits the options to build directly on experiences from operational systems when defining requirements of gravity-based data products, such as fast-track products, towards improving such systems. To our knowledge, the only system worldwide that currently makes use of GRACE/GRACE-FO TWS data in an operational way is NASA’s Goddard Space Flight Center groundwater and soil moisture drought indicating system (https://nasagrace.unl.edu). This system assimilates GRACE/GRACE-FO-based monthly Mascon TWS data into a land surface model to separate TWS into individual water storage compartments such as groundwater and soil moisture, to bridge data gaps and to overcome the coarse spatial and temporal of the gravity-based TWS input. In an optimal case, the observation-based TWS information would inform the modelling system directly at the desired spatial and temporal resolution of the output products, i.e., the drought indicators. Their current product specifications could thus be taken as tentative target requirements for the gravity-based TWS input to this application. They are defined by a spatial resolution of 0.25 degree globally (Li et al. 2019) and 0.125 degree at the CONUS scale (Getirana et al. 2020), a daily temporal resolution, and an update at weekly intervals, indicating a latency of less than one week.

In an earlier prototype of an operational near-real time gravity-based service, the European Service for Improved Emergency Management (EGSIEM) (Jäggi et al. 2019) developed a catchment wetness index based on daily GRACE TWS data as an indicator for flood early warning applications. The EGSIEM prototype had a short operational test run period at the very end of the lifetime of the GRACE mission in 2017 only. Nevertheless, from hindcast experiments in the Danube river basin, it could be shown that for selected flood events with major inundation impacts the gravity-based basin-average flood index revealed unusual high wetness conditions in the basin already about 40 days before the flood peak registered in the GRACE period at a downstream station of the Danube river. In a test application for DLR's Center for Satellite-Based Crisis Information (ZKI), the added value of this early flood indication was illustrated: the Charter 'Space and Major Disasters', which is an agreement of space agencies and satellite operators worldwide with the aim of providing a uniform system for the quick acquisition and delivery of Earth Observation data in case of disasters (Voigt et al. 2016), could have been activated much earlier when using the gravity-based flood indicator than it was actually activated during the flood events in the Danube basin. In this way, the programming and the efficient use of Earth observations satellites for rapid flood mapping could have been largely improved. For instance, this proactive early satellite tasking would have offered the possibility to have satellite data available for disaster response teams a few hours instead of several days after a dam break that caused widespread flooding in southern Romania (Jäggi et al. 2019). The EGSIEM prototype service specifications described in Jäggi et al. (2019) could be considered as threshold requirements for fast-track gravity-based TWS data for this type of application: daily resolution, while a non-independent daily solution in the form of an, e.g., 5-day moving window is acceptable, with maximum latency of 5 days.

Related to EGSIEM, the Center for Satellite Crisis Information (ZKI) at DLR is highly interested in gravity-based TWS data within flood and drought monitoring applications in the context of disaster management, including the possible benefit of TWS information for an early tasking of other Earth observation satellites towards areas of disasters (G. Strunz, personal communication). High temporal resolution of few days and high spatial resolution is required for these applications, the required latency needs to be investigated. A daily TWS product based on a 5-day moving window processing approach with 300 km resolution is considered as a probably useful data set. In a similar application context, the Research Group Natural Hazards at DLR (DLR-NH) reports comparable requirements in the frame of flood and drought hazard warning and forecasting (S. Martinis, personal communication). It is stressed that a higher spatial resolution is preferred over temporal resolution, the desired spatial resolution of 100 km is comparatively coarse, though, and the desired temporal resolution is in the order of 2 to 3 days. Required latencies are in the range of 3 to 5 days.

As groundwater storage tends to vary more slowly in time compared to near-surface soil moisture or surface water storage, product requirements for operational groundwater services may be less strict in terms of latency and temporal resolution. Towards an operational Copernicus service for a global gravity-based groundwater product (G3P), a survey among potential scientific, applied and institutional users (Ruz Vargas et al., 2022) revealed a monthly resolution of the groundwater product to be useful (86% of all answers) whereas only 9% of the users requested a higher temporal resolution. In terms of product latency, the largest fraction of users (40%) requested a monthly latency while 27% asked for shorter latencies, and for 33% of the users even larger than monthly latencies would be acceptable for their applications.

Considerably higher temporal resolution and shorter latencies are required for applications related to atmospheric processes and hydro-meteorological extremes including floods. Within the Integrated Forecast System (IFS) of the European Centre for Medium Range Weather Forecasts (ECMWF), for instance, the land data assimilation system (LDAS) assimilates satellite-based soil moisture data as information on the wetness state of the land surface (e.g. de Rosnay et al. 2022). In this framework of the operational forecast system, the required temporal resolution and latency of the input data for assimilation is at the sub-daily scale, which would also apply to a gravity-based data product if, alternatively or additionally, used for characterizing the landscape wetness state. This requirement presumably cannot be matched by the NGGM / MAGIC mission. As the requirement cannot be achieved with ASCAT or SMOS soil moisture Level 2 data neither, a neural network processor trained beforehand on the level 2 soil moisture and on soil temperature data has been developed. By this way, short latency level 1c data from the satellite observations can be used within the LDAS (Baugh et al., 2022; Rodríguez-Fernández et al., 2017). In a preliminary inquiry in the course of this CCN1, ECMWF stated that they don't have any further explicit requirements for gravity missions for numerical weather predictions or hydrology (F. Pappenberger, personal communication).

In an inquiry for this CCN1 at the Joint Research Centre of the European Commission (JRC), the high relevance of gravity-based TWS data for water resources management and modelling was stressed by JRC, being useful for the Copernicus Emergency Management Service (CEMS) applications GloFAS (Global Flood Awareness System), EFAS (European Flood Awareness System), GDO (Global Drought Observatory) and EDO (European Drought) (P. Salamon, personal communication). Application areas of gravity-based TWS data at JRC are seen as standalone product for water resource management, as indicators for possible droughts or precursors of flooding, and for assimilation into their hydrologic model LISFLOOD that is run within the aforementioned CEMS services. While the harmonization of TWS products from future satellite gravity missions with those of GRACE and GRACE-FO was stressed as highly important for these applications to have long-term consistent time series of TWS anomalies, requirements for fast-track products for the CEMS applications were suggested as follows: Given that TWS is not a very rapidly changing property, a temporal resolution of about 5 days deems to be useful and is clearly preferred over a daily solution that would have lower spatial resolution. As a threshold latency, 10 days is suggested; 5 days as a target latency. A gravity-based TWS product is required to coincide at best with the spatial resolution of the (hydrological) model used in their applications, i.e. 3 arcmins (about 5 km). A lower spatial resolution is possible but not ideal. A daily TWS product with a spatial resolution of about 1300 km (d/o 15) is considered to be of no use for their applications.

As a private sector example, the company Mozaika (Sofia, Bulgaria) (M. Damova, personal communication) contributed to this inquiry on fast-track requirements. Dealing with applications in the field of water resources management, including hydrological forecasting of river discharge, water levels, or water stocks in the snow cover, the company sees potential use of TWS data as an additional input for their forecasting models. Given that applications are run for catchments and water management units at sub-national, rather small spatial scales, data requirements are of high temporal (1-day) and high spatial (order of magnitude 1 km) resolution, corresponding to the requested outputs of their activities. While models have also been trained with data of, e.g., 100 km spatial resolution, the target requirements are at the output resolution. Mozaika can be seen as a typical SME player in the broad commercial market of regional water resources management and forecasting applications so that their requirements can be seen as a benchmark for many in this field.

The above inquiries and reviews of possible fast-track requirements are summarized in Table 27-6. It should be noted that with 8 services and institutions, the conclusions provided here are based on a small sample only. Overall, the results are quite diverse, depending on institution and specific service applications, and vary in particular for the required spatial resolution of gravity-based fast-track products. As a common result, though, a daily gravity-based TWS data set with low spatial resolution (here 1300 km) is not considered to be useful. There is a tendency among the users that a daily product with higher temporal resolution but not fully independent daily data (moving window approach over 5 days) is preferred, both over the low spatial resolution real daily product as well as over a 5-day average data set. A target latency of 1 day is noted by the majority of users, while the threshold latency varies among the users mostly between 3 and 7 days.

Table 27-6: Preliminary summary of fast-track gravity-based TWS product requirements for operational applications in the field of hydrology and water management, from literature review and ad-hoc inquiries at selected institutions (for details and sources, see full text)
Q1: What is a useful temporal resolution (3, 5, 7 days)?
Q2: Which is the desired temporal resolution (days)?
Q3: Is a 1-day product with about 1300 km resolution (d/o 15) of use?
Q4: Is a 1-day product (with ~300 km resolution), where the day is solved by considering 2 days before and after it, preferred over a real 1-day product with about 1300 km resolution?
Q5: Is a 1-day product (with ~300 km resolution), where the day is solved by considering 2 days before and after it, preferred over a 5-day product?
Q6: What is an acceptable latency of a gravity-based TWS product (threshold requirement) (days)?
Q7: What is the desired latency of a gravity-based TWS product (target requirement) (days)?
Q8: What is the desired spatial resolution?
Units for Q1, Q2, Q6, Q7 are [days]. n/a: no answer available or not applicable

Institution/ Service	Type of application	Q1	Q2	Q3	Q4	Q5	Q6	Q7	Q8
NASA / UNL	Drought monitor	7	1	n/a	n/a	n/a	7	1	0.125°
JRC / CEMS	Flood and drought forecasting / alerting	5	5	no	no	no	10	5	5 km
ECMWF	Numerical weather forecast	<1	<1	n/a	n/a	n/a	<1	<1	0.1°
EGSIEM	Flood indication and warning	5	1	no	yes	yes	5	1	0.5°
DLR-ZKI	Disaster management and satellite tasking	3	1	no	yes	yes	n/a	n/a	n/a
DLR-NH	Flood/drought hazard warning and forecasting	3	2	no	yes	n/a	5	3	100 km
G3P	Groundwater resources assessment	30	7	no	n/a	n/a	30	7	0.1°
Mozaika	Regional hydrological forecasting (floods, water resources)	3	1	no	yes	yes	1	<1	1 km

In cooperation with ESA's QSG4EMT (Quantum Space Gravimetry for monitoring Earth's Mass Transport Processes) project a user requirement survey was carried out during the period April – July 2023. In total 135 questionnaires were completed by users from a broad field of geoscientific disciplines (Figure 27-12). Focusing on fast-track data sets, a larger fraction of users considers a weekly to monthly temporal resolution to be an acceptable threshold requirement, while a higher temporal resolution is noted as desired requirement, with 35% of users requesting a daily resolution (Figure 27-13, top plot). The distribution of the user needs regarding the temporal resolution are differentiated for the different application areas (Figure 27-13, bottom plots). Here it can be noted that particularly atmospheric applications, hydrology, and geodesy request a 1-week resolution (threshold) and a 1-day resolution (desired). Similarly to the temporal resolution, the threshold latency is mainly seen at 1 week to 1 month, while in terms of the desired latency, a considerable fraction of users also votes for a latency of 1 day (Figure 27-14), again particularly from the atmospheric, geodetic and hydrological user groups.

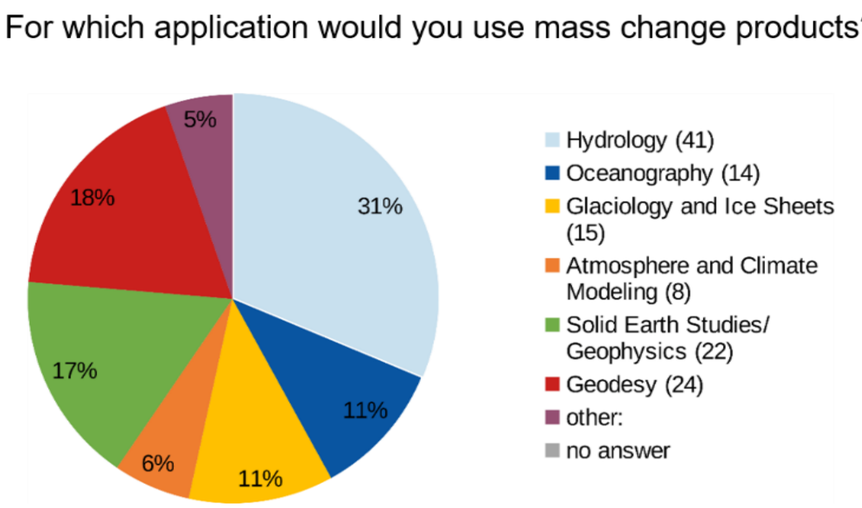

Figure 27-12: Evaluation of the QSG4EMT survey: disciplines of application of mass change products.

With respect to the trade-off of gravity data between temporal and spatial resolution, the majority of users (55%) prefers a higher spatial over a higher temporal resolution (Figure 27-15, left plot). However, in total 45% considers the temporal resolution at least as important as the spatial resolution showing the substantial interest of the user community regarding fast-track products. While the disciplines hydrology, glaciology, and oceanography have a stronger tendency towards a higher spatial resolution, the atmospheric, solid Earth, and geodesy users tend more towards considering both to be equally important.

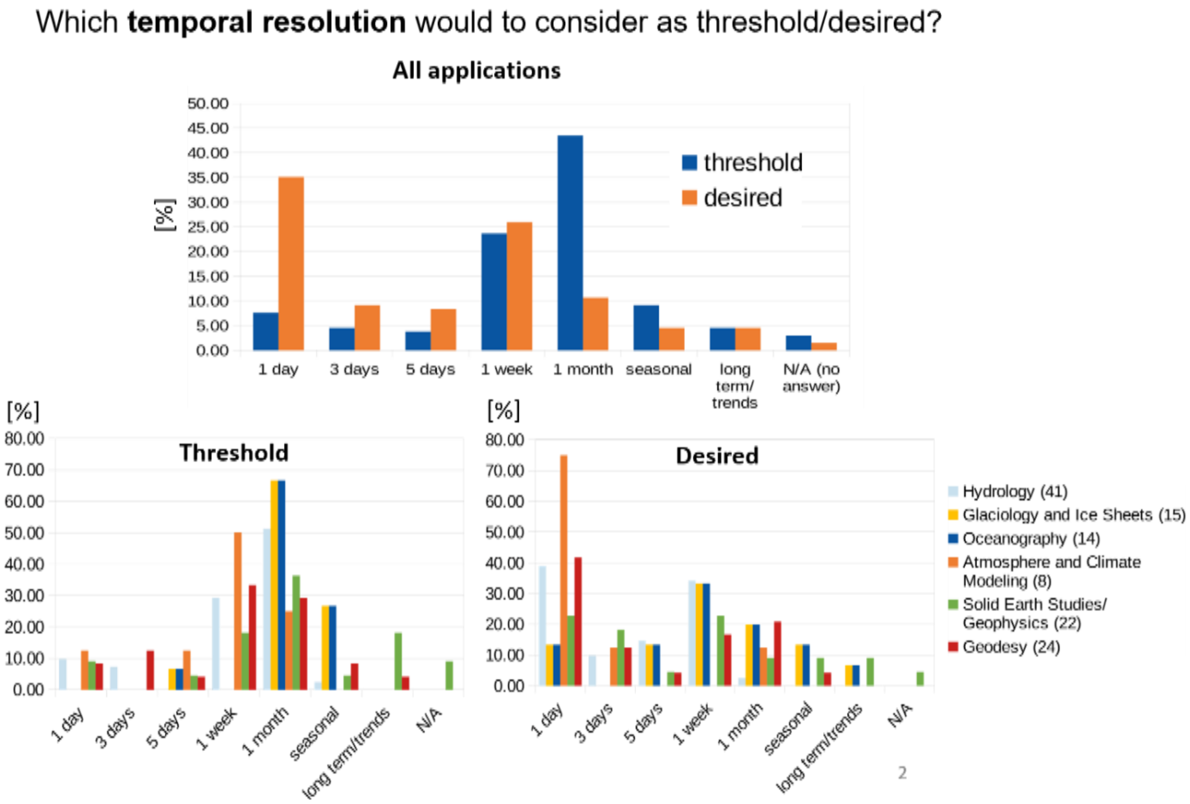

Figure 27-13: Evaluation of the QSG4EMT survey: requirements for temporal resolution of mass change products, separated for threshold and desired requirements (top) and for the different scientific disciplines (bottom).

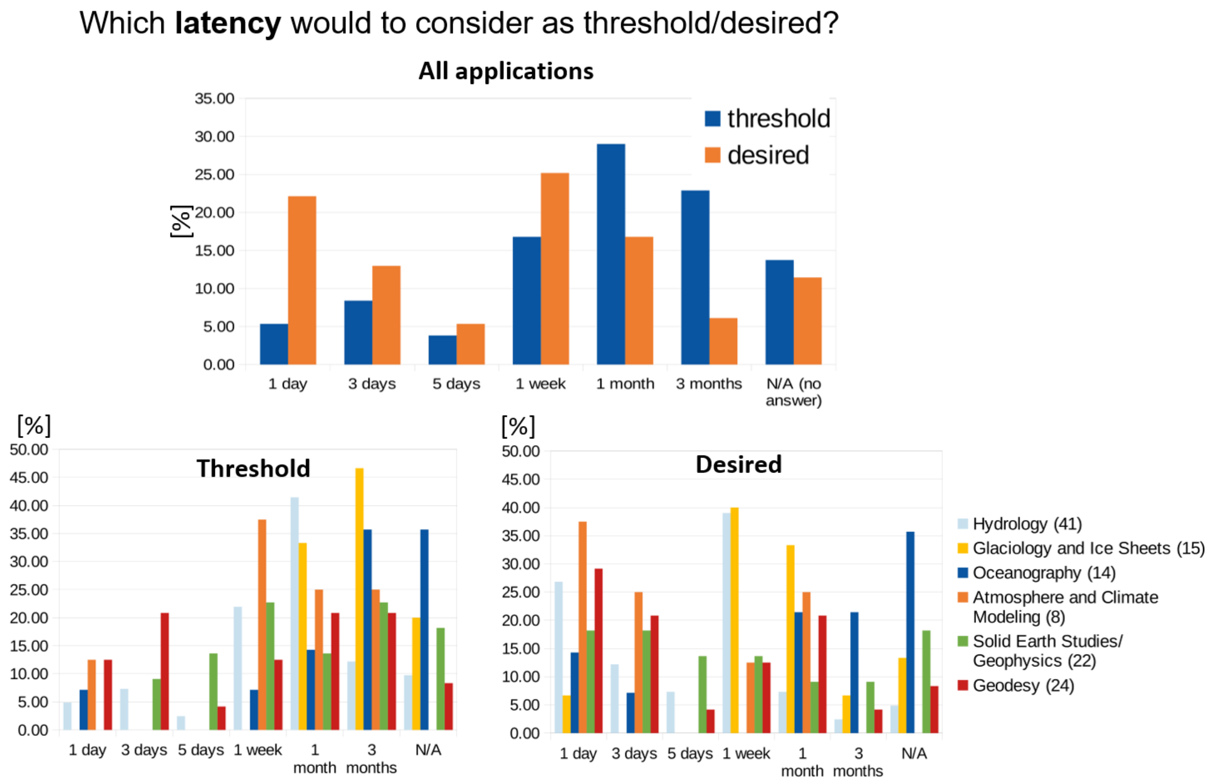

Figure 27-14: Evaluation of the QSG4EMT survey: requirements for latency of mass change products, separated for threshold and desired requirements (top) and for the different scientific disciplines (bottom).

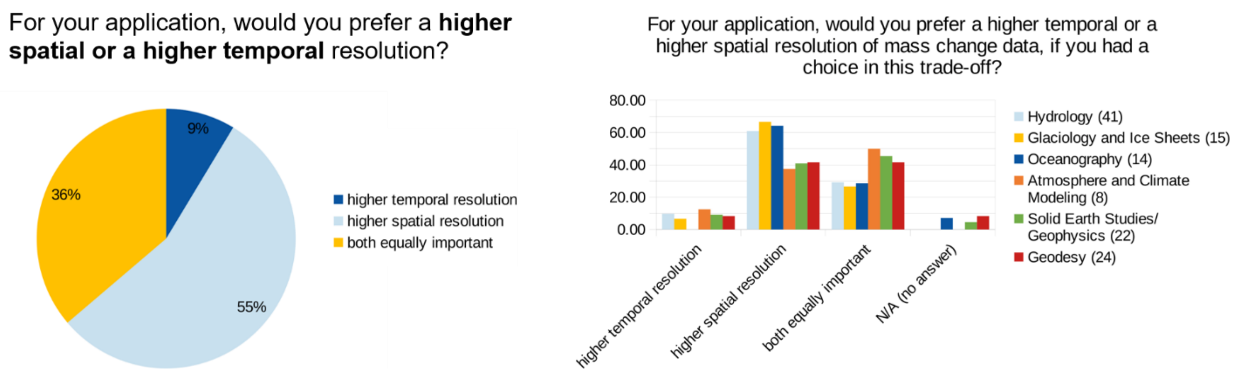

Figure 27-15: Evaluation of the QSG4EMT survey: requirements on temporal versus spatial resolution

In the ad-hoc inquiry presented above in this chapter, users replied that they prefer fast-track solutions with higher spatial resolution that are dependent/smoothed over more than one day over independent daily solutions with very low spatial resolution. When asked more generally if it is acceptable that daily mass change data is temporally smoothed, the answers to the questionnaire were 50:50 (Figure 27-16, left plot). Thus, it can be concluded that there is potential usability for both versions: dependent and independent daily data sets. While a majority (63%) of the users taking part in the survey use mass change data only episodically for research purposes (Figure 27-16, right plot), there is also a considerable portion (37%) interested in a regular/operational use of the data.

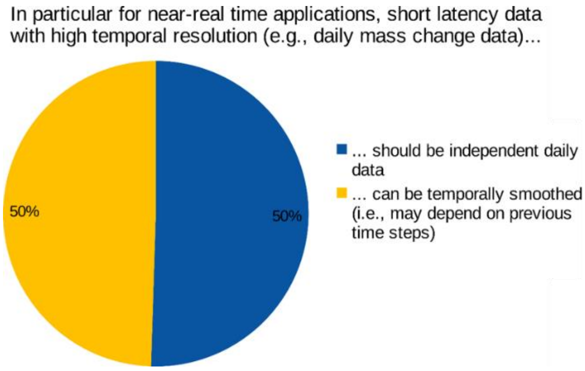

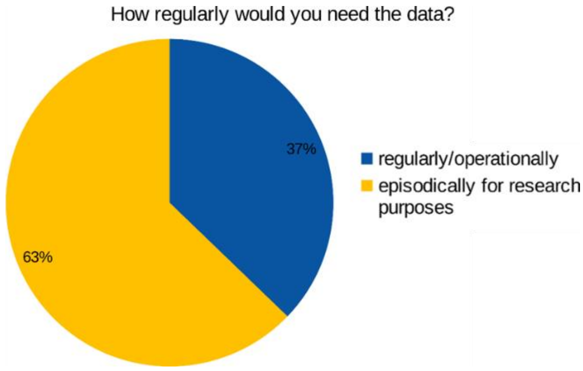

Figure 27-16: Evaluation of the QSG4EMT survey: requirements on the preferred characteristics of daily data (left) and on the kind of use (research vs. operational, right)

In summary of literature review, service inquiries and user survey with a focus on fast-track requirements of mass change data with high temporal resolution, it can be concluded that the requirements are quite diverse depending on the discipline and the actual data product or service application of interest. The threshold values for both temporal resolution and latency are in the range of 1 week to 1 month, the target values in the range of 1 day to 1 week. Overall, specifications of a NRT/fast-track mass change product that can satisfy a large part of applications and users in this field can be concluded from the results as follows: data with 5-day resolution, with daily updates and a maximum latency of 2 days.

27.6. EVALUATION FOR ICE MASS LOSS IN MOUNTAIN GLACIERS (FIRST STEPS) (WP1660)

Introduction

Mountain glaciers are highly sensitive to climate change and serve as prominent indicators of global warming. Despite storing much less ice than the Antarctic and Greenland Ice Sheets, glaciers have been the largest contributor to 20th-century sea-level rise, responsible for 0.5–0.6 mm yr^{-1} (IPCC, 2018). Models predict that glaciers will remain important contributors to sea-level rise in the future, potentially raising sea levels by 9-15 cm by the century's end (Rounce et al., 2023). On local scales, glacier mass loss may lead to habitat degradation, altered water availability, and disruption of marine ecosystems (Huss et al., 2017; Wester et al., 2019). Moreover, the release of freshwater from melting glaciers can interfere with the crucial thermohaline circulation, further affecting global climate (Yang et al., 2016; Bamber et al., 2018). GRACE provided the first continuous global mass balance estimates of mountain glacier mass balance (e.g., Wouters et al., 2019; Ciracì et al., 2020), yet measuring these systems using gravimetry remains challenging. Their small size leads to a low signal-to-noise ratio, and to leakage effects of non-glacial signals, especially in non-polar regions with pronounced hydrological variations. In this work, we assess the performance of different mission scenarios for the future MAGIC mission.

Data and Method

As in the earlier study on the Antarctic and Greenland Ice Sheets, four cases were considered: one GRACE/GRACE-FO-like, single-pair configuration, and three Bender double-pair configurations with varying orbit constellations of the polar and inclined pair (3d_H, 5d_Ma and 5d_Mb). For each of these scenarios, 52 weekly simulated solutions were provided. In addition, 12-yr long (1995-2006), monthly time series for a single and double pair mission were also considered.

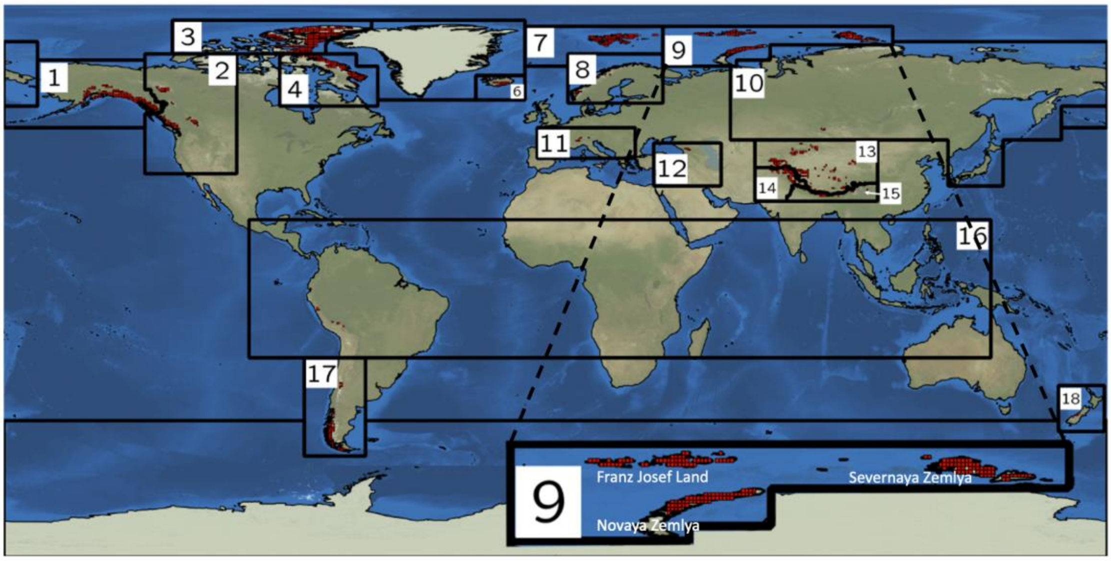

Figure 27-17: Overview of the global glacier distribution. In this study, Randolph Glacier Inventory regions 3, 4, 6, 7, 9 and 17 were considered (adapted from Wouters et al., 2019)

Except for linear mass trends for four glaciated regions (Alaska, European Alps, Himalayas, and the Karakoram Mountain Range), glacier mass signals are not included in the ESA Earth System Model (ESM) HIS fields which were used as input for the simulations. Therefore, monthly mass variations were derived regional climate models. Surface mass balance (SMB) data were available for Arctic Canada North, Arctic Canada South, Iceland, the Southern Andes, Svalbard and Arctic Russia (further subdivided into Novaya Zemlya, Severnaya Zemlya and Franz Josef Land), see Figure 27-17. For the former four regions, downscaled output was used from the Regional Atmospheric Climate Model (RACMO; Noël et al., 2018; Noël et al., 2022, Noël et al., in preparation), for the latter three from the Modèle Atmosphérique Régional (MAR; Maure et al., 2023). These models provide monthly surface mass balance fields. It should be kept that the total glacier mass balance also includes mass change due to glacier dynamics, however insufficient data are available to constrain this component properly. To avoid unrealistic mass build up in the glacier accumulation zones (where annual SMB is positive), and unrealistically negative signals in the ablation zones (annual SMB < 0) , SMB anomalies were computed with respect to a reference period, following Van Den Broeke et al. (2009). These anomalies were then summed in time to obtain cumulative mass changes for the period 1995-2006 and scaled where necessary to match the GRACE mass change observations in Wouters et al. (2019) for the period 2002-2006. Finally, the cumulative SMB (cSMB) fields, which were provided on regional model grids with a resolution between 0.5 and 6 km, were downscaled to a global geographic grid at a 0.5 x 0.5 degree resolution, and converted to spherical harmonics coefficients up to degree/order 180.

These were then used as input for the algorithm of Wouters et al. (2019) to retrieve the mass change signals in the 8 glacier regions of interest. This was done for the full set of coefficients (d/o 180), which yields the reference time series, $\dot{m}(t)_{glac,\ d/o\ 180}$. This procedure was repeated using different cut-off values for the spherical harmonic coefficients (d/o 80, 90, 100, and 120), yielding time series ($\dot{m}(t)_{glac,\ d/o\ X}$) of how the glacier signal would be observed under the different mission configurations, in noise-free conditions.

The SMB model data were only available at monthly temporal resolution. Therefore, the weekly simulation data were aggregated to monthly field as well. The simulated observations and the HIS model were differenced in order to obtain the noise signal for each mission configuration ($\dot{m}(t)_{noise,\ d/o\ X}$). Furthermore, the HIS spherical harmonics were also used to estimate the expected leakage signal from hydrological, solid earth and ocean signals in the surroundings of the glacier systems. For a cut-off degree/order X, this is given by:

$$\dot{m}(t)_{leakage,\ d/o\ X} = \dot{m}(t)_{HIS,\ d/o\ X} - \dot{m}(t)_{HIS,\ d/o\ X}$$

where the last term on the right-hand side accounts for the fact that the ESA ESM HIS fields also contain signals in the glaciated area.

The observed signal can then be written as:

$$\dot{m}(t)_{obs,\ d/o\ X} = \dot{m}(t)_{glac,\ d/o\ X} + \dot{m}(t)_{noise,\ d/o\ X} + \dot{m}(t)_{leakage,\ d/o\ X}$$

To benchmark the performance of each mission configuration against the target and threshold requirements listed in the MRD, the RMSD is computed based on the difference between the reference glacier time series $\dot{m}(t)_{glac,\ d/o\ 180}$ and the observed signal $\dot{m}(t)_{obs,\ d/o\ X}$.

Table 27-7: User requirements for the cryosphere at monthly time scales, specified in the Mission Requirements Document. Units of the target/threshold accuracies are cm equivalent water height.

Cryosphere	**M**	Threshold-a: 250 km @ 5.5 cm; Threshold-b: 150 km @ 50.0 cm	Target-a: 250 km @ 0.55 cm; Target-b: 150 km @ 5.0 cm

Results

1-year simulations

In Figure 27-18, results are visualized for three regions (Arctic Canada South, Iceland, and Southern Andes) situated at latitudes below 70 degrees, the region where the largest gain can be expected from an inclined satellite pair. Compared to the single-pair results all three mission configurations with such an inclined pair show a strongly reduced noise level and are more consistent with the reference signal, in particular for the Southern Andes region. The best visual agreement is observed for the 5d_Mb and 3d_H scenarios. A quantitative analysis is presented in Figure 27-19, where the RMSD is shown for all mission configurations, and summarized in Table 27-8. When using the full set of spherical harmonic coefficients, i.e., d/o 120 for the dual-pair configurations, and d/o 100 for the single-pair configuration, it becomes clear that the RMSD is reduced by 1-2 orders of magnitude in the mid-latitude regions when including a second, inclined pair. For the 5d_Mb configuration, the 150-km threshold criterion is met for all regions, while the target is only reached for Arctic Canada North. For the 3d_H scenario this holds for all regions except for Severnaya Zemlya, which has an area smaller than 150x150 km^2. Under the 5d_Ma scenario, the RMSD of 6 out 9 regions falls below the threshold, two of which are smaller than the specified resolution. Interestingly, the single pair passes the threshold in only 3 regions, but performs better than the 5d_Ma and/or 3d_H configuration in Arctic Canada North (5d_Ma and 3d_H), Severnaya Zemlya (3d_H), and Franz Josef Land (5d_Ma and 3d_H). It should be noted that only spherical harmonic coefficients up to d/o 100 were provided for the single-pair solution. Therefore, it is likely that the comparatively worse performance of the 5d_Ma and 3d_H configurations - processed up to d/o 120 - is caused by increasing noise in the higher coefficients.

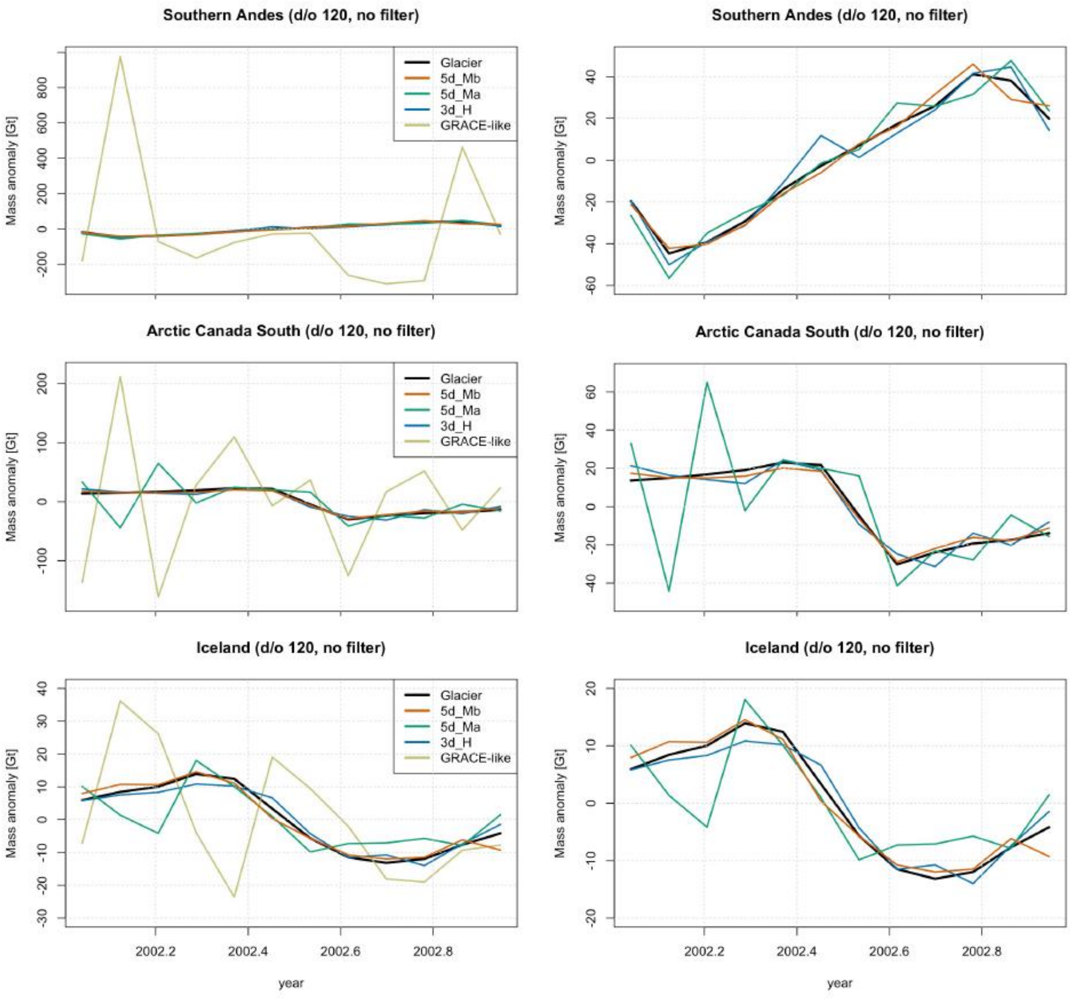

Figure 27-18: Examples of mass variations in three of the glacier regions of interest, retrieved from the four mission scenarios for maximum degree/order 120 (approx. 166 km spatial resolution) and the reference glacier $\dot{m}(t)_{glac,\ d/o\ 180}$ (black lines). In the right column, the single-pair, GRACE-like results are omitted for clarity.

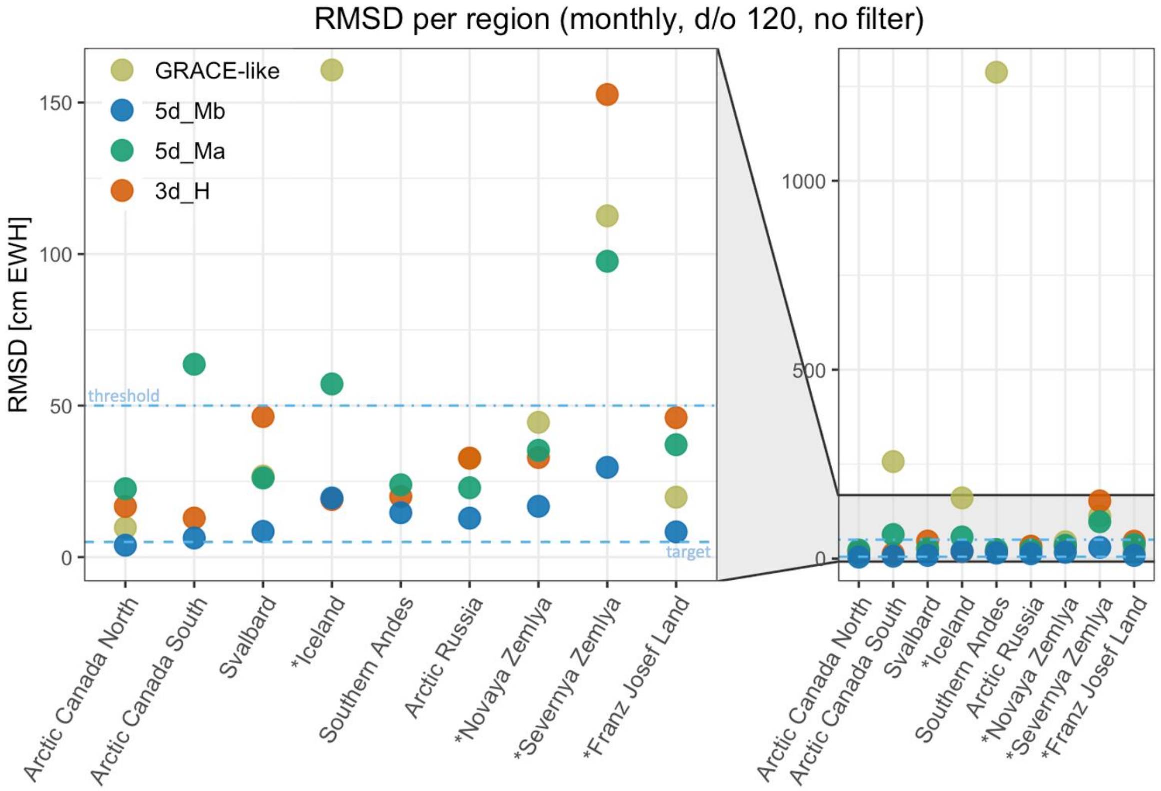

Figure 27-19: RMS difference for the 1-yr simulation of the four mission configurations, for each of the glacier regions considered. Coefficients up to degree/order 120 were used for the dual-pair configurations, corresponding to a spatial resolution of approximately 166 km, and degree/order 100 (~ 200 km) for the single-pair, GRACE-like concept. The dotted and dashed-dotted line indicate the target and threshold RMSD criteria at monthly time scales, respectively. An asterix (*) in front of the region name indicates that the region is smaller than 150x150 km^2.

Table 27-8: Number of regions (out of 9 in total) for which the monthly threshold and target criteria are met for the four different configurations, with and without filtering.

Configuration	threshold 150 km (50.0 cm)			target 150 km (5.0 cm)		
	no filter	VADER 10	VADER 100	no filter	VADER 10	VADER 100
GRACE-like	5	9	-	0	6	-
5d_Ma	6	9	9	0	5	5
5d_Mb	9	9	9	1	7	7
3d_H	8	9	-	0	4	-
Configuration	**threshold 250 km (5.5 cm)**			**target 250 km (0.55 cm)**		
	no filter	**VADER 10**	**VADER 100**	**no filter**	**VADER 10**	**VADER 100**
GRACE-like	0	6	-	0	0	-
5d_Ma	0	3	4	0	0	0
5d_Mb	3	5	6	0	0	0
3d_H	0	4	-	0	0	-

This is supported by the results for lower 250 km (d/o 80) target resolution (Figure 27-20), where the dual-pair simulations now generally outperform the single-pair. The only exception is the Arctic Canada North region, where the 5d_Ma configuration has the largest RMSD. As before, the 5d_Mb configuration performs best in all regions, and is the only one to pass the threshold criterion in 3 out of the 9 regions. For the other configurations, the criterion is not met in any of the regions. However, limited conclusions can be drawn from this, since Arctic Canada North is the only region larger than the specified 250x250 km^2 resolution. Focusing on the mid-latitude glacier regions, it is evident that an inclined pair is required to obtain a step forward improvement in monitoring their mass changes.

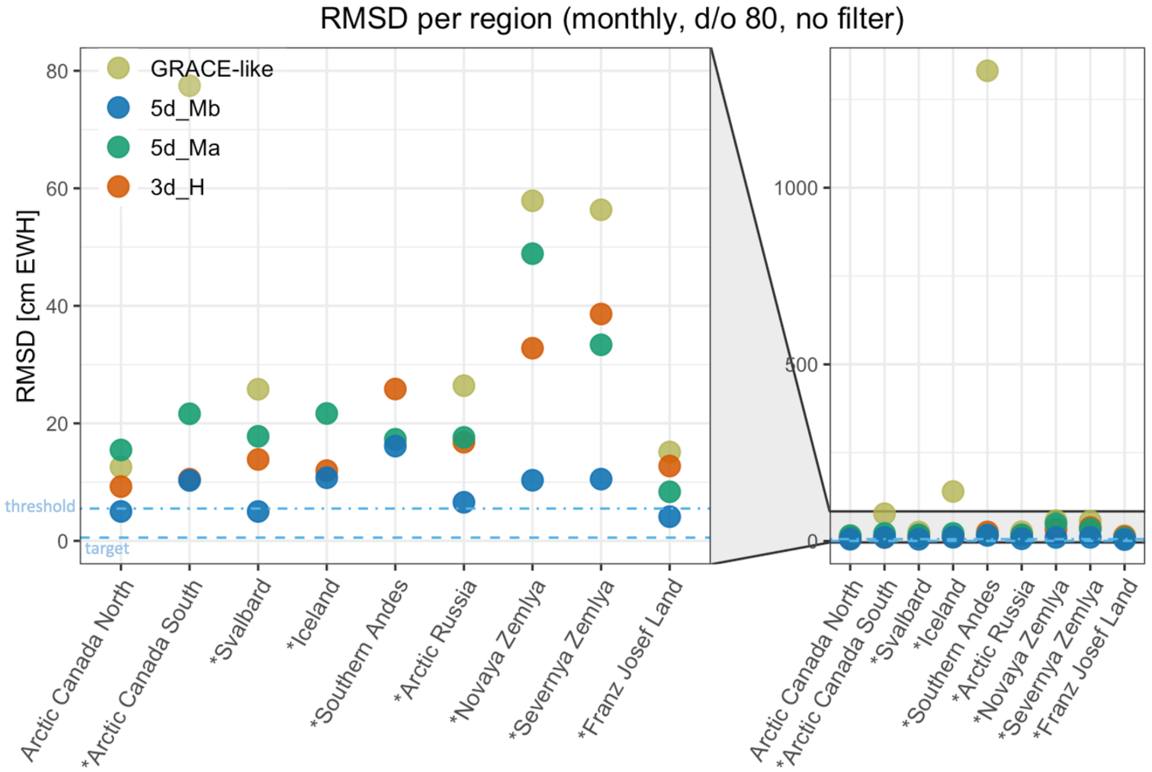

Figure 27-20: RMS difference for the 1-yr simulation of the four mission configurations, for each of the glacier regions considered. Coefficients up to degree/order 80 were used for all mission configurations, corresponding to a spatial resolution of approximately 250 km. The dotted and dashed-dotted line indicate the target and threshold RMS criteria at monthly time scales, respectively. An asterix (*) in front of the region name indicates that the region is smaller than 250x250 km^2.

Since it can be expected that the end users will apply postprocessing to the spherical harmonic coefficients, we also analyzed the performance after applying a weak (α = 10) VADER-filter (Horvath et al., 2018). For the 5d_Ma and 5d_Mb configurations, solutions with a weak (α = 10) and strong (α= 100) VADER filtering were also provided. Results are shown in Figure 27-21. At 150 km resolution, the threshold is now met for all configurations, and for 5d_Mb the RMSD is below the target criteria for all but 2 regions. For both filter settings, the Southern Andes region does not meet the target. In addition, for the weak filter (α = 10) Severnaya Zemlya, and for the stronger setting Arctic Canada South have a too high RMSD. The fact that results differ may be attributed to the fact that the VADER filter was originally developed for the single-pair GRACE mission. This may also explain why the filtered results for the single-pair constellation are on par with those of the dual-pair 5d_Mb configuration, and outperform the 5d_Ma and 3d_H scenarios in many (but not all) regions. Further analysis is needed to optimize the filter parameters for the double-pair constellations.

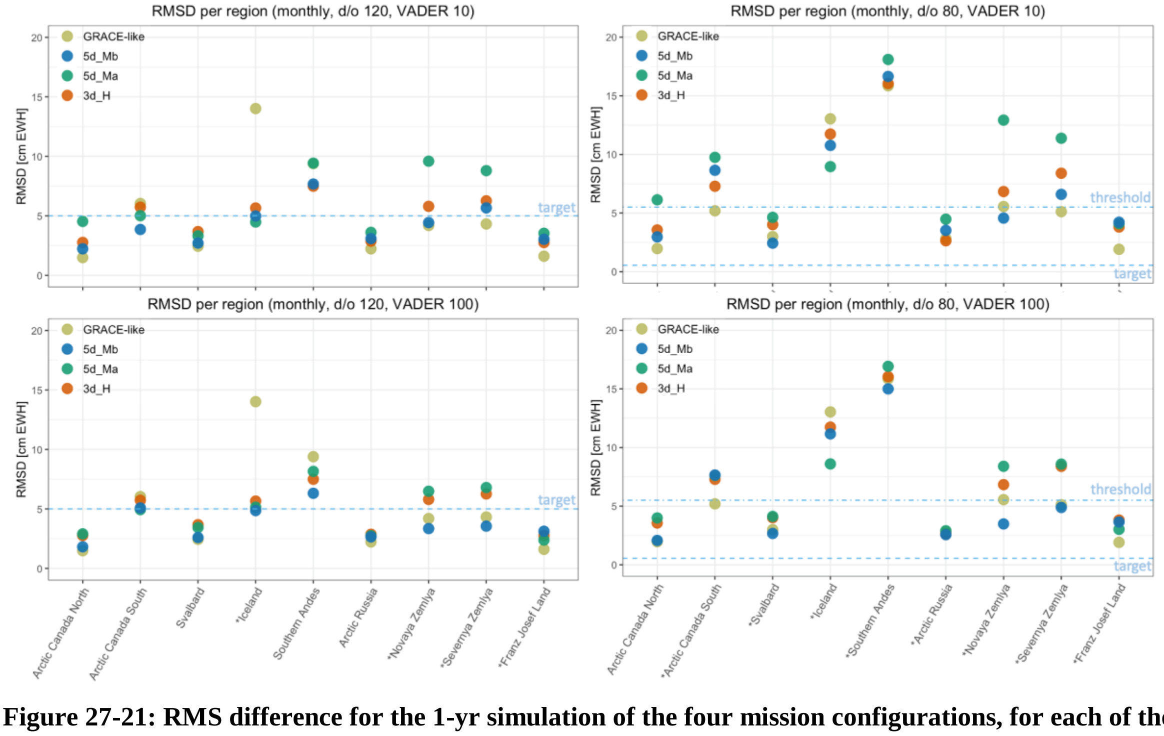

Figure 27-21: RMS difference for the 1-yr simulation of the four mission configurations, for each of the glacier regions considered, when applying the VADER-filter (top row: α = 1; bottom row: α = 100). Coefficients up to degree/order 120 and 80 were used in the left and right column, respectively. The dotted and dashed-dotted line indicate the target and threshold RMS criteria at monthly time scales, respectively. An asterix (*) in front of the region name indicates that the region is smaller than 150x150 (left column) or 250x250 km^2 (right column).

Depending on the filter setting and mission constellation, the threshold criterion for the lower 250 km resolution is met for 3 (5d_Ma) to 6 (5d_Ma) regions. Except for the weakly filtered 5d_Ma, all configurations meet the threshold criterion for Arctic Canada North, the only regions larger than the specified resolution. The target, however, is not reached in any setting.

12-year simulations

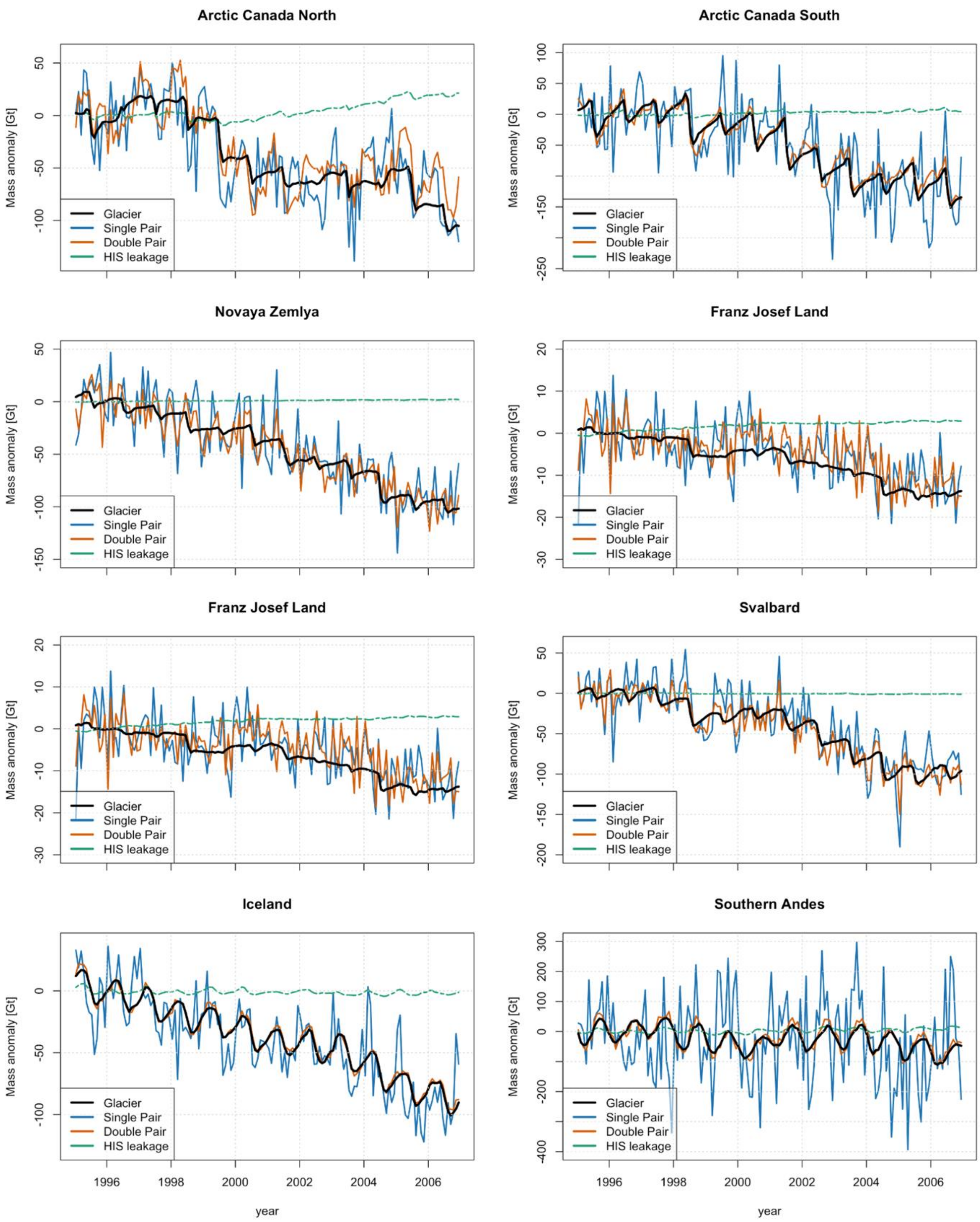

Figure 27-22: Time series of mass variations in glacier regions retrieved from the 12-yr closed loop simulations for a single (blue) and dual (orange) pair mission concept. The green lines show the leakage signal from non-glacier components in the HIS model.

To study the performance at longer time scales, 12 years of simulated observations from a numerical closed-loop simulations for a single and dual pair mission concept (Schlaak et al., 2022) were used. Monthly spherical harmonic coefficients up to d/o 90 were made available, covering the years 1995-2006. Mass variations were derived in a similar manner as the 1-yr solutions, described above.

Time series for all regions are displayed in Figure 27-22. Both the single and double pair results track the long-term change in glacial mass well, although significant noise can be observed at short time scales. In most regions, a seasonal cycle appears to be present the noise signal, in particular in the single-pair configuration, which requires further investigation. As in the 1-yr simulations, the noise level at the mid-latitude regions (Arctic Canada South, Iceland, and Southern Andes) is reduced by an order of magnitude when adding an inclined satellite pair. At higher latitudes, the double pair constellation still outperforms the single pair in all regions, although the noise reduction is less substantial. This is in line with the findings of Schlaak et al. (2022), who found that the added value of a second satellite pair mainly can be observed in the areas which are covered both polar and inclined pairs.

When considering the long-term trends, it can be seen that in some regions, the simulated results diverge from the reference glacier signal. This is particularly pronounced in Arctic Canada North and South, where the cumulative divergence amounts to 10-25 Gigatonnes at the end of the 12-yr period. In both regions are located near the former Laurentide Ice Sheet, hence the glacial isostatic adjustment (GIA) signal is pronounced here. The majority of the divergence can therefore very likely be attributed to GIA leakage from the regions surrounding the glacier systems, combined with a possible small contribution from mass variations in the tundra and neighboring Greenland Ice Sheet.

Table 27-9: Standard error of the linear trend fitted to the mass change time series of the 12-yr single and dual pair simulations. The last column shows the ratio of the standard error of the single pair to that of the double pair.

region	$\sigma_{\text{single pair}}$ [cm/yr]	$\sigma_{\text{dual pair}}$ [cm/yr]	$\sigma_{\text{single pair}} / \sigma_{\text{dual pair}}$
Arctic Canada North	0.51	0.33	1.5
Arctic Canada South	2.69	0.49	5.5
Svalbard	1.84	0.99	1.8
Iceland	4.20	0.39	10.8
Southern Andes	11.41	0.92	12.4
Arctic Russia	0.91	0.57	1.6
Novaya Zemlya	2.49	1.44	1.7
Severnya Zemlya	2.57	2.29	1.1
Franz Josef Land	0.82	0.60	1.4

It is common practice to correct for the GIA leakage using viscoelastic solid earth models, so this divergence can be expected to be minimized in future real-life applications. Therefore, to assess the performance of the single and dual pair in estimating long-term mass glacial mass trends, the HIS leakage signal was excluded. A linear trend, together with a annual and semi-annual harmonic, was fitted to the noise time series $\dot{m}(t)_{noise,\ d/o\ 90}$ and the standard error of the trend was computed, assuming uncorrelated noise. As reported in Table 27-9, the standard error is larger for the single pair configuration in all regions, by a factor 1.1 (Severnya Zemlya) to 12.4 (Southern Andes). Again, the most striking improvement is found at mid-latitude. A one-on-one comparison with the requirements in the MRD is not possible, since these were specified for resolutions of 130 and 170 km, which would require spherical harmonic coefficients up to at least d/o 117. However, for the double pair, all regions except Severnaya Zemlya, have a standard error well below the 170 km threshold of 2.6 cm/yr.

Conclusions

As for the ice sheet, the analysis presented here clearly demonstrates the added value of a dual-pair constellation. Irrespective of the configuration, including an inclined satellite pair increases the accuracy of glacier mass change observations by orders of magnitude at mid latitudes, both a short and long time scales. In the most optimal configuration, 5d_Mb, the threshold at 150 km resolution is met for all regions, whereas the target is also reached for Arctic Canada North. At 250 km resolution, the RMSD for this configuration falls below the threshold for three regions. It should be pointed out that all regions where the threshold accuracy is not achieved are smaller than the target 250 x 250 km^2 resolution. The 3d_H and 5d_Ma still meet the 150 km threshold for 8 and 6 regions, respectively, but result in an RMSD exceeding the 250 km threshold for all regions. Filtering the solutions results in an increased number of regions where the thresholds and targets accuracy are reached, also for the single-pair configuration. It is recommended that future efforts are invested in designing filters optimized for a dual-pair mission.

At longer time scales, no conclusive statements could be made about the threshold and target requirements listed in the MRD. Yet, the results of the double pair provide confidence that the threshold might be met for a number of regions. Regardless, the added value of an inclined satellite pair is clear and the improved accuracy provided by a mission such as MAGIC will significantly further our understanding of long and short-term glacial mass change and their contribution to sea level rise. This is particularly true for glaciers located at lower latitudes, where glacier shrinkage has profound socio-economic impactss.

A limitation of this case study is that the Alaska glacier region, among the largest glacier systems outside the ice sheets, could not be included. Model SMB simulation are available from the MAR model (Maure et al., 2023), but the ESA Earth System Model already includes linear mass trends for this region, which would bias the analysis as the ice mask of the two models differ. It is therefore recommended that in a future update of the ESM model, realistic glacier signals are included based on SMB models, and where possible additional data on ice discharge.

27.7. EXTENDED EVALUATION OF OCEAN SIGNALS, INCLUDING THE EFFECT OF LARGE-SCALE OCEANIC BOUNDARY SIGNALS (WP1670)

Preliminary investigations established the clear superiority of the dual satellite pair configuration over the single pair, and showed that it was capable of resolving order 2 cm variations over small ocean basins, as exemplified by a 120-day period resonant mode of the Caribbean Sea. Investigations into the possibility of resolving the Atlantic Meridional Overturning Circulation (AMOC) were very promising but inconclusive for two reasons. First, the simulation time series was too short to apply to the multi-year timescales of the AMOC, so error estimates relied on unreliable $1/\sqrt{t}$ scaling of the simulated errors. Second, it was found that the modelled ocean pressures on the western Atlantic continental slope, known to be associated with the AMOC, were also correlated on the dominant decadal timescales with pressures on very large scales. Although this might prove useful, it is poorly understood at this time, so it is unsafe to rely on this large-scale correlation for monitoring the AMOC.

The aim of this extended study is to address these two issues. The first is addressed by using monthly means of 12 years of simulated observations (Schlaak et al., 2023) from a complete Earth System Model (Dobslaw et al., 2014), in which the ocean component combines a global ocean average, a coarse resolution model used for dealiasing GRACE observations and, at degrees and orders beyond 60, the 1/10 degree resolution STORM simulation with realistic mesoscale variability (Storch et al., 2012). Data are provided as monthly-mean gravity potential spherical harmonics to degree and order 90, for years 1996-2012 inclusive. These are converted via downward continuation and application of appropriate Love numbers to harmonics of surface mass anomaly in metres of water equivalent.

The second issue is addressed by using data only from the western Atlantic continental slope, from the 1/12 degree resolution NEMO ocean model. We use 54 years (1959-2012 inclusive) of monthly mean values from a model which has realistic mesoscale variability, and in which it has been demonstrated that boundary pressures can be used to reconstruct the AMOC accurately (Hughes et al., 2018). We subtract the time-average, annual and semiannual cycles from all model time series, and set to zero all pressures except those between depths of 100 m and 3200 m on the West Atlantic continental slope. The data are averaged onto a half-degree Gaussian grid, and converted to spherical harmonics of surface mass anomaly as above.

Use of the NEMO simulation overcomes several issues. It allows us to link the pressures to the AMOC, which is known from NEMO but is ambiguous in the simulation model. The 54-year timeseries allows us to focus on that relationship at the longer, decadal timescales which are of most interest for the AMOC. It also allows us to have a boundary signal which is not correlated with the ocean interior pressures, as these are coming from a different model.

While it is known that boundary pressures are a good measure of the AMOC, this calculation works best if they are averaged with respect to ocean depth. When projected onto the horizontal plane, as appropriate for satellite observations, this would require weighting the pressures with the steepness of the slope. Such weighting would imply very fine scale information, making it impractical to apply in this work. Instead, we rely on the spatial coherence of the signals (most apparent at decadal time scales), and simply divide the continental slope into "upper slope" and "lower slope", separated by the depth at which the AMOC direction reverses (taken as 1200 m here). Preliminary investigations identified the North Atlantic between 25°N and 45°N as the most promising and relevant region. The ideal averages were found to be over the regions 200-1200 m and 1200-3200 m depth, with negative and positive weightings respectively. However, the upper slope region thus defined was extremely narrow. Extending upwards to 100 m depth resulted in only slight degradation of the relationship with AMOC, while substantially expanding the horizontal area. Extending to the coast degraded the relationship rather more, and was not pursued further.

Figure 27-23a shows the actual model AMOC (black) and its reconstruction (blue) using the ideal simple weighting function (the oceanographer's non-standard unit of the sverdrup, Sv, represents a flow of $10^6 m^3 s^{-1}$; for comparison, the AMOC is about 18 Sv). It can be seen that this does a very good job at long time scales (5-year means or longer), but the simplification of the weighting function and the different spatial patterns of pressure at higher frequencies means that interannual variability is not well reconstructed. Thus, this investigation is of most relevance at the longer time scales, but it is still useful to look at shorter time scales as they still reflect the average pressures, if not the AMOC. This reconstruction used the weighting function shown in Figure 27-23b, at full resolution.

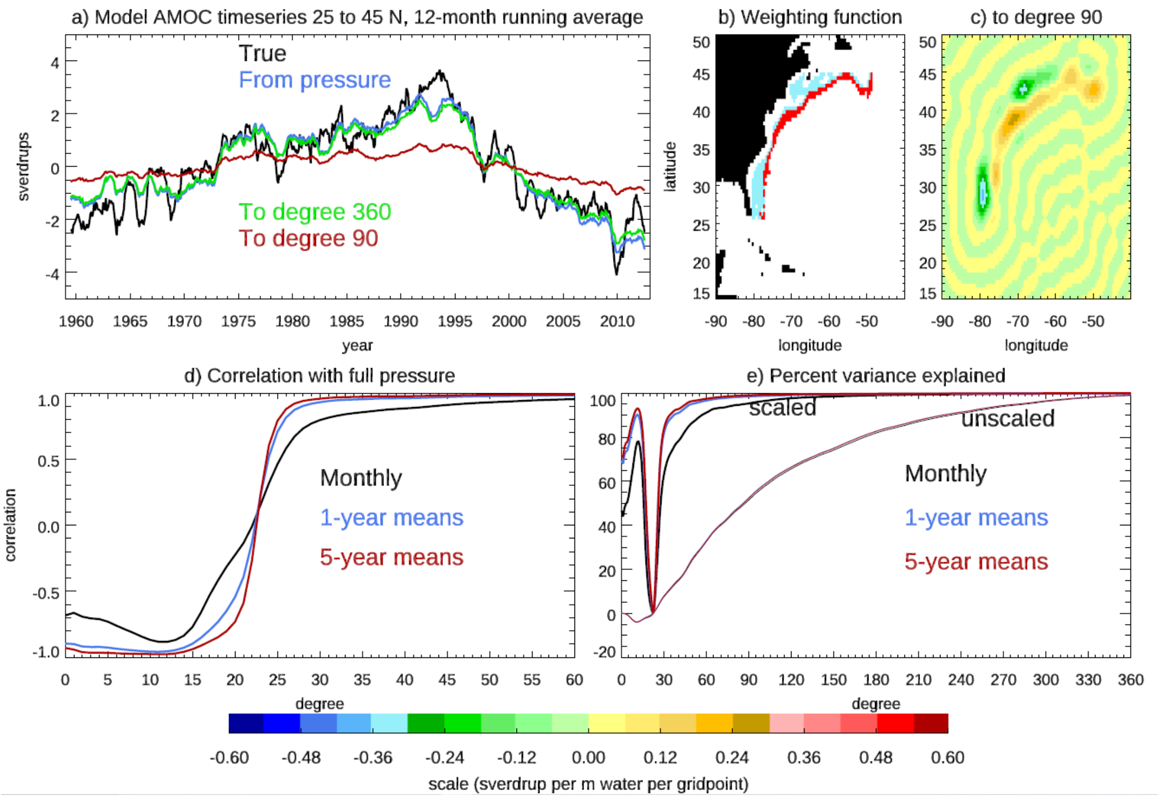

Figure 27-23: AMOC and its reconstruction from boundary pressures in NEMO. a) The true model AMOC (black), its reconstruction using pressures with the best, simple weighting function (blue), and when the pressure data are truncated at degree 360 (green) and 90 (red). b) The simple weighting function used. c) the simple weighting function when truncated at degree 90. d) correlation and e) percent variance explained of full-resolution AMOC reconstruction with that truncated at different resolutions. Monthly, running annual mean, and running 5-year mean time series are considered, and percent variance is shown with unscaled values and values scaled with the optimum factor based on the running annual mean data.

To simulate the effect of reduced-resolution pressure data, we truncate the pressures at degree 360 and degree 90 before calculating the weighted averages, producing the green (360) and red (90) curves in Figure 27-23a. Truncating pressures at degree 90 is equivalent to using full resolution pressures and a weighting function truncated at degree 90, as shown in Figure 27-23c.

The blurring produced by reduced resolution has the effect of reducing the AMOC amplitude, but the correlation is still very high at degree 90 for all time scales. Figure 27-23d shows correlations of time series using pressures truncated at different degrees with the ideal pressure time series. Interestingly, correlations at all time scales pass through zero at about degree 22, telling us that it is only substantially beyond degree 22 that the calculation is meaningfully resolving the negative weighting on the upper slope, and positive weighting on the lower slope.

Figure 27-23e shows the percent variance explained using data truncated at different resolutions. The thin lines show the case with no scaling, reflecting the reduced amplitudes when using low resolution data. Using a least-squares fit allows the calculation of an ideal amplification factor for each truncation (about 4 at degree 90), and the scaled curves (equivalent to correlation squared) show variance explained after this scaling has been applied. For all the following work, this scaling is applied to all time series, thus amplifying the noise as well as the signal.

The above results establish that pressures from the continental slope can be used at a wide range of truncations, with appropriate scaling, to reproduce the ideal weighted average, and that ideal weighted average is a good measure of the AMOC with smoothing of about five years or more.

There are two distinct ways in which the practicalities of measurement can contaminate this retrieval. There is noise in the actual harmonics that are retrieved, and leakage of signals from outside the continental slope due to the limited resolution. To assess these sources of noise, we use the “truth” harmonics from the Earth System Model (ESM) to calculate leakage, and “simulation minus truth” to assess the measurement noise, and simply apply the same weighted average calculation to each of these sets of harmonics, followed by applying 1-year and 5-year running averages. Note that the leakage calculation will also include a retrieval of boundary pressures from the ESM – we expect leakage to dominate over this at most truncations, but it is worth bearing in mind that this sets a floor on the leakage noise estimate which actually reflects real signal. For a realistic high resolution model run for 12 years this could be up to a standard deviation of about 1 Sv, and a trend of up to 0.2 Sv/yr, like the values seen in NEMO.

What would be a useful level of accuracy? A standard target is 1 Sv, and this is quite a challenging target for in-situ observations (Hughes et al., 2018). Climate simulations predict a reduction of the AMOC through the 21st century, with a range of predictions for the size. Roberts et al. (2020) report typical rates of decline of 3% per decade, or a little over 1 Sv every 20 years. Weijer et al. (2020) report fairly linear rates resulting in typically 6 Sv by the end of the century for low emissions scenarios, increasing to about 8 Sv for high emissions. Overall, trends of about 0.05 to 0.1 Sv/yr are predicted in the long term, requiring 10-20 years to produce a 1 Sv change.

Figure 27-24 shows the noise calculations, with the upper panels representing the actual time series of erroneous AMOC from fields truncated at degree 90, and the lower panels giving summary statistics for the same cases at different truncations. In panels a-e, black is for monthly values, blue for running annual mean, and pink for running 5-year mean. Thin lines (except the black lines in b) and c)) are single-pair noise, thick lines for double-pair noise, and dots for signal leakage.

It is clear that the dual-pair noise is substantially below that for a single pair. The degree 90 truncation is the worst case for the single pair in this comparison, but comparing thick and thin lines with matching colours in Figure 27-24d shows that this is the case at all truncations (note the logarithmic scale).

Although the double-pair configuration produces noise below 1 Sv for a wide variety of truncations, for annual and 5-year mean time series, this is somewhat academic as the leakage signal is much higher over most of this range.

While the measurement noise increases towards degree 90, the leakage noise decreases, and the optimal retrievals occur where the best compromise is found. For 5-year means, this is at about degrees 75-90, and gives RMS errors of about 0.4 Sv from each source (0.6 Sv total if added in quadrature).

This is a very good result at the time scales of most interest. However, it should be noted that a 5-year running average applied to a 12-year time series, represents rather few degrees of freedom and may underestimate the variability. Nonetheless, the result is in line with a reasonable averaging applied to the 1-year running average results, for which the measurement noise and leakage noise intersect at 1 Sv (total 1.4 Sv) at around degree 70-80.

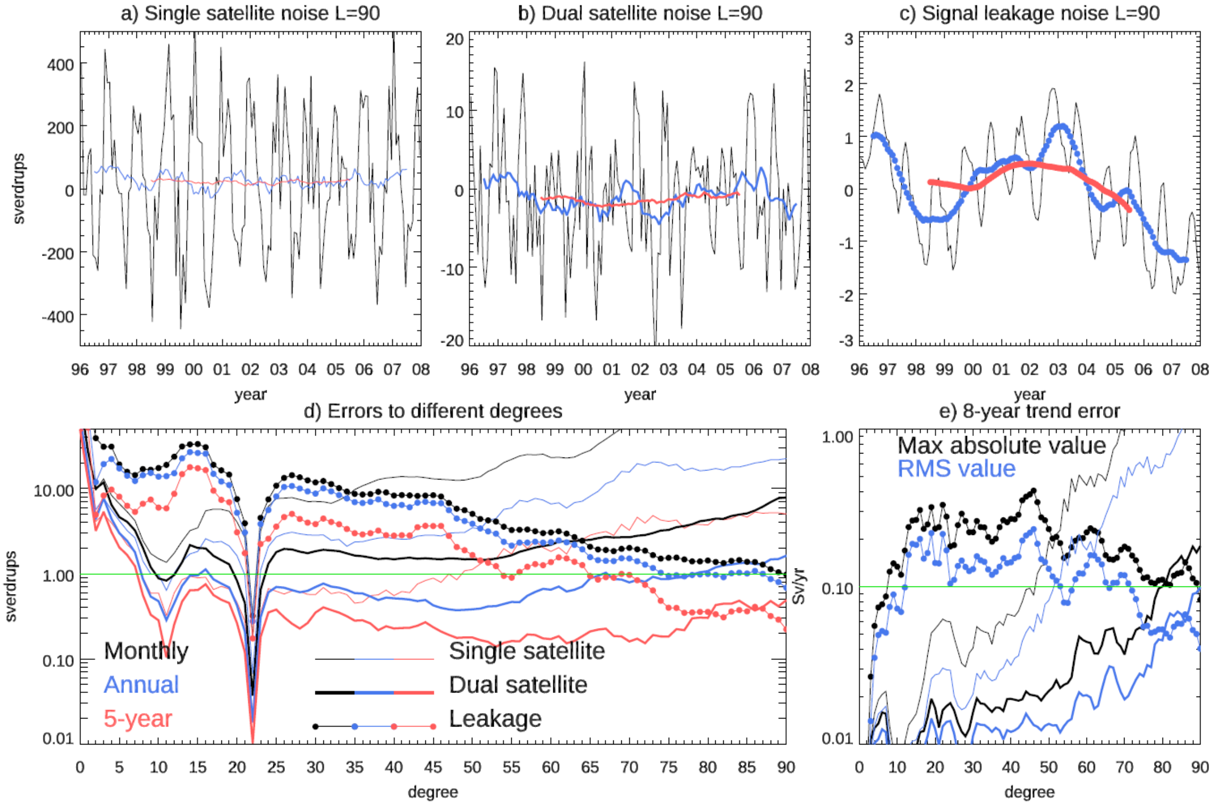

Figure 27-24: Noise in the pressure-predicted AMOC retrieval under different observation scenarios. a) measurement noise in a single pair scenario, showing monthly values, running annual means, and running 5-year means for a retrieval truncated at degree 90. b) as for a), but using a two-pair scenario. c) leakage effects due to truncation for the "truth" model. d) Standard deviations of the above time series, but for different truncations. e) maximum absolute value and rms value of linear trends fitted to all 8-year subsets of the three noise time series, with no smoothing. Thin lines represent single-pair noise, thick lines for double-pair, and dots for leakage.

Regardless of the details, it is clear that the measurement noise component will reduce as the time-averaging increases, and that sub-sverdrup accuracies are attainable using data to about degree 80. The leakage is more complex. Geophysical signals can have long timescales, and we see that the proportional suppression of noise by averaging is reduced in the leakage timeseries compared to the measurement noise. The biggest issue is the linear trend, and this is addressed in Figure 27-24e, where the maximum absolute value and the RMS value of the 8-year linear trend errors is plotted as a function of truncation degree (in this case using just the monthly data). Again, even more than for 5-year running averages, 8-year trends on subsets of a 12-year time series are not statistically independent and can only provide an indication of the approximate size of the trend error. Nonetheless, we find that both double-pair noise and leakage noise drop well below 0.1 Sv/yr RMS values at around degree 80.

Without longer simulations, we cannot say for sure how stable the estimates would be at multidecadal timescales, but the indications are very positive. Recalling that the leakage signal includes a "true" component from the continental slope which we estimated might produce a noise floor of 1 Sv and 0.2 Sv/yr, it is clear that these results are consistent with having reached the noise floor, so these already good results may in fact be dominated by signal interpreted as noise.

In conclusion, full ESM simulations show that the 5-year running mean AMOC changes can be measured at sub-sverdrup RMS accuracy level with the dual-pair satellite configuration, a level of accuracy comparable with (and independent of) the best in-situ measurements and of great value for ocean climate monitoring. If this holds at longer periods (which is consistent with the data we have, but not proven), then we should be able to detect anthropogenic trends at the 2-sigma level with 20-40 years of measurement, and rapid changes of several sverdrups, as suggested by some models in the case of a threshold effect would be detected within a year of such changes occurring.

27.8. CO-SEISMIC AND POST-SEISMIC DATA BASE (WP1680)

The aim of the work package is to compute the co- and post-seismic gravity change due to earthquake dislocations, described by their moment tensor, using the QSSPSTATIC code (Wang et al., 2017). We devoted a considerable effort to automate the construction of the necessary QSSPSTATIC input files, which include all the information necessary to compute the gravity change fields due to an earthquake event. The automatization process populates the input file with the earthquake source parameters, the time window and time sampling of interest, and the rheological model of a radially layered Earth. Because QSSPSTATIC computes the change in radial gravity, including a vertical gravity gradient correction, requested for simulating measurements of a gravimeter solidly connected to the deforming topography – we counter-correct for this effect, using the modelled terrain displacement. The observables are computed at the provided computation points, which are defined as general, sparse points (i.e. not structured grids), which QSSP treats as source-receiver couples – as it is customary in seismology.
The input for each earthquake comes from a *quakeML* format XML file (https://quake.ethz.ch/quakeml/), as available in the USGS catalogue. A provided list of files is downloaded and parsed, extracting the parameters required to model a point-source: location (longitude, latitude, depth), origin time, and the 6 components of the symmetric moment tensor: $M_{rr}, M_{tt}, M_{pp}, M_{rt}, M_{rp}, M_{tp}$.

While the Green functions computation is carried out serially (for each source depth, while different depths and/or models are computed concurrently), we employ data parallelism to accelerate the computation of the observed gravity change at a given time. By using a set of ad-hoc scripts, we split (fork) the amount of global computation points on a number of separate QSSPSTATIC input files, each one containing only a portion (chunk) of the global grid. All the forked input files are then provided as a job list to the GNU Parallel, to which the orchestration of process-based parallelism is delegated. The fork phase also produces the scripts required to join all the separate points into one output.

Afterwards, the global points are reshaped to a global grid with accompanying coordinates (a labelled array). The grids are then stored in a COARDS compliant netCDF file (NOAA, 1995). This procedure is carried out systematically for all the produced snapshots (co-seismic and a selection of post-seismic times), including the computation of the isolated post-seismic signal (through subtraction of the co-seismic signal from a post-seismic grid).

To store the data in a consistent format, used later in the operations part of the detectability analysis and to easily convert it to different derived functionals of the geopotential, all the gravity change grids are transformed to a spherical harmonic expansion. Coefficients are expressed as it is customary for global gravity models, as unit-less 4π fully normalized spherical harmonics coefficients of the gravitational potential at a nominal ground-level radius.

We impose that the sampling of the global grids that we compute is equiangular along latitude and longitude, resulting in N × 2N points (latitude times longitude). This allows employing the transform routines according to the (Driscoll & Healy, 1994) sampling theorem, as available in SHTOOLS (Wieczorek & Meschede, 2018). After transforming the gravity grids to their surface SH coefficients (of the change in radial gravity, akin to gravity disturbance) to unit-less coefficients (through division by the degree-dependent term that is used in the potential-to-gravity differentiation, see following equation), the coefficients are stored in an ICGEM '.gfc' format file. The main result, for a given event, is a time series of SH coefficients, which is also represented with the derived quantity of degree variance spectra (with or without spatio-spectral localization in a spherical cap centered on the earthquake source).

$$\overline{C_{l,m}} = w_l \cdot \overline{C_{l,m}^{V_r}}\,,\ w_l = \frac{-R^2}{GM(l+1)}$$

The above equation defines the conversion from the spherical harmonic coefficients of the gravity change ($\overline{C_{l,m}^{V_r}}$) to unit-less spherical harmonics coefficients ($\overline{C_{l,m}}$), with w_l degree (l) dependent weights used in the a-dimensionalization.

We have calculated the earthquake gravity signals of the co-seismic and post-seismic signal for a selection of events, with magnitude ranging from M 7.6 to 9.2. For the sensitivity analysis the events of most importance are those at the magnitudes close to M 8.3, where the improvement of detectability by MAGIC compared to GRACE is most significant. Presently the modelling is carried out with a point source approach, which has differences reaching 10 % respect to a finite fault model, for magnitudes close to M 8.8. The differences reduce, the smaller the seismic moment is - a result we have obtained from comparison tests, where for a given fault mechanism both the finite fault and point source model was used, and the co-seismic disturbance gravity field was calculated.

Another input on which the modelled fields depend is the lithosphere and mantle structure. Presently we use a standard model for the different earthquakes, with a purely elastic crust and a viscoelastic mantle. The lowest interface defines the rheologic properties of a homogeneous sphere underlying the interface.

Spherical layers that have different top and bottom parameter values, are assumed to have a constant gradient for each parameter and will be discretized automatically to a number of homogeneous sublayers. The relaxation of the shear modulus is implemented through a Burgers rheology, in which a Kelvin-Voigt body (m_1, h_1) and a Maxwell body (m_2, h_2) are connected in series. m_2 is the unrelaxed modulus and is derived automatically from the S wave velocity Vs and the density ρ with the following equation:

$$m_2 = r\, {v_s}^2$$

The other parameters are as follows, and use the following convention in the QSSPSTATIC software:

h_1 = transient viscosity (dashpot of Kelvin-Voigt body; ≤ *0* means infinity value).
h_2 = steady-state viscosity (dashpot of Maxwell body; ≤ *0* means infinity value).

The rigidity of the Kelvin-Voigt body is calculated through the following equation, using the parameter a defined in the table:

$$m_1 = m_2 \cdot a/(1 - a) \; with \; a = m_1/(m_1 + m_2) \; (> 0 \; and \; \leq \; 1)$$

The parameter convention for special cases of the layers, using the values in the table are:

1. Elastic: *h1* and *h2 ≤ 0* (infinity); a meaningless.
2. Maxwell body: *h2 > 0* and [*h1 ≤ 0* (infinity) or *a = 1*].
3. Standard-Linear-Solid: *h2 ≤ 0* (infinity) and *0 < a < 1*, whose fully relaxed modulus is given by *a*unrelaxed_modulus*.

The bulk modulus is not affected by the relaxation.

The rheologic model used for the calculations is given in Table 27-10 and Figure 27-25.

Table 27-10: Rheologic layering of the spherical earth model used for the computations of the gravity change generated by an earthquake

	depth [km]	vp [km/s]	vs [km/s]	〉 [g/cm^3]	η1 [Pa s]	η2 [Pa s]	α	remark
1	0	5,8	3,36	2,72	0	0	1	
2	20	5,8	3,36	2,72	0	0	1	
3	20	6,5	3,75	2,92	0	0	1	Hooke
4	35	6,5	3,75	2,92	0	0	1	
5	35	8,04	4,47	3,32	0	0	1	
6	40	8,041	4,472	3,323	0	0	1	
7	40	8,041	4,472	3,323	1,00E+18	1,00E+19	0,5	
8	120	8,05	4,5	3,371	1,00E+18	1,00E+19	0,5	Burgers
9	210	8,3	4,518	3,426	1,00E+18	1,00E+19	0,5	
10	210	8,3	4,522	3,426	0	1,00E+20	1	
11	410	9,03	4,87	3,547	0	1,00E+20	1	Maxwell A
12	410	9,36	5,07	3,756	0	1,00E+20	1	
13	660	10,2	5,6	4,065	0	1,00E+20	1	
14	660	10,79	5,95	4,371	0	1,00E+21	1	
15	760	11,056	6,209	4,431	0	1,00E+21	1	
16	1000	11,464	6,384	4,5698	0	1,00E+21	1	Maxwell B
17	1200	11,771	6,512	4,6839	0	1,00E+21	1	
18	1400	12,052	6,627	4,7951	0	1,00E+21	1	

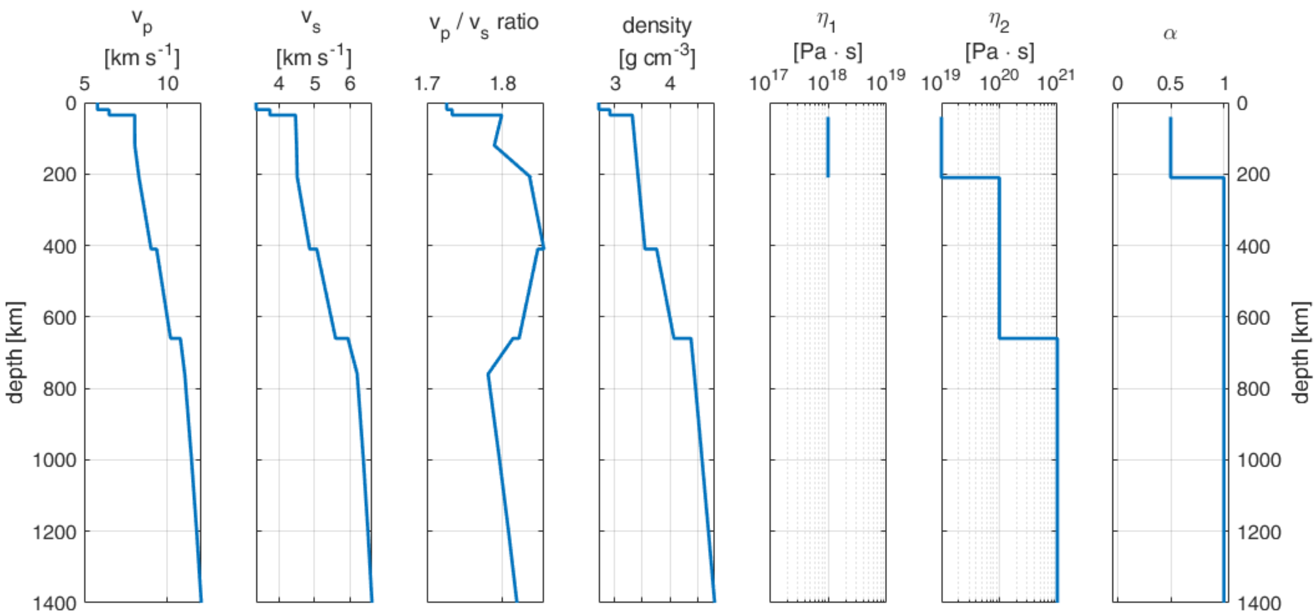

Figure 27-25: Graphics of the rheologic layering of the spherical earth model used for the computations of the gravity change generated by an earthquake. The values correspond to Table 27-10.

We have provided the SH geopotential coefficients in the ICGEM GFC format. The file names are such to allow to retrieve the gravity change for a given event at a given time. The file name convention is as follows:

[event_name]_[days]d[hours[h].gfc

Metadata are included in the gfc header, including a link to the data source (e.g. the USGS-provided quakeML file), to ensure reproducibility of the results. We deem this format and filename structure suitable to populate a database of events. A list of the available events and a short description of the modelled data is provided in plain text format.

The input for the point source is given by the moment tensor components and the hypocenter location (longitude, latitude, depth). The information on the focal mechanism is retrieved for all events from the USGS catalogue (https://www.usgs.gov/programs/earthquake-hazards). The finite fault solution for the greater events in the same catalogue, are published in the global CMT (Centroid Moment Tensor) project format. In this case we can model each patch using the 6 components of the moment tensor, i.e. in the same form as a point source. Finite fault modelling was used to compare the omitted signal due to the point source approximation, as mentioned above, using the co-seismic of Maule 2010 M 8.8 earthquake as a benchmark.

Even if we showed that the point-source approximation can be deemed acceptable for these purposes, the strategy we devised allows to be extended to finite-fault modeling for all the events - albeit at the cost of increased computational effort. For the events of great magnitude, at the higher end of the considered magnitudes, for instance from M 8.5 upwards, finite-fault modelling gives significant difference in the high end of the spectrum (from SH degree 80 upwards), increasingly so with increasing fault length and fault area (which are proportional to magnitude, albeit not trivially scalable). Run time scales up with the number of finite fault patches, and thus finite fault modelling shall be carried out for selected events for which the difference to the point source becomes critical for the sensitivity evaluation.

We computed the spherical harmonic coefficients of the gravity change due to the co-seismic and post-seismic deformation for the earthquakes listed in Table 27-11.

Table 27-11: List of earthquakes for which the coseismic and postseismic deformation is planned to be calculated with the approach of Wang et al. (2017)

Name	Mw	time	longitude	latitude	depth [km]
Sumatra 2004	9.2	2004-12-26 00:58:50Z	94,0772	3,6000	13,5
Tohoku 2011	9.1	2011-03-11 05:46:23Z	142,8799	38,2200	11,5
Maule 2010	8.8	2010-02-27 06:34:15Z	-72,7100	-35,9500	30,5
Sumatra 2012	8.6	2012-04-11 08:38:36Z	92,8598	2,3300	30,5
Doublet of Sumatra 2012	8.2	2012-04-11 10:43:09Z	92,4500	0,7700	16,0
Singkil 2005	8.6	2005-03-28 16:09:36Z	97,1100	2,0800	30,0
Bengkulu 2007	8.4	2007-09-12 11:10:26Z	101,3700	-4,4400	34,0
Okhotsk 2013	8.3	2013-05-24 05:44:49Z	153,3340	54,8700	610,0
ChiChi 1999	7.6	1999-09-20 17:47:18Z	120,8707	23,9700	15,5

The forward modelling of the gravity disturbance field changes requires the fault mechanism and seismic moment tensor, which are retrieved from the USGS earthquake data centre. The web pages of each event are found in Table 27-12.

Table 27-12: Links to the fault mechanism and moment tensor of the earthquakes listed in Table 27-11.

Name	URL
Sumatra 2004	https://earthquake.usgs.gov/earthquakes/eventpage/official20041226005853450_30/executive
Tohoku 2011	https://earthquake.usgs.gov/earthquakes/eventpage/official20110311054624120_30/executive
Maule 2010	https://earthquake.usgs.gov/earthquakes/eventpage/official20100227063411530_30/executive
Sumatra 2012	https://earthquake.usgs.gov/earthquakes/eventpage/official20120411083836720_20/executive
doublet of Sumatra 2012	https://earthquake.usgs.gov/earthquakes/eventpage/usp000jhjb/executive
Singkil 2005	https://earthquake.usgs.gov/earthquakes/eventpage/official20050328160936530_30/executive
Bengkulu 2007	https://earthquake.usgs.gov/earthquakes/eventpage/official20070912111026830_34/executive
Okhotsk 2013	https://earthquake.usgs.gov/earthquakes/eventpage/usb000h4jh/executive
ChiCh i1999	https://earthquake.usgs.gov/earthquakes/eventpage/usp0009eq0/executive

As an example, we show the gravity change of the 2013 Sea of Okhotsk Mw 8.3, 611 km deep, event. The gravity signal has been modelled by (Tanaka et al., 2015), using GPS observations and the GRACE gravity field as constraints. They find that the for modeling the coseismic GPS observation for such deep earthquakes the point source and the finite fault give the same results. They find as criterion for adequacy of the point source, that the fault size should be smaller than the earthquake depth. Their model uses the shallowly dipping nodal plane as the fault plane, and they constrain strike, dip, and rake to the values from the GCMT (Global Centroid-Moment-Tensor (CMT) Project, https://www.globalcmt.org/) solution (189°, 11°, and −93°, respectively). Slip was assumed to be uniform on a rectangular fault 100 km wide, 40 m wide downdip, and the best fitting moment was calculated to be 4.25×10^{21} N · m (i.e., $M_w = 8.35$) assuming a value of $\mu = 122.5$ GPa from the PREM Earth model at a depth of 611 km and calculating an average slip of 6.94 m. They document a coseismic gravity change of up to -1.5 microGal, with an NS elongated negative change east of the epicentre. This result is rotated by 90° to (Chao & Liau, 2019), who analyse the GRACE observation with an alternative method. The parameters we find on the USGS site are a moment of 3.844 10^{21} Nm, Magnitude 8.32, Depth 610.0 km. The two nodal planes are NP1: Strike 12°, Dip 81°, Rake -89°, and NP2: Strike 184°, Dip 10°, Rake -98°. The plane NP2 is very similar to the one used by (Tanaka et al., 2015). The coseismic displacement measured by GPS on the Kamchatka peninsula was modelled by (Steblov et al., 2014). (Xu et al., 2017) study the postseismic deformation and gravity effect of the Okhotsk 2013 earthquake, concluding that the GPS station on Kamchatka has recorded the viscoelastic relaxation, with the post-seismic effect being opposite to the coseismic displacement. They conclude that no afterslip is present, and that the postseismic gravity change is too small to be recorded by GRACE.

The coseismic gravity change we obtain is shown in Figure 27-26.

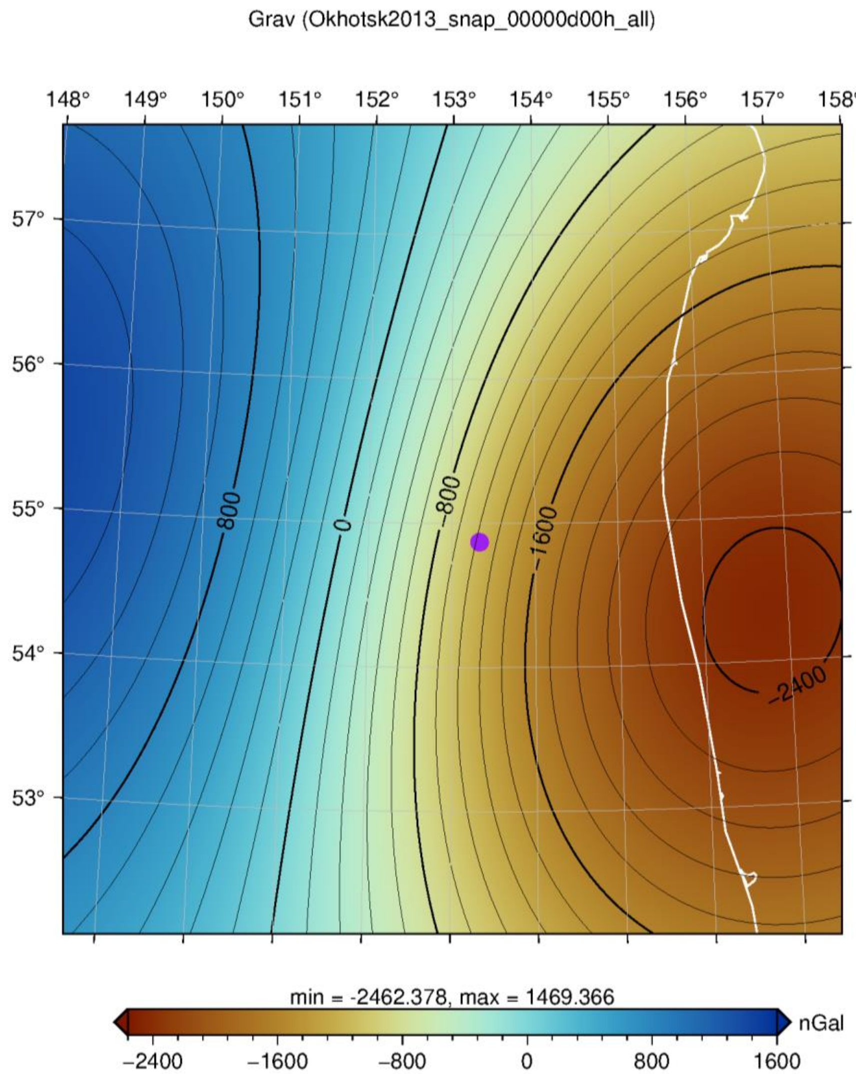

Figure 27-26: Modelled coseismic gravity change for the Okhotsk 2013 deep earthquake

The postseismic gravity change, after 1 month is seen in Figure 27-27, and seen to be in opposite direction as the coseismic field. The change after one month is very small, up to about 70 nGal.

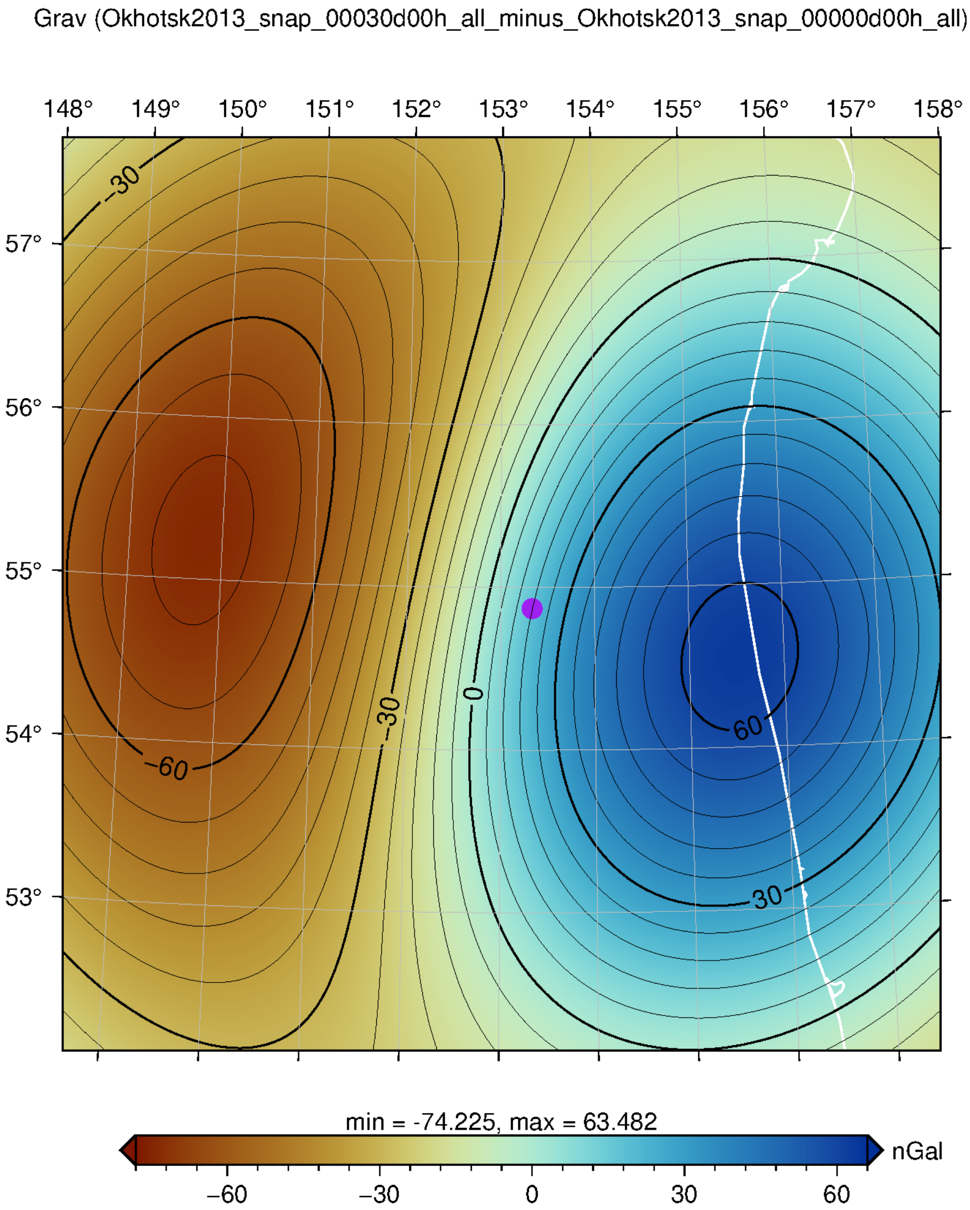

Figure 27-27: Modelled postseismic gravity change for the Okhotsk 2013 deep earthquake, 1 month after the main shock.

We calculate the gravity fields as a merger of a near field, calculated with sampling 0.0625°×0.0625° in a box of 40°×40° centred on the earthquake, and the far field, calculated with 1° sampling. The final merged and global grids have been resampled on a grid spacing of 0.0625°×0.0625°. The spherical expansion of the global grids is then calculated for each time step, the header being as shown in Figure 27-28.

```
name = Okhotsk2013
url = https://earthquake.usgs.gov/product/moment-
tensor/usb000h4jh_Mww/us/1369377496690/quakeml.xml
M0_Nm = 3.800000E+21
lon_deg = 153.334000
lat_deg = 54.870000
depth_km = 610.000
origin_time = 2013-05-24T05:44:49.686Z
elapsed_days = 0.0000
begin_of_head ============================================================
modelname              Okhotsk2013
product_type           gravity_field
gravity_constant       398600441800000.0
radius                 6378137.0
max_degree             180
tide_system            unknown
norm                   fully_normalized

key    L    M          C                        S
end_of_head ================================================
gfc    0    0    1.7573661995352803e-14    0.0000000000000000e+00
gfc    1    0    5.3985532687718434e-10    0.0000000000000000e+00
gfc    1    1    9.0226714013074200e-10    4.5618296594589038e-10
gfc    2    0    2.0201467527756358e-10    0.0000000000000000e+00
gfc    2    1   -2.4426081312090637e-10   -7.9599939919386313e-10
gfc    2    2   -5.5276110424137955e-10   -1.4601392253982419e-10
gfc    3    0    1.5624659884326526e-10    0.0000000000000000e+00
gfc    3    1   -3.3160770861834031e-10   -6.7804621336888704e-10
gfc    3    2   -8.8649096730819545e-10   -3.6383422530197606e-10
gfc    3    3   -4.1139219076741893e-10    8.7519613544141807e-11
...
```

Figure 27-28: Header file of the ICGEM format of the SH coefficient file of the gravity potential of a snapshot of the gravity change induced by a given earthquake, at a given time following the occurrence.

The files of the SH coefficients for the different earthquakes have been uploaded to the TUM MAGIC repository on LRZ Sync+Share (in directory MAGIC/CCN1/Deliverables/Data/Data1-CCN1/WP1680/earthquakes_shc). They will be used for comparing the gravity signals with the noise levels of the different mission scenarios.

We also provide the global grids of the gravity change at ground level, with a regular grid step of 0.0625°×0.0625° (interpolated from 1°×1° outside the 40°×40° near-field region). These contain the full, not band-limited, spectral content of the modelling output, well beyond the spatial scales employed in the comparison with simulations. The grids have been uploaded in directory MAGIC/CCN1/Deliverables/Data/Data1-CCN1/WP1680/earthquakes_grd. They follow the same naming convention of SH coefficients files. The grids file format is COARDS netCDF, each earthquake time series of grids provided in a compressed tar.xz archive.

For illustration we show the degree spectral amplitudes of the gravity field for two time snapshots in Figure 27-29.

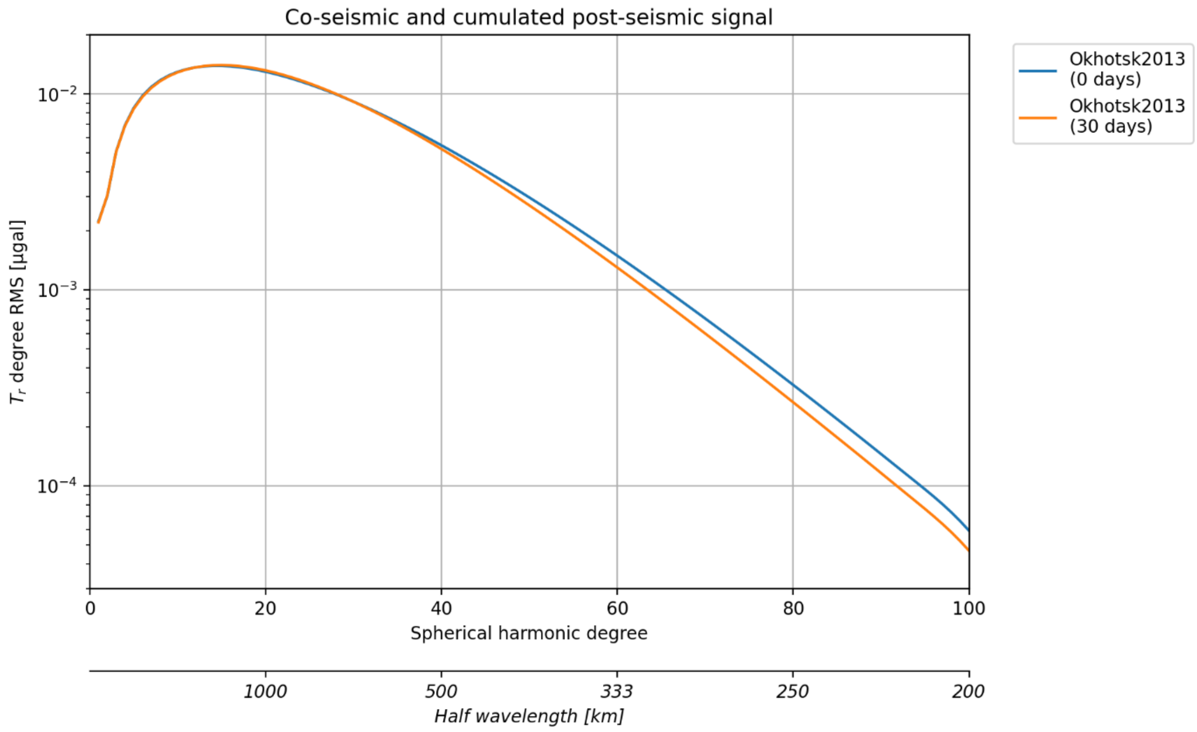

Figure 27-29: Degree spectral amplitudes of the gravity field for two time snapshots. Okhotsk 2013 deep earthquake.

We also show the spectral amplitude variation for the first month in Figure 27-30.

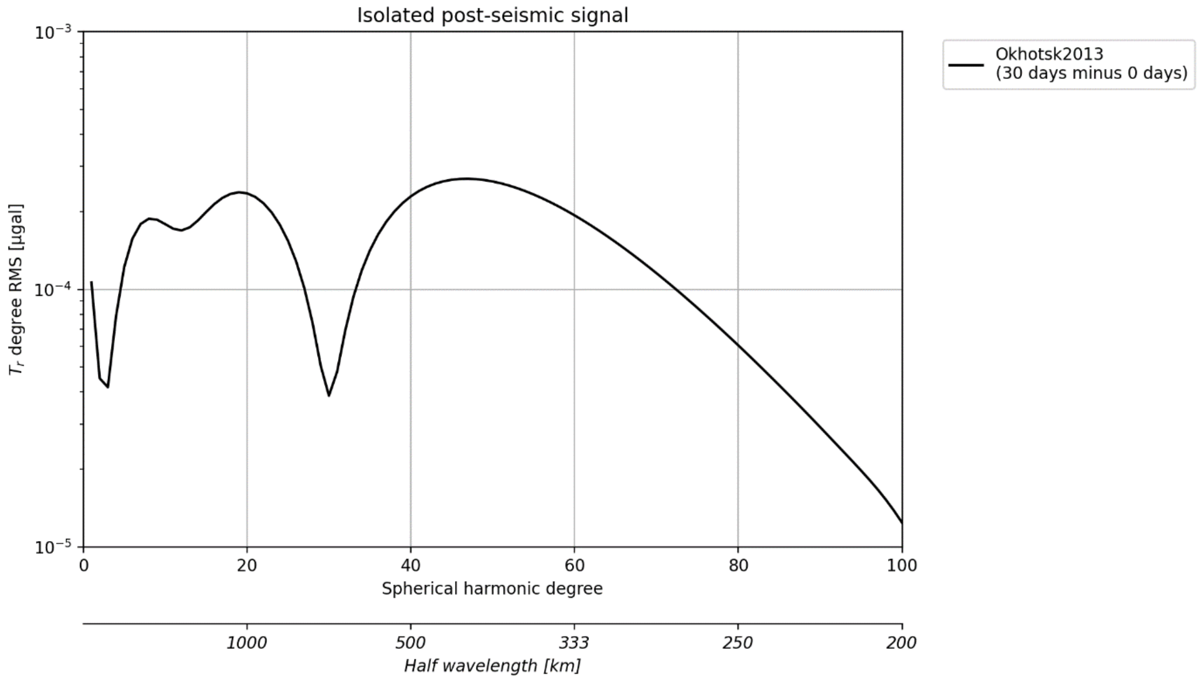

Figure 27-30: Degree spectral amplitude change of the gravity field for the first month after the earthquake. Okhotsk 2013 deep earthquake.

A way to represent the time variation of the spectrum is to code the amplitude in color of horizontal spectral bars, each of which represents the spectrum of the gravity change rate, shown in Figure 27-31. A slight dependency on the degree can be observed, although minor, respect to the gravity change in time over the entire spectrum.

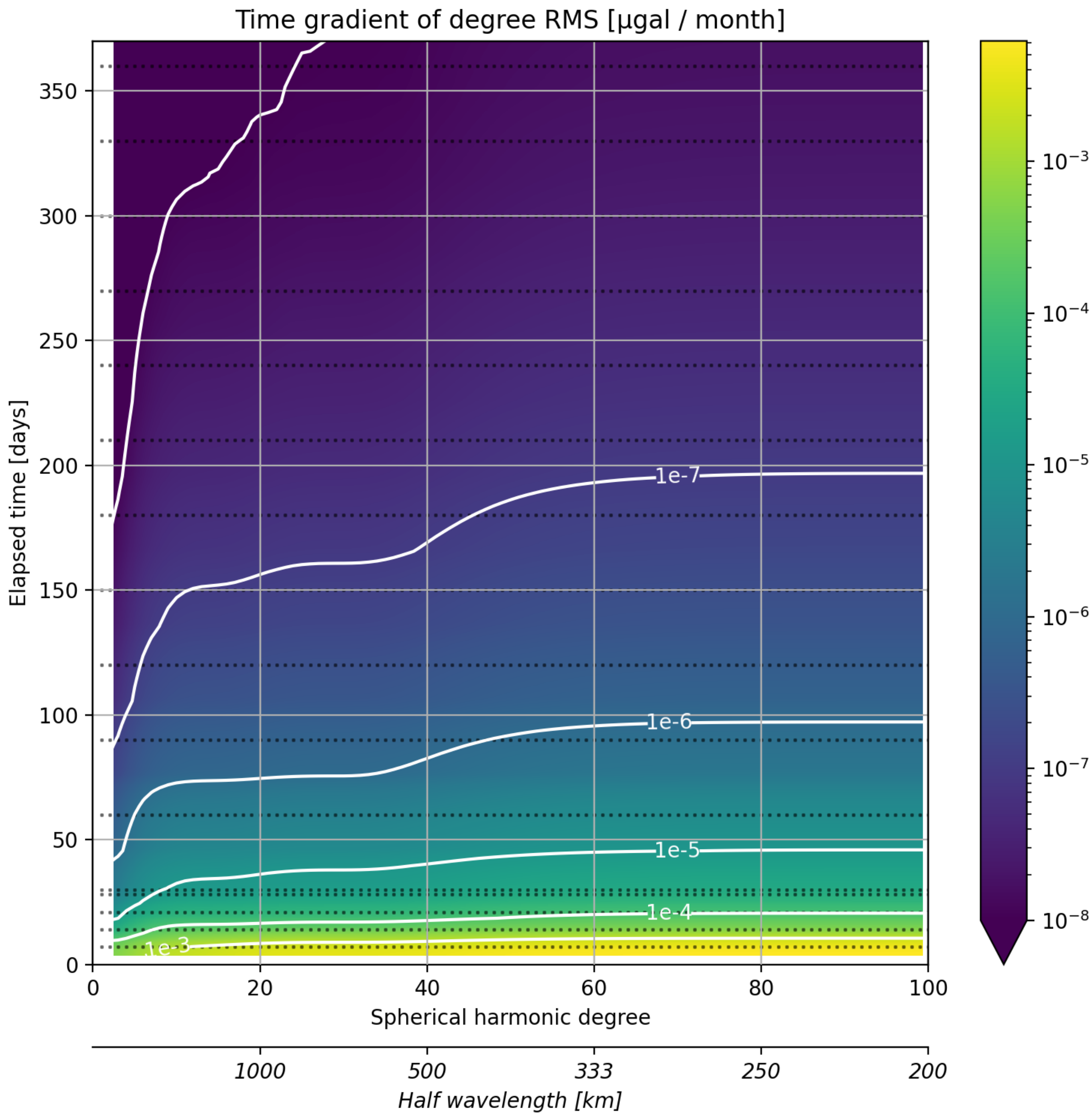

Figure 27-31: Degree spectral amplitude change rate of the gravity field over the period of 1 year after the earthquake. The stippled horizontal lines are the times of the snapshots, the color values in between have been interpolated along time. Okhotsk 2013 deep earthquake.

27.9. SENSITIVITY ANALYSIS EARTHQUAKES (WP1690)

The strategy of analysing the sensitivity to earthquakes is done by comparing the signal strength of the gravity field of a given earthquake to the noise of the satellite mission calculated from the difference of the recovered gravity field with the time variable gravity field which includes atmosphere, ocean, hydrology, postglacial rebound, but no earthquake, besides the Sumatra coseismic signal for the year 2004. For the comparison in the spectral domain we use the average error degree variance of the HIS retrieval error calculated for a defined time resolution window (e.g. 5 days, 1 month, 1 year) and the degree variance of the signal. For illustration we show the satellite noise curves compared to the earthquake signals modelled in WP1680 for the polar only, inclined pair only and MAGIC double pair constellation. We follow the indication received from TUM to deleting the SH coefficients that suffer from poor observation coverage due to the polar gap. This is particularly evident for the inclined pair, which has a large polar gap of 20°, given its inclination of 70°. Following Sneeuw and van Gelderen (1997) the SH coefficients with order m less than $m\_max=\theta\ l$, with θ the angle of polar gap in radians and l the degree, must be blanked before calculating the noise degree variances. The effect on the spectral error curve of not blanking these coefficients is a large increase of the noise at low degrees, between degree 5 and up to about degree 50.

The polar-gaps blanking effect on the inclined pair is shown in Figure 27-32, where the spectral error curves for the Bender and inclined pair are drawn. The noise curves are valid for a 5 days long acquisition. The inclined only pair without blanking has a higher noise at low-mid degrees than the Bender case, but has lower noise in this window after the blanking. Comparing the inclined only case, with near-zonal blanking applied, and the Bender case introduces an inconsistency, which must be considered when evaluating their performance: the retrieval error over the polar caps in the Bender solution is not nulled. A slight increase in the Bender error curves with respect to the inclined only errors is thus expected. The effect of the blanking is more evident in the 1 year averages of the SH coefficients recovered over a 5 day interval. In the averaged curves the noise is over 1 order of magnitude lower after blanking for the inclined pair. When the 20° blanking is applied to both the Bender and the inclined pair, the noise curves are close to equal. The blanking has close to no effect on the polar pair. These observations can be made in Figure 27-32 (lower plot).

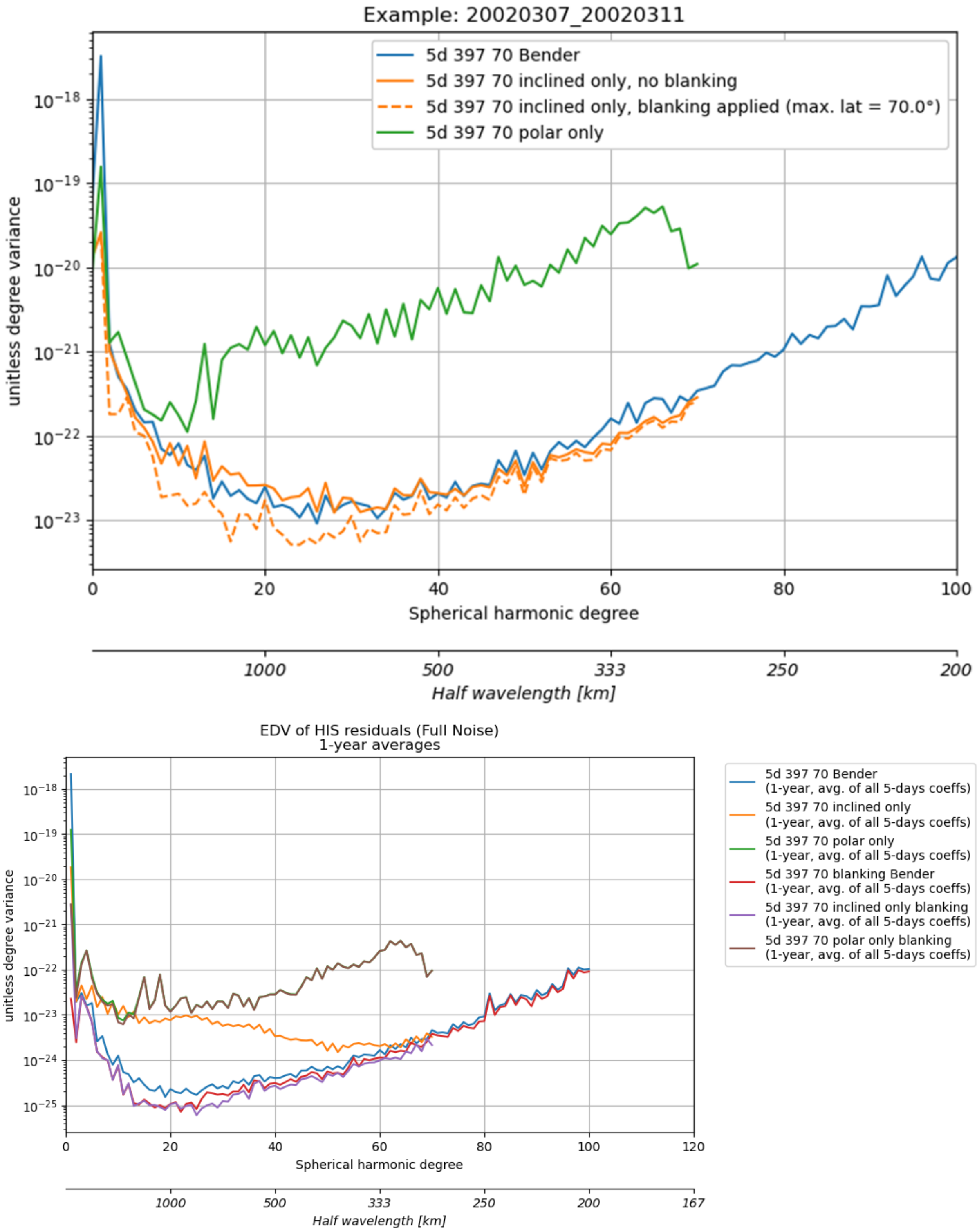

Figure 27-32: Unitless error degree variances of the MAGIC mission scenarios: polar only, inclined only and Bender double-couple. For the definition of the polar-gaps blanking see text. Upper plot: error curves for 5 days sampling. Lower plot: error curves for the averages over 1 year of the HIS full noise SH coefficients, with and without polar-gaps blanking.

We now proceed to compare the noise curves with the coseismic earthquake signal, for the noise corresponding to a sampling of 5 days (Figure 27-33). Since the signal is local and not global, a spatial localization of the spectrum is required. We apply the spatio-spectral localization method in the spherical harmonic domain proposed by (Wieczorek et al. 2007), in its implementation in the SHTOOLS software (Wieczorek et al., 2018), and adopt the spherical cap as localization domain. If the localization operation is not applied, an observable earthquake spectrum results to be much lower and seemingly undetectable by the mission, which is not realistic when comparing the earthquake signal amplitude with the noise amplitude calculated on the earth surface. Examples of the localized spectra for lakes and glaciers, and hydrologic basins is found in Pivetta et al. (2022).

The signal degree variance spectra are obtained with a spatio-spectral localization procedure inside a spherical cap with a radius of 9°. We find it is relevant to analyse the spectral amplitudes of signal and noise, due to the fact that the signal decays, the noise increases with decreasing spectral wavelength. This means that only up to a certain wavelength the observations can be used to detecting the earthquake, as for greater wavelength, the noise is higher than the signal. This critical wavelength decreases the greater the time window is, used for integrating the signal. The crossing of the noise and signal spectral curves defines the maximum degree at which it is beneficial to synthesize the observed field in the spatial domain for detection of an earthquake, because by adding SH coefficients above this limit adds gravity signal which is affected by noise larger than the earthquake signal which shall be recovered.

The earthquake signals have similar spectral dependency, increasing in amplitude with increasing degree, and scaling with the magnitude. The exception is the deep Okhotsk earthquake, which lacks high frequency signal. It can be seen that the Bender and inclined only solution recovers a much broader bandwidth of the signal, compared to the polar only pair. The latter has overall a high noise level. The Chichi 1999 earthquake is below resolution, all other earthquakes would be seen by the Bender or inclined-only mission.

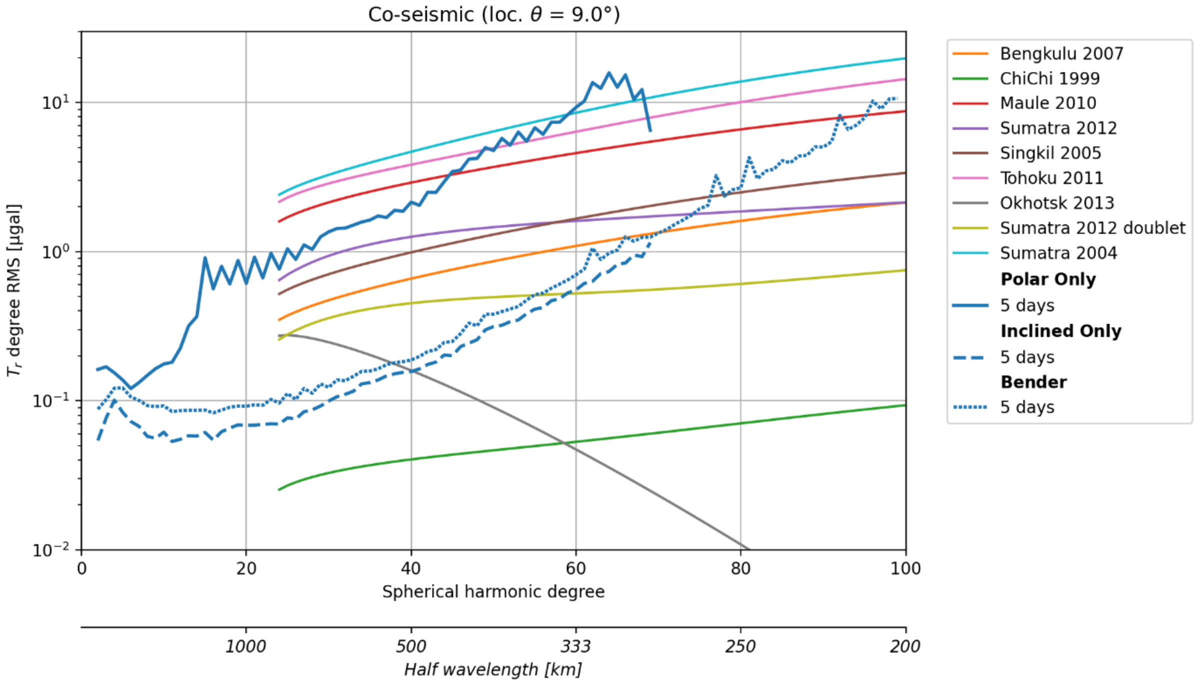

Figure 27-33: Error degree amplitudes of the MAGIC mission scenarios: polar only, inclined only and Bender double-couple and the signal degree amplitudes (localized) of the coseismic signal for selected earthquakes discussed in WP 1680. Polar-gaps blanking has been applied to the inclined noise solutions. 5-day time integration for the gravity acquisition at the satellite.

We now consider the detection of a postseismic gravity change, integrated over 1 year. Since we wait for 1 year to detect the postseismic gravity change, we estimate the SH expansion of the errors of a 1-year solution by averaging the HIS retrieval error SH coefficients of all the 5-day solutions over 1 year. The averaging process lowers the error curves considerably. Coherently with the 5-day analysis, the blanking of near-zonal coefficients in the inclined pair only case was applied also here, for each of the 5-day solutions used in the average.

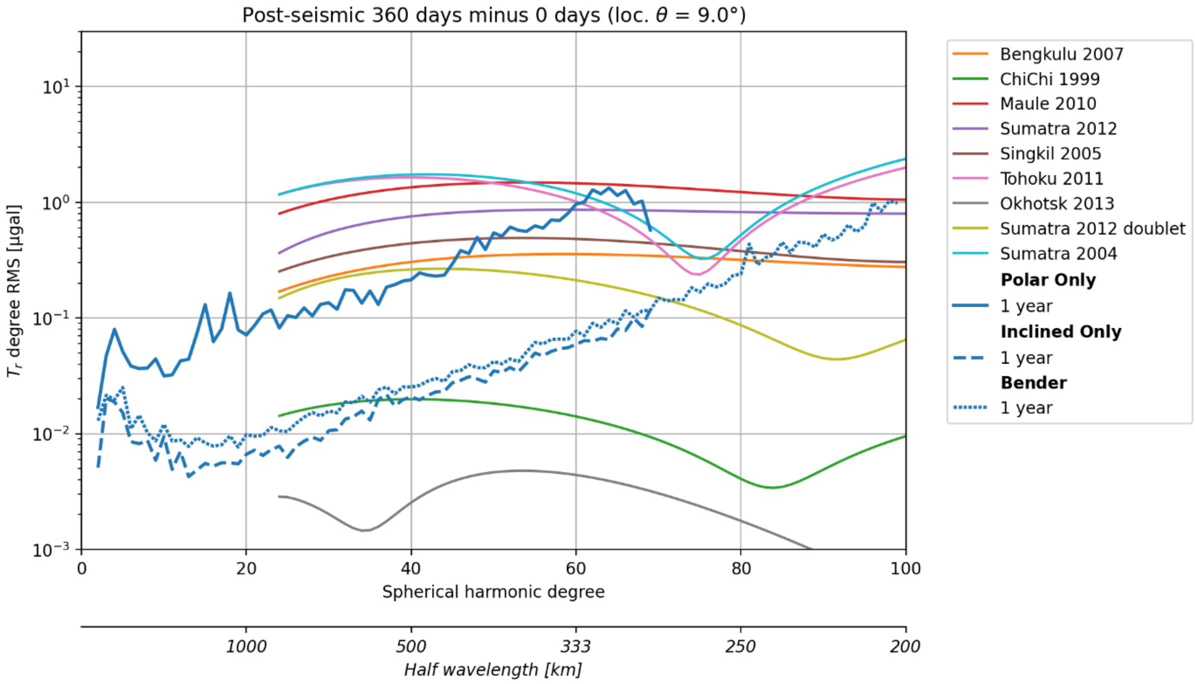

Figure 27-34: Error degree amplitudes of the MAGIC mission scenarios: polar only, inclined only and Bender double-couple and the signal degree amplitudes (localized) of the postseismic gravity change for selected earthquakes discussed in WP 1680. Polar-gaps blanking has been applied to the inclined noise solutions. One-year averages of the noise for a year of 5-day solutions.

For the post-seismic spectrum over an interval of 1 year the spectral characteristics are similar for most earthquakes, independently of depth. For some events a characteristic minimum is found at a given degree, with an increase in the spectral amplitude for greater degrees. At the moment it is unclear what this minimum represents, or what it is due to. The inclined only and Bender are similar in their performance. The Bender double pair is slightly less performant than the inclined pair only, but as shown above, this can be in part attributed to the lack of blanking, so there is a bias between the inclined and Bender error curves. The polar only pair has much higher noise than both the inclined and Bender solution. Given the gravity change spectra for these particular events the Bender and inclined only solutions give the same sensitivity. The ChiChi 1999 and Okhotsk 2013 events are two exceptions: the former of considerably smaller magnitude than the others, the latter a peculiar deep-focus source. The near equivalence of inclined pair only and Bender in this analysis is seen very well also in the SNR curves shown in the next graph, where the inclined-only pair is traced over the Bender SNR curve.

As we have shown in the example in Chapter 27.8, the greatest postseismic gravity change occurs in the first month following the earthquake, with the gravity change between the end of the first month and the end of the first year being close to 0.1 % of the signal after one month.

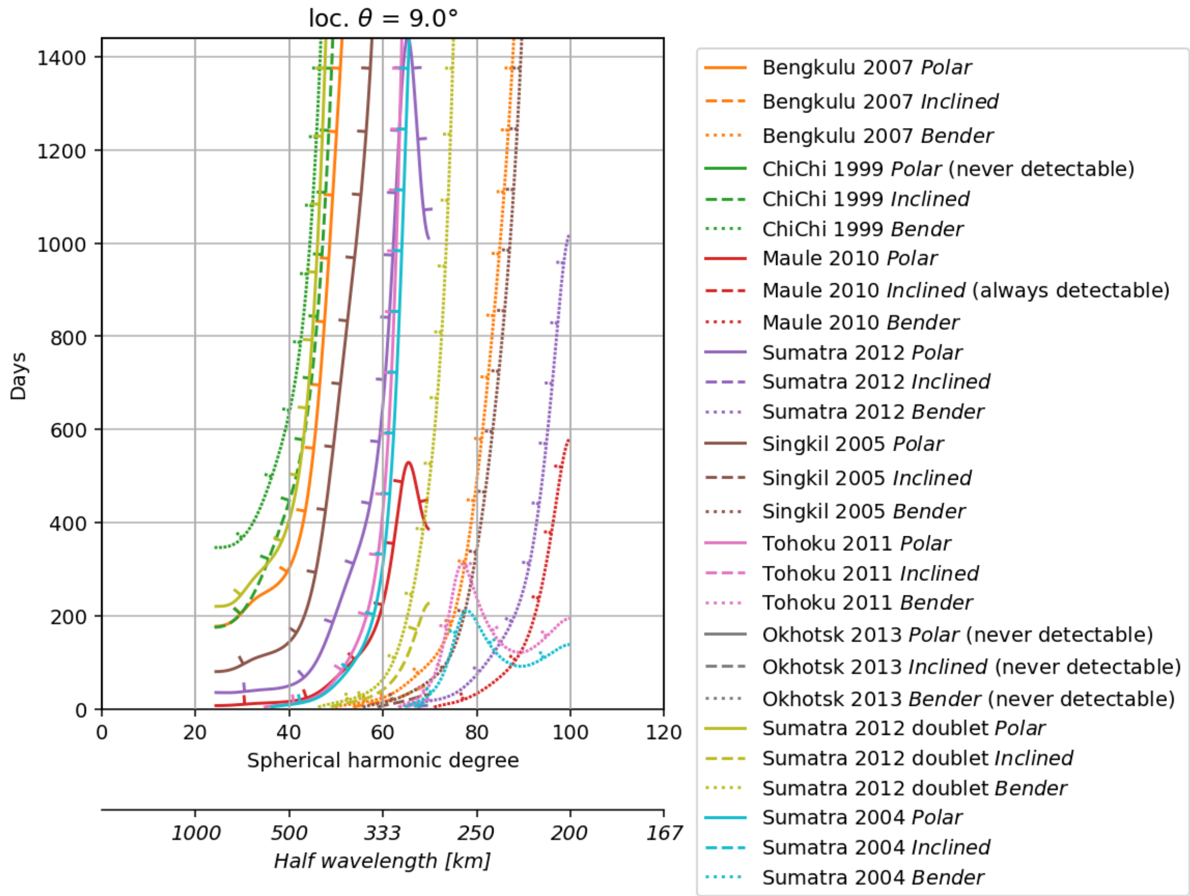

Figure 27-35: Post-seismic detectability through time. The signal and error values are compared at each time (y axis: days) using the same, consistent length of observed signal and scaled errors. The contours are given at signal to noise ratio (SNR) SNR = 1, and contour ticks point towards SNR > 1. The inclined pair noise has been blanked.

The SNR curves shown in Figure 27-35 depict in compact form the sensitivity to the post-seismic gravity change. The ChiChi 1999 change is not detectable by the polar pair, but only by the inclined and Bender pair. The Okhotsk 2013 SNR curve is also not visible, because the signal is not resolved. All other events are visible by the polar pair, with an increase in the maximum resolved spherical harmonic degree over time. The greatest increase is found in the first 150 days (from degree 25 to degree 60 according to the earthquake, after which the curves verticalize, so little increase in the maximum degree is found. For all events, except the Chichi 1999 and Okhotsk 2013, the Bender and Inclined missions bring a gain in close to 40 degrees of maximum resolution. Since the Bender simulations are available up to degree 100, they allow to assess by how much the maximum detectable degree increases through time. The diminishing impact of time frames longer than 400 days reflects the decreasing temporal gradient of the post-seismic gravity signal, as shown in Figure 27-34.

The SNR curves can be used to define the maximum resolved degree for the different scenarios. For instance, tracing an imagined horizontal line in the graph of Figure 27-35 at 365 days, leads to a series of intersections of the SNR curves. These intersection-points correspond to the point of intersection of the signal spectral curves with the noise spectral curves. For the Tohoku 2011 and Sumatra 2004 mega-earthquakes at 365 days no intersection of the Bender and inclined only pair curves with the horizontal lines is found. This matches the observation that after 365 days the signal spectral curves are well above the Bender and inclined noise curves. Observing the SNR curves, we see that the detectability is lower than the maximum degree 80 only for the first 100 days after the earthquake: after 100 days the lowest degrees up to degree 70, and above degree 90 are resolved, with a gap between degrees 70 and 90 for the Sumatra 2004 event. Similar resolving power is present for the Tohoku 2011 earthquake.

A means to check the consistency of the noise per degree spectra with the signal per degree spectra obtained from the localization analysis, is to also calculate the localized spectrum of the noise, in the same window used for the signal localization. We show this using the 1-year average of the HIS retrieval error for the 5-day solutions. We calculate the localized spectrum of the average HIS retrieval error using the same localization radius of 9° used for the signal localization. The 1-year global noise curves, the localized noise curves, and the localized signal spectrum are all displayed in Figure 27-36.

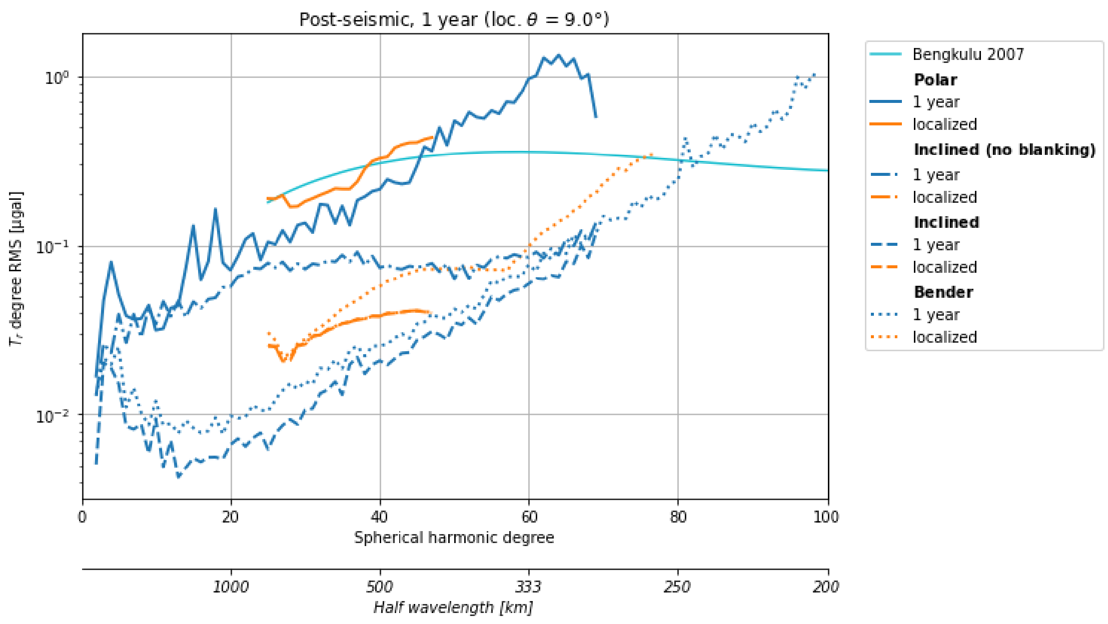

Figure 27-36: The 1 year global noise curves, the localized noise curves averaged over 1 year, and the localized signal spectrum of the Bengkulu 2007 earthquake. Localization radius is 9°.

Figure 27-36 shows that the polar-gaps blanking effect which is applied to the inclined pair has no effect on the localized noise spectrum, which is understandable by the fact that the earthquake location (and the 9° cap around it) is comprised in the observed latitudes of the inclined mission and is thus unaffected by the gap in the polar regions. Instead, the non-blanked global spectrum is different from the blanked spectrum of the inclined pair, as the global spectrum includes the polar regions. Systematically the localized spectrum is a bit higher than the global spectrum, which we attribute to the fact that the earthquake is located in a region with higher noise than the global average noise – the global spectrum in spherical harmonics being akin to an average over the whole globe. In this case, the earthquake signal spectrum is above the localized and the global spectrum, so positive detectability is conserved, albeit with a different maximum SH degree.

Localization results in a loss of SH degrees in the localized spectrum, at the low and high end of the domain, by an amount equal to the bandwidth of the localization window, due to the convolution-like operator involved. Since the simulations of the three mission scenarios are provided at different maximum degree (70, 70, and 100 for polar-only, inclined-only and Bender, respectively) and the localization window is expanded up to degree 23, this results in the localized error curves being limited to degree 48, 48, and 77 respectively (i.e. maximum degree minus the window bandwidth). The earthquake signal was expanded up to SH degree 180, thus resulting in a maximum degree after localization of 157, therefore it is not the limiting factor in the spectra shown here.

The maps of the noise, synthesized in the spatial domain from the SH expansions, are displayed in Figure 27-37. All maps are expanded up to degree and order $N=70$, for consistency – therefore the Bender solution is truncated from N=100 to 70. Otherwise, since the errors at N=100 reach higher values than those of the other configurations at N=70, the Bender map would have shown much larger amplitudes – an inconsistent comparison.

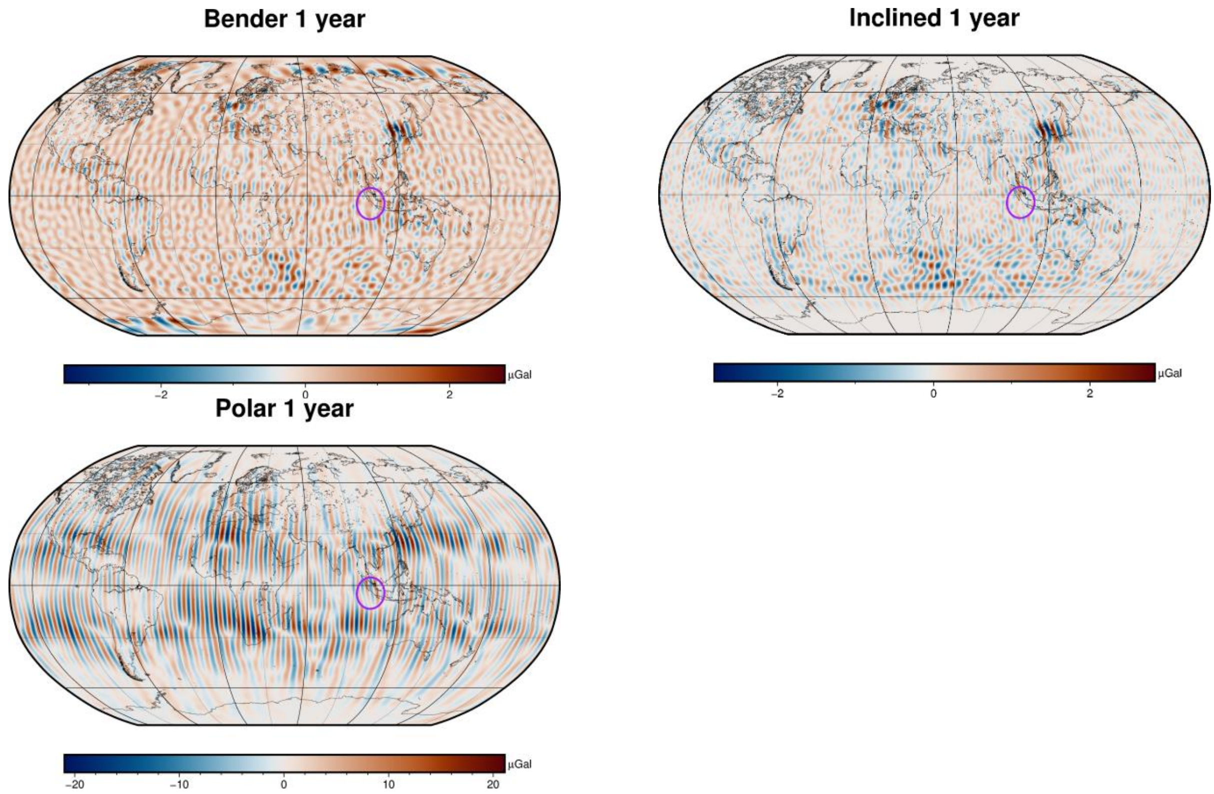

Figure 27-37: Global maps of the noise distribution for the Bender, inclined only, and polar only mission designs. The degrees of 0, 1 and 2 have been nulled, the maximum degree of the synthesis is N=70. The Inclined pair is shown after polar-gaps blanking is applied. The purple circle shows the cap of the spectral localization for the Bengkulu 2007 earthquake.

Global maps of the noise distribution for the Bender, inclined only, and polar only mission designs. The degrees of 0, 1 and 2 have been nulled, the maximum degree of the synthesis is $N=70$. The Inclined pair is shown after polar-gaps blanking is applied. The purple circle shows the cap of the spectral localization for the Bengkulu 2007 earthquake.

We also show a zoom on the spatial variation of the gravity field of the average noise over 1 year for the three mission scenarios, which is put in comparison to the postseismic signal over an interval of 1 year. As expected from the spectral analysis, the signal is well above the noise level, as seen in Figure 27-38.

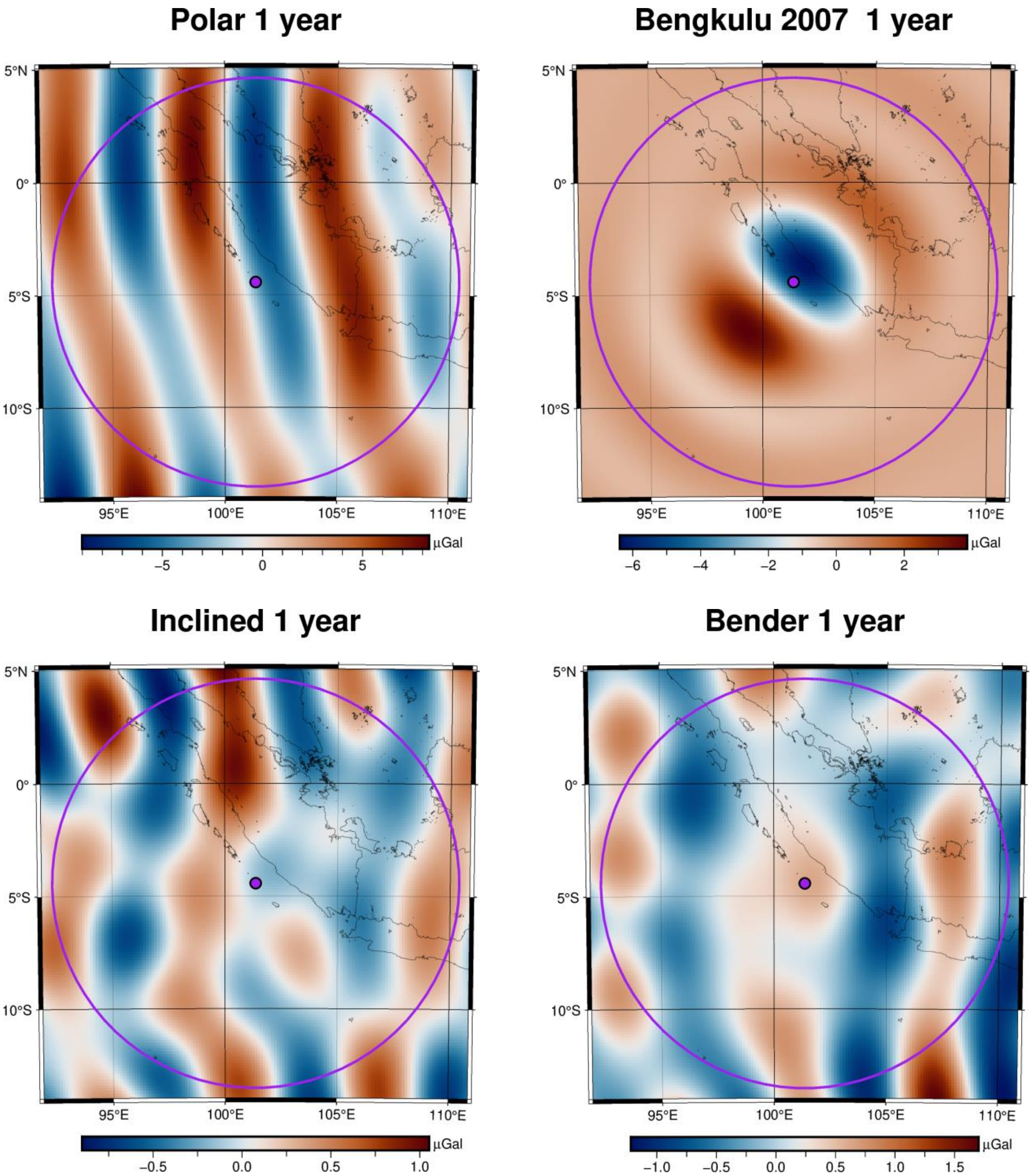

Figure 27-38: Localized maps of the noise distribution for the Bender, inclined only, and polar only mission designs, and for the postseismic gravity change over 1 year of the Bengkulu 2007 earthquake. The degrees of 0, 1 and 2 have been nulled, the maximum degree of the synthesis is N=70. The inclined pair is shown after polar-gaps blanking is applied. The purple circle shows the cap of the spectral localization.

Comments and Conclusions

A computing framework has been defined with which the gravity signals of earthquakes can be computed, based on the USGS-NEIC earthquake catalog. The automatic computational approach calculates grids and SH expansions of the grids for one earthquake, representing the time evolution of the gravity field change generated by the earthquake starting from the co-seismic signal and continuing with the post seismic field. The first collection of events has been uploaded to the server and is available for further inclusion as a input time variable gravity field that can be added to the AOHIS gravity change. The database of earthquake signals is expandable to a greater number of earthquakes, for instance lowering the maximum earthquake magnitude. The co-seismic and post seismic SH coefficients of the time evolution of the gravity field are available and copied to the server.

Given the earthquakes, we have proceeded to evaluate their detectability from the inclined, polar, and Bender mission design, with a 5-day sampling of the gravity change. The sensitivity of the 5-day solution of the inclined and Bender mission design are equivalent, and both are greatly better than the polar only pair, in terms of noise level compared to the earthquake signal curves. The Bender solution has the advantage of the higher maximum degree of the field recovery, which is of value in observing the co-seismic and the post seismic signal. The criterion to define an earthquake as detectable if at least a part of its spectrum is above the spectral noise curves of the mission is coherent with the comparison in space domain of the noise and signal. The spectral analysis is useful, since it defines the spectral window of the observed gravity field that can be summed to define the cumulated field. In the case that the signal amplitude falls below the spectral noise amplitude at a given degree (K), an approach can be to synthesize the noise for one-time realization of the recovered signal, up to different degrees, for instance below and above degree K. This noise realization is required to have lower amplitude than the earthquake signal if the earthquake should be detected.

In space domain one more approach to estimate the sensitivity of the mission design to earthquakes, could be to perturb an earthquake signal with the noise realization and test whether the earthquake parameters can be recovered through an inversion process. Of particular interest is the rheology involved in the postseismic visco-elastic relaxation.

28. APPLICABLE DOCUMENTS, REFERENCE DOCUMENTS, AND PUBLICATIONS TO PART 5

28.1. APPLICABLE DOCUMENTS

[AD-1] Mission Requirements Document, Next Generation Gravity Mission as a Mass-change And Geosciences International Constellation (MAGIC) - A joint ESA/NASA double-pair mission based on NASA's MCDO and ESA's NGGM studies (2020). ESA-EOPSM-FMCC-MRD-3785

[AD-2] Scientific Readiness Levels (SRL) Handbook, Issue 1, Revision 0, 05-08-2015

[AD-3] Statement of Work - ESA Express Procurement - EXPRO NGGM/MAGIC science support study during Phase A, Issue 1, Revision 0, 18/01/2021 Ref ESA-EOPSM-FUTM-SOW-3813

28.2. REFERENCE DOCUMENTS

Astafyeva, Elivira, Irina Zakharenkova et al. (2017) Global Ionospheric and thermospheric effects of the June 2015 geomagnetic disturbances: multi-instrumental observations and modeling: Global effects of June 2015 disturbances, Journal of Geophysical Research: Space Physics 122(11), https://doi.org/10.1002/2017JA024174

Balidakis, K., Dobslaw, H., Zus, F, Eicker, A., Dill, R. and Wickert, J. (in preparation): Current and Future Contributions of Global Geodesy to Large-Scale Atmospheric Modelling (to be submitted to Surveys in Geophysics)

Bamber, J. L., Tedstone, A. J., King, M. D., Howat, I. M., Enderlin, E. M., van den Broeke, M. R., and Noel, B.: Land Ice Freshwater Budget of the Arctic and North Atlantic Oceans: 1. Data, Methods, and Results, Journal of Geophysical Research: Oceans, 123, 1827–1837, https://doi.org/10.1002/2017JC013605, 2018.

Baugh, C., de Rosnay, P., Lawrence, H., Jurlina, T., Drusch, M., Zsoter, E. and Prudhomme, C. (2020) The Impact of SMOS Soil Moisture Data Assimilation within the Operational Global Flood Awareness System (GloFAS). Remote Sensing 12(9).

Brandt, Daniel A., Charles D. Bussy-Virat, Aaron J. Ridley, 2020: A Simple Method for Correcting Empirical Model Densities During Geomagnetic Storms Using Satellite Orbit Data. Space Weather. https://doi.org/10.1029/2020SW002565

Bruinsma S, Boniface C, Sutton EK & Fedrizzi M 2021. Thermosphere modeling capabilities assessment: geomagnetic storms. J. Space Weather Space Clim. 11, 12. https://doi.org/10.1051/swsc/2021002.

Bruinsma, S., Claude Boniface: The operational and research DTM-2020 thermosphere models. J. Space Weather Space Clim., Volume 11, 2021. https://doi.org/10.1051/swsc/2021032

Boniface, C. and Sean Bruinsma (2021) Uncertainty quantification of the DTM2020 thermosphere model, Journal of Space Weather and Space Climate 53, https://doi.org/10.1051/swsc/2021034

Bussy-Virat, Charles D., Aaron J. Ridley: Estimation of the thermospheric density using ephemerides of the CYGNSS and Swarm constellations. Journal of Atmospheric and Solar-Terrestrial Physics. Volume 221, 15 September 2021, 10568.7 https://doi.org/10.1016/j.jastp.2021.105687

Calabia A, Tang G, Jin S (2020), "Assessment of new thermospheric mass density model using NRLMSISE-00 model, GRACE, Swarm-C, and APOD observations", Journal of Atmospheric and Solar-Terrestrial Physics, Vol. 199, 105207 https://doi.org/10.1016/j.jastp.2020.105207

Callejón, Miguel, Christian Siemes, Alejandro Pastor (2023) Improving orbit prediction via thermospheric density calibration. In: 2nd NEO and Debris Detection Conference, Volume 2, Issue 1, ESA Space Debris Office, Editors: T. Flohrer, R. Moissl, F. Schmitz; Darmstadt, Germany, 24 - 26 January 2023.

Ceren Kalafatoglu Eyiguler, E., J. S. Shim, M. M. Kuznetsova, Z. Kaymaz, B. R. Bowman, M. V. Codrescu, S. C. Solomon, T. J. Fuller-Rowell, A. J. Ridley, P. M. Mehta, E. K. Sutton: Quantifying the Storm Time Thermospheric Neutral Density Variations Using Model and Observations. Space Weather, 2019. https://doi.org/10.1029/2018SW002033

Chao, B. F., & Liau, J. R. (2019). Gravity Changes Due to Large Earthquakes Detected in GRACE Satellite Data via Empirical Orthogonal Function Analysis. Journal of Geophysical Research: Solid Earth, 124(3), 3024–3035. https://doi.org/10.1029/2018JB016862

Ciracì, E., Velicogna, I., and Swenson, S.: Continuity of the Mass Loss of the World’s Glaciers and Ice Caps From the GRACE and GRACE Follow-On Missions, Geophysical Research Letters, 47, e2019GL086926, https://doi.org/10.1029/2019GL086926, 2020.

Dobslaw H, Bergmann-Wolf I, Dill R, Forootan E, Klemann V, Kusche J, Sasgen I (2014) Updating ESA’s Earth System Model for Gravity Mission Simulation Studies: 1. Model Description and Validation, (Scientific Technical Report; 14/07), Potsdam: Deutsches GeoForschungsZentrum GFZ, 69p.

Doornbos E. 2011. Thermospheric density and wind determination from satellite dynamics. Ph.D. Thesis, Department of Astrodynamics and Satellite Missions, Delft University of Technology. Available at http://resolver.tudelft.nl/uuid:33002be1-1498-4bec-a440-4c90ec149aea

Driscoll, J. R., & Healy, D. M. (1994). Computing Fourier Transforms and Convolutions on the 2-Sphere. Advances in Applied Mathematics, 15(2), 202–250. https://doi.org/10.1006/aama.1994.1008

Drob, D. P., et al. (2015), An update to the Horizontal Wind Model (HWM): The quiet time thermosphere, Earth and Space Science, 2, 301–319, doi:10.1002/2014EA000089.

Forootan, E., S Farzaneh, M Kosary, M Schmidt, M Schumacher: A simultaneous calibration and data assimilation (C/DA) to improve NRLMSISE00 using thermospheric neutral density (TND) from space-borne accelerometer measurements. Geophysical Journal International, Volume 224, Issue 2, February 2021, Pages 1096–1115, https://doi.org/10.1093/gji/ggaa507

Forootan, Ehsan, Mona Kosary, Saeed Farzaneh, Timothy Kodikara, Kristin Vielberg, Isabel Fernandez-Gomez, Claudia Borries, Maike Schumacher (2022) Forecasting global and multi-level thermospheric neutral density and ionospheric electron content by tuning models against satellite-based accelerometer measurements. Nature Scientific Reports, 12:2095. https://doi.org/10.1038/s41598-022-05952-y

Fernandez-Gomez, I., Kodikara, T., Borries, C. et al. Improving estimates of the ionosphere during geomagnetic storm conditions through assimilation of thermospheric mass density. Earth Planets Space 74, 121 (2022). https://doi.org/10.1186/s40623-022-01678-3

Förster, M., Haaland, S. E., and Doornbos, E.: Thermospheric vorticity at high geomagnetic latitudes from CHAMP data and its IMF dependence, Ann. Geophys., 29, 181–186, https://doi.org/10.5194/angeo-29-181-2011, 2011.

Getirana, A., M. Rodell, S. Kumar, H.K. Beaudoing, K. Arsenault, B. Zaitchik, H. Save, and S. Bettadpur, GRACE improves seasonal groundwater forecast initialization over the U.S., J. Hydrometeor., 21 (1), 59-71, doi:10.1175/JHM-D-19-0096.1, 2020.

Gondelach, David J., Richard Linares, 2021: Real-Time Thermospheric Density Estimation via Radar and GPS Tracking Data Assimilation. Space Weather. https://doi.org/10.1029/2020SW002620

Gondelach, David J., Srinivas Setty, Christoph Bamann, Paul Cefola: Atmospheric density estimation for improved orbit determination and conjunction assessment. 8th European Conference on Space Debris, 2021, ESA Space Debris Office. Vol 8, issue 1, Editors: T. Flohrer, S. Lemmens, F. Schmitz.

Horvath, A., Murböck, M., Pail, R., and Horwath, M.: Decorrelation of GRACE Time Variable Gravity Field Solutions Using Full Covariance Information, Geosciences, 8, https://doi.org/10.3390/geosciences8090323, 2018.

Hughes, C. W., Williams, J., Blaker, A., Coward, A. and Stepanov, V. (2018). A window on the deep ocean: The special value of ocean bottom pressure for monitoring the large-scale, deep-ocean circulation. Progress in Oceanography 161, 19-46. https://doi.org/ 10.1016/j.pocean.2018.01.011.

Huss, M., Bookhagen, B., Huggel, C., Jacobsen, D., Bradley, R. S., Clague, J. J., Vuille, M., Buytaert, W., Cayan, D. R., Greenwood, G., Mark, B. G., Milner, A. M., Weingartner, R., and Winder, M.: Toward mountains without permanent snow and ice, Earth's Future, 5, 418–435, https://doi.org/10.1002/2016EF000514, 2017.

IPCC: Special Report on the Ocean and Cryosphere in a Changing Climate, IPCC Geneva, 2018.

Jaggi, A., Weigelt, M., Flechtner, F., Güntner, A., Mayer-Gurr, T., Martinis, S., Bruinsma, S., Flury, J., Bourgogne, S., Steffen, H., Meyer, U., Jean, Y., Susnik, A., Grahsl, A., Arnold, D., Cann-Guthauser, K., Dach, R., Li, Z., Chen, Q., van Dam, T., Gruber, C., Poropat, L., Gouweleeuw, B., Kvas, A., Klinger, B., Lemoine, J.M., Biancale, R., Zwenzner, H., Bandikova, T. and Shabanloui, A. (2019) European Gravity Service for Improved Emergency Management (EGSIEM)-from concept to implementation. Geophysical Journal International 218(3), 1572-1590.

Kodikara, Timothy (2022) Data assimilation in the thermosphere-ionosphere-electrodynamics general circulation model (TIE-GCM). IAGA GeoDAWG Virtual Seminar Series, 25 Jan 2022, Virtual.

Kodikara, T., Carter, B., & Zhang, K. (2018). The first comparison between Swarm-C accelerometer-derived thermospheric densities and physical and empirical model estimates. Journal of Geophysical Research: Space Physics, 123(6), 5068–5086. https://doi.org/10.1029/2017JA025118

Li, B., M. Rodell, S.V. Kumar, H.K. Beaudoing, A. Getirana, B.F. Zaitchik, L.G. Goncalves, C. Cossetin, S. Bhanja, A. Mukherjee, S. Tian, N. Tangdamrongsub, D. Long, J. Nanteza, J. Lee, F. Policelli, I. B. Goni, D. Daira, M. Bila, G. de Lannoy, D. Mocko, and S. C. Steele-Dunne, Global GRACE data assimilation for groundwater and drought monitoring: advances and challenges, Water Resour. Res., 55, doi:10.1029/2018WR024618, 2019.

Licata, R. J., & Mehta, P. M. (2023). Reduced order probabilistic emulation for physics-based thermosphere models. Space Weather, 21, e2022SW003345. https://doi.org/10.1029/2022SW003345

Licata, Richard J., Piyush M. Mehta, W. Kent Tobiska, S. Huzurbazar (2022) Machine-Learned HASDM Thermospheric Mass Density Model With Uncertainty Quantification. Volume 20, Issue 4, Number e2021SW002915, https://doi.org/10.1029/2021SW002915

Manzi, Matteo, Sai Abhishek Peddakotla, Emma Stevenson: IntelLIgent Atmospheric Density Modelling for Space Operations. Stardust-R Project Working Group. Stardust-R Global Virtual Workshop - I, Pisa, September 2020. H2020 project. http://www.stardust-network.eu/wp-content/uploads/2021/05/PWG-ILIAD-presentation-1.pdf

Oliveira, Denny M., Eftyhia Zesta et al. (2021) The Current State and Future Directions of Modeling Thermosphere Density Enhancements During Extreme Magnetic Storms, Frontiers in Astronomy and Space Sciences, https://doi.org/10.3389/fspas.2021.764144

March G, Doornbos E, Visser P. 2019a. High-fidelity geometry models for improving the consistency of CHAMP, GRACE, GOCE and Swarm thermospheric density data sets. Adv Space Res 63: 213–238. https://doi.org/10.1016/j.asr.2018.07.009

March G, Visser T, Visser P, Doornbos E. 2019b. CHAMP and GOCE thermospheric wind characterization with improved gas-surface interactions modelling. Adv Space Res 64: 1225–1242. https://doi.org/10.1016/j.asr.2019.06.023

March G, Van den IJssel J, Siemes C, Visser P, Doornbos E, Pilinski M. 2021. Gas-surface interactions modelling influence on satellite aerodynamics and thermosphere mass density. J Space Weather Space Clim 11, 54. https://doi.org/10.1051/swsc/2021035

Maure, D., Kittel, C., Lambin, C., Delhasse, A., and Fettweis, X.: Spatially heterogeneous effect of the climate warming on the Arctic land ice, The Cryosphere Discussions, 2023, 1–20, https://doi.org/10.5194/tc-2023-7, 2023.

Mehta PM, Paul SN, Crisp NH, Sheridan PL, Siemes C, March G, Bruinsma S. 2022. Satellite drag coefficient modeling for thermosphere science and mission operations. Adv Space Res. https://doi.org/10.1016/j.asr.2022.05.064

Mehta, P. M., and R. Linares (2017), A methodology for reducedorder modeling and calibrationof the upper atmosphere,Space Weather,15, 1270–1287,doi:10.1002/2017SW001642.

NOAA. (1995). Cooperative Ocean/Atmosphere Research Data Service: Conventions for the standardization of NetCDF files. https://ferret.pmel.noaa.gov/Ferret/documentation/coards-netcdf-conventions.

Noël, B., van de Berg, W. J., Lhermitte, S., Wouters, B., Schaffer, N., and van den Broeke, M. R.: Six decades of glacial mass loss in the Canadian arctic archipelago, Journal of Geophysical Research: Earth Surface, 123, 1430–1449, https://doi.org/10.1029/2017JF004304, 2018.

Noël, B., Aðalgeirsdóttir, G., Pálsson, F., Wouters, B., Lhermitte, S., Haacker, J. M., and van den Broeke, M. R.: North Atlantic Cooling is Slowing Down Mass Loss of Icelandic Glaciers, Geophysical Research Letters, 49, e2021GL095697, https://doi.org/10.1029/2021GL095697, 2022.

Park, Jaeheung, Joseph S. Evans, Richard W. Eastes, Jerry D. Lumpe, Jose van den IJssel, Christoph R. Englert, Michael H. Stevens, 2022: Exospheric Temperature Measured by NASA-GOLD Under Low Solar Activity: Comparison With Other Data Sets. Journal of Geophysical Research: Space Physics. https://doi.org/10.1029/2021JA030041

Pivetta, T., Braitenberg, C., & Pastorutti, A. (2022). Sensitivity to Mass Changes of Lakes, Subsurface Hydrology and Glaciers of the Quantum Technology Gravity Gradients and Time Observations of Satellite MOCAST+. Remote Sensing, 14(17), 4278. https://doi.org/10.3390/rs14174278

Ponte, R. M., & Schindelegger, M. (2022). Global ocean response to the 5-day Rossby-Haurwitz atmospheric mode seen by GRACE. Journal of Geophysical Research: Oceans, 127, e2021JC018302. https://doi.org/10.1029/2021JC018302.

Qian, L., Wang, W., Burns, A. G., Chamberlin, P. C., Coster, A., Zhang, S.-R., & Solomon, S. C. (2019). Solar flare and geomagnetic storm effects on the thermosphere and ionosphere during 6–11 September 2017. Journal of Geophysical Research: Space Physics, 124, 2298–2311. https://doi.org/10.1029/2018JA026175

Riviere-Casanova, Guillaume, and Nathan S. Collins (2021) Investigating parameter effects on atmospheric density estimation using satellite mega-constellation. ASCEND 2021, November 15-17, 2021, Las Vegas, Nevada & Virtual, AIAA 2021-4192, Session: Space Situational Awareness. https://doi.org/10.2514/6.2021-4192

Roberts, M. J., Jackson, L. C., Roberts, C. D., Meccia, V., Docquier, D., Koenigk, T., et al. (2020). Sensitivity of the Atlantic Meridional Overturning Circulation to model resolution in CMIP6 HighResMIP simulations and implications for future changes. Journal of Advances in Modeling Earth Systems, 12, e2019MS002014. https://doi.org/10.1029/2019MS002014

Rodríguez-Fernández, N.J.; Muñoz Sabater, J.; Richaume, P.; de Rosnay, P.; Kerr, Y.H.; Albergel, C.; Drusch, M.; Mecklenburg, S. SMOS near-real-time soil moisture product: Processor overview and first validation results. Hydrol. Earth Syst. Sci., 21, 5201–5216, 2017.

de Rosnay, P., Browne, P., de Boisseson, E., Fairbairn, D., Hirahara, Y., Ochi, K., Schepers, D., Weston, P., Zuo, H., Alonso-Balmaseda, M., Balsamo, G., Bonavita, M., Borman, N., Brown, A., Chrust, M., Dahoui, M., Chiara, G., English, S., Geer, A., Healy, S., Hersbach, H., Laloyaux, P., Magnusson, L., Massart, S., McNally, A., Pappenberger, F. and Rabier, F. (2022)

Coupled data assimilation at ECMWF: current status, challenges and future developments. Quarterly Journal of the Royal Meteorological Society 148(747), 2672-2702.

Rounce, D. R., Hock, R., Maussion, F., Hugonnet, R., Kochtitzky, W., Huss, M., Berthier, E., Brinkerhoff, D., Compagno, L., Copland, L., Farinotti, D., Menounos, B., and McNabb, R. W.: Global glacier change in the 21st century: Every increase in temperature matters, Science, 379, 78–83, https://doi.org/10.1126/science.abo1324, 2023.

Ruz Vargas, C., Güntner, A., Haas, J., Contreras, S., User requirements of the Global Gravity-based Groundwater Product (G3P) – Survey results. Technical report of the G3P project, https://www.g3p.eu/fileadmin/user_upload/G3P_survey_report.pdf, 2022.

Schindelegger, M., Harker, A. A., Ponte, R. M., Dobslaw, H., & Salstein, D. A. (2021). Convergence of daily GRACE solutions and models of submonthly ocean bottom pressure variability. Journal of Geophysical Research: Oceans, 126(2), e2020JC017031. https://doi.org/10.1029/2020JC017031.

Schlaak, M., Pail, R., Jensen, L. and Eicker, A (2023). Closed loop simulations on recoverability of climate trends in next generation gravity missions, Geophys. J. Int. (2023) 232, 1083–1098. https://doi.org/10.1093/gji/ggac373

Siemes, Christian, Claudia Borries, Sean Bruinsma, Isabel Fernandez-Gomez, Natalia Hładczuk, Jose van den IJssel, Timothy Kodikara, Kristin Vielberg, and Pieter Visser (2023) New thermosphere neutral mass density and crosswind datasets from CHAMP, GRACE, and GRACE-FO. J. Space Weather Space Clim. 2023, 13, 16. https://doi.org/10.1051/swsc/2023014

Sneeuw, N. and M. van Gelderen M., 1997, The polar gap, Geodetic Boundary Value Problems in View of the One Centimeter Geoid, 1997, Volume 65, ISBN : 978-3-540-62636-7.

Steblov, G. M., Ekström, G., Kogan, M. G., Freymueller, J. T., Titkov, N. N., Vasilenko, N. F., Nettles, M., Gabsatarov, Y. V., Prytkov, A. S., Frolov, D. I., & Kondratyev, M. N. (2014). First geodetic observations of a deep earthquake: The 2013 Sea of Okhotsk M w 8.3, 611 km-deep, event: KOGAN ET AL.: GEODETIC OBSERVATIONS OF DEEP EARTHQUAKE. Geophysical Research Letters, 41(11), 3826–3832. https://doi.org/10.1002/2014GL060003

Storch J.-S. V., Eden .C, Fast I., Haak H., Hernández-Deckers D., Maier-Reimer E., Marotzke J. and Stammer D (2012) An estimate of the Lorenz energy cycle for the world ocean based on the STORM/NCEP simulation. J Phys Oceanogr 42(12), 2185–2205. https://doi.org/10.1175/JPO-D-12-079.1

Sutton, Eric K., Jeffrey P. Thayer, Marcin D. Pilinski, Shaylah M. Mutschler, Thomas E. Berger, Vu Nguyen, Dallas Masters: Toward Accurate Physics-Based Specifications of Neutral Density Using GNSS-Enabled Small Satellites. Space Weather. 2021. https://doi.org/10.1029/2021SW002736

Sutton, E. K., J. M. Forbes, R. S. Nerem (2005) Global thermospheric neutral density and wind response to the severe 2003 geomagnetic storms from CHAMP accelerometer data. Journal of Geophysical Research Space Physics, Volume 110, Issue A9, https://doi.org/10.1029/2004JA010985

Tanaka, Y., Heki, K., Matsuo, K., & Shestakov, N. V. (2015). Crustal subsidence observed by GRACE after the 2013 Okhotsk deep-focus earthquake: GRAVITY CHANGE OF DEEP-

FOCUS EARTHQUAKE. Geophysical Research Letters, 42(9), 3204–3209. https://doi.org/10.1002/2015GL063838

Thomson, R. E. and Fine, I. V. (2021). Revisiting the ocean's non-isostatic response to 5-day atmospheric loading: New results based on global bottom pressure records and numerical modeling. Journal of Physical Oceanography, 51, 2845–2859. https://doi.org/10.1175/JPO-D-21-0025.1.

Van Den Broeke, M., Bamber, J., Ettema, J., Rignot, E., Schrama, E., Van Berg, W. J. D., Van Meijgaard, E., Velicogna, I., and Wouters, B.: Partitioning recent Greenland mass loss, Science, 326, 984–986, https://doi.org/10.1126/science.1178176, 2009.

van den IJssel, Jose, Eelco Doornbos, Elisabetta Iorfida, Günther March, Christian Siemes, Oliver Montenbruck (2020) Thermosphere densities derived from Swarm GPS observations, Advances in Space Research, Volume 65, Issue 7, 1758-1771, https://doi.org/10.1016/j.asr.2020.01.004

van Helleputte T, Doornbos E, Visser P. 2009. CHAMP and GRACE accelerometer calibration by GPS-based orbit determination. Adv Space Res 43: 1890–1896. https://doi.org/10.1016/j.asr.2009.02.017

Visser P, van den IJssel J. 2016. Calibration and validation of individual GOCE accelerometers by precise orbit determination. J Geod 90: 1–13. https://doi.org/10.1007/s00190-015-0850-0

Voigt, S. et al., 2016. Global trends in satellite-based emergency mapping, Science, 353(6296), 247–252.

Wang, R., Heimann, S., Zhang, Y., Wang, H., & Dahm, T. (2017). Complete synthetic seismograms based on a spherical self-gravitating Earth model with an atmosphere–ocean–mantle–core structure. Geophysical Journal International, 210(3), 1739–1764. https://doi.org/10.1093/gji/ggx259

Weijer, W., Cheng, W., Garuba, O. A., Hu, A., & Nadiga, B. T. (2020). CMIP6 models predict significant 21st century decline of the Atlantic meridional overturning circulation. Geophysical Research Letters, 7, e2019GL086075. https://doi.org/10.1029/2019GL086075

Weimer, D. R., M. G. Mlynczak, J. T. Emmert, E. Doornbos, E. K. Sutton, and L. A. Hunt: Correlations Between the Thermosphere's Semiannual Density Variations and Infrared Emissions Measured With the SABER Instrument. J Geophys Res Space Phys. 2018 Oct; 123(10): 8850–8864. https://dx.doi.org/10.1029%2F2018JA025668

Wester, P., Mishra, A., Mukherji, A., and Shrestha, A.: The Hindu Kush Himalaya Assessment: Mountains, Climate Change, Sustainability and People, https://doi.org/10.1007/978-3-319-92288-1, 2019.

Wieczorek, M. A., & Meschede, M. (2018). SHTools: Tools for Working with Spherical Harmonics. Geochemistry, Geophysics, Geosystems, 19(8), 2574–2592. https://doi.org/10.1029/2018GC007529

Wieczorek, M.A. (2007): Simons, F.J. Minimum-Variance Multitaper Spectral Estimation on the Sphere. J Fourier Anal Appl, 13, 665–692, doi:10.1007/s00041-006-6904-1).

Wouters, B., Gardner, A. S., and Moholdt, G.: Global Glacier Mass Loss During the GRACE Satellite Mission (2002-2016), Frontiers in Earth Science, 7, 96, https://doi.org/10.3389/feart.2019.00096, 2019.

Xu, C., Su, X., Liu, T., & Sun, W. (2017). Geodetic observations of the co- and post-seismic deformation of the 2013 Okhotsk Sea deep-focus earthquake. Geophysical Journal International, 209(3), 1924–1933. https://doi.org/10.1093/gji/ggx12

Yang, Q., Dixon, T. H., Myers, P. G., Bonin, J., Chambers, D., van den Broeke, M. R., Ribergaard, M. H., and Mortensen, J.: Recent increases in Arctic freshwater flux affects Labrador Sea convection and Atlantic overturning circulation, Nature Communications, 7, 10525, https://doi.org/10.1038/ncomms10525, 2016.

Yuan, Liangliang, Shuanggen Jin, Andres Calabia: Distinct thermospheric mass density variations following the September 2017 geomagnetic storm from GRACE and Swarm. Journal of Atmospheric and Solar-Terrestrial Physics, Volume 184, March 2019, Pages 30-36. https://doi.org/10.1016/j.jastp.2019.01.007

Zhang, Keke, Xingxing Li, Chao Xiong, Xiangguang Meng, Xin Li, Yongqiang Yuan, Xiaohong Zhang: The Influence of Geomagnetic Storm of 7-8 September 2017 on the Swarm Precise Orbit Determination. JGR Space Physics. https://doi.org/10.1029/2018JA026316

PART 6:

NRT CONCEPT: DESCRIPTION, RESULTS, ANALYSIS AND APPLICATIONS

29. INTRODUCTION

The purpose of this document is to describe strategies related to the generation of fast-track products (NRT) and their application in the frame of the DMD processing, and for space weather applications. This refers to WP 1700 of the WBS.

30. NRT CONCEPT OF L2 PRODUCTS WITH DMD APPROACH (WP1710)

30.1. OVERVIEW

Fast-track processing strategies are applied to produce short-term gravity products with short latencies as input for operational service applications. Since short-term solutions are generally limited in spatial resolution, either Kalman filtering (Kurtenbach et al. 2012) or averaging (sliding window) approaches (Purkhauser et al. 2019) can be applied to increase their spatial resolution (max. SH degree). We prefer a purely data-driven approach such as the sliding window technique for fast-track processing.

In order to generate L2 data, all necessary Level-1B and Level-2a data must be provided as fast as possible. They should be available within 24 hours, and have a comparable quality as the final products. The main difference between fast-track and final products is that the fast-track data generation and distribution relies on an automated process.

For the setup of a fast-track processing chain, cronjobs would regularly check for data availability and automatically start the fast-track Level-2 processing chain for a particular day once all required input data are available. The processing scheme uses the algorithms of the baseline standard processing as well as the DMD approach (Abrykosov et al. 2022).

30.2. NRT WITH DMD

Within the DMD approach, low-resolution gravity fields are estimated over short time intervals (e.g. daily up to d/o 15). These fields' deviation to their mean is then transformed to the observation domain and reduced from the observation vector containing the full gravity signal. In a final step, the reduced observation vector is used to estimate a full-resolution, long-term (e.g. monthly) gravity product. Note that the DMD scheme is not limited to a single de-aliasing step, which in the example above corresponds to the estimation and reduction of daily fields, but can be expanded by multiple intermediate steps, e.g. the subsequent estimation of two- and three-daily interval fields, before obtaining the final long-term gravity product. The limitation to this multi-step scheme is dictated by the trade-off between the reduction of temporal aliasing errors and the addition of misparametrization errors introduced within each de-aliasing step. The methodology is also presented and discussed in detail in Abrykosov et al. (2022).

The benefit of a multi-step DMD parametrization for an NRT-type processing is evident – DMD yields stand-alone gravity products at each processing step which can be used to recover changes in temporal gravity over various short time periods at various spatial scales. To demonstrate this, an exemplary processing scheme is presented in the following. Here, we assume that observations as well as any additional required auxiliary data become available at daily intervals and is then processed on the basis of a DMD scheme with three de-aliasing steps where one-, two and three-day fields are consecutively estimated up to d/o 15, 30 and 45 (this scheme has been proven to work well both for a double-pair as well as an inclined-pair-only constellation) in addition to the full-resolution field up to e.g. d/o 100. It is further assumed that the data processing is carried on the basis of a six-day moving window. Effectively, this means that the NRT-type processing is triggered for the first time once six days of data become available and is then repeated daily by adding the data of the current day I while simultaneously excluding the data of day $I-7$. Figure 30-1 graphically summarizes the obtainable data products for this processing scheme over three subsequent processing periods – days 1-6, 2-7 and 3-8.

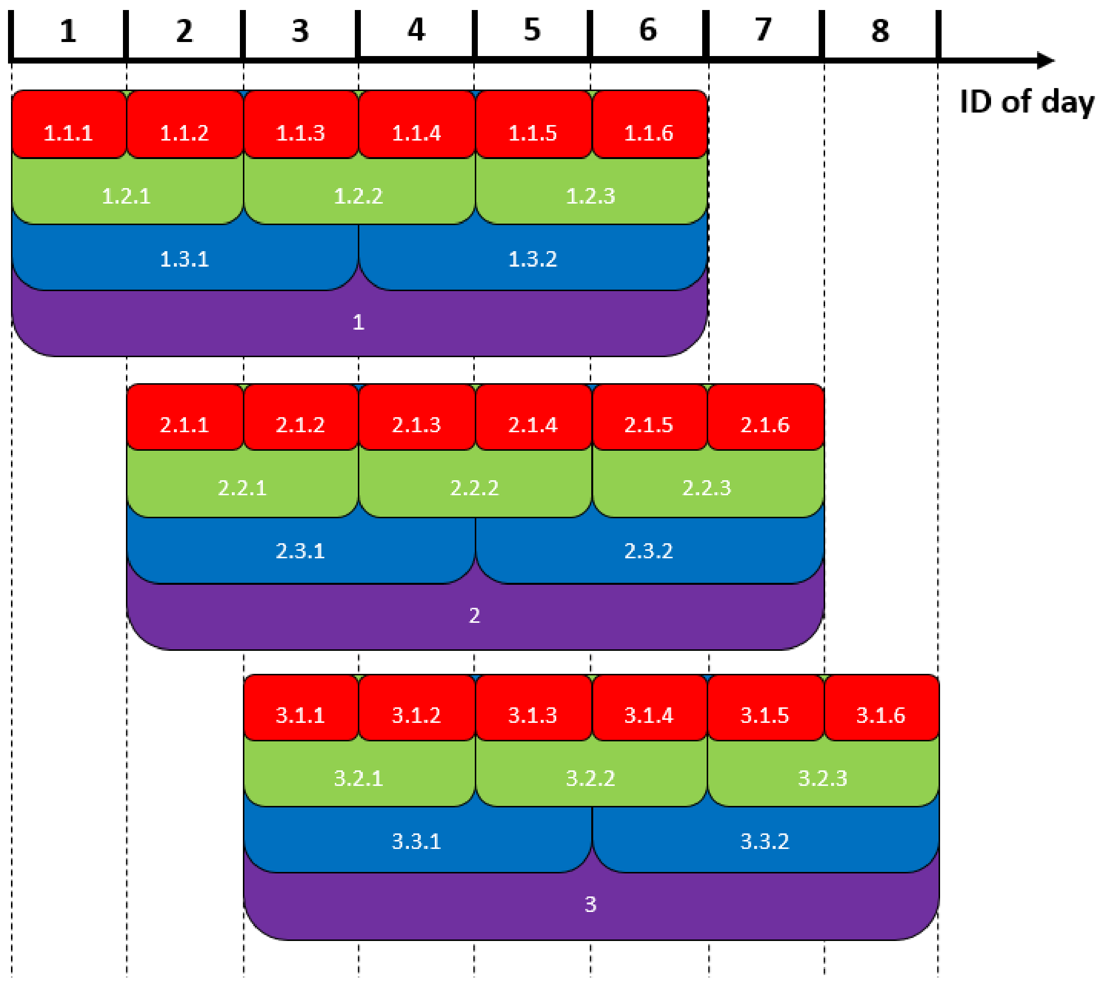

Figure 30-1: NRT-type processing with DMD on the basis of a sliding window approach. In this example, de-aliasing fields are estimated over periods of one (red), two (green) and three (blue) days, until the final six-day gravity product (purple) is computed. In the nomenclature X.Y.Z, Z denotes the ID of the interval solution estimated over the period of Y days within retrieval block X (which also corresponds to the ID of the full, i.e. purple, solution).

The full-resolution fields (solutions 1, 2 and 3) can be retrieved once over each six-day period. Thus, the six-day solutions have a latency time of seven days, as they are processed on the day after the last required day of data (day 6) becomes available. If one is interested in the variations between the consecutive six-day solutions which in the example above effectively describe the change in temporal gravity between days 1 and 7 or 2 and 8, respectively, the latency time increases by one additional day (eight days in total). This type of retrieval is analogous to that presented in Purkhauser et al. (2019).

While the six-day solutions obtained here benefit greatly from the de-aliasing capabilities of the multi-step DMD scheme, the resulting latency time is clearly suboptimal. What is more, even if the quantification of variations would be based on the interval products, i.e. 1-, 2- or 3-day solutions, the latency time would not change, as these would also become available at the earliest after the respective six-day data accumulation period. Thus, a possible solution is to continuously expand the processing blocks with new data without excluding the oldest days until the maximum processing period is achieved, while continuously reprocessing it by means of DMD with a sequentially increasing number of de-aliasing steps.

In case of the exemplary parametrization presented above, the scheme would be as follows. For the example, a two-day solution could be processed with DMD (daily de-aliasing fields) in block 1 on day three. In processing block 2, the first two-day solution would be ready on day 4, and one could quantify the variations between days 1 and 3 with a latency time of four days. Both block 1 and 2 and two could then be expanded with two additional days of data, which would then respectively yield a three-day solution. In case of block 1 it would become available on day 5 and in case of block 2 on day 6. Alternatively, the latency time could be reduced by one additional day if the estimation of the two-daily de-aliasing fields were to be cancelled. However, one should evaluate whether the trade-off between increase in temporal aliasing effect through the exclusion of an intermediate de-aliasing step is justifiable. The expansion can in principle be carried out to an arbitrary extent, but is effectively only useful as long as the requirements for the latency time are met. The evident trade-off in this type of retrieval is that the spatial resolution scales with the latency period.

This processing strategy is also schematically presented in Figure 30-2. Note that this type of processing is not possible with the methodology presented in Purkhauser et al. (2019), since, firstly, the underlying Wiese approach requires the availability of the entirety of data necessary for the set-up of the full – in the example above, six-daily – gravity solution, and, secondly, the Wiese parametrization only allows for a single de-aliasing step.

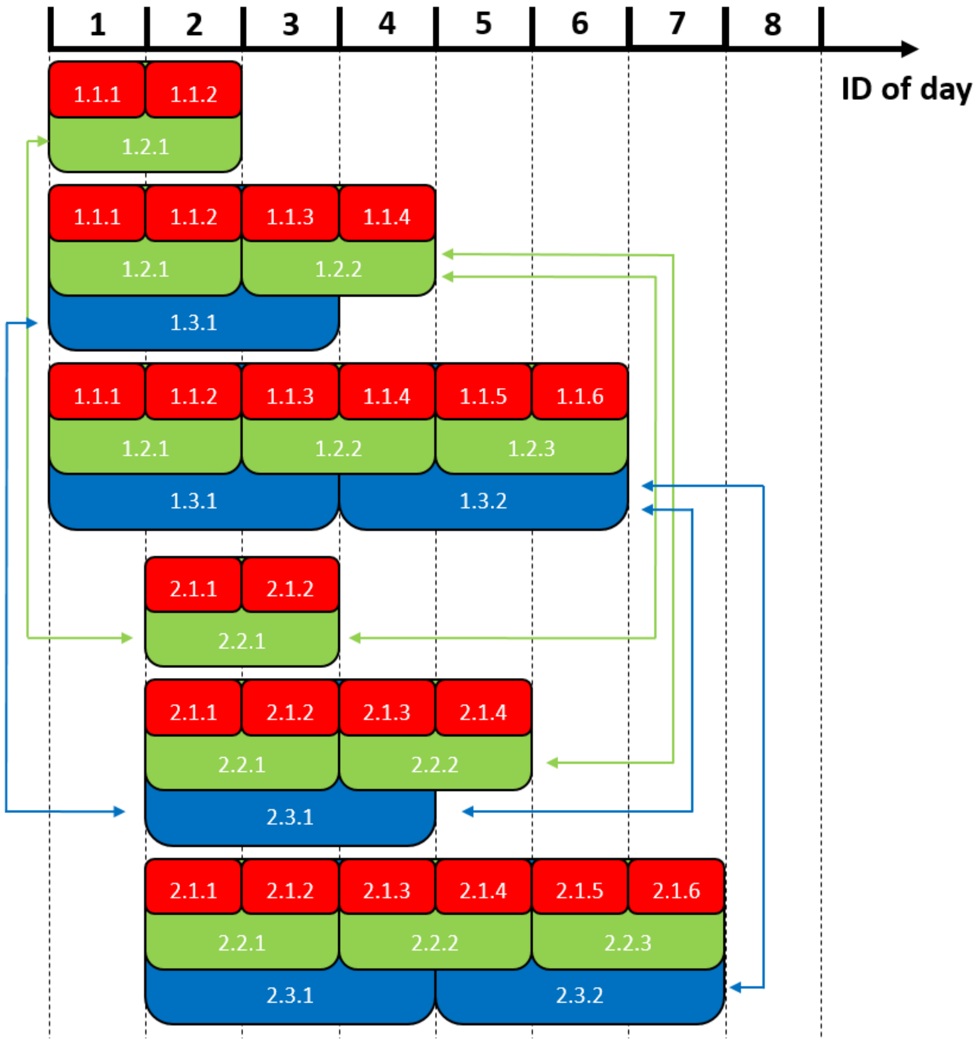

Figure 30-2: Stepwise set-up of gravity fields within individual retrieval blocks on the basis of DMD. The underlying data sets are continuously expanded with data of the current day once it becomes available. The arrows indicate which gravity products can be inter-compared in order to obtain a quantification of the variations in temporal gravity.

30.3. SUMMARY

We present a functional NRT-type retrieval scheme on the basis of a sliding window approach as presented in Purkhauser et al. (2019). Here, however, we apply the DMD parametrization scheme instead of the Wiese approach, which facilitates the retrieval of gravity products over shorter time scales. In turn, this allows for a reduction of the latency time at which variations in temporal gravity can be computed, as comparisons can already be carried out on the basis of interval (de-aliasing) products. The clear drawback, of course, is that a shorter latency also results in a reduced spatial resolution. On the other hand, there is freedom to compute interval fields over – in principle – arbitrary time intervals, which allows one to better tailor the retrieval scheme to the user groups' requirements regarding latency times.

31. NRT CONCEPT OF L2 PRODUCTS WITH RESPECT TO SPACE WEATHER (WP1720)

31.1. ROADMAP OF NRT PROCESSING CHAIN FOR NGGM/MAGIC

There are two important aspects of data provision for space weather applications: Timeliness and robustness. The first aspect is simple to explain. Since the thermosphere is a highly driven and volatile system, conditions can change within minutes—hours during active solar and geomagnetic activity and within hours—days during moderate to low solar and geomagnetic activity. Therefore, data that is several days old has little to no value for now- and forecasting of the state of the thermosphere. Achieving an as low as possible latency for data provision is paramount. However, this implies that the processing has to be as fast as possible and, therefore, must run in a fully automated way without human interaction. This is complicated because accelerometer data is prone to perturbations from the satellite or the instrument itself.

Further, the accelerometer data will be subject to a bias, which needs to be estimated and removed in the processing. The estimation is typically performed via precise orbit determination based on the GNSS receiver and satellite attitude data, augmented with Earth orientation data from the IERS and GNSS satellite positions and clock corrections from the IGS. From this brief overview, it is already clear that the processing needs to be robust against artifacts in the data, handle several data providers, and deal with failed or late data provision and potentially unclear data quality. Notably, the latter two are almost irrelevant when the processing occurs with a latency of one month or longer because the data providers will have fixed most issues by then. In summary, we expect that establishing a robust NRT processing chain for space weather applications will require substantial effort for development and testing.

In the following, we outline the processing from raw telemetry to Level 2 neutral density data products and identify potential Level 3 data products for application in space weather. We will provide a few references and point to Siemes et al. (2023) and the references therein. Also, the references provided in WP1630 apply.

Raw telemetry

In the context of NRT processing of accelerometer data for space weather applications, it is essential to realize that the data will be collected and stored onboard the satellite until a downlink event occurs during contact between the satellite and the ground station. For many geodetic missions, we have one primary and one backup ground station contact per day. When both contacts are fully utilized for downlinks and spread out as evenly as possible over time, we have a latency between data collection and reception of raw telemetry of 0—12 hours. More ground station contacts will reduce the latency. Considering that NGGM/MAGIC is a constellation of two pairs of satellites, interleaving the ground station contacts of the satellite pairs can potentially halve the latency to 0—6 hours. The downlink of the raw telemetry might need a few minutes, depending on the data volume and hardware used for the downlink. The data transfer from the ground station to the ground processing center might take another few minutes. Thus, the critical part is the number of downlinks and how they are distributed over time, where practicalities such as office hours must be considered.

Level 1b data products

The conversion of the accelerometer data in the raw telemetry to Level 1b data is straightforward. Here, we outline a possible subdivision of processing steps across processing levels. The first step in the conversion will be extracting the accelerometer data packets into a sorted stream of accelerometer data records stored in Level 0 data products. The next step will be converting engineering units to physical units, leading to Level 1a data files. Then, corrections will be applied to reverse the transfer function of the instrument's read-out chain, apply a time correction to shift the accelerometer data to the exact measurement epochs, and transform from the instrument to the satellite reference frame. The resulting data will be stored in the Level 1b data products. These simple, lightweight processing steps will only take a fraction of a second. Likely, the writing to the data storage device will be the slowest link in the chain.

Level 2 data products

An overview of the processing was provided in WP1630. Input to the processing is the following (Siemes et al., 2023):

- Level 1b accelerometer data,
- GNSS tracking data,
- Satellite attitude data,
- Satellite mass, including remaining fuel mass,
- Satellite geometric information such as locations of center-of-mass and GNSS antenna,
- Auxiliary data such as:
    - Earth orientation data from the IERS (https://www.iers.org),
    - GNSS position and clock data from the IGS (https://igs.org),
    - Space weather indices, such as the F10.7 radio flux index and the ap index of geomagnetic activity, for evaluating thermosphere models to obtain atmospheric temperature, composition, and wind
    - Radiation flux data to evaluate the albedo and Earth infrared radiation pressure acceleration.

The output of the NRT processing will be neutral density, augmented with uncertainty quantification.

Assuming that the satellite is equipped with more than one accelerometer, averaging the right combination of accelerometers or using the center accelerometer will eliminate accelerations due to satellite dynamics, the Euler and centrifugal accelerations, and gravity gradients between the satellite center of mass and the center of the proof mass. This will yield the acceleration that applies to the satellite center of mass. The data must be thoroughly screened for outliers and artifacts, a lesson learned from past missions.

The next step is the calibration, which includes estimating scale factors, quadratic factors, axes couplings, and so on, from dedicated maneuvers and science mode data and estimating the accelerometer bias via precise orbit determination based on GNSS tracking data (see, e.g., the WP1800 Technical Note). The output of this step is the calibrated non-gravitational acceleration that applies to the satellite center of mass.

Then, we need to extract the aerodynamic acceleration from the non-gravitational acceleration. This is achieved by removing the accelerations due to thrusts and radiation pressure. Since both accelerometer and GNSS tracking are sensitive to the sum of non-gravitational accelerations, the accelerations due to thrusts and radiation pressure must be known accurately. Neutral density is derived from the acceleration in the along-track direction. It is convenient because estimating the accelerometer bias via GNSS tracking is most accurate in this direction and simplifies the required radiation pressure modeling.

In the case of radiation pressure acceleration, the main contributor in the along-track direction is the solar radiation pressure. The solar radiation flux is accurately known and shows a less than 0.1% variability. The radiation pressure acceleration can be accurately modeled when the satellite geometry, the reflection and absorption coefficients for visible light and infrared radiation, and the heat capacitance of the outer panels are known well. Accurate data from thermistors located outside the exterior panels will be an asset for modeling the satellite's thermal emissions, representing the second-largest contributor to the radiation pressure acceleration after solar radiation pressure. The effects of albedo and Earth's infrared radiation are minimal in the along-track direction, assuming a GRACE-like satellite shape and attitude. Also, we expect the altitude of NGGM/MAGIC to be well below 500 km, where the radiation pressure acceleration is small compared to the aerodynamic acceleration in the along-track direction, making minor radiation pressure modeling errors less critical.

Thrusts can be impulsive and continuous, or even a combination of both. As for radiation pressure, we need to accurately know the acceleration due to thrusts. In the case of short impulse thrusts of only a few seconds, the simplest solution is to cut out and interpolate the affected accelerometer data because neutral density changes at the scale of tens of seconds to minutes along the orbit. In the case of continuous thrust, the thrust force and direction need to be known with sufficient accuracy and temporal resolution, i.e., the thruster data is part of the science data. It is also important to realize that in the case of continuous thrust, the thrust force will have the same magnitude as the aerodynamic drag. Thus, an error in the thrust force (scaling or bias) will translate one-to-one into an error in the aerodynamic acceleration and, therefore, neutral density. We advise to aim for an accuracy of 1% for the thrust force. A better accuracy is welcome if it is possible to achieve with a reasonable effort.

Once the radiation pressure acceleration and the thrust acceleration have been removed to obtain the aerodynamic acceleration, the latter needs to be converted into neutral density observations. This requires aerodynamic modeling based on the satellite geometry and gas-surface interaction models. Again, we expect the NGGM/MAGIC satellite to fly at an altitude well below 500 km, which puts it into an altitude range where the gas-surface interaction is represented accurately by the diffuse reflection with incomplete energy accommodation (DRIA) model. This model prescribes that a gas atom or molecule is diffusely reflected off the satellite surface, i.e., following Lambert's cosine law for the directional distribution. The velocity of the reflected gas atom or molecule will adjust to a certain degree to the satellite surface temperature, described by the energy accommodation coefficient. For non-experts, we note that the velocity of a gas atom or molecule is proportional to the square root of its temperature. The aerodynamic modeling provides the aerodynamic force coefficient vector as a function of the direction of the atmospheric flow relative to the satellite and atmospheric temperature and composition, often pre-calculated and stored as a lookup table.

Once the dynamic force coefficient vector is available, the last missing piece of data is the wind velocity in the along-track direction, which has to be added to the satellite velocity. The along-track wind has to be calculated from a thermosphere wind model, noting that an increase in headwind is indistinguishable from an increase in neutral density. Typically, the thermosphere wind magnitude is small (<100 m/s) compared to the satellite velocity (~7.6 km/s), so the accuracy of the thermosphere wind model is not critical. Only during intense geomagnetic storms the wind velocity may reach 1 km/s, increasing the uncertainty of the neutral density observations during such events. Finally, we can use the direct algorithm described in Doornbos (2011) to invert the aerodynamic acceleration to a neutral density observation, which is a straightforward processing step.

Even though auxiliary data need to be fetched from several providers, two thermosphere models have to be evaluated (one for atmospheric composition and temperature, e.g., NRLMSIS 2.0, and another for wind, e.g., HWM14), we expect that the processing of neutral density observations will take a few minutes at most for a 6—12 hours-batch of data (typical CPU time is 10 min for a daily GRACE-FO run as done in the framework of the TOLEOS project, using a standard Desktop with a Linux OS).

Because of the wide variety of input data and processing steps, the neutral density observations are subject to many error sources. As part of a contract with the Community Coordinated Modeling Center (CCMC, https://ccmc.gsfc.nasa.gov), Delft University of Technology developed a software tool to propagate the uncertainty of the input data consistently to obtain a quantification of uncertainty in the neutral density observations. The development of the software tool is completed. However, a manual and a scientific publication must be written before the software can be made public (expected within the next few months). This means the method and the software for the uncertainty quantification of neutral density observations are completed. In the context of NGGM/MAGIC, we would still need to assess the uncertainty of the input data listed above to arrive at a realistic uncertainty quantification of neutral density observations. The latter is highly beneficial for all users of the neutral density data, particularly within data assimilation into thermosphere models for space weather applications. The processing of the uncertainty quantification is slightly heavier than for the neutral density observations. Nevertheless, we expect the uncertainty quantification to be processed within a few minutes. Therefore, the total time for processing the Level 0 data to Level 2 neutral density observations, including the uncertainty quantification, and also including the bias calibration via precise orbit determination, should be less than 20 minutes. Of course, this processing time estimate should be confirmed while developing a dedicated NRT processing chain.

Level 3 data products

The assimilation of neutral density observations into a reduced-order model (ROM), empirical or physics-driven model is the single highest impact space weather application of neutral density observations. As discussed in WP1630, while proof of concept studies demonstrated the feasibility of the neutral density observation assimilation, the methods are still in their infancy. Further, most studies focused on the ability to forecast density while using ‘final’ space weather indices, i.e., neglecting the need to forecast indices such as the F10.7 radio flux index for solar activity and the ap index for geomagnetic activity. In the case of high geomagnetic activity, other approaches, such as using simple correlation relationships between the interplanetary magnetic field and changes in neutral density, might provide more accurate short-term forecasts (Kraus et al, 2020).

The Level 3 data product targeting space weather could be any thermosphere model assimilating density data. The data product must be simple to evaluate to account for limited computing resources wherever such a model is employed, including onboard a satellite. Timely provision, robustness, and reliability are paramount to ensure that such a data product is accepted and implemented by users, particularly the space agencies responsible for space situational awareness. Such a Level 3 data product would assimilate Level 2 neutral density observations, augmented with uncertainty quantification, whenever new data becomes available. Depending on the ground station contacts, this could be every 3, 6, 12, or 24 hours. The uncertainty of the neutral density observations, the model itself, and the forecasted space weather indices need to be propagated at the model level, such that the Level 3 data product is also augmented with reliable uncertainty quantification.

Roadmap

We have developed a fully automated screening of GRACE-FO accelerometer data. Assuming that NGGM/MAGIC is of superior quality, this part of the processing is considered solved. However, we advise revisiting this point once the satellite enters operations and the data quality is known. Given the actual data quality, tailoring the processing chain is a likely action.

One should review the timely availability of all required information and input data listed above. If some input data is classified as ‘preliminary,’ ‘fast-track,’ or ‘rapid’ data, we need to analyze the accuracy compared to the final data. This includes checking for potential data gaps, as some data products might be delayed, and assessing the accuracy of the rapid data or data that needs to be extrapolated ahead of time.

Another concern is the latency at which the accelerometer bias can be estimated. This might be impacted by the accuracy of ‘rapid,’ ‘ultra-rapid,’ or ‘predicted’ data from the IERS and IGS. An interesting question is whether we should rely on the estimated bias based on ‘ultra-rapid’ data or if it might be better to extrapolate the accelerometer bias, assuming that the instrument and the temperature environment are highly stable. Similarly, we should study the impact of other auxiliary data, such as the F10.7 solar radio index, the ap index for geomagnetic activity, and CERES radiation flux data, used within the Level 2 neutral density processing chain.

We need to study the uncertainty in all input data for a reliable uncertainty quantification of the neutral density observations. This will also need to be adapted to the case of NGGM/MAGIC-specific input parameters, such as the satellite geometry and our knowledge of the surface properties. This goes as far as quantifying the uncertainty of the gas-surface interaction at the altitude targeted by NGGM/MAGIC.

Further, we should review methods for assimilating neutral density observations into thermosphere models, which primarily emerged in the last few years. We need to compare their skill for now- and forecasts of neutral density and study the impact of having more frequent observation updates (every 3, 6, 12, 24 hours) and multi-point observations because of having two satellite pairs covering distinct local times and, potentially, different altitudes. In the case of forecasting neutral density, we need to study the influence of predicting the required space weather indices, particularly the F10.7 solar radio flux index and the ap index indicating geomagnetic activity, which are the most frequently used model drivers. The study should separately assess quiet and active conditions.

For an honest assessment, one should also study the impact of improved now- and forecasts of neutral density on orbit prediction for various space objects. The latter should include active satellites with known and unknown attitude control laws, debris objects of known size and shape but unknown varying attitude, and debris objects of unknown size, shape, and attitude. The objects should also be spread across various altitudes and have well-known and poorly-known initial states (position and velocity). This will allow us to identify under which circumstances the neutral density observation assimilation effectively improves orbit predictions, including the propagation of orbit uncertainty, which is crucial for conjunction analysis and collision risk assessment. Involvement from the space agencies responsible for space situational awareness is desirable to establish an early link to the most critical users.

32. NRT SIMULATIONS WITH PRR BASELINE SCENARIO (WP1730)

The user requirements regarding fast-track (NRT) products were consolidated only at the PM2, and the data for of the PRR scenario were provided even afterwards. Due to these delays, no activities could be done in this project phase, but the task will be transferred to the next project phases.

33. APPLICABLE DOCUMENTS, REFERENCE DOCUMENTS, AND PUBLICATIONS TO PART 6

33.1. APPLICABLE DOCUMENTS

[AD-1] Mission Requirements Document, Next Generation Gravity Mission as a Mass-change And Geosciences International Constellation (MAGIC) - A joint ESA/NASA double-pair mission based on NASA's MCDO and ESA's NGGM studies (2020). ESA-EOPSM-FMCC-MRD-3785

[AD-2] Scientific Readiness Levels (SRL) Handbook, Issue 1, Revision 0, 05-08-2015

[AD-3] Statement of Work - ESA Express Procurement - EXPRO NGGM/MAGIC science support study during Phase A, Issue 1, Revision 0, 18/01/2021 Ref ESA-EOPSM-FUTM-SOW-3813

33.2. REFERENCE DOCUMENTS

Abrykosov P, Murböck M, Hauk M, Pail R, Flechtner F (2022) Data-driven multi-step self-de-aliasing approach for GRACE and GRACE-FO data processing. Geophys. J. Int. 232, 1006-1030, https://doi.org/10.1093/gji/ggac340

Doornbos E. 2011. Thermospheric density and wind determination from satellite dynamics. Ph.D. Thesis, Department of Astrodynamics and Satellite Missions, Delft University of Technology. Available at http://resolver.tudelft.nl/uuid:33002be1-1498-4bec-a440-4c90ec149aea

Krauss S., Behzadpour S., Temmer M., Lhotka C. (2020). Exploring Thermospheric Variations Triggered by Severe Geomagnetic Storm on 26 August 2018 Using GRACE Follow-On Data. Journal of Geophysical Research Space Physics, Volume 125, Issue 5, Number e2019JA027731. https://doi.org/10.1029/2019JA027731

Kurtenbach E., Eicker A., Mayer-Gürr T., Holschneider M., Hayn M., Fuhrmann M., Kusche J. (2012). Improved daily GRACE gravity field solutions using a Kalman smoother, J. Geodyn. 59–60, 39-48, https://doi.org/10.1016/j.jog.2012.02.006.

Purkhauser A.F., Pail R. (2019). Next generation gravity missions: near-real time gravity field retrieval strategy. Geophys. J. Int. 217(2), 1314–1333, https://doi.org/10.1093/gji/ggz084.

Siemes C., Borries C., Bruinsma S., Fernandez-Gomez I., Hładczuk N., van den Ijssel J., Kodikara T., Vielberg K., Visser P. (2023). New thermosphere neutral mass density and crosswind datasets from CHAMP, GRACE, and GRACE-FO. J. Space Weather Space Clim. 2023, 13, 16. https://doi.org/10.1051/swsc/2023014

PART 7:

IN-FLIGHT CALIBRATION OF ACCELEROMETERS

34. INTRODUCTION

This document is part of deliverable TN D7 in accordance with the CHANGE REQUEST No.1 [RD-1] and reports about the WP 1800 (1810, 1820 & 1830) activities.

35. PARTICIPATION IN CO-ENGINEERING SESSIONS WITH INDUSTRY (WP1810)

This chapter provides an overview of the tests that have been conducted to interpret and verify the contents of data sets of simulated observations provided by the industrial System Simulators of TASI (Section 35.1) and ADS (Section 35.2). The data sets include time series of simulated observations by the Laser Ranging Instrument (LRI), accelerometer and reconstructed attitude quaternions plus their errors. Moreover, typically time series of orbit positions are provided (e.g., [RD-5]).

35.1. TASI

The following 4 test data sets have been defined and provided:

- MIN 1D/3D: minimum solar activity 1/3-dimensional drag-free control;
- MAX 1D/3D: maximum solar activity 1/3-dimensional drag-free control.

The drag-free control is either only along the accelerometer X axis (predominantly along the flight axis, 1D) or along all three accelerometer axes (3D). The convention for the axes, along with the format of the provided data files, is described in [RD-5]. The data sets cover a period of 7 days (or 1 week).

The System Simulator data sets include time series for the LRI instrument in terms of LRI range noise. The accelerometer calibration referred to in this Technical Note nominally relies on GNSS-based Precise Orbit Determination and does not include LRI – or low-low Satellite-to-Satellite Tracking (ll-SST) – observations. However, it has been tested if inclusion of such observations might enhance the quality of estimated calibration parameters. In that case, range-rates are derived by simple differencing of consecutive range observations. Time series of range noise and derived range-rate noise are displayed in Figure 35-1 for 1 day together with their Power Spectral Densities (PSDs) derived from the full week of data: note the steep decrease of the power for frequencies at the far right of the spectrum. The Root-Mean-Square (RMS) for the 1-week time series is respectively equal to 2,7 μm and 12 nm/s for the range and range-rate noise. The PSDs display the expected behavior, i.e., higher noise level for the (very) low frequencies.

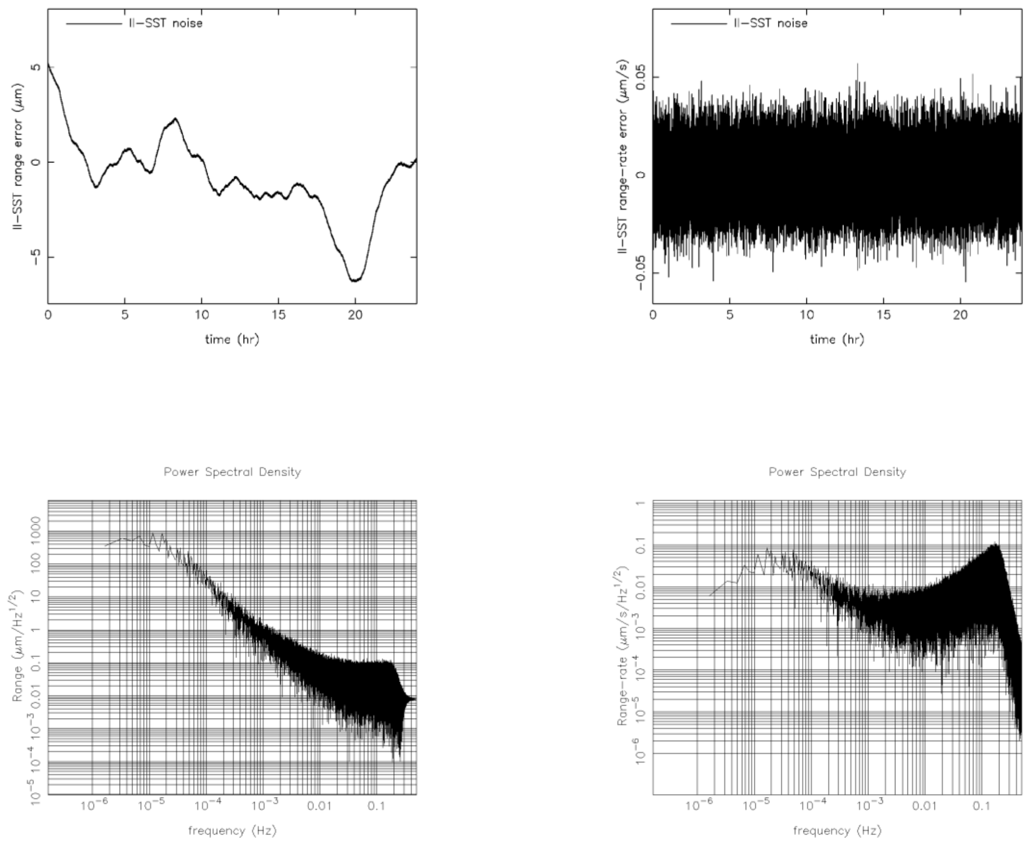

Figure 35-1 ll-SST observation noise (left: range, right: derived range-rate) - TASI System Simulator.

Figure 35-2 displays noise for 1 day of accelerometer 1 onboard satellite 1 (noise patterns are similar for all accelerometers onboard all 2 satellites) together with their PSDs derived from the full-week data set. Time series and PSDs are in accordance with expectation (e.g., PSD level below 10^{-11} m/s^2 in the measurement bandwidth).

Time series of non-gravitational accelerations are displayed in Figure 35-3 (1 day), Figure 35-4 (1 week), and Figure 35-5 (1 day) for selected solar-minimum and solar-maximum cases, and for 1D and 3D drag-free control (DFC). For the 1D DFC, it can be observed that the remaining acceleration signal along the X-axis is typically a few nm/s^2 maximum. The remaining signal for the Y-axis amounts up to 200 nm/s^2 and 20-100 nm/s^2 for the Z axis with a 1 cycle-per-orbital-revolution (cpr) component, where for the Z axis a systematic difference between satellites 1 and 2 can be observed. The latter can be explained by the leader/follower concept, where the follower satellite is aligned such as to guarantee acquisition of the LRI instrument. For the 3D DFC, an extremely low non-gravitational acceleration signal remains for the Y and Z axes (Figure 35-5), even much below 0.1 nm/s^2. This can only be achieved with a DFC system which is throttleable to a very low force level (assuming for example a 500 kg satellite, 0.1 nm/s^2 leads to a force level of 50 nanonewton, or 0.05 μN).

Based on these time series, it can be anticipated that for the 1D DFC, accelerometer scale factors can be estimated for the Y and Z axes with a certain confidence level, but not for the X axis (see Chapter 36, Section 36.2.2, and Chapter 37, Section 37.2). For 3D DFC, no reliable estimation of accelerometer scale factors seems feasible. Figure 35-4 has been included to show that for the 1D case, the non-gravitational accelerations along the Y-axis is systematically decreasing in the course of the week, which will result in a less reliable estimation of accelerometer scale factors in this direction (see again Chapters 36 and 37).

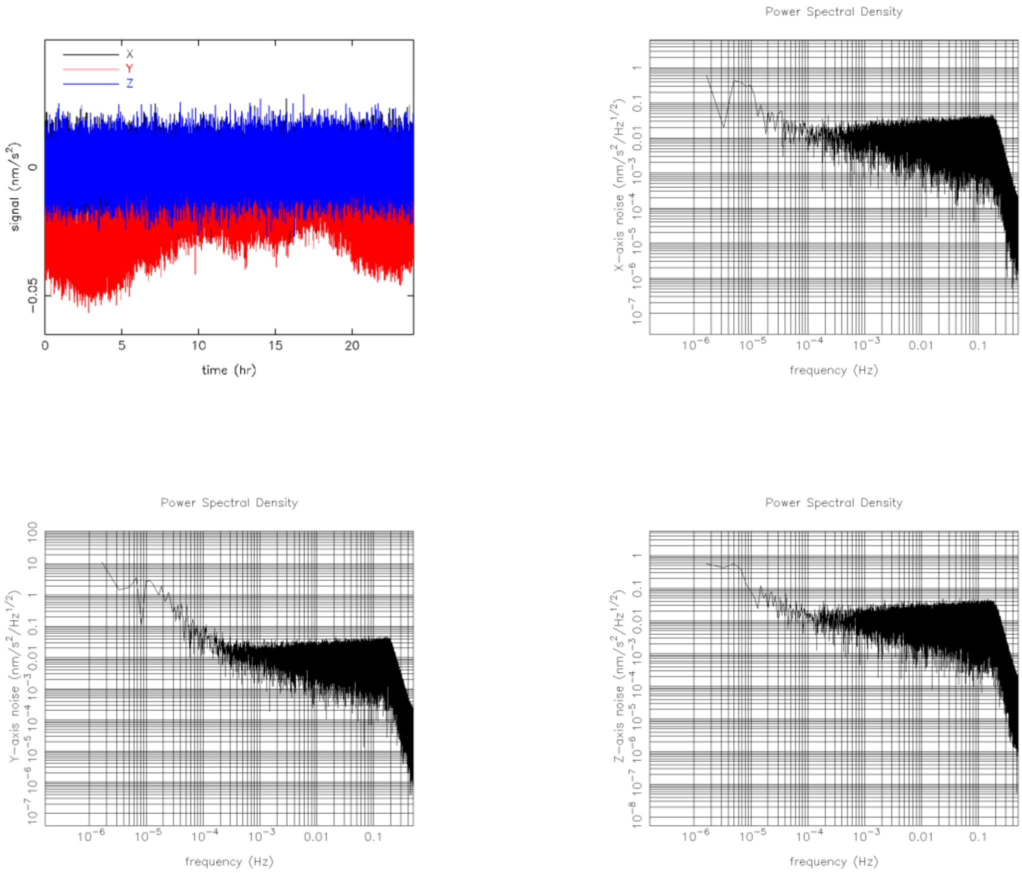

Figure 35-2 Accelerometer noise for MAX_1D case - TASI System Simulator.

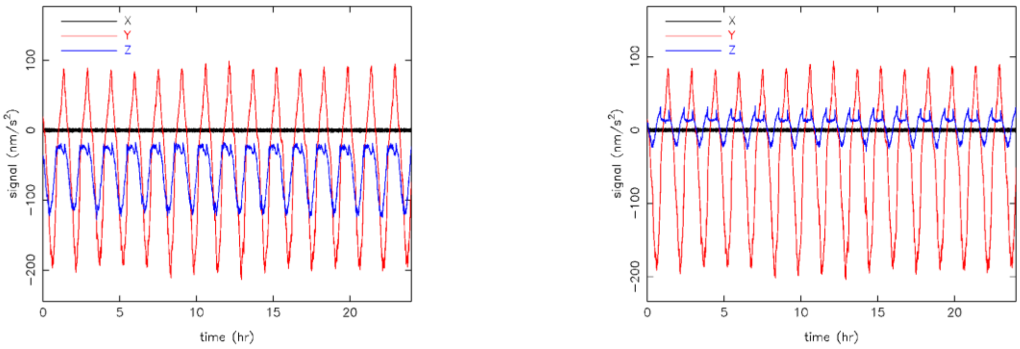

Figure 35-3 Non-gravitational signal for satellites 1 (left) and 2 (right) for MAX_1D case - TASI System Simulator (1st day).

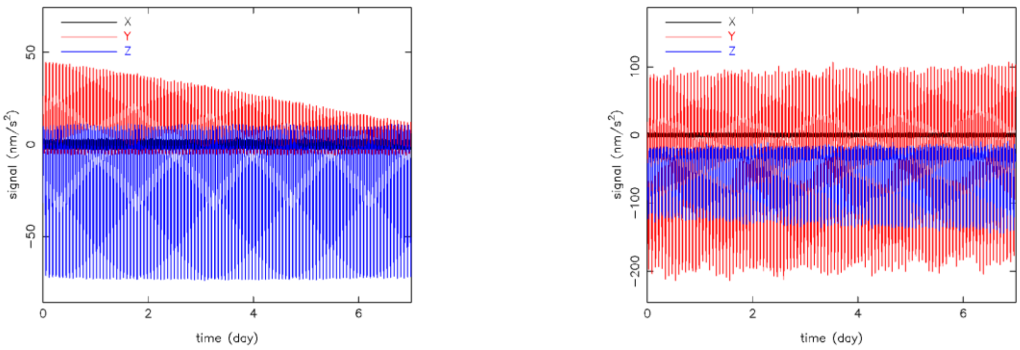

Figure 35-4 Non-gravitational signal for satellite 1 for MIN_1D (left) and MAX_1D (right) cases - TASI System Simulator (full week).

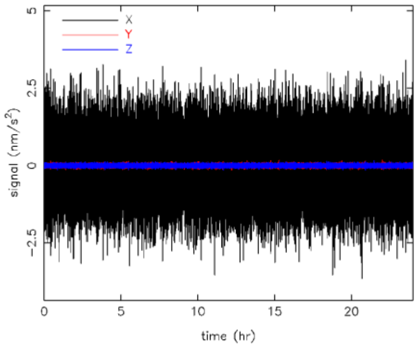

Figure 35-5 Non-gravitational signal for satellite 1 for MAX_3D case - TASI System Simulator.

Finally, Figure 35-6 displays a representative 1-day time series of attitude reconstruction errors in terms of rotation around the X- (roll), Y- (pitch), and Z-axis (yaw). For the roll and yaw axis, the attitude reconstruction errors are significantly below the 1 arcsec level, whereas these errors are up to 15 arcsec for the pitch axis including lower frequency errors. This is consistent with expectation, given the attitude reconstruction is based on a fusion of star tracker observations and differential accelerometer observations based on one gradiometer arm along the Y axis.

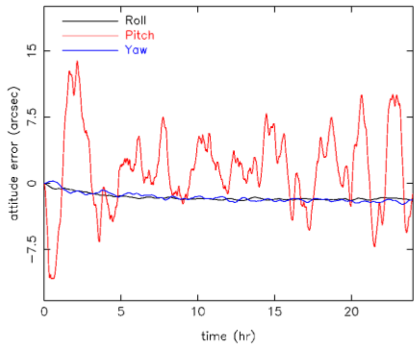

Figure 35-6 Attitude reconstruction error for satellite 1 for MAX_3D case - TASI System Simulator.

35.2. ADS

The first provided test data set covers a period of 100,000 (about 28 hours) seconds starting on 1 August 2027. The formats and contents of provided files are like those of the TASI data sets.

Time series of range noise and derived range-rate noise are displayed in Figure 35-7 for the full time series together with their PSDs. The Root-Mean-Square (RMS) for the 1-week time series is respectively equal to 0.55 **μ**m and 21 nm/s for the range and range-rate noise. The range noise is lower compared to the TASI data sets (higher noise at very low frequencies), whereas the range-rate noise is higher.

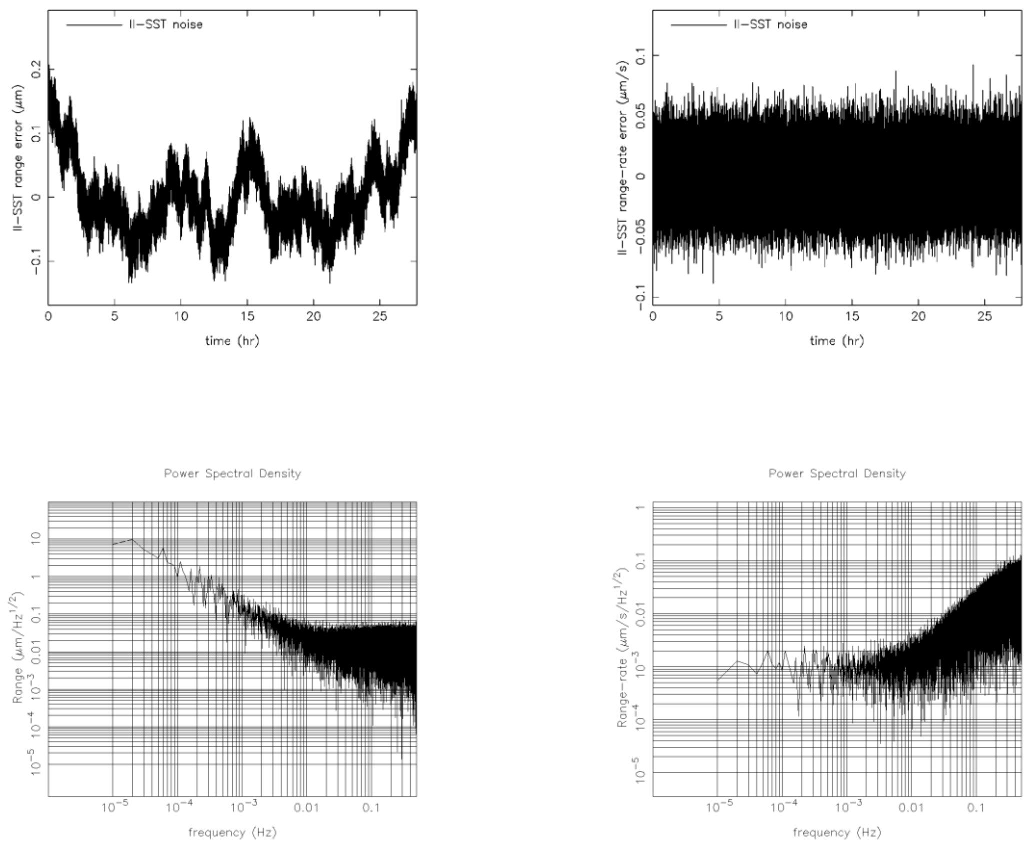

Figure 35-7 ll-SST observation noise (left: range, right: derived range-rate) - ADS System Simulator.

Figure 35-8 displays time series of accelerometer noise for the ADS test data set. For this test data set, the. Noise time series are identical for all accelerometers. The accelerometer noise is at the same level as for the TASI data set (Figure 35-2).

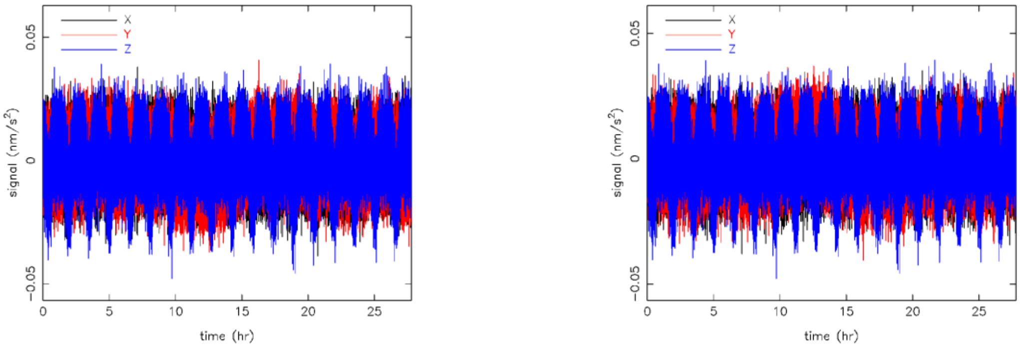

Figure 35-8 Typical noise accelerometers ADS System Simulator for satellite 1: accelerometers 1 (left) and 3 (right).

Time series of non-gravitational accelerations are displayed in Figure 35-9 and Figure 35-10. It can be observed that DFC is applied for the X and Y axes resulting in remaining accelerations with low variance: for the Z axis a signal remains up to 50-75 nm/s^2, again with a clear 1 cpr component. Opposite to the accelerometer time series of the TASI data set, the ADS time series include the effect of gravity gradient and rotational terms (please note that for this data set, accelerometer 3 is in the center-of-mass and accelerometers 1 and 2 are off-centered by 25 cm along the Y axis). For this scenario, it is anticipated that only for the Z axis, reliable accelerometer scale factors can be estimated.

Finally, Figure 35-11 displays a representative 1-day time series of attitude reconstruction errors in terms of rotation around the X- (roll), Y- (pitch), and Z-axis (yaw). For all rotation axes, variations of around 10 arcsec can be observed, opposite to the time series of the TASI data set (Figure 35-6, only for the pitch axis). In addition, opposite to the TASI data set, significant biases can be observed, especially large for the pitch axis: about 75 arcsec. These biases probably represent simulated uncertainties of the star tracker instrument mounting/orientation onboard the satellite.

Disclaimer: please note that it was reported that the ADS test data set referred to in this Technical Note did not represent a realistic scenario. It thus served to test interfaces between the ADS and End-to-End simulators of TU Delft and CNES. Therefore, Sections 36.2.2 and 37.2.2 below have not been populated.

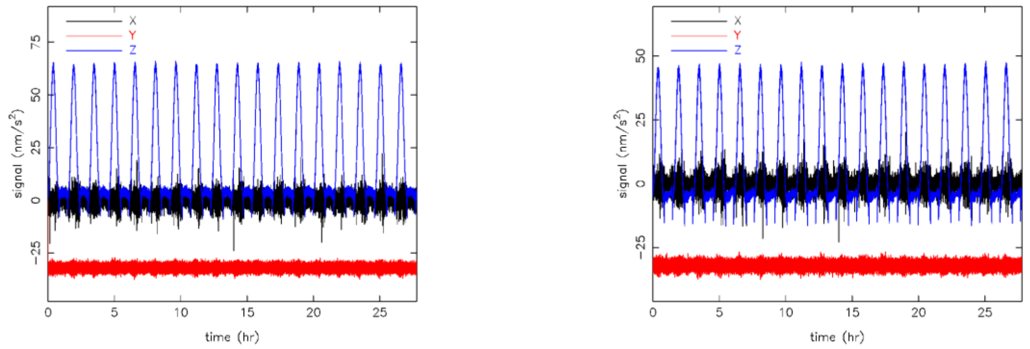

Figure 35-9 ADS non-gravitational accelerations for accelerometer 2 for satellites 1 (left) and 2 (right).

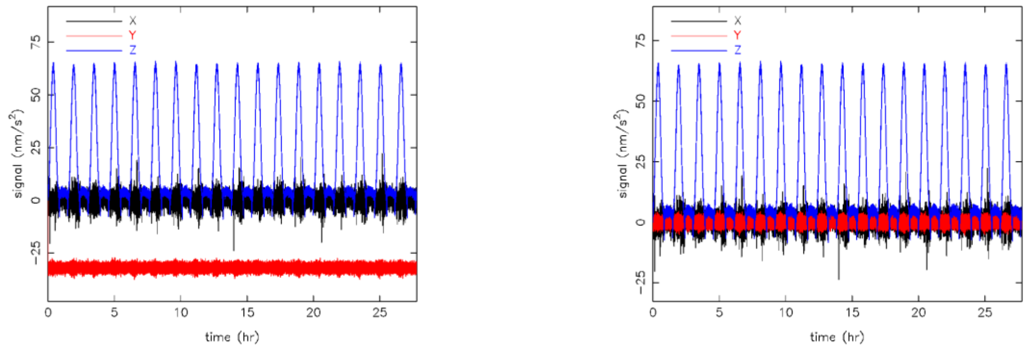

Figure 35-10 ADS non-gravitational accelerations for accelerometers 2 (left) and 3 (right) for satellite 1.

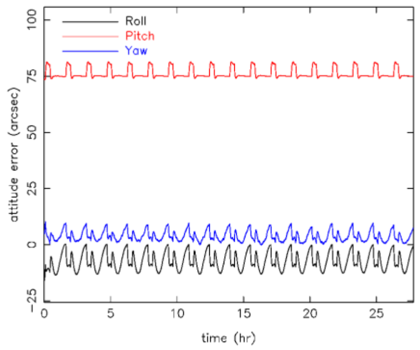

Figure 35-11 ADS attitude reconstruction errors.

36. WP1820 REFINED ANALYSIS OF IN-FLIGHT CALIBRATION OF ACCELEROMETERS - TUD

For the POD-based accelerometer calibration parameter retrieval simulations, the End-to-End simulator infrastructure as described and referred to in [RD-2][RD-3] is used. Please note that the following convention is used for the accelerometer observations:

$$a_{cal} = S \times a_{meas} + b$$

where S represents the accelerometer scale factor and b the accelerometer bias. The observed acceleration is represented by a_{meas}, whereas the calibrated accelerometer observation is represented by a_{cal}.

36.1. Introduction

The setup for the simulations resembles the one used before in the MAGIC/NGGM study [RD-3]. Table 36-1 provides details of the employed force models (“truth” and “reference”), observations and observation error models (TASI, ADS), estimated parameters, and observation weights. In case of inclusion of LRI range-rate observations, especially the relative weight with respect to the GNSS-based orbit coordinates is relevant (for GNSS-only retrievals, a change of weight does not change the actual retrieval, but only the values for the formal errors which are directly proportional to these weights).

Table 36-1 Simulation set-up for scenario **5d_Mb** (see [RD-6]). In addition, the error models and estimated parameters are specified.

Period	1-31 January 2002
True force model	• GOCO05s 120x120 • AOHIS 120x120 • Solid-earth tides (IERS) • Ocean tides: EOT11a (120x120) • 3rd body perturbations (JPL ephemeris) • Drag-free (residual drag ≈ 10 nm/s^2) based on TASI or ADS time series
Reference force model = true force model except for:	• GOCO5s 1-sigma clone • AO+AOerr (120x120) [RD-4] • Ocean tides: GOT4.7 (120x120)
Observables generated in daily batches:	• ll-SST @ 1 s • X,Y,Z position coordinates @ 10 s
Observation noise/errors	• ll-SST: colored noise according to TASI or ADS system simulator • Accelerometer: colored noise according to TASI or ADS system simulator • X,Y,Z position coordinates: 1 cm • Star tracker: attitude reconstruction errors according to TASI or ADS system simulator
Estimated parameters	• Daily epoch position & velocity for each satellite (2x2x6=24 per day) • Accelerometer calibration parameters: selection of biases and scale factors
Nominal weights	• ll-SST: 1.0 μm/s • X,Y,Z position coordinates: 2.0 cm
Weights (based on observation fits)	• ll-SST: 0.2 μm/s • X,Y,Z position coordinates: 1.5 cm

36.2. Results

POD-based accelerometer calibration parameter retrieval simulations have been conducted with the TU Delft End-to-End simulator using the data sets of observation errors provided by TASI (36.2.1) and ADS (36.2.2).

36.2.1. Using observation errors according to TASI System Simulator

Data sets of observation signals and errors have been generated for 4 different scenarios, including solar minimum and solar maximum periods (Section 35.1). For solar minimum and maximum, the TASI simulator selected respectively 1-7 September 2023 and 15-21 January 2035. Since the AOHIS models are available for the period 1995-2006 [RD-4], these dates were shifted to 1-7 January 1996 and 2002, respectively, when using the TU Delft End-to-End simulator.

First, the impact of individual errors sources on the GNSS-based Cartesian orbital position coordinates and LRI range-rates was assessed for daily estimation runs for 1D DFC (Table 36-2). In these runs, the initial position, velocity and three accelerometer biases were estimated. In addition, for 1D DFC, accelerometer scale factors were estimated for the Y and Z axes. It can be observed that for fir for the "Noise" case is indeed consistent with the simulated noise levels. The attitude reconstruction errors affect the orbital position coordinates and the LRI observations through coupling with non-gravitational accelerations (thus expected to be smaller for 3D drag-free control, which is indeed the case). For the orbit coordinates, the impact is very small, even orders of magnitude below the 1 cm level. For the LRI observations, it can be observed that the impact is at the same order of magnitude as the LRI instrument noise. The accelerometer noise leads to a fit level for the LRI observations at about 3 times the LRI instrument noise, showing the need indeed for very precise accelerometers to take full advantage of the LRI observations for observing temporal gravity. The largest residuals are caused by the tide model uncertainty and the signal due to HIS plus the error in the de-aliasing product AO. It might be argued that ignoring the full HIS signal in the reference gravity field model leads to pessimistic results. In reality, this signal will be retrieved to a large extent in the gravity field processing. However, it can then be argued that one partly bites its own tail, because in the gravity field processing calibrated accelerometer observations are to be used. Regarding the impact of tide model errors, it can be observed that the impact on LRI range-rate observations for 1D DFC is significantly lower by about a factor of 3 than for 3D DFC. This can be explained by the estimation of accelerometer scale factors for the Y and Z axis. The non-gravitational signals have a large 1 cpr component which leads to absorption of resonances caused by the tide model errors. The latter is also reflected by the lower residuals for the GNSS-based orbit coordinates.

Formal errors of estimated accelerometer biases and scale factors are included in Table 36-3 and Table 36-4. If no constraints are applied for the scale factors along DFC axes, the estimation becomes unreliable and in fact impossible. For the DFC axes, the formal errors are close to or orders of magnitude above 1 or 1000 part-per-thousand (Table 36-3). For all cases, accelerometer bias estimates are very accurate and below the 1 nm/s^2 level. When constraining the scale factors for the DFC axes (X-axis for 1D DFC, and all axes for 3D DFC), the impact on the predicted quality of estimated accelerometer bias parameters is limited, but for the 1D

DFC case it is expected that the accelerometer scale factors for the Y and Z axes can be reliably estimated.

Table 36-2 Examples impact individual error sources on position and ll-SST residuals: biases unconstrained, 1D cases: X-axis scale factor fixed to 1, 3D cases: all scale factors fixed to one – 1 January 2002 (nominal weights).

MAX_1D	**X (cm)**	**Y (cm)**	**Z (cm)**	**ll-SST (μm/s)**
Noise	1,0060	0,9992	0,9979	0,0124
Attitude error	0,0058	0,0015	0,0041	0,0138
Accelerometer error	0,0178	0,0065	0,0167	0,0375
Tide model error	0,9518	0,3327	0,3825	0,0663
AO errors + HIS	0,9000	0,4014	0,6388	0,1750
Static grav. mod. error	0,0578	0,0279	0,0629	0,0425
All	1,4714	1,1601	1,2843	0,1851
MAX_3D				
Noise	1,0060	0,9992	0,9979	0,0124
Attitude error	0,0002	0,0001	0,0002	0,0007
Accelerometer error	0,0179	0,0066	0,0169	0,0376
Tide model error	0,9913	0,4549	0,4066	0,1771
AO errors + HIS	0,9000	0,4014	0,6388	0,1750
Static grav. mod. error	0,0578	0,0279	0,0629	0,0425
All	1,4872	1,1662	1,2872	0,2629

Table 36-3 Accelerometer calibration parameter retrieval formal errors (biases: nm/s^2, scale factors: 1 part per thousand): all biases and scale factors unconstrained – 1 January 1996/2002 for solar minimum/maximum.

GNSS only (σ=2cm)	**Bias X**	**Bias Y**	**Bias Z**	**Scale X**	**Scale Y**	**Scale Z**
Sat 1/MIN_1D	0,00089	0,27569	0,82738	997,15300	1,23277	0,39860
Sat 1/MAX_1D	0,00077	0,27577	0,82681	998,09900	0,22352	0,27341
Sat 1/MIN_3D	0,00089	0,62374	0,83271	1018,46000	41494,70000	83135,40000
Sat 1/MAX_3D	0,00077	0,62397	0,83290	1022,04000	41502,60000	83234,30000
Sat 2/MIN_1D	0,00504	0,27570	0,82756	2019,58000	1,25043	0,42932
Sat 2/MAX_1D	0,00496	0,27583	0,82702	2009,22000	0,23260	0,80281
Sat 2/MIN_3D	0,00896	0,54524	0,83618	4303,22000	22283,20000	84011,80000
Sat 2/MAX_3D	0,00852	0,54536	0,83614	4126,63000	22288,20000	83230,30000

Table 36-4 Accelerometer calibration parameter retrieval formal errors (biases: nm/s^2, scale factors: 1 part per thousand): biases unconstrained, 1D cases: X-axis scale factor fixed to 1, 3D cases: all scale factors fixed to one – 1 January 1996/2002 for solar minimum/maximum.

GNSS only (σ=2cm)	**Bias X**	**Bias Y**	**Bias Z**	**Scale X**	**Scale Y**	**Scale Z**
Sat 1/MIN_1D	0,00060	0,27569	0,82706	0,00000	1,23277	0,39766
Sat 1/MAX_1D	0,00034	0,27577	0,82652	0,00000	0,22352	0,27251
Sat 1/MIN_3D	0,00060	0,27516	0,82595	0,00000	0,00000	0,00000
Sat 1/MAX_3D	0,00034	0,27541	0,82612	0,00000	0,00000	0,00000
Sat 2/MIN_1D	0,00060	0,27570	0,82706	0,00000	1,25043	0,42608
Sat 2/MAX_1D	0,00034	0,27583	0,82656	0,00000	0,23260	0,80088
Sat 2/MIN_3D	0,00060	0,27516	0,82597	0,00000	0,00000	0,00000
Sat 2/MAX_3D	0,00034	0,27541	0,82615	0,00000	0,00000	0,00000

The impact of individual errors sources on GNSS-based retrieved accelerometer calibration parameters is displayed in Table 36-5 for the 1st day of January 1996/2002, for satellite 1. Maximum accelerometer bias retrieval errors are caused by tide model errors and by uncertainties in the AO de-aliasing product plus the HIS signal. For the X axis (predominantly in the flight direction), the bias retrieval errors are always very low and orders of magnitude below the 1 nm/s^2 level. The bias retrieval errors are in general the largest for the Z axis (predominantly height direction) and can reach up to 2 nm/s^2, whereas this is up to 1 nm/s^2 for the Y axis (predominantly cross-track direction). Accelerometer scale factors are estimated only for the Y and Z axes for 1D DFC. Maximum retrieval error is at about 65 part-per-thousand or 0.065 for the Y axis and about 39 part-per-thousand or 0.039 for the Z axis. For solar minimum, the scale factor retrieval errors are larger due to the smaller remaining non-gravitational acceleration signal.

Table 36-5 Impact of error sources - accelerometer calibration parameter retrieval errors (biases: nm/s^2, scale factors: 1 part per thousand): biases unconstrained, 1D cases: X-axis scale factor fixed to 1, 3D cases: all scale factors fixed to one – 1 January 1996/2002 for solar minimum/maximum.

GNSS only (σ=2cm)	**Error**	**Bias X**	**Bias Y**	**Bias Z**	**Scale X**	**Scale Y**	**Scale Z**
Sat 1/MIN_1D	Attitude	-0,00006	0,00005	-0,00193	0,00000	-0,01100	0,00000
Sat 1/MAX_1D	Attitude	-0,00083	0,00074	0,00271	0,00000	0,00000	-0,04300
Sat 1/MIN_3D	Attitude	0,00000	0,00000	-0,00004	0,00000	0,00000	0,00000
Sat 1/MAX_3D	Attitude	0,00000	0,00000	-0,00003	0,00000	0,00000	0,00000
Sat 1/MIN_1D	Accelerometer	0,00067	0,01374	-0,02390	0,00000	0,00000	-0,02700
Sat 1/MAX_1D	Accelerometer	0,00069	0,01332	-0,02260	0,00000	0,00000	0,02000
Sat 1/MIN_3D	Accelerometer	0,00067	0,01289	-0,02283	0,00000	0,00000	0,00000
Sat 1/MAX_3D	Accelerometer	0,00069	0,01293	-0,02308	0,00000	0,00000	0,00000
Sat 1/MIN_1D	Tracking noise	-0,00012	0,04281	0,30854	0,00000	-0,03000	0,29000
Sat 1/MAX_1D	Tracking noise	-0,00051	0,00948	0,61226	0,00000	0,04000	-0,25100
Sat 1/MIN_3D	Tracking noise	-0,00013	0,05180	0,29793	0,00000	0,00000	0,00000
Sat 1/MAX_3D	Tracking noise	-0,00051	0,01144	0,62601	0,00000	0,00000	0,00000
Sat 1/MIN_1D	AO errors + HIS	-0,03145	-0,93767	1,11302	0,00000	65,37000	39,32000
Sat 1/MAX_1D	AO errors + HIS	-0,00398	-0,03421	0,39142	0,00000	3,56000	5,24000
Sat 1/MIN_3D	AO errors + HIS	-0,03063	0,91551	1,99436	0,00000	0,00000	0,00000

Sat 1/MAX_3D	AO errors + HIS	-0,00400	-0,33715	0,57131	0,00000	0,00000	0,00000
Sat 1/MIN_1D	Tide model err.	-0,00422	-0,16481	-0,52897	0,00000	-17,27800	1,70000
Sat 1/MAX_1D	Tide model err.	-0,01037	-0,24900	-1,32398	0,00000	-2,88700	-11,52100
Sat 1/MIN_3D	Tide model err.	-0,00459	-0,27305	-1,15720	0,00000	0,00000	0,00000
Sat 1/MAX_3D	Tide model err.	-0,01028	0,12121	-1,19943	0,00000	0,00000	0,00000
Sat 1/MIN_1D	Static grav. err.	-0,00027	-0,01058	-0,01283	0,00000	-0,35500	0,02000
Sat 1/MAX_1D	Static grav. err.	-0,00045	-0,00825	-0,04393	0,00000	-0,00200	-0,20400
Sat 1/MIN_3D	Static grav. err.	-0,00028	-0,01322	-0,02537	0,00000	0,00000	0,00000
Sat 1/MAX_3D	Static grav. err.	-0,00045	-0,00461	-0,03641	0,00000	0,00000	0,00000

Note the different impact of AO errors for 1 January 1996 and 2002

Table 36-6 displays the accelerometer calibration parameter retrieval errors when all error models are combined for both satellites of the inclined tandem. It can be observed that the accelerometer scale factor errors are smaller than caused by only the AO de-aliasing uncertainty plus HIS signal, which can be explained that for the selected day the impact of the tide model uncertainty has the opposite sign (Table 36-5). Bias retrieval errors are below 1 whereas scale factor retrieval errors amount up to about 0.05 for both the Y and Z axes for 1D DFC during solar minimum.

Table 36-7 shows the impact of adding LRI range-rate observation in the POD-based accelerometer calibration parameter retrieval. For the selected days, the impact on the estimated scale factors for 1D DFC is limited ranging from slight improvement to degradation. Except for the X axis, the impact on the bias estimation is significant: retrieved biases for the Y and Z axes have much bigger errors. The POD-based estimation process aims at minimizing observation residuals, where in the case of adding LRI observation this results in minimized LRI residuals at the expense of much less accurate bias estimates for the Y and Z axes.

Table 36-6 Accelerometer calibration parameter retrieval errors - full error model (biases: nm/s^2, scale factors: 1 part per thousand): biases unconstrained, 1D cases: X-axis scale factor fixed to 1, 3D cases: all scale factors fixed to one – 1 January 1996/2002 for solar minimum/maximum.

GNSS only (σ=2cm)	**Bias X**	**Bias Y**	**Bias Z**	**Scale X**	**Scale Y**	**Scale Z**
Sat 1/MIN_1D	-0,03545	-1,05584	0,86525	0,00000	47,69000	41,31000
Sat 1/MAX_1D	-0,01547	-0,26513	-0,34537	0,00000	0,72000	-6,75200
Sat 1/MIN_3D	-0,03494	0,69470	1,09760	0,00000	0,00000	0,00000
Sat 1/MAX_3D	-0,01457	-0,19314	-0,02246	0,00000	0,00000	0,00000
Sat 2/MIN_1D	-0,03332	-0,91294	0,57224	0,00000	46,90000	43,32000
Sat 2/MAX_1D	-0,01299	-0,41298	-0,62501	0,00000	0,47000	-26,04900
Sat 2/MIN_3D	-0,03297	0,81172	0,87772	0,00000	0,00000	0,00000
Sat 2/MAX_3D	-0,01245	-0,20924	-0,89547	0,00000	0,00000	0,00000

Table 36-7 Accelerometer calibration parameter retrieval errors - full error model (biases: nm/s^2, scale factors: 1 part per thousand): biases unconstrained, 1D cases: X-axis scale factor fixed to 1, 3D cases: all scale factors fixed to one, scale factors – 1 January 1996/2002 for solar minimum/maximum.

GNSS (σ=1.5cm) + ll=SST (σ=0.2 μm/s)	**Bias X**	**Bias Y**	**Bias Z**	**Scale X**	**Scale Y**	**Scale Z**
Sat 1/MIN_1D	-0,03696	8,45396	-1,98305	0,00000	54,23000	27,70000
Sat 1/MAX_1D	-0,01582	-1,93257	2,12697	0,00000	0,70000	-0,46300
Sat 1/MIN_3D	-0,03639	4,20968	-1,32229	0,00000	0,00000	0,00000
Sat 1/MAX_3D	-0,01388	0,24832	-1,91733	0,00000	0,00000	0,00000
Sat 2/MIN_1D	-0,03467	-9,49056	-1,18459	0,00000	40,59000	30,65000
Sat 2/MAX_1D	-0,01162	1,47822	-5,93516	0,00000	0,51000	-1,04900
Sat 2/MIN_3D	-0,03420	-0,69338	-0,80204	0,00000	0,00000	0,00000
Sat 2/MAX_3D	-0,00980	5,56590	-10,92140	0,00000	0,00000	0,00000

Finally, Table 36-8 and Table 36-9 display retrieved biases and scale factors (1D DFC only) for the remaining days of the week of 1-7 January 1996/2002. In general, results are consistent with those displayed in Table 36-6, except for the accelerometer Y-axis scale factor errors for

1D DFC, which display a (strong) growing trend in the course of the week up to about 0.18 or 180 part-per-thousand. This can be explained by the strongly decreasing variance of the residual non-gravitational signal for the Y axis (see Figure 35-4).

Table 36-8 GNSS-only accelerometer calibration parameter retrieval errors - full error model (biases: nm/s^2, scale factors: 1 part per thousand): biases unconstrained, 1D cases: X-axis scale factor fixed to 1.

Satellite/Scenario	**Date**	**Bias X**	**Bias Y**	**Bias Z**	**Scale X**	**Scale Y**	**Scale Z**
Sat 1/MIN_1D	960101	-0,03545	-1,05584	0,86525	0,00000	47,69000	41,31000
Sat 1/MIN_1D	960102	-0,04089	-0,84144	0,22041	0,00000	9,87000	20,46000
Sat 1/MIN_1D	960103	-0,03415	-0,27923	0,06951	0,00000	-5,59500	35,02000
Sat 1/MIN_1D	960104	-0,02779	-1,27614	0,05723	0,00000	36,18000	22,80000
Sat 1/MIN_1D	960105	-0,02591	-1,06290	2,45830	0,00000	87,50000	14,72000
Sat 1/MIN_1D	960106	-0,03329	-1,68277	0,82088	0,00000	184,55000	28,90000
Sat 1/MIN_1D	960107	-0,03991	-0,73242	2,20753	0,00000	181,97000	17,38000
Sat 1/MAX_1D	020101	-0,01547	-0,26513	-0,34537	0,00000	0,72000	-6,75200
Sat 1/MAX_1D	020102	0,00564	0,86966	-0,08615	0,00000	-4,09600	1,34000
Sat 1/MAX_1D	020103	-0,00131	-0,88209	-1,67624	0,00000	-3,80800	0,23000
Sat 1/MAX_1D	020104	-0,00931	-0,32363	-1,49752	0,00000	-9,63100	-2,87800
Sat 1/MAX_1D	020105	0,00936	-0,59676	-2,33455	0,00000	-13,39300	-1,00900
Sat 1/MAX_1D	020106	0,00622	0,14356	-1,87737	0,00000	-11,41900	-2,71300
Sat 1/MAX_1D	020107	0,02105	-0,36743	-1,87513	0,00000	-13,81800	2,34000

Table 36-9 GNSS-only accelerometer calibration parameter retrieval errors - full error model (biases: nm/s^2, scale factors: 1 part per thousand): biases unconstrained, 3D cases: all scale factors fixed to one.

Satellite/Scenario	**Date**	**Bias X**	**Bias Y**	**Bias Z**	**Scale X**	**Scale Y**	**Scale Z**
Sat 1/MIN_3D	960101	-0,03494	0,69470	1,09760	0,00000	0,00000	0,00000
Sat 1/MIN_3D	960102	-0,04025	-0,06523	0,43779	0,00000	0,00000	0,00000
Sat 1/MIN_3D	960103	-0,03414	0,85564	-1,25461	0,00000	0,00000	0,00000
Sat 1/MIN_3D	960104	-0,02729	-0,22247	0,65817	0,00000	0,00000	0,00000
Sat 1/MIN_3D	960105	-0,02443	-0,16353	3,68561	0,00000	0,00000	0,00000
Sat 1/MIN_3D	960106	-0,03188	-0,09805	2,89848	0,00000	0,00000	0,00000
Sat 1/MIN_3D	960107	-0,03785	0,22277	3,89564	0,00000	0,00000	0,00000
Sat 1/MAX_3D	020101	-0,01457	-0,19314	-0,02246	0,00000	0,00000	0,00000
Sat 1/MAX_3D	020102	0,00641	-0,74525	-0,61101	0,00000	0,00000	0,00000
Sat 1/MAX_3D	020103	-0,00033	-0,66986	-2,05628	0,00000	0,00000	0,00000
Sat 1/MAX_3D	020104	-0,00844	0,03591	-2,24338	0,00000	0,00000	0,00000
Sat 1/MAX_3D	020105	0,01018	0,05027	-3,54712	0,00000	0,00000	0,00000
Sat 1/MAX_3D	020106	0,00702	0,60650	-2,79974	0,00000	0,00000	0,00000
Sat 1/MAX_3D	020107	0,02150	0,06346	-3,32088	0,00000	0,00000	0,00000

36.2.2. Using observation errors according to ADS System Simulator

Not populated, please see end of Section 35.2.

36.3. Conclusions

GNSS-based accelerometer calibration allows for a very precise determination of accelerometer biases for the X axis (predominantly the flight direction): precisions much better than 0.1 nm/s^2 are feasible when using the full error model. For the Y and Z axes (predominantly in the cross-track and height direction, respectively), these precisions are typically better than 1 and 4 nm/s^2, respectively. Of the error sources investigated, uncertainties in the tide model and uncertainties/omissions in the temporal gravity field model (e.g., errors in the de-aliasing models) are the dominant ones. The latter might be mitigated by co-estimating the gravity field (with the risk of "biting one's own tail").

The capability of GNSS-based accelerometer calibration for estimating accelerometer observations strongly depends on the magnitude of the (residual) non-gravitational accelerations. Four scenarios have been investigated based on the possible combinations of flying during solar minimum or maximum on the one hand and flying 1D or 3D DFC. In case of 3D DFC, no reliable estimation of accelerometer scale factors is feasible. In case of 1D DFC, where the DFC is aligned with the X axis, only reliable scale factors for the Y and Z axes can be estimated with precisions ranging between about 0.001 and 0.18 for the Y axis and 0.001 and 0.04 for the Z axis. Better precisions are obtained for the solar maximum period, when the 1D DFC leaves bigger non-gravitational accelerations. During solar minimum, the uncertainty of the estimated scale factors is about 10 times worse than during solar maximum. Especially for the Y axis, the TASI simulations display a decreasing trend of the order of magnitude of the residual accelerations, leading to larger errors in the retrieved Y axis accelerometer scale factors.

Including the LRI observations in the POD-based accelerometer calibration, i.e., together with the GNSS-estimated orbit coordinates, might lead to a degraded estimation of accelerometer calibration parameters. Finding the optimal relative weight of the GNSS and LRI observations is not straightforward. Remaining gravity field modeling errors (as in, e.g., the de-aliasing products) have a relatively big impact on the LRI observations as compared to the GNSS observations. This is a contributing factor to less precise accelerometer calibration parameter estimates, despite the very high precision of the LRI observations themselves.

37. REFINED ANALYSIS OF IN-FLIGHT CALIBRATION OF ACCELEROMETERS – CNES (WP1830)

For the POD-based accelerometer calibration parameter retrieval simulations, the End-to-End simulator infrastructure as described and referred to in [RD-2][RD-3] is used.

37.1. Introduction

The setup for the simulations listed in Table 37-1 is nearly identical to Table 36-1, which provides details of the employed force models ("truth" and "reference"), observations and observation error models (TASI), estimated parameters, and observation weights.

Table 37-1 Simulation set-up for scenario **5d_Mb**. In addition, the error models and estimated parameters are specified.

Period	1-31 January 2002
True force model	• GOCO05s 120x120 • AOHIS 120x120 • Solid-earth tides (IERS) • Ocean tides: EOT11a (120x120) • 3rd body perturbations (JPL ephemeris) • Drag-free (residual drag ≈ 10 nm/s^2) based on TASI or ADS time series
Reference force model = true force model except for:	• GOCO5s • AO+AOerr (120x120) [RD-4] • Ocean tides: GOT4.7 (120x120)
Observables generated in daily batches:	• ll-SST @ 1 s • X,Y,Z position coordinates @ 10 s
Observation noise/errors	• ll-SST: colored noise according to TASI or ADS system simulator • Accelerometer: colored noise according to TASI or ADS system simulator • X,Y,Z position coordinates: 1 cm • Star tracker: attitude reconstruction errors according to TASI or ADS system simulator
Estimated parameters	• Daily epoch position & velocity for each satellite (2x2x6=24 per day) • Accelerometer calibration parameters: selection of biases and scale factors for uncompensated axes
Nominal weights	• LRI: 0.4 μm/s • X,Y,Z position coordinates: 1.0 cm

37.2. Results

POD-based accelerometer calibration parameter retrieval simulations have been conducted with the CNES End-to-End simulator using the data sets of observation errors provided by TASI (Section 37.2.1).

37.2.1. Using observation errors according to TASI System Simulator

The same data sets of observations and noise generated for 4 different scenarios, including solar minimum and solar maximum periods, described in Section 35.1 were used by CNES. For solar minimum and maximum, the AOHIS model for the period 1-7 January 2002 was used in the CNES End-to-End simulator.

Table 37-2 displays the accelerometer calibration parameter retrieval errors for the first day of 2002, in black for TU Delft and in blue for CNES, when all error models are combined for both satellites of the inclined tandem. CNES and TU_Delft bias retrieval errors are generally of the same order of magnitude. This is also the case for scale factors, except for the MIN_1D case. Also, the TU Delft scale factor results improve for the MAX_1D cases, which can be explained by the larger residual non-gravitational accelerations (this is also reflected by the formal errors).

Table 37-2 Accelerometer calibration parameter retrieval errors with GNSS - full error model (biases: nm/s^2, scale factors: 1 part per thousand): biases unconstrained. 1D cases: X-axis scale factor fixed to 1. 3D cases: all scale factors fixed to one. TU Delft/CNES: black/blue

GNSS only (σ=2cm) **GNSS only (σ=1cm)**	**Bias X**	**Bias Y**	**Bias Z**	**Scale X**	**Scale Y**	**Scale Z**
Sat 1/MIN_1D	-0,03545	-1,05584	0,86525	0,00000	47,69000	41,31000
	0,00976	-0,31079	-0,98087	0,00000	2,53038	-5,35664
Sat 1/MAX_1D	-0,01547	-0,26513	-0,34537	0,00000	0,72000	-6,75200
	0,00980	-0,42646	-1,08637	0,00000	0,62741	6,45664
Sat 1/MIN_3D	-0,03494	0,69470	1,09760	0,00000	0,00000	0,00000
	0,00974	-0,27274	-1,15761	0,00000	0,00000	0,00000
Sat 1/MAX_3D	-0,01457	-0,19314	-0,02246	0,00000	0,00000	0,00000
	0,00974	-0,27274	-1,15760	0,00000	0,00000	0,00000
Sat 2/MIN_1D	-0,03332	-0,91294	0,57224	0,00000	46,90000	43,32000
	0,00794	-0,36290	-1,00612	0,00000	2,53123	-5,69591
Sat 2/MAX_1D	-0,01299	-0,41298	-0,62501	0,00000	0,47000	-26,04900
	0,00795	-0,47615	-0,13243	0,00000	0,51745	24,37550
Sat 2/MIN_3D	-0,03297	0,81172	0,87772	0,00000	0,00000	0,00000
	0,00794	-0,32561	-1,15514	0,00000	0,00000	0,00000
Sat 2/MAX_3D	-0,01245	-0,20924	-0,89547	0,00000	0,00000	0,00000
	0,00794	-0,32561	-1,15515	0,00000	0,00000	0,00000

Table 37-3 shows the impact of adding LRI range-rate observation in the POD-based accelerometer calibration parameter retrieval, compared with the GNSS-only estimations. The X-bias retrieval is not improved, whereas the Y-bias and especially Z-bias have much bigger errors. Table 37-4 shows the LRI range-rate observation and GNSS-based accelerometer calibration parameter retrieval calculated by TU Delft and CNES. The TU Delft and CNES results are close, except for the MIN_1D case.

Table 37-3 Accelerometer calibration parameter retrieval errors with GNSS (top line) and GNSS and LRI (bottom line) - full error model (biases: nm/s^2, scale factors: 1 part per thousand): biases unconstrained. 1D cases: X-axis scale factor fixed to 1. 3D cases: all scale factors fixed to one. Significantly better/worse for GNSS+LRI: green/red.

GNSS (σ=1cm) & LRI (σ=0.4 μm/s)	**Bias X**	**Bias Y**	**Bias Z**	**Scale X**	**Scale Y**	**Scale Z**
Sat 1/MIN_1D	0,00976	-0,31079	-0,98087	0,00000	2,53038	-5,35664
	0,00964	-0,60981	7,04000	0,00000	3,54987	-4,74491
Sat 1/MAX_1D	0,00980	-0,42646	-1,08637	0,00000	0,62741	6,45664
	0,00957	-0,46787	-2,94627	0,00000	0,60748	0,63471
Sat 1/MIN_3D	0,00974	-0,27274	-1,15761	0,00000	0,00000	0,00000
	0,00964	0,28076	6,16624	0,00000	0,00000	0,00000
Sat 1/MAX_3D	0,00974	-0,27274	-1,15760	0,00000	0,00000	0,00000
	0,00964	0,28082	6,16719	0,00000	0,00000	0,00000
Sat 2/MIN_1D	0,00794	-0,36290	-1,00612	0,00000	2,53123	-5,69591
	0,00805	-0,01864	-9,03788	0,00000	1,99887	-4,92027
Sat 2/MAX_1D	0,00795	-0,47615	-0,13243	0,00000	0,51745	24,37550
	0,00810	-0,20966	0,91464	0,00000	0,52974	2,29833
Sat 2/MIN_3D	0,00794	-0,32561	-1,15514	0,00000	0,00000	0,00000
	0,00804	-0,85584	-8,56222	0,00000	0,00000	0,00000
Sat 2/MAX_3D	0,00794	-0,32561	-1,15515	0,00000	0,00000	0,00000
	0,00804	-0,85589	-8,56318	0,00000	0,00000	0,00000

Table 37-4 Accelerometer calibration parameter retrieval errors with GNSS and LRI - full error model (biases: nm/s^2, scale factors: 1 part per thousand): biases unconstrained.
1D cases: X-axis scale factor fixed to 1. 3D cases: all scale factors fixed to one. TU Delft/CNES: black/blue

GNSS (σ=2cm) + LRI (σ=0.2 μm/s) **GNSS (σ=1cm) + LRI (σ=0.4 μm/s)**	**Bias X**	**Bias Y**	**Bias Z**	**Scale X**	**Scale Y**	**Scale Z**
Sat 1/MIN_1D	-0,03696	8,45396	-1,98305	0,00000	54,23000	27,70000
	0,00964	-0,60981	7,04000	0,00000	3,54987	-4,74491
Sat 1/MAX_1D	-0,01582	-1,93257	2,12697	0,00000	0,70000	-0,46300
	0,00957	-0,46787	-2,94627	0,00000	0,60748	0,63471
Sat 1/MIN_3D	-0,03639	4,20968	-1,32229	0,00000	0,00000	0,00000
	0,00964	0,28076	6,16624	0,00000	0,00000	0,00000
Sat 1/MAX_3D	-0,01388	0,24832	-1,91733	0,00000	0,00000	0,00000
	0,00964	0,28082	6,16719	0,00000	0,00000	0,00000
Sat 2/MIN_1D	-0,03467	-9,49056	-1,18459	0,00000	40,59000	30,65000
	0,00805	-0,01864	-9,03788	0,00000	1,99887	-4,92027
Sat 2/MAX_1D	-0,01162	1,47822	-5,93516	0,00000	0,51000	-1,04900
	0,00810	-0,20966	0,91464	0,00000	0,52974	2,29833
Sat 2/MIN_3D	-0,03420	-0,69338	-0,80204	0,00000	0,00000	0,00000
	0,00804	-0,85584	-8,56222	0,00000	0,00000	0,00000
Sat 2/MAX_3D	-0,00980	5,56590	-10,92140	0,00000	0,00000	0,00000
	0,00804	-0,85589	-8,56318	0,00000	0,00000	0,00000

37.2.2. Using observation errors according to ADS System Simulator

Not populated, please see end of Section 36.2.2.

37.3. Conclusions

The CNES results in general verify the TUD results and lead to similar conclusions as in Section 36.3.

38. APPLICABLE DOCUMENTS, REFERENCE DOCUMENTS, AND PUBLICATIONS TO PART 7

38.1. APPLICABLE DOCUMENTS

[AD-1] NGGM/MAGIC – SCIENCE SUPPORT STUDY DURING PHASE A – EXPRO, RFP Proposal No. TUM/2021-MAGIC-Science, ESA RFP/3-17035/20/NL/FF/tfd, 16-03-2021

[AD-2] Assessment of a Next Generation Mission for Monitoring the Variations of Earth’s Gravity. Final Report, ESTEC Contract No. 22643/09/NL/AF, Issue 2, Date: 22.12.2010

[AD-3] Assessment of a Next Generation Gravity Mission to Monitor the Variations of Earth’s Gravity Field. Final Report, ESTEC Contract No. 22672/09/NL/AF, Issue 1, Date: 10.10.2011.

[AD-4] Assessment of Satellite Constellations for Monitoring the Variations in Earth Gravity Field “SC4MGV”, ESA Contract No 4000108663/13/NL/MV, Final Report, 04 November 2015

[AD-5] R.D. Ray, Precise comparisons of bottom-pressure and altimetric ocean tides, J. Geophys. Res.: Oceans, Vol. 118, pp. 4870-4584, doi: 10.1002/jgrc.20336, 2013

[AD-6] Savcenko, R. and Bosch, W. (2012): EOT11A - Empirical Ocean Tide Model from Multi-Mission Satellite Altimetry, München, Deutsches Geodätisches Forschungsinstitut (DGFI), hdl:10013/epic.43894

[AD-7] GOCO, Gravity observation combination (GOCO), www.goco.eu, accessed 23 September 2021

[AD-8] D.E . Pavlis, S. Poulouse, J.J. McCarthy, GEODYN operations manual, Contractor report, SGT Inc. Greenbelt, 2006

[AD-9] D.N. Wiese, P. Visser, R.S. Nerem, Estimating Low Resolution/High Frequency Gravity Fields to Reduce Temporal Aliasing Errors, Adv. Space Res., 48(6), pp. 1094-1107, doi: 10.1016/j.asr.2011.05.027, 2011

[AD-10] TU Munich LRZ server (https://syncandshare.lrz.de/).

38.2. REFERENCE DOCUMENTS

[RD-1] CHANGE REQUEST No. 1 to Contract No. 4000134613/21/NL/FF/ab, NGGM/MAGIC – Science Support Study during Phase A, 28 November 2022

[RD-2] Next Generation Gravity Mission as a Mass-change And Geosciences International Constellation (MAGIC), Science Support Study During Phase A, Technical Note WP300 DORIS aided orbits and relative gravity field observables, Issue 1.0, 17 October 2022 (Ref. ESA-EOPSM-FUTM-SOW-3813, 18/01/2021)

[RD-3] Next Generation Gravity Mission as a Mass-change And Geosciences International Constellation (MAGIC), Science Support Study During Phase A, Technical Note WP700 Calibration of accelerometers, Issue 1.0, 20 June 2022 (Ref. ESA-EOPSM-FUTM-SOW-3813, 18/01/2021)

[RD-4] ESA Earth System Model for Mass Distribution and Transport, https://isdc.gfz-potsdam.de/esmdata/esaesm/, last accessed 23 September 2021

[RD-5] Sabrina Dionisio, NGGM TN 21, e-MAGIC Architecture, Design and Interface Document, TASI-SD-NGGM-TNO-0484, 25/JAN/2022

[RD-6] Statement of Work - ESA Express Procurement - EXPRO NGGM/MAGIC science support study during Phase A, Issue 1.0, Date 18/01/2021 Ref ESA-EOPSM-FUTM-SOW-3813

PART 8:

AD-HOC:
IMPACT OF FROZEN VS. CIRCULAR ORBIT FOR P2

39. INTRODUCTION

In this study, we compare gravity retrieval performance on the basis of a circular and a frozen P2 orbit in order to understand whether one is more beneficial than the other. In case of the circular orbit (standard for simulations of the MAGIC/NGGM science study) which features a very small eccentricity, the primary goal is to keep fluctuations in orbital altitude as small as possible with respect to the mean altitude. In case of the frozen orbit, its perigee remains invariant in space (around either pole), and, consequently, also its orbital altitude over any given geolocation remains close-to constant. This, however comes at the cost of a larger eccentricity, and, therefore, overall larger fluctuations in altitude. This matter is visualised in Figure 39-1.

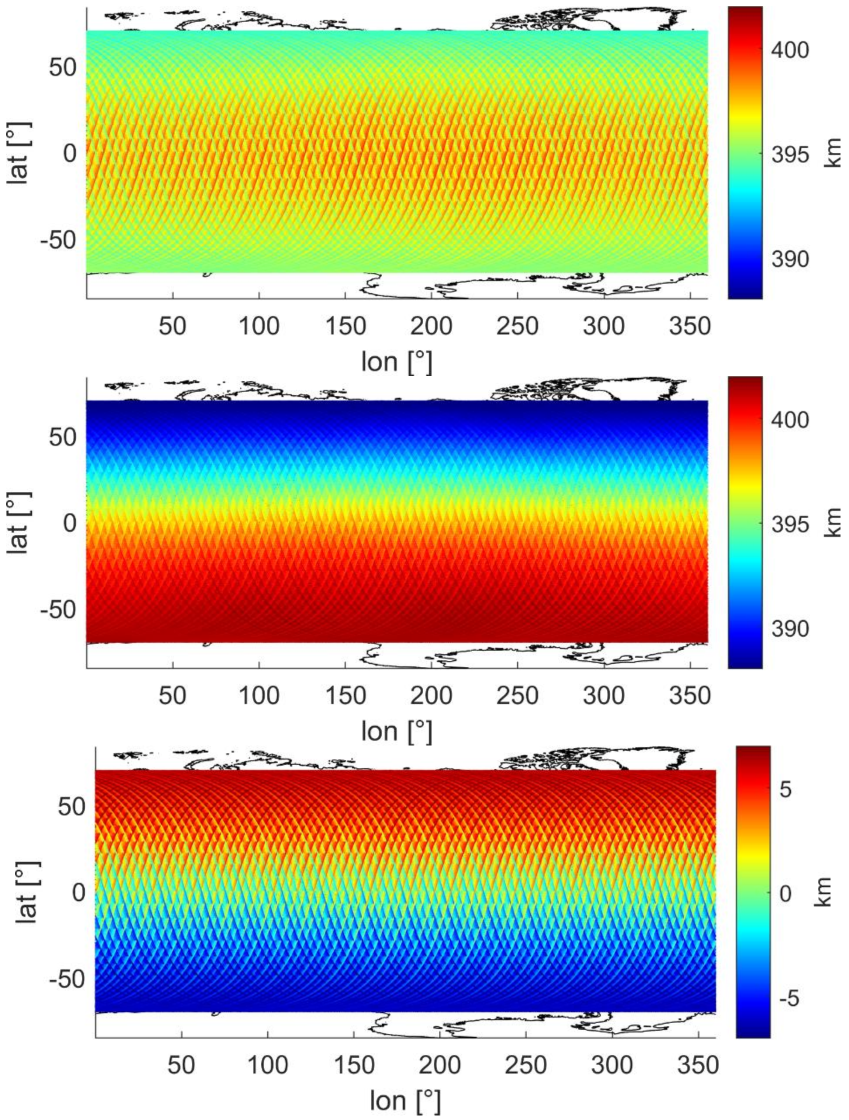

Figure 39-1 Orbital altitude over January 2002. Top – circular orbit, center – frozen orbit, bottom – difference between altitudes of circular and frozen orbit.

40. SIMULATION SETUP

For this study, we run a gravity retrieval on the basis of a Bender-type double-pair as well as a P2-only observation geometry. For P1, we assume the parameters of scenario 5d_H. For the circular P2, the parameters of 5d_Mb are used, while for the frozen P2 they are altered accordingly. The parameters are summarized in Table 40-1.

Table 40-1: Orbital parameters

	Semi-major axis [m]	eccentricity	incl. [°]	asc. node [°]	arg.of perigee [°]	mean anomaly [°]
P1-A	6871210.979	0.0016	89	359.98	27.78	331.51
P1-B	6871208.124	0.0016	89	359.98	29.17	331.95
P2-A circular	6780418.955	0.0008	70	2.34	5.46	353.82
P2-B circular	6780416.219	0.0008	70	2.34	8.46	352.68
P2-A frozen	6780409.532	0.0011	70	2.34	65.95	293.33
P2-B frozen	6780409.377	0.0011	70	2.34	66.91	294.26

Based on these flight formations, we simulate 5-day and 31-day gravity retrieval for a FN and a IO scenario. It is noted that TEs are included in both noise scenarios, but are treated differently in terms of stochastic modelling. In IO, tailored weighting is applied for the TEs (*w1*-type weighting), while in FN the stochastic modelling is based only on the instruments (ACC and LRI/LTI; *w0*-type weighting).

41. SIMULATION RESULTS

41.1. DOUBLE-PAIR

The double-pair-based retrieval error for the full-noise scenario is shown in Figure 41-1 in terms of degree amplitudes as well as in Figure 41-2 in terms of coefficient and formal error triangular plots. It is evident that the differences in retrieval performance are absolutely minor both in the 5- and 31-day scenario. The largest difference can be found in C10, followed by C20 and C30. The same overall behaviour can be seen in the product-noise-only simulation results (Figure 41-3 and Figure 41-4), though the error in C30 seems to be lower in comparison to respective the full-noise results.

41.2. P2-ONLY

In case of gravity retrieval on the basis of a stand-alone P2, the results show an identical overall behaviour. This can be seen clearly in Figure 41-5 and Figure 41-6 (FN) as well as Figure 41-7 and Figure 41-8 (IO). Note that the degree amplitudes presented here include the near-zonals affected by the spherical cap regularization. Consequently, the largest differences can be found in these spherical harmonic coefficients. Also, since the regularization is the dominant effect in the near-zonals, the difference between *w0*- and *w1*-type weighting is almost non-existent.

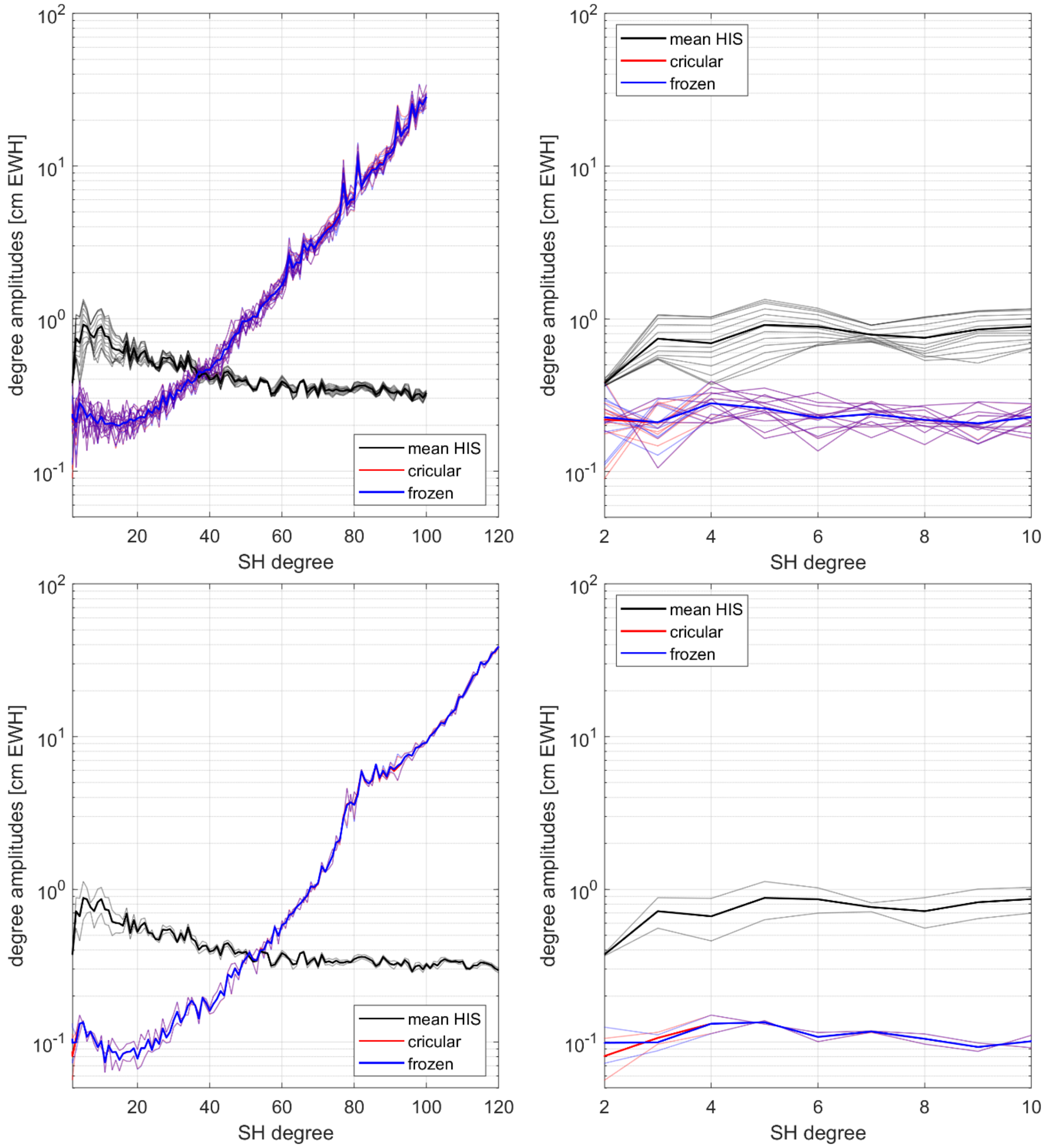

Figure 41-1: retrieval error of the 5- (top) and 31-day (bottom) double-pair-based FN gravity solutions. The low-degree spectrum of the left-hand side plots is shown in more detail on the right.

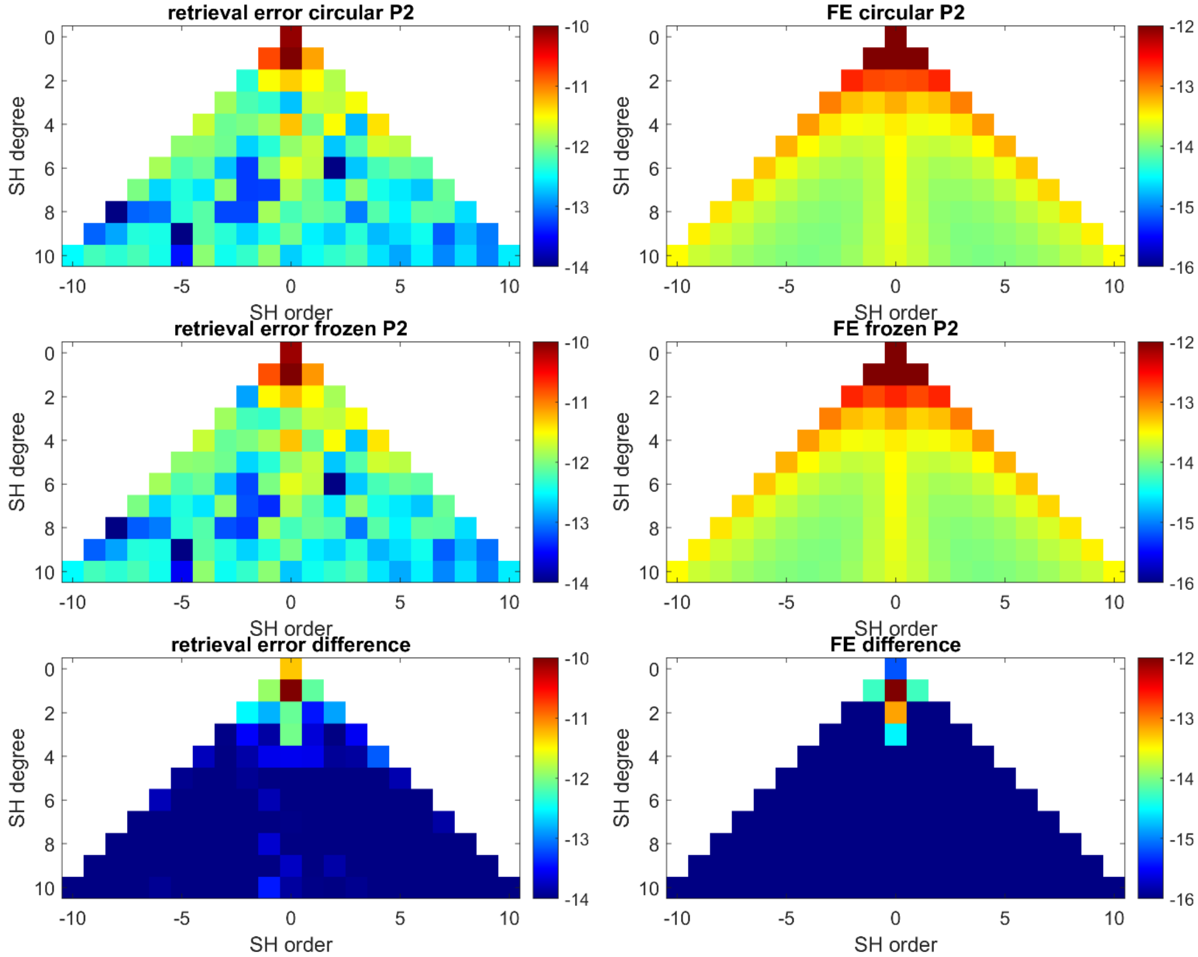

Figure 41-2: retrieval error of the 5-day double-pair-based FN gravity solutions (left) and the corresponding formal errors (right) zoomed to the low-degree spectrum. The bottom row shows the difference between coefficients and formal errors, respectively.

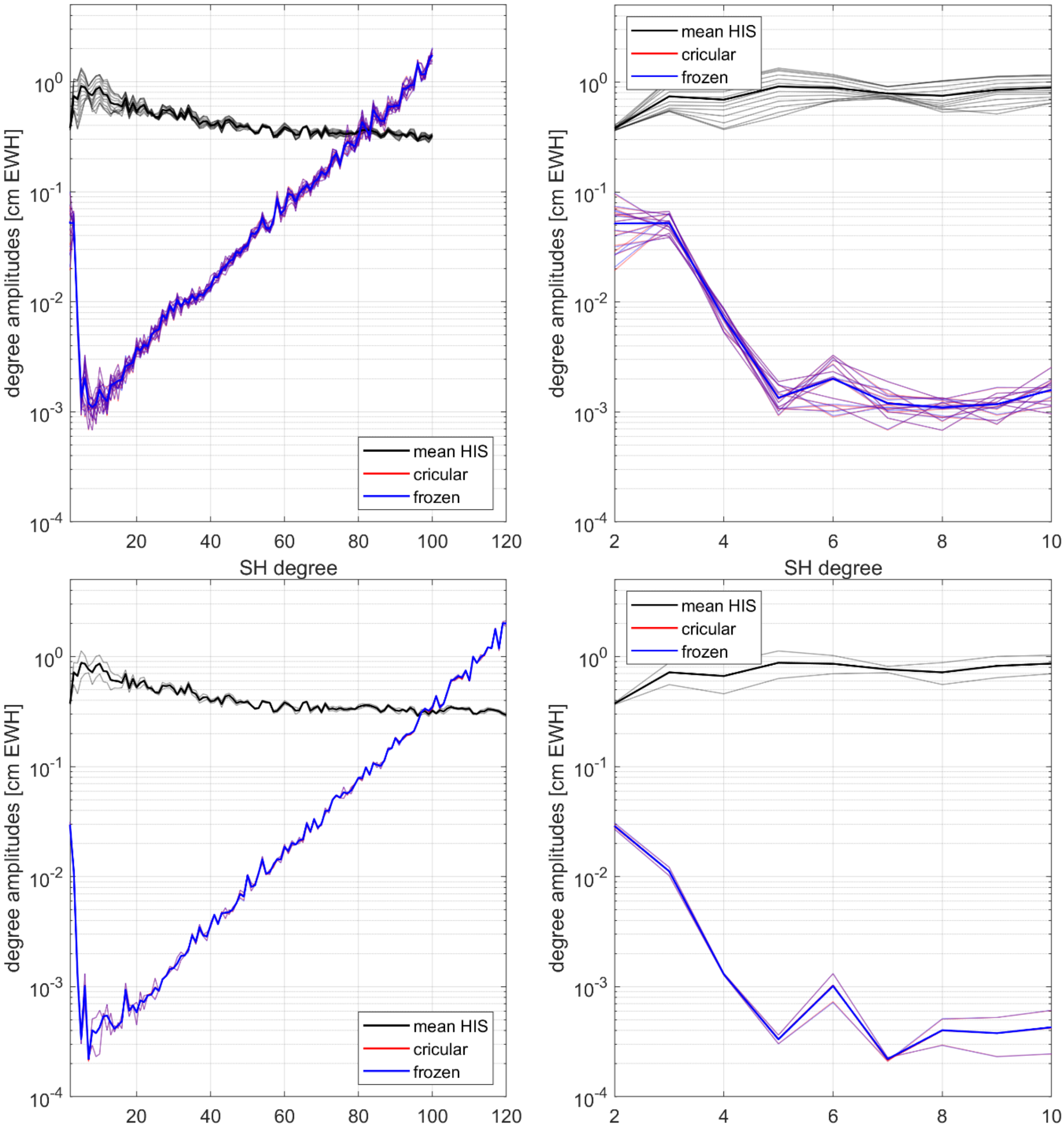

Figure 41-3: retrieval error of the 5- (top) and 31-day (bottom) double-pair-based IO gravity solutions. The low-degree spectrum of the left-hand side plots is shown in more detail on the right.

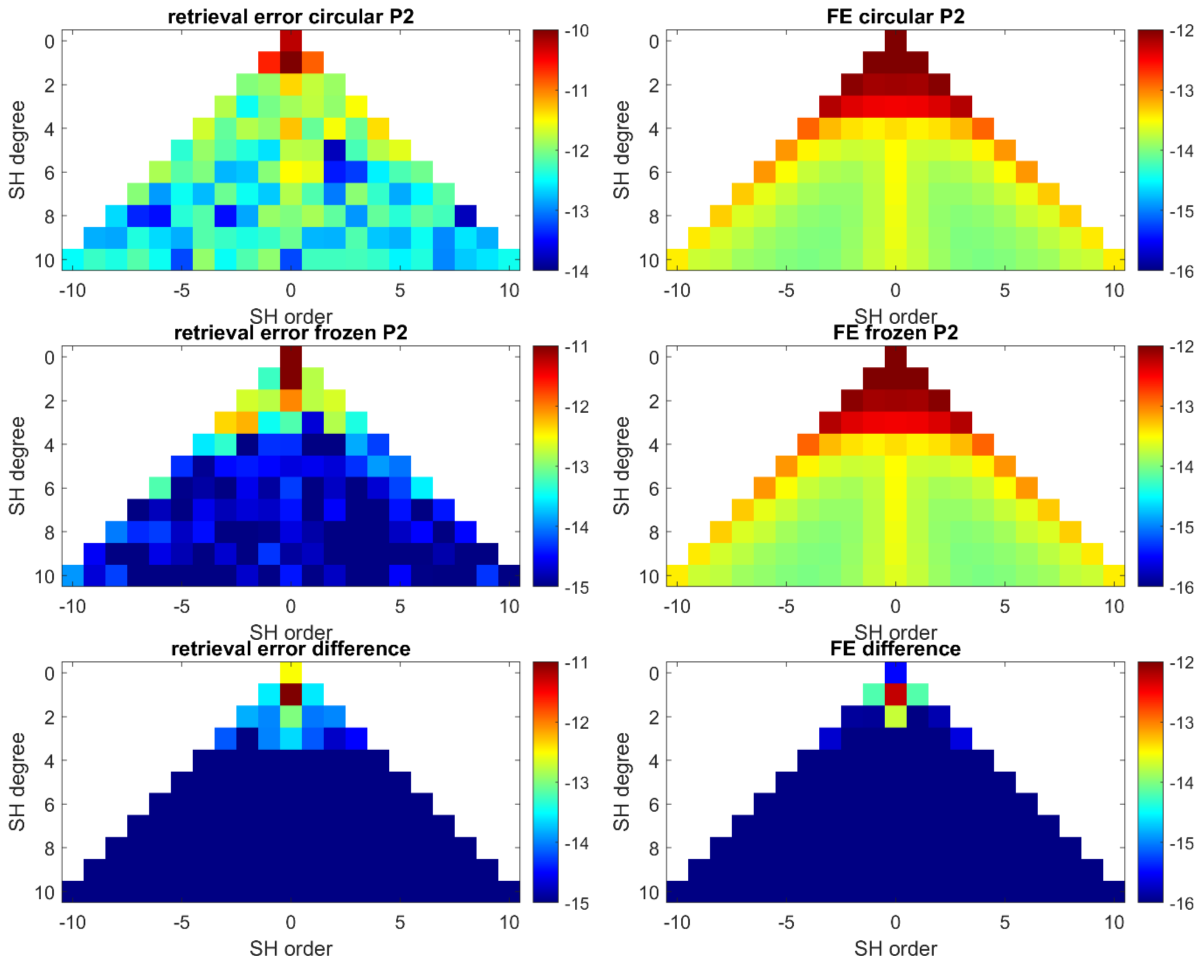

Figure 41-4: retrieval error of the 5-day double-pair-based IO gravity solutions (left) and the corresponding formal errors (right) zoomed to the low-degree spectrum. The bottom row shows the difference between coefficients and formal errors, respectively.

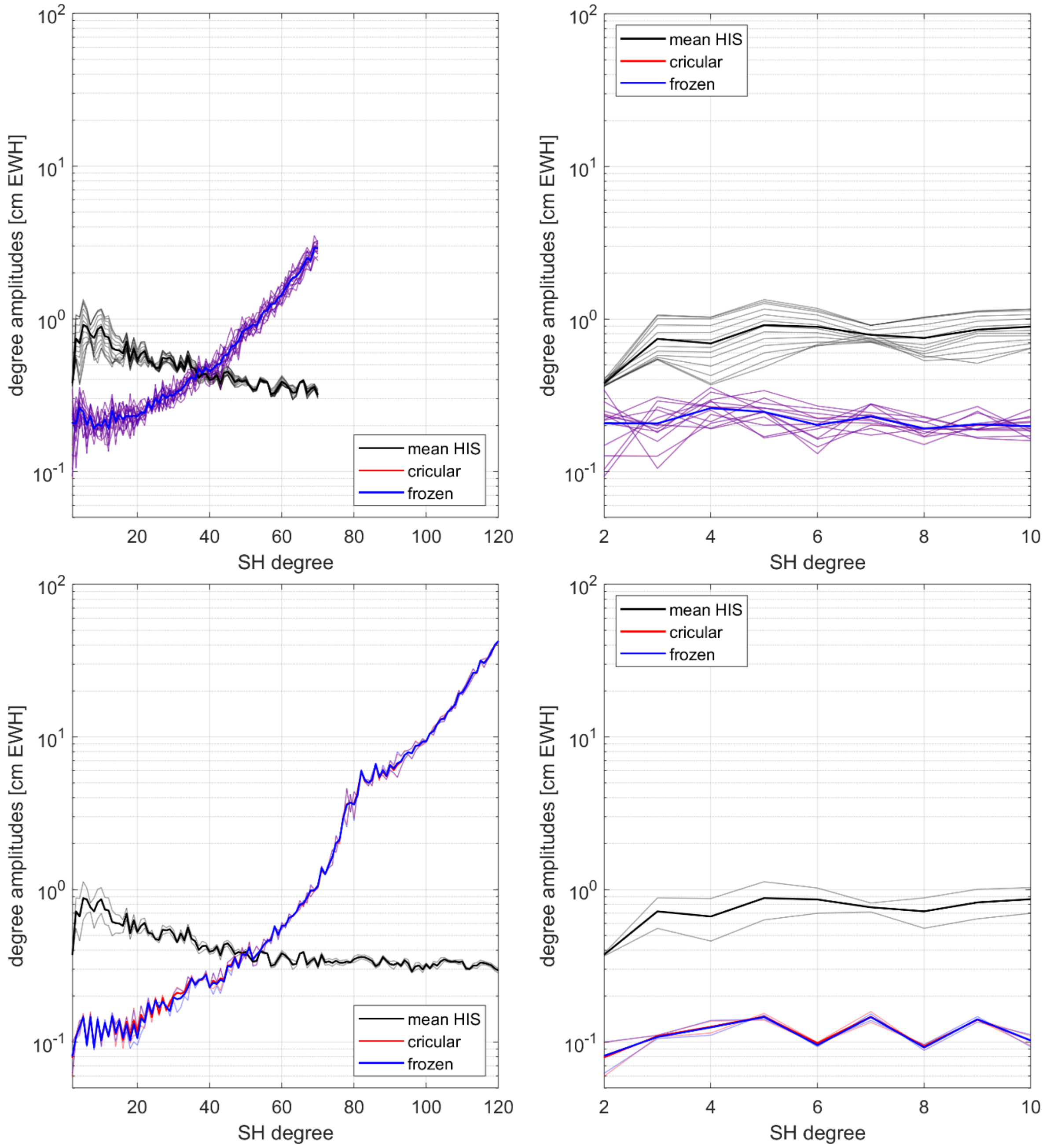

Figure 41-5: retrieval error of the 5- (top) and 31-day (bottom) P2-only-based FN gravity solutions. The low-degree spectrum of the left-hand side plots is shown in more detail on the right.

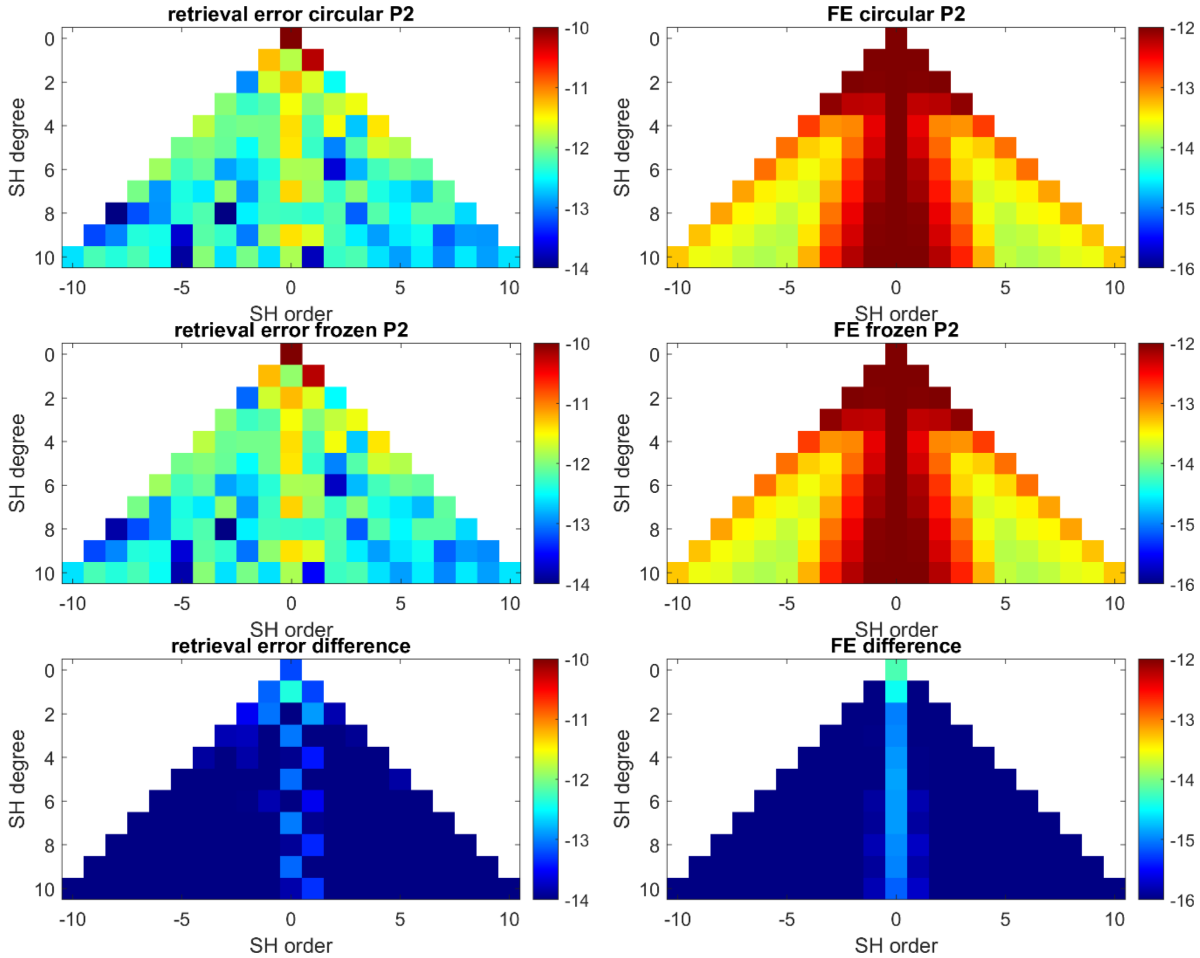

Figure 41-6: retrieval error of the 5-day P2-only-based FN gravity solutions (left) and the corresponding formal errors (right) zoomed to the low-degree spectrum. The bottom row shows the difference between coefficients and formal errors, respectively.

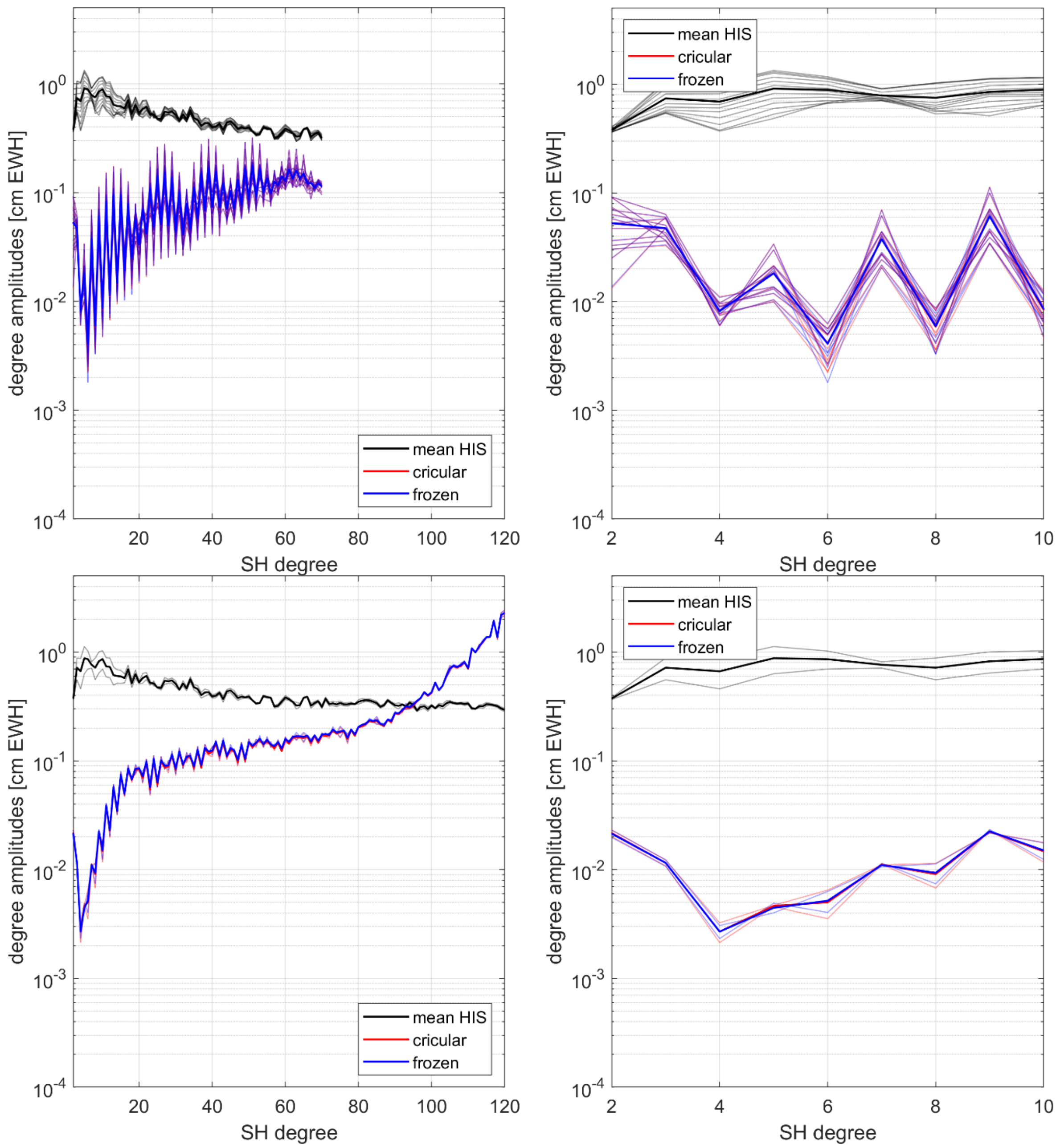

Figure 41-7: retrieval error of the 5- (top) and 31-day (bottom) P2-only-based IO gravity solutions. The low-degree spectrum of the left-hand side plots is shown in more detail on the right.

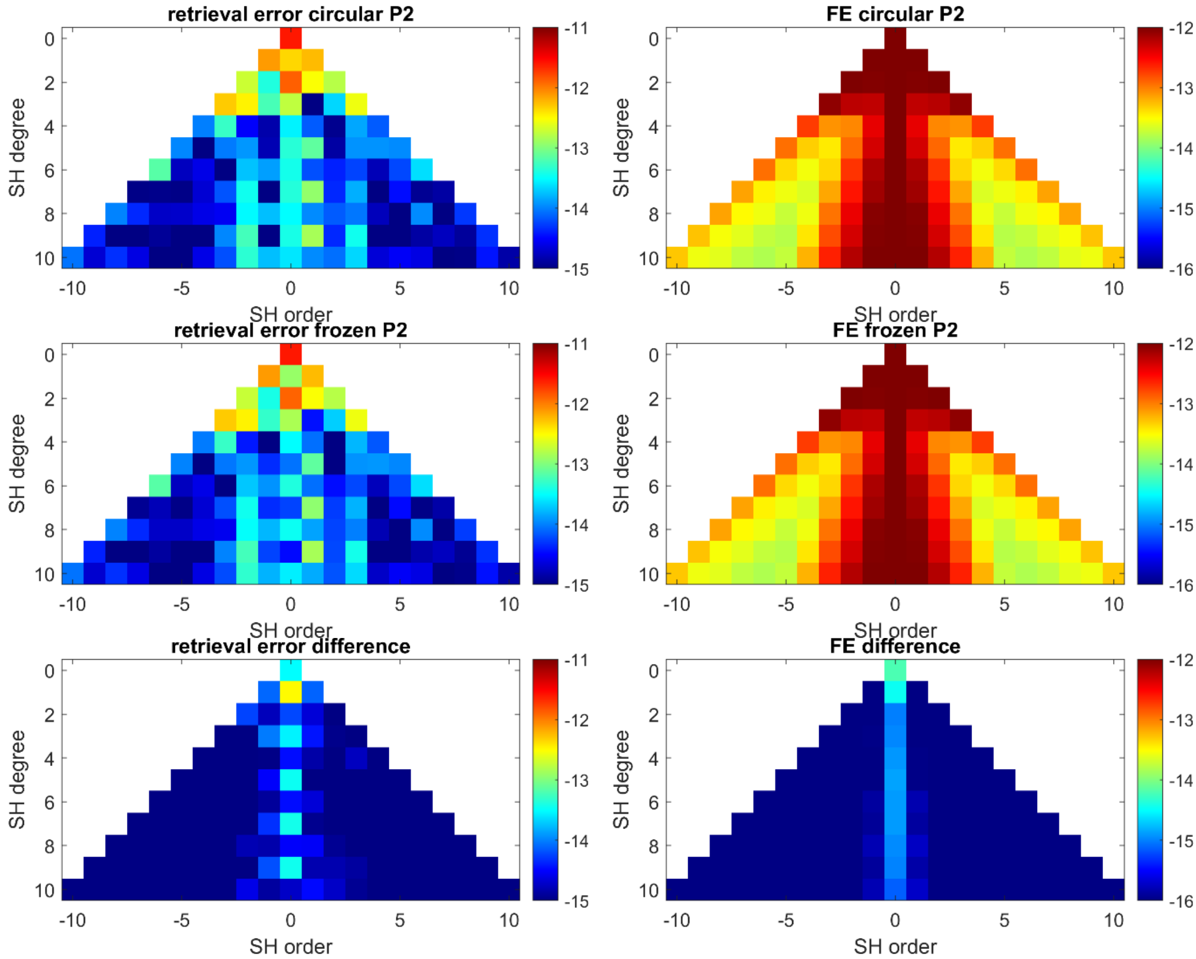

Figure 41-8: retrieval error of the 5-day P2-only-based IO gravity solutions (left) and the corresponding formal errors (right) zoomed to the low-degree spectrum. The bottom row shows the difference between coefficients and formal errors, respectively.

41.3. ERROR PROPAGATION INTO THE SPATIAL DOMAIN

For the sake of completeness, we rigorously propagate the co-variance matrix $\Sigma_{\hat{x}\hat{x}}$ of the estimated coefficients onto a regular global 1°x1° grid, since the varying altitudes of the frozen orbit should have been mapped into it. For this, we generate a design matrix A containing the functionals of a synthesis which yields dimensionless grid values according to

$$Y(\theta,\lambda) = \sum_{n=0}^{n_{max}} \sum_{m=0}^{n} P_{nm}(\cos\theta)(C_{nm}\cos m\lambda + +S_{nm}\sin m\lambda) \qquad [1]$$

with n_{max} set to 70.
Consequently, the resulting co-variance matrix of the grid values reads

$$\Sigma_{grid} = A\Sigma_{\hat{x}\hat{x}}A^T. \qquad [2]$$

The standard deviations of the grid values, i.e. the square root of the diagonal of Σ_{grid} is then plotted onto the grid. Figure 41-9 shows such standard deviations for the 5-day product-noise-only retrieval scenarios based on a double-pair and P2-only in an exemplary manner. Other scenarios are not explicitly shown in this document, since they feature an identical relative behaviour. It can be seen that the propagation of the coefficients' co-variances primarily yields a C20-type pattern with larger values close to the equators and smaller ones towards the poles. The underlying reason is the varying observation spacing – since ground tracks are sparser at the equator and converge towards the poles, more observations per areal element are present at higher latitudes, thereby formally enhancing the performance there. A C10-type pattern similar to the altitude distribution of the frozen orbit (c.f. Figure 39-1) cannot be discerned here. It is only revealed once the difference between the grid values obtained on the basis of the frozen and circular orbit is taken. It can thus be concluded that while the orbital altitude is indeed mapped into the co-variances of the estimated coefficients, the effect is entirely superimposed by the contributions of the ground track density, and is therefore negligible.

42. CONCLUSIONS

Overall, the choice of a frozen orbit for P2 features no notable drawbacks or advantages over a respective circular orbit in terms of gravity field retrieval – the performance remains practically unchanged. This holds for both a Bender-type-based as well as for a P2-only-based retrieval scenario. Some differences can be found in the low zonals (up to d/o 3), though they are very small in terms of amplitudes. The effect of the orbital altitude fluctuations is further present in the co-variances of the retrieved gravity field, but is entirely superimposed by the impact of ground track density.

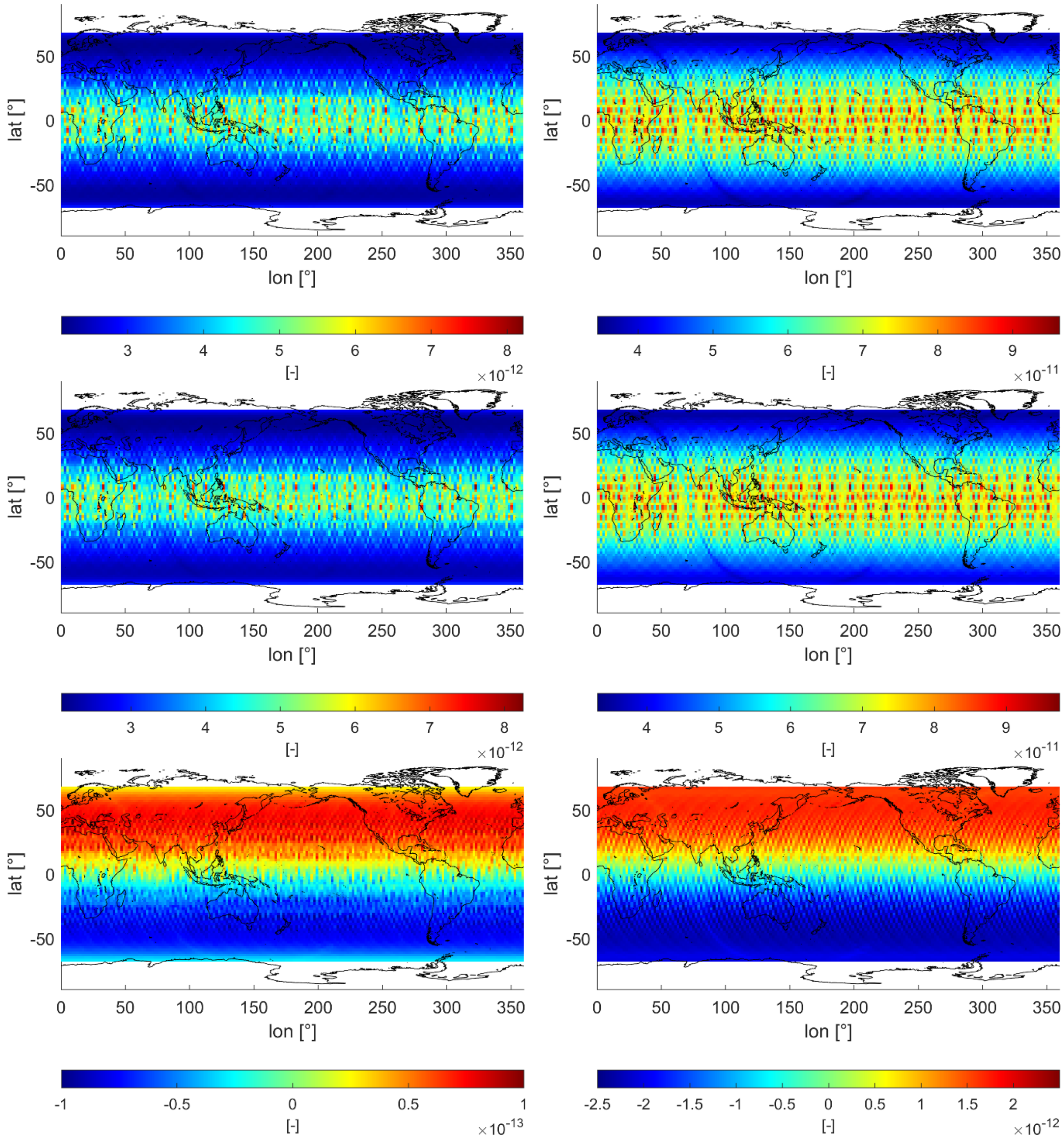

Figure 41-9: co-variances for d/o 1 to 70 of the retrieved 5-day double-pair- (left) and P2-only-based (right) full-noise gravity solutions propagated onto a regular global grid. Polar regions (over |φ|=70°) have been removed to highlight the effect of the P2 orbit. Top – circular P2 orbit as basis, center – frozen P2 orbit as basis, bottom – differences between the above two.

PART 10:

CONCLUSIONS CCN1

- The **performance** of the MAGIC constellation is mainly **driven by** the **inclined pair** (NGGM) in the region |φ|<70°.
- Several **methodological improvements** were investigated, e.g.,
  - Stochastic modelling of AO background model errors. It shows promising results for static AO VCM, but does not work for time-variable VCM yet.
  - Extended parameterization schemes such as DMD approach show advantages over "Wiese" co-parameterization; also multi-step DMD shows promising results.
  - Correlations and couplings among extended parameterization and stochastic modelling schemes are still to be investigated and assessed.
- **NGGM** (P2-only) and **MAGIC** (P1+P2) simulation results (with conservative assumptions regarding background model errors) can **largely meet NGGM/MAGIC MRD threshold requirements** both, for monthly and short-term solutions, with the exception of the very low degrees.
- A **third numerical simulator** was developed at **CNES**. It achieves promising results, but does not yet reach the same degree of maturity as TUM and GFZ simulators.
- The **scientific benefit of NGGM/MAGIC** could be demonstrated in simulation for:
  - Continental hydrology, especially detection of wet and dry extremes
  - Larger glacier systems
  - Resolving AMOC and potential anthropogenic influence
  - Detectability of co-seismic and post-seismic earthquake signals
- A **novel processing chain L0 to L1b for LRI/LRT observations**, which is independent of existing Level-1a to Level-1b processing chain, was **set up** and successfully tested.
- High-accuracy bias estimates were achieved by **GNSS-based accelerometer calibration**. The estimation of scale factors mainly depends on the magnitude of residual non-conservative accelerations. Adding LRI information to the calibration procedure does not improve the results.
- An initial version of the Algorithm Theoretical Basis Document (**ATBD**) was generated.
- In the frame of a Science Readiness Assessment (SRA), the Science Readiness Level **SRL 5** was **evaluated** for the numerical simulators of TUM and GFZ.